PATTERNS IN ONTOGENY OF HUMAN TRABECULAR BONE FROM SUNWATCH VILLAGE IN THE PREHISTORIC OHIO VALLEY

DISSERTATION

Presented in Partial Fulfillment of the Requirements for

The Degree Doctor of Philosophy in the Graduate

School of The Ohio State University

By

James Howard Gosman, B.A., M.A., M.D.

* * * * *

The Ohio State University
2007

Dissertation Committee:

Professor Clark Spencer Larsen, Advisor

Professor Robert A. Cook

Professor Douglas E. Crews

Professor Christopher B. Ruff

Professor Paul Sciulli

Professor Samuel Stout

Approved by

_____

Advisor
Anthropology Graduate Program

ABSTRACT

The goal of this research was to study trabecular bone microarchitecture during growth and development, producing new quantitative and structural knowledge about the development and remodeling of normal trabecular structure as demonstrated in a subadult archaeological skeletal sample from the Late Prehistoric Ohio Valley. Trabecular bone microarchitecture has a predictable relationship to functional and external loading patterns applied throughout ontogeny and maturity. Relatively little research has been directed toward the structure of and variation in trabecular bone during ontogeny, creating a deficiency in the foundation upon which trabecular bone adaptation can be used for bioarchaeological inferences. This research project tests hypotheses characterizing the temporal sequence and variation in trabecular bone volume fraction and degree of anisotropy as a reflection of growth and development, as associated with the timing and acquisition of normal functional activities (initial and maturation of bipedal gait), and as associated with changing body mass.

A selected skeletal sample from the Late Prehistoric site (A.D. 1200-1300) of SunWatch Village consisted of 37 subadult and three young adult proximal tibiae. The sample as a whole, as well as four maturity stage-related groups, was analyzed.

The analyses consisted of nondestructive microCT scanning of the proximal metaphyseal tibia visually demonstrating the microarchitectural trabecular structure, and quantitative 3-D structural analyses measuring bone volume fraction, degree of anisotropy, trabecular thickness, and trabecular number. Bone volume fraction and degree of anisotropy are highest at birth, decreasing to a low value at one year of age, and then gradually increasing to the adult range around six to eight years of age. Trabecular number is highest at birth and lowest at skeletal maturity; trabecular thickness is lowest at birth and highest at skeletal maturity. The results of this study provide quantitative morphological and scan-image data on the ontogenetic patterned changes in human trabecular bone structure from birth to skeletal maturity, highlighting the dynamic sequential relationships between growth/development, general functional activities, and trabecular distribution/architecture.

Trabecular bone analysis is situated within the broad framework of research in musculoskeletal biology with society-wide implications in the areas of skeletal adaptation in varying genetic and environmental settings, serious public health conditions (osteoarthritis and osteoporosis), and skeletal regenerative and implant investigations. This study enhances the infrastructure of research by incorporating recent technological and methodological advances, fostering a multidisciplinary approach towards understanding skeletal biology, and augmenting relevance to biocultural studies of ancient and recent populations.

ACKNOWLEDGMENTS

This dissertation is the culmination of guidance, encouragement, discussions, and support from many individuals. Special thanks go to my advisor Clark Spencer Larsen who guided, with a steady hand, the transformation of this seasoned clinical physician into a neophyte physical anthropologist. His focused mentoring and example of academic excellence has made this new chapter in my life-journey exciting and productive. Each individual on my dissertation committee receives my most sincere gratitude for their roles in my initiation into the discipline of Anthropology and their ongoing enthusiasm and guidance in this dissertation research: Drs. Robert Cook, Douglas Crews, Christopher Ruff, Paul Sciulli, and Samuel Stout.

The anthropologists from the Dayton Society of Natural History (DSNH) at the Boonshoft Museum of Discovery were incredibly generous in lending their time and knowledge to this project. Lynn Simonelli (DSNH Curator of Anthropology), William Kennedy (DSNH Assistant Curator of Anthropology), and Andy Sawyer (DSNH/SunWatch Site Anthropologist/Manager) all gave invaluable assistance in assembling the SunWatch juvenile skeletal sample, making available key data and resources, and providing continuous encouragement and interest.

The University of Texas High Resolution X-ray Computed Tomography research scientists and lab personnel played a key role in this project. It is their infrastructure, experience, and willingness to share their know-how, which made this project of the visualization and quantification of human trabecular architecture during growth and development possible. I particularly wish to thank Dr. Richard Ketcham for his interest in taking this project on and his guidance in all phases of the scanning and analysis procedures. In addition, Dr. Matthew Colbert, Phillip Watson, Alison Mote, and Ashley Gosselin-Idari all made significant contributions.

Lisa Nichols, research librarian at the St. Vincent Mercy Medical Center Health Science Library, has given me exceptional support throughout this research. Her unfailing attention and uncanny ability to produce the most obscure research publications are most gratefully acknowledged. Dr. Hyagriv Simhan, my son-in-law, deserves singular thanks for his unflinching patience in helping this researcher develop statistical procedures for this project. Brian Begg has my gratitude for his assistance in the details of the bibliography and tables.

My office staff at Independent Evaluators, Inc. has contributed mightily to the completion of this dissertation. My special thanks to Dawn Schmidt for her assistance and creative problem solving.

This late-in-life redirection of my professional journey would not have been possible without the unfailing support of my wife, life-partner, and best friend- Mary Ellen Gosman- and the extended Gosman family: Dr. Gabriella Gosman and family, Dr. Amanda Gosman, and Nathaniel Gosman and family.

I would like to acknowledge financial support of this dissertation research by National Science Foundation Dissertation Improvement Grant # 0650727 to Dr. Clark S. Larsen and Dr. James H. Gosman and National Science Foundation grant EAR-0345710 to UTCT.

VITA

October 27, 1944……Born – Toledo, Ohio

1966……B.A. History, University of Michigan

1970……M.D., University of Michigan

1975……Completion Residency in Orthopedic Surgery

1975 – 2002……Attending Orthopedic Surgeon and Clinical Professor of Orthopedic Surgery, St. Vincent Mercy Medical Center and Medical College of Ohio, Toledo, Ohio

2002 – present……..Consulting Orthopedic Surgeon, Toledo, Ohio

2002……..M.A. Archaeology and Heritage, University of Leicester, UK

PUBLICATIONS

Research Publication

1. Gosman JH, and Crews DE. 2007. From Evolution to Osteoarthritis: Examining Injury-Related OA of the Human Knee Joint as an Evolutionary Cost of Bipedalism. American Journal of Human Biology *19:* 257.

2. Gosman J. 2006. Patterns in Ontogeny from SunWatch, a Late Prehistoric Ohio Valley Village. Current Research in Ohio Archaeology 2006*,* http://www.ohioarchaeology.org/joomla/index.

3. Gosman JH, and Koslowski T. 2006. Scoliosis: Taphonomy or Pathology. Paleopathology Newsletter Supplement. March 2006: 15.

4. Gosman JH. 2005. Most Falls Occur at Home: A Bio-Architectural Study. Paleopathology Newsletter Supplement. April 2005: 4.

FIELDS OF STUDY

Major Field: Anthropology

Research Interests: Skeletal Biology; Bioarchaeology; Postcranial Bone Functional Adaptation; MicroCT and Quantitative Skeletal Analysis

TABLE OF CONTENTS

LIST OF TABLES

LIST OF FIGURES

LIST OF ABBREVIATIONS

Full Name	Abbreviation
Bone Volume Fraction	BV/TV
Degree of Anisotropy	DA
Star Volume Distribution	SVD
Volume of Interest	VOI
Trabecular Thickness	Tr,Th
Mean Trabecular Thickness	Tr.Th.Mn
Maximum Trabecular Thickness	Tr,Th.Mx
Trabecular Number	Tr.N
Mean Intercept Length	MIL
Medial	M
Lateral	L
Anterior	A
Posterior	P
Femoral Bicondylar Angle	FBA
Field of Reconstruction	FOR
Hypertrophic Chondrocyte	HC

CHAPTER 1

GENERAL CONSIDERATIONS FOR TRABECULAR BONE RESEARCH

INTRODUCTION

Research focused on the morphology and structure of human long bone joints and diaphyses has demonstrated the relationships among morphology, lifestyle, and loads engendered during physical activity (Bridges et al., 2000; Larsen, 1997; Ruff, 2000). Trabecular bone density and microarchitecture is likewise influenced by mechanical forces during growth and development resulting in the adult configuration, through the process of bone functional adaptation (Huiskes et al., 2000; Ryan and Kravitz, 2005; Carter and Beaupre, 2001; Martin et al., 1998). Relatively little work has been directed toward the structure of or the variation in trabecular bone during ontogeny (Ryan and Krovitz, 2006; Ryan et al., 2007; Tanck et al., 2001), creating a deficiency in the foundation upon which trabecular bone adaptation can be used for bioarchaeological inferences. Garn (1980) has asserted the William Wordsworth quote, "the child is the father of the man;" trabecular bone may represent a stepchild in this particular case. In the strict sense, the term cancellous

bone is used for the complex three-dimensional structure composed of multiple trabeculae; the term trabecular bone is used for the bone of discrete trabeculae (Parfitt et al., 1987; Odgaard, 1997). However, for the purposes of this dissertation the meaning of these two terms is considered to be identical and terms are used interchangeably.

Appreciation of differences in growth patterns among populations as well as growth pattern as basic human ontogenetic process will lead to better understanding of adult morphological variation and inform on the underlying biological, environmental, and sociocultural conditions that produce this variation (Larsen, 1997). The goal of this study is to develop and interpret new quantitative knowledge about the development and remodeling of normal human trabecular structure during ontogeny. This is demonstrated via the analysis of a subadult archaeological skeletal sample from SunWatch Village, a Late Prehistoric Ohio River Valley site. The methods specifically engage the advanced technologies of microCT imaging and three-dimensional quantitative computational analysis.

Age effects on bone structural adaptation are important considerations for accurate behavioral interpretations. There is age-specificity in bone response to mechanical loading, both qualitative and quantitative (Bertram and Swartz, 1991; Ruff et al., 1994). Age-related research has been primarily focused on cortical bone size and strength. Increased mechanical loading stimulates subperiosteal bone apposition and endosteal resorption prior to mid-adolescence and relatively greater endosteal apposition thereafter (Ruff et al., 1994; Bass et al., 2002). The growth and development

period generates constant shape changes requiring a highly active and responsive modeling/remodeling process; a process which moderates substantially after skeletal maturity (Pearson and Lieberman, 2004).

Diaphyseal cross-sectional strength and cancellous microarchitecture are responsive to mechanical loads, while bone length and articular size are less so (Ruff, 2003; Lieberman et al., 2001). The relationship of articular structure and function has been studied by Rafferty and Ruff (1994) using nonhuman primates. These authors suggest that the internal trabecular mass and structure is independent of the external articular surface volume and area. Their findings indicate that trabecular mass (internal) corresponds to differences in mechanical loads borne by the joint and articular shape (external) corresponds to aspects of joint mobility.

Swartz et al. (1998) investigated the variation in trabecular architecture from the point of view of the size of the individual elements. That is, how does the size of the individual trabeculae scale with body size in mammals? The authors compared an empiric scaling analysis of trabecular dimensions in mammals ranging in mass from four to $40X10^6$ grams to two divergent models for pattern of trabecular size change associated with body size change. One model held the individual trabeculae uniform in size and shape over all joint/body sizes, with increases in trabecular volume occurring through the addition of new elements of the same size. The other model maintained constant trabecular geometry, with increases in trabecular volume occurring through an isometric increase in trabecular size. The results of this analysis suggested that trabecular size had little dependence on body size, thus favoring the constant trabecular

size model. It should be noted that this was an analysis of skeletally mature animals. The results do not exclude positive allometric scaling of trabecular size and body size during growth and development of any particular individual.

Swartz and co-authors (1998) make several additional observations on aspects of trabecular architecture: (1) trabecular architecture may be driven to some degree by the necessity of an adequate trabecular surface for calcium homeostasis, (2) trabecular architectural connectivity is qualitatively different for small *versus* large animals (small animals have few trabeculae, which connect primarily to cortical bone and larger animals have trabeculae, which connect primarily to other trabeculae), and (3) no systematic differences were found in trabecular size or scaling patterns related to locomotor form. The importance of these observations is the indication that the mechanical behavior of trabecular bone is not determined solely by the volume fraction. The trabecular architectural patterns, interconnections, and orientations affect trabecular bone mechanics and these patterns can change fundamentally with body size (Swartz et al., 1998).

The interaction of mechanical loading, growth and development, and skeletal responsiveness accounts for skeletal adaptation into early adulthood (Duppe et al., 1997; Turner and Robling, 2003). Following this period, the skeletal response is greatly reduced (Forwood and Burr, 1993). It does, however, continue over a longer time frame with the possibility of cumulative long-term effect (Ruff et al., 2006; Valdimarsson et al., 2005). Adult bone morphology represents a retention of those structural features established during ontogeny modified by biological factors and

functional adaptive changes (albeit markedly reduced) accumulated during maturity (positive or negative). Therefore, bioarchaeological behavioral interpretations in regard to subsistence strategy, mobility, gender roles, and technologies need to take into account the patterning of skeletal changes, especially during ontogeny (Ruff, 2005).

Trabecular bone is believed to be adapted to external loading conditions (Biewener et al., 1996; Huiskes et al., 2000; Ryan and Kravitz, 2005; Wolff, 1892), based on tissue strain (Rubin et al., 2002), and acting through a regulatory system with numerous feedback loops resulting in modeling/remodeling. This model requires "mechanosensors," which are proposed to be osteocytes (You et al., 2001). Bone has a customary equilibrium strain window, above which bone deposition occurs and below which resorption occurs (Frost, 1987). This adaptive strain level is highly context specific, varying with skeletal location (Bass et al., 1999; Lieberman et al., 2001), systemic factors of age, disease state, hormonal status, genetic background (Frost, 1987; Pearson and Lieberman, 2004), and loading characteristics, including type of strain, strain history, magnitude, frequency, and rate (Burr et al., 2002; van der Meulen et al., 1993; Carter and Beaupre, 2001, Huiskes et al., 2000). Bone functional adaptation for this investigation is considered to be biomechanically relevant regional variations and temporal changes in trabecular bone structural and material organization that are produced by modeling and remodeling processes during normal skeletal development, growth, and changing patterns of functional behavior. These processes are mediated by genetic, epigenetic, and extragenetic (i.e., microdamage) influences (Skedros et al., 2004).

MicroCT and High Resolution X-Ray Computed Tomography

MicroCT/HRXCT technology combined with 3D structural computational analyses can produce non-invasive, high-resolution 3D images (Muller et al., 1994; Ruegsegger et al., 1996). Measurements of cancellous bone architecture and material properties correlate with skeletal adaptation to daily internal and external loads (Ding et al., 2002). MicroCT is a particularly robust technology for cancellous bone analysis closely correlating with histomorphology and experimental structural analysis, allowing the accurate reconstruction of the complex latticework construction of trabecular bone (Fajardo et al., 2002; Muller and Ruegsegger, 1995; Uchiyama et al., 1999; Van Rietbergen et al., 1998). The scanner's spatial resolution can be much finer than the range of trabecular sizes and thicknesses, allowing accurate reconstruction and quantification of cancellous structures (Kothari et al., 1998). Serial scan data produces slice images of specified thickness and spacing, which can be converted into smaller elements for finite element method (FEM) modeling and in this investigation three-dimensional structural analysis (Ryan and van Reitbergen, 2005).

Structural data direct from microCT scanning permits the 3D computational quantitative analysis (Quant 3D) of primary microstructural properties of interest to this study, namely bone volume fraction and degree of anisotropy. The bone volume fraction (BV/TV) is the ratio of volumes: bone present to the total volume. This is a statement of how a certain volume of trabecular bone is distributed. In theory, its significance is based on Parfitt's plate model of cancellous bone (Parfitt et al., 1987),

which describes the distribution of trabecular plates and rods under varying conditions of mechanical load or disease. However, in practice BV/TV is directly measured from primary scan data without bias or prior model assumptions. The degree of anisotropy (DA) demonstrates the quantifiable directionality and orientation of trabeculae within the cancellous bone microstructure (Ketcham and Ryan, 2004). This is a fundamental property of bone: relating mechanics and architecture, the adaptive response of cancellous bone to load direction (Pontzer et al., 2006).The combination of bone volume fraction (BV/TV) and degree of anisotropy (DA) are the most effective predictors of the mechanical properties of cancellous bone (Ding et al., 2002; Jacobs et al., 1997).

These two parameters are the core data points for this study, to be used as key indicators of continuity and change in trabecular bone during ontogeny. Additional parameters include trabecular thickness (Tr.Th) and trabecular number (Tr.N), both of which have specific ontogenetic patterning as well. The objective of this research is to study the temporal sequence and variation in bone volume fraction, degree of anisotropy, trabecular thickness, and trabecular number as reflections of ontogeny and as associated with the timing and acquisition of normal functional activities (crawling, initial bipedal gait, and independent physical activities).

ONTOGENETIC STUDIES

Ontogenetic studies can address several important problem areas, including general health of a population, age-related behavioral changes, and the influence of lifestyle on growth and development. In the realm of bone functional adaptation, these analyses aim to define age changes that would be characteristic of individuals within a population. Several issues have been identified which may confound growth-related studies from archaeological samples (Saunders, 2000). These include questions of sampling, sex determination, and age estimation. Biological mortality bias in subadult skeletal series was examined in reference to long bone lengths by Saunders and Hoppa (1993). Their findings suggested that, although present, the effect of mortality bias is minimal and overshadowed by other methodological concerns. Ontogenetic studies using skeletal series are, by necessity, cross-sectional samplings of different age groups as opposed to longitudinal tracking of single individuals. The assumption is that this cross-sectional sample represents an accurate description of growth.

Trabecular skeletal adaptation is responsive to typical external loads of daily living in both density and architecture. During growth, load (body mass and muscle strength) increases gradually, which implies that density and architecture would change as well (Tanck et al., 2001). The increase in density due to increasing loading would involve primarily bone formation; architectural adaptation must involve both formation and resorption. Computer simulation of trabecular adaptation (Huiskes et al., 2000) found that trabecular thickness (density) due to increased loading would occur much

faster than trabecular reorientation due to changes in loading direction. At the present time, limited quantitative morphological data are available on the development of architecture and structural adaptation in juvenile human trabecular bone. This study aims to ameliorate this situation and lay the groundwork for future research in trabecular bone adaptation from the anthropological perspective.

Archaeological and modern human trabecular ontogenetic studies

A selective review of previous ontogenetic trabecular bone research indicates that human studies have been primarily qualitative until very recently. Kneissel et al. (1997) studied cancellous bone structure in both the growing and aging lumbar spine in a Medieval Nubian population, finding that cancellous bone structure in children consisted of a densely packed uniform network of small rod-like trabeculae. Adolescence was the stage of greatest bone volume with more small plate-like trabeculae. The adult configuration was large plate-like trabeculae in the central zone and smaller trabeculae in the superior and inferior zones. Mielke et al. (1972) published the analysis of a skeletal sample from Sudanese Nubian cemeteries (350 BC - AD 1400) studying the rate of development and age-related changes in the internal structure of the femur. They demonstrated that the density of the femoral head trabecular bone decreases with age in both sexes, while the average thickness of femoral head trabeculae decreases with age in males and increases with age in females. Atkinson (1967) described changes in vertebral cancellous bone in the age range of 5-

90 years, suggesting that children have the highest numerical density of trabeculae. There is a predominant loss of horizontal trabecular throughout life. Korstjens et al. (1995) investigated the radiographic trabecular pattern in the distal radius of Netherlander children (age 4-14 years) from the Nijmegan Growth Study. Their findings noted a gradual loss of primary trabeculae, thickening of the rest, and an increase in the degree of anisotropy just proximal to the epiphyseal plate during the period of growth.

Animal trabecular ontogenetic studies

Investigation of the architectural properties of trabecular bone using direct three-dimensional methods is relatively recent and is in the process of refinement (Fajardo et al., 2002). Quantitative three-dimensional variations in the architectural and mechanical characteristics of trabecular bone during skeletal growth were largely unknown and unstudied until the end of the last decade. Nafei et al. (2000a, 2000b) undertook an ontogenetic animal model study using lambs in three age groups and sheep in two age groups with the purpose to investigate the relationship between age, architectural, and mechanical properties of trabecular bone. The process of growth and development of trabecular bone as observed by these researchers indicates that in order to withstand the increasing demands on the bone tissue of an organism more bone tissue forms. This results in an increased bone volume fraction, changes in the trabecular number and morphology, and changes in the trabecular orientation in space (Nafei et al., 2000a, b). Tanck et al. (2001), continuing on the theme of developmental

architecture and mechanical adaptation in juvenile trabecular bone, studied the hypothesis that a time lag occurs between the adaptation of trabecular density and the adaptation of trabecular architecture (based on computer simulations of bone-cell-based modeling and remodeling) (Huiskes et al., 2000). Three-dimensional morphological and mechanical parameters were studied from the vertebrae and proximal tibiae of immature pigs, using microCT and finite element analysis. The findings indicated that bone volume and stiffness increased rapidly in the initial growth phase. Morphological anisotropy started later and was still progressing at the time of peak bone mass. The implications are that bone density is adapted from the early phase of growth (body mass), whereas trabecular architecture is adapted later in development, during which mechanical adaptation produces a more efficient architecture. Pontzer et al. (2006) report an experimental test of Wolff's law in an ontogenetic study of mechanical loading and trabecular orientation in juvenile guinea fowl. This study of different knee flexion angles in birds running on a treadmill supported the prediction that the orientation of "trabecular bone adapts dynamically to the orientation of peak compressive forces" (2006, p. 57). A question of interest to this research is, "does the ontogenetic patterning for human trabecular bone parallel these particular models?"

MICROCT RESEARCH IN ANTHROPOLOGY

Nonhuman primate studies

MicroCT was introduced to the field of skeletal biology in the late 1980s by Layton et al. (1988) and Feldkamp et al. (1989), applying it primarily to the study of osteoarthritis and osteoporosis. The use of microCT in anthropological studies was initially limited to primate inner ear morphology (Spoor et al., 1994). The first published preliminary analysis of examining the potential of microCT for functional studies of nonhuman primate trabecular architecture was conducted by Fajardo and Muller (2001). These researchers used microCT and microCT-based morphometric methods to compare the microarchitectural features of trabecular bone among four anthropoid species that vary in behavior from suspensory-climbing to quadrupedal locomotion. The expectation was that trabecular trajectories and degree of trabecular bone anisotropy are correlated with the bone's loading regime. The results of this and other nonhuman primate studies (MacLatchy and Muller, 2002; Rafferty and Ruff, 1994; Ryan and Ketcham, 2002a, b; Ryan and van Rietbergen, 2005) have demonstrated the potential usefulness of microCT in examining the relationship between loading regimes, locomotion behavior, and trabecular architectural orientation. Fajardo and Muller also addressed important methodological issues of microCT imaging such as trabecular bone heterogeneity and the importance of location and scaling of the volumes of interest (VOI) in order to identify anatomically and biomechanically homologous VOIs. Bone density (BV/TV) and anisotropy combined

accounted for over 92% of the variance in yield strength and 70-82% of the variance in stiffness (Young's modulus).

Human Studies

Very recently, microCT data on human trabecular structural changes during growth and development as well as adult morphology have been published (Ryan and Krovitz, 2005, 2006; Ryan et al., 2007; Richmond et al., 2004). Richmond et al. (2004) studied the differences in trabecular bone structure in adult human and chimpanzee knee joints using HRXCT imaging and 3D structural computations. The focus of this research was on the effect of the differing degree of knee flexion during locomotion. Under normal circumstances, chimpanzees "walk" on a flexed knee, whereas humans extend the knee fully in the stance phase of gait. Human trabecular bone patterns have increased bone volume in the medial femoral condyle and exhibit a stronger orientation perpendicular to the articular surface. These changes are consistent with greater habitual loads (relative to body mass) and to the different joint posture (more extended knee) in human bipedal gait.

Ryan and Krovitz (2005, 2006) have recently presented microCT studies on human growth and development of trabecular bone in the proximal femur. The purpose of these HRXCT/Quant 3D studies was to quantify changes of trabecular bone in relation to changing functional and external loading patterns with age. Clear differences in bone structure were noted between younger and older individuals.

Bone volume fraction and degree of anisotropy decreased between the ages of 6 and 12 months. This then reverses, and by age 2-3 years the bone volume, thickness, and anisotropy increased slightly. Regions in the femoral neck became more anisotropic corresponding to cortical thickening of the inferior femoral neck. These changes in the proximal femur are consistent with the shift in external loading associated with the initiation of unassisted walking in infants around one year of age. The ontogenetic development of trabecular bone in the proximal tibia, the objective of the present study, provides an additional locomotor signal for assessing human behavior and physical activity during childhood.

TIBIAL STUDIES: GENERAL AND AUXOLOGICAL

"Anatomy is a process, not a state" (Count, 1943, p.1).

The tibia has a distinguished history in skeletal research. This section provides a chronological sampling of general studies focusing on tibial growth and development. It is a frame of reference and is not meant to be exhaustive. Its purpose is to highlight the broader context into which this research on the patterning of trabecular bone development is positioned, within the overall model of human skeletal growth. A brief digression into explanatory definitions is in order. Puberty is the developmental time of greatest sex differentiation since early intrauterine months, characterized by changes throughout the body in size, shape, composition, and physiology. The word puberty refers to the period of sudden enlargement of reproductive organs (Tanner, 1990). The word adolescence is increasingly used to

refer to the psychological and behavioral changes occurring around this time. However, the phrase "adolescent growth spurt" has been (and continues) to be prevalent in the literature of human growth. For the purposes of this dissertation "puberty" and "adolescence" will be used interchangeably (Tanner, 1990).

Beginning with the end product, the adult tibia, Hrdlička (1896) published "Study of the Normal Tibia" based on the examination of nearly 2000 normal adult bones of persons of mixed ethnicity and sexes in the collection of the New York College of Physicians and Surgeons. Hrdlička was impressed by the marked variability in shape, stating: "The bone is hardly ever alike in two skeletons…" (Hrdlička, 1896, p.307). While variations in the shape of sections of the tibial shaft were frequent, differences in the epiphyseal/metaphyseal articular regions were relatively less so. These observations foreshadow later research documenting adaptive plasticity of the long bone diaphyses and relative stability of external joint shape (Ruff, 2000; Rafferty and Ruff, 1994).

Francis's "Growth of the Human Tibia" (1939) is stated to be the first published longitudinal study of tibial growth. This research was part of a larger human growth and development study carried out by the Brush and Associated Foundations at Western Reserve University. The left tibia was measured by both standard anthropometric techniques and roentgenographic measurements. The cohort was white children, free of any serious illness or any gross mental or physical defect. Measurements were taken from 3 months to 13 years. The general pattern

demonstrated a typical “growth pattern”: high growth rate up to 3 years (although reduced relative to the growth rate at birth), linear growth rate 3-10 years, and increased growth rate 10-13 years. Sex differences were noted with females entering the pubertal growth spurt earlier.

Count (1943) fitted mathematical exponential equations to describe the human growth curves based on the quantitative relationship between dimensions of the body expressed as ratios (indices). These formulae allow the derivation of growth velocities, which is equivalent to the value of growth-in-time. Stature becomes an event. Count notes that based on the parametric indices studied, growth accelerations occur at about the ages of first and second permanent molar completion. Growth ceases in the third molar period. He argues that the accelerations are a time-phenomenon, speeding up the process of growth. They do not necessarily alter the growth pattern of bodily proportions. The value of these concepts is their usefulness in comparative growth studies expressed on a graph of a set of measurements over a time continuum [represented by the graphic displays in the Results section of this dissertation].

The Child Research Council carried out a longitudinal study of physical growth known as the Denver Growth Study from 1927 to 1967 (McCammon, 1970). Subjects in this study were mostly of northern European ancestry, middle and upper socioeconomic class, and lived in the Denver area. Long bone data were, in part, based on standardized radiographs taken at two to six month intervals from six

months of age through late adolescence (Ruff, 2007). This project resulted in reports on the growth of major long bones of the extremities in health children including the tibia (Maresh 1955). Maresh describes long-bone growth in children as "both complex and orderly" (1955, p.742).

The results from the Denver growth Study suggest that the infancy period is characterized by marked variability in linear growth rates and patterns, within and between individuals (as great as 50 percentiles) (Maresh, 1955). This is considered to represent a shift in adaptation from the maternal environment to an adaptation to the complex postnatal factors influencing growth (Bogin, 1999a, b). The childhood pattern (from three years of age to the prepubescent years) was found to be relatively stable and orderly. The adolescent years are a return to variability: variability in onset, magnitude, and duration of the adolescent growth spurt. The three age periods (infancy, childhood, and adolescence) describing the linear growth processes will be shown by this dissertation research to have relevance in describing the trabecular microarchitectural growth processes as well.

Partially longitudinal analyses of normal tibial growth at and after various ages were published by Anderson, Green, and Messner (1963). The purpose of this clinical work was to assess the progress of abnormalities of growth and to serve as a guide in estimating the timing for surgical invention for correction of leg length discrepancy (epiphyseal arrest). The comparison of the extent of variation in amount of growth measured according to chronological ages with that according to skeletal

ages in the same children is instructive. The wide range in growth values observed in children after a given age may be effectively reduced when growth is related to common levels of maturity rather than to chronological ages (Anderson et al., 1963). Observed variation was found to be as much as 60% less when using biological rather than chronological ages. These data are important and relevant to this dissertation project in support of the ordering of the tibial samples according to developmental maturation characteristics rather than specified chronological age estimation. This technique (seriation), a significant asset to this research, will be discussed in detail in a later section of this chapter.

Gindhart's (1973) study presented mixed longitudinal data on the tibiae and radii of several hundred normal North American white children to provide a source for standards of long bone length and incremental growth in children. The study used radiographs from the Fels Research Institute for the Study of Human Development longitudinal program. The results were concordant with other major studies (Francis, 1939; Maresh, 1955; Anderson et al., 1963). Findings relevant to this research include: "only at ages 6 and 12 months are there statistically significant differences between sexes until the age of thirteen years and older; the male tibia is longer in all these cases" (Gindhart, 1973, p.43). This provides support for combining sexes, at least up to ages greater than 13 years, for the generation of quantitative skeletal growth data. After age 13, tibial growth demonstrates relatively increased variability due, in part, to adaptive changes, catch up growth (or lack of), and sex-specific

adolescent growth patterns. These factors may constrain the quality of the quantitative data in the older nonadult group.

Recent re-working of the Denver Child Research Council data has focused on the sequential development of limb components and variation in this growth process from childhood through adolescence (Smith and Buschang, 2004, 2005). These radiographic studies confirmed earlier studies demonstrating, that at age ten, long bone lengths for girls and boys are similar; by age 16, the leg bones in boys are longer. Girls consistently demonstrated higher variation in long bone length and growth velocity. The tibia proved to have the most variable relative growth velocity (relative to its mean growth velocity) of the four major long bones at age 13 years, especially in girls (3.4-3.7x). On a theoretical note, West- Eberhard (2003) suggests that the modular organization of growth allows the timing relationships of various components to change in response to various environmental conditions (i.e. nutrition, infection, and physical activity) in order to reduce the risk to the normal development of vital structures. Hallgrimson et al. (2002) predicted that because distal segments (e.g. tibiae) are formed later, they are affected by more, earlier events, and thus may have greater variation. Empirical data and theoretical mechanism combine to indicate greater environmental and developmental plasticity of the tibia relative to the other long bones (humerus, radius, and femur) (also see Holliday and Ruff, 2001). On a practical note, these observations suggest that tibial trabecular bone quantitative growth data may become increasingly variable and noisy from ~age 13 years and older.

The studies discussed above are longitudinal surveys of modern healthy subjects designed to establish standards for assessing the growth status of the individual child and to explore variation in the growth process. This research has lead to an understanding of the roles that heredity and environment play in regulating growth and development and the extent that these forces play in the morphological variation of human groups living in diverse circumstances (Eveleth and Tanner, 1990). The summary position is that growth processes demonstrate remarkable biological plasticity in adaptations to environmental conditions.

Mensforth's article (1985), "Relative Tibia Long Bone Growth in the Libben and Bt-5 Prehistoric Populations," addresses the hypothesis that "modification in the rate and timing of growth events provide a more direct measure of a group's developmental response to environmental circumstances" (Mensforth, 1985, p.248). This influential study examines the patterns of tibia long bone growth in two archaeological nonadult skeletal samples. The tibia was selected because past research had shown (Tanner, 1990) the rapidly growing long bones of the lower limb exhibit the most pronounced effects from stress-induced growth retardation and the tibia was the most frequently preserved long bone in the archaeological skeletal samples providing the best continuous sampling of the nonadult period (Mensforth, 1985).

The Mensforth study demonstrated that variations in the growth patterns in the Libben tibiae occurred early in life and were primarily restricted to the weaning

period. It was suggested that the high level of infectious disease experienced early in life in the Libben children was a prime agent for early growth retardation. An interesting side-bar to this publication is its reference to the term *secotrant*: second year transitional (Jeliffe, 1969). Secotrant refers to young children (1-2 years of age) in traditional societies at high risk for infectious disease and/or malnutrition (Mensforth, 1985). This time period proves to be important in the developmental re-organization of trabecular bone to be demonstrated in the results of this investigation. Although the Mensforth study was not intended to quantify the overall magnitude of developmental differences, it did identify differential skeletal growth of biological significance consistent with research on extant developing and/or preindustrial populations. The focus of Mensforth's research on the *patterns* of long bone ontogeny using archaeological skeletal remains, places it in an ancestral position to this dissertation's investigation ontogenetic patterning of trabecular bone.

Ding's (2000) study on age variation of adult human proximal tibial trabecular bone investigates normal age-related changes in mechanical, physical/compositional, and 3D microstructural properties. The importance of Ding's research is that it outlines adult boundaries towards which the ontogenetic pattern of trabecular bone of the proximal tibia is directed by genetic and environmental influences. The materials for Ding's research on 3D structural properties were 40 tibiae retrieved from 40 donors aged 16 to 85 years. The specimens were human autopsy proximal tibiae without macroscopic pathological changes. They were harvested from individuals who had been normally active until two weeks before

death. Two randomly selected cylindrical trabecular bone specimens were obtained from both medial and lateral tibial condyles.

Ding's procedure for three-dimensional reconstruction and analysis included scanning the specimens with a high resolution microtomographic system (μ-CT 20, Scanco Medical AG, Zurich, Switzerland) and quantification of structural properties including, but not limited to: anisotropy (star volume distribution method, SVD), mean trabecular volume, connectivity, and bone volume fraction (bone volume per total specimen volume). Ding demonstrated that the decrease in mechanical properties of trabecular bone in the proximal tibia with ageing is mainly a consequence of the loss of trabecular substance. The study showed that the bone volume fraction and mean trabecular volume decreased significantly with age; connectivity did not have a general relationship with age; and the degree of anisotropy increased with age. These age-related changes had the same trend and pattern for both the medial and lateral condyles of the tibia. Interpretation of these findings suggests a pattern of continuing bone functional adaptation to age-related bone loss: the aging trabeculae aligning strongly with the primary direction of mechanical forces which are parallel to the longitudinal loading axis of the tibia.

Ding's observations, which chronologically are commencing at the end-age point of this dissertation research, indicate the trend and pattern of changes in trabecular bone after ontogeny throughout life's remaining course. The principle of mechanical factors determining trabecular structural organization remains operative

throughout life. Control of bone formation is of primary concern during ontogeny; control of bone resorption and remodeling are of concern in maturity.

ENVIRONMENTAL FACTORS AFFECTING TRABECULAR BONE IN GENERAL AND ABOUT THE KNEE IN PARTICULAR

Mechanical loading and nutrition are key environmental factors known to affect bone development (Bass et al., 2005). This section summarizes current concepts and data concerning the mechanical environment of the knee joint, exercise, and human walking, and how those mechanical forces are determinants in trabecular bone structural organization. These loading forces will be seen to be of importance to the ontogenetic patterning demonstrated by this research. The observed effects of nutritional differences on trabecular bone density are discussed in Chapter 2.

Trabecular bone and changes in mechanical loading: recent animal studies

The published literature on the mechanical factors influencing trabecular bone structure is vast. The following discussion selects several very recent studies, which have investigated the influence of changes in mechanical loading on the trabecular bone about the knee joint, the region of interest to this research. This is an attempt to summarize the specific effects of mechanical forces on knee joint-derived trabecular bone, as observed by different researchers in the past two to three years. Richmond et al. (2005) examined the influence of bipedal locomotion on the trabecular structure in the distal femur, comparing a bipedally trained macaque to a sample of wild-collected

macaques. Previous research had demonstrated that bipedally trained macaques acquire some humanlike skeletal features (i.e., lumbar lordosis and deepened patellofemoral grooves) (Richmond et al., 2005). The results of this microCT study indicated a more anisotropic trabecular structure, primarily oriented in the sagittal plane, in the distal femur of the trained macaque. This trabecular directionality suggests a correspondence to the knee range of motion in flexion and extension present in the bipedally trained macaque, but not in the quadrupedal wild-collected macaques (also see Richmond et al., 2004). This is thought to be an example of trabecular bone adaptation during growth brought about by a change in loading patterns and activities.

Fritton et al. (2005) compared volumetric bone mineral content (and other structural parameters) between loaded and contralateral (unloaded) proximal tibiae in an experimental adolescent mouse model using microCT technology. The proximal metaphyseal region of the loaded tibia demonstrated an increase in bone mineral content, bone volume fraction, and average trabecular thickness. These results indicated a site-specific increase in bone structural parameters generated in the proximal tibial metaphysis by a daily regimen of controlled axial loading during skeletal growth.

Van der Meulen et al. (2006) investigated the effects of mechanical loading to trabecular bone formation and (re)alignment of the distal lateral femoral condyle in a rabbit model. The experimental method tested the hypothesis that cyclic loading applied directed to cancellous bone would result in new bone formation aligned with the loading direction. The loading in this model was applied in a direction *not*

(emphasis mine) habitually loaded- perpendicular to the lateral surface of the condyle. This required an implantable loading device, which may have added an additional variable to the experimental results, namely activation of an accelerated bone remodeling process (Frost, 1986). The results of microCT and histomorphometric examination showed that *in vivo* cyclic loading significantly increased the trabecular bone volume fraction, trabecular thickness, and mineral apposition rate in the loaded limb. Interestingly, trabecular realignment as measured by degree of anisotropy did not change in this experimental model, perhaps because of the predominance of the already established primary loading direction which is perpendicular to the medial-lateral experimental loading force.

The Pontzer et al. (2006) study on trabecular orientation in the distal femur is an elegant demonstration of the dynamic adaptation of trabecular bone to changes in the orientation of peak compressive forces. The experimental design used two age-matched groups of juvenile guinea fowl, each running on a treadmill set at level (0°) or on an incline (20°). The incline group had used their knee joints in a more flexed posture than did the level group. Trabecular orientation and density was measured with a radon transform-based method from microCT scan data. The results demonstrated that the difference in orientation of the thickest trabecular struts (13.6°) in the sagittal plane corresponded to the difference in knee flexion (13.7°) between the two groups of running fowl. The authors state that these results suggest that trabecular architecture during ontogeny is "both responsive and highly sensitive to its mechanical environment" (Pontzer et al., 2006, p. 64).

Trabecular bone and exercise: recent studies in children

Longitudinal studies of prepubertal and adolescent boys and girls have been recently published, examining the relationship between physical activity and bone structural parameters in the trabecular bone regions of the femoral neck, radius, and tibia, as well as the cortical bone of the femur, humerus, and tibia (Forwood et al., 2006; Janz et al., 2004; Lloyd et al., 2002; MacKelvie et al., 2004; Koutulainen et al., 2005; Sone et al., 2006; Uusi-Rasi et al., 2006). These studies incorporate structural metrics (bone size, density, geometry, and strength) derived from dual-energy x-ray absorptiometry (DXA) scans using the Hip Structure Analysis program (Hind and Burrows, 2007), magnetic resonance imaging (Bass et al., 2002), and peripheral quantitative computed tomography (Bass et al., 1998; Koutulainen et al., 2002).

This research into bone functional adaptation during growth and development indicates that physical activity and high-impact exercise intervention have a positive site-specific effect on cortical (increased cross-sectional area) and cancellous (increased trabecular bone density) bone strength parameters (after controlling for biological maturity age and body size) (Bass et al., 2002; Hind and Burrows, 2007; Sundberg et al., 2001; Ward et al., 2005). The effect is greatest in the prepubertal and early pubertal years when there may be an increased skeletal responsiveness to loading, due of new quantities of bone-active hormones such as estrogens, androgens, growth hormone, and insulin-like growth factor-1 (Hind and Burrows, 2007; Mauras et al., 1996; Ward et al., 2005). A provisional summary position is that “exercise during growth has been shown to lead to large increases in bone mass and the biomechanical

strength of bones – much greater than achieved at any other time of life" (Ducher and Bass, 2007, p. 171).

Human walking

The initiation and maturation of the human bipedal gait are key contributors to skeletal loading patterns, expressed in this research by changes in the ontogenetic pattern of proximal tibial trabecular bone. The observed natural history of human walking and in particular, the differences between the gait of toddlers and adults are instructive. The infant walks without support at around one year of age (Sutherland, 1997). The toddler gait shows a low average walking speed, high cadence (steps/minute), short step length, a wide support base, and a prolonged double support phase (standing on both feet) (Hallemans et al., 2005). Kinematic differences between toddlers and adults include, in toddlers, the guard position of the arms, external rotation of the feet, absence of heel strike, and simultaneous flexion of the hip and knee in swing and stance (Sutherland, 1997). The toddler gait is further characterized by a lack of muscle force and balance issues (Woollacott and Assaiante, 2002).

With walking experience and further neurological development, the young child's gait matures in two phases. The first phase is evident after around six months of walking and is indicated by rapid changes in all gait parameters: decrease in cadence, increases in step length and walking speed, and an increase in single limb support. The second phase, beginning around age two years, is a further refinement of the gait pattern. The adult pattern is characterized by a narrow mediolateral base of support, predictable limb stability, a consistent cadence, and mechanical efficiency (Sutherland,

1997). Sutherland (1988, 1997) presents data establishing the attainment of gait maturation and stabilization between 3.5 and 4 years. He states that the changes that occur through the remainder of the growing years are explained by growth alone. Recent research has extended that age, arguing that continued improvements in walking balance and stability occur until age six to eight years (Hallemans et al., 2005; Woollacott and Assaiante, 2002). The developmental sequence of human walking begins at gait initiation with segments of the body moving *en bloc*, and ends at gait maturation with an articulated, independent operation and control of those segments (Woollacott and Assaiante, 2002).

Knee joint forces

The determination of *in vivo* forces acting at the human knee during normal gait and other activities (e.g., stair descent, stair ascent, and jogging) provides an essential "input" to the investigation of loading mechanisms and bone functional adaptation. It should be noted that the published data are adult-based. The knee joint intersegmental forces have three major contributors: muscle, ligament, and contact forces. Intersegmental joint forces are calculated by modeling the leg as a collection of rigid links or segments representing the thigh, leg, and the foot (Hurwitz et al., 1998). These knee joint loads varying according to activity, phase of gait cycle, and knee flexion angle. The range of forces at the knee joint is generally reported in terms of body weight.

The two main techniques which have been used to determine joint loading are telemetry (a direct experimental technique using the femoral component of a total hip

replacement) and mathematical modeling (a theoretical approach) (Komistek et al., 2005). Unfortunately, there currently is not an implantable design to measure knee joint loads directly and thus verify the mathematical modeling approaches. The knee joint interactive tibio-femoral forces derived from various approaches are listed in Table 1.1. These data demonstrate the range of knee joint forces with varying activities, with tibio-femoral contact forces ranging from 2.1 times body weight (normal walking) to 5.4 times body weight (stair ascent). The relationships of tibio-femoral contact forces, gait cycle, and knee joint angle are represented in Figure 1.1. The linkage of the actual biomechanical loading of the knee joint and the microarchitecture of the trabecular bone of the proximal tibia remains to be established.

Alignment

The magnitude and distribution of total knee joint forces between the medial and lateral plateaus of the proximal tibia is related to the static axial alignment of the knee (tibiofemoral angle) and the dynamic adduction moment during gait (Andrews et al., 1996; Heller et al., 2003; Hurwitz et al., 1998). Deviations from normal alignment (3-5°, valgus) of the knee have been shown to increase the tibio-femoral joint contact forces during gait and stair climbing (Heller et al., 2003). Increased valgus/varus (tibia angled away/toward the midline relative to the femur) angulation resulted in increases in the peak contact forces, from an average of 3.3 times body weight (BW) up to 7.4 BW.

Authors	Approach	Activity	Knee Force
Taylor and Walker (2001)	Telemetry	Walk	2.2-2.8 BW
		Stair descent	3.1 BW
		Stair ascent	2.8 BW
		Jogging	3.6 BW
Paul (1976)	Math Modeling	Normal walk	2.8 BW
		Fast walking	4.3 BW
		Stair descent	4.9 BW
		Stair ascent	4.4 BW
Heller et al. (2003)	Math Modeling	Walk	3.3 BW
		Stair ascent	5.4 BW
Komistek et al. (2005)	Math Modeling	Walk	2.1-3.4 BW
		Deep Knee Bend	1.8-3.0 BW

Table 1.1 Knee joint interactive tibio-femoral contact forces derived from various approaches (from Komistek et al., 2005). BW, body weight.

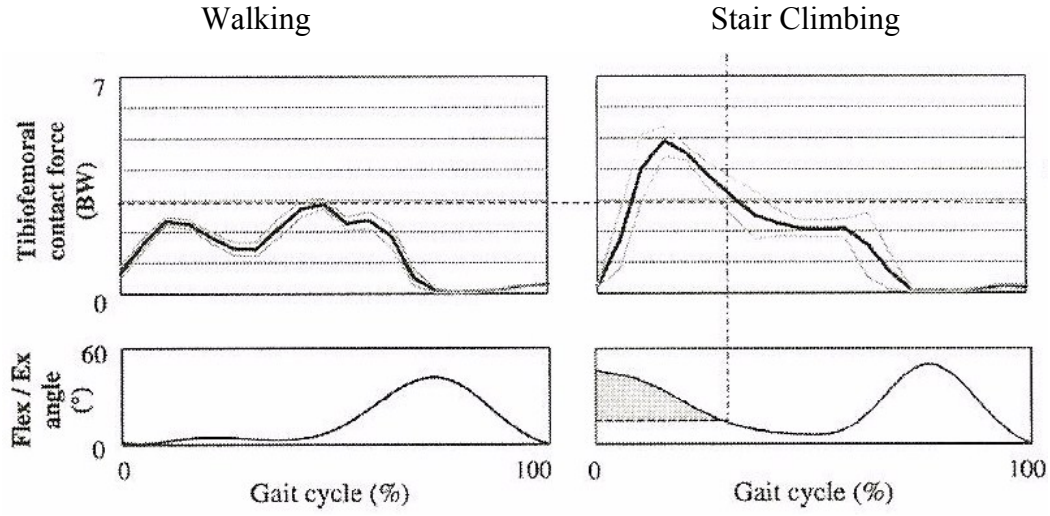

Figure 1.1 Tibio-femoral contact forces and knee joint position during both normal walking and stair climbing. The dotted horizontal lines correspond to the average peak axial force during walking. Forces are shown in body weight (BW). Flex/Ex angle is the knee joint position (Taylor et al., 2004).

The distribution of knee joint loads during walking is typically calculated as approximately 70% of the total load passing through the medial compartment of the knee (Hurwitz et al., 1998). The adduction moment is a dynamic measure of the forces across the medial compartment. It is calculated with considerations of body weight, height, vector of loading forces, and distance of the center of the knee joint from the body midline. Hurwitz et al. (1998) investigated the relationship between the distribution of medial to lateral tibial bone mineral content and the knee adduction moment. Their results showed a positive correlation, with an increased adduction moment associated with relatively greater bone mineral content in the proximal tibial medial condyle compared to the lateral condyle. The adduction moment has been correlated with the tibio-femoral angle, in that lower tibio-femoral angles (varus) have higher adduction moments and vice versa (Andrews et al., 1996). The importance of

this study is that it demonstrates a "significant correlation between the dynamic medial-lateral load distribution and the corresponding bone distribution (Hurwitz et al., 1998, p. 429).

An intriguing application of these data lies in the consideration of the connections between the development of the femoral bicondylar angle and the ontogenetic changes in the trabecular bone microarchitecture of the proximal tibia. The formation of the human bicondylar angle is considered to be an epigenetic phenomenon, in which growth of the distal femur is modulated by the mechanical loading environment related to the initiation and development of bipedal walking (Shefelbine et al., 2002; Tardieu et al., 2006). Femoral metaphyseal growth differentials result in a stable femoral bicondylar angle of 8°-10° by the age of eight years. This corresponds to an increased valgus tibio-femoral angle between ages two to four years of 5°-7°, with establishment of the normal alignment by eight years of age (Salenius and Vankka, 1975). The possible relationships between the ontogenetic changes in the femoral bicondylar angle, tibio-femoral angle, and proximal tibial trabecular bone structure will be discussed in the Results chapter.

This chapter has compiled background data on current concepts of the mechanical environment of the tibia and the response of trabecular bone about the knee to changes in mechanical loading. These findings, which contribute to the formulation of the hypotheses of this research project include (but are not limited to):

- An increase in loading to trabecular bone (body mass + physical activity) elicits an increase in bone density and trabecular thickness.

- A change in loading direction elicits a change in trabecular orientation, aligned with the loading direction.
- Exercise during growth tends to result in increased trabecular thickness and bone density.
- Locomotor behaviors may be key variables in the patterning of proximal tibial trabecular bone structure.

HYPOTHESES

Trabecular bone ontogenetic analysis, as proposed in this study, is made possible and justified by recent advances in non-invasive imaging technologies (microCT/MRI), computational methodologies (3D computer simulation, finite element analysis), and experimental data (animal models, implant telemetry and recovery). Trabecular bone analysis can be thought of as part of the mechanobiology model developed to explain skeletal tissue differentiation, maintenance, and adaptation in response to biophysical stimuli within the environment (Carter and Beaupre, 2001; Jacobs, 2000; Ruimerman et al., 2005; van der Meulen and Huiskes, 2002). Skeletal morphogenesis has two components: intrinsic (genetic) skeletal patterning and extrinsic (epigenetic) modulation based on the variable regulation of genetic expression from environmental, physical, and biochemical factors. The essence of cancellous mechanobiology lies in developing a complex understanding of the influences of mechanical loads on skeletal biology, geometry and internal organization at all scalar

levels, including nanostructural, molecular, cellular, tissue, and organic. This study is concerned with the *tissue* level analysis of trabecular strut structure.

The initial architecture of tibial metaphyseal trabecular bone is dictated by the patterned organization of cartilage cells and the process of endochondral ossification forming bone (primary spongiosa) characterized by randomly organized interconnecting trabeculae (Carter and Beaupre, 2001; Wong and Carter, 1990). This bone is subsequently remodeled (secondary spongiosa) with changes in porosity, architecture, and directionality in response to loading history modified by biological factors in a fashion that is site, surface, age, and sex-specific. Skeletal ontogeny, the key aspect of this project, interacts with this process by establishing a "normal" trajectory of shape, size, and internal structure based on "normal" mechanical requirements. The changes in loading history related to the adoption of bipedal gait, increased body mass and physical activity contribute to this process. Daily cyclic loading of cancellous bone is produced by customary and habitual activities (e.g., walking, running, climbing, and carrying) applied consistently over a long period of time with bone formation, resorption, and directionality determined by the specifics of the daily stress stimulus (Rubin et al., 2002).

This study develops quantifiable, repeatable, unbiased, morphological and scan image data on ontogenetic microarchitectural changes to relative bone volume, anisotropy, and trabecular thickness/number in human trabecular bone structure from a Late Prehistoric Ohio Valley archaeological subadult skeletal sample. The combined parameters are optimally studied by microCT scanning and 3D computational

structural analysis; they form the data core of this project. The results highlight the dynamic relationships and sequences between growth/development, general functional activities, and trabecular distribution/architecture. The following hypotheses, based on previous literature and general modeling/remodeling theory, are tested in this project to characterize the temporal sequence of change in two selected trabecular bone structural parameters, bone volume fraction (BV/TV) and degree of anisotropy (DA), during human growth and development:

1. *Infancy (0-1 year): pre-walking is characterized by homogeneous, thin, relatively low density (low BV/TV) primary trabeculae with random orientation (low DA).*

2. *Early childhood (1-5 years): increased body mass, beginning and independent walking is characterized by increasingly dense (higher BV/TV) secondary remodeled trabeculae with multiaxial anisotropic orientation (low DA).*

3. *Middle childhood (5-10 years): increased body mass, adult gait pattern, and independent activities is characterized by statistically significant increased bone volume (higher BV/TV) and an increase in anisotropy (higher DA).*

4. *Late puberty/early adult (15-20 years): increased body mass related to pubertal growth spurt, fully active adult lifestyle is characterized by statistically significant increased bone volume (higher BV/TV) and statistically significant increase in anisotropy (higher DA).*

SUMMARY

The theoretical and experimental foundations for an ontogenetic trabecular bone research program have been discussed using recent technological advances in microCT imaging and three-dimensional structural analyses. Hypotheses were developed based on mechanobiological theory, recent animal models, and human studies. The robust and unbiased characteristics of these methods are applied to an archaeological juvenile skeletal series from SunWatch village, a Late Prehistoric site in the Ohio Valley. The results of this study are expected to contribute to the development of new quantitative "reference" data for the ontogenetic patterning of human trabecular bone.

Organization of dissertation

This dissertation consists of eight chapters including this general introduction and statement of hypotheses. Chapter 2 places trabecular bone into the broader context of skeletal biology, discussing the current state of understandings. Chapter 3 is the cultural background chapter. It combines a brief review of the Fort Ancient concept with a selected, but detailed, examination of relevant archaeological investigations of SunWatch village. Chapter 4 is a biological continuation of the preceding chapter and presents a summary of the biologically-related and bioarchaeological research data on the SunWatch and related Fort Ancient skeletal remains. Chapter 5 discusses the

characteristics of the materials (SunWatch juvenile tibiae) that form the basis for this investigation, age-at-death estimation, and the seriation procedure. It also details the methods of the research including microCT scanning technology and protocol, the structural analysis program Quant 3D, and statistical procedures. Chapter 6 is a compilation of the results emphasizing the visual interpretation of the quantitative data. Chapter 7 provides an interpretative framework for an understanding of the meaning of the quantitative patterns of trabecular bone ontogeny. Chapter 8 summarizes the results of this project and places it into the broader context of skeletal research. Finally, three appendices are included for reference: the complete quantitative dataset, selected enlarged figures of CT slice images and 3D rose diagrams, and the scan-related Quant 3D log files of the primary medial and lateral volumes of interest.

CHAPTER 2

SKELETAL BIOLOGY OF TRABECULAR BONE

Adult trabecular bone morphology reflects lifelong accumulated strain history superimposed upon the biological and mechanical-related structural changes occurring during growth and development. The biological factors (discussed below) include, but are not limited to, genetics, metabolic influences, and nutrition. Analysis of cancellous microarchitecture and directionality (anisotropy) has the potential to provide a window into the assessment of human behavior and physical activity in the archaeological context over the life course of individuals, groups, and populations. A compelling broad-based research framework is the exploration of cancellous bone adaptation from a life course perspective extending from prenatal stages to birth, childhood, adolescence, young adulthood, and later adult life (Ben-Shlomo and Kuh, 2002). This includes studies of growth and development, human variation, the effects of lifestyle change, aging and senescence, and chronic degenerative conditions. It incorporates the influences of socially structured health and disease, diet and nutrition, mobility and sedentism, and workload.

This research perspective uses mechanobiology of cancellous bone as the theoretical scaffold, providing the continuity in a life course of change through the processes of growth, modeling, remodeling, skeletal adaptation, aging, and disease. Mechanobiological factors during ontogeny, responsible for the development of skeletal mass and distribution, are also in play at the opposite stages of life: aging, senescence, and the development of osteoarthritis (Beaupre et al., 2000). The purpose of this chapter is to present an overview of the current conceptual models for endochondral ossification, trabecular bone development, and adaptation. This is followed by discussions of basic concepts and recent advances in skeletal biology, theories of bone remodeling, and research on the biomechanics of trabecular bone. The scope of this chapter is not meant to be exhaustive, but rather to highlight selected current perspectives in skeletal biology in reference to trabecular bone adaptation. This sets the stage for a research program studying the variation in human trabecular bone structure over a life history perspective, beginning with ontogeny. Developing trabecular bone in the metaphyseal and epiphyseal regions of long bones is a result primarily of the endochondral ossification process.

ENDOCHONDRAL OSSIFICATION

Long bones grow by the process of endochondral ossification (Scheur and Black, 2000). This process is influenced by both biological and mechanical factors, the tibia is no exception. This section will describe general aspects of endochondral

ossification and recent research on regulatory processes, outline specific morphological changes in the tibia during ontogeny, and place this bony element (both cortical and cancellous envelopes) within a continuum of life course perspective.

"Endochondral ossification is the process by which the skeletal cartilage anlagen are replaced by bone" (Olsen et al., 2000). This process involves the formation of a cartilage primordium and growth plate, where chondrocytes initially undergo proliferation and a series of differentiation steps secreting a cartilage template that is eventually replaced by bone (Lai and Mitchell, 2005). The anlagen elongate and expand in width by proliferation of chondrocytes and deposition of cartilage matrix. Chondrocytes undergo further maturation to hypertrophic chondrocytes (HC) and synthesize an altered (from proliferating cartilage) extracellular matrix. Angiogenic factors secreted by hypertrophic chondrocytes induce angiogenesis from the perichondrium; osteoblasts, osteoclasts, and hematopoietic cells come with the blood vessels. The primary ossification center is thus formed.

Within the ossification center, the hypertrophic chondrocytic matrix is degraded, the hypertrophic chondrocytes undergo apoptosis, and osteoblasts replace the disappearing cartilage with trabecular bone. Bone marrow is also formed. Simultaneously, osteoblasts in the perichondrium form a collar of compact bone around the diaphysis of the cartilage, locating the primary ossification center within a tube of bone. At one or both ends (epiphyses) of the cartilage, secondary ossification centers are formed, leaving a plate of cartilage (growth plate) between the epiphysis

and diaphysis. Elongation of the long bone from the growth plate results from a coordinated sequence of chondrocyte proliferation, hypertrophy, and apoptosis. It is this choreographed process that creates the initial framework of trabecular bone and thus, the foundation upon which the ontogenetic patterning of interest to this investigation rests. Concurrently, these processes are coordinated with growth in the epiphysis and radial appositional growth of the diaphysis (Olsen et al., 2000). Bone growth at the growth-plate cartilage or at an ossification center is, on its own, insufficient to form the complex shapes of complex bones. Constant (re)modeling occurs within the bone tissue and also at the internal and external bone surfaces in the form of bone deposition and resorption (Aiello and Dean, 2002).

A complex, carefully coordinated sequence of perichondral development, angiogenesis, chondrocyte proliferation, and chondrocyte differentiation is required for the progression of endochondral bone formation and maintenance of normal childhood growth (Stevens and Williams, 1999). Recent research is beginning to bring understanding to the fundamental regulatory processes for control of endochondral bone formation. Studies have identified Indian hedgehog (Ihh) as a key coordinating molecule in these processes: stimulating growth plate chondrocyte proliferation, preventing chondrocyte hypertrophy, and regulating bone formation in the perichondrial collar and trabecular bone below the growth plate (Olsen et al., 2000). Parathyroid hormone-related peptide (PTHrP) is another important signaling molecule which is instrumental in regulating chondrocyte maturation and differentiation (Stevens et al., 1999). “Ihh and perichondrial PTHrP are thought to be

components of a feedback loop that regulate the relative proportions of proliferating and hypertrophic chondrocytes in growth plates" (Olsen et al., p. 204). Bone morphogenic protein (BMP) is thought to be a downstream mediator of Ihh signaling; it may also be a positive inducer of Ihh expression (Pathi et al., 1999). These factors and, as yet, unknown molecules are in involved in a complex autoregulatory network.

The major systemic hormones that regulate linear growth through endochondral bone formation during childhood include growth hormone (GH) and insulin-like growth factor-1 (IGF-1), thyroid hormone (T3), and glucocorticoids. The major contribution during adolescence comes from sex steroids (Stevens at al., 1999). Recent research has demonstrated the importance of these hormones to the control of growth, although the underlying molecular mechanisms are largely unknown. The GH-IGF-1 signaling system is required for normal growth of the skeleton. Targeted disruption studies have consistently demonstrated severe growth retardation and delayed bone development (Stevens et al., 1999).

Childhood hypothyroidism results in a reversible but complete arrest of linear bone growth from disorganization of epiphyseal growth plate chondrocytes and disrupted endochondral bone formation. These changes can be rescued by thyroid hormone replacement. Androgens and estrogens are crucial for peri-pubertal growth and skeletal maturation and for the cessation of linear growth in adulthood as they induce epiphyseal growth plate fusion at the end of puberty. Both sex steroids influence GH secretion, exert direct effects on the growth plate, and are important in the bone responsiveness to mechanical loading.

The effects of glucocorticoids on bone turnover and osteoporosis is well established. Their actions on endochondral bone formation are less clear. The skeletal effects of targeted disruption on the growth plate by glucocorticoids are still largely unknown. In contrast, vitamin D and retinoids have important roles in bone formation (lack of which leads to rickets in children and osteomalacia in adults). Studies have demonstrated that deficiencies cause severe impairment of bone formation and expansion of the epiphyseal growth plate due to widening of the hypertrophic zone. The latter effect is thought to be secondary to accelerated differentiation of proliferating chondrocytes to hypertrophic cells (Kato et al., 1990).

This brief overview of endochondral ossification, the foundation of linear growth of human long bones, highlights the process and the recent research into normal regulatory control. This latter aspect is a relatively young and emerging field set to grow rapidly (Stevens and Williams, 1999). The current study is focused on the zone of primary endochondral bone (primary spongiosa) (Figure 2.1).

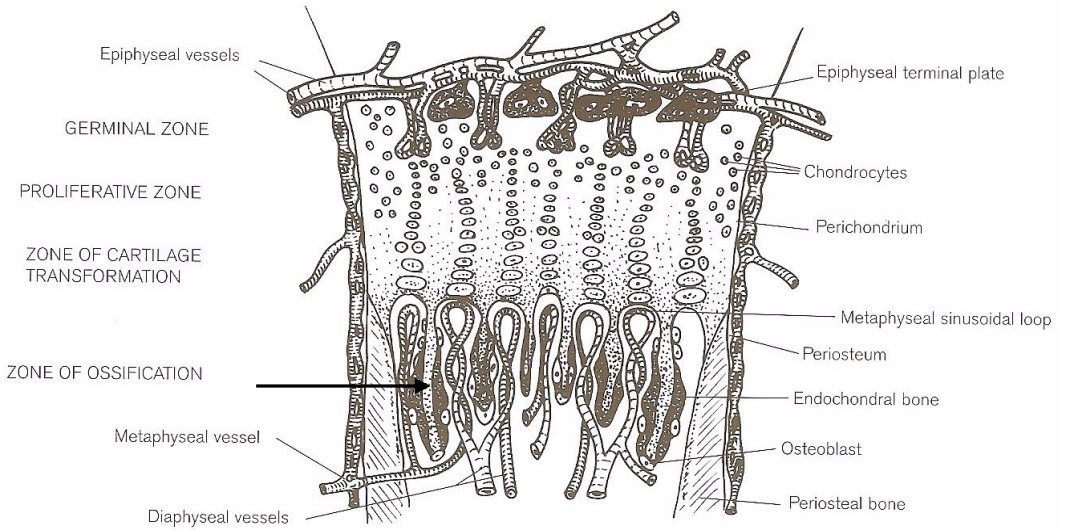

Figure 2.1 Summary of features of endochondral ossification. Black arrow points to a primary spongiosa trabecula (from Scheuer and Black, 2000).

TIBIAL DEVELOPMENT

This descriptive section is abstracted from Scheur and Black (2000). At birth, 80% of the overall length of the tibia is occupied by ossified shaft. The shaft is arched somewhat posteriorly in the proximal third and straight in the distal two-thirds. The anterior border is a sharp ridge turning medially at its distal end. The proximal metaphyseal surface is convex, smooth and oval in outline. The distal metaphyseal surface is flat and quadrangular or oval.

The tibia is reported to grow at a uniform rate throughout childhood, in contrast to the femur which grows more slowly up to puberty and then increases rapidly with the pubertal growth spurt. This results in an increasing crural index (total tibial length x 100/total femoral length) from age six to puberty and then decreasing.

Smith and Bushang (2005) in a recent study of longitudinal adolescent growth of the humerus, radius, femur, and tibia, found the tibia to have the most variable pattern of growth velocity.

A morphological summary of tibial development (Scheur and Black, 2000, p.414) is indicated in Table 2.1.

Age	Event
Birth	Shaft and proximal epiphysis
6 weeks	Proximal secondary center present
3-10 months	Distal secondary center appears
3-5 years	Medial malleolus starts to ossify
8-13 years	Distal tuberosity starts to ossify
12-14 years	Proximal and distal tuberosity unite
14-16 years	Distal epiphysis fuses in females
15-18 years	Distal epiphysis fuses in males
13-17 years	Proximal epiphysis fuses in females
15-19 years	Proximal epiphysis fuses in males

Table 2.1 Tibial developmental morphology

LIFE HISTORY PERSPECTIVE

Bone morphology, linear growth, repair, and maintenance are influenced by a variety of genetic, nutritional, environmental, and mechanical factors acting over a lifetime. A broad framework for consideration of skeletal adaptation is from a life history perspective extending from fetal development to birth, childhood, adolescence, young adulthood, and later adult life (Ben-Shlomo and Kuh, 2002). This includes studies of fetal and postnatal growth and development, the effects of lifestyle change, aging and senescence, and chronic degenerative conditions. From the bioarchaeological agenda, the influences of socially structured health and disease, diet and nutrition, mobility and sedentism, and workload are additional factors. This research perspective uses mechanobiology as the theoretical scaffold, providing the continuity in a life course of change through the processes of growth, modeling, remodeling, and skeletal adaptation. Mechanobiological factors during ontogeny, responsible for the development of skeletal mass and distribution, are also in play at the opposite stages of life: aging, senescence, and the development of osteoarthritis (Beaupre et al. 2000).

Applying this perspective to the tibia specifically, the outline of the journey is known; the beginning is fetal skeletal morphogenesis, the destination is death. The actual course traveled is variable, individually and for populations. During ontogeny tibial morphology and linear growth is influenced by genetic background for general patterning; diet, nutrition, and illness burden for growth parameters; and hormonal

balance and mechanical loading (physical activity) for growth, acquisition of bone mass, and bone shape/architecture. The tibial shaft in early childhood is relatively round (eurycnemic). It demonstrates over time a variable but definite change in shape towards being more triangular with mediolateral flattening (platycnemic) reflecting adaptation to anteroposterior bending loads (Lovejoy et al., 1976; Ruff and Hayes, 1983). The tibial ontogenetic trabecular microarchitectural patterns demonstrated in this research are expected to be influenced by similar complex interactions.

After skeletal maturity, in early adult years, influences on tibial cortical morphology and geometry involve mechanical forces and age-related factors. The processes are maintenance of the skeletal structure established at the end of development; continued, but substantially reduced, skeletal adaptation with periosteal apposition and endosteal contraction (or expansion); and repair of microdamage.

After this relatively homeostatic phase, advanced age-related changes in the tibial morphology/microstructure begin (Ding, 2000). The bone loss process in both sexes begins from an imbalance of bone formation versus bone resorption, accentuated in women by the loss of estrogen. This is reflected in the tibial diaphysis by medullary expansion and some compensatory periosteal apposition (hopefully maintaining structural strength parameters). It is reflected in the tibial trabecular bone by trabecular thinning and loss of connectivity. Separate from age-related changes in the tibial metaphyses are trabecular bony modifications associated with the initiation and progression of osteoarthritis. Taking osteoarthritis of the knee as an example, the tibial subchondral cancellous bone has specific trabecular changes involving

thickening, fatigue damage, increased remodeling rate, and possibly reactivation of endochondral ossification. The life history perspective as just outlined provides a framework for an integrated research program in skeletal biology of which this research is a single module.

MECHANOBIOLOGICAL MODELS FOR TRABECULAR BONE

The interrelationship between biology and mechanical environment is the foundation of the term mechanobiology: the influence of loading environment on bone structure and biology (Jacobs, 2000). Understanding the influence of mechanical loads on cancellous bone structure began in the mid-19th century with Swiss anatomist von Meyer's drawings of the internal structure of the proximal femur (Roesler, 1987). Wolff's outspoken advocacy of the concept he termed the "Trajectorial Theory" of trabecular alignment lead to widespread acceptance that has carried into the present day (Wolff, 1892). Foreshadowing current research, Wolff proposed that cancellous bone architecture was based on "law according to which alterations in the internal architecture clearly observed and followed mathematical rule…" (Roesler, 1987). Wolff's statement on the form and function of bone referred to a static mathematical relationship between trabecular architecture and stress trajectories. Wolff's long shadow casts onto research approaches attempting to find appropriate parameters "by which structural and geometrical properties can be described under a more-or-less general principle" (Huiskes, 2000, p.146).

There is another paradigm passed down from the 19th century. Wilhelm Roux focused on the relationship of biological processes to trabecular architecture and external load. Roux (1881) suggested that functional adaptation of trabecular bone is "regulated locally by cells, governed by mechanical stimuli, in a self-organized process." This is the modern equivalent of a biological regulatory system producing a structure adapted to mechanical demands based on its own characteristics (Huiskies, 2000). Huiskes argues (2000) that it is the study of bone "production technology" (versus design) from which understanding will develop on the nature of bone architecture and adaptation.

Recent research in cancellous bone analysis includes computational, imaging, experimental, and cellular/molecular studies designed to determine the structural and material consequences and biological processes of various loading regimes (Lanyon, 1996) based on advances in theoretical modeling of the mechanobiology of cancellous bone (Jacobs, 2000). It is these advances (microCT imaging, quantitative 3D analysis, and large-scale finite element method of computer-based simulation) which have stimulated the emerging interest in trabecular bone as a robust portal for understanding skeletal adaptation and behavior in extant and past human populations.

Studies of skeletal adaptation have proven to be invaluable tools for the study of human behavior and lifestyle. Long bone cortical cross-sectional properties described by Ruff et al. (1994) have linked human ontogeny, maturation, and behavior with skeletal response to mechanical loading, providing an influential, explanatory framework for the observations of evolutionary biologists and bioarchaeologists.

"There has been a decline in overall skeletal strength relative to body size over the course of human evolution that has become progressively steeper in recent millennia, probably due to increased sedentism and technological advancement" (Ruff, 2005, p. 202). The large body of published research in this area has demonstrated its value by contributing to the understanding of temporal/spatial changes in human skeletal morphology as related to behavior, lifestyle, and workload. Trabecular bone adaptation research complements this established body of understanding of cortical bone, focusing on a different envelope of bone with its own unique properties and responses.

"APPARENT LEVEL" MODELING OF MECHANOBIOLOGICAL ADAPTATION

A goal of trabecular bone modeling studies is the formulation of a mathematical description of the relationships between mechanical and biological behavior. The *apparent level* approach is taken. The best way of understanding this approach is that it considers the *net effect* of cellular or mechanical behavior without needing to account for each cell, trabecula, or action individually (Jacobs, 2000). The apparent level of skeletal modeling takes a complex microarchitectural structure and homogenizes the various structures and mechanical forces. This type of analysis is part of the engineering field of continuum mechanics. When combined with advances in Finite Element Method, it allows the study of mechanobiological interactions of trabecular microarchitecture and anisotropy (Carter and Beaupre, 2001).

Carter and Beaupre (2001) have used the apparent level to describe a comprehensive equilibrium model, the "mechanobiological hypothesis" (Pearson and Lieberman, 2004) based on a "simple mathematical rule relating cyclic tissue stress to bone apposition and resorption" (Carter et al., 1996, p. 5S). The general equilibrium model assumes that bone acts to maintain a mechanically stable, stress-strain range in response to mechanical loads. Bone requires a certain level of daily mechanical stimulation from various activities of daily living (e.g., walking, running, and climbing) for maintenance. The appropriate level of mechanical stimulation for bone apposition versus resorption is site specific and based on biologically interdependent influences of genetic influences, systemic factors, and local tissue interactions (see Beaupre and Carter, 2001 for the mathematical model).

The mechanobiological hypothesis considers bone growth as having two components: biological and mechanobiological. The biological component is controlled by genes and hormones, thus following the normal growth trajectory and velocity: decreasing in mid-childhood, increasing during the adolescent spurt, and decreasing to near zero at maturity. The mechanobiological component models an optimal strain level in bone in response to load (Bertram and Biewener, 1988). The mechanical influences become increasingly dominant and the systemic biological influences decrease in influence during growth and development. After age 10, mechanobiology predominates, maintaining daily stress stimulus (strain magnitude x loading cycles) within a "lazy zone" in which little bone apposition or resorption occurs (Carter et al., 1996).

Biological factors (i.e., genetic, hormonal, nutritional, and local tissue interactions) interrelate with and change the mechanobiological response (Carter and Beaupre, 2001). These local tissue interactions may involve physiochemical influences between adjacent cells and tissues, involving local expression of growth factors, cytokines, and bone induction factors (e.g., BMPs). There may be a cellular response involving the recruitment and activity of osteoblasts and osteoclasts, which results in the alteration of the mechanobiologically-mediated rate of bone apposition and resorption. In addition, there may be an interaction and change in the mechanobiological sensitivity, responsiveness, and/or regulatory signaling (Carter and Beaupre, 2001).

During ontogeny, increased loads above the lazy zone results in bone apposition; decreased loads results in bone resorption. Mature bone is predicted to respond to similar changes by periosteal deposition and endosteal resorption. This model accounts for site-specific and age-specific variability based on cellular factors such as the availability of osteoblast precursor cells and/or osteoclasts (Carter and Beaupre, 2001). Multiple simulation studies demonstrate that this model "successfully predicts the appositional bone growth and modeling observed in the diaphyseal cross section" beginning from the fetal femoral anlagen to maturity (Carter et al., 1996, p. 5S). Most pertinent to this discussion of cancellous bone, the same mechanobiological hypothesis predicts the observed macro- and micro-architecture of proximal (or distal) cancellous bone formed by endochondral ossification (Carter and Beaupre, 2001). Furthermore the geometry, microarchitectural, and density changes in mature cortical

and cancellous bone occurring as a result of skeletal adaptation to physical activities can be accurately simulated. Changes in bone mass (thickness and density) occur with increases or decreases in load magnitude or cycle. Changes in architectural patterns (distribution and anisotropy) occur with alterations in the direction of load (Carter and Beaupre, 2001).

The strength of the mechanobiological hypothesis is the ability to accurately predict observed skeletal changes. It is clearly an oversimplification of the complex, hierarchical biologic system for bone growth, development, (re)modeling, and repair. One of the shortcomings of the mechanobiological hypothesis model directly related to cancellous bone architecture is that it can not provide optimal trabecular orientations in some cases involving multiple loading directions (i.e., nonperpendicularity). Jacobs and Eckstein (1997) initially addressing this question, expanded this model to account for both trabecular density and alignment, demonstrating that tensile stresses play a dominant role in subchondral cancellous bone architecture which may not, therefore, correspond with areas of joint contact. These studies still leave the question of the observed nonperpendicular aspect of cancellous bone unresolved. A proposed solution is directly modeled trabecular architectural patterns.

DIRECT MICROSTRUCTURAL MODELING

The application of the continuum assumption (apparent behavior of cancellous bone is approximated by a continuum) to the tissue level of analysis accounting for

individual trabeculae is termed direct microstructural modeling (DMM) (Jacobs, 2000). The micromechanical environment of individual trabeculae of cancellous bone can be studied *in vivo* in small animals and *in vitro* whole human bones. Detailed microstructural cellular response behaviors and mechanobiological consequences can be modeled, supporting for example, Huiskes et al. (1998) hypothesis that "the stress concentration surrounding osteoclast resorption cavities is responsible for localizing osteoblastic bone formation during infilling of the cavity" (Jacobs, 2000). This developing technology specifically avoids some of the simplifying assumptions made in the apparent level modeling and holds the promise for a more precise determination of quantitative mechanical loading on an individual trabecula scale. This method has been made possible by advances in ultra-high-resolution CT scanners and finite element solutions for very large dataset models (100 million- 1 billion elements).

Advances in understanding trabecular bone mechanobiology, structure, and adaptation will develop along the lines of microstructural (possibly nanostructural) and cellular models ultimately providing the capability of evaluating temporospatial changes of trabecular bone. And from the anthropological perspective, the relationships of these changes to human populations and socially structured behavior, health, and disease. Some basic consideration of the cellular "actors" and their regulatory interactions are essential to understanding the proposed models as well as the empirical data from this current research on ontogenetic patterns of trabecular bone.

SKELETAL BIOLOGY: CELLS

Osteoblasts

Bone strain (or lack of) is mediated through the cellular responses of the osteoblast and osteoclast lineages. The osteoblast lineage is comprised of mesenchymally-derived cells including osteoblasts, osteocytes, and bone-lining cells. In general terms, osteoblasts form bone by synthesizing collagen matrix and secreting calcium-phosphate mineral; osteocytes and bone-lining cells may regulate metabolic and sensory functions (Pearson and Lieberman, 2004). Each cell type is phenotypically unique with particular identifying biochemical markers (Massaro and Rogers, 2004). Differentiation along a specific lineage is triggered by a genetic regulatory cascade, which for osteoblasts includes genes coding for core binding factor alpha 1, collagen 1, bone sialoprotein, osteopontin, and osteocalcin (St-Arnaud, 2003).

Osteoblasts are genetically sophisticated fibroblasts (Ducy et al., 2000) originating in a variety of tissues including the periosteum and endosteum. The only morphological feature specific to osteoblasts versus fibroblasts is the presence of a specific extracellular matrix. Differentiated osteoblasts produce a mucoprotein matrix, called osteoid, in which collagen fibrils are enmeshed. This is followed with mineralization of the osteoid by deposition of inorganic crystals of calcium phosphate on the collagen fibers. The search for osteoblastic differentiation factors has lead to the identification of Cbfa1 (core-binding factor-α1) as a dominant osteoblast-specific transcription factor (Harada and Rodan, 2003). Other transcription factors are involved

in osteoblast differentiation, including the Indian hedgehog (Ihh) growth factor (Ducy et al., 2000). The regulatory genetic architecture and mechanisms are presently poorly understood.

Bone formation by differentiated osteoblasts is controlled by complex, hierarchical, homeostatic, biological systems. Modulators of bone mass include a polygenic regulatory system, calcium availability, sex steroids, nutrition, and mechanical usage. The central regulation of osteoblast function features the endocrine system comprising parathyroid hormone (PTH); 1, 25$(OH)_2$ vitamin D; calcitonin; and the sex steroids. These hormones have varied roles in different contexts. Estrogen is particularly important in bone formation and resorption, up-regulating osteoblast activity. Estrogen receptors (ERα and ERβ) in osteocytes and osteoblasts have critical roles in mechanotransduction and the osteogenic response to strain (Pearson and Lieberman, 2004). PTH and vitamin D are mineral sensitive hormones stimulating osteoclasts and inhibiting osteoblasts. Calcitonin is a mineral-building hormone secreted by the thyroid which up-regulates osteoblasts and down-regulates osteoclasts. Recent research has demonstrated a possible central "master-regulator" of bone formation in the hormone Leptin (Ducy et al. 2000), produced in adipose tissue, inhibiting osteoblast function through hypothalamic and sympathetic nervous system signaling pathways (Harada and Rodan, 2003).

Transcriptional and growth factor regulation of osteoblastic function is controlled with temporal and spatial specificity by a system of autocrine and paracrine signaling. *Cbfa1* is currently the key player, bridging the gap between osteoblast

differentiation and osteoblast function. *Cbfa1* is regulated by several growth factor families, including BMPs, fibroblast growth factors, insulin-like growth factors, transforming growth factors, and platelet-derived growth factors (Jee, 2001).

Research on the effects of aging on osteoblast and osteoprogenitor cells has demonstrated the possible effects of senescence on these cells in respect to diminished synthetic capacity, a decline in the number of progenitor cells which can be recruited to differentiate into osteoblasts (Nashida et al., 1999), and a reduced sensitivity to mechanical signals (Donahue et al., 2001). These are important factors (in addition to changes in hormone levels) in the age-related imbalance of bone deposition and resorption- especially notable in trabecular bone.

Osteocytes

Osteocytes are differentiated osteoblasts that have become embedded in the mineralized matrix they have created as osteoblasts. These abundant cells (Mullender et al., 1996) reside within cavities termed lacunae, making physical contact with each other, osteoblasts, bone lining cells, and possibly osteoclasts by way of cellular processes passing through tunnels called canaliculi (Donahue et al., 2003; Martin et al., 1998). Gap junctions allow osteocytes to form a functional syncytium linking all cells within bone, forming the basis of their possible role as mechanosensory cells.

Mechanosensitivity of osteocytes has been demonstrated by in vitro and in vivo studies of pulsating, steady, and oscillating fluid flow, as well as changing substrate strain levels, resulting in increased mRNA expression, gene up-regulation, and metabolic synthesis of various active compounds (Donahue et al, 2003). Interestingly,

osteocytic cells contribute little to bone formation or resorption directly. Their role is thought to involve the communication of load-induced signals to the affector cells: osteoblasts and osteoclasts. Recent research has demonstrated functionally coupled gap junctions between osteocytes, themselves, and osteoblasts (Yellowley et al., 2000), supporting the hypothesis that osteocytes appraise mechanical signals and regulate bone adaptation (Mullender and Huiskes, 1997).

The aging effects on osteocytes include a reduction in the density of lacunae and number of osteocytes and decreased ability of the surviving cells to respond to biochemical and mechanical stimuli (Pearson and Lieberman, 2004). Concurrent with these aging changes is the accumulation of microcracks in bone, rendering the bone prone to fracture.

Bone Lining Cells

Bone lining cells (BLC) are quiescent osteoblasts that "escaped being buried by newly formed bone and remained on the surface when bone formation ceased" (Martin et al., 1998, p. 48). These cells flatten against the bone surface, maintaining communication with osteocytes and each other with gap-junctioned processes, while maintaining receptors for parathyroid hormone, estrogen, and paracrine signaling. The BLCs are thought to be part of a system responsive to chemical and mechanical stimuli, responsible for mineral transfer (Martin et al., 1998), and may activate bone (re)modeling to deposit or resorb bone according to strain levels (Martin, 2003). Mullender and Huiskes (1997, p 527) examined regulatory computer models for whether BLCs could potentially regulate bone remodeling in cancellous bone by

themselves, without input from osteocytes. They concluded "that mechanical information at the bone surface may not be sufficient to adequately regulate functional bone adaptation."

Osteoclasts

Osteoclasts are derived from a fusion of multiple (10-20) hematopoietic precursor cells (mononuclear phagocytes) originating in the bone marrow (Boyle, 2003). As part of the macrophage lineage, these cells differentiate at or near the bone surface and function to resorb bone. The activated osteoclasts (osteoclastogenesis) adhere to bone by a ruffled surface which creates a seal (Teitelbaum, 2000), allowing bone resorption to occur from the effects of decreasing the local pH (H_2CO_3) and from the secretion of various anti-collagen proteolytic enzymes.

Osteoclast differentiation and function is regulated by at least 24 known genes, including those encoding tartrate-resistant acid phosphatase (TRAP), cathepsin K (CATK), calcitonin receptor, and the β_3-integrin (Boyle et al., 2003). Two hematopoietic factors are necessary and sufficient for osteoclastgenesis and maturation: TNF-related cytokine RANKL and the polypeptide growth factor CSF-1 (colony-stimulating factor-1).

Regulation of osteoclast transcription includes important molecules synthesized by osteoblasts (and other cells). Two important molecules are RANK/RANK-L and osteoprotegerin (OPG). Osteoclastogenesis and bone resorption are coordinated by the RANKL/RANK/OPG regulatory axis (See Boyle et al., 2003 for review). RANK-L (cytokine) and RANK (transmembrane signaling receptor) are required for osteoclast

differentiation, activation, and bone resorption. OPG (soluble protein) blocks osteoclast formation, bone resorption, and induces apoptosis by acting as a decoy receptor and blocking RANKL binding to its cellular receptor RANK. OPG over-expression blocks osteoclast production resulting in osteopetrosis. OPG deletion results in enhanced bone resorption and osteoporosis. "Expression of RANKL and OPG is therefore coordinated to regulate bone resorption and density positively and negatively by controlling the activation state of RANK on osteoclasts" (Boyle et al., 2003, p.338). Additional stimulators of osteoclast function are PTH; 1, 25 $(OH)_2$ vitamin D; thyroid hormone; glucocorticoids; IGF-1, and BMP-2 and -4. Additional inhibitors of osteoclast function are calcitonin, nitric oxide, gonadal steroids, and interleukin-1 and -6 (Boyle et al., 2003).

The effect of aging on osteoclasts is usually framed in terms of adult skeletal disease (osteoporosis, periodontal disease, rheumatoid arthritis, multiple myeloma, and metastatic cancers) in which there is evidence for excess osteoclastic activity, leading to an imbalance in bone remodeling which favors resorption (Duong and Rodan, 2001). Specific age-related metabolic changes in these cells have not been identified (Boyle et al, 2003).

The strain stimulus responsible for osteoclastic activity and ultimately trabecular bone adaptation is likely to work through a regulatory system of soluble signals released by osteoblasts (bone lining cells) integrating these two cellular functions (osteoblast/osteoclast). Research is progressing rapidly in the direction of reconstructing the osteoclast signaling network and its role in bone (re)modeling,

density, maintenance, and adaptation (e.g., Martin et al., 1998; Martin, 2003; Mullender and Huiskes, 1997).

SKELETAL BIOLOGY: (RE) MODELING

Bone is composed of four skeletal envelopes on which modeling and remodeling occurs: the trabecular, endosteal, periosteal, and Haversian surfaces (Martin et al., 1998). The effects of the modeling and remodeling processes differ at each surface. Although this project is focused on trabecular bone, a general description of (re)modeling and the instrument of remodeling, the basic multicellular unit (BMU) follows.

General Definitions: Modeling and Remodeling

Modeling is "the principle mode of bone cell coordination in the growing skeleton" (Parfitt, 2003, p. 4). During ontogeny, bone is formed in one location and resorbed in another to accommodate the changes of bone size and shape. This is orchestrated by the combination of genetic, systemic biological, and local mechanical factors. As bones grow in length and width, the result of endochondral ossification and periosteal intramembranous bone apposition, they are sculpted by periosteal and endosteal resorption at different locations (Martin et a., 1998).The modeling process involves independent actions of osteoblasts and osteoclasts. The periosteal envelope is especially active in the modeling process during ontogeny and to a much lesser extent during adult life. It is responsible for increasing bone diameter. This redistribution of

bone is a relatively continuous process resulting in a net gain in bone mass (Parfitt, 2003) corresponding to the increase in body mass during growth and development. The rate and extent of modeling is greatly reduced after skeletal maturity.

The end result of the modeling process is skeletal shape, architecture, and mass appropriate to biological and mechanical requirements. Examples include tibial metaphyseal "cut-back," diaphyseal enlargement or drift, and cranial re-shaping to accommodate increase in brain size. The mechanical control of this growth and adaptation process is thought to be explained by the osteoblast-osteocyte-bone lining cell signal transduction syncytium responding to increased strain in the local matrix triggering bone formation or resorption until the strains are normalized (Huiskes et al., 2000; Sommerfield and Rubin, 2001).

Bone remodeling (bone maintenance) is the "mechanism of bone replacement in the vertebrate skeleton" (Parfitt, 2002, p.5). This process is characterized by the sequentially synchronized "coupled" actions of osteoclasts and osteoblasts (activation-resorption-formation) occurring on the same surface. Remodeling, continuing throughout life, generally does not affect the size and shape of the bone, but a net bone loss may result. Remodeling is a process occurring on the Haversian, trabecular, and endosteal envelopes. Bone replacement is initiated by osteoclastic resorption followed soon after by osteoblastic formation. The temporary, cyclic anatomic structure responsible for this process has been named the basic multicellular unit (BMU) by Frost (1969) (see also Parfitt, 2002). This will be discussed in the following section.

Bone remodeling has three apparent purposes: (1) its metabolic function provides a mechanism to maintain calcium homeostasis by promoting the exchange of calcium ions at the bone surface (Martin et al., 1998); (2) its structural function provides a mechanism for skeletal adaptation to the mechanical environment; and (3) its maintenance function provides a mechanism to repair fatigue damage created in bone by repetitive cycles of mechanical loading (Burr, 2002). It is argued that the "main purpose of remodeling is to prevent degradation of function (microdamage) as bone becomes older" (Parfitt, 2002). The load bearing function of bone is threatened by the accumulation of fatigue microdamage which is targeted for remodeling (Burr, 2002).

Basic Multicellular Unit (BMU)

Remodeling is carried out by a cyclic, temporary anatomic structure: the BMU. These anatomical units are most readily identified in cortical bone (osteonal). They have also been described in cancellous bone (hemi-osteonal) (Parfitt, 1994). Parfitt argues that BMUs in cancellous bone "travel across the surface digging a trench rather than a tunnel, but maintaining its size, shape and individual identity by the continuous recruitment of new cells, just as in cortical bone" (Parfitt, 1994, p.273).

A fully developed BMU consists of a team of osteoclasts forming the cutting (hemi) cone, a team of osteoblasts behind forming the closing cone, some form of vascular supply, and associated connective tissue (Parfitt, 1994). The capillary in cortical bone or specialized sinusoid in cancellous bone (Melsen, 1995) is at the heart of the BMU, ideally situated to coordinate the coupled functions activation, resorption,

and formation (Parfitt, 2000). Preosteoclasts, originating in the bone marrow, arrive at the resorption site via the circulation. The individual differentiated osteoclasts are short-lived (12 days), turning over at a rate of eight percent per day. Osteoblasts from precursors in the local connective tissue, refill the resorbed bone at each successive cross-sectional location, maintaining three-dimensional organization. Some of the osteoblastic team become buried as osteocytes, some die (average life span is measured in weeks), and some become relatively quiescent bone lining cells. The BMU exists and travels in three dimensions, excavating and refilling a trench in cancellous bone of 2000μm at about 10μm/day for 100 days, while maintaining the proper spatial and temporal relationships among its cellular elements (Parfitt, 1994).

The life span of the BMU has a beginning (origination), middle (progression), and end (termination). Its duration in cancellous bone is approximately three months. The origination is described as beginning on a small area of quiescent bone surface and involves digestion of the endosteal membrane by enzymes released from lining cells. These changes in lining cell morphology expose the mineralized bone surface. The process of neoangiogenesis provides the capability for the egress of circulating mononuclear osteoclast precursors at precisely the correct location. Their attraction to the region of exposed mineral and subsequent fusion to form osteoclasts allows the assembly of a sufficient number of osteoclasts to form the cutting (hemi)cone (Parfitt, 2002). Progression is travel in a particular direction for a particular time. Constant re-supple of osteoclast precursors is necessary. At termination the BMU stops moving forward, the supply of osteoclast precursors is turned off, and refilling by osteoblasts is

completed. BMU remodeling can function in two modes: (1) the conservation mode in which the completed BMU has resorbed and formed equal amounts of bone; and (2) the disuse mode, in which the completed BMU forms less bone than has been resorbed, resulting in net bone loss (Frost, 2003).

Activation frequency is a two-dimensional concept of the overall intensity of bone remodeling. It has recently been re-defined as the conversion of a region of bone surface from quiescence to remodeling activity (Parfitt, 2002). As applied to cancellous bone it refers to the probability that a new cycle of remodeling will be initiated at any point on the surface (Parfitt et al., 1987). This index incorporates both the birthrate of new BMUs and the average distance that each one moves.

The BMU remodeling process is thought to have targeted and nontargeted components (Burr, 2002). Parfitt (2002) and Burr (2002) have recently summarized concepts: (1) some remodeling is targeted for the replacement of fatigue-microdamaged bone; and (2) a substantial amount (70%) of total remodeling is not targeted for this specific purpose. Non-targeted remodeling is surplus to load-bearing issues, provides a margin of safety, and may have several purposes or mechanisms: (1) removal of hypermineralized bone; (2) initially targeted BMUs may overshoot their target; and (3) stochastic BMU origination. Many unsolved issues exist, especially as related to the signaling mechanisms for bone remodeling. Advances in analytical technology are contributing to recent refinements in bone remodeling theory.

DEVELOPMENTS IN BONE REMODELING THEORY

General Model

The concept that bone remodeling is controlled by mechanical as well as metabolic influences has been subject to intense study in recent years. Current consensus focuses on four fundamental observations or hypotheses. First, bone is thought to contain sensor cells monitoring mechanical strain (or other load-related variables), comparing these levels to a physiologically desirable range, and activating biological processes if necessary to bring the sensed variable back inside the acceptable range (Frost, 1987, 1989). This concept assumes that bone remodeling removes bone when the mechanical stimulus is too low and adds bone if the stimulus is too high (Carter and Beaupre, 2001; Martin, 2000). Second, osteocytes have been identified as possible bone mechanosensing cells producing a signal proportional to strain on bone surfaces by sensitivity to ion channels, interstitial fluid flow, electrical signals, or other perturbations (Mullender and Huiskes, 1997).

The third key concept is that osteocytes sense fatigue damage and transmit signals to activate remodeling and remove the damage. Research has been focused on cortical bone showing that increased activation of remodeling is associated with microdamage (Burr, 2002). “It is generally assumed that the same is true in cancellous bone” (Martin, 2000, p.1). The fourth hypothesis suggests that cells of the osteoblast lineage control the initiation of remodeling. The bone lining cells are thought to be

responsible for activating BMUs in response to osteocytic signals or hormones. These four concepts are the foundation for a current general model of bone remodeling.

Mechanostat

The modern offspring of Roux's concept of a biological control process (Roesler, 1987) is Frost's mechanostat theory (1987, 1989). This theoretical construction holds that local strains regulate bone mass, in the same way that the local temperature in a room regulates the heater through a thermostat (Frost, 1987). The basic multicellular units maintain local bone mass controlled by a mechanical feedback loop and a set point, which is the threshold setting for the balance between strain and bone formation/resorption. Frost emphasizes this is a biologically-mediated process regulated by mechanical loads. Relevant to this current research, Frost and Jee, (1994a, b) have applied this model directly to the endochondral ossification process during ontogeny.

Frost's mechanostat theory is credited with distinguishing between modeling and remodeling. The theory is built on the premise that disuse and overload have opposite effects on these two processes. Disuse activates remodeling, but inhibits formation mode modeling, leading to bone loss. Overload inhibits remodeling and activates formation mode modeling, leading to bone gain. Presented in this way the initial mechanostat model is at odds with the general model described above, ignoring the activation of remodeling in response to tissue overload and fatigue damage. Experimental data indicates that remodeling is elevated when strains are either excessively low, or so excessively high that damage occurs.

The fully elaborated form of Frost's mechanostat theory accounts for these concerns (Burr, 1992). It holds that bone adapts by different biological processes within four mechanical usage windows defined by minimum effective strains for activating adaptive processes, called setpoints (Frost, 1987). Remodeling, which removes or conserves bone, is activated by reduced mechanical usage in the "trivial loading zone" or by microdamage in the "pathological loading zone." Remodeling is suppressed in the "physiological zone."

Modeling, which can add bone (cortical and trabecular), reshapes surfaces by resorption or lamellar formation drift and is activated by increased mechanical usage in the "overload zone." It remains quiescent within or below the physiological zone. The threshold loads for activation (setpoints) of these processes may be influenced by various systemic, hormonal, or local factors. For example, the theoretical *perceived* upward shift of the remodeling setpoint is thought to be associated with the loss of estrogen, resulting in activated remodeling and bone loss. Experimental research has provided examples of bone adaptation in adult animals consistent with the mechanostat theory (Jee, 1990, 1991).

Frost has significantly contributed to the increasing awareness of mechanical factors in the regulation of bone (re)modeling and repair. Recent advances in large-scale computer simulation are driving research towards integrated quantitative models attempting to explain the morphological/biological phenomena in bone. Striving for a unifying paradigm, Martin proposes a theoretical approach, "assuming that the

[osteocytic] signal inhibits rather that stimulates remodeling" (2000, p.2). Huiskes et al. (2000) have developed a unified self-regulating model.

Inhibitory Theory of Bone Remodeling

The concept of an inhibitory osteocytic signal is derived from research suggesting that osteocytes send inhibitory signals to nearby osteoblasts to slow the production of osteoid allowing contact with the bone surface to be maintained (Marotti, 1996). Martin (2000) hypothesizes that "this inhibitory osteocytic signal is identical to that which others have hypothesized to be produced by mechanical loading" (2000, p.2). Bone lining cells activate remodeling unless inhibited by the osteocytic signal. In this system, activation of remodeling is increased when the generation or transmission of the inhibiting signals are diminished. Examples are a disuse state (reduction of strain-generated signal), mechanical damage (interrupting signal transmission); osteocyte apoptosis (interrupting signal generation), and hormonal alteration of signal generation, transmission, or interpretation. Martin (2000) argues that the essential point of his hypothesis is its "unifying nature." He states it accounts for a common signal to guide osteoblasts into bone matrix as osteocytes, gauges mechanical load and microdamage, and signals bone lining cells to remove/replace bone tissue.

Unified Trabecular Bone Paradigm

The "third method of science" is the application of large-scale computer simulation, after "theory" and "empiricism" (Kelly, 1998). This approach has been used to model a self-regulatory paradigm for cancellous bone adaptation and maintenance (Huiskes et al., 2000). Trabecular architecture emerges as an optimal

mechanical structure adapted to alternative external loads during modeling and remodeling. The central focus of this theory is to provide a framework for investigative computational explanation of the "effects of mechanical forces on trabecular bone morphogenesis, maintenance and adaptation by relating local mechanical stimuli in the bone matrix to assumed expressions of the cells actually involved in bone metabolism' (Ruimerman et al., 2005).

Bone remodeling involves the formation of cavities by osteoclasts and the subsequent filling of these cavities by osteoblasts. The coupling factor between these two cellular functions in remodeling is mechanical, as it is in modeling. Modeling is thought to be under the control of external forces changing the strains in the mineralized bone at large, while remodeling resorption cavities have a similar strain-enhancing effect locally. Huiskes and co-authors state, "modeling and remodeling could both be described as being governed by strain perturbations, be they generated externally by the load or internally by resorption cavities" (2000, p.704). Osteoclastic resorption cavities weaken their trabecula, causing a local elevation of strain, perceived by osteocytes. Osteoblasts are then recruited by the osteocytes to form bone.

This cancellous bone regulatory model involves several key points which have been discussed previously in different contexts. First, the mechanical variable that triggers feed-back from external forces to bone metabolism is a typical strain-energy density (SED) rate in the bone as produced by recent loading history. The SED includes loading rate, frequency, and amplitude. Interestingly, relatively few loading cycles per day are required to maintain bone mass (Huiskes et al., 2000). Second,

osteocytes respond to loading in their local environments producing a biochemical messenger in proportion to the typical SED rate. Third, the biochemical signal creates an osteoblastic recruitment stimulus as long as it is above a threshold value. The model links the bone formation stimulus to the SED rate, modulated by osteocyte mechanosensitivity and distance attenuation. Fourth, the probability of osteoclast resorption is regulated by either the presence of microcracks within the bone matrix or by disuse.

Osteoclasts are activated by cytokines produced by osteoblasts, including bone ling cells (RANK/RANKL/OPG). The activation process may originate from an osteocyte signal. This theory now merges with Martin's inhibitory concept in assuming that the osteocytic network normally suppresses osteoclast activation while transporting signals to the surface through mechanical loading. Disuse hampers suppression by reducing the inhibitory signal; microcracks hamper suppression by disconnection of the canaliculi. Parameters in the model can be linked to various metabolic factors.

Iteration of the computer simulation starting with a generic regular grid obtains homeostatic trabecular architecture. In homeostasis, the remodeling process continues to renew bone without altering mass or architecture generally. When the external load applied to the homeostatic architecture was rotated 30 degrees, the trabeculae gradually assumed a reorientation aligned with the load (demonstration of Wolff's Law). Reduced load reduced trabecular thickness; increased load increased bone mass; a new homeostatic configuration resulted. Huiskes et al. argue that the mechanical feedback

model is a “potent and stable regulator of the complex biochemical metabolic machinery towards lasting optimality of form” (2000, p.706). Large-scale finite element modeling (Ruimerman et al., 2005) confirms 19th century speculation for a self-regulating biological system of cancellous bone adaptation (Roux, 1881) and trajectorial architecture (Wolff, 1892).

NUTRITIONAL INFLUENCES: CURRENT CONCEPTS

The nutritional environment is accommodating to skeletal development. That is, enough is good enough. There is no indication that an excess of nutrients will result in greater bone development (other than an indirect effect associated with increased body weight) (Bass et al., 2005). The most significant effect of nutrition on bone development (trabecular and cortical) is when there is a state of deficiency of nutritional status. Nutritional status is the balance between nutrient-energy intake and nutrient-energy requirements. The immediate effect of malnutrition in children is reduced longitudinal growth. The longer term effect is bone loss due to increased endosteal resorption and trabecular thinning (Bass et al., 2005). Nutrient deficiencies documented to lead to skeletal growth disturbances, and for which the requirements are known are: energy, protein, calcium, iron, zinc, vitamin D, and vitamin A (Berti et al., 1998).

Nutrition influences skeletal development (linear growth and bone density) indirectly through hormone systems, namely sex steroids, thyroid hormone, growth

hormone (GH), and insulin-like growth factor-1 (IGF-I). In terms of the trabecular bone envelope, total energy, protein, and calcium are key nutrients. In animal models, protein and caloric restriction results in reduced linear growth, cortical thinning, and *trabecular wasting*. This is associated with a disruption in the sex steroid and GH-IGF-axes inducing osteoblast resistance to IGF-I in both the cortical and trabecular bone envelopes (Bourrin et al., 2000).

Human studies agree with the animal models, demonstrating that an energy deficit and protein deficiency both lead to an apparent reduction in bone formation and an increase in bone resorption (Cooke and Zanker, 2004). In the growing skeleton, these result in retarded longitudinal growth, less trabecular bone accrual, and decreased trabecular bone density. The biochemical pathway by which energy and protein malnutrition influence bone growth and development is thought to be by suppressing IGG-I levels or the bone cells' sensitivity to IGF-I (Bourrin et al., 2000). This reduces bone formation. In addition to affecting the GH-IGF-I axis, these deficiencies, when severe, are also associated with imbalances in the sex steroid axis, namely estrogen deficiency or resistance (Ammann et al., 2000). This increases bone resorption. A contributing factor, in the context of energy and protein deficiencies, may be reduced mechanical loading associated with reduced muscle mass, body weight, and physical inactivity (Bass et al., 2005).

Calcium is important to skeletal growth and tissue mineralization. It is commonly thought to be a key determinant for maximizing bone density during growth. Fortunately, bone density appears to be maintained across a broad range of

dietary calcium intakes, until a variable physiological threshold is reached. Reduced calcium intake has not been found to influence bone growth and development to the same degree as energy and protein malnutrition (Bass et al., 2000). Calcium supplementation has been associated with increased bone density. However, a recent review of dietary calcium intake-related studies suggests that the *independent* effect of calcium supplementation in children has not been verified (Lanou et al., 2005).

BIOMECHANICS OF TRABECULAR BONE

This section reviews current research and concerns of trabecular bone biomechanics. But first, what is the difference between biomechanics and mechanobiology? Is this simply a term inversion? Van der Meulen and Huiskes (2002) address this point exceptionally well in their article based on a European Society of Biomechanics keynote lecture in 2000. To quote, biomechanics can be defined as "the science that studies the effects of forces on biological tissues, organs and organisms, in relation to biological and medical problems" (ESB, 1978). Mechanobiology, the inverse, shifts the emphasis from mechanics to biology, studying how "load-bearing tissues are produced, maintained, and adapted by cells as an active response to biophysical stimuli in their environment" (van der Meulen and Huiskes, 2002).

Mechanobiology emphasizes the processes behind "form follows function." Given this focus, what does function follow? In the evolutionary sense, function follows form through the process of natural selection. This results in a biological

ostinato, “form follows function follows form…” Within this repetitive phrase, biomechanics of skeletal adaptation studies form following function; mechanobiology of skeletal adaptation studies how function determines form (van der Meulen and Huiskes, 2002).

Mechanical behavior of trabecular bone

Returning to the mechanics perspective of trabecular bone, it is described as a complex, highly heterogeneous material with substantial variations of strength and elastic modulus within and across anatomic sites affected by aging, disease, and density (Keaveny et al., 2001). Current research interests focus on two broad areas: the characterization of mechanical properties based on trabecular bone composition and microstructure and the role of trabecular bone micro/macro damage in fracture risk and remodeling.

Trabecular tissue material itself is morphologically similar to cortical bone. That is, it is an anisotropic composite of hydroxyapatite, collagen, water, and other proteins. It is arranged in “packets” of lamellar bone (Keaney et al., 2001). The components of heterogeneity of structure are thought to be responsible for wide variations in mechanical properties of cancellous bone, including variations in volume fraction, microarchitecture, and tissue properties. When discussing the specifics of mechanical properties, age, site, and disease need to be explicitly designated (Goldstein et al., 1983). This is a key concept of trabecular bone biomechanics.

Trabecular bone is anisotropic in material direction and trabecular architecture. The principle structural direction and degree of anisotropy are important components

of cancellous bone analysis. Recent advances in micro-imaging and computational techniques have lead to the development of a quantitative 3D visualization of the anisotropy in trabecular bone providing the opportunity to gain additional insights from this type of data (Ketcham and Ryan, 2004). The variation in the combination of bone volume fraction, trabecular orientation, and degree of anisotropy provides explanation for up to 94% of trabecular elastic behavior. Cancellous bone strength depends on the same variables with the additional factor of differences in relation to load type (asymmetry in tension versus compression versus shear). Interestingly, despite all this complexity, the strain-based description of failure trabecular bone is linear and relatively uniform (Kopperdahl and Keaveny, 1998). Carter and Hayes (1977) published key data, contributing to the foundation for understanding the relationships between trabecular bone strength and stiffness and apparent bone density. Their investigation found that the compressive strength of trabecular bone was proportional to the apparent density squared, and that the compressive stiffness was proportional to the apparent density cubed.

Gibson (1985) advanced the understanding of the mechanical behavior of trabecular bone by investigating the mechanisms of deformation. He modeled cancellous bone as a porous network of interconnecting rods and plates (cells). Gibson described three regimes of behavior within the stress-strain curve of cancellous bone with increasing compression: linear elastic bending, cell wall failure, and collapse of the cell walls onto one another. His work contributed to the understanding of how

trabecular mechanical properties (stiffness and strength) depend on structural conditions, such as relative density, cell wall properties, and geometry.

Multiaxial and whole bone failure behavior is important clinically (falls, trauma, implant interfaces). The importance of the combination of both cortical and trabecular bone morphology and density to predict bone apparent stiffness, strength, and possible fracture risk has been recently investigated in an *in vivo* study using a newly developed high resolution quantitative computed tomography scanner (MacNeil and Boyd, 2007).

Trabecular damage

Damage and repair of individual trabeculae is recognized as a normal physiologic process with important implications in osteoporotic fracture risk, stimulus for remodeling, and osteoarthritis. Damage can range from macro to the nanometer scale of collagen and hydroxyapatite. Recently, large-scale finite element models have been used to study the failure properties of trabecular bone related to the accumulation of damage from overloads, fatigue, or creep loading (Niebur et al., 2000). These types of studies will form the basis for addressing possible strain-specific biological responses to damage in bone, an important issue in understanding the mechanobiology of trabecular bone (Burr et al., 1997).

This section has provided a glimpse of the substantial body of current knowledge about trabecular bone mechanics. The multidisciplinary approach combining sophisticated experimental-computational techniques with advances in

molecular/cellular biology is poised for continued success in addressing the complexities for trabecular/cancellous bone tissue (Keaveny et al., 2001).

SUMMARY

The study of trabecular bone adaptation is part of an incredibly dynamic broad-based scientific interest in skeletal form and function. Advances in genomics, cellular, and molecular biology have combined with finite element computer simulation and micro-imaging techniques to make visible the previously invisible, make knowable the previously unknowable, and make the previously inaccessible accessible. This chapter presents current concepts and theoretical models concerned with trabecular bone skeletal biology.

The initial architecture of trabecular bone in the metaphyseal region of human long bones reflects the organization of the growth plate and the endochondral process. This is a columnar trabecular pattern oriented perpendicular to the growth surface. The newly formed cancellous bone is quickly (re)modeled, resulting in changes in local bone density, orientation, and architecture. A summary of the current understanding of the trabecular bone modeling/remodeling process is that it is closely influenced by the local loading environment. A mechanotransduction system monitors mechanical strain-related variables within bone and compares these levels to a physiologically desirable range. Biological processes are activated, if necessary, to bring the sensed variable back inside the acceptable range (Frost, 1987, 1989) by bone formation and/or

resorption. Developing trabecular bone is patterned by the combination of biological factors (decreasing in influence with age) and ongoing mechanically-directed modeling/remodeling. This results in an internal trabecular structure for which the distribution of bone density and architecture is closely matched to its customary mechanical loading environment (Wolff, 1892).

The application of a multidisciplinary approach for examining all aspects of skeletal adaptation offers great promise to the broad field of anthropology, helping to unravel the mysteries of growth and development, behavior, health, and lifestyle of ancient human populations through their skeletal remains. The current ontogenetic research utilizing the juvenile skeletal remains from SunWatch Village is a small step in this direction.

CHAPTER 3

CULTURAL BACKGROUND: FORT ANCIENT AND SUNWATCH VILLAGE

CULTURAL HISTORY

Early populations of the Upper and Middle Ohio Valley are divided into five temporal periods and cultural traditions (Sciulli and Oberly, 2002; Abel et al., 2000): Paleoindian (ca. 10,000- 4000 BC), Archaic (ca. 4000- 1000 BC), Woodland (ca. 1000 BC- AD 900), Late Prehistoric (ca. AD 900- 1400), and Protohistoric (AD 1500-1700). The skeletal record becomes available in the Late Archaic, when the elaboration of burials appears archaeologically visible. The Upper and Middle Ohio Valley encompasses areas of Pennsylvania, West Virginia, Ohio, and Kentucky. This region includes the hilly, western portion of the unglaciated Appalachian plateau to the glacial till plains of central and western Ohio. Five different ecozones are described for this region: Great Lakes, Lake Plains, Till Plains, Glaciated Appalachian Plateau, and Unglaciated Appalachian Plateau (Kozarek et al., 1994). The topography ranges from narrow upland valleys with lower fertility, low-calcium soil in the Unglaciated Plateau

to broad river valleys in the Till Plains with fertile high-calcium soil (Sciulli and Oberly, 2002). This is a deciduous environment, ecologically diverse and resource rich.

The Archaic phase (ca. 4000- 1000 BC) is characterized by mobile populations, increasing in size, and expanding throughout the region. Archaeological evidence from seasonal habitation sites and burials in this region during the Archaic phase indicates that subsistence was based primarily on hunting, fishing, and gathering, possibly combined with the inclusion of some domesticated native plants (Smith, 1989). Lithic analysis suggests four general settlement types, namely large and small occupations, chert processing sites, and food procurement/processing sites. The annual subsistence cycle is one of repetitive land-use, involving larger spring and summer riverine or lacustrine settlements and smaller interior fall and winter hunting camps (Lepper, 1988).

Settlements in the Late Archaic phase (ca. 1000 BC) were used by increasingly larger populations on a repeated seasonal basis, burying their dead in distinctive but diverse cemeteries. The Late Archaic burials were frequently marked by mounds of earth and may contain grave goods including red ochre, grooved axes, atlatls, and objects made of precious materials (copper, marine shell). These mortuary complexes are known as “Glacial Kame” along western Lake Erie and “Red-Ochre” in southern Ohio (Sciulli and Oberly, 2002).

Early Woodland populations exhibit biocultural continuity with the preceding Late Archaic groups. Increasing elaboration of mortuary practices (burial mounds) was

a characteristic change, culminating in the Hopewell phase of the Middle Woodland. The Middle Woodland settlement pattern is considered to have been a dispersed system of hamlets with central ritual precincts characterized by mounds and earthworks (Dancy, 1994). This more sedentary lifestyle was associated with an increased reliance upon what are known as Eastern Agricultural Complex crops (Smith, 1989). The term Eastern Agricultural Complex refers to the group of plants that originally formed the basis of agriculture in the eastern regions of North America north of Mexico. These plants included squash (*Cucurbita pepo*), goosefoot or lambsquarter (*Chenopodium berlandieri*), sumpweed or marshelder (*Iva annua*), and sunflower (*Helianthus annuus*) (Gremillion, 2004). The morphological characteristics of the seeds and fruits of these plants suggest manipulation by human management. Other plants (maygrass, *Phalaris caroliniana*; knotweed, *Polygonum erectum*; and giant ragweed, *Ambrosia trifida*) found in archaeological contexts suggest cultivation, but do not have the morphological changes consistent with domestication (Gremillion, 2004). These native seed crops are thought to have formed the basis for what Smith (2001) has termed a "low level food production" economy.

The Late Woodland phase (ca. AD 600- 800) continued the same subsistence practices as the Middle but the settlement structure, material culture, and ritual activity (more village-focused) changed substantially. The archaeological record demonstrates larger, sometimes fortified settlements with or without organization around central plazas (Sciulli and Oberly, 2002). Habitation sites, consisting of family-related groups expanded from the riverine into the uplands. The bow-and-arrow gained predominance

in the Eastern Woodland by AD 600. Increased hunting activities, intergroup competition/violence (Seeman, 1992), and further reliance on maize agriculture (Kelly, 1990a, b) occurred during this period.

The Late Prehistoric period of the Ohio Valley, beginning around AD 900 is marked by a subsistence shift centered on intensive maize agriculture and other tropical domesticates (beans, cucurbits, etc.). The cultural correlates are large fortified villages located on major drainages, sedentary aggregated populations, and maize dependency. This phase is characterized by five parallel, geographical, indigenous cultural traditions consisting of Fort Ancient in the south and southwestern areas, Sandusky in the north close to the south shore of Lake Erie, Monongahela and Belmont in the unglaciated east, and Whittlesey in the northeast (Sciulli and Oberly, 2002). Regional population packing was evident in areas of diverse wild resources and potentials for intensive maize production. Settlements typically consisted of large fortified villages with associated cemeteries, located in major river valleys.

The Sandusky Tradition is a cultural manifestation in North Central Ohio, along Lake Erie drainages, continuing from a Middle Archaic population base (Abel et al., 2000). The archaeological record demonstrates a mixed horticultural- collector seasonal subsistence cycle including intensification of maize agriculture. The increased sedentism and community nucleation are evident in spring, summer, and autumn fortified villages. Monongahela Tradition populations formed nucleated maize farming communities in adjacent regions of Ohio, northern West Virginia, and southwestern

Pennsylvania. Their circular dwellings are associated with silo-like storage pits. They are built around a central plaza with or without a fortified palisade. Fort Ancient populations consolidated along the main trunk and tributaries of the Ohio River. These groups were river-edge agriculturalists living in nucleated, planned year-round villages (Carskadden and Morton, 2000). The Fort Ancient culture (SunWatch) is described as "transegalitarian," having a stable subsistence for 750 years consisting of intensive maize/bean agriculture supplemented by hunting deer, bear, elk, and turkey (Pollack and Henderson, 2000).

FORT ANCIENT

The term *Fort Ancient Culture* is shrouded in misunderstanding. Coined by William C. Mills (1906), it was used initially to refer what is now known to be a Middle Woodland hilltop enclosure in southern Ohio. Working at South Fort Village, Mills (1906, p. 135-136) defined Fort Ancient Culture as a "pre-Columbian way of life represented by established homes, developed agriculture, stored food, and intertribal trade" (Cook, 2004, p. 31). Archaeological investigators in the earlier 1900s had concluded that Fort Ancient settlements were lower on the cultural evolutionary scale and thus preceded the more elaborate Hopewell groups (Moorehead, 1908). It was not until the 1930s that stratigraphic analyses demonstrated that Hopewell people preceded Fort Ancient.

James B. Griffin's 1943 publication, *The Fort Ancient Aspect*, is the seminal study on the Fort Ancient culture. Griffin's study defined the initial classification of

Fort Ancient and has influenced all subsequent investigations to a greater or lesser degree. The format and title of Griffin's descriptive analysis utilized the Midwestern Taxonomic System (McKern, 1939), which was developed to bring order to archaeological "chaos." This system developed four archaeological constructs based on groupings of shared attributes: component (single site), focus (closely related sites), aspect (series of foci), and phase (many aspects) (Cook, 2004). Griffin divided the Fort Ancient Aspect geographically (centered on river drainages) into four foci based on trait lists (primarily ceramic). Limitations of the work are considered to be the inclusion of relatively few sites, lack of a temporal dimension, and perhaps over-reliance on "intuitive judgment" (Henderson and Turnbow, 1992; Kennedy, 2000). For the purposes of this discussion, the terms Fort Ancient "aspect," "culture," and "tradition" will be used interchangeably.

Fort Ancient populations occupied the central Ohio Valley including southern Ohio, southeastern Indiana, northern Kentucky, and western West Virginia from roughly AD 1000 until European contact (Griffin, 1978). These groups were characteristically maize intensive agriculturalists, settled in permanent villages of several hundred individuals. The Fort Ancient settlements typically were established in alluvial settings with early Fort Ancient sites being distributed widely throughout the region; later sites became concentrated along the Ohio River. Figure 3.1 is a map of Fort Ancient sites which traverse three broad ecoregions, including the Western Allegheny Plateau, the Eastern Corn Belt Plains, and the Interior Plateau (Woods et al., 2000).

It may be argued that Fort Ancient is a regional concept within an environmentally diverse region. In spite of environmental and cultural heterogeneity, the Fort Ancient populations practiced a similar economy. It should be noted that the Fort Ancient "culture" (Griffin, 1943) does not represent a homogeneous unit. It is rather a regional grouping of autonomous village units responding to varied environmental, economic, and cultural circumstances. These villages have been characterized as maintaining a largely egalitarian social structure without evidence of social stratification and/or chiefdoms (Henderson, 1998; Schurr and Schoeninger, 1995). Varying degrees of Mississippian influences have been discussed (Henderson, 1998; Cook, 2004, 2007).

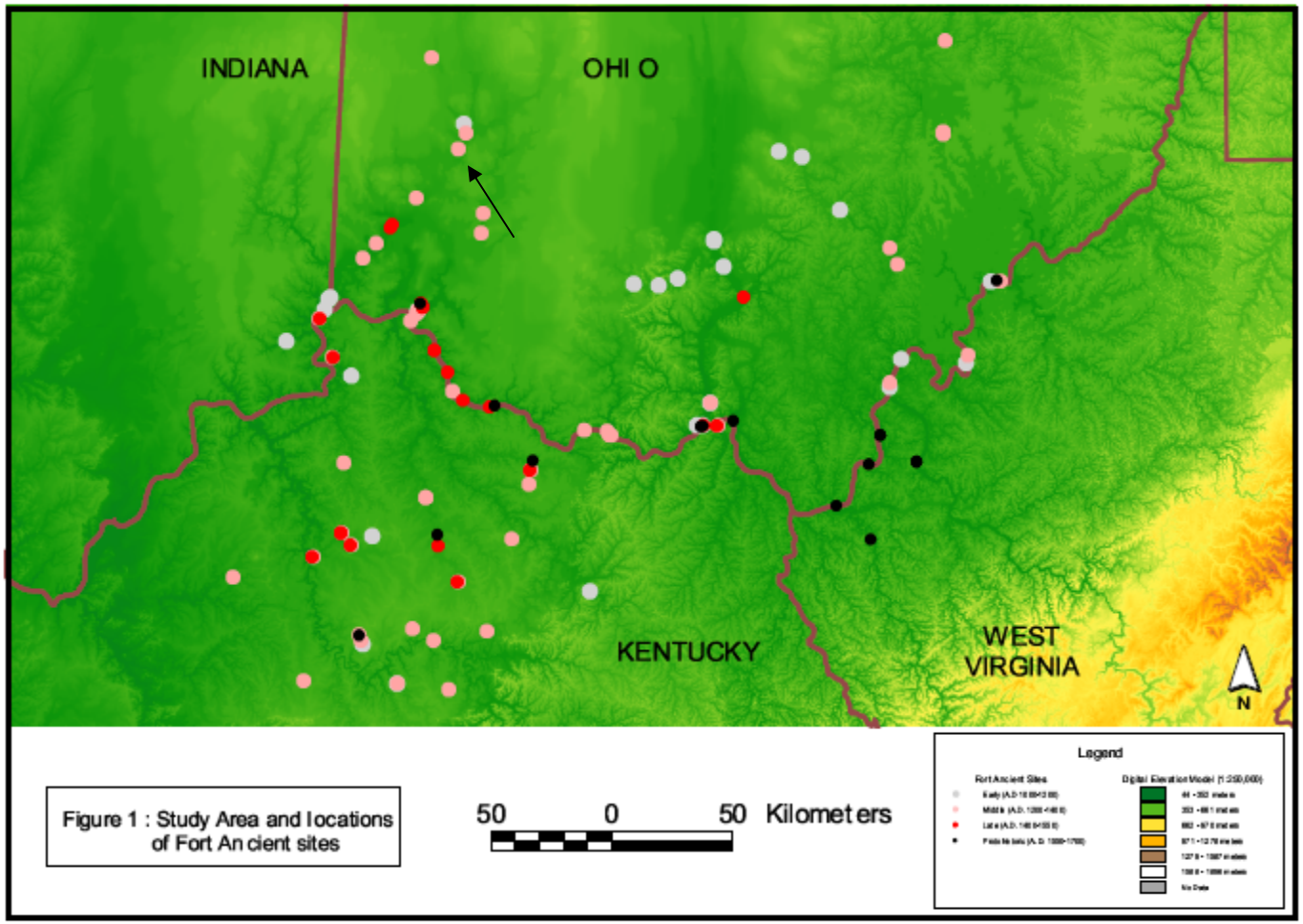

Figure 3.1 Map of Fort Ancient site regional distribution. SunWatch Village is marked by circle with a black arrow directed towards it (From Kennedy, 2000).

Numerous chronological divisions for Fort Ancient have been proposed over the past four decades as archaeological chronological control improved. The Griffin foci have been lumped and split into alternatively defined groupings with differing spatial and temporal extent. The term *Late Prehistoric*, used frequently in this research, refers to the entire duration of the Fort Ancient culture- AD 1000 to AD 1700. A useful, recent temporal taxonomy is:

- Early Fort Ancient: AD 1000-1200
- Middle Fort Ancient: AD 1200-1400
- Late Fort Ancient: AD 1400-1550
- Protohistoric: after AD 1550

Table 3.1 is a selective compilation of relatively current Fort Ancient taxonomonic terminology with source citations (Kennedy, 2000). Although the validity of some "phases" in this culture-historical scheme has been disputed, the organization of Fort Ancient culture into defined units has (and remains) the basis for current research and discussion.

Time	Phase	Geographic Coverage	Time Span	Source
Protohistoric (A.D. 1550-1700)	Montour	North central Kentucky	A.D. 1550-1750	Henderson et al. 1992
	Madisonville phase	West half Central Ohio Valley	A.D. 1400-late 1600s	Prufer and Shane 1970; Griffin 1978
Late (A.D. 1400-1500)	Madisonville horizon	Central Ohio Valley	post A.D. 1400/1450	Essenpreis 1988:9
	Clover phase	East half Central Ohio Valley	A.D. 1450-1650	Griffin 1978; Graybill 1981
	Gist	North central Kentucky	A.D. 1400-1500	Henderson et al. 1992
	Mariemont	Southwestern Ohio (lower)	A.D. 1450-1670	Cowan 1987
	Philo	Upper Muskingum River valley	A.D. 1250-1450	Gartley et al. 1976; Gartley 1977
	Elkhorn	Central Kentucky	A.D. 1200-1400	Sharp and Pollack 1992
	Manion	North central Kentucky	A.D. 1200-1400	Henderson et al. 1992
	Feurt (original definition)	South central and southeastern Ohio	A.D. 1250-1400	Prufer and Shane 1970
Middle (A.D. 1200-1400)	Feurt (redefined by Graybill)	South central and southeastern Ohio	A.D. 1050-1450	Graybill 1981
	Shoemaker	Southwestern Ohio (lower)	A.D. 1250-1350/1400	Cowan 1987
	Anderson	Southwestern Ohio (upper)	A.D. 1100-1400	Griffin 1943; Prufer and Shane 1970; Essenpreis 1982
	Blennerhasset	Eastern Ohio and northwestern West Virginia	A.D. 1250-1450	Graybill 1986
	Woodside	Eastern Kentucky and western West Virginia		Dunnell 1972
Early (A.D. 1000-1200)	Croghan	North central Kentucky	A.D. 1000-1200	Henderson et al. 1992
	Osborne	Central Kentucky	A.D. 950-1200	Turnbow 1988
	Baum, Baldwin, Brush Creek	South central and southeastern Ohio	A.D. 950-1250	Prufer and Shane 1970
	Turpin	Southwestern Ohio (lower)	A.D. 1000-1250	Cowan 1987
	Roseberry	Eastern Ohio and northwestern West Virginia	A.D. 1050-1250	Graybill 1986

Table 3.1 Compilation of Fort Ancient terminology (From Kennedy, 2000).

It is notable that Fort Ancient has come to be defined by a summation of variable constructs of material culture as a manifestation of adaptation within an environmentally diverse region. For the record, according to the schematic outline, SunWatch is a Middle Fort Ancient village of the Anderson phase located in southwestern Ohio.

The current understanding of Fort Ancient origins and development suggests a continuity with Late Woodland predecessors with a variable influence by Middle Mississippian groups (migration and/or interaction) (Henderson, 1998; Pollack and Henderson, 1992, 2000; Griffin, 1943; Prufer and Shane, 1970; Nass and Yerkes, 1995; Robertson, 1980). Cook (2004, 2007b) has recently investigated Fort Ancient as a peripheral Mississippian expression studying SunWatch "village structure and growth in relation to exposure to Middle Mississippian populations" (Cook, 2004, p. 8).

Archaeological data demonstrates an apparent temporary abandonment of the Ohio Valley by Fort Ancient groups between AD 1650 and AD 1750 (prior to direct European contact) marking an end to the Fort Ancient Aspect. It is unclear at this time, whether this was a process of decreasing population or decreasing archaeological visibility of settlement patterns (Pollack and Henderson, 1992). Subsequently, the historic Ohio Valley was occupied by groups moving [back] into the region, namely Huron (Wyandot), Shawnee, Delaware, and Seneca. The Shawnee have been proposed as the most probable historic group with connections to Fort Ancient, but this remains

a point of discussion (Griffin, 1943; Drooker, 1997; Henderson et al., 1992; Pollack and Henderson, 1992).

SUNWATCH VILLAGE: ARCHAEOLOGICAL ANALYSES

Site background

The SunWatch village is the type site for Middle Fort Ancient social structure and settlement form (Heilman et al., 1988; Drooker, 1997; Henderson and Pollack, 2001) in part due to its excellent preservation, coherency, and relatively short-term occupation. Radiocarbon dates support thirteenth century occupation (1250 A.D. ± 100 years) (Heilman et al., 1988; Cook, 2004). The social structure of the site is indicative of an autonomous village with kin-centered households organized in dual corporate organizations (possible clans) (Cook and Sunderhaus, 1999; Cook, 2004). Social integration is thought to have been achieved by way of a specified ritual area and Green Corn ceremonialism (Heilman et al., 1988).

Research has indicated a well-planned circular village organized around a red cedar center pole thought to be part of a solar alignment system (Heilman and Hoefer, 1981). Concentric circles of clusters of burials, storage pit structures, and houses emanate outwardly from the center pole, culminating in a stockade around the periphery (Figure 3.2). Visual inspection of structure and stockade relationships, posthole analysis, and radiocarbon dates suggest that the village was remodeled at least once. Current evidence suggests that SunWatch was occupied year around (Ramsey-

Styer, 1995; Wagner, 1996). SunWatch village provides archaeological data for the examination of Middle Fort Ancient settlement developmental patterns. In addition, SunWatch village provides well preserved juvenile skeletal remains allowing for the quantitative examination of trabecular bone developmental patterns, as exemplified by this dissertation research.

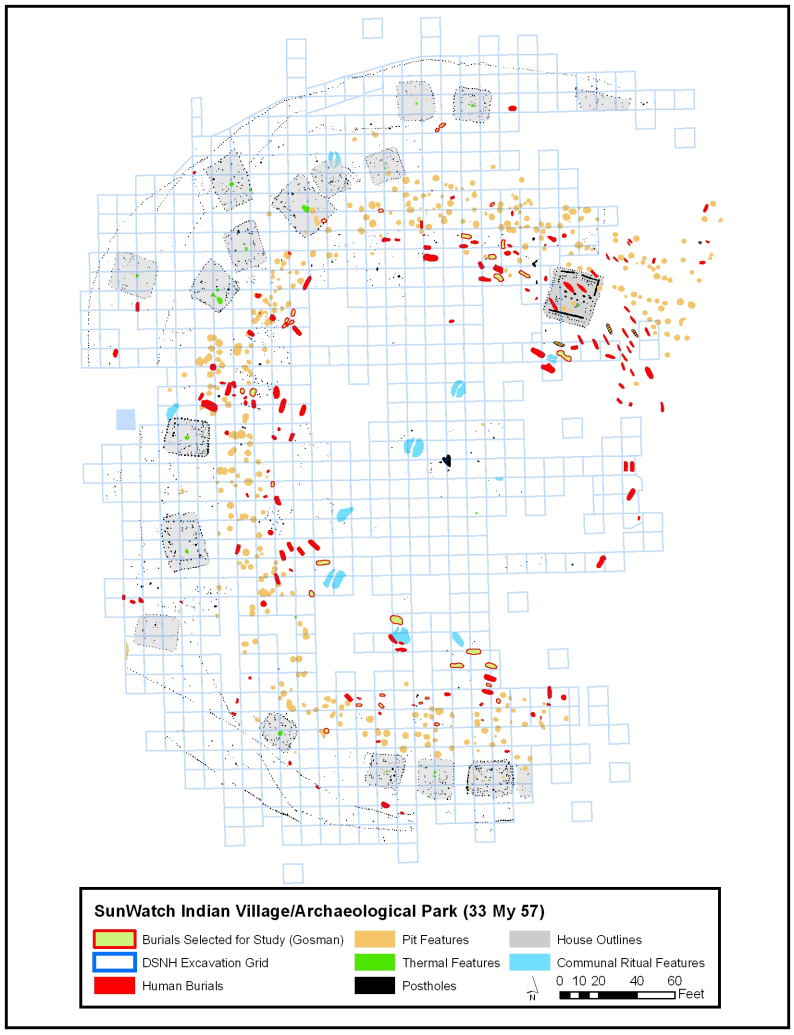

Figure 3.2 SunWatch Village and archaeological features (courtesy of W. Kennedy).

The SunWatch site (33My57) (Figure 3.3) is located on the west bank of the Great Miami River, south of Dayton, Ohio, beneath the plowed field of the previous Vance family farm (Lileas, 1988). The site was initially named the Incinerator site because of the proximity of a disposal incinerator and land ownership by the City of Dayton. The name was changed to SunWatch in 1988 as part of site recognition as a National Historic landmark (Heilman et al., 1988).

Early collection of plow-surface prehistoric artifacts by collectors and avocational archaeologists was common during the early portion of the twentieth century. Excavations in the northeastern portion of the site were carried out by avocational archaeologists John Allman and Charles Smith between 1964 and 1969. Numerous burials, pit features, and a house were uncovered (Allman, 1968; Smith, n.d.). It should be noted that several of the skeletal remains used in the current research were excavated by Smith.

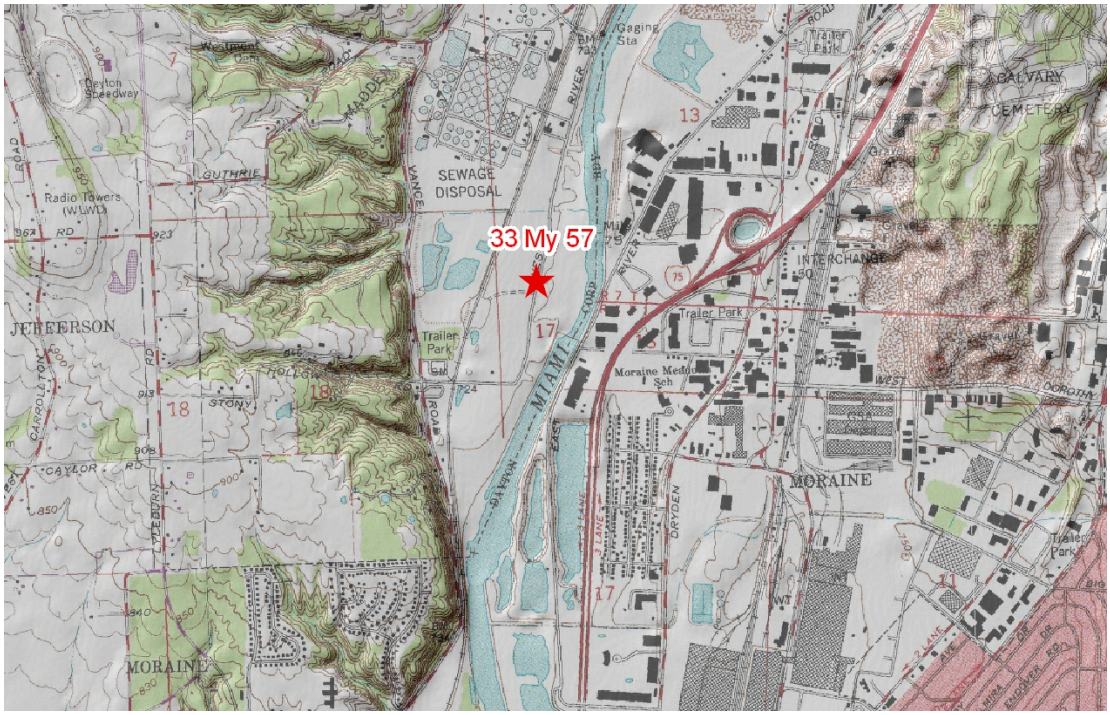

Figure 3.3 SunWatch Village site (33 My 57) (courtesy of W. Kennedy).

Charles Smith was instrumental in bringing the site to the attention of James Heilman, curator of Anthropology at the Dayton Museum of Natural History (DMNH), in 1969. In 1970, the City of Dayton was developing plans for expanding a sewage treatment facility which would have substantially damaged the site. Salvage excavations by the DMNH were begun in 1971, continuing until 1975 at which time the site was granted federal protection (Heilman et al., 1988). Archaeological efforts carried out into the 1980s gradually shifted from excavation to reconstruction and analyses. The site and interpretive center opened to the public in 1988- the same year that formal excavations were stopped. This combination of avocational and DMNH excavations have generated an incredibly broad-spectrum database from which

analytical investigations have been carried out over the past 30 years. Archaeologically-focused research has been concerned with astronomical alignments; settlement structure, organization, and development; ritual behavior; and food production economy. Selected aspects of these analyses most relevant to the current work are discussed. Biologically-focused research will be discussed in the subsequent chapter.

Astronomical alignments

Heilman and Hoefer (1981) advanced the initial interpretation of the village center pole complex as a type of astronomical indicator. The Eastern Red Cedar found in the center posthole is a high value, ritual-specific wood found in another documented Mississippian alignment/calendrical system – Cahokia's "Woodhenge" (Wittry, 1969). The SunWatch center and associated poles are aligned with particular houses, pit features, burials, and hearths two times a year on dates coinciding with spring planting and summer harvesting (April 29 and August 14) (Goss, 1988). The SunWatch solar alignment system allows 107 frost-free days between planting and the first harvest. The Green Corn ceremony was held at a point when the corn crop is first edible. A double harvesting is thought to have taken place (green and mature) in order to minimize the risk to the corn from an early fall frost, late drought, pests, or other calamities (Kennedy, 2000).

Additional alignments mark the winter solstice and equinox, which are integral components of many calendar systems in prehistory (Aveni, 2003) (Figure 3.4). Various other alignments have been subjected to speculative interpretation including linkages to stellar appearances and a burial with materials aligned along cardinal axes. Of interest, potential center posts have been found at the Madisonville Fort Ancient site (Drooker, 1997).

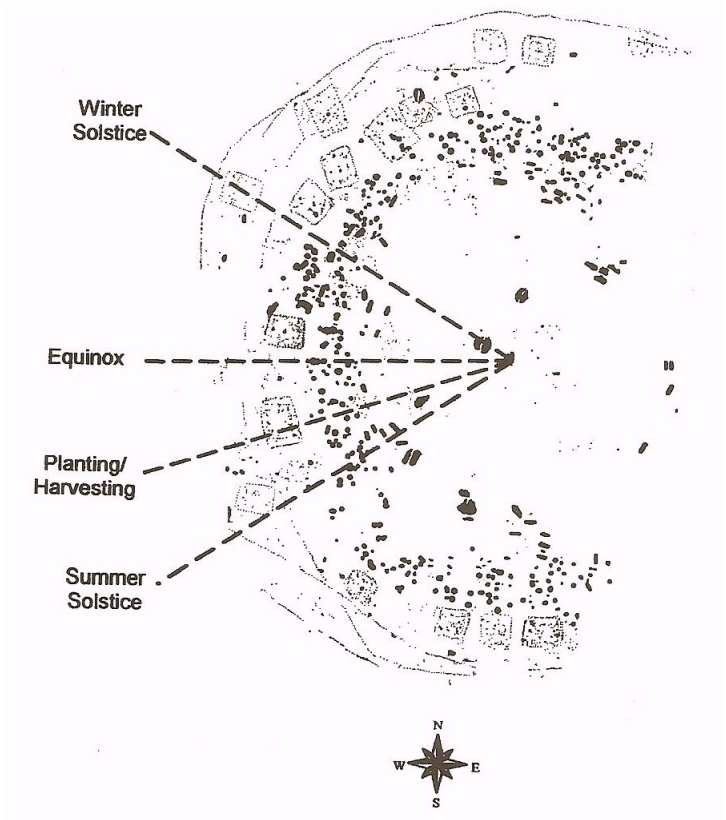

Figure 3.4 SunWatch astronomical alignment interpretations (from Heilman and Hoefer, 1981 and Cook, 2004).

Social organization and village formation

SunWatch social structure has been inferred from spatial analysis of pottery and lithic refit distributions, burnt corn concentrations, relative house structure and storage pit sizes, and burial patterning (Cook, 2004). Heilman (1988) interpreted a refit analysis of pottery rim sherds as evidence for household-based patterns and localization. This initial investigation suggested three to four spatial units. Recent re-investigation of an expanded pottery assemblage, as well as selected burial features concluded that SunWatch was organized in a dual division structure with possible components consisting of localized households, clans, sodality, and elite/ritual area (Cook, 2004).

Robertson (1980, 1984) expanded Heilman's initial work, focusing on lithic refits. The lithic linkages were distinct from those of the pottery refits, indicating connections between a single house and the rest of the village. This house was termed the Men's House on the assumption that men were responsible for the manufacturing of lithic tools. The Men's House is part of a group of structures in the west portion of the village which has come to be recognized as a ritual-focused area. The Green Corn ceremony is thought to be an important part of social integration at SunWatch (Heilman et al., 1988). This ceremony was widespread among the Eastern Woodland and Mississippian populations (Hudson, 1976). It consisted of both a harvest celebration and a renewal observance. Activities included household and village cleansing as well as firing large quantities of corn.

The archaeological correlates for the various aspects of the Green Corn ceremony consist of the distribution of burnt artifacts and corn and pottery refits (from disposal) within a ritual area. The spatial analysis of burnt corn and large storage pits revealed increased concentrations in this west sector, consistent with communal activity of the Green Corn ceremony. This, in combination with the presence of a large house structure constructed with red cedar and the positioning of solar alignments, augmented the interpretation of this sector as a ritual area. The large house structure has been termed Big House (Heilman and Hoefer, 1981) or "chief's lodge" (Nass, 1989).

Mortuary analyses (Evans-Eagle, 1998) have enhanced the understanding of SunWatch as having an egalitarian social organization with burials clustered in kin grouping and differentiated by age and gender. Evans-Eagle does present an argument of some internal ranking within clans or corporate structures. This agrees with an autonomous local group type of social structure without evidence of any systematic hierarchical organization (Griffin, 1992; Johnson and Earle, 2000; Pollack and Henderson, 2000).

Cook (2004, 2007a) has used multiple lines of archaeological data, consisting of burial groups, house rebuilding/remodeling, feature attributes, lithics, radiocarbon dates, and pottery refits, to examine the pattern of SunWatch village formation. He argues in a summary statement that "four corporate groups and an elite area developed during two stages of village formation" (Cook, 2004, p. 218). Two kin groups came together to initially form the village, settling in the southern and northern sectors of the

site (Area 1 and Area 4). Steady growth characterized the southern group; an additional group characterized the growth of the northern group. A stockade enclosed the village structures. The second phase of village formation was concentrated in Areas 2, 3, and 4 with additional houses being built, existing houses expanded, and the elite/leadership/ritual area formed. An enlarged stockade enclosed all the known village structures. Figure 3.5 is a graphic representation of the proposed SunWatch growth model.

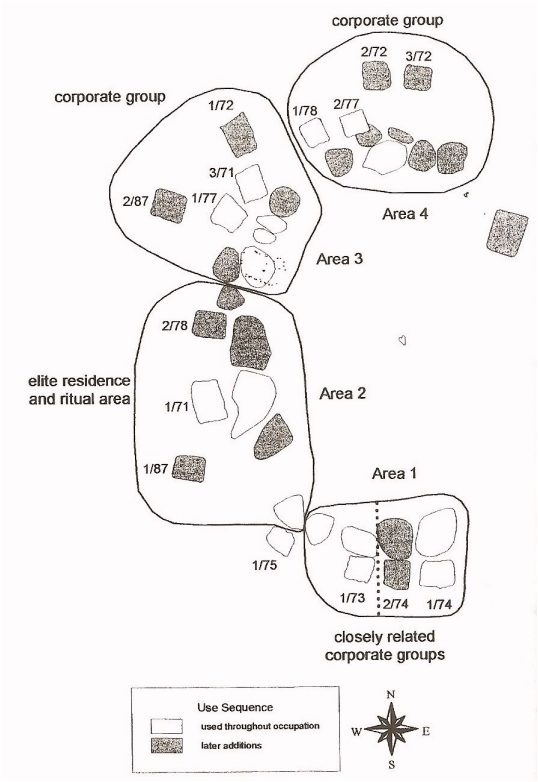

Figure 3.5 SunWatch village formation model (from Cook, 2004, p. 225).

Cook (2007a) has recently published an expanded reappraisal of SunWatch village examining site occupation and growth. Of primary interest was reconciling the wide range of radiocarbon dates from the site (ca. AD 1000 to 1500) to the archaeological temporal indicators (house rebuilding, feature form and size, and material attributes). Cook argues that the results from this enquiry suggest two possible scenarios for SunWatch occupation: (1) a single occupation of 10-30 years approximately 100 years later (late AD 1200s- early AD 1300s) than that suggested by earlier researchers, or (2) two separate shorter occupations of 5-15 years by Fort Ancient groups, once in the late AD 1100s and once during the late AD 1300s. Site reuse has been identified as a pattern of agricultural management during the Middle Fort Ancient period (Cook, 2007; Henderson and Pollack, 2001). Groups migrating into SunWatch are not ruled out. The data at this point does not permit a definitive conclusion "with any degree of confidence" (Cook, 2007, p.457). The important point for this current research is that either scenario represents relatively short village occupation(s).

Food production economy

The subsistence pattern for SunWatch is an important underpinning to this current biological investigation of trabecular bone ontogeny as it establishes the nutritional framework (i.e. maize-focused) for skeletal growth and development. Climatic reconstruction using faunal and floral analyses (Shane, 1988; Wagner, 1988) reveal relatively warmer conditions during the site's occupation compared to the subsequent cooling of the Little Ice Age. SunWatch was located within a diverse range

of ecosystems consisting of wetlands/floodplain, pocket prairie, and semi-forested habitats. The economic strategy could be characterized as maize-intensive small-scale agriculturalist. Short-term inherent risks were thought to be buffered by some resource diversification, food storage, and inter-village or regional exchange. Long-term risk buffering of food shortages related to soil depletion and climatic stress may have been managed by eventual village abandonment (O'Shea and Halstead, 1989).

Although faunal and floral analyses have demonstrated a subsistence pattern based on wild and domesticated goods, the archaeological, ethnographical, and carbon isotope ratios data have established that the primary food production economy of SunWatch was maize intensive. It has been estimated from several carbon isotope analyses that 50-75% of the diet was maize (Kennedy, 2000; Broida, 1983; Conard, 1988; Schurr and Schoeninger, 1995; van der Merwe et al., 1978). This proportion of maize in the SunWatch diet is similar to other Late Prehistoric and Protohistoric groups (Farrow, 1986; Katzenberg et al., 1995; Stothers and Bechtel, 1987). The SunWatch villagers and other Fort Ancient populations to the east and north grew the frost-resistant Eastern Eight-Row maize which requires a shorter growing season than the variety it replaced (Midwestern Twelve Row) (Smith, 1992). SunWatch village was initially occupied during a climatic time period thought to be of low agricultural risk; the growing season subsequently may have decreased by as much as twenty days in the later portion of the Late Prehistoric period (Kennedy, 2000). The SunWatch village organization and calendrical alignments emphasize the importance of the delineation of the growing season for maize as the primary subsistence staple. Climatic variables are

clearly potential high-voltage stressors on the Fort Ancient/SunWatch village agricultural systems.

Additional domesticated plants found commonly within the village include beans, squash, sunflowers, and tobacco. Beans play an important nutritional role, supplying a source of protein and complementing the lysine and tryptophan deficiencies of maize. A fully adequate corn-bean diet requires consumption of one gram of beans for every 2.6 grams of maize (Kennedy, 2000; Bresssani, 1967). Modern subsistence farmers are unable to maintain these proportions; it is likely that SunWatch farmers fell short as well.

The floral data supports the use of a wide range of wild grasses and small seeded annuals, nuts, and fruits. These resources were exploited to a lesser degree by the SunWatch/Fort Ancient groups than by their Late Woodland predecessors or contemporaneous Mississippian populations (Rossen, 1992). It should be noted that it is possible that some of these differences may be related to preservation issues (Rossen, 1992; Wagner, 1987).

Hunting was of considerable importance to the SunWatch food economy supplying food during the winter and most notably a protein source. The faunal data indicates an exploitation of deer (principally), elk, bear, and turkey (Heilman et al., 1988; Wagner, 1996). The faunal assemblages were primarily mammalian (~80%) and are typical of edge/open forest habitats. Fish, shellfish, waterfowl, and small terrestrial mammals were all underrepresented in the subsistence scheme (Kennedy, 2000). In a co-evolutionary model, the SunWatch population apparently exploited animals and

"wild" species drawn to their agricultural fields and the surrounding transition zones (MacCauley, 1990; Wheelersburg, 1992).

Food storage is an important component of maize agricultural risk management. SunWatch has numerous deep pit features arranged concentrically around the central plaza. These pits were used initially to store harvested maize and other plant products; they were subsequently filled with refuse after the maize was consumed (Mills, 1904; Grooms, 1999). Experimental archaeological studies (Grooms, 1999) suggest that maize can be stored successfully for eight to 12 months in deep in-ground storage pits. In a study of the capacity of the SunWatch storage features, Grooms (1999) calculated that seven individuals could be *sustained* (emphasis mine) for three- five months depending upon the individual size of the pit and actual proportion of maize in the diet. The archaeological data suggests that the SunWatch food production economy ranged from life sustaining to somewhat-less-than-optimal. The quantitative bone growth microarchitectural data generated in this investigation must be viewed within this specific context.

SUMMARY

Fort Ancient is a regional concept describing a pre-Columbian way of life centered in permanent villages between 1000 A.D and 1550 A.D. The populations relied on a maize-intensive agricultural system. SunWatch Village, used for this investigation, is the type site for the Middle Fort Ancient period (1200 A.D.-1400 A.D.). Characteristics of SunWatch, which will prove to be important components of

this dissertation research, include its putative egalitarian social structure, the local continuity with preceding populations, the relatively short occupation timeframe, and the maize- focused food production economy.

A consideration of the adequacy of the SunWatch food production economy indicates that it was permissive of high fertility, but conducive to a change in general health. Its nutritional deficiencies were manifested biologically by shorter stature compared to earlier populations and high prevalence of dental disease. The biological data is discussed in the following chapter.

CHAPTER 4

FORT ANCIENT TRADITION AND SUNWATCH VILLAGE: PHYSICAL ANTHROPOLOGY

The methodology and theoretical perspective of analysis of skeletal remains from the Ohio Valley runs on the rails of two major themes of North American physical anthropology during the latter one half of the twentieth century: descriptive typological analysis giving way to an adaptational, functional biocultural approach and an intense interest in the biological and social consequences of the transition from a hunter-gathering life style to a settled agricultural economy based on maize. This chapter is a focused review of skeletal research at SunWatch and related sites within the Fort Ancient tradition. It chronicles the emergence of bioarchaeology as a major constituent in understanding the health, nutrition, and lifestyle of past human groups. As such, this chapter lays out what is known and inferred about the individuals who lived in SunWatch village and lays the foundation upon which an understanding of the patterns of ontogenetic changes in trabecular bone can be developed.

The skeletal material from SunWatch has been studied in terms of cranial typology, biological affinity, paleopathology, and bioarchaeological stress markers. Many of the early reports are non-published manuscripts stored at Dayton, Ohio's

Boonshoft Museum of Natural History and made available to this researcher. In the past two decades, the complete SunWatch skeletal sample excavated by both the Smith and Heilman excavations has undergone detailed bioarchaeological study by Paul Sciulli, Myra Giesen, and others (Sciulli et al., 1990; Sciulli, 2007; Giesen, 1992). Biological studies focused primarily on SunWatch and/or relevant Fort Ancient sites are reviewed chronologically.

CRANIAL TYPOLOGY

The inception of Robbins and Neumann's (1972) published study of cranial metrics, morphology, and biological affinity from Fort Ancient samples was in 1936 when Eli Lilly of Indianapolis agreed to underwrite such a study by Georg K. Neumann then working at the Museum of Anthropology in Ann Arbor, Michigan. Neumann collected skeletal data from various sites in the Ohio Valley; unfortunately he was unable to complete the study. Neumann's collected data, however, formed an important part of Louise Robbins's subsequent work and joint authorship of a monograph on biodistance. This skeletal study is important for two reasons. First, the only previous study of Fort Ancient people was Hooton's (1920) analysis of the skeletal material from the Madisonville site near Cincinnati, Ohio. And second, it is excellent example of the descriptive and typological research focus in North American skeletal biology and anthropology in the mid-20th century (Armelagos et al., 1982), which has now given way to a problem-focused biocultural adaptational approach.

Robbins and Neumann's analysis used Griffin's scheme of four archaeological foci within the Fort Ancient Tradition (Baum, Feurt, Anderson, and Madisonville) to organize their typological examination. SunWatch is considered an example of the Anderson focus; however, the SunWatch skeletal remains were not included in this particular research. Five North American physical "types" were "identified" for comparison of Fort Ancient morphology to other Eastern Woodland populations: Lenid, Ilinid, Iswanid, Muskogid, and Dakota.

The Lenid type is identified as the predominant physical form in the northeastern Woodland area during the Middle Archaic through the Middle Woodland archaeological periods. Crania, in general, are described as being large, longheaded, and robust with large brow ridges. Facial characteristic include a medium to large height and breadth, resulting in a long, broad face. Neumann (1960) had observed that the Lenid populations displayed a gradual change in a number of traits during the latter part of the Middle Woodland period. He argued that the Ilinid cranial type of the Late Woodland and Upper Mississippi periods was derived from these earlier changes (Robbins and Neumann, 1972).

The Ilinid type is typified by a large ovoid cranial vault and medium robusticity. The facial dimensions are moderate in size, flatness, and prognathism. The rear of the skull is stated to have a pronounced amount of occipital curvature, which according to the authors is a Lenid-like morphology. Neumann (ibid) had previously asserted that the Ilinids were metrically distinct from the earlier Lenids. However, there

appears to be morphological overlap as well as an admission of the possibility of "intermixture" of skeletal groups used in the analysis.

The Iswanid type series was derived from the Indian Knoll population and is representative of earlier physical type of the pre-Ceramic Archaic shell mound culture of the Ohio Valley. The skull is described as small and relatively high. The face lack robusticity and is small compared to the cranium. As described, the Iswanid variety is stated to have a number of metrical and morphological differences, making it an easily identifiable type.

The Dakotid variety is thought to have evolved as a result of the migration pattern of the Plains groups into the Ohio Valley region. It is considered to be of trihybrid origin: a mixture of Lenid, Walcolid (Muskogid), and Deneid characteristics. The skull is described as medium is size with a high braincase. The face is large, flat and rugged with only a small degree of prognathism.

The Muskogid type is considered representative of the Middle Mississippi archaeological horizon of the Late Prehistoric period. The skull is described as large with a high braincase and short ovoid form. Artificial cranial deformation is common among the Muskogid populations. The face is considered large relative to the braincase. The face is broad with frequently a prominent chin.

These authors' conclusion from this examination of Fort Ancient crania was that the Fort Ancient Ilinid "type" was "found to be fairly widespread throughout the [Fort Ancient] aspect" (Robbins and Neumann, 1972, p.105) - found in nearly all Fort

Ancient components. The second physical variety associated with Late Fort Ancient sites (primarily Madisonville) was Muskogid. The authors contend that the Fort Ancient Ilinids display temporal and spatial relatedness with several populations-ancestrally and contemporaneously. It is proposed that the Fort Ancient Ilinid peoples represent the original inhabitants of the Fort Ancient cultural area in continuity and having evolved from a Woodland cultural base. This study came under early criticism (Giesen, 1992) as being subjective, arbitrary, and typologically restrictive. Issues with the study samples were identified as originating from a relatively small geographical area, including culturally deformed skulls, small sample size, and male specimen bias. Having stated these positions, however, this study is relevant to this dissertation research by implying a relative genetic homogeneity and common ancestral population for the Fort Ancient village of SunWatch; thus establishing a relatedness framework for ontogenetic research.

INFANTICIDE

The term infanticide covers a broad range of cultural and historical contexts; it includes neonatal/infant neglect, abandonment, or immediate smothering. Most of these methods do not leave forensic traces, resulting in significant difficulty of detecting infanticide in the archaeological record (Scott, 1999). Additional confounding factors for archaeological samples center on unknown, and possibly unknowable, culturally-specific burial practices for neonates and young infants. The detection of skewed sex ratios is one suggested methodology for identifying

infanticide. The resultant findings for prehistory remain assumptions with a putative modern western-mind bias. It is likely that infanticide has been practiced by prehistoric peoples. It is equally likely that infanticide and fertility ideologies have co-existed (Scott, 1999).

Louise Robbins turned away from typological categorization and towards examination of biological and cultural causes of skeletal variation in subsequent work. One of the first reports based solely on skeletal remains excavated at SunWatch is a speculative investigation of infanticide (Robbins, 1975). Robbins analyzed the 31 young children and infants recovered from the site at that time, noting that these nonadults were found buried in storage pits, middens, and intentional burial cuts. Robbins argued that the "evidence for infanticide seems irrefutable," based on absence of intentional burial ritual treatment for many young infants. According to Robbins, the correlative physical evidence included vertical burial in storage pits with associated fragmentation of the cranial bones and odd body angles and articulations as if the infant was made to fit into the pit not *vice versa*. No useful data concerning skewed adult sex ratios was possible from the limited sample of the total burial population. No corroboration of Robbins' assumption of infanticide at SunWatch, as indicated by divergent burial treatment of young infants or any other indicator, has been forthcoming.

PALEOPATHOLOGY

Stanley Knick undertook a survey of the pathological conditions of adult skeletal remains excavated between 1971 and 1975 as partial fulfillment of a Masters degree (Knick, 1976, 1977). The sample analyzed consisted of 25 adult individuals aged ≤ 25 years to > 45 years: 13 males and 11 females. The distribution of trauma, pathological conditions, and skeletal anomalies were considered in relation to age, sex, and spatial distribution within SunWatch village house groups. The quality of Knick's observations and interpretations were somewhat hampered by inexperience. However, several interesting findings were elucidated. No sex differences were noted. All individuals over 15 years of age demonstrated evidence of active dental disease including caries, wear, tooth loss, abscess formation, and periodontal changes. These findings are consistent with similar analyses of other prehistoric, agricultural, maize-centric groups (Larsen, 1997). All individuals over the age of 25 years had skeletal changes consistent with osteoarthritis (elbow, costovertebral, sacro-iliac, ankle, spine facet joints, and feet) and degenerative intervertebral disc disease (cervical, thoracic, and lumbar). These conditions were identified by Knick on the basis of the presence of osteophytes.

Arguably, the most interesting findings were the concentration of vertebral anomalies to three house structures on the south side of the central plaza which are thought to delineate family groups (Knick, 1977). The skeletal analysis demonstrated varying degrees of spinal dysraphism, abnormalities of vertebral segmentation, sacral asymmetry with cranial/caudal shift, and cranial sutural anomalies. Sacral anomalies

consisting of varying degrees of sacral spina bifida were found in 33 percent of the skeletal sample. All of these individuals were in three burial groups associated with three corresponding house structures. The association between individuals and specific house structures has been inferred from spatial analysis of burials, house structures, and central plaza (Cook, 2004). Knick (1977) argued that the concentration of sacral anomalies described lends an additional line of supportive primary skeletal data.

Steve Paquette's unpublished manuscript "An Analysis of Demographic and Pathological Correlations at Incinerator Site, Fort Ancient Culture, Montgomery County, Ohio" (1981) reports on the examination of 103 burials excavated at SunWatch during the 1976 through 1979 seasons. Paquette's sample contains 57 nonadults, 11 individuals between adolescence and 25 years of age, 21 individuals between 26-45 years of age, and 11 individuals over age 45 years. This report is a continuation of Knick's work on the burials excavated from 1971- 1975 discussed above. Paquette's findings support the high prevalence of spina bifida, but suggest that it may be more widespread among house groups; 26% of the adult "population" was stated to exhibit spina bifida. The high frequency of osteoarthritis and dental pathological conditions (100% in the age group >25 years) was also confirmed. Osteoarthritis was stated to be most commonly manifested as vertebral osteophytosis. Dental disease consisted of caries, alveolar abscess, and tooth loss.

BIOARCHAEOLOGY

A change in research perspective from descriptive analysis within a typological framework to biocultural functional and adaptation studies began in the 1970s. A broad-scale model linking subsistence change to population pressure (Cohen, 1977) stimulated research on population size, dietary quantity and quality, and bioarchaeological markers of stress (Cohen and Armelagos, 1984). A central focus for physical anthropology was the cultural adaptations and associated skeletal changes imbedded in the process of a transitioning food production economy. A biologically successful transition was characterized by a dietary shift which yielded an adequate amount of energy and nutrients: "A biologically less successful transition was that characterized by the use of a high energy-low nutrient diet (Fort Ancient)" (Cassidy, 1984).

Perzigian et al. (1984), from the University of Cincinnati, report on the comparative dental and skeletal biology of four groups from southwest Ohio ranging from the Late Archaic period (ca. 1000 BC) to the Mississippian-Fort Ancient period (AD 700-1600). The results from the two Fort Ancient samples (Turpin and State Line) will be discussed and used to provide a framework for later analyses more specific to SunWatch. This study is significant for undertaking a comprehensive bioarchaeological approach. The Turpin site is located on the Little Miami River, three miles north of the Ohio River; the State Line site is located on the Ohio-Indiana border, two miles north of the Ohio River. Based on radiocarbon dates (A.D.1175 ±150, 60), these sites were nearly contemporaneous with SunWatch; based on archaeological

data, these sites were culturally similar to SunWatch. Perzigian states explicitly that the authors' explanatory model is based on *in situ* cultural change and adaptation of the indigenous population with "little or no migration from or genetic interchange with other regions" (Perzigian et al., 1984). Osteometric data indicated that the two Fort Ancient groups were essentially phenotypically indistinguishable and thus justified combination into one sample.

The analysis of stature variation indicated that Fort Ancient people were more sexually dimorphic than earlier groups (Late Archaic). The pattern of mean stature change was estimated from measurements of the femur (Genoves, 1967). Results suggested an increase in stature from Late Archaic to Middle Woodland followed by an apparent *decrease* to lower than Late Archaic levels in the Fort Ancient period. Similar change was noted for both sexes. Significant limitations of Perzigian et al.'s study are the small sample size for the Archaic and Woodland groups and the possibility that the samples derived from Woodland burial cult groups (Adena and Hopewell) may represent only higher status groups. The data suggest, however, at the least, that there were no enhancements of growth for the increasingly sedentary, maize agricultural, Fort Ancient groups.

The relative intensity of weight-bearing demands of physical activity can be *generally* assessed by comparisons of the femoral midshaft index (ML/AP × 100). The anteroposterior diameter of the femur may be relatively increased and circularity is decreased. This assumes that a greater degree of mediolateral flattening of the femur is an indicator of greater physical demands. This construct is an oversimplification as

femoral cross-sectional shape also depends on additional factors, such as body build and types of activity (Ruff et al., 2006). Stocky bodies tend to have increased femoral mediolateral bending strength, while individuals with a lifestyle requiring mobility over rugged terrain tend to have increased anteroposterior bending strength. Perzigian et al. argue, the lower indices point to "a more biomechanically stressful existence" (Perzigian et al., 1984, p.13.6). The mean index for the Fort Ancient samples of both sexes is higher than the combined earlier Late Archaic-Woodland samples suggesting that "a somewhat less physically demanding way of life seems to characterize Fort Ancient people vis-à-vis earlier Archaic and Woodland groups" (ibid, p.13.6).

Group comparisons of linear enamel hypoplasia (LEH) data for the permanent dentition indicated that exposure to stressors associated with LEH (nutritional deficiencies, anemia, and infections) was three times greater for Fort Ancient children compared to Middle Woodland or Late Archaic groups (60% vs. 20%). Perzigian's findings are similar to those reported for other Ohio Valley groups (Sciulli and Oberly, 2002). The frequency of these findings in Fort Ancient sites points toward a decline in general health and nutrition attending the increasing commitment to sedentary village life and agriculture.

Turning from indicators of growth and development to specific pathological conditions, dental caries increased from a frequency of 2.5% in the Late Archaic to 25% in the Fort Ancient period. These findings have been confirmed in other studies of Ohio Valley groups and globally. As Perzigian et al. state, "The evidence is unequivocal that caries became a prominent feature and characteristic burden of the

late groups who relied more heavily on maize agriculture" (1984, p. 13.10). The frequency of nonspecific inflammatory lesions of the long bones (periostitis) is considered a relative general measure of health and disease in spite of a multiplicity of etiological processes. Perzigian reports that long bones in general and the tibia specifically had a significantly higher frequency of periosteal lesions in Fort Ancient periods than in earlier phases. The frequency of porotic hyperostosis and cribra orbitalis follows the same pattern (Mensforth et al., 1978). The interplay among nutrition, population density, occupational activity, and microbial action was stated to have resulted in "at least a modest decline in skeletal health" coincident with the adoption of agricultural economies (Perzigian et al., 1984; Lallo, 1979).

Perzigian et al. (1984) state that paleodemographic analysis suggests high fertility with a life expectancy at birth of 33 years for the Fort Ancient group, compared to lower fertility and a life expectancy at birth of 20 years for earlier groups (Late Woodland). Limitations to this paleodemographic reconstruction include inherent bias from the small sample size and under-representation of both infants and subadults in general. The findings, however, are consistent with the now known, profound demographic changes, which occurred associated with the growing commitment to maize agriculture (Schurr and Schoeninger, 1995). Villages arose and increased in size and number and population densities increased (Perzigian et al., 1984). These demographic changes during the Fort Ancient adaptational shift were associated with the observation of an apparent increase in interpersonal hostility and violent death. Earlier Late Woodland groups are stated to have no strong evidence for warfare

(Lovejoy and Heiple, 1981). Numerous authors have reported cranial and postcranial wounds in Fort Ancient skeletal collections (Hooton, 1920; Lovejoy and Heiple, 1970; Morgan, 1946).

The summary position of Perzigian et al. (1984) (see also Sciulli and Oberly, 2002) is that dental and skeletal health declined significantly in the Fort Ancient times in southwestern Ohio. This was associated with an increased commitment to maize agriculture and reinforced by the synergy among diet, population density, and disease. It is within this wider regional and cultural context that SunWatch village is situated.

The Dayton Museum of Natural History published in 1988 an edited two volume summary of SunWatch research: "A History of 17 Years of Excavation and Reconstruction- A Chronicle of 12th Century Human Values and the Human Built Environment." Chapter 5.8 entitled "Burials – the Human Factors" (Dunn, 1988) presents a general overview of the "business of physical anthropologists" directed primarily at a lay audience. Dunn summarized the analyses of Robbins, Knick, and Paquette, characterizing the population of SunWatch as having:

1. Bad dentition
2. Prevalent osteoarthritis
3. "Generally poor health"
4. Medium build
5. Multiple examples of injury
6. Foci of spina bifida associated with house groups

7. Cultural skull deformation in older individuals (not confirmed by subsequent research).

This data-free summary concludes that to answer "the many questions remaining with regard to the skeletal population recovered from this most important Fort Ancient site… Time, and continued collaboration, will tell" (Dunn, 1988. p.311).

Myra Giesen's Ph.D. dissertation (1992) reports on a large set of skeletal samples analyzed by her and Paul Sciulli from the Late Prehistoric period, studying biological affinities and stress indicators. The Fort Ancient Tradition sites include Anderson, Buffalo, Madisonville, and SunWatch. The Sandusky Tradition sites include Indian Hills, Pearson, and Peterson. The material from SunWatch consists of 104 subadult and 63 adult skeletons, representing all the known materials excavated from the site. These biodistance and biocultural stressor investigations contributed substantially to the slowly developing understanding of the population-based "biological" aspects of the Late Prehistoric Period of the Ohio Valley generally and of people from SunWatch Village specifically. Results relevant to this trabecular ontogeny research project are discussed.

Biological affinities examinations, based on cranial metric and non-metric traits, indicated a relationship between all samples with respect to shape. It was stable through time, suggesting a common ancestral population. The variation of cranial size was stated to be a function of time, sedentary settlement patterns, relatively restricted gene flow and micro-evolutionary changes resulting from adaptations to differences in specific local environments. The important point for SunWatch ontogenetic research is

that the SunWatch population appears to have significant degree of genetic homogeneity, thus reducing the potential for variability of auxological data due to genetic factors.

Stature estimates calculated by regression equations developed by Sciulli et al., 1990) confirm the previous finding of significant sexual dimorphism for adult heights at all the Late Prehistoric sites. SunWatch Village had the tallest adult stature for men and was in the middle of the group for women. Table 4.1 is organized in chronological order from the earlier to the more recent Late Prehistoric sites.

♂	N	X ± SD	♀	N	X ± SD
SunWatch	30	166.8 ± 4.4	SunWatch	30	153.7 ± 4.2
Anderson	15	165.2 ± 6.9	Anderson	15	154.9 ± 4.6
Pearson	52	165.3 ± 5.3	Pearson	52	154.5 ± 4.5
Petersen	7	157.8 ± 2.7	Petersen	5	147.0 ± 7.2
Indian Hills	26	163.8 ± 3.5	Indian Hills	25	153.2 ± 4.1
Buffalo	99	165.3 ± 6.0	Buffalo	108	154.4 ± 4.1
Madisonville	78	160.7 ± 7.1	Madisonville	95	154.2 ± 6.8

.

Table 4.1 Stature estimates of Late Prehistoric Ohio Valley populations (from Giesen, 1992). Chronological order. Measurement in centimeters.

Giesen (1992) found that adult stature proportion in postcranial elements maintained stability over time and place. Postcranial data thus shows the same pattern as cranial data, namely shape stability and size variability. This is understandable on

the basis of the differential response and time scale for body shape and size to the complex interaction of genetic and environmental forces. Body shape, in general, is responsive to long time-scale factors, especially geoclimatic (Ruff, 1994). Body size and some body proportions (lower limb) are responsive to relatively short time-scale factors, such as nutritional, disease, sociocultural, and sociopsychological conditions (Tanner, 1990; Bogin et al., 2002). Better living circumstances seem to result in a relatively longer lower extremity body shape (Bogin et al., 2002).

Long bone growth is discussed within the framework of biocultural stressor and stress indicators. The rate of growth has been identified as a better reflection of health in some cases than attainment of adult stature, which is influenced significantly by catch-up growth (Larsen, 1997). Giesen's research fitted subadult bone measures to a human growth equation (Count, 1943) for the Buffalo, Pearson, and SunWatch sites. Of interest to this ontogenetic study are the growth curves and velocities Giesen plotted for the tibia. These were compared to a Late Archaic sample (Giesen and Sciulli, 1988) and to the Denver Growth Study of modern Euro-Americans (Maresh, 1955). Figures 4.1 and 4.2 are plots of tibial growth parameters generated by Giesen. The Late Prehistoric samples tend to be grouped together. The SunWatch tibial growth curves are in line with the Denver samples (when corrected for magnification, personal communication, Ruff, 2007). What may be notable, however, is the slightly reduced growth velocity in early childhood for most of the Late Prehistoric samples, possibly suggesting a relatively more stressed environment for these individuals (Giesen, 1992). These findings have a significant point of relevancy to the current investigation. The

general overall similarities of the Late Prehistoric SunWatch growth curves and modern growth curves lend credibility to using the SunWatch juvenile sample for an ontogenetic study. Additional data discussed below addresses the possibilities of nutritional stressors affecting the Late Prehistoric populations.

The indications of increased frequencies of pathological conditions (e.g. linear enamel hypoplasia) in the dentition of Late Prehistoric agriculturalists compared to early non-agricultural groups confirmed previous studies indicating poorer dental health with the transition to maize agriculture (Giesen, 1992). Giesen's research provided one of the first extensive surveys and comparisons of biological data of Late Prehistoric populations in the Ohio area. The inclusion of SunWatch provided an important biocultural perspective on long bone linear growth patterns germane to this trabecular project.

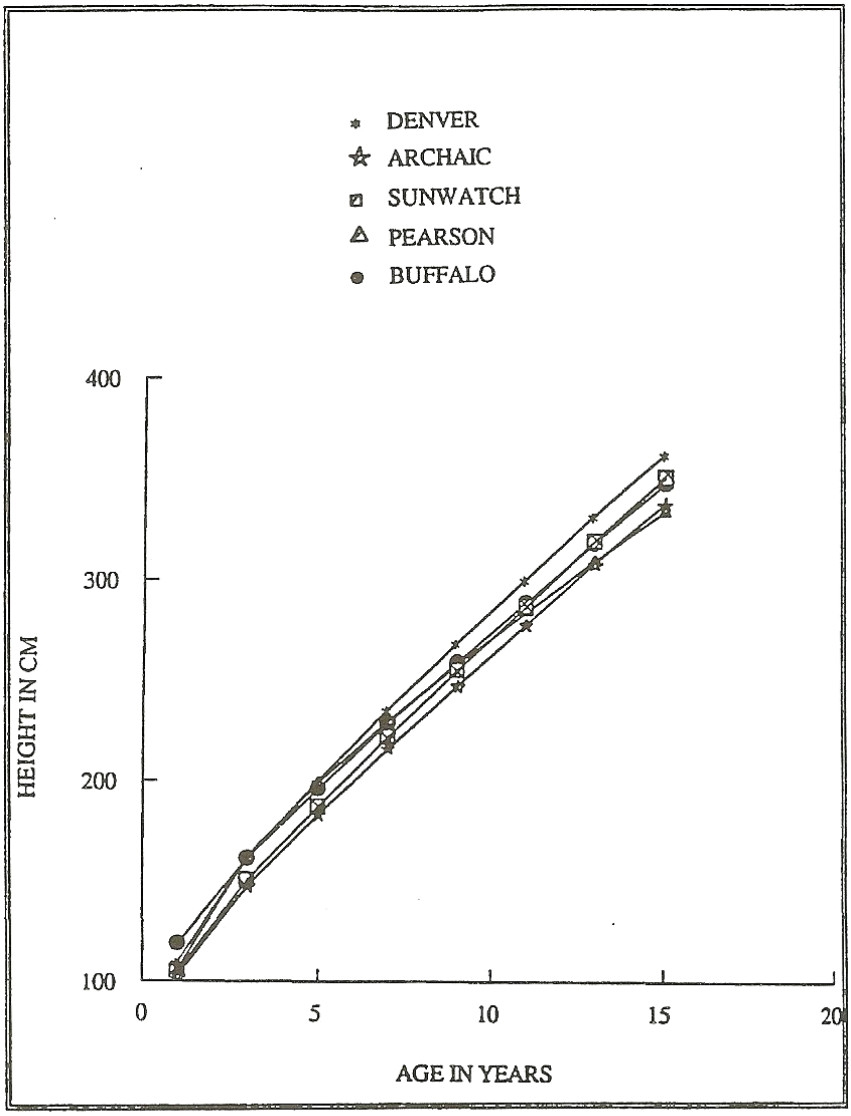

FIGURE 9.

Tibia growth curves.

Figure 4.1 Plot of tibial growth in Late Prehistoric Populations. SunWatch juveniles fall between the modern Denver sample and Late Archaic populations (from Giesen, 1992).

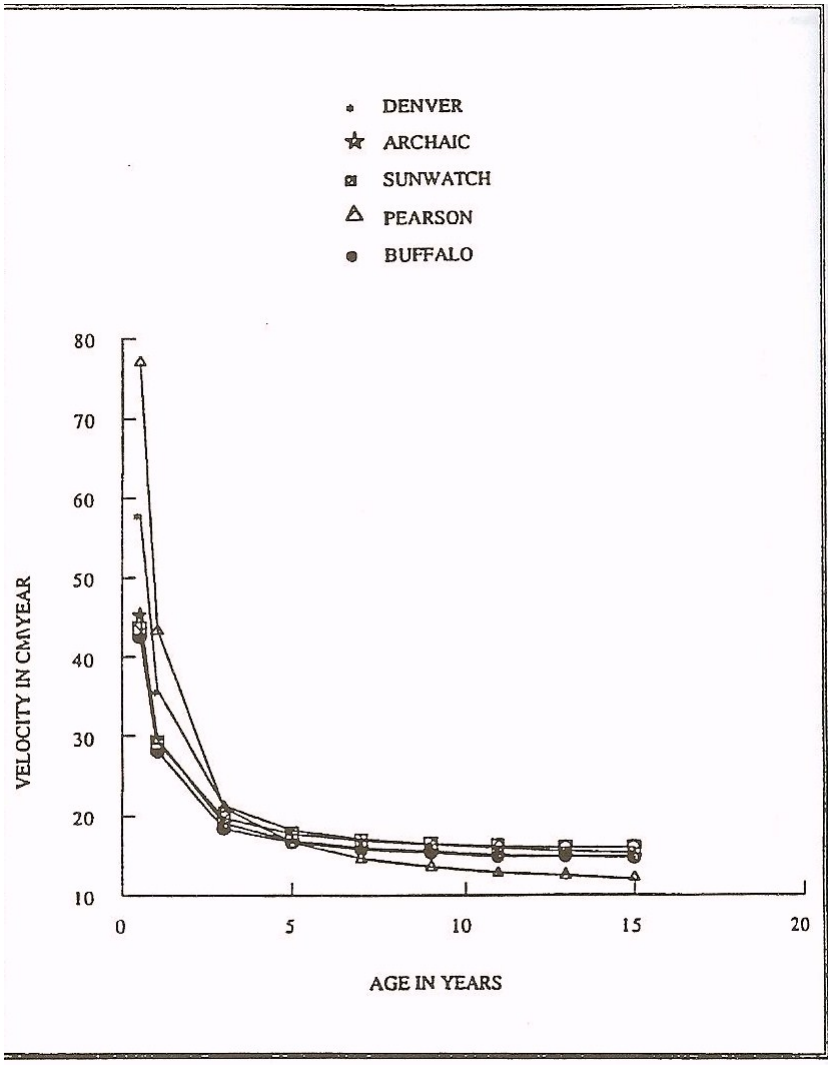

FIGURE 13.

Tibia velocity curves.

Figure 4.2 Late Prehistoric tibial growth velocity curves demonstrating slightly reduced growth velocity at SunWatch early in childhood (from Giesen, 1992).

Sciulli and Oberly (2002) consider the health of Native American populations of Eastern North America, published as a book section in Steckel and Rose's edited volume (2002), "The Backbone of History: Health and Nutrition in the Western Hemisphere." Sciulli and Oberly's study samples 469 individuals from the Late Archaic (ca. 1000 BC) to the Late Prehistoric (ca. AD 1000) periods and represents the most recent comprehensive analysis of various health indicators of the Ohio region. SunWatch, as one of the best preserved and most completely analyzed Late Prehistoric villages, contributes essential health-related biological data to this project, supporting a summary position and framework upon which to appraise the ontogenetic changes in trabecular bone structure and organization.

Findings specific to SunWatch, within the broader culture history, in regards to dental pathology, stature, paleodemography, postcranial metrics, femoral growth, trauma, degenerative joint disease, hyperostosis, and infection are discussed in detail by the authors. One important note emphasized by Sciulli and Oberly is that the paleodemographic reconstructions of these prehistoric groups may not be representational of the once living populations. The frequencies of pathological conditions should be viewed as "broad estimates subject to significant error" (Sciulli and Oberly, 2002, p. 456). The tables of data summaries in this section have been adapted from those in the Sciulli and Oberly publication or created from their dataset. Caries, abscesses, and premortem tooth loss for permanent and deciduous teeth demonstrate a 2-3 time increase between the Archaic hunting-gathering groups and SunWatch samples (Tables 4.2 and 4.3). This pattern is consistent with archaeological

chronology for the adoption of maize agriculture superimposed on normal age-related processes. These findings parallel the changing pattern of carbon isotope values among these populations over time. The $\delta^{13}C$ values increase (become less negative) with increasing C_4 (maize) plant contribution in the diet. Values range from -27.4 to -21.5 in the Late Archaic to -15.6 to -10.7 in the Late prehistoric (Sciulli and Oberly, 2002). These later values indicate maize contributed up to 50% of the carbon in the diet at SunWatch (Conard, 1985).

Phase	Caries	Antemortem Loss	Abscess
Late Archaic	4.1	9.0	4.1
Sun Watch	16.0	21.6	7.1

Table 4.2 Disease in permanent dentition (from Sciulli and Oberly, 2002).

Phase	Caries	Antemortem Loss	Abscess
Late Archaic	0.25	0.00	0.00
Sun Watch	15.3	0.00	0.36

Table 4.3 Disease in deciduous dentition (from Sciulli and Oberly, 2002).

Stature data was summarized from earlier analyses of native populations of the Ohio Valley (Sciulli et al., 1990; Sciulli and Giesen, 1993) which had been derived from femoral lengths using sex-specific regression equations developed in Ohio Valley natives. Restating Giesen's (1992) findings, Sciulli and Oberly (2002) observed that

limb proportions were constant throughout the prehistoric chronology. They comment that this is as expected in populations with a common ancestral lineage. Both sexes have a decrease in stature during the Late Prehistoric phase attributed in part to the inadequacies of diet in agriculturalists (Table 4.4). The authors also noted that differences in stature between samples had an association with soil type, with samples located on high-calcium soils having a greater stature than samples located on lower-calcium soils. Sciulli and Oberly state, "This indicates that ecological differences, *possibly* (my emphasis) related to calcium availability, are primary factors affecting overall growth and development and that these factors may be at least as significant as changes in diet" (2002, p. 455). For relevance to this trabecular bone study, SunWatch is located on high lime glacial drift soil.

Period	Males	N	Females	N
Late Archaic	168.6 ± 6.2	72	154.5 ± 6.1	68
Early Late Prehistoric	165.2 ± 5.5	94	154.9 ± 4.5	98
Mid Late Prehistoric	162.4 ± 5.4	37	151.7 ± 6.9	38
Proto-historic	162.9 ± 7.0	202	152.4 ± 6.5	228

Table 4.4 Stature variation over time in the Ohio Valley (from Sciulli and Oberly, 2002).

Postcranial osteometric data (humeral length/circumference, femur length/midshaft A-P/M-L/ area) indicates somewhat longer and thicker measures for the Archaic samples. Of the Late Prehistoric samples, the SunWatch individuals are generally the longest. Area measures and robustness show few differences among the samples. The Ohio Valley individuals may be characterized metrically as moderately large and robust (Sciulli and Oberly, 2002). Femoral growth models during the age range 0-17 were similar in all samples indicating a broadly similar effect of stressors (or lack of) on all populations as represented among these nonsurvivors to adulthood.

The Ohio Valley samples have a low level of trauma: healed fractures (≤6%) and cranial vault, facial, hand, and weapon-related trauma (<1%). Time period and/or culture are stated to have no significant effect on trauma frequency (Sciulli and Oberly, 2002) (Table 4.5). As expected, males have a somewhat higher frequency of healed fractures. Overall, the exposure and risk of trauma is cumulative and thus the frequency increases with age.

Phase	Arm	Leg	Vault	Total
Late Archaic	3	4	1	8
SunWatch	5	2	3	10

Table 4.5 Percent Trauma in Ohio Valley populations (from Sciulli and Oberly, 2002).

The frequencies of degenerative joint disease (DJD) were analyzed for the adult axial and postcranial skeleton. The highest prevalence was noted for the

vertebral column, reflecting the continuum of the age-related intervertebral disc degenerative cascade (Boos, 2002). No sex differences were revealed. The sex-combined samples, however, did disclose a significant association between DJD frequency and culture period with the frequency of postcranial DJD being slightly higher in the Archaic sample compared to SunWatch. The effect of time period/ culture is insignificant on the rankings of vertebral DJD (Sciulli and Oberly, 2002).

The frequencies of hyperostosis, infections, and hypoplasia demonstrated no significant sex differential. Late Prehistoric group frequencies ranked higher than did groups from early time periods (Table 4.6).

Pathology	Archaic			SunWatch		
	Male	Female	Child	Male	Female	Child
Cribra O	3.3	2.4	7.8	0.00	4.8	14.1
Porotic H	6.5	9.1	8.5	12.9	22.7	15.0
Tibial Inf.	10.3	7.1	1.9	12.9	16.8	25.7
Skel. Inf.	32.0	24.9	13.6	45.3	37.5	25.3
LEH UIs	19.0	4.5	0.00*	9.0	28.6	2.2*
LEH UCs	12.0	20.0	0.00*	15.3	27.8	3.5
* = deciduous teeth						

Table 4.6 Frequencies (%) of hyperostosis, infections, and hypoplasias (adapted from Sciulli and Oberly, 2002). Cribra O, cribria orbitalis; Porotic H, porotic hyperostosis; Tibial Inf., tibial infections; Skel. Inf., skeletal infections; LEH UIs, linear enamel hypoplasia upper incisor; LEH UCs, linear enamel hypoplasia upper canine.

Sciulli and Oberly (2002) report the results of the patterns of associations among these pathological conditions and the associations of these conditions with stature and dental disease, comparing the Archaic sample and a pooled Late Prehistoric sample (including SunWatch). The Archaic short individuals exhibit LEH, anemia, and infections at a higher frequency and at a younger age-at-death than do the tall individuals. The other primary association was between older age and dental pathology as well as the non-specific pathological conditions (LEH, anemia, and infection). The authors suggest that these pathological conditions can be viewed as effective stressors affecting growth, development, and life span.

The Late Prehistoric analysis reveals a different pattern. Dental caries and abscesses are associated with older individuals, but not LEH, anemia, and infection. LEH is primarily associated with short stature. Anemia and infections are common in younger children (age <5) and LEH in older children (age>5) and adults. The association of infections and anemia with younger Late Prehistoric children and the resultant overall increase in LEH may be a marker of the nutritional inadequacies in the Late Prehistoric. Sciulli and Oberly (2002, p.474) argue that the LEH, "which indicates potent stress, apparently remained a severe consequence of stress and is associated both with growth deficiencies (short size) and early mortality." This author notes that the growth data on SunWatch individuals do not support the presence of significant growth deficiencies.

The Ohio Valley Native American samples, with the exception of SunWatch, are all above the median for the Health Index for the total Western Hemisphere sample

(Steckel and Rose, 2002). The Health Index represents a quantification of health status for individuals and groups based on multiple skeletal indicators of nonspecific stress: growth/stature, linear enamel hypoplasia, porotic hyperostosis/ anemia, periosteal reactions/infectious disease, trauma, degenerative joint disease, and caries, dental abscesses, and tooth loss. Stress is defined in accordance to the general stress perspective (Goodman and Armelagos, 1989) as "measurable physiological disruption or perturbation that has consequence for individuals and populations" (Steckel and Rose, 2002, p, 12). The Health Index is calculated by scoring the attributes of health enumerated above for individuals on a severity scale of 0 (lowest) to 100 (highest). These scores are then pooled by site, converted to age-specific rates, and adjusted by the distribution of person-years lived by age in a reference population. The resulting indexes (0 to 100%) for each attribute are averaged to create an overall health index that is comparable across sites.

SunWatch is situated only slightly below the median: placed here primarily because of the high frequency of acquired pathological conditions of dentition and infection (Table 4.7).

Description	Index	Stature	Hyp.	Anemia	Dental	Inf.	DJD	Trauma
SunWatch	71.6	31.6	83.3	89.3	68.9	66.7	75.2	86.5
Average	78.1	32.2	86.7	94.7	81.7	81.6	82.4	90.6
Std. Dev.	5.6	14.1	8.8	3.6	15.3	12.9	9.9	5.6

Table 4.7 Health Index and Components of SunWatch and Eastern North Native American Populations (from Steckel and Rose, 2002).

Overall, the skeletal samples analyzed by these authors have a generally low frequency of pathological conditions. Trauma and degenerative joint disease are age-related and of similar frequencies and severity throughout the temporal span. The Late Prehistoric individuals have a higher frequency of linear enamel hypoplasia and associated growth depression resulting in smaller average adult stature. The SunWatch individuals were the tallest of the Late Prehistoric sample. The increased frequency of acquired dental pathological conditions in the maize agricultural Late Prehistoric samples is a defining characteristic. The specific pattern of health, disease, and general stressors exhibited by SunWatch and other Ohio Valley Late Prehistoric agricultural groups may be in part related to the fact that Ohio Valley populations were experimenting with maize agriculture for a relatively short time span prior to European contact. These groups still had considerable reliance on hunted and gathered foods. They were likely to have had an even poorer health record if they had relied solely on maize for food production and nutrition. Sciulli and Oberly (2002) suggest that the full

diet, health, and sociocultural consequences of an intensive maize agricultural economy may not have had time to be fully elaborated.

SUMMARY

Genetic and environmental (nutrition, infection, and socioeconomic) factors have a systemic influence on bone ontogeny, maintenance, and architecture (Eveleth and Tanner, 1990; Johnston and Zimmer, 1989; Larsen, 1997). The Ohio Valley adult and juvenile Late Prehistoric skeletal collections, exemplified by SunWatch Village, are characteristic of past agricultural populations demonstrating increased population growth and density, relative undernutrition and increased disease burden, and associated skeletal and dental changes (Larsen, 1995). These factors may have influenced the developmental and lifestyle changes in cancellous bone microarchitecture, quantitatively and qualitatively, thus adding presently unknown variables to this analysis. The assumption is that given the Fort Ancient/SunWatch transegalitarian social organization, then the diet, environment, and lifestyle were apt to have been relatively similar throughout the SunWatch village population. Even though a mortality bias undoubtedly exists in the SunWatch juvenile skeletal sample used in this research and some of these individuals may have had some early growth faltering (Giesen, 1992; Sciulli and Oberly, 2002), there is no systematic evidence that these subadults had not remained physically active for most of their life span. The

quantitative trabecular “skeletal growth profile” of this research is expected to be environmentally-specific in terms of the relative timing, rate, and extent of ontogenetic changes. The patterned sequence, however, may demonstrate some universal aspects of human growth and development.

CHAPTER 5

MATERIALS AND METHODS

This chapter is organized into three sections. The initial section discusses the characteristics of the skeletal sample. The second section is concerned with details of computed tomography scanning and quantitative structural analysis of trabecular bone. The final segment discusses biological measures and methods of vital importance to this research including age-at-death estimations, maturity stage seriation, body mass estimations, and femoral bicondylar angle determination.

THE SKELETAL SAMPLE

Juvenile human skeletal remains used in this study are drawn from the Late Prehistoric site SunWatch, an agricultural 13th Century village. The SunWatch skeletal sample is curated and housed by the Dayton Society of Natural History at the Boonshoft Museum of Discovery, Dayton, Ohio. Appropriate permissions have been obtained for use of selected individuals as part of this research project. The proximal

tibia is the skeletal element used in this research to quantify to the pattern of ontogenetic morphological architecture changes in trabecular bone.

The skeletal collection from SunWatch is comprised of 103 nonadult and 63 adult individuals. These skeletal remains have previously had determinations of age and sex (when possible) estimations (Sciulli and Oberly, 2002). They are represented by all age groups from 0.0 to 50+ years. The SunWatch subadult series exhibits geographical and cultural coherency and relative genetic homogeneity. Although, population movement, admixture, and aggregation were occurring during this period contributing to the large, dense settlements, biodistance studies demonstrate a common ancestral pattern (Robbins and Neumann, 1972; Giesen, 1992). The lifestyle of this group was characterized by intensive maize agriculture combined with variable seasonal subsistence-settlement cycles.

The SunWatch skeletal series was chosen for this study because of its regional, cultural, biological, and topographical consistency; the well-studied archaeological context; and the number and age distribution of well-preserved subadult individuals. The proximal tibia has been chosen for this study of loading history analyses because of its excellent preservation characteristics. The proximal tibia's central position in weight-bearing loading and the fact that during the stance phase of gait the loading direction is generally orthogonal and uniaxial (Freeman and Pinskerova, 2005) are expected to enhance the structural analysis by reducing the influences of multiaxially-directed forces.

Selected juvenile proximal tibiae from the larger subadult skeletal series and three young adults form the sample selected for microCT imaging and 3-D structural analysis. Selection criteria included preservation/pathological condition status, distribution within the developmental maturity scheme and age-related groupings, and the relative dispersal in spatial distribution of burials within SunWatch village. Bones with pathological conditions (rickets, scurvy, infection) or poor preservation were excluded from the sample. Adequate preservation is defined as an intact proximal metaphyseal surface and proximal third of the bone, with or without the proximal tibial epiphysis. Subadults were ordered (seriation; see Methods) according to a relative developmental maturity based on dental developmental criteria, epiphyseal fusion, and long bone diaphyseal metrics. The age/developmental groupings are intended to demonstrate the mechanical influences of normal functional activities on bone adaptation superimposed on the ontogenetic substrate. These age groups were initially set up and described in the hypotheses section of this dissertation (Chapter 1) as follows:

1. 0-1.0 years: infancy (not walking)
2. 1.0-5 years: early childhood (walking)
3. 5-10 years: middle childhood (independent activities)
4. 15-24 years: adolescence/ early adult (full adult lifestyle)

The sample was anticipated to consist of 40 proximal tibiae from juvenile individuals; 10 individuals distributed into each of 4 age groups. The full realization of this plan was constrained by the not atypical low number of skeletal remains in the

late childhood/adolescent ages. Tibiae from three young adult individuals (ages 19-24 years) are included in the sample representing the near-term target for the ontogenetic pattern. Three juvenile individuals were eventually excluded from quantitative analysis after scanning because of taphonomic changes of intratrabecular mineral inclusions (two individuals) and trabecular structural anomaly associated with suspected treponemal disease (one individual). The complete sample analyzed was composed of 36 tibiae [see Appendix A for the comprehensive dataset].

PROJECT METHODS: OVERVIEW

Micro computed tomography (microCT) and High Resolution X-Ray Computed Tomography (HRXCT) technology combined with three-dimensional (3D) structural computational analyses can produce non-invasive, high-resolution skeletal images and quantitative data, ideal for the investigation of ontogenetic patterns of change in trabecular bone (Muller et al., 1994; Ruegsegger et al., 1996). Measurements of trabecular bone architecture and material properties have been shown to correlate with skeletal adaptation to internal and external loads inherent to human growth, development, and aging (Ding et al., 2002). MicroCT is a particularly robust technology for trabecular bone analysis closely correlating with histomorphology and experimental structural analysis; allowing the accurate reconstruction of the complex latticework construction of trabecular bone (Fajardo

et al., 2002; Muller and Ruegsegger, 1995; Uchiyama et al., 1999; Van Rietbergen et al., 1998).

In this dissertation terms *CT* and *microCT* are used for "generic" discussion purposes; the terms *HRXCT* and *UTCT* apply specifically to the University of Texas computed tomography scanner. This section begins with an overview of CT scanning and structural analyses. It then presents the specifications of the UTCT scanner used for this research, and proceeds to detailed discussions of the particular methods and protocols of this research using as source material: published literature, information derived from the UTCT website, personal experience, and discussions with UTCT research scientists.

The microCT scanner employs an array of X-ray point source beams producing information in a number of projections, allowing a three-dimensional image to be calculated. MicroCT was initially used qualitatively to study osteoporosis. The high resolution CT scanner (HRXCT) has several important modifications compared to the microCT scanner resulting in reduced distortions, higher spatial resolution, and lower radiation dose (Odgaard, 1997). Recent studies have been published on the trabecular architecture of non-human primates (Fajardo and Muller, 2001; Ryan and van Reitbergen, 2005) using both types of imaging. These studies demonstrated that microCT and HRXCT accurately image micron-sized trabecular struts allowing measurements related to cancellous bone mechanical properties. The development of three-dimensional computational

methods has now provided exciting possibilities for bioarchaeology, skeletal biology, and human growth and development.

The high-resolution X-ray computed tomography scanner at the University of Texas at Austin, Department of Geological Sciences, was used in this project to produce sequential scan data of the entire proximal tibial metaphysis of the SunWatch juvenile skeletal sample. Samples were scanned at nominal resolutions ranging from 22- 80μm in all planes (x, y, and z). This allowed for accurate reconstruction and quantification of trabecular microstructural architecture (Ryan and van Rietbergen, 2005; Kothari et al., 1998). Spherical volumes of interest and biomechanically-appropriate scaling for sample size were defined within each scan dataset from which structural computations were made. This protocol, in general according to the published literature, calibrates for an accuracy of 0.5% (Ryan and van Rietbergen, 2005). An evaluation of the measurement process specifically for this investigation was carried out using the methodology of Gage R&R studies (Wheeler and Lyday, 1989).

3D structural analysis consists of measurements of specific parameters: bone volume fraction (BV/TV), trabecular number (Tb.N), trabecular thickness (Tb.Th), and degree of anisotropy (DA). These are calculated from the HRXCT images using the Quant 3D software program. The measured structural parameters, describing the trabecular fabric, are indicators of cancellous bone microarchitecture, mechanical properties, and skeletal adaptation to loading history (Ulrich et al., 1999; van Reitbergen et al., 1995; Zysset, 2003).

CT: BASIC PRINCIPLES AND GENERAL BACKGROUND

X-ray computed tomography (CT) was developed as a medical diagnostic tool in Great Britain in 1971, gaining its inventors, A.M. Cormack and G.N. Hounsfield, the Nobel Prize for Medicine in 1979 (Hounsfield, 1973; Ledley, 1974). CT is now an established and rapidly expanding technology in clinical medicine. Its potential for application to industrial use and anthropological, paleontological, and geological research has been gathering influence in the past two decades (Conroy and Vannier, 1984; Ketcham and Carlson, 2001; Ruff and Leo, 1986). CT allows for the nondestructive three-dimensional mapping of the variation of X-ray attenuation within objects producing straightforward, intuitive imagery in a digital format, lending itself to quantitative analysis.

The basic common elements for X-ray radiography include an X-ray source, an object to be imaged through which the X-rays pass, and a series of detectors that measure the extent to which the X-ray signal has been attenuated by the object (Ketcham and Carlson, 2001). Important aspects of an x-ray source include the size of the focal spot, the spectrum of energies generated, and the x-ray intensity. The focal-spot size is one determining factor for the potential spatial resolution of a CT system: the fewer source-detector paths, the finer the resolution. The energy spectrum of x-ray accounts, in part, for the relative attenuation of the beam passing through materials. Higher x-ray intensity accounts for more effective penetration and more image clarity (reducing the signal-to-noise ratio). If all waves

have the same frequency they are called *monochromatic* (one color): a source like a laser or an x-ray synchrotron. A source like a light bulb, the sun, or an x-ray tube generates *polychromatic* (white light) radiation (many wavelengths).

The effective energy spectrum of a system depends on the energy input of the x-ray source, beam filtration, beam hardening in the object scanned, and the relative efficiency of the detectors to different energies. Scanning artifacts are possible from changes in the X-ray spectrum caused by passage of the beam through an object. Compensation for these will be discussed in a later section.

The attenuation (photoelectric absorption, Compton scattering, and pair production) of the X-ray beam as it passes through an object/medium is used to reconstruct images. In photoelectric interactions, the energy of the x-ray is absorbed by, or transferred to, an inner electron in an atom of the imaged medium. This electron is then ejected at an angle. This interaction is related to the atomic number of the material scanned, resulting in a material differential in attenuation. For example, the calcium component of bone has a higher atomic number than non-bone constituents producing a relatively higher photoelectric interaction and greater total attenuation.

Compton scattering is another interaction of the x-ray beam with the scanning medium. X-ray imparts energy to an outer electron of an atom of the material scanned, to be ejected at an angle, scattering in another direction at reduced energy. Compton interactions are dependent upon electron density which

is related to the physical mass density of the material (Hendee, 1983). Collimation of the x-ray beam and detectors removes most of the photons produced by Compton and photoelectric interactions. Collimation refers to the divergence of the waves in a beam. Beams with waves which are all progressing in the same direction are termed a well collimated beam. A light bulb produces uncollimated light which spreads in all directions. The third attenuation process, pair production involves a photon interaction with a nucleus, transforming it into a positron-electron pair. This is associated with transfer of excess photon energy.

The linear attenuation coefficient, μ, is the rate of removal of x-rays per unit path length of material traversed (Ruff and Leo, 1986). Attenuation numbers for different materials generated by a CT scanner are expressed relative to the linear coefficient of water at that x- ray energy. The Hounsfield scale (H) is the most widely used constant for this expression. Water is 0 H (by definition); air is -1000 H (no attenuation). Bony structure CT numbers range from 500- 2000 H; soft tissue CT numbers range from -100- +100 H.

The essentials of image acquisition involve the measurement of attenuation coefficients from a series of detectors at small intervals along the path of collimated x-ray beams passing transversely through the object scanned. Detectors make use of scintillating materials to record flashes of light generated by the incoming X-rays. The detectors influence image quality through their size, quantity, and efficiency in detecting the energy spectrum emanating from the

source. Detector images are converted to digital data producing a video signal divided into pixels.

A single set of X-ray intensity measurements on all detectors for a given object position and scanner geometry is termed a *view* (Ketcham and Carlson, 2001). This process is repeated through rotations of 360 degrees, acquiring multiple sets of views of an object over a range of angular orientations. Continuity of views produces an image, sonogram. These data, converted by a mathematical process, are used to create two-dimensional images, *slices*, corresponding to what would be seen if the object were sliced along the scan plane. Spatial resolution of CT images is determined by numerous factors including the focal spot of the X-ray beam, the size and spacing of the detectors, and the dimensions of the field of reconstruction. Contrast resolution, which is the ability to distinguish between materials of different attenuation properties (i.e. bone / non-bone), is typically 0.5% or better (Hendee, 1983).

Image reconstruction and display are based on visual images generated by the attenuation coefficients placed within a matrix of 1024 x 1024 picture elements (pixels). Pixel size is multiplied by slice thickness to produce volume elements (voxels) in which CT number/value intervals are represented by a continuum of "gray levels." The raw intensity data is formed in a sinogram, which is converted to CT values in a range specified and relevant to the material being scanned. As already discussed, medical systems generally use the Hounsfield Unit. CT systems with flexible geometry, scanning modes, and multiple uses (i.e. UTCT) develop

differing and specific optimization techniques for different materials, which in principle maintain an assumed linear relationship between CT number and density. For example, x-ray attenuation differs between marrow-filled cancellous bone (autopsy specimen) and archaeological bone samples. “The presence of fatty marrow in the pore spaces of cancellous bone increases its overall density, but decreases its attenuation of x-rays relative to mass density” (Ruff and Leo, 1986, p.190).

CT scanners can be grouped into four categories based on their spatial resolution and the size of objects they are most suitable for scanning (Table 5.1). Medical scanners generally are in the category of conventional CT; recently developed exceptions are the cardiovascular multidetector scanners. Industrial scanners are designed to image a wide range of scales. The University of Texas high-resolution X-ray CT Facility is a custom designed scanner combining, in tandem, a high-resolution system and an ultra-high-resolution system, capable of microtomographic resolution. This scanner will be discussed in detail in subsequent sections.

Type	Resolution	Scale of Observation
Conventional	mm	m
High Resolution	100µm	dm
Ultra-high Resolution	10µm	cm
Microtomography	µm	mm

Table 5.1 Types of CT scanners (from Ketcham and Carlson, 2001)

CT scanners can also be classified according to a generational taxonomy. The scanners utilizing only x-rays in the scan plane range from first- through fourth-generation systems. First-generation CT directs a pencil beam through the object to a single detector. The source-detector pair is translated across the object in the scan plane: repeating from a number of angular orientations (Figure 5.1A). Second-generation CT uses the same procedure with a fan beam and a series of detectors (Figure 5.1B). Third-generation CT uses fan beam and detector arrays which are wide enough to scan the entire object; only rotation of the object or source-detector pair is required (Figure 5.1C). Third-generation scanners are faster than second-generation. The offset technique (Figure 5.1 D) permits larger objects to be scanned and smaller objects to be closer to the narrower section of the fan beam. This results in improved resolution through enhanced utilization of detectors. These scanners maintain relative motion between the object and source-detectors. The object may move or the source-detector pair may move. The UTCT

scanner used in this research was in the third-generation mode. Fourth-generation scanners are typically modern medical devices in which a single x-ray source rotates around the object being scanned with a fixed complete ring of detectors.

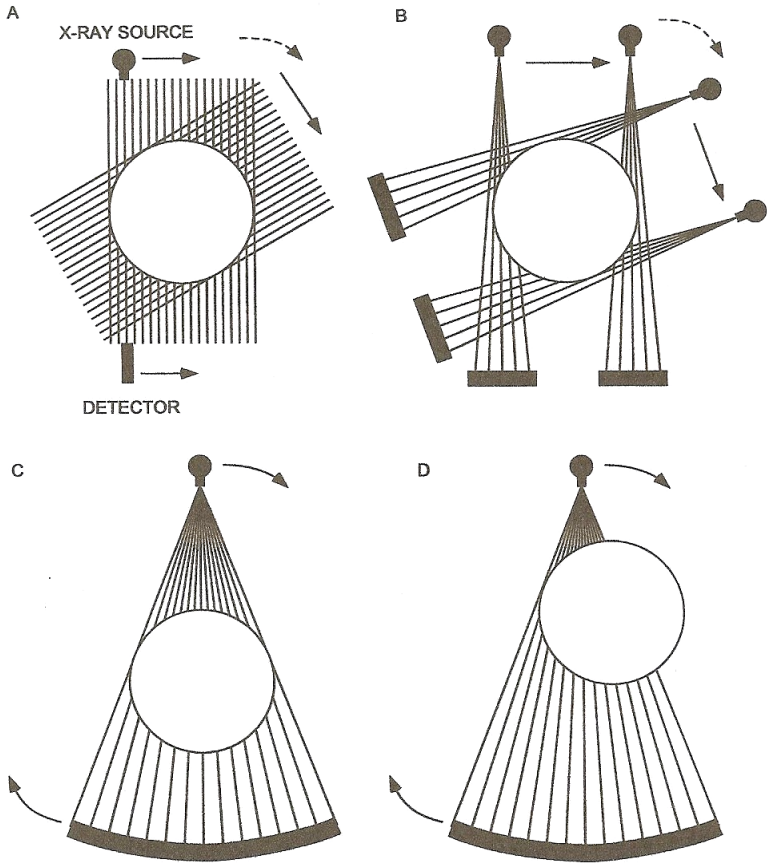

Figure 5.1 A-D Characteristic geometries of first (A), second (B), third (C), and offset mode third (D) generation CT scanners. White circles represent the object scanned and thin black lines the x-ray beams (from Ketcham and Carlson, 2001).

Volume scanning uses a cone beam or a highly collimated, thick, parallel beam rather than a fan beam. The linear series of detectors is replaced by a planar

grid allowing faster data acquisition by compiling data for multiple slices in one rotation. The UT facility is capable of second- and third-generation scanning on the high-energy system, and third generation and volume scanning on the ultra-high-resolution system. Third- generation scanning is usually the method of choice (Ketcham and Carlson, 2001).

Artifacts

Computed tomography has subtle associated complications which can make the data problematic for quantitative use. The identification and management of the more commonly encountered problems requires discussion: beam hardening, ring artifacts, and partial-volume effects. Beam hardening is the most common CT scanning artifact, causing the edges of an object to appear brighter than the center even in a homogeneous material (Figure 6.2 A-D). This artifact is caused by the increase in mean x-ray energy (*hardening*) of the X-ray beam as it passes through the object scanned. Lower-energy X-rays are attenuated more easily than higher-energy X-ray; a polychromatic beam preferentially losses the lower-energy portion of its spectrum. The process results in a higher average energy in the effective beam leading to more attenuation of the short ray paths than the long ray paths. Image manifestations of beam hardening are an artificial darkening at the center and brightening near the edges of the object scanned, which may make differentiation between artifact and actual material variation difficult. Beam

hardening artifact thus changes the CT value of a material depending upon its location in an image.

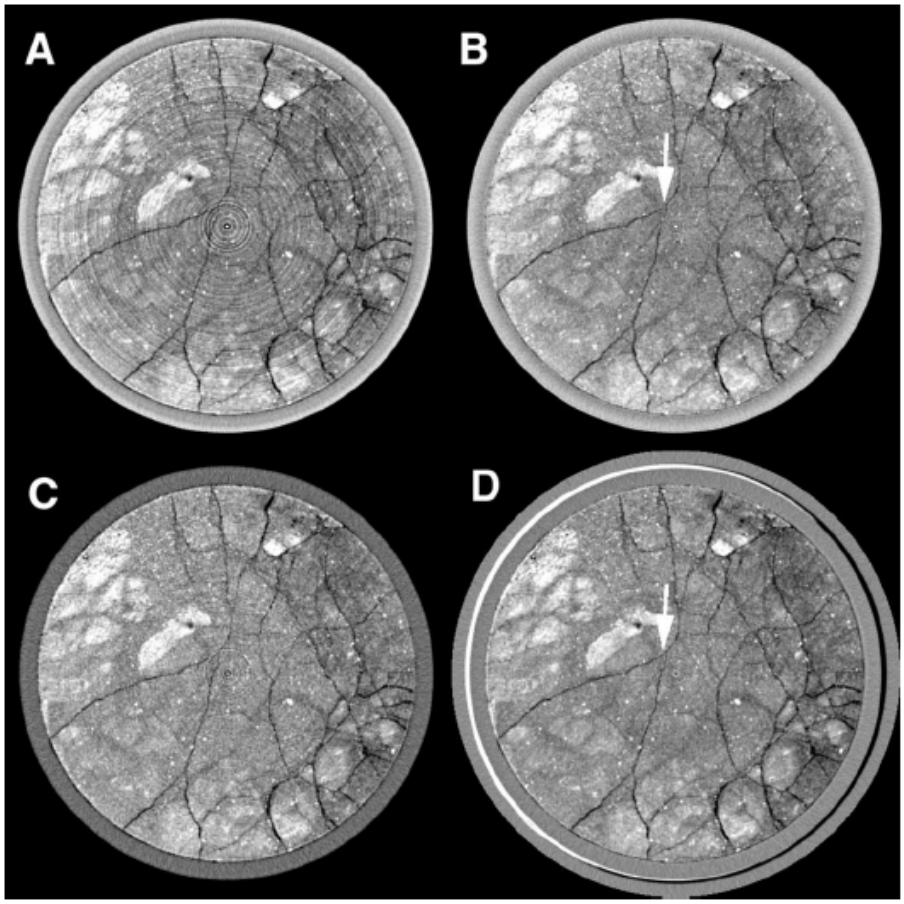

Figure 5.2 A-D Examples of beam hardening CT artifact with artificial darkening at the center and brightening near the edges of the object scanned. A. also demonstrates ring artifacts (from Ketcham and Carlson, 2001).

Remedies for beam hardening include using an X-ray beam of sufficient energy to ensure that beam hardening is negligible, remove the outer edges of an image and use only the center, pre- or post-harden the X-ray beam through an attenuating filter (copper, brass, or aluminum), and/or use a wedge packing

material creating an overall cylindrical form of material of similar attenuation. These measures have varying degrees of effectiveness depending on the particulars involved. Beam hardening can also be addressed at the data processing stage if the object scanned is materially uniform. A correction can be applied to the raw scan data converting each reading to a non-beam-hardened equivalent before reconstruction. Other techniques include after-the-fact software wedge correction or application of a Fourier filter that removes long-wavelength variations in CT value.

Ring artifacts appear in third-generation scanning as circles centered on the rotational axis (Figure 6.2 A). Shifts in the output of various detectors cause the corresponding x-rays in each view to have inconsistent values accentuated during reconstruction. Detector variability is related to changes in scanning conditions including: change in temperature or beam strength and differential sensitivity to varying beam hardness. This link to beam hardness allows ring artifacts to be mitigated at the scanning stage by the same methods used for beam hardening alone. In addition, ring artifacts are open to software solutions by removing the apparent linear feature in the sinogram before or during the reconstruction procedure. A downside of these methods is that any actual linear feature may be altered even if it does not coincide with a ring,

Partial-volume effects are related to the fact that the CT value of a specific material volume represents the average of the attenuation properties of the various

substances in that volume. Material boundaries are blurred to some extent as constrained by the resolution limitations of X-ray; material in any one voxel can affect the CT values of neighboring voxels. This provides both a problematic aspect for quantitative interpretations as well as an opportunity for fine-scale data extraction. Interpretation of CT values in voxels containing multiple components (i.e. bone/non-bone) may or may not be reasonable straightforward. For example, if a voxel contains to components of similar attenuation values, a linear combination of the CT values based on their volumetric proportions provides a satisfactory resolution. In the case for two components with attenuation values far apart (bone/non-bone) error can result if their boundary is parallel with the scan plane; fortunately this error is frequently negligible. These issues are discussed below in more detail in the section on thresholding.

Data generation

The framework for developing scanning procedures, resolution requirements, and case-specific scanning parameters is termed *optimization*, the objective of which is to "maximize the contrast between features of interest while minimizing or eliminating artifacts than can interfere with analysis" (Ketcham and Carlson, 2001, p.392). This current scanning project follows the optimization process: identify imaging objectives, define necessary image resolution, slice thickness, and attenuation discrimination. These decisions provide guidance for the best scanning parameters including source-detector combination; scanning mode;

X-ray energy, intensity, and spot size; beam filtration, scanned in air or packed; and wedge material. This is an adaptive process, refining scanning technique to match the study's objectives. The results of this optimization process for this project will be specified in a later section of this chapter.

The visualization of the CT scan depends upon a three-dimensional matrix of relative attenuation values, a *data brick*. The actual presentation of this data depends on the scientific application and study objectives. Skeletal structures are frequently investigated using two-dimensional data (slices) along three orthogonal axes (coronal, sagittal, and horizontal). Three-dimensional representations have also proven useful: isocontouring and volume rendering. The isocontouring process defines one (bone) or more of the surfaces that marks the boundaries of the object and constructs a topographic map from the gridded data. Isocontour positions are interpolated among data points, defining the surfaces on a subpixel scale (Figure 5.3), resulting in detailed surface information and the possibility for volumetric measurements. Isocontouring may at times be arbitrary in the definition of a surface. In addition these data sets require more memory and processing power than does volume rendering.

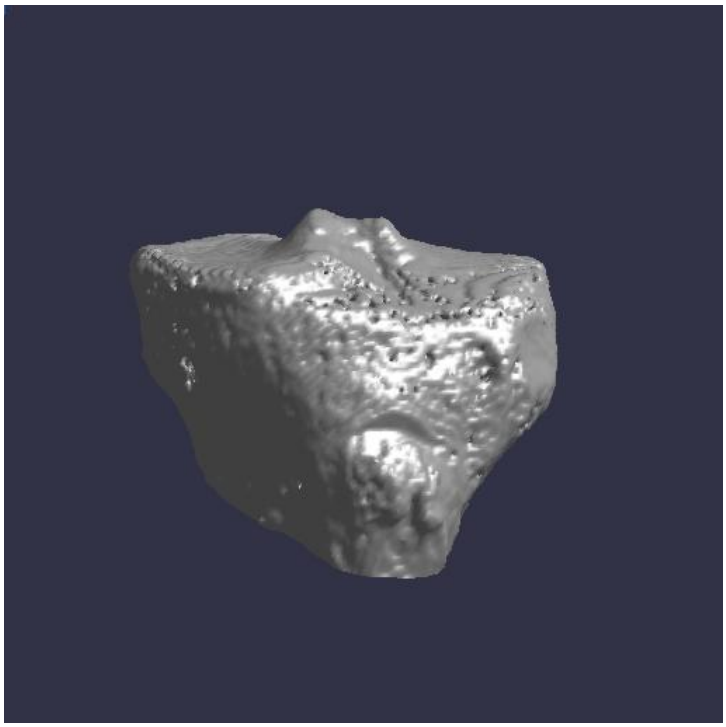

Figure 5.3 Example of an isocontour image of the proximal tibia from three-dimensional reconstruction of CT scan data.

Volume rendering assigns each voxel a red-green-blue color or alternatively a gray scale and opacity based on that voxel's CT number. By setting some voxels' opacity to zero it is possible to see into a material of interest. Volume rendering is especially suited to CT imagery, allowing discrimination between two materials based on their average CT value or textural differences. A larger range of information is available in the volume rendering technique compared to isocontouring. It is especially useful for visualization of internal structures such as in fossil crania.

Segmentation is a necessary procedure to convert CT data into an isocontour analysis. This a collection of computational and statistical techniques used to separate features of interest from "the rest" (Glasbey and Horgan, 1995). Various steps assisting segmentation include noise reduction, edge enhancement and tracking, and region growing. Two common techniques are *thresholding* and *edge finding*. No segmentation technique is universally applicable for all images and no segmentation technique is designated as perfect. This study uses a consistent thresholding technique which will be presented in a section to follow. The discussion now turns to the specific descriptions for this study of the UTCT HRXCT, the research-specific scanning protocol developed by the process of optimization, and the particulars of three-dimensional structural analyses using Quant 3D software.

UTCT

The University of Texas HRXCT scanner (Figure 5.4) is a custom designed, high performance imaging system built by Bio-Imaging Research in Lincolnshire, Illinois with an objective of having the capabilities of scanning objects ranging from meteorites to bony trabeculae, from decimeters to meters in size, and with a spatial resolution on the order of a few micrometers to millimeters. Discussion that follows is a synopsis of the description of the UTCT scanner on the www.ctlab.geo.utexas.edu website, in the published literature, and gleaned from personal experience and discussions at the UTCT installation.

.

Figure 5.4 UTCT scanner (image from www.ctlab.geo.utexas.edu).

The scanner is a tandem design of two subsystems within a signal radiation-safety enclosure (i.e. lead box): an ultra-high resolution subsystem and a high-energy subsystem. The ultra-high-resolution subsystem, used for this research, has a recently upgraded 225 kV X-ray source with a microfocal spot (one micron). This is associated with an image intensifier detector sampled by a 1024 X 1024 CCD (charge-coupled device) video camera to sample images from 3 to 70 mm in diameter. The limits of spatial resolution of this system are determined by the specimen's proximity to the X-ray source (magnification increases with proximity), combined with the fixed pixel size of the video image, and the

dimensions of the data voxels. This results in a highly flexible system capable of imaging specimens from several cm to a few mm in diameter with spatial resolution from ~250 μm to ~ 5 μm.

The microfocal, high- energy X-ray source is polychromatic and allows for stable X-ray output throughout a range of mean energies. This permits a high level of discrimination among materials of closely similar attenuation penetrated by relatively low-energy radiation, as well as reliable scans for small fossils and rocks requiring higher energy X-ray. The high-energy subsystem for tomography of large specimens (up to 50 kg in weight) employs a 420-kV tungsten X-ray source, a rotating turntable, and either of 2 available high-energy detectors. This system is appropriate for geological specimens such as segments of drill cores or large fossils.

The UTCT system's flexibility is further enhanced by the ability to acquire data in several different modes, thus optimizing performance. Both subsystems can collect data in third-generation geometry (rotate-only; centered and variably offset). The high-energy subsystem can also operate in second-generation geometry (translate-rotate). This flexibility allows for increased resolution within subvolumes by selective reconstruction of the raw attenuation data. Complete control over translational positioning of the object scanned ensures that maximum resolution can always be achieved. This system has a "multi-slice" mode which acquires data from several slices simultaneously significantly reducing scan times

at minimal cost in scan data quality. Both subsystems are fully enabled for digital radiography in standard 2-D X-ray projection: real-time (continuous) or as a separate study. It is the combination of high-energy X-ray source, microfocal spot, highly sensitive detectors, and precision positioning mechanisms that makes the UTCT exceptionally capable of acquiring high resolution CT scan data, essential to this study of quantitative changes in trabecular bone.

The digital image analysis laboratory adjacent to the UTCT scanner is dedicated to the reconstruction of digital images from the raw CT data. Visualization requires advanced computational resources capable of processing very large blocks of data. These techniques often rely on 3-D rendering, animation into sequential views, and interactive examination of the reconstructed images. Software and techniques have been developed by the UTCT research scientists to extract and ensure full scientific value from scan data, including proper interpretation of the data and maintenance of integrity of the reconstructive process. This researcher benefited greatly from the expertise in CT data acquisition, reconstruction, and software application of the UTCT research scientists. All samples were scanned at the High-Resolution X-ray Computed Tomography Facility (HRXCT) at the University of Texas at Austin (UTCT; http://www.ctlab.geo.utexas.edu).

SPECIFIC IMAGING PROTOCOL

Data collection

Individual tibiae were mounted in a vertical position with the proximal end down, embedded on florist foam block and stabilized with bee's wax. Care was taken to ensure that the proximal tibia was oriented vertically and thus the scan plan was perpendicular to the long axis. Each tibia was scanned individually with serial cross-sectional slice thickness and spacing ranging from 0.0215 to 0.0857 mm depending on the size of the proximal tibia. The entire proximal tibial metaphysis (and epiphysis if present) was imaged beginning at the proximal-most margin and continuing distally until approximately the beginning of the diaphyses. This protocol produced 600-700 slices, which equals 600-700 million data bricks (1024 x 1024 pixels) per specimen for computational analyses. Because of growth-related proximal tibial breadth size differences, four reconstructed fields of view (FOR) were used (22, 40, 60, and 80mm) yielding an in-plane pixel size of 21-78μm for each specimen (see Appendix A). This effective resolution is within the documented range necessary for accurate trabecular bone quantitative studies (Kothari et al., 1998; Majumdar et al., 1998; Laib and Ruegsegger, 1999; Ryan and Ketcham, 2002a, b).

Tibiae were scanned with source energies of 150 kV and between 0.1 and 0.19 mA depending on size with no filter, no offset and air wedge. Wedge refers to packing material used to create an overall cylindrical form of material of similar

attenuation. This can reduce beam-hardening artifact. In this case no packing material was necessary. The distance from the X-ray spot to the center of rotation of the object scanned (source-object distance; S.O.D) ranged from 66 to 245 mm depending again on the size of the tibia. Scans were collected with 1600 views, 1 sample per view, and 31 slices per rotation. Views is the number of angular positions that data is obtained at (e.g., 360 views is data collection every 1 degree).

Imaging processing

The scan data sinogram was processed for ring removal using the IDL (Research Systems, Inc., Boulder, CO, U.S.A.) routine "RK_SinoRingProc Simul" with default parameters. Rotational correction processing was performed with IDL routine "DoRotationCorrection." Images were reconstructed in a 1024 X 1024 16 bit TIFF format. TIFF (Tagged Image File Format) is a flexible and adaptable file format used for storing images. It can handle multiple images and data in a single file through the inclusion of "tags" in the file header. Tags can indicate the basic geometry of the image, such as its size, or define how the image data is arranged and whether various image compression options are used. The ability to store image data in a lossless format makes TIFF files a useful method for archiving images. Unlike standard JPEG, TIFF files can be edited and resaved without suffering a compression loss.

The images were then reduced from 16-bit to 8-bit data using the IDL platform program "Do16to8." This processing produced a reduction of the number

of grayscale values in the histogram to 256 (from 0- 4095) with no loss of voxel resolution. Gray values represent X-ray attenuation, which is a close function of density (Ketcham and Carlson, 2001; Maga et al., 2006).

The structural analysis software program developed at UTCT specifically for trabecular bone, Quant3D, was used for this research (Ryan and Ketcham, 2002a, b; Ketcham and Ryan, 2004). Quant3D is written in the Interactive Data Language (IDL) v. 6.3 (Research Systems, Inc.). This program implements common quantification parameters of trabecular architecture such as bone volume fraction (BV/TV), trabecular thickness (Tb.Th), trabecular number (Tb.N), and fabric anisotropy.

BASIC EFFECTS AND LIMITATIONS OF DATA ACQUISITION

CT thresholding protocols

The quantitative interpretation of images derived from CT scanning requires a method to clearly distinguish the structure of interest from the surrounding structure- in the case of this research, bone from non-bone. A CT slice displays a spectrum of gray-scale images representing the densities of the structures. The threshold value (gray-scale value) is that which sets the boundary. The difficulties arise from the fact that the boundaries between adjacent structures are never clearly defined, but instead are characterized by a continuum of gray-scale values (Coleman and Colbert, 2007). The accuracy of the thresholding protocol lies in its capability to minimize this "blurring of the edges." Compounding this consideration is the situation in which

measurements are taken on a three-dimensional VOI (sphere) as in the current research. The threshold value must be applied to a dataset of tens or hundreds of slices, as opposed to a single slice. Research into the effects of threshold selection suggests its importance for the accurate determination of bone volume fraction and mechanical properties, especially in cases of low BV/TV. The architectural directionality of bone fabric appears to be less sensitive to changes in threshold (Hara et al., 2002).

Each individual's dataset in this research was thresholded to discriminate between bone and air using the iterative segmentation algorithm of Ridler and Calvard (1978; Trussel, 1979). In this method, the mean grayscale values above and below a proposed threshold are calculated and used as the threshold for the next iteration. The process continues until a stable solution is found. This method has been validated by several reseachers (Glasbey and Horgan, 1993; Leung and Lam, 1996) as having performed best against other thresholding processes using objective standards such as precision, consistency, and approximation of the correct threshold (when using synthetic images). Benefits in the iterative thresholding technique as implemented for CT data are: (1) the approach takes the entire three-dimensional volume and all grayscale values into consideration in determining the optimal threshold value, (2) the iterative method is automated, and (3) it reduces the possibility of calculational errors of the threshold values. In every instance the appropriateness of the implementation was verified by visual examination of the images and the calculated thresholds.

The automated Ridler and Calvard 1978/Trussel 1979 thresholding system is based on the assumptions that the data encompass the full range of gray levels and that the sample has two components (air and bone). The presence of a third material (marrow, dirt, mineral intrusions) may make results less reliable. The stability of this thresholding method in this research is demonstrated in the 100% repeatability of bone volume fraction values for every specific VOI analyzed within a specimen. This does not exclude, however, variation between VOIs in the same specimen or variation between specimens from diagenetic effects, differential trabecular preservation, or subtle mineral intrusion. Careful visual inspection of the placement of the spherical VOIs in this research was undertaken in order to not include regions with intrusive materials or trabecular damage. The importance of the influence of thresholding on microstructural parameters, in this particular research, lies in being attentive to the explicit methods of data acquisition. This is especially important when comparing microCT-derived quantitative data between and among researchers.

Resolution Dependency of Microstructural Properties

The CT scanning optimization process and the flexibility of the UTCT scanner used in this research resulted in all scans being performed at the maximum resolution possible given the size of the object, field of reconstruction , voxel size and slice spacing, inherent geometry, and X-Ray energy. Because of the striking change in tibial size from birth to adulthood, four fields of reconstruction (FOR) with corresponding voxel sizes and effective resolution (22, 40, 60, and 80 μm) were

required for the complete scanning dataset. An important question to be asked is: what is the dependency of the three-dimensional microstructural properties on the measurement resolution? It should be noted that because various CT scanners have differing flexibility, focal spots, X-ray energy, and geometry a portion of the answer to this question is scanner-specific. The literature discussed below reports results from diverse scanners. No specific data are available for the UTCT scanner.

Muller et al. (1996) studied the question of resolution dependency using a microCT system providing a nominal isotropic resolution of 14 μm. Resolution in the volumes of interest were then subjected to reduction factors ranging from 2 to 20. Bone volume fraction (BV/TV), trabecular number (Tr.N), and trabecular thickness (Tr.Th) were assessed. BVTV was found to remain constant up to a resolution of 100 μm. Trabecular number decreased gradually from resolutions of 14-100 μm-approximately 10%. Trabecular thickness, similar to BV/TV, was relatively constant up to a resolution of 100 μm. All properties were found to either decrease (BV/TV, Tr.N) or increase (Tr.Th) "monotonously up to a nominal resolution of about 175 μm" (Muller et al., 1996, p.118).

Kothari et al (1998) reported on human trabecular bone imaged at a resolution of 40 μm and then artificially degraded to an in-plane resolution of 100 μm and a slice resolution of 100-1000 μm. The results of this study indicated that the morphometric measures of BV/TV and trabecular number showed weak resolution dependency. Structural anisotropy demonstrated strong resolution dependency for the

femur, but not the vertebrae. The measure of trabecular thickness was noted to have strong resolution dependency. The increase in trabecular thickness has been attributed to the averaging out of thinner trabeculae at the lower resolutions (Kothari et al., 1998; Muller et al., 1996). The authors state that the resolution dependency of these parameters could be minimized if the slice direction was taken transversely along the superior-inferior axis. It is important to note that this orientation was part of the scan protocol for this current investigation and that the structural data was assessed for resolution dependency.

VOLUME OF INTEREST (VOI) SELECTION

Spherical volumes of interest (VOIs) were extracted from the proximal tibial metaphysis/epiphysis. The two primary VOIs were placed in each proximal tibia: the center of the medial plateau and the center of the lateral tibial plateau. These were located by a systematic VOI selection strategy devised to produce volumes homologous in size, location, and sampling density (Fajardo and Muller, 2001) across individuals of differing size and maturity. The microarchitecture of trabecular bone is spatially heterogeneous and thus the quantitative parameters derived from scan data are highly dependent on VOI position and size. The general strategy in individuals prior to fusion of the proximal tibial epiphysis was a method based on scan slice measurements to position biomechanically and developmentally homologous sampling volumes, tracking the leading edge of ossification in a zone reflecting the initial primary bone response to external loads-

as opposed to remodeled secondary trabeculae (Ryan and Krovitz, 2005)(Figure 6.6). Each VOI was visually inspected to ensure it did not include areas of mineral intrusions or significant preservation damage. The goal was to provide quantitative morphological data on the pattern of trabecular bone architecture in similar anatomical and biomechanically -relevant regions of the proximal tibia at different stages of development.

When applying this sampling procedure (just distal to the growth plate) to individuals 16.9 years and older with the epiphysis present, it became apparent that the volumes of interest contained essentially remodeled secondary spongiosa and not primary trabeculae. The VOIs were moved to the subchondral growth front in order to sample newly formed trabecular bone (Figure 6.7). This position is *not* homologous to that of the younger individuals. In addition, the growth plate contributes an extra horizontal component not present in younger specimens. The advantage of shifting the VOIs proximally in older individuals is that the trabecular bone, which is sampled, is that which is primarily responsive to load. The subchondral spongiosa experiences joint forces directly (Hayes et al., 1978) and is more likely to exhibit the strongest architectural response to differences in loading regimes (Pontzer et al., 2006).. The disadvantage is that the VOIs of the older individuals are not strictly comparable or homologous to those of the younger individuals. The effect of this on the results of this research will be discussed in the following Chapter (Results).

The maximal medial/lateral breadth of the proximal tibia midway between the anterior and posterior cortices defined the x axis (the primary anatomical axis) for the primary VOIs. The y-axis is orthogonal to the x-axis and on the same scan slice. The x-axis line (x) was measured in mm directly from the scan slice data selected at 5mm from the proximal surface of each tibia. The center of the medial plateau was defined as a point on this line, 0.25x lateral to the medial edge; the center of the lateral plateau was defined as a point on this line, 0.75x lateral to the medial edge and bisected by the x-axis (Figure 5.5). The radius (mm) of medial and lateral spherical volumes sampled was based on 50% of the 0.25x dimension. This was converted to the voxel radius by dividing the radius (mm) by the voxel size (mm) of the particular sample, thus relating the voxel sample size of the VOI to a consistent fraction of tibial breadth for each specimen [0.50 X 0.25(x)/ voxel size = voxel radius] . The position of the VOIs along the z-axis (proximal/distal) was selected so that the proximal extent of the spherical volume (north pole) is ≤5mm below the growth plate in younger individuals without the epiphysis present (Figure 5.6) and ≤5mm below the articular subchondral plate in older individuals with the epiphysis present (Figure 5.7).

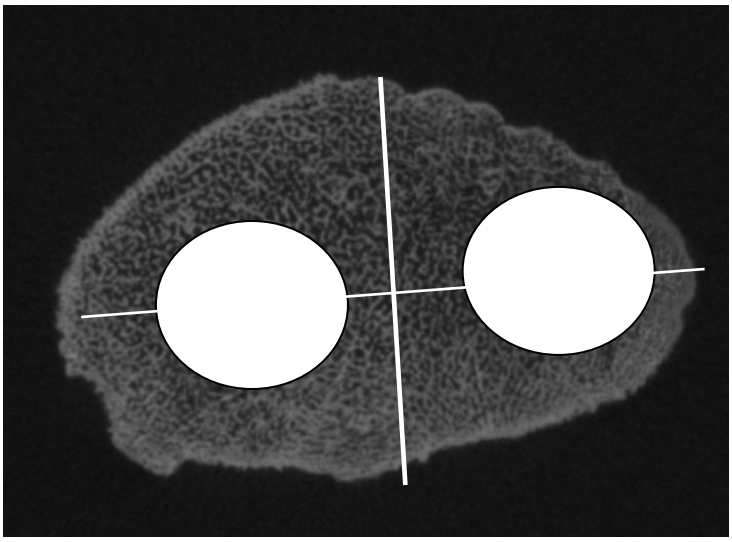

Figure 5.5 Representation of primary medial and lateral VOIs on a CT slice. The x-axis is the thin white line and y-axis is the thicker white line. Spherical VOIs are represented by white circles and are centered in the medial and lateral condyles. Secondary VOIs (not shown) are placed in the center of the each quadrant created by the midline axis intersection. The central VOI (not shown) is centered on the intersection. Image not geometrically precise.

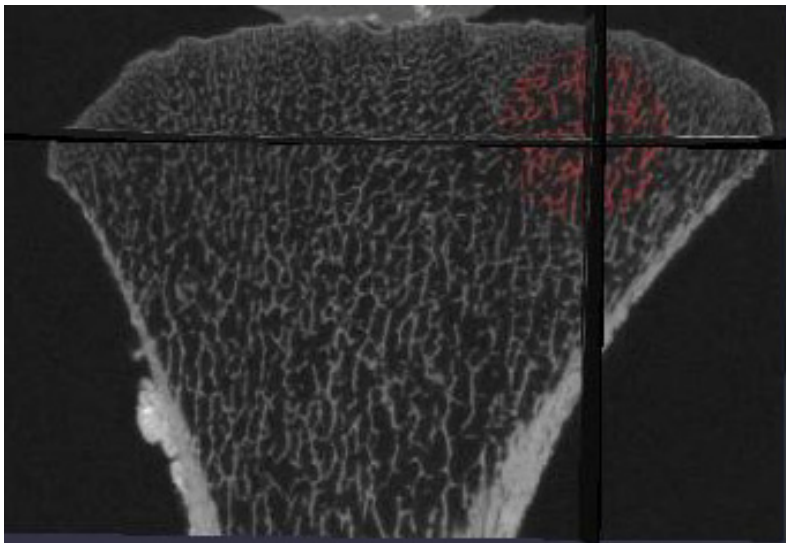

Figure 5.6 Medial VOI z-axis (proximal/distal) location represented by the sphere with transverse, sagittal, and coronal planes indicated by dark shading for reference and orientation. Epiphysis is not present (Burial 15_74).

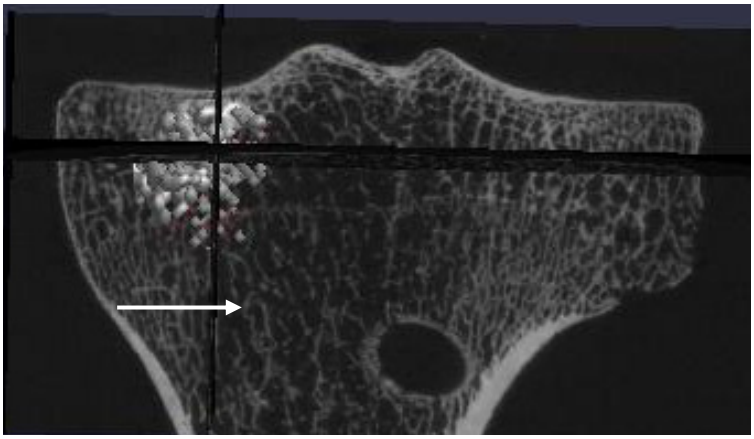

Figure 5.7 Medial VOI location (Burial 3A_76) in older individual with epiphysis present. Transverse, sagittal, and coronal planes are indicated by dark shading for reference and orientation. White arrow locates center of VOI homologous to that in the younger individuals with the epiphysis present.

In addition to the analysis of the two primary VOIs, a separate investigation of the developmental intra-tibial spatial variation of trabecular architecture was undertaken using multiple secondary VOIs located in anterior, posterior, and central regions of the proximal tibial metaphysis/epiphysis. The anterior/posterior VOIs were placed in the center of the anteromedial, posteromedial, anterolateral, and posterolateral quadrants of the proximal tibial as determined by the previously determined x and y axis (see Figure 6.5). They were positioned in the same relative z position as the primary VOIs (see Figure 6.6). The size of these multiple VOIs was smaller (66%) than the primary VOIs in order to avoid any overlap [0.50 X 0.25(x) X 0.66/ voxel size = voxel radius]. Finally, a central VOI was placed at the intersection of the x and y axes. The relative z position and voxel sample size of this VOI were identical to those of the primary VOIs. A selected subsample of eight individuals ranging from fetal to young adult ages was used for these portions of the project.

Quantification of trabecular bone structure

Quant3D was used to analyze trabecular architecture within the various volumes of interest. The morphological parameters quantified by Quant3D include:

- Bone volume fraction (BV/TV): number of bone voxels/total voxels in the VOI.

- Trabecular number (Tb.N): an estimated parameter based on the number of intersections between a grid of lines and the bone normalized by total grid-line length.
- Trabecular thickness (Tb.Th): calculated as the shortest intercept lying in bone.
- Fabric structure and anisotropy: quantified using the star volume distribution (SVD) method.

This research is aimed at quantifying the interrelationships of various structural parameters in developing trabecular bone. Trabecular bone structure and its relationship to joint loading and locomotor behavior is generating increasing research interest with results suggesting a close correspondence between the distribution and arrangement of trabecular bone and the orientation and magnitude of loads experienced (Biewener et al., 1996; Pontzer et al., 2006; Swartz et al.,1998). Cowan (1986) is credited with defining the concepts of three-dimensional fabric structure and fabric tensor to bone mechanics. Fabric describes the local anisotropy of a material; fabric tensor is a mathematical description of the material's fabric. Several methods have been developed to quantify and describe the relative anisotropy and orientation of trabecular bone in three dimensions. Three well-documented techniques used to calculate a second-rank fabric tensor (defined below) are the mean intercept length (MIL) (Cowin, 1986), the star length distribution (SLD) (Odgaard et al., 1997; Smit et al., 1998), and the star volume distribution (SVD). The MIL method measures linear traverses extended to cross multiple material intersections over a range of orientations. The MIL traverses,

crossing multiple boundaries on either 2D orthogonal sections or full 3D VOIs, reflect features of both the material of interest and the surrounding material. The SLD and SVD (the SVD was used for this research), characterize the distribution of bone in three dimensions in only the material of interest: linear intercepts for SLD and infinitesimal cone intercepts for SVD. The principle directions and magnitudes (eigenvectors and eigenvalues) are derived from the fabric tensor and represent the principle trabecular component directions and their relative magnitudes.

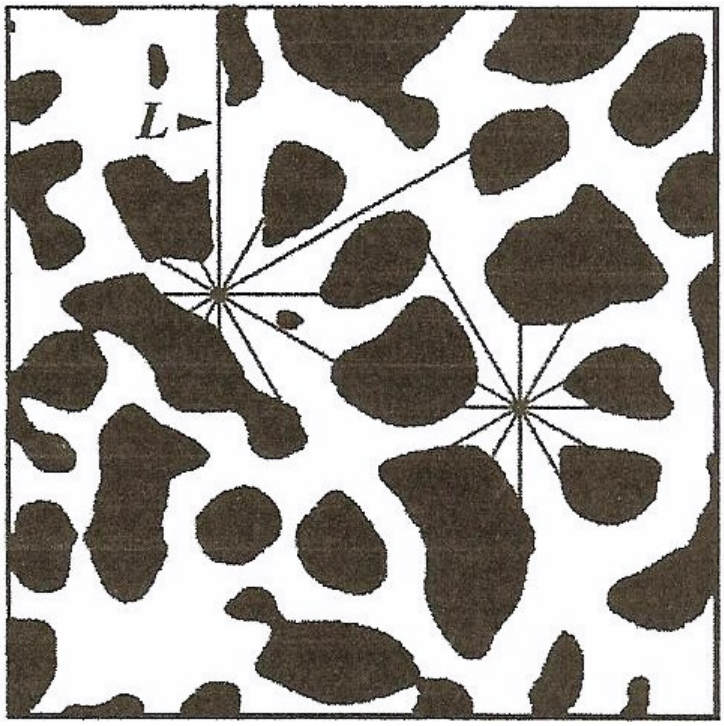

Figure 5.8 Representation of the SVD method (From Ryan and Ketcham, 2002). White is bone; black is marrow space.

The star volume distribution (SVD) method (Cruz-Orive et al., 1992; Ketcham and Ryan, 2004; Ryan and Krovitz, 2006) for quantifying trabecular bone fabric anisotropy expresses the distribution of bone around random points lying within the bone phase and measuring the lengths of lines emanating from them in three dimensions until they encounter a boundary (intercepts). The intercept is the longest uninterrupted "line" passing through each point that lies entirely within a bone at a particular orientation (Figure 5.8). These lines are considered infinitesimal cones with their vertex at the point of origin and their bases at the bone/nonbone interface. The complete set of such cones within an object (VOI) is the star volume component summed over all orientations. The SVD method uses the cubed length of the star component. This tends to amplify differences between major and minor components, resulting in increasing the inferred anisotropy and augmenting data visualization. In the Figure 5.8 depicted above, the SVD method is shown in two dimensions. The white areas are trabecular bone and the black areas marrow space/air. The dark radial "stars" represent how intercepts lengths are measured at several orientations at random points within the bone. *L* is the length of the longest intercept that lies entirely within bone at this particular orientation.

In the current study, the SVD intercepts lengths were measured for 513 uniformly distributed orientations at each of 2000 points lying in the bone phase of each spherical VOI. Researched VOI shapes have included spheres (MacLatchy and Muller, 2002), cubes (Hildebrand et al., 1999; Ryan and Ketcham, 2002b), and

irregular polyhedra (Fajardo and Muller, 2001). Ketcham and Ryan (2004) have noted uneven voxel sampling towards the edges and corners of a cubic VOI. They state that "a spherical VOI is preferable when possible" (Ibid, p.161). The point sampling is random with only points within bone selected for the SVD. Orientation sampling for the distribution of points is based on the algorithm generating unique directions (513) in angular increments projected outward to vertices on the sphere surface. A random rotation is applied to the vector set of each analysis to impart a degree of randomness to the uniform distribution of directions. This uniform angular sampling scheme has advantages over a purely random method in enhancing repeatability and visualization (Ketcham and Ryan, 2004). The reproducibility of the SVD anisotropy and other structural measurements in this study was assessed by the measurement evaluation methodology for Gage R&R studies (Wheeler and Lyday, 1989) using the central VOIs, identical parameters (sampling method, number of points and orientations, and uniform orientations with a random set), and three complete replications on eight different specimens. This will be discussed further in the Results chapter.

A tensor expresses the relation between material response or force with respect to the axes of its underlying symmetry or reference frame. A first rank tensor is a spatial vector: its three components (*x, y, and z*) refer to the axes of some reference frame. A second rank tensor has 9 components (3×3 matrix). Each component is associated with two axes: one from the set of the reference frame axes and one from the material frame axes. This can be thought of as a linear

relationship between two vectors (Pruffle, 2007). A second rank tensor was derived from the orientation and intercept data, which were compiled into a weighted 3×3 orientation matrix (Odgaard et al., 1997; Ryan and Ketcham, 2005). The orientation matrix and the fabric tensor derived from it describe the distribution of trabecular bone in the VOI. The principle component directions and magnitudes (primary, secondary, and tertiary material axes) are represented by the tensor eigenvectors $\hat{\mathbf{u}}_1, \hat{\mathbf{u}}_2, \hat{\mathbf{u}}_3$ and eigenvalues τ_1, τ_2, τ_3 respectively. The eigenvectors represent the orientation in 3D space of the material axes of bone structure; the corresponding eigenvalues represent the relative magnitude of each of the three material axes. The estimates of principal directions are influenced by two primary factors: the analytical method and the character of the underlying trabecular distribution. The anisotropy of trabecular bone described by the primary eigenvector is considered to hold potentially important mechanical information on aspects of skeletal loading. The underlying assumption is that the methods of quantification can accurately capture the true primary direction. Previous research (Ketcham and Ryan, 2004; Ryan and Ketcham, 2005) has demonstrated that the methods used in this research (SVD) are "appropriate and accurate for effectively quantifying trabecular bone structure" (Ryan and Ketcham, 2005, p.255).

Several summary parameters can be quantified using the SVD method in Quant3D in addition to the eigenvectors and eigenvalues. The degree of anisotropy (DA) is calculated as the ratio of the primary eigenvalue (τ_1) to the tertiary eigenvalue (τ_3); this scalar index generally describes the anisotropy of the

trabecular structure. A fully isotropic structure has a DA of 1. The higher the value the more anisotropic the material becomes, indicating a more highly oriented structure. Eigenvalues can also be used to calculate the elongation index (E) as ($1-\tau_2/\tau_1$). This index varies between 0 and 1. The lower values indicate a more plate-like structure with higher degree of similarity between primary and secondary eigenvalues; the higher values indicate a more rod-like structure with the primary orientation predominating (Maga et al., 2006). These indices in combination, describe a continuum of fabric shapes: spheres, plates, and rods (Benn, 1994). Spheres are isotropic structures with similar eigenvalues: $\tau_1 \approx \tau_2 \approx \tau_3$. Plate-like trabeculae have unequal eigenvalues: $\tau_1 \approx \tau_2 \gg \tau_3$. Rods are linear structures with characteristic eigenvalues: $\tau_1 \gg \tau_2 \approx \tau_3$. The capacity for computer-generated data visualization provides a powerful and interactive tool for analyzing these relationships.

Data visualization

The orientation and intercept measurements can be visualized with either a standard stereonet or by using a three-dimensional version of a rose diagram (Figure 5.9). The rose diagram, used in this project, provides a biologically intuitive representation of the distribution of trabecular bone. The three-dimensional rose plots augment the eigenvector/eigenvalue numerical approach by providing a visualization of the complexity of trabecular architecture (Ketcham and Ryan, 2004) not constrained by the necessity for orthogonal components. The

SVD shows the most contrast of the various methods (SVD, MIL, SLD), clearly demonstrating a visual interpretation of multidimensional architecture and variation. Although the information contained in a rose diagram is no greater than that in a standard stereo contour plot, the novel interactive capabilities offer powerful insight into the organization of trabecular bone fabric. The trabecular plates appear as disc-like structures; the linear trabecular struts appear as rod-like structures. The rose diagram is viewed in the VRML (virtual reality modeling language) format, readable by a number of freeware applications and browser plug-ins (access: http://www.web3d.org/vrml/browpi.htm). Representative static images are displayed in this dissertation. Because colors are an important aspect of the rose diagram visual display, selected figures are available in color in Appendix B. This is done in recognition that a significant component of data envisioned is lost by black/white image reproduction. Ketcham (2005) describes SVD data visualization:

> A 3D rose diagram is created by projecting each analysis direction vertex from the unit sphere inward or outward from the origin according to the star component measurement. Vertex positions and colors are normalized by dividing by the maximum measurement value. The normalized value of 1.0 plots in red at a distance from the origin equal to the coordinate length; lower values plot in "cooler" rainbow colors and proportionately closer to the origin. This coloring convention allows the relative measurements values to be easily ascertained; for example, the appearance of dark blue indicates that there is a roughly factor 10 difference between minimum and maximum measurements. Also plotted on these diagrams are the eigenvector directions, with axis lengths scaled by their associated eigenvalues.

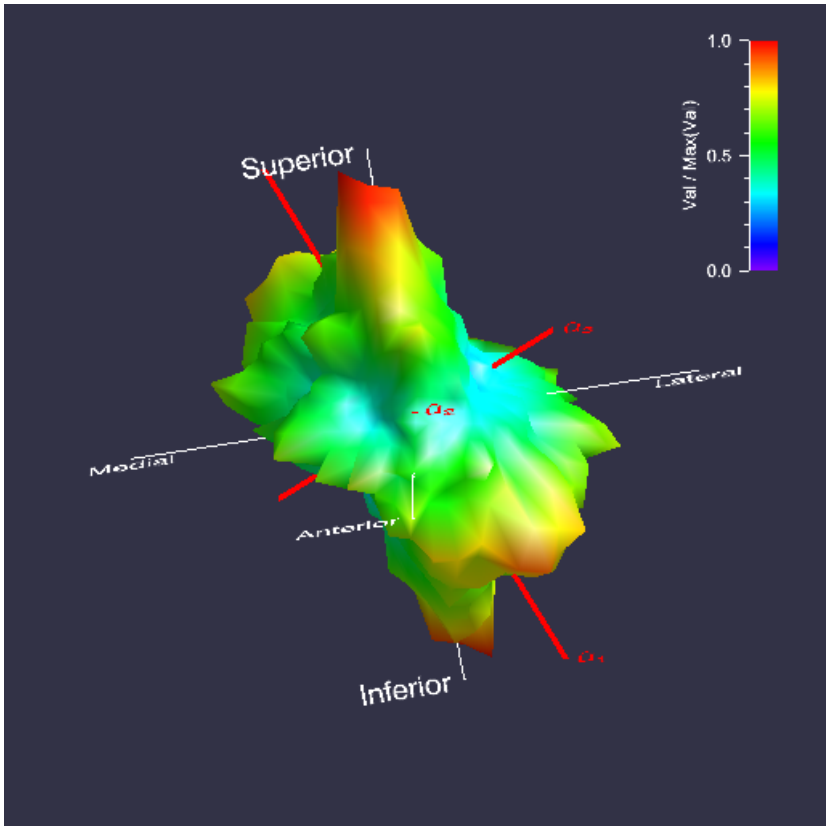

Figure 5.9 SVD 3D Rose Diagram. The distance from origin and color (violet = minimum, red = maximum) indicate relative component value within a single analysis. Red axes show principle component directions and relative magnitudes. White axes are anatomical designations (from Ketcham and Ryan, 2004).

The Quant3D SVD/rose diagram methodology provides insight into the relationship of the fabric structure and the principal component directions. The primary eigenvector provided by the principal component analysis does not necessarily coincide with the direction having the highest SVD values on the rose diagram. The discrepancy may seem counter intuitive. This discordance is based on a fundamental difference in focus: the principal components are mutually constraining to orthogonal axes and represent *global averages*; the SVD rose

diagrams highlight *localized features* and may display non-orthogonal axis orientation.

The output of Quant3D measurements and computations is formatted into a specimen-specific data-log from which the parameters of interest are extracted. Appendix C contains the full set of Quant3D data-logs for the primary volumes of interest. The validity and credibility of the results of the ontogenetic trabecular bone scan and morphometric data of this research are critically linked to the population-specific maturity staging of the SunWatch juvenile skeletal series. The following section discusses the principles and practice of age-at-death estimation and maturity-related seriation, which provide the infrastructure upon which the results may be interpreted.

AGE-AT-DEATH ESTIMATION

Estimation of age-at-death in a skeletal sample, generally speaking, involves identifying morphological features in the skeletal remains and comparing these features with a reference sample of known ages. Estimation of sources of variability is an essential step in this process (Ubelaker, 1989). The resulting age-at-death "determination" is one of the foundations of understanding the structure of ancient populations. Other important components of paleodemographic reconstruction are sex determination, fertility, and migration. Demographers are interested in aspects of population growth, mortality, and human ecology. Bioarchaeologists are concerned

with primary skeletal data correlated with age: the effects of physiological stress, diet/nutrition, infection, trauma, and physical activity (Larsen, 1997).

Research questions of a biological anthropological nature ask "how the distribution of individual health and well-being vary across time and space" (Milner et al., 2000, p. 471). This variation is linked to population dynamics, environmental conditions, and socioeconomic factors. The demographic aspects and consequences of ontogenetic changes and variability have at their core the necessity of age-at-death estimations. In general, the composition of mortality samples in terms of age, sex, and social status is a critical source of information about the functioning of past societies. Age estimation is a primary supporting pillar for this ontogenetic study.

Subadults

Ontogenetic studies of skeletal morphology may examine questions of the general health of a population (growth disruption and other indicators of physiological stress), developmental growth patterns, age-related behavioral changes (developmental or cultural), and the influence of bone functional adaptation (Ruff, 2000). These types of studies, in the archaeological context, are a cross-sectional sampling of single individuals in an attempt to define age changes that could be characteristic of a population. In essence, these are examinations and comparisons of imposed waypoints in a continuous (but not linear) developmental process. Clearly, control of these waypoints (age-at-death) must be defined in order to make any credible interpretation of subadult skeletal morphological data.

Age estimation of the juvenile skeleton involves establishing physiological age (developmental changes) and attempting to correlate this with chronological data. Confounding factors include the difficulties determining sex in subadults (females have adolescent developmental changes 1-2 years earlier than males), individual variation in maturation, and effects of environmental and genetic factors on growth.

Subadult age-at-death estimation of archaeological skeletal remains is an exercise in attempting to place biological growth and development on a chronological age continuum. The inherent variability of growth may arguably be its most consistent characteristic. Growth varies within and between individuals and populations based on, but not limited to, genetic factors, sex, nutrition, disease, season, and socio-economic circumstances. It is this lack of a simple linear relationship between growth and age that makes age-at-death assessments in a number of situations uncertain- estimates, not determinations (Scheuer and Black, 2000).

A discussion of subadult age-at-death as a key variable in population, lifestyle, and developmental reconstructions would be incomplete without a consideration of the prevalent analytical tools used for age control. Biological age, encompassing skeletal and dental age, is used as the indicator for progress of an individual along the developmental pathway: a correlate (possible/hopeful) of chronological age. The estimation of skeletal age utilizes the times of appearance and fusion of ossification centers and the size and morphology of bones. Dental age is

most usefully expressed in the archaeological context in terms of the state of maturation of the teeth assessed from various stages of mineralization.

Skeletal age

Three phases of development are useful in establishing age from skeletal elements: (1) the time of first appearance of an ossification center; (2) the morphological appearance of the bony element and size of the ossification center; and (3) the time of fusion of the center with another separate ossification center. These phases vary according to bone, function, and developmental timescale.

Primary ossification centers form generally in the embryonic and early fetal periods of life; secondary centers usually appear after birth. The times for appearance of prenatal ossification centers are highly variable due to fetal and postnatal environmental factors. The detection of early ossification centers varies with the technique of observation (histological and radiological). Postnatal ossification centers appear from birth to early adult life. Data from systematic, longitudinal radiographic growth studies on predominantly white, middle-class children, carried out between 1930-1960, form the basis for various reference atlases. These consist of a series of standards (cited in Scheur and Black, 2000) (male and female) deemed representative: Greulich and Pyle (1959), hand and wrist; Hoer et al. (1962), foot and ankle; Pyle and Hoerr (1955), knee region.

Skeletal age of an individual can be estimated by comparing the radiographic pattern of ossification centers to the maturity stages in the atlas. Problems occur in observational technique and in assuming a fixed pattern and order of development.

These atlases are useful in clinical contexts, in part due to the numerous centers of ossification available to grade and the relatively ease of radiographic examination of peripheral regions. However, they are of little use in an archaeological skeletal assemblage where the remains are usually disassociated (exception: mummified material), ossification centers displaced and/or not excavated, and various carpal/tarsal bones upon which bone age can be determined are not ossified or not present.

Skeletal morphology is useful for age assessment through recognition of a skeletal element, size, and morphological stage of development. Primary ossification centers are usually identifiable as specific bones. Prenatal (fetal) osteology has focused on age and size creating regression graphs from the gestational age of three lunar months to term (Scheuer and Black, 2000) for crown-heel and long bone diaphyseal length. Other indicators include the union of major elements of the sphenoid, temporal, and occipital bone (Kosa, 1989). Scheuer and MacLaughlin-Black (1994) have reported on the usefulness of changing dimensions of the pars basilaris for age estimation between early fetal periods and six years of age.

Postnatal diaphyseal length standards have been developed from numerous cross-sectional and longitudinal studies (quoted in Scheuer and Black, 2000: Maresh, 1955; Anderson et al., 1963; Gindhart, 1973). This data is primarily from white Europeans or individuals in the USA of European descent. Long bone lengths and the timing of epiphyseal fusion are environmentally sensitive. Standards are population-specific; systematic bias is introduced to age-at-death estimations when using

standards generated from one population to evaluate another, unrelated group. Explicit understanding of the use of reference standards and skeletal growth perturbations are critical to the accuracy of age-at-death assessment using skeletal data.

The morphological appearance of the ossification centers has potential for age estimations of juveniles in archaeological skeletal remains. The use of bone elements undergoing distinct changes within a short time could improve accuracy. Problem areas include lack of information on the anatomy of all these bony elements, the non-random age distribution of mortality in children, and poor excavation retrieval rate.

The timing of fusion of ossification centers varies in different parts of the skeleton. Postcranial fusion occurs primarily at the growth plate between a primary and secondary center (epiphysis). There are areas of fusion of primary centers (mandible, sternum, scapula, pelvis, spheno-occipital synchondrosis). The epiphyses of the major long bones, hands and feet, and spheno-occipital synchondrosis fuse during adolescence. Secondary centers of the vertebrae, scapula, clavicle, sacrum, and pelvis fuse in the early adult age period. The variability in reported times of ossification center fusion increases with age and observational methodology. Fusion timing data have been generated by radiographic studies and dry bone examination. The resulting reference standards have the same specificity problem as previously discussed: matching an individual to a particular standard pattern.

Epiphyseal union is a process; intra- and interobservor error is significant when trying to determine stages: unobservable, open, partial, and complete (Buisktra

and Ubelaker, 1994). The association of observations from dry bones with radiographs is also problematic; union is judged at an older age on dry bone examination. The timing of fusion has a broad range depending in part by variation in the onset of the adolescent growth spurt. The inability to determine sex in juvenile skeletal remains further broadens the timing-range as females have an onset of skeletal maturation at least two years earlier than males. Age estimates without sex assignation are an average of those for both sexes.

Dental age

Dental age is the other major indicator of maturity in the juvenile. It has significant advantages over skeletal aging. Teeth survival may exceed bone, making them possibly the only surviving structures for certain fossil species and the least damaged in more recent archaeological skeletal assemblages. Tooth growth, including deciduous and permanent teeth, spans the entire subadult lifespan. Finally, dental formation is probably less susceptible to environmental perturbations (nutrition, infection, endocrine function) exhibiting less variability to a given chronological age than skeletal age (Smith, 1991).

The eruption of teeth and the stage of mineralization of the crowns and roots have been used for dental aging. Mineralization is thought to be less affected than eruption by intrinsic and extrinsic factors (Lewis and Garn, 1960; Scheuer and Black, 2000). The formation process has a genetic basis, while eruption is affected by tooth loss, inadequate spacing, infection, and other factors (Ubelaker, 1987).The definition

of eruption may be ambiguous, including the whole process of tooth emergence from its crypt to emergence through the gingiva. The assessment of eruption is problematic in dry bone specimens and must be defined as the "appearance of the tooth cusp at or above the level of the crestal alveolar bone" (Scheuer and Black, 2000). Given this definition, dental eruption can be useful in the archaeological context.

Studies arrange eruption into three periods during childhood and early adulthood: (1) deciduous dentition, (2) mixed, and (3) permanent dentition (Hillson, 1996). Schour and Massler (1941) published their chart for the development of the human dentition. This has been reworked by Ubelaker for studies of Native Americans. It is reproduced in "Standards" (Buikstra and Ubelaker, 1994). Although the chart was originally based on a small number of terminally ill children, its performance throughout the world has made it a recognized standard.

Mineralization, as opposed to eruption, can be studied at any point along the developmental continuum of the tooth. "Age estimation of children based on dental development is accurate because of the highly canalized nature of human tooth development" (Pfau and Sciulli, 1994). Early development of deciduous dentition begins in the prenatal period. The deciduous roots and early stages of permanent crown formation take place postnatally. Population reference standards have been created by radiographic studies in living populations of children (Moorrees, 1963; Pfau and Sciulli, 1994; Smith, 1991; Hillson, 1996). Pioneer work on dental development was carried out in the Fels Longitudinal Study on Ohio children. Moorrees et al. (1963) combined clinical and radiographic data to produce a series of

plots of developmental stages. The assignation of archaeological teeth to these stages allows interpolation of age. This methodology has proven to produce age estimations +/- six months (Hillson, 1996; Liversidge, 1994).

Smith (1991) revised the Moorrees, Fanning and Hunt (MFH) data with the aim of predicting age. Each tooth is assigned to a developmental stage and a "mean age calculated using the values from all available teeth" (Hillson, 1996). In the present study the age estimates of male and female tables were averaged for juveniles without sex determinations. This method was found reliable in archaeological material (Smith, 1991). Hillson (1996) assessed Smith's method as the easiest to use and as "the standard of the future."

Problem areas include accuracy, repeatability, statistical methodology, sampling, and appropriateness of the available standard to the skeletal assemblage being studied (Smith, 1991; Hillson, 1996; Lampl and Johnston, 1996). Different methods may produce different age estimates; mismatches exist between population reference standards and archaeological skeletal series. Lampl and Johnston (1996) identify two primary sources of error. First, there is random error, which is normal variability of maturation within a population of children. Second, there is systematic error, which is produced by shared environmental circumstances within a local population.

Specific problems of inherent bias in dental aging of archaeological remains also include the fact that reference standards are based on radiographic studies, which have poor definition of unmineralized tissue; there is not a one-to-one

correspondence of x-rays to skeletal remains, introducing systematic error (over/under). Taphonomonic factors may be responsible for the more accurate anterior mandibular teeth to be missing. Finally, archaeological remains are death assemblages; the children were sick and died. How abnormal were they and what was the influence on dental formation? Having said all this, the consensus opinion is that the average of age ranges for maturation on available teeth does provide the most reliable estimation of subadult age. However, it is important to maintain the distinction between dental development stage and assigned age: the first is observation; the second is interpretation (Hillson, 1996).

Dental enamel microstructure has been shown to have a regular time dependency (Fitzgerald, 1998). The cross striations between adjacent striae of Retzius (circaseptan interval) are uniform within a tooth and between all teeth in an individual. Fitzgerald (1998) has reviewed published data and presented independent results supporting the usefulness of enamel microstructural analysis in age estimation and growth/development studies. Technological development (confocal microscopy, microCT imaging, and computer analyses) and large-scale validation studies are required before this method is applicable for routine anthropological use.

Accuracy of age-at-death estimates

The accuracy of age-at-death of an individual in any skeletal sample is, in reality, a probability statement. It is the identification of the probability of a certain age range given specific conditions (if …; then…). The accuracy (degree to which an estimate conforms to reality) and precision (degree of refinement with which an

estimate is made) is based on numerous factors and methodological issues (White and Folkens, 2005):

- Age categories and distribution strongly influence accuracy. Younger individuals are aged with more precision than adults in which degenerative changes are the indicators. Variation in the aging process starts to increase in the third decade of life between individuals and within a single skeleton (Meindl and Russell, 1998).
- The preservation and availability of skeletal elements constrains which methodology and diagnostic features may be used. The recognition of sample bias is important within this concern.
- Sample composition is important. Admixture of populations or small isolated samples increases the prediction error. Differing analytical methods have variable reliability and accuracy. The Bocquet-Appel and Masset (1982) critique argues that the methods applied for estimating skeletal age result in an age distribution for skeletal series that reflect "the age structure of the reference sample on which the methods were devised" (Wright and Yoder, 2003, p.48). Seriation may be possible in larger samples allowing comparison within a single biological population. Many deficiencies can be removed by the systematic application of seriation: arrangement of all individuals in a sequence of increasing age prior to individual estimated age assignment (Lovejoy et al., 1985). Groups of individuals are assembled that display similar degree of expression of an age indicator. Age determination is not

completed for any individual until the entire sequence is established. Age-related differences within categories are established.

- The rate and timing of dental and skeletal development may be variable within a population resulting in some unknown degree of estimation bias.

Lovejoy et al. (1985) have argued for a multifactorial determination of skeletal age-at-death as a way of reducing bias and improving accuracy. The method uses a principal components weighting of five indicators (pubic symphyseal face, auricular surface, radiographs of the proximal femur, dental wear, and suture closure). This results in a *summary age*, which the authors argue "may be presumed not to differ significantly from the original real age distribution of the population" (Lovejoy et al., 1985). Other authors agree that if age-estimation is essential, a multifactorial approach (dental development, long bone growth, and epiphyseal union) producing a subadult summary age combined with multivariate analysis may be the most accurate for age-at-death estimations in subadults (Pfau and Sciulli, 1994). Dental development is best for the entire age range of birth to 18 years. Bone length is useful as a second choice for this age range (in research not studying morphological growth). Epiphyseal fusions are helpful from 0.5 to 7 years [mandible (.5 years), vertebral aches/body (2-7 years)]; no fusions occur between ages 7 and 12; fusions are again useful from ages 12 to 18 (acetabulum, long bones). Skeptics remain, however. Jackes (2000) suggests that age-based preservation differences control the result of this principal components analysis and that using more than one indicator in concert may not increase the accuracy of age estimation.

In this research, subadult age estimations are based on the following references (measures and scoring are from Buikstra and Ubelaker (1994) (see Appendix A for complete dataset):

- Dental age: deciduous (Sciulli, 1992); permanent (Smith, 1991).
- Long bone age: fetal (Sherwood et al., 2000); postnatal (Maresh, 1955).
- Epiphyseal fusion (Scheuer and Black, 2004).

And adult sex and age-at-death estimates:

- Sex: pubis (Phenice, 1969)
- Age estimate (Lovejoy et al., 1985)

SERIATION

Seriation, in reference to subadult age-at-death estimations, is a sorting and ordering of progressive developmental stages of all the individuals *within* the sample *without* reference to standards or particular age ranges (Hillson, 1992; Jackes, 2000; Sciulli, 2007). This results in the possibility for comparative analysis among and between individuals of the same developmental stage (not same age), eliminating the bias and possible error produced by the assumptions inherent to reference standards discussed above. Age control of a particular sample is still desirable, but it would be a by-product of indicator stage seriation, not a pre-determined age category.

Seriation of relative dental development produces within-sample stages, eliminating the systematic bias and assumptions intrinsic to reference standards, and

producing a framework for incorporation of other age-at-death assessments. Because this process provides an internally consistent measure of maturity within a specific population, it offers a *significant asset* to this ontogenetic study of trabecular bone by placing the skeletal data within maturity scale independent of imposed standards and reducing data "noise." The SunWatch 103 subadult skeletal remains have been developmentally sequenced by Paul Sciulli and reported on as part of a recent publication "Relative Dental Maturity and Associated Skeletal Maturity in Prehistoric Native Americans of the Ohio Valley Area" (2007). The following description of the seriation procedure is based on Sciulli's work (2007), experience, and personal communications between this author and Dr. Paul Sciulli.

Deciduous and permanent teeth were scored for dental development according to tooth formation stages published by Moorrees et al. (1963a, b). Teeth were observed macroscopically and were assigned to a tooth formation stage, assuming the crown and root regions maintained morphological integrity. The following minimal criteria were met by each individual: (1) two deciduous teeth of different classes, (2) or two permanent teeth of different classes, (3) or a combination of deciduous and permanent teeth, and (4) at least one tooth which had not completed development (Sciulli, 2007). The teeth and individuals were then sequenced from the least to most mature, based on the assumption that dental development proceeds from the occlusal surface of the crown to the root apex.

A scalar dental maturity progression of 16 stages was established based on initial root formation and complete apex closure. The criteria for selecting these two

tooth formation stages as the basis for the seriation sequence included: exclusivity from one another, easy observability, and high repeatability (Sciulli, 2007). This seriation of deciduous and permanent tooth development resulted in a familiar sequence for modern humans (Hillson, 1996): di1>di2>dm1>dc>dm2>M1>L1>U1>C>P1>P2>M2>M3. The sixteen stages using macroscopic observation were constructed beginning with the appearance of a given tooth formation stage for specific teeth and progressing to the appearance of other specific tooth formation stages defining the developmental increments. Explanation of the 16 stages is as is listed in Table 5.2.

Additional developmental observations recorded were: scoring for tooth as erupted into occlusion or not, replacement of the deciduous teeth, and skeletal development indicators. Eruption into occlusion was determined by the position of the tooth relative to adjacent teeth and the presence of occlusal wear facets. Deciduous replacement was identified, "if a permanent successor was present and erupting or erupted into occlusion or neither deciduous nor permanent tooth was present but the socket was that of a permanent tooth" (Sciulli, 2007, p. 549). Skeletal development was recorded as maximum long bone lengths (excluding fused epiphyses and epiphyseal union (fused or not fused) and positioned within the dental maturity stage matrix for that individual. Variations in the skeletal development pattern when skeletal development indicators are placed within this framework may indicate adaptations or interactions between individuals or populations to their environmental conditions. If an individual has no teeth available, a dental maturity

stage can be determined based associated skeletal data. Sciulli (2007) recommends, in this particular case, that a *range* of dental maturity stages would be appropriate, considering the assumption that skeletal and dental maturation may run on different developmental clocks.

Stage	Event
1	only deciduous incisor tooth crown development and no deciduous incisor roots
2	appearance of deciduous incisor roots
3	appearance of dm1 roots
4	appearance of the deciduous canine roots
5	appearance of the dm2 roots
6	completion of the deciduous incisor root apex
7	completion of the dm1 root apex
8	completion of the deciduous canine root apex
9	completion of the dm2 root apex
10	appearance of permanent anterior premolar roots
11	appearance of permanent posterior premolar or M2 roots
12	completion of M1 root apex
13	completion of root apex of lower permanent incisors or appearance of M3 roots
14	completion of canine and both premolar root apex
15	completion of M2 root apex
16	M3 root ≥ one-half completed and <apex closed

Table 5.2 Dental Developmental Maturity Stages (Sciulli, 2007).

Populational variation has been shown to exist in the relative timing of dental development with Native American teeth developing in earlier stages compared to Old World samples (Hillson, 1992; Lovejoy et al., 1990; Owsley and Jantz, 1983; Smith, 1991; Tompkins, 1996). This finding is accentuated with increasing maturity; once more highlighting the difficulties associated with using a reference developmental standard for age-at-death estimation (Sciulli, 2007).

Sciulli (2007) argues that the seriated dental developmental staging may represent a basic, biologically-meaningful, maturation sequence for Ohio Valley samples encompassing tooth development, fusion pattern, and bone lengths. The sequences of dental stages and epiphyseal fusions (from distal humerus to distal radius) correspond to each other and to those reported from other Native American samples (Sciulli, 2007; Stewart, 1934; Johnson, 1961). The seriation method as described is both constraining and enabling. It is sample-specific and relative; it is standard-free and flexible. Samples or populations with different developmental patterns and sequences can be sorted into various maturity categories which remain assumption-free in regards to developmental timing and age estimation. The results of this work suggest that distinguishing ontogenetic patterns of trabecular bone change is enhanced by the ordering of the SunWatch subadults into biologically meaningful maturity stages.

OTHER IMPORTANT CONSIDERATIONS

Body mass

Ruff (2007) has presented body mass estimation formulae for juvenile skeletal remains ranging in age from 1 to 17 years. These prediction equations, utilizing distal femoral metaphyseal and femoral head breadth, suggest better estimation of body mass with the former in younger children and the latter in individuals greater than 15 years. The equations are applied in this project. Criticism could be applied to the use of the distal femoral metaphyseal breadth in a study of the microarchitecture of the proximal tibia as being biomechanically related and thus circular. The counter arguments are that the parameters studied are significantly different (metaphyseal breadth *vs*. trabecular microarchitecture) and experimental data demonstrate a lack of correlation between changes in mechanical load and metaphyseal growth/articular size after early to mid- childhood years (Lieberman et al., 2001; Ruff, 2007).

The maximal mediolateral breadth of the distal metaphyseal surface of the femoral diaphysis was measured by sharp-tipped calipers to the nearest 1.0mm. The measurement was taken between the most medially and laterally projecting points on the metaphyseal surface, approximating, but not necessarily perpendicular to the long axis of the shaft. All available ipsilateral femurs corresponding to the tibial element sample with relevant morphological integrity and characteristics were measured (Appendix A). This measurement was possible from perinatal age to the age

corresponding to distal femoral epiphyseal fusion. In older children, with femoral epiphyses present, maximum femoral head breadth was measured according to standard technique as measured on the periphery of the articular surface of the head (Bass, 1995). These measurements had been made by previous investigators and are part of the burial record. This author repeated the measurements on randomly selected individuals with essentially the same results as those recorded (+/- 0.5 mm).

Femoral bicondylar angle

Measurement of the femoral metaphyseal bicondylar angle was performed on all available nonadult ipsilateral femurs corresponding to the tibial element sample with suitable morphological integrity and without fusion of the distal femoral epiphysis. These were the same femurs for which distal metaphyseal medial/lateral breadth measurements were taken (Appendix A). The metaphyseal bicondylar angle was recorded by direct skeletal measurement with a clinical goniometer to the nearest 0.5 degree. The angle was observed, according to Tardieu (1994), as the measurement between the diaphyseal longitudinal axis and the sagittal plane perpendicular to the distal metaphyseal plane. "The distal metaphyseal plane was defined by the two most distally projecting points of the metaphyseal surface" (Tardieu, 1994, p. 187). It should be noted that there is a degree of freedom or "wobble" in the direct skeletal measurement of the bicondylar angle due to positioning, rotation, and an irregular metaphyseal surface. Radiographic measurement technique could result in more reliable data, but falls outside of the scope and budgetary framework of this dissertation research. This is part of future studies on specific aspects of trabecular

bone ontogeny. The direct skeletal measurement may generate a data precision imbalance when viewed relative to quantitative microCT data and thus make for increased data variability. This subject will be discussed more fully in the Results section.

STATISTICAL ANALYSIS

Two categories of analysis were performed to evaluate the maturity/age-related variation of trabecular bone structural parameters of the various VOIs. First, taking the seriated sample dataset as a whole, as well as the selected subsample, OriginLab scientific graphing and analysis software (OriginLab Corporation, Northampton, MA; www.originlab.com) was used to produce the graphic displays, statistical, and curve fitting analyses. The focus is on scatterplots, curve smoothing, and non-linear curve fitting procedures. Origin provides a NLSF Wizard, which is a user-friendly tool for performing nonlinear least squares fitting (NLSF). This flexible fitting tool has a five-step process, which includes: (1) select fit dataset, variable ranges, and scatterplot parameters; (2) select Origin Basic Functions for approximating curves and their equations (exponential, logistic, and allometric equations were useful for this research); (3) select weighting of select data if indicated (none in this research); (4) set Fitting Control for display features (i.e., confidence bands and number of iterations); and (5) create output graph.

Second, the sample was divided into four maturity-related groups; one-way ANOVA was used to compare BV/TV and SVD DA in the four groups. If the F-test showed a significant level, a multiple comparison was performed with the Bonferroni test to find differences between the groups. For all statistical analyses, a p-value <0.05 was considered significant. Stata 9 for Windows (Stata Corp, College Station, Texas) was used for these analyses. Variation within and among the four groups was further explored by side-by-side box plots generated by the OriginLab software.

SUMMARY

The characteristics of the SunWatch juvenile sample of tibiae have been outlined. The excellent state of preservation of the juvenile tibiae of the skeletal sample point stands out as a significant asset to this project. The analytical methods presented are optimally suited to evaluating the ontogenetic patterning of human trabecular bone and creating culturally-specific "reference" quantitative data not previously existing. The advanced technologies offer a totally non-destructive, assumption-free examination of the microarchitecture of trabecular bone. The combination of microCT scan images, quantitative dataset of structural parameters, and intuitive rose-diagram displays demonstrate specific patterning on how we became the way we are, with regard to trabecular bone of the proximal tibia, as well as some likely aspects of a universal sequence in human growth and development.

The principles and practice of the estimation of key biological parameters are discussed, namely age-at-death estimation, maturity staging/seriation, body mass assessment, and consideration of the femoral bicondylar angle. The seriation method is a key component to this research. It allows the data to be systematically ordered in a population-specific manner. The advanced technologies used in this research take full advantage of this strength.

CHAPTER 6

RESULTS

The pattern of ontogeny of trabecular bone is a reflection of a staged continuum defined by the range of responses of the biological systems and regulatory mechanisms (Lovejoy et al., 2003; Turner, 2007). Within this framework, the human body is developmentally plastic, as well as having the potential for plasticity throughout life. Plasticity is defined as "systematic changes within the person in his or her structure and/or function" (Lerner, 1984, p.xi). The specific manner and outcome of development (skeletal in this research) are related to complex interactions with the environment, both cultural and physical (Roberts, 1995), in which the individual is situated (Sofaer, 2006). Environmental factors are interwoven into this developmental biological fabric with multifaceted reciprocities between self and the world.

This theoretical scaffold is important to the results of this research. This study is *not about* SunWatch; it *is about* skeletal developmental biology *at* SunWatch. The quantitative and microarchitectural changes in the organization of trabecular bone during ontogeny reported are specific to the genetic framework and epigenetic

processes to be found in this Fort Ancient village. There are currently no additional data of this type for comparative studies. The results of this research are presented in three formats followed by a discussion of potential data limitations of the microCT methodology. These formats are: (1) the visual display of qualitative and quantitative data with narrative description, (2) statistical analyses of the morphometric data, and (3) exploration of important components of variation including body mass, femoral bicondylar angle, and within-tibial heterogeneity.

The exposition of results falls naturally and most intuitively (to this author) into two genres: the big picture and age-related groupings. The "big picture" considers the continuity and change over the entire age range of the sample of 36 individuals– birth to young adulthood. The age-related groupings provide imposed, but biologically meaningful stages of growth and development with differences in hormonal control, behavior, and physical activity between them. As such, comparisons between the age-related groupings allow some general inferences to be made within the framework of the overall ontogenetic pattern. The meaningfulness and legitimacy of these particular statistics, however, must be considered critically in light of the different genetic, epigenetic, and hormonal regimes operative for each group. In addition, the majority of individuals (seven out of ten) in the oldest group have the epiphysis present and volumes of interest in positions not homologous with those in the younger groups. This eliminates the oldest group from direct comparability with the others; general trends, however, may be evident. The planned groupings have been previously presented as part of the hypotheses outlined in

Chapter 1. The *actual* age-related groupings based on the final skeletal sample are stated below. The ultimate age groupings reflect the natural patterning of the skeletal data into biologically meaningful sets:

I. 0- 0.5 years: infancy (maternal-fetal hormonal system, dependency, not walking, n = 9).

II. 0.8- 2.1 years: early childhood (growth hormone, thyroid hormone, dependency, early walking, n = 10)

III. 2.75- 9.8 years: middle childhood (growth hormone, thyroid hormone, maturation of gait, independent activities, n =8)

IV. 15- 24 years: adolescence/ early adult (sex hormonal system, full adult lifestyle, n = 9)

The results aim to demonstrate the diachronic *pattern, continuity, and change* of trabecular bone architecture and quantitative structural parameters of the non-adult human proximal tibia. Trabecular bone displays marked heterogeneity: within and between elements. The exact quantitative values are important only as part of the pattern, as they are regionally variable within the proximal tibia and among the individuals. *The pattern is the message*. This study is specific to these tibiae. Some inferences in regards to "general biological patterns" will be considered, to be confirmed or refuted by future research.

VISUAL DISPLAY OF DATA

Qualitative aspects of trabecular bone organization

The visualization of qualitative and quantitative information is arguably a highly intuitive way of data presentation (Tufte, 1983, 1990). This is particularly effective for the display of microarchitectural and Quant 3D parameters of ontogenetic changes in trabecular bone. Figures 6.1- 6.5 are high-resolution CT cross-sections from individuals of different ages spanning late fetal age (0.00 years) to young adulthood (24 years). The upper portions of the figures (A) contain transverse cross-sections (slices) as collected from the CT scanner. The middle portions of the figures (B) are coronal sections reconstructed from the scan data. The lower portions of the figures (C) are three-dimensional reconstructions with the transverse, coronal (background), and sagittal planes of the medial volume of interest indicated by dark shading. The anatomical orientation of a slice is anterior above and medial to the left. The anatomical orientation of the coronal section is medial to the left, viewing from anterior to posterior. The anatomical orientation of the three-dimensional reconstruction is with the viewer looking from anterior to posterior. All sections are taken through the plane of the medial volume of interest (MVOI) which has been located within 5mm of the proximal margin of the bone with the center of the spherical VOI in the anatomical center of the medial tibial condyle (as defined in the Methods section). The pattern of change in architectural and structural

parameters of the lateral volume of interest (LVOI) follows the same course as that of the MVOI.

This series of imaging sections exhibit changes in size and shape. In addition, they provide qualitative evidence of the reorganization of trabecular structure in the proximal tibia with age. Quantitative parameters are calculated from this scan data and will be discussed in following sections. Trabecular bone at birth is characterized by a dense relatively undifferentiated structure with a large number of small trabeculae organized in interconnected parallel columns reflecting the fetal structural morphology of the growth plate and the endochondral ossification process (Figure 6.1 A,B,C).

By approximately 12 months of life the bone volume fraction is diminished by approximately 40%; thinning the lattice with greater spacing between trabeculae and relatively less anisotropy (Figure 6.2 A,B,C).

anterior

medial

A.

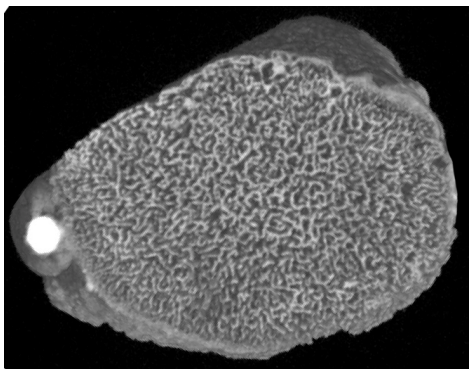

B.

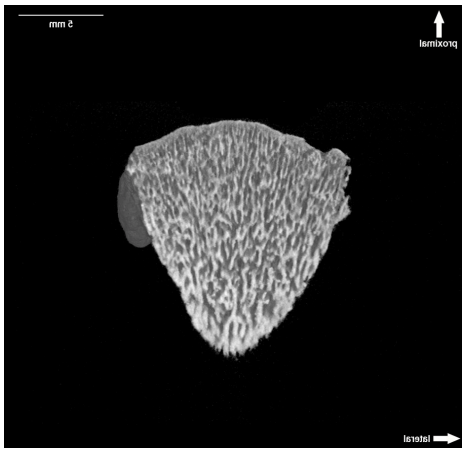

C.

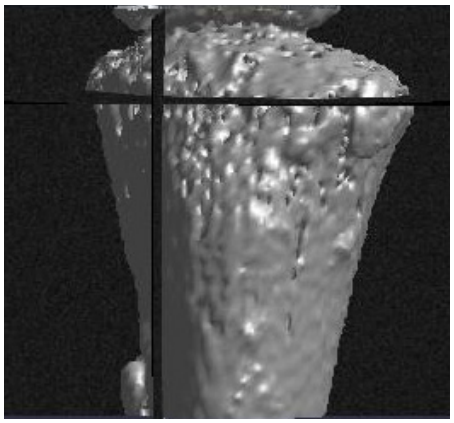

6.1 Transverse CT slice (A), coronal CT reconstruction (B), and reference image (C) of neonatal skeleton (Burial 10_72). BV/TV is 0.4117; SVD DA is 6.5148.

A.

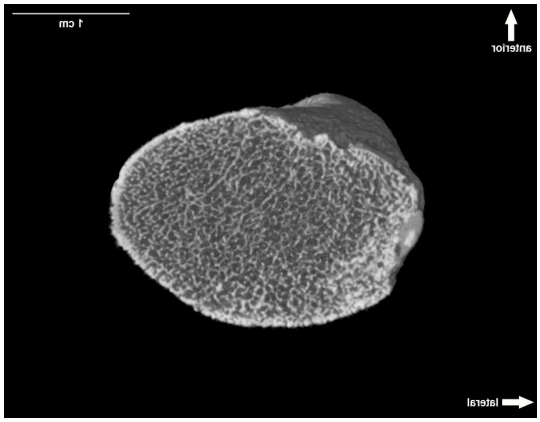

B

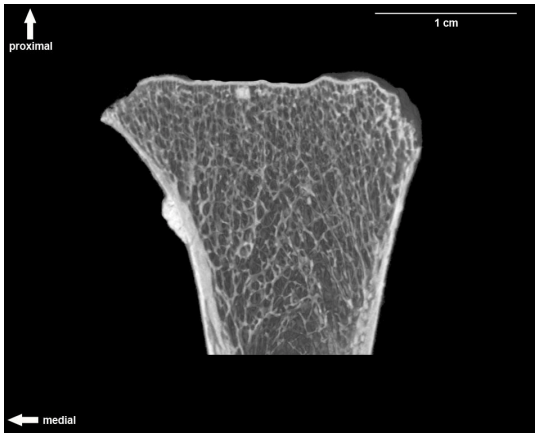

C.

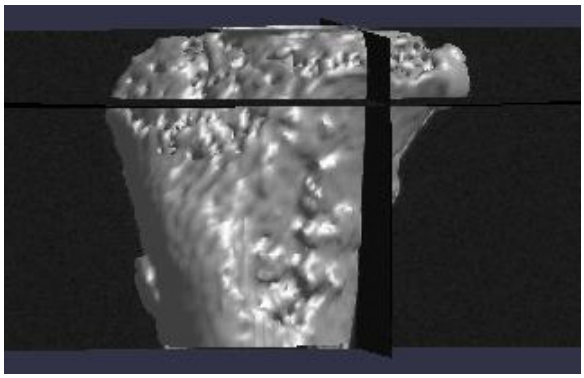

Figure 6.2 Transverse CT slice (A,) coronal CT reconstruction (B), and reference image (C) of estimated 1.3 year old skeleton (Burial 4_72). BV/TV is 0.2841; SVD DA is 4.7457.

From about 1.5 to 2.5 years of age, more mature bone architecture begins to appear with a shift in the arrangement, number, and distribution of trabecular bone coinciding with the early attempts and subsequent acquisition of bipedal gait (Figure 6.3 A,B,C). This transitional period is characterized by biologically significant variability in trabecular structure and arrangement: decreased trabecular number, increased trabecular thickness, and relatively less directional organization.

From ages 2.5 to 10 years, trabecular bone gradually conforms to a more adult configuration of rod and plate structures (Figure 6.4 A,B,C) characterized by an increase in trabecular thickness, decrease in trabecular number, and increasing anisotropy.

Adolescent/young adult years are characterized by continued bone functional adaptation of the trabecular bone with structural changes demonstrating increased trabecular spacing, trabecular thickness, isotropy, and regional variation (Figure 6.5 A,B.C). It is important to note that the three young adults in this sample are all female. It has been documented that up to 10% of bone mineral density can be lost during a single pregnancy (Javaid and Cooper, 2002). Some characteristics of their bone volume fraction may reflect prior pregnancies- possibly a relative decrease. Unfortunately, there are currently no data on corresponding changes in bone volume fraction. This remains an unknown.

A.

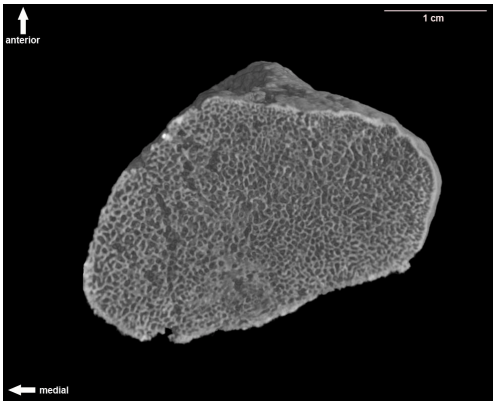

B.

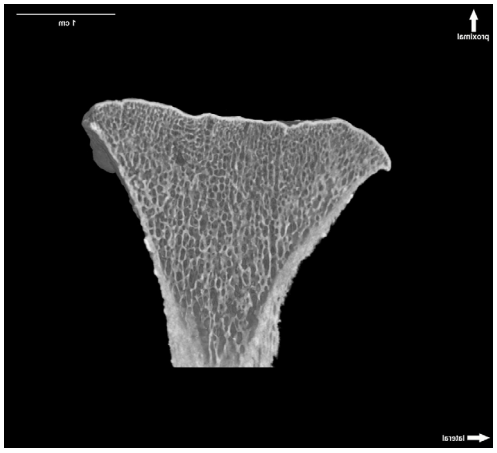

C.

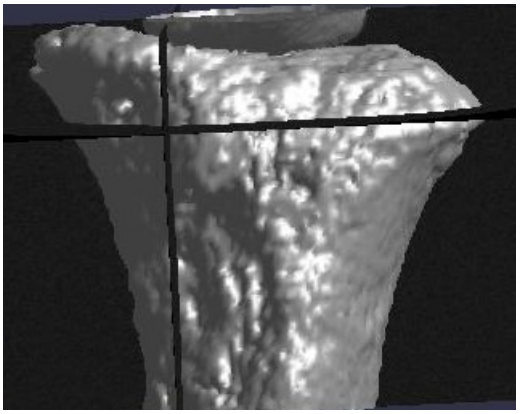

Figure 6.3 Transverse CT slice (A), coronal CT reconstruction (B), and reference image (C) of estimated 2.1 year old skeleton (Burial 6_80). BV/TV is 0.3759; SVD DA is 2.0306.

A.

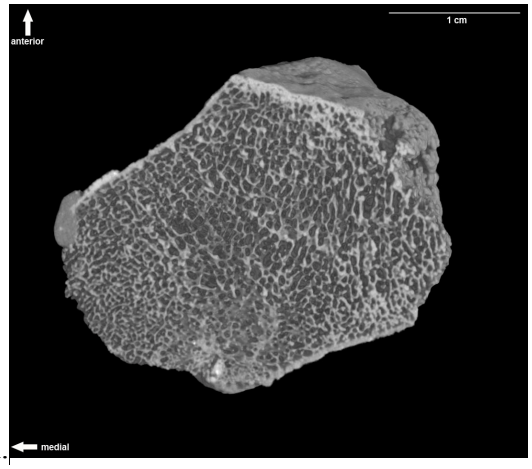

B.

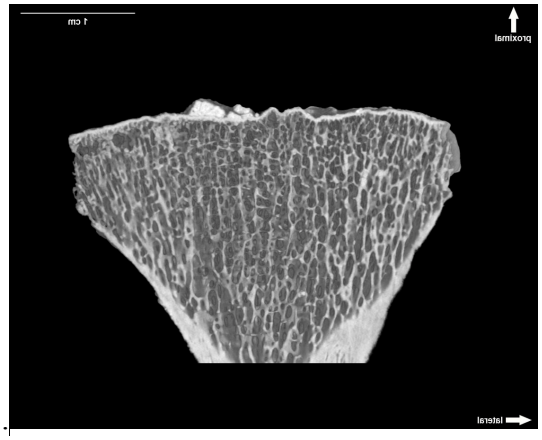

C.

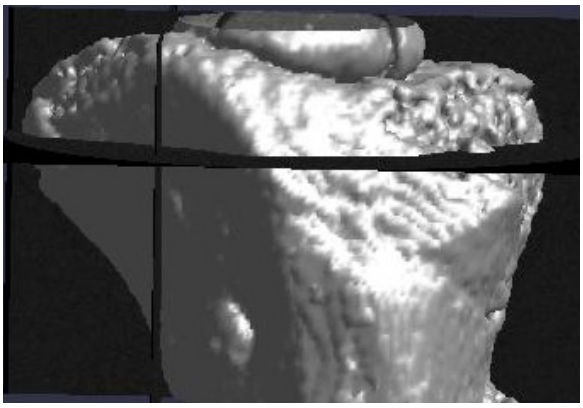

Figure 6.4 Transverse CT slice (A), coronal CT reconstruction (B) and reference image (C) of estimated 7 year old skeleton (Burial 2_73). BV/TV is 0.3266; SVD DA is 4.6258.

A.

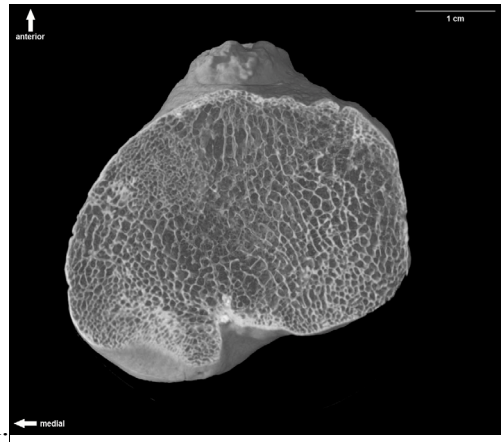

B.

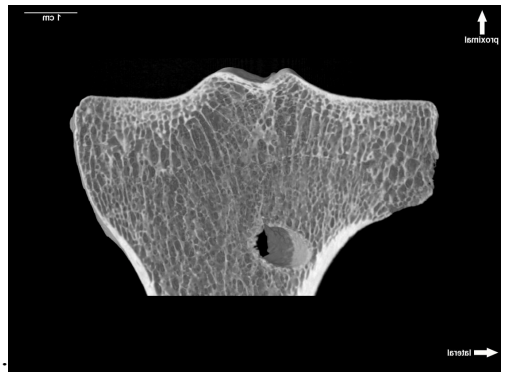

C.

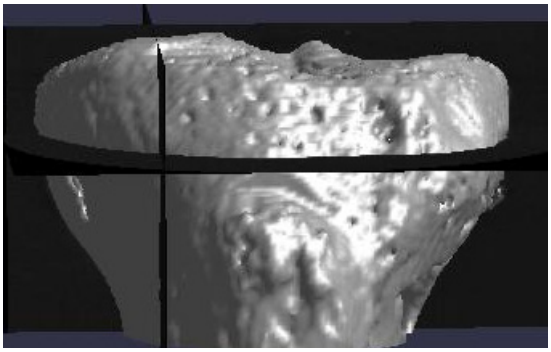

Figure 6.5 Transverse CT slice (A), coronal CT reconstruction (B), and reference image (C) of estimated 21 year old female skeleton (Burial 3A_76). BV/TV is 0.3366; SVD DA is 1.3673.

Three-dimensional rose diagrams: anisotropy

The continuum of bone volume fraction changes described above is associated with corresponding ontogenetic changes in trabecular directional organization (anisotropy). Figures 6.6-6.13 are renderings of the star volume distribution degree of anisotropy (SVDDA) of the media/lateral VOIs with 3D rose plots generated by the IDL Quant 3D software (Ketcham and Ryan, 2004). The three-dimensional rose diagrams capture the structural variation within the VOI providing an easy to interpret visual representation. Highly anisotropic structures can be differentiated from more isotropic structures (Maga et al., 2006). These plots allow the display of the *complexity* of trabecular architecture, preserving *nonorthogonal* components of variation. These enhancements can be compared to the more traditional numerical method of utilizing eigenvalues and eigenvectors by placing the measured intercept and orientation data into a 3 x 3 matrix resulting in fabric tensors. Visualization is then commonly presented by way of non-intuitive stereoplots in which the tensor method necessarily results in three orthogonal eigenvectors regardless of the actual trabecular organization.

The rose diagrams examples given are viewed along the antero-posterior axis (*y*). They are combined side-by-side with a corresponding reconstructed CT coronal slice on the anatomical *y* axis through the center of the MVOI from the same individual. The orientation and anatomical directions therefore match those of the rose diagram resulting in an intuitive visual display of the concordance between the vectors plotted on the rose diagrams and the orientation of the trabecular structure.

The 3D rose diagrams are fully 3D structures, viewable from any angle. They are stored as 3D computer graphics in VRML-format files.

Although regional variation of anisotropy within and among the proximal tibiae is evident, the *principal eigenvector as demonstrated by the rose diagrams is similar across all ages with a superoinferior orientation* and some variable posteroanterior and mediolateral obliquity for medial volumes of interest and lateromedial obliquity for lateral volumes of interest (Figures 6.6 and 6.7). These directions are consistent with the mechanical properties of trabecular bone as related to the major weight-bearing loads and constrained by the age-related shape changes in the proximal tibia (Ding, 2000; Ryan et al., 2007). Significant age-related directional *change* of the principal eigenvector of the proximal tibia is *not* evident in this study. The relative eigenvalues of the primary, secondary, and tertiary vectors change with age; the eigenvectors remain relatively similar in direction. Quantitative parameters are discussed in the following section.

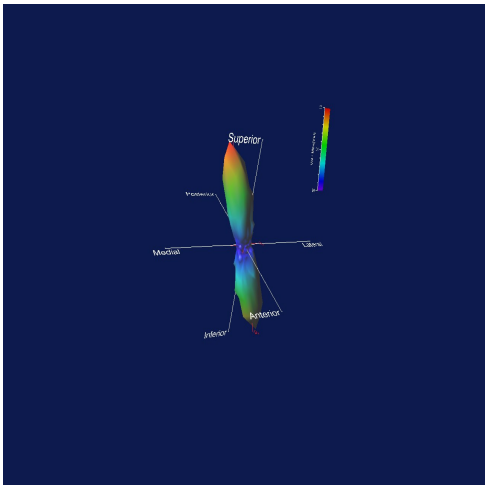

Figure 6.6: Medial VOI SVD (Burial 10_72) demonstrating slight anteroposterior/mediolateral obliquity.

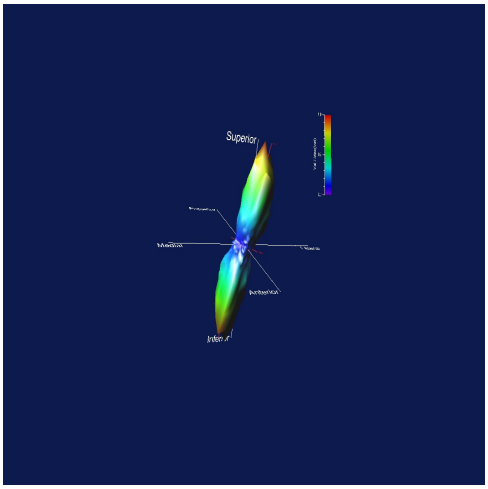

Figure 6.7 Lateral VOI SVD (Burial 10_72) demonstrating slight anteroposterior/lateromedial obliquity.

The following figures are progressive-maturity selected examples of trabecular architecture and SVD rose diagrams (Figures 6.8- 6.14). Their orientation is with medial to the left, posterior behind, and superior above: looking along the *y*

axis from anterior to posterior at a coronal plane through the center of the medial volume of interest sphere (bone on the left, rose 3D diagram on the right). Anatomical axes are in white; eigenvectors are in red.

The trends with age and SVDDA parallel those of the bone volume fraction (BV/TV) in producing a "lazy U" shaped pattern (high-low-higher). The rose diagram is relatively smooth and cylindrical when representing the primary eigenvector/eigenvalue in highly anisotropic trabecular bone. It becomes more irregular in shape as the secondary and tertiary eigenvectors/eigenvalues gain representation in trabecular bone that is less directional (i.e. more isotropic, less anisotropic). The youngest individuals of the sample have a very anisotropic trabecular structure representing the constraints of columnar endochondral ossification process (Figure 6.8). The values of degree of anisotropy decrease over the first year of life as the bone architecture becomes relatively isotropic; both medial and lateral condyles are partners in change (Figure 6.9). The SVDDA then begins to increase in association with bipedal weight-bearing with the early differentiation of the trabecular rod and plate configuration and a more complex shaped rose 3D diagram (Figure 6.10). The degree of anisotropy begins to approaches average adult values by age 6 years.

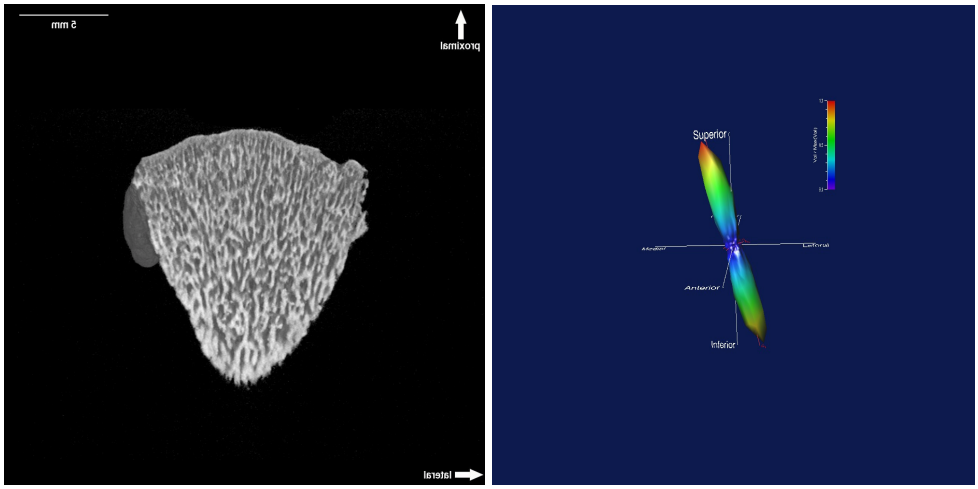

Figure 6.8 Burial 10_72 is 0.00 years old and medial VOI SVD DA is 6.5148.

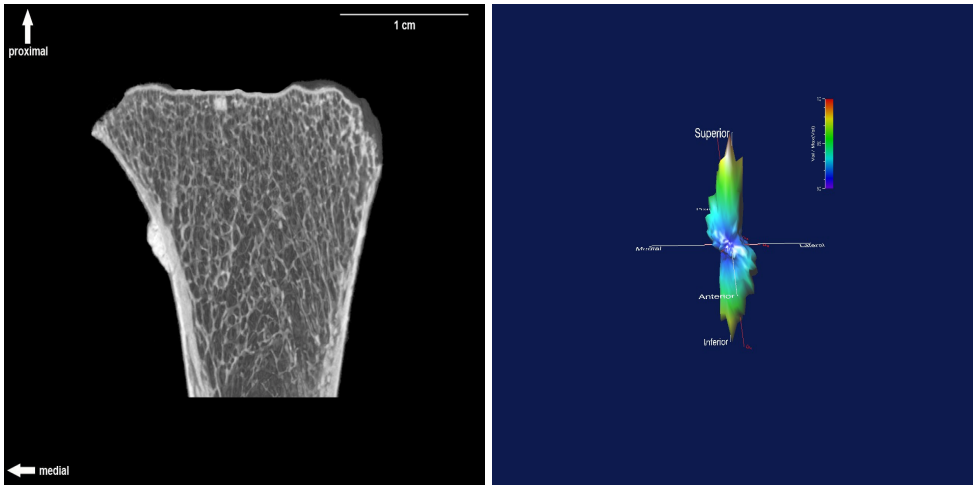

Figure 6.9 Burial 4_72 is 1.3 years old and SVD DA is 4.7457.

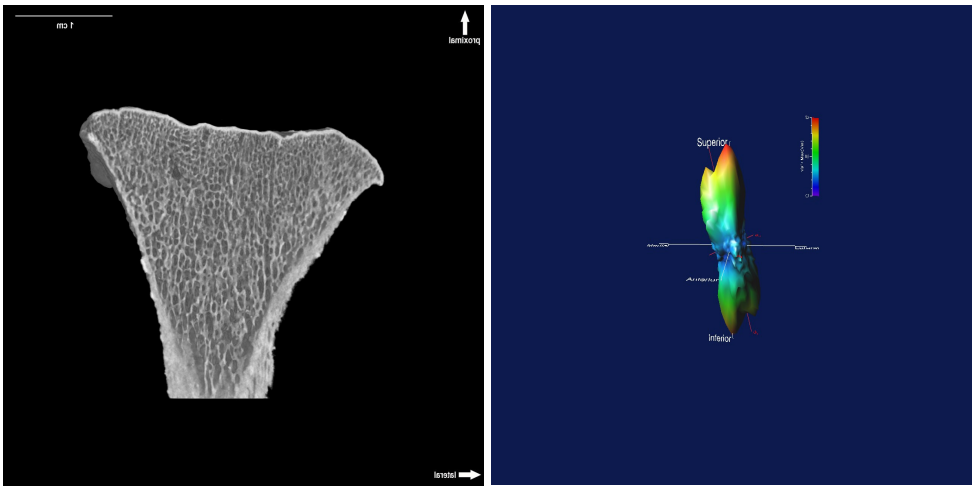

Figure 6.10 Burial 6_80 is 2.1 years old and SVD DA is 2.0306.

Trabecular microarchitecture becomes well-defined by middle childhood (6-8 years) with evidence of a distinctive plate and rod structure, defined anisotropy, decreased trabecular number, and increased trabecular thickness (Figure 6.11).

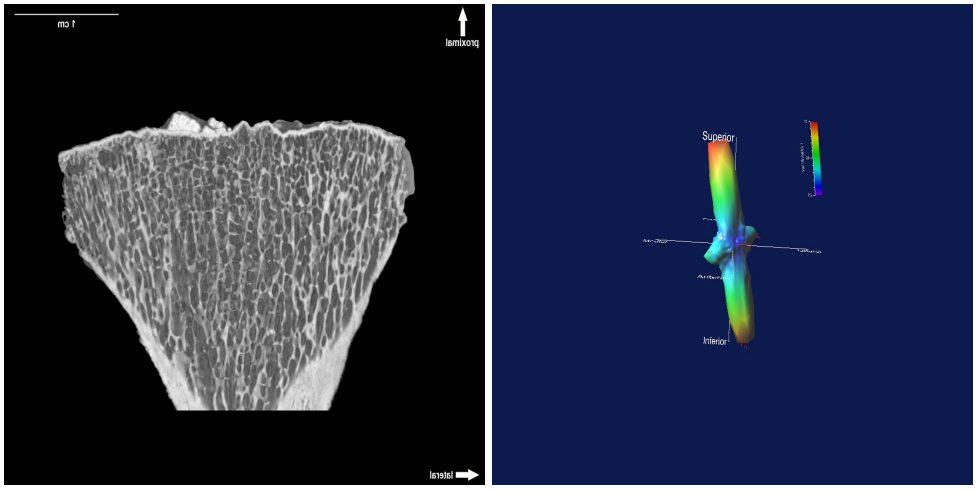

Figure 6.11 Burial 2_73 is estimated 6.8 years and SVD DA is 4.6258.

Late childhood/pre-puberty trabecular structure (10-11 years) demonstrates a further refinement of the degree of anisotropy with the primary eigenvector gaining predominance. Intra-tibial variation in BV/TV suggests continued bone functional adaptation to the types of mechanical loads (physical activity, muscle forces, and changing body mass) experienced. This is especially notable in the posterior aspects of both the medial and lateral tibial condyles, responding to increased loads in knee flexion.

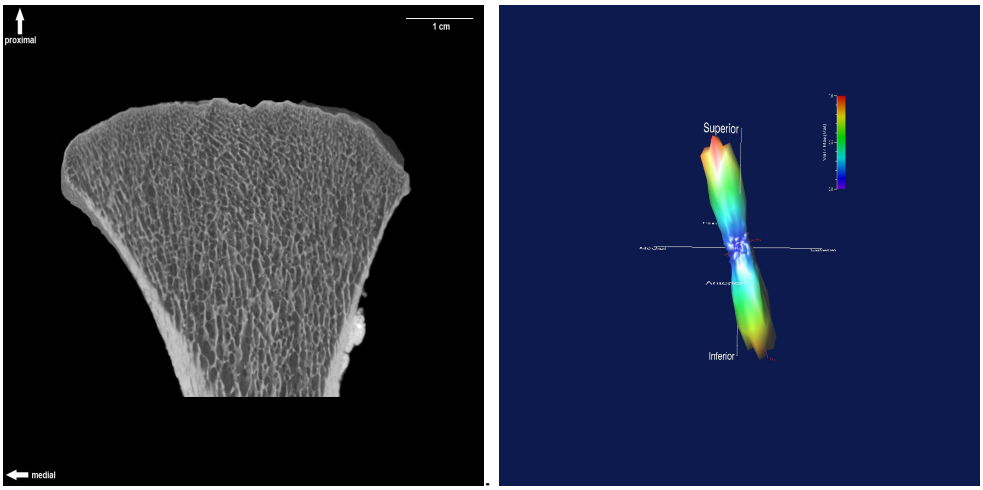

Figure 6.12 Burial15_74 is 9.8 years and SVD DA is 5.6836.

The following two individuals have volumes of interest in the subchondral position. A skeletal example of late adolescent maturity (near fusion of proximal tibial epiphysis) reveals the often-described coarsening of the trabecular structure which is increased trabecular spacing secondary to a decrease in trabecular number and an increase in thickness in those trabeculae remaining. These findings suggest

the combined effects of the pubertal sex hormone regime modulated by mechanobiological forces. The primary eigenvector remains oriented superoinferiorly. The rose 3D diagram has become more complex in shape reflecting both the horizontal component of the epiphyseal growth plate and a much more resolute plate/rod pattern (Figure 6.13).

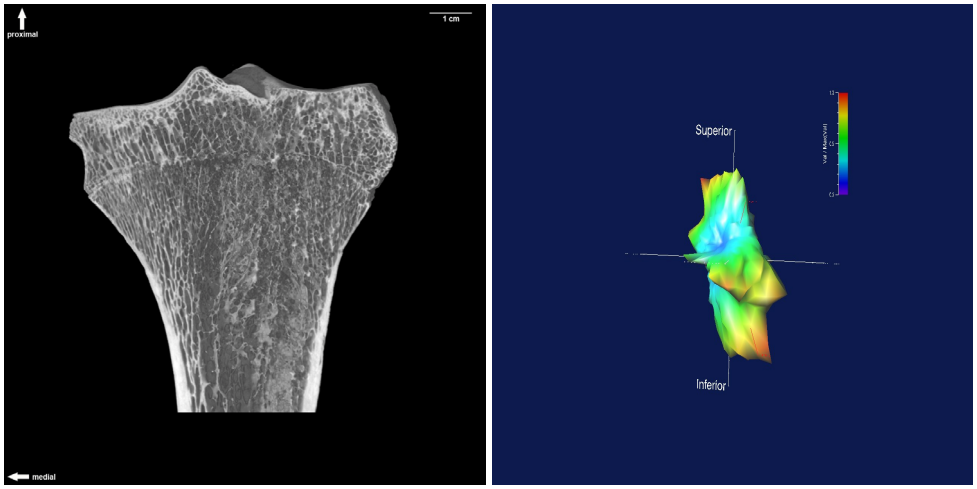

Figure 6.13 Burial SM_16 is 16.9 years and SVD DA is 4.5041.

The images of the proximal tibia of a young adult woman represent one particular endpoint of the ontogenetic pattern for trabecular bone (Figure 6.14). The trabecular pattern medial condyle is organized to accept loading forces (60/40: medial/lateral) with an increase in the orthogonal plate-like conformation under the subchondral plate in the primary spongiosa. Secondary and tertiary eigenvectors of the SVD are emphasized producing a 3D rose diagram with a parallelogram-like shape as opposed to the smooth vertical columnar shape of infancy.

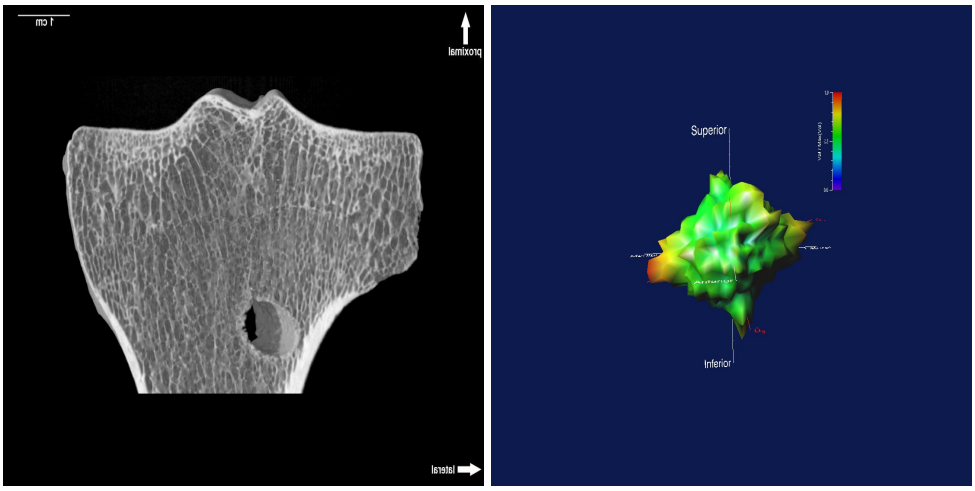

Figure 6.14 Burial 3A_76 is 21 years and SVD DA is 1.3673.

The visual journey

This section has been an attempt to "envision information" (Tufte, 1990): intersecting words, biologically-derived images, and mathematically-calculated diagrams. The goal was to seek simplicity and clarity, while representing the rich texture of data, a comparative context, and an understanding of complexity (Tufte, 1990). The skeletal examples for the journey from birth to adulthood have been chosen carefully to *highlight* waypoints in the continuous and variable process of growth and development (Figure 6.15), suggesting (but not confirming) to the reader that there *may* be a general pattern to be perceived. This will be explored further with quantitative data.

Figure 6.15 Proximal tibiae from burials 10_72 and 3A_76: birth to maturity.

QUANTIFICATION OF TRABECULAR BONE STRUCTURE

The results of the three-dimensional morphometric analyses of the central medial and lateral tibial condyle VOIs are listed for each specimen in Tables 6.2 and 6.3 respectively. The overall ontogenetic-related patterns for both the medial and lateral VOIs are similar. The structural data for the trabecular architecture include:

1. Bone volume fraction (BV/TV)
2. Star volume distribution degree of anisotropy (SVD DA)
3. Elongation index (E)
4. Trabecular thickness mean (Tb.Th Mean [mm])
5. Trabecular thickness maximum (Tb.Th Max [mm])
6. Trabecular number (Tb.N/mm)
7. Field of reconstruction (FOR [micrometers])

Trabecular structure data are plotted relative to age estimate for each individual as well by age-related groupings (I-IV).The overall patterns are presented first and the groupings follow. OriginLab scientific graphing and analysis software (OriginLab Corporation, Northampton, MA; www.originlab.com) was used to produce the graphic displays, statistical, and curve fitting analyses. The comparative non-linear curve fitting analytical aspect of this software was used to define the fit most descriptive of the data, determine statistical significance when relevant, and to indicate the general patterns of change which are frequently irregular and nonlinear. The actual fitted-curve lines serve primarily an illustrative purpose, consistent with the framework for "envisioning quantitative data" (Tufte, 1990). No claim is being made to the general applicability of the specific equations. Ruff (2003) has argued that plots of log-transformed data (ratios as well as individual parameters) may provide some additional insights into changes in ontogenetic trajectories. An advantage to the use of logged data with ratios is that proportionality over different size ranges is preserved; an advantage to the use of log-transformed data for individual properties is that the specific (percentage) growth rate is emphasized as opposed to the absolute (Ruff, 2002; 2003). During the data exploration process for this research, plots were provisionally constructed using both raw and log-transformed data. This researcher was unable to discern any advantage to the latter in terms of the visual display of quantitative data or the depth of interpretations possible. For these reasons, raw data is used throughout this dissertation. Appendix A contains the complete skeletal sample dataset.

The three scales of developmental maturity used in this study (seriation, age estimation, and maturity stage) are highly correlated (Table 6.1). The plots using each of these developmental measures have the same pattern, shape, and curve fitting equations. Age estimation was chosen as the maturity scale in this exposition for reasons of clarity and simplicity as well as obviating the need for the reader to repeatedly refer back to the seriation and maturity stage schemes.

	Seriation	Age	Maturity
Seriation	1.0000	0.8025	0.9156
Age	0.8025	1.0000	0.9675
Maturity	0.9156	0.9675	1.0000

Table 6.1 Coefficient of Correlation: Developmental Scales

Burial No.	Age Est.	Mat. Stage	Seriation	FOR	BV/TV	SVD DA	MIL DA
10/72	0.1	1	7	22	0.4117	6.5148	1.4851
14B/72	0.1	1	8	22	0.4606	7.7742	1.5115
9/72	0.25	1	21	22	0.4041	7.1332	1.5914
5/71	0.25	1	23	22	0.4393	6.0874	1.4618
8/72	0.4	2	29	22	0.2958	7.4439	1.4895
15AB/73	0.4	2	30	22	0.4362	7.6417	1.5438
15A+B/73	0.4	2	31	22	0.4361	5.7339	1.4501
12/73	0.4	2	42	22	0.2975	9.231	1.7042
5/72	0.4	2	45	22	0.2609	6.4366	1.4807
7/73	0.7	3	48	22	0.2596	8.8512	1.6295
8/73	0.9	4	56	22	0.2416	4.8926	1.4758
4/72	1.3	5	61	40	0.2841	4.7457	1.408
9/73	1.3	5	62	40	0.2613	3.0029	1.2658
4/73	1.3	5	63	40	0.2359	5.0708	1.4987
8/76	1.3	5	67	40	0.334	1.4019	1.1749
7/76	1.3	5	69	40	0.288	4.2776	1.4692
6/80	2.1	6	79	40	0.3759	2.0306	1.1254
14/74	2.75	7	84	40	0.2087	7.2195	1.3204
6/71	4.7	9	86	40	0.2812	4.1905	1.2596
13/72	6.8	11	87	60	0.3784	4.8028	1.4292
2/73	6.8	11	88	40	0.3266	4.6258	1.3086
7/80	9.8	12	89	60	0.4485	3.5887	1.2552
1/81	9.8	12	93	60	0.3305	5.9331	1.3163
SM3	9.8	12	94	60	0.287	5.0216	1.2551
15/74	9.8	12	95	60	0.3468	5.6836	1.2897
9/75	14.3	15	96	80	0.3699	4.013	1.3668
7/81	14.3	15	97	80	0.4255	7.1248	1.4996
9/77	14.3	15	98	80	0.3693	5.799	1.4242
SM18	16.9	16	99	80	0.365	3.0487	1.4678
SM16	16.9	16	102	80	0.3507	4.5041	1.4497
SM9B	16.9	16	103	60	0.3281	5.5952	1.4476
474	19	-	-	80	0.3156	1.755	1.5805
3A/76	21	-	-	80	0.3366	1.3673	1.44
9/74	24	-	-	80	0.2955	13.0283	1.5893

Table 6.2 Structural parameters of the entire sample for the medial VOI (continued). FOR, field of reconstruction; BV/TV, bone volume fraction; SVD DA. Star volume distribution degree of anisotropy; MIL DA, mean intercept length degree of anisotropy; TrTh Mean, mean trabecular thickness; TrTH Max, maximum trabecular thickness; TrN, trabecular number.

Table 6.2 Continued

Burial No.	TrTh Mean	TrTh Max	TrN
10/72	0.0778	0.2639	5.1179
14B/72	0.0873	0.2216	5.0443
9/72	0.0952	0.2792	4.2415
5/71	0.0956	0.2931	4.5043
8/72	0.0865	0.2891	3.4476
15AB/73	0.0762	0.2387	5.5363
15A+B/73	0.0782	0.2372	5.4617
12/73	0.0967	0.3083	2.9699
5/72	0.0902	0.3052	2.968
7/73	0.0921	0.2517	2.6766
8/73	0.1031	0.2784	2.177
4/72	0.1187	0.4043	2.3089
9/73	0.1178	0.3593	2.1869
4/73	0.1267	0.3539	1.7588
8/76	0.1422	0.3908	2.285
7/76	0.1354	0.5117	2.013
15/72	0.1545	0.448	2.0797
3/72	0.1362	0.4743	2.1601
6/80	0.1449	0.5286	2.4577
14/74	0.1305	0.4495	1.5697
6/71	0.1419	0.4425	1.9312
13/72	0.1952	0.7	1.8532
2/73	0.1796	0.6401	1.7108
7/80	0.2319	0.7161	1.8607
1/81	0.203	0.5722	1.6022
SM3	0.1913	0.6341	1.4664
15/74	0.203	0.6404	1.7068
9/75	0.4293	1.8456	0.9258
7/81	0.2933	0.9561	1.3725
9/77	0.2827	1.2861	1.2092
SM18	0.3091	1.155	1.1074
SM16	0.3789	1.6524	0.9454
SM9B	0.2298	0.7061	1.3263
474	0.2686	1.1998	0.9709
3A/76	0.4186	1.9205	0.7846
9/74	0.3174	1.0248	0.9278

Burial No.	Age Est.	Mat. Stage	Seriation	BV/TV	SVD DA	MIL DA
10/72	0.1	1	7	0.3933	4.3401	1.5226
14B/72	0.1	1	8	0.4452	7.2108	1.5331
9/72	0.25	1	21	0.3893	9.2954	1.7191
5/71	0.25	1	23	0.4871	6.5367	1.5221
8/72	0.4	2	29	0.2575	6.4801	1.5219
15AB/73	0.4	2	30	0.4333	10.1475	1.7422
15A+B/73	0.4	2	31	0.4269	8.1035	1.5833
12/73	0.4	2	42	0.245	8.7033	1.637
5/72	0.4	2	45	0.241	5.9625	1.5507
7/73	0.7	3	48	0.2299	4.2553	1.4329
8/73	0.9	4	56			
4/72	1.3	5	61	0.248	3.2046	1.3227
9/73	1.3	5	62	0.2615	3.4891	1.2908
4/73	1.3	5	63	0.252	6.086	1.4832
8/76	1.3	5	67	0.2967	2.5436	1.2903
7/76	1.3	5	69	0.2911	3.8551	1.3537
15/72	1.3	5	70	0.3221	2.9556	1.2616
3/72	2.1	6	76	0.3081	4.5957	1.3869
6/80	2.1	6	79	0.3843	3.2213	1.3043
14/74	2.75	7	84	0.2353	7.8451	1.4308
6/71	4.7	9	86	0.2328	3.6072	1.2661
13/72	6.8	11	87	0.3779	3.075	1.3451
2/73	6.8	11	88	0.3004	6.3244	1.5781
7/80	9.8	12	89	0.3626	6.5612	1.6243
1/81	9.8	12	93	0.3247	6.7363	1.5703
SM3	9.8	12	94	0.2888	9.4249	1.6524
15/74	9.8	12	95	0.3377	7.2213	1.4039
9/75	14.3	15	96	0.3271	10.1058e	1.2157
7/81	14.3	15	97	0.3899	6.1774	1.4299
9/77	14.3	15	98	0.3291	2.7257	1.23
SM18	16.9	16	99			
SM16	16.9	16	102	0.2997	2.152	1.1474
SM9B	16.9	16	103	0.2851	3.2475	1.243
474	19	-	-	0.3218	3.9402	1.3544
3A/76	21	-	-	0.3557	11.4669	1.5022
9/74	24	-	-	0.2958	4.4036	1.3492

Table 6.3 Structural parameters of the entire sample for the lateral VOI (continued).

Table 6.3 Continued

Burial No.	TrTh Mean	TrTh Max	TrN
10/72	0.0788	0.2206	4.9331
14B/72	0.0904	0.2358	4.75123
9/72	0.0929	0.2587	4.1646
5/71	0.1063	0.3048	4.2839
8/72	0.0939	0.2931	2.8217
15AB/73	0.0853	0.2323	4.9319
15A+B/73	0.0806	0.2168	5.1197
12/73	0.0957	0.2947	2.5562
5/72	0.0884	0.2961	2.6903
7/73	0.1019	0.2822	2.1179
8/73			
4/72	0.1201	0.3544	1.9351
9/73	0.1141	0.3187	2.3225
4/73	0.1282	0.3583	1.796
8/76	0.1356	0.414	2.1138
7/76	0.1268	0.3811	2.105
15/72	0.1562	0.5134	1.9555
3/72	0.135	0.3345	2.2167
6/80	0.1463	0.3967	2.5902
14/74	0.1299	0.5019	1.8271
6/71	0.1348	0.4048	1.7146
13/72	0.2307	0.9789	1.25
2/73	0.173	0.5977	1.7037
7/80	0.2308	0.8566	1.4974
1/81	0.2109	0.7185	1.5402
SM3	0.2077	0.9374	1.4011
15/74	0.1986	0.5956	1.6419
9/75	0.4128	1.7103	0.9449
7/81	0.2507	0.6479	1.4939
9/77	0.2505	0.8957	1.2642
SM18			
SM16	0.3761	2.0326	0.8441
SM9B	0.2317	0.7783	1.1752
474	0.2897	1.2353	1.071
3A/76	0.3181	1.0675	1.0775
9/74	0.2946	1.2328	0.9461

EVALUATION OF THE MEASUREMENT PROCESS

The basic interrogation of a measurement system, in this investigation the combination of microCT scan and Quant3D computations, is whether or not it is precise enough to detect real differences for the trabecular bone structural parameters across individuals in the entire sample as well across the four maturity-related groups. The analysis was performed under the advisement of Thomas Bishop of The Ohio State University Statistical Consulting Services. The data consisted of three complete repeat measurements of the Quan3D derived structural parameters from the central VOI in eight individuals dispersed evenly within the entire sample and across the maturity-related groups.

Of particular interest is the relative contribution (%) of the measurement process to the total variation. The components-of-variation portion of the measurement evaluation analysis indicates that virtually all of the variation detected is due to differences across individuals/groups and only a negligible portion is due to the measurement system. The percent variation attributed to the measurement system (0.06-0.6%) is consistent with that of other published microCT studies of trabecular bone (0.5%) (e.g., Maga et al., 2006). The results of this study indicate that the measurement system is more than adequate for its application to this research project. The relevant aspects of the Gage R&R analysis (Wheeler and Lyday, 1989) results are summarized in Table 6.4.

Parameter	Measurement-related variation (%)
BV/TV	0.00
SVD DA	0.63
TrTh Mean	0.06
TrN	0.00

Table 6.4 Results from measurement evaluation study.

OVERALL QUANTITATIVE PATTERNS

Bone volume fraction

The BV/TV for both the medial and lateral primary VOIs (Figures 6.16 and 6.17) is the highest in the youngest individuals: remaining high from late fetal age to postnatal ages of 4-6 months. The range of values during this time period is remarkably consistent: 0.4041 to 0.4606 (40- 46% bone). This particular range and the general overall pattern are consistent with the findings of Ryan and Krovitz's (2006) work on trabecular bone ontogeny of the proximal femur. Their results for BV/TV for the youngest age group, in a similar type of archaeological sample, are reported as "ranging from approximately 0.45 to 0.59 (45% to 59% bone)" (Ryan and Krovitz, 2006, p. 595). Decreases in the bone volume fraction begin to appear by five

months of age (Table 6.2). The bone volume fraction decreases nearly 40% between the ages of 6 and 12 months- lowest values reached are between 0.2300 and 0.2400. The BV/TV then increases incrementally after age 12 months reaching the average for adult values after age 6 years. Ding (2000) studied the age variation in normal human trabecular bone from the proximal tibiae in a human autopsy series aged 16 to 83 years. The overall mean and 95% confidence interval for BV/TV in adults were 0.2300 and 0.2300- 0.2500. The pattern is characterized by an age-related decrease. These results are skewed by the age distribution (older) of Ding's study. However, the volume fraction reported in Ding's young adults (16-30 years old) was around 0.3000, similar to that in this research. The "lazy-U" ontogenetic pattern for BV/TV seen in the plots of the current research is best described by an exponential-decay model. This pattern is repeated in the degree of anisotropy analyses.

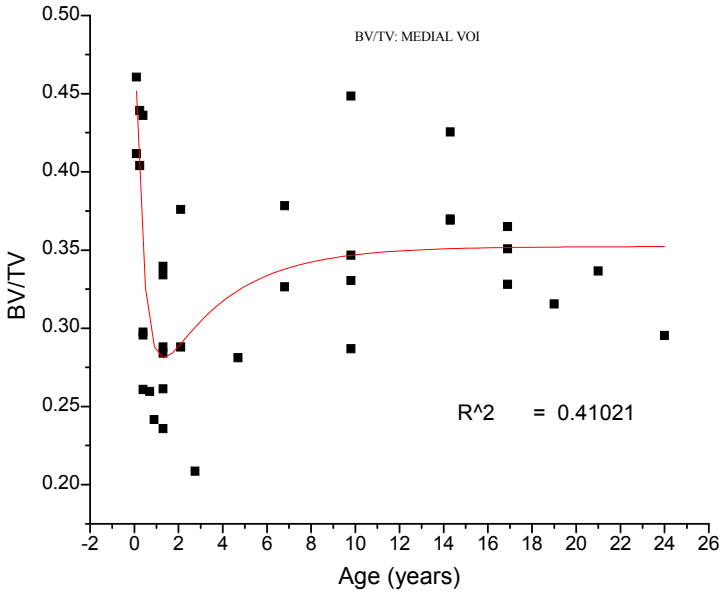

Figure 6.16 BV/TV: MEDIAL VOI. Black squares represent individual tibiae. Red [black] line represents the exponential-decay curve.

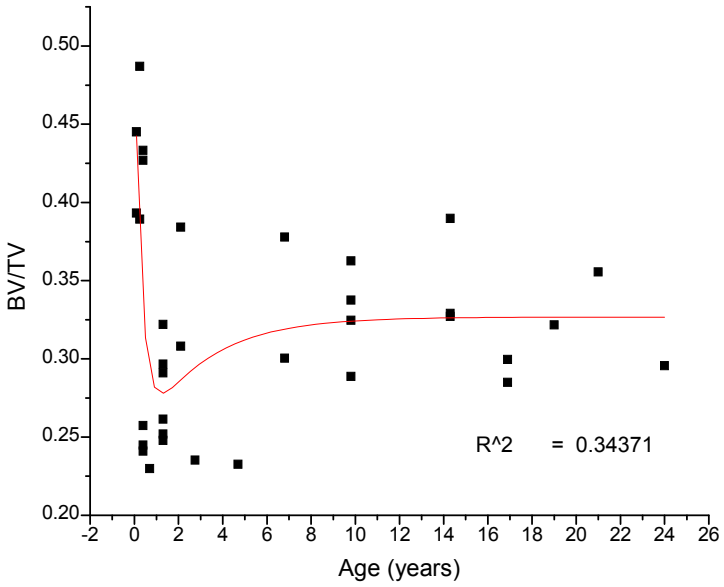

Figure 6.17 BV/TV: LATERAL VOI. Black squares represent individual tibiae. Red [black] line represents the exponential-decay curve.

Anisotropy

The results for fabric structure for both the medial and lateral VOIs follow the same age-related course as that for BV/TV (Figures 6.18 and 6.19). The star volume distribution degree of anisotropy (SVDDA) is calculated as the eigenvalue of the primary direction divided by the eigenvalue of the tertiary direction. The resultant units are dimensionless. This morphometric data, which are the basis for the previously displayed 3D rose diagrams, exhibit a very anisotropic trabecular structure in the youngest individuals. The range of values is between 8.85 and 5.73. The degree of anisotropy decreases during the latter one half of the first year of life, becoming relatively isotropic at about one year. The range of values is between 1.40 and 5.07. Both VOIs then return to a more directional fabric (increased anisotropy), reaching average adult values by age 6 years. Similar to BV/TV, the scatterplot of SVD DA is best described by an exponential-decay model.

Ding's (2000) research on the age variations of human adult tibial trabecular bone reports for SVD DA an overall mean and 95% confidence interval of 5.44 and 6.22-8.38. The degree of anisotropy reported for Ding's young adults (16-30 years old) was around 4.0, similar to that in this research. The three adults (female) incorporated into this study exhibit this wide range of variability. The plot for the lateral VOI has four missing values: two due to poor preservation/mineral intrusion of the lateral condyle, one adult omitted because of outlier value >2x median, and one adolescent omitted because of influence of partial epiphyseal plate fusion.

The non-homologous VOI positioning in the six oldest individuals contributes to the data scatter for these individuals. The effect of the horizontal component of the growth plate and epiphysis in some individuals tends to increase the value of the tertiary eigenvector and thus decrease the degree of anisotropy in these individuals. It should be noted, however, that the pattern of biologically significant changes in SVD DA occurs at an earlier age and thus the impact of this VOI positioning on the overall SVD DA results appears low.

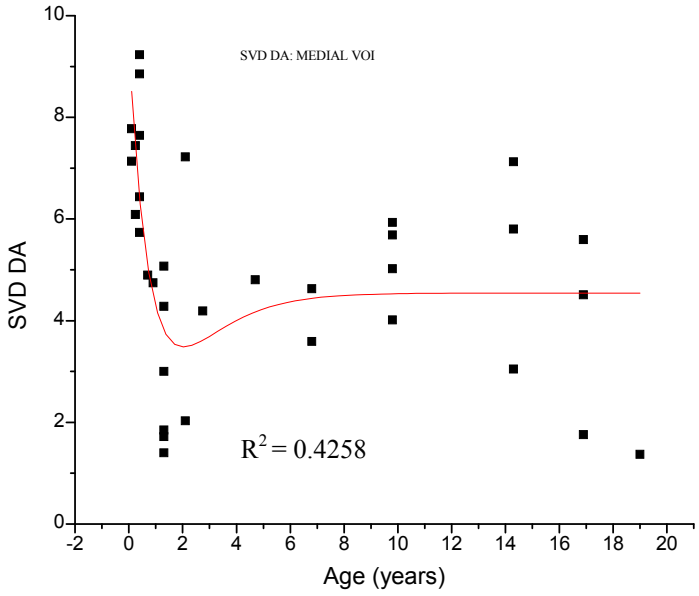

Figure 6.18 SVD DA: MEDIAL VOI. Black squares represent individual tibiae. Red [black] line represents the exponential-decay curve.

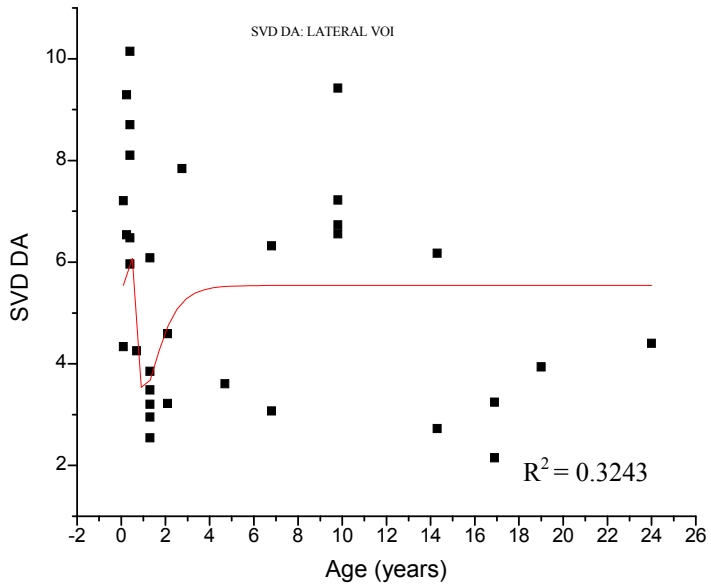

Figure 6.19 SVD DA: LATERAL VOI. Black squares represent individual tibiae. Red [black] line represents the exponential-decay curve.

Elongation index

Additional information from structural analysis can be extracted using eigenvalues to calculate the elongation index (E) as $(1- \tau_2/\tau_1)$. This index varies between 0 and 1. The lower values indicate a more plate-like structure with higher degree of similarity between primary and secondary eigenvalues; the higher values indicate a more rod-like structure with the primary orientation predominating (Maga et al., 2006). This is another way to demonstrate the changes in the trabecular architecture of the proximal tibia, which is initially rod-like, changing to more plate-like during the second year of life as walking begins, and then eventually developing a more "lattice-work" structure (Figures 6.20 and 6.21). These analyses do not include those individuals with epiphyses present (see Appendix A for the E data).

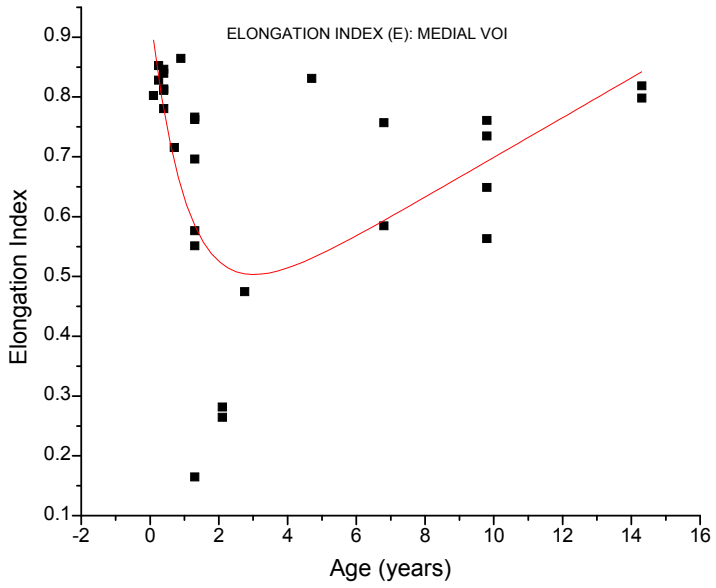

Figure 6.20 ELONGATION INDEX (E): MEDIAL VOI. Black squares represent individual tibiae. Red [black] line represents the exponential-decay curve.

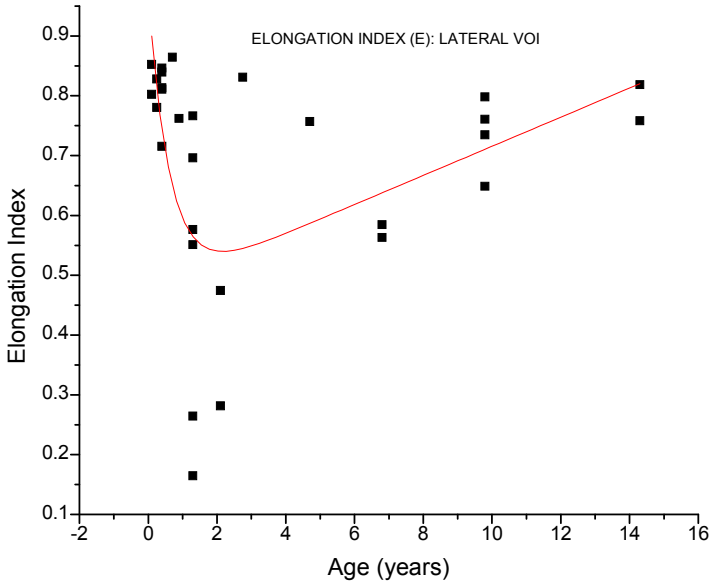

Figure 6.21 ELONGATION INDEX: LATERAL VOI. Black squares represent individual tibiae. Red [black] line represents the exponential-linear curve.

Trabecular thickness

The measured mean and maximum trabecular thicknesses (Tr.Th.Mn; Tr.Th.Max) of the proximal tibia reveal an age-related linear relationship (increase) from birth to maturity. The trends with age are comparable for both the medial and lateral VOIs. The Tr.Th.Mn scatterplots are displayed below (Figures 6.22 and 6.23). Ryan and Krovitz's (2006) ontogenetic study of the proximal femur included ages 0.00 to 9 years. Their reported range of values of TrThMn, using a comparable scanner and the same Quant 3D software, in this age range is 0.093 – 0.215 mm. The range of values of this ontogenetic study of the proximal tibia in the same age range is a very comparable 0.078-0.200 mm.

Extending the age scope of this study into young adulthood, the data demonstrate a continual, relatively linear increase in mean trabecular thickness through the adolescent growth spurt and into maturity. The range of young adult values in this study (extremely limited sample, n =3) is 0.270- 0.4200 mm. Reported values from the literature of adult mean trabecular thickness vary from 0.123-0.217 mm (Hildebrand et al., 1999; Lai et al., 2005; Link et al., 1998; Majumdar et al., 1998; Ryan and Krovitz, 2006; Ulrich et al., 1999). Although some of these studies contain significant differences in methods, sampling procedures, and bone elements studied, the values obtained may provide a general benchmark. It is perhaps not surprising that a Late Prehistoric agricultural population with a high physical demand lifestyle would have mean trabecular thickness values on the high end of those reported in the literature for contemporary individuals.

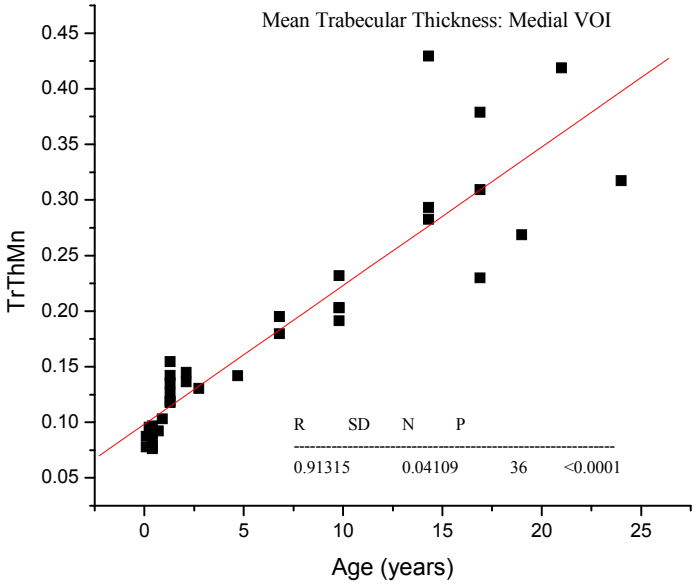

Figure 6.22 Tr.Th.Mn: MEDIAL VOI. Black squares represent individual tibiae.

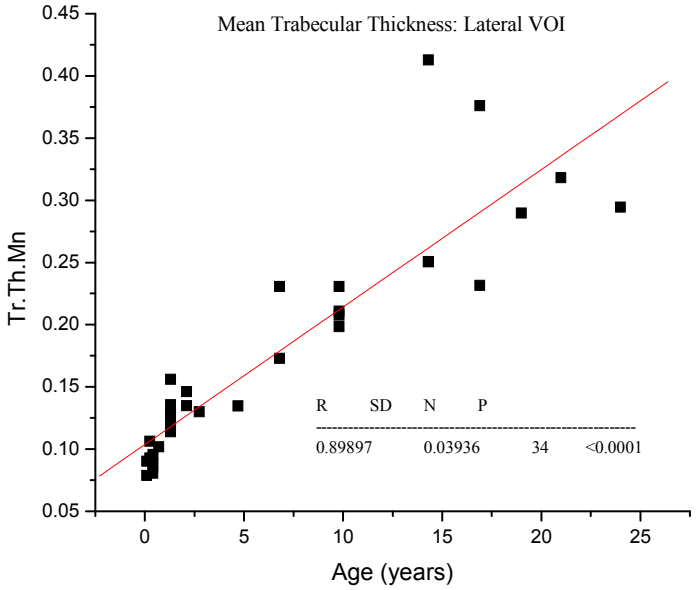

Figure 6.23 Tr.Th.Mn: LATERAL VOI. Black squares represent individual tibiae.

Trabecular number

The ontogenetic pattern for trabecular number (Tr.N) is opposite of that for Tr.Th (Figure 6.24). The measured values for Tr.N decrease strikingly from the youngest individuals through approximately one year of age. The Tr.N then continues a gradual decrease, reaching in the medial VOI the range consistent with adult values by late adolescence (0.93-1.33/mm). Reported values from the literature of adult mean trabecular number vary from 1.12 to1.60/mm (Hildebrand et al., 1999; Lai et al., 2005; Link et al., 1998; Majumdar et al., 1998; Ryan and Krovitz, 2005; Ulrich et al., 1999). As with the previous parameters discussed, the trends with age are similar for both the medial and lateral VOIs (Figures 6.25 and 6.26). This nonlinear relationship of Tr.N with age is best described by a nonlinear polynomial regression curve.

These results of this research for the ontogenetic pattern of trabecular number in the proximal tibia partially diverge from those reported by Ryan and Krovitz (2006) for the proximal femur. These authors found the same decline from birth through one year, but then an apparent stabilization of trabecular number "after about one year and remains at or near adult values after that age" (ibid, p. 598). This may be more apparent than real, due to the fact that they studied only two individuals past three years of age.

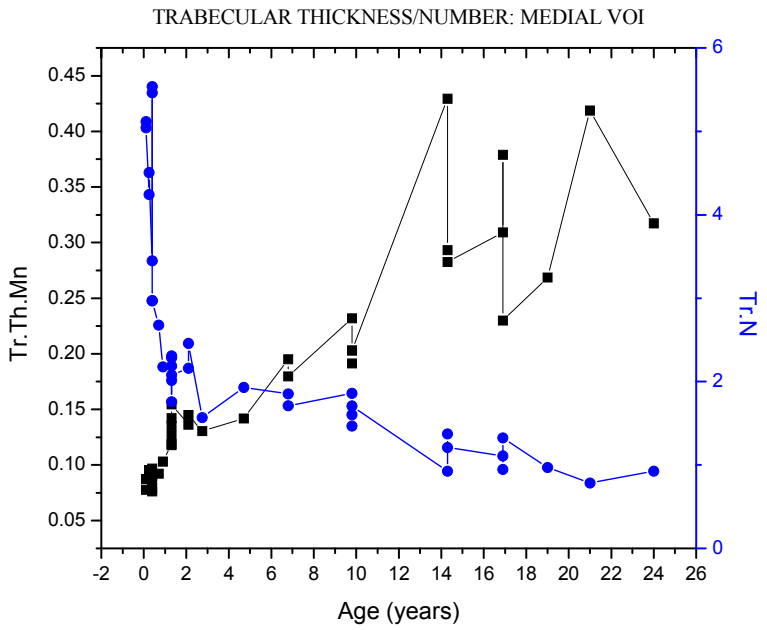

Figure 6.24 Double Y scatterplot of TrTh and TrN from the medial VOI. Black squares (TrTh) and blue (TrN) circles represent individual tibiae. In black/white reproduction TrN is described by circles in a non-linear curve with high values in the upper left and low values in the lower right.

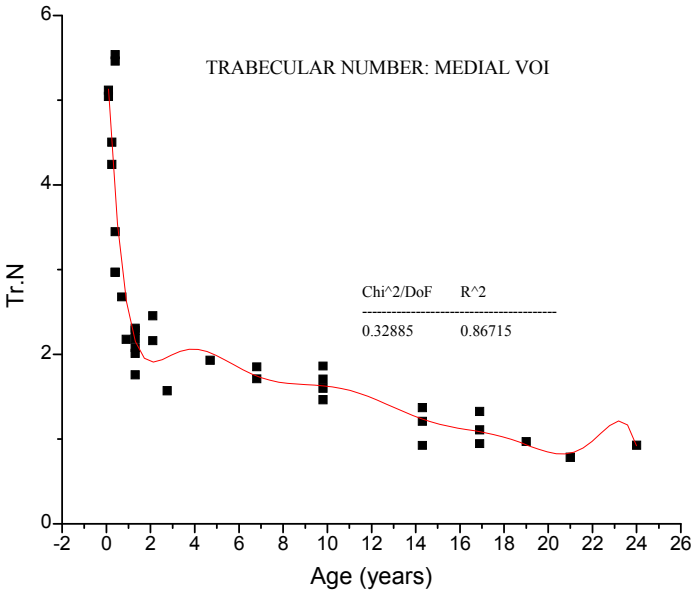

Figure 6.25 Tr.N: Medial VOI. Black squares represent individual tibiae. Red [black] line represents the nonlinear polynomial regression curve.

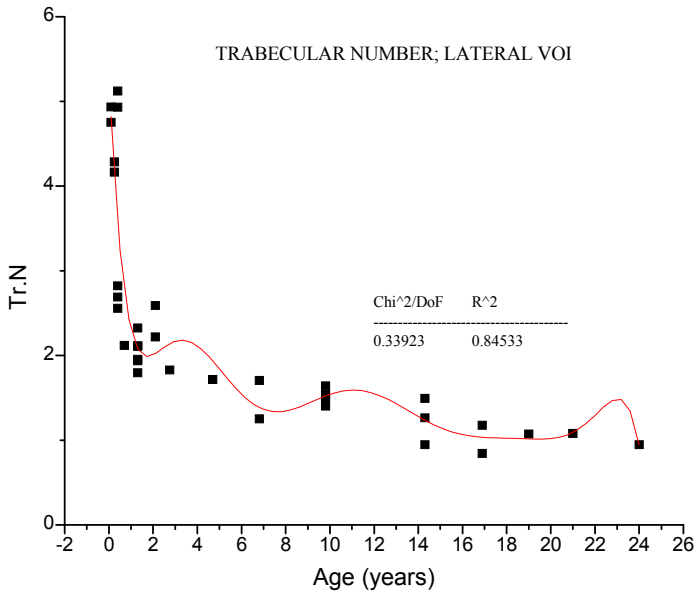

Figure 6.26 Tr.N: LATERAL VOI. Black squares represent individual tibiae. Red [black] line represents the nonlinear polynomial regression curve.

The results presented document the overall pattern of trabecular structural change during ontogeny, influenced by increasing body mass, the acquisition and maturation of mature bipedal gait, and the transition from dependency of physical behavior to independent adult activities. The data indicate that the initial primary spongy bone is replaced by remodeled bone with fewer, thicker struts. These results support earlier work studying other skeletal elements (Ryan and Krovitz, 2006) and other taxa (Byers et al., 2000; Fazzalari et al., 1997; Mulder et al., 2005; Parfitt et al., 2000; Wolschrijn and Weijs, 2004, 2005).

The rapid reorganization of trabecular bone in the first two years of life includes changes in bone volume fraction, anisotropy, trabecular thickness, and trabecular number. The initial, relatively dense trabecular columnar structure is progressively reduced as unloaded or underloaded bone is removed. The remaining trabecular grid is then differentially remodeled/modeled, directed by mechanical stimuli related to physical activity and body mass. This derived pattern suggests that mechanical loading as a result of locomotor maturation is one of the essential driving forces for bone functional adaptation in the early years. The overall trabecular changes have a complex relationship with, but are not limited to, genetic factors, age, locomotion, physical activity, increases in body mass, and hormonal systems.

MATURITY/AGE -RELATED GROUPS (I-IV)

Maturity-stage combinations (I-IV) provide additional insight to the quantitative data by allowing comparisons to be made within and among biologically meaningful groups (Table 6.5).

Maturity Group	Maturity Stage	N	Mean Age (years)
I.	1-2	9	0.311
II.	3-6	10	1.360
III.	7-12	8	7.538
IV*	15-24	9	17.511

* seven individuals of group IV have the epiphysis present or fused.

Table 6.5 Maturity stage- related groups.

Results for the grouped maturity stage analyses are listed in Table 6.6 A/B, which includes group means and standard deviations. Structural parameters of interest are BV/TV, SVD DA, TrTh, and TrN. Figures 6.26 -6.29 (A/B; medial VOI/lateral VOI) display the data for each trabecular bone parameter among the groups in side-by-side box plots.

A. MEDIAL VOI				
Maturity Group	BV/TV	SVDDA	Tr.Th.Mn	Tr.N
I.	0.383 (0.076)	7.111 (1.065)	0.087 (0.008)	4.366 (1.023)
II.	0.291 (0.046)	3.784 (2.288)	0.127 (0.020)	2.211 (0.249)
III.	0.326 (0.071)	5.134 (1.131)	0.185 (0.033)	1.713 (0.162)
IV.	0.351 (0.038)	5.137 (3.510)	0.325 (0.069)	1.063 (0.202)

B. LATERAL VOI				
Maturity Group	BV/TV	SVDDA	Tr.Th.Mn	Tr.N
I.	0.369 (0.095)	7.420 (1.816)	0.090 (0.008)	4.028 (1.052)
II.	0.288 (0.047)	3.801 (1.069)	0.129 (0.016)	2.128 (0.234)
III.	0.308 (0.054)	6.349 (2.101)	0.190 (0.040)	1.572 (0.188)
IV.	0.326 (0.034)	5.528 (3.482)	0.303 (0.064)	1.102 (0.208)

Table 6.6 Grouped morphometric results: Mean and (Standard Deviation).

The maturity-stage group box plot presentations exhibit interesting contrasts of variation in the structural parameters within and among the groupings. For this data set the boxes depict a six-number summary, which consists of: the smallest observation [(▼): bottom whisker], lower quartile [(Q1): bottom of box], median (horizontal bar through box), mean (■), upper quartile [(Q3): top of box], and the largest observation [(▲): upper whisker]. The spacing between different parts of the

box helps indicate data variance and skew. A provision is made for the representation of extreme values which are computed as the upper/lower quartile range ± 1.5 x IQR. None of the data, after eliminating those extreme outliers among the older individuals, exceeds these values. The IQR (enclosed within the box) is the *interquartile range* which is the range within which the middle 50% of the ranked data are found (Massart et al., 2007).

Figure 6.27 A/B representing the bone volume fraction (BV/TV) data demonstrates important transitions in trabecular bone functional adaptation. The youngest individuals (group I) have the largest IQR reflecting the dramatic reconfiguration of the internal trabecular structure in the first six months of life. The onset of walking (group II) appears to channel the trabecular volume into a more constrained range. The middle childhood group (group III) displays the widest range of values which may be associated with the differences in the chronology and rate of maturation between males and females in this cross-sectional, pooled sex study. The late adolescent/young adults (group IV) reach an apparent "target" characterized by the smallest IQR. The means for BV/TV values are highest in the youngest group, decline in group II; the BV/TV means then increase, reaching adult levels in group IV which are 85-90% of the starting value. Oneway ANOVA testing for BV/TV of the medial and lateral VOIs, overall, indicated a statistically significant p-value = 0.001 and 0.003 respectively. Bonferroni posthoc testing demonstrated significant statistical differences between groups I and II ($p = 0.001$) and between groups I and III ($p = 0.030$) for the MVOI only.

A.

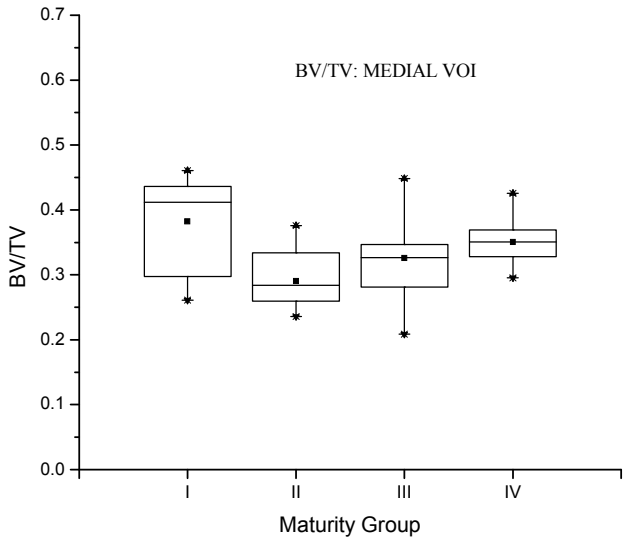

B.

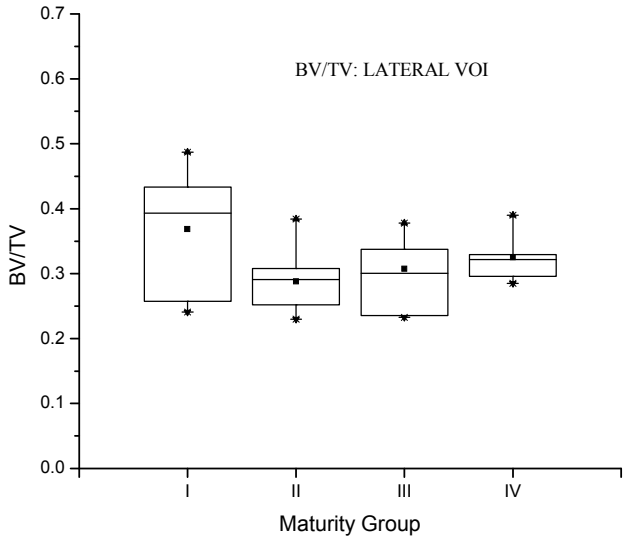

Figure 6.27 BV/TV: Side-by-side box plots by maturity-staged groups.
MVOI (A) overall p = 0.001, between Groups I/II p = 0.001, between Groups I/III P = 0.030. LVOI (B) overall p = 0.003, Group comparisons are not significant at the 0.05 level.

.

Figure 6.28 A/B displays the quantitative data for the degree of anisotropy (SVD DA). The pattern of SVD DA between the maturity-related groups is similar to that for BV/TV. The mean is the highest and the IQR is the lowest for SVD DA of the youngest group highlighting the fetal organization of the endochondral ossification process. Growth and development combined with trabecular reorganization associated with function behavioral changes (nonwalking-to-walking; dependency-to-independent physical activities) contribute to a decline followed by an increase in the mean value for anisotropy as well as increased variability in groups II-IV. Oneway ANOVA testing of SVD DA overall indicated a non-significant p-value = 0.070. Bonferroni posthoc testing confirmed the lack of significant statistical differences between groups.

A.

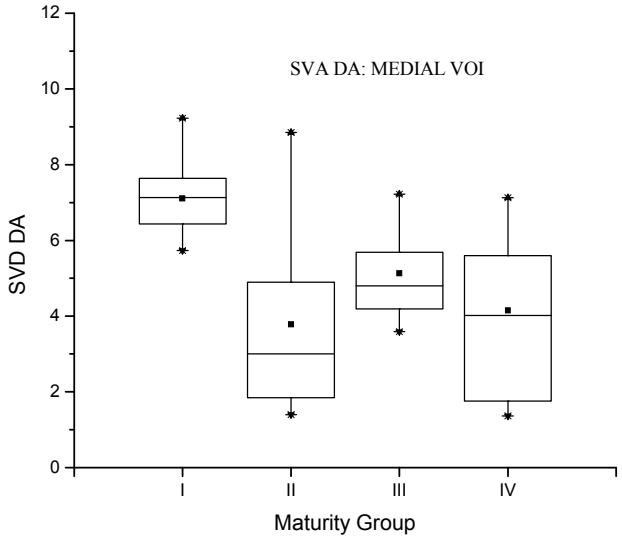

B.

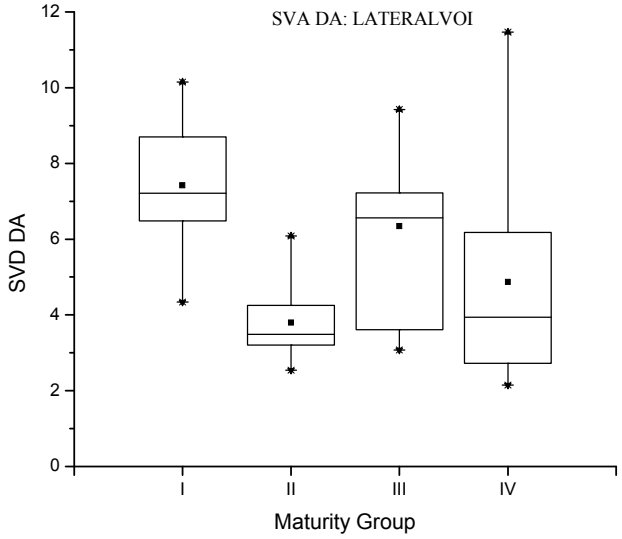

Figure 6.28 SVD DA. Side-by-side box plots by maturity-staged groups. P= 0.070 which is not statistically significant for either the medial and lateral VOI (A,B).

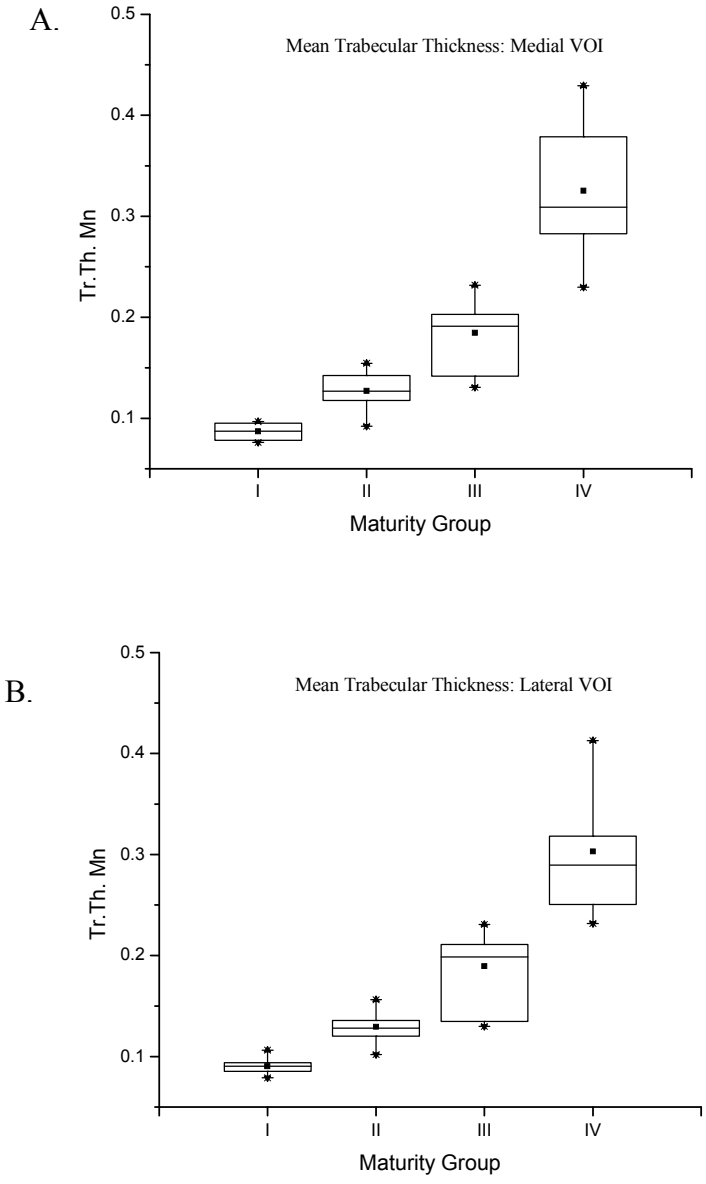

Figure 6.29 Mean trabecular thickness. Side-by-side box plots by maturity-staged groups.

The group-related analysis of trabecular thickness (Figure 6.29 A/B) reiterates the apparent linear age-dependency with progressive increases in median, mean, IQR, and minimum/maximum values. Figure 6.30 (Medial VOI) displays the group-related analysis for trabecular number demonstrating the largest mean, median, IQR, and spread of values in the youngest group I with a decline in each of the remaining groups (II-IV). Lateral VOI (not shown) has an identical pattern.

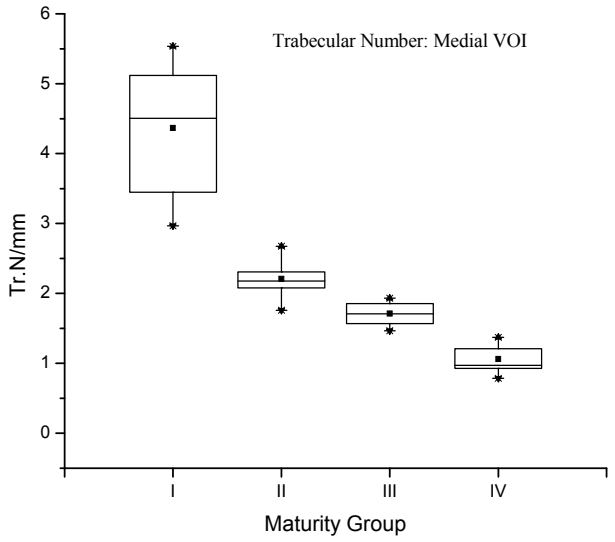

Figure 6.30 Tr.N. Side-by-side box plots by maturity-staged groups.

An interesting aspect of this particular data display (Figure 6.30) is that decreasing trabecular number appears to be an inherent part of the ontogenetic pattern for trabecular bone and not solely an adult age-related phenomenon associated with osteoporosis. The results suggest that the decreasing bone mass

characteristic of osteoporosis may be considered on a continuum of the ontogenetic scheme modified by various internal and external risk factors. This will be discussed further in the following chapter.

This completes the exposition of the ontogenetic pattern of quantitative structural data for human trabecular bone from the SunWatch village juvenile skeletal sample. It is apparent from the results presented that trabecular bone weaves a complex interaction with age and functional locomotor changes. The fundamentals of the construction of trabecular bone rely on the modulation of trabecular volume and geometry in response to some function of the magnitude, direction, and/or frequency of applied loads (Wong and Carter, 1990). One important factor which is not incorporated into the 3D analytical framework of this research is the consideration of changes in bone material properties that occur during ontogeny. Compact and trabecular bone in young children has been demonstrated to be less stiff and strong than that of adults (Currey and Butler, 1975). A relatively early age-related increase in material strength (Mulder et al., 2007) may contribute to the ontogenetic pattern by making the trabecular bone seem apparently less loaded during early childhood (Frost and Jee, 1994; Ruff, 2003b). This may account for some of the early decrease in BV/TV. Relative homeostasis of BV/TV appears around age six, even though material strength continues to increase due to progressive mineralization.

The relationships of additional important components of structural variation in the trabecular ontogenetic pattern including body mass, femoral bicondylar angle

(reflection of attainment of bipedal gait), and within-tibial trabecular heterogeneity (ontogenetic adaptation to bipedalism) are explored in the following section.

COMPONENTS OF VARIATION

Body mass

Previous trabecular bone research (animal models and human investigations) has demonstrated that bone volume fraction and trabecular thickness increase while trabecular number decreases during development (Byers et al., 2000; Mulder et al., 2005; Nafei et al, 2000a, b; Nuzzo et al., 2003; Parfitt et al., 2000; Ryan and Krovitz, 2006; Salle et al., 2002; Tanck et al., 2001; Wolschrijn and Weijs, 2004). Some animal models including immature pig and sheep (Tanck et al., 2001; Nafei et al., 2000a, b) found that the initial adaptive mechanism was additional bone density as a response to an early and rapid increase in body mass. Fabric anisotropy developed later. These particular animal models do not fully conform to the lazy U-shaped pattern of age-related changes revealed for bone volume fraction and anisotropy in human development. Trabecular thickness and number do conform to the animal models. Ryan and Krovitz have commented that the animals used in these trabecular bone ontogenetic studies were "already too old to show the same age-related changes that we found" or that the models did not include analysis of the role of locomotor changes in trabecular development (2005, p.600). Body mass appears to have less of a defining role in human trabecular architectural adaptation in regards to BV/TV,

SVD DA, and Tr.N during the first two years of life than does delayed locomotor maturation. Bone volume fraction and anisotropy first decrease, and then increase with increasing age, body mass, and locomotion. Trabecular number decreases with increasing body mass and age. This pattern of structural change was replicated in Wolschrijn and Weijs's (2004) study of the trabecular architecture of the ulnar coronoid process of dogs ranging in age between 4 and 24 weeks old. These authors note that dogs do not stand until 1.5 weeks and don't walk with a steady gait until 3 weeks. The results to be presented suggest that increased body mass becomes increasingly important to trabecular structure after the early acquisition and maturation of normal human walking.

The method for calculation of body mass in this research has been discussed in Chapter 5. The presence and preservation of the relevant skeletal element (distal femoral metaphysis, femoral head) dictated the number of measurements possible (17/36; 47%). One year (± 0.5) of age is the youngest for which the distal femoral metaphyseal breadth regression formulae published by Ruff (2007) are applicable. It is with initiation of walking that the correlation between body mass and femoral distal metaphyseal breadth become significant. Table 6.7 lists the relevant skeletal data for this research.

Burial No.	Age	Distal Femoral (mm)	Femoral Head (mm)	Body Mass (kg)
10/72	0.1			
14B/72	0.1			
9/72	0.25			
5/71	0.25			
8/72	0.5			
15AB/73	0.5	18		5.68
15A+B/73	0.5			
12/73	0.5			
5/72	0.5	25		7.3
7/73	0.7			
8/73	0.9			
4/72	1.3			
9/73	1.3			
4/73	1.3			
8/76	1.3	35		9.18
7/76	1.3	30		8.24
15/72	1.3	37		9.56
3/72	2.1	40		10.92
6/80	2.1	38		10.38
14/74	2.75	40		11.78
6/71	4.7	48.5		16.2
13/72	6.8			
2/73	6.8			
7/80	9.8	59		29.03
1/81	9.8	48		18.12
SM3	9.8			
15/74	9.8	61		31.01
9/75	14.3			
7/81	14.3			
9/77	14.3			
SM18	16.9		48	66.8
SM16	16.9			
SM9B	16.9		39	51.1
474	19		44	64.5
3A/76	21		41	57.9
9/74	24		42	60.1

Table 6.7 Body mass skeletal data

Figure 6.31 displays the cross-sectional growth "curve" based on the available data for body mass-for-age. A fairly traditional plot is evident described by non-linear logistic curve fitting. Inserting body mass estimates into the CDC standard weight-for-age growth charts (Figure 6.32 and 6.33), the younger SunWatch subadults are plotted along the 5-10th percentiles. The chart for males was chosen arbitrarily. While this is clearly not a population-specific comparison, some insights may be evident. A few adolescents are in the mid-percentile range, suggesting the possibility of some catch-up growth occurring during the adolescent growth spurt. This is speculative given the incomplete and cross-sectional nature of the data.

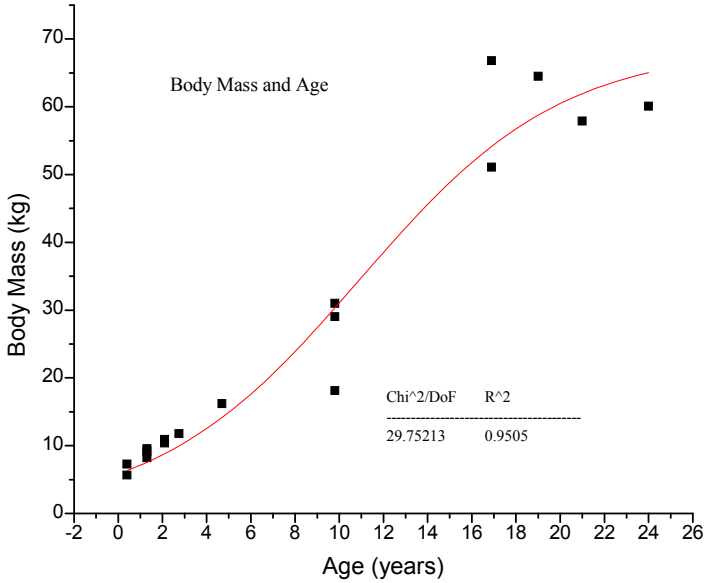

Figure 6.31 Body Mass-For-Age of SunWatch juvenile sample. Black squares represent individual tibiae. Red [black] line represents the nonlinear logistic curve.

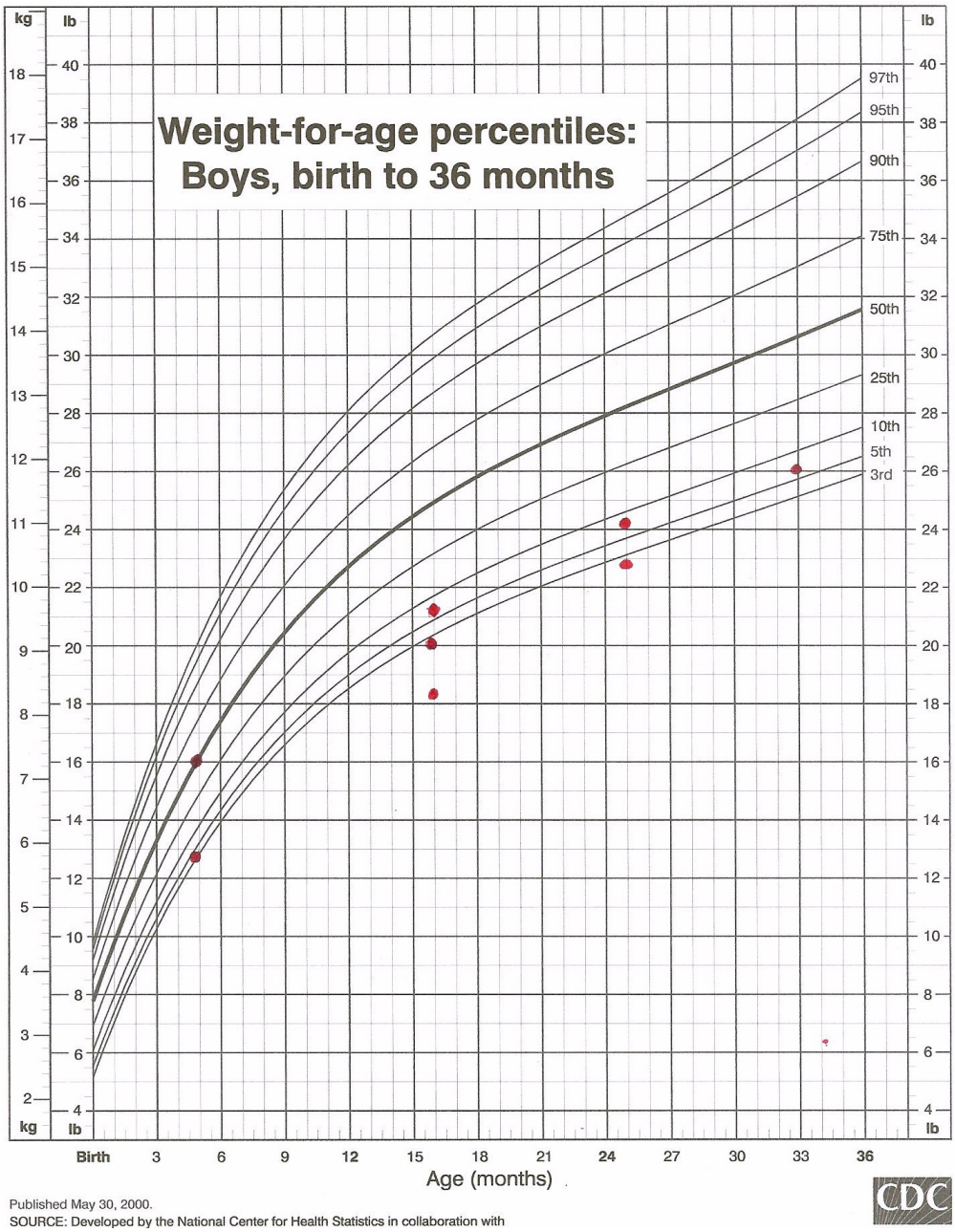

Figure 6.32 CDC weight-for-age chart from birth to 36 months (boys). SunWatch individuals are represented by red [black] circles.

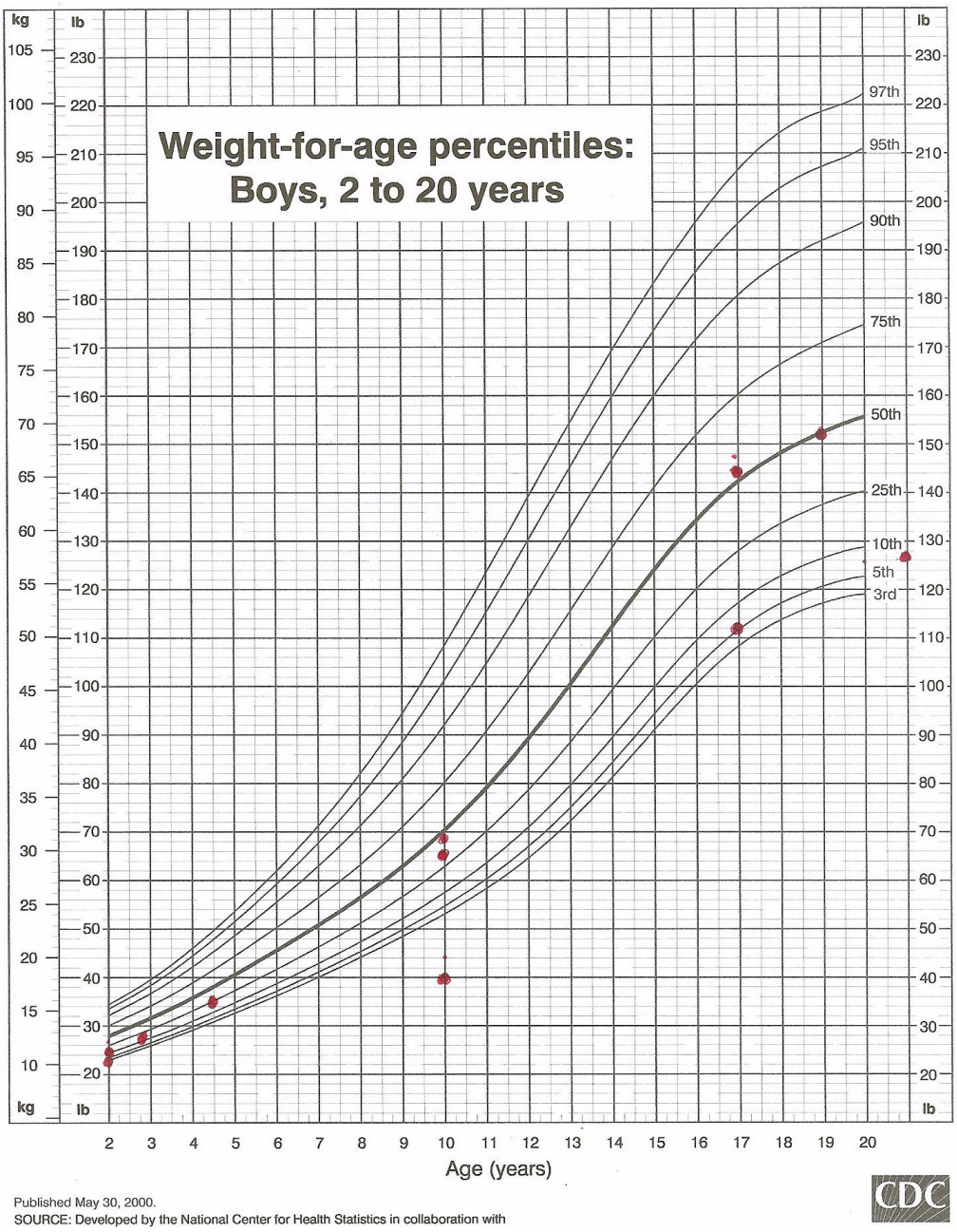

Figure 6.33 CDC weight-for-age chart from 2 to 20 years (boys). SunWatch individuals are represented by red [black] circles.

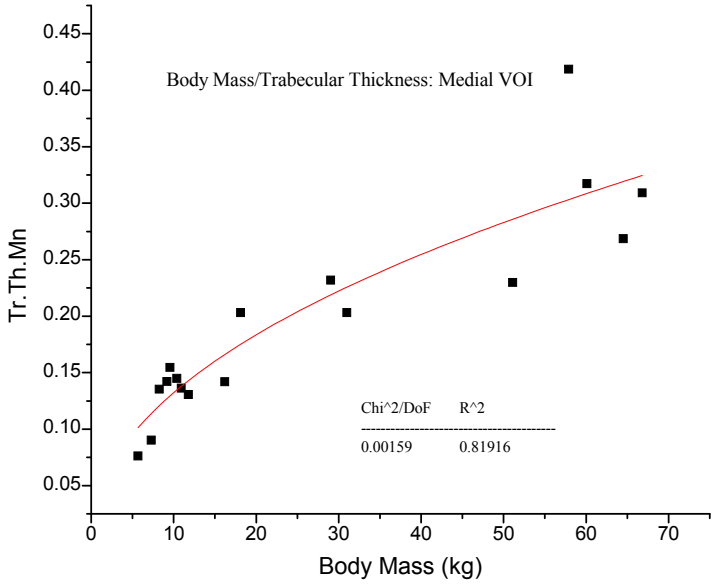

A.

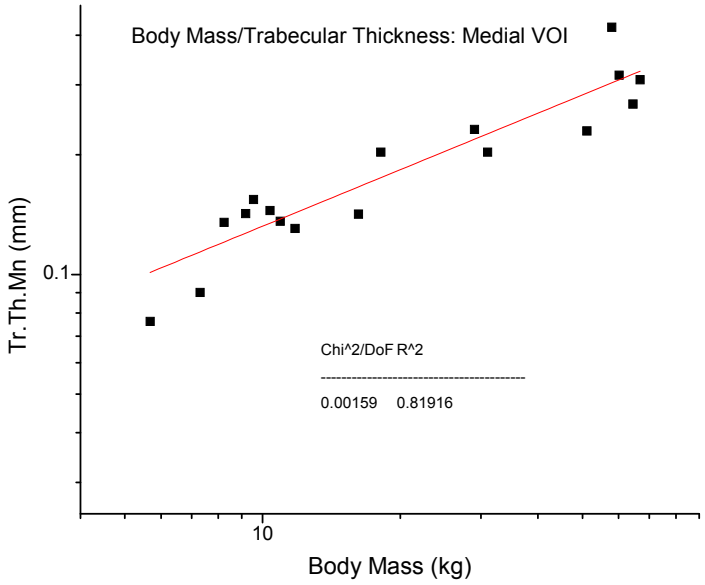

B.

Figure 6.34 A/B Body mass and trabecular thickness from the medial VOI. Black squares represent individual tibiae. Plot A is a raw data, nonlinear allometric curve. Plot B is a log-log plot.

Trabecular thickness is the only structural parameter in this study with a positive correlation to increasing body mass. Figure 6.34 A/B displays this relationship described best by a non-linear allometric curve for the raw data and a linear relationship for the logarithmic-logarithmic plot (isometric/slightly positive allometric). Fajardo et al. (2005) reported on research using 3D microCT methods to study the interspecific relationship in adults between body weight and femoral neck trabecular microarchitecture in six anthropoid species. BV/TV was stated to show an increasing but non-specific trend with body weight. Trabecular number decreased, scaling negatively allometrically. Trabecular thickness increased with body weight in both sexes, exhibiting positive allometric scaling; the trabecular become more plate-like as they thicken. The authors argue that increases in bone volume fraction are produced by increases in trabecular strut thickness rather than increasing the relative number of trabeculae. The only published results comparable to the current study are Ryan and Krovitz's (2006) work on "Trabecular Bone Ontogeny in the Proximal Femur." The age estimates of this study range from 0.0-9.0 years. Although calculations for body mass are not included in the report, one can reasonably infer that body mass did increase over this age interval. Mean trabecular thickness increased from 0.093 mm to 0.186 mm.

The research literature concerned with trabecular thickness scaled to body mass is focused on skeletally mature configurations (Frost, 1999; Maga et al., 2006). Variation in trabecular thickness exists within a nest hierarchy: within a single bony element, between the same element, among different elements, and between/among

individuals, groups, and taxa. The prevailing concept in regards to trabecular thickness and body mass is expressed by Swartz et al. (1998) as the "broadly overlapping range of values for the very smallest and very largest taxa in our sample: there is little difference in absolute trabecular size even when the extremes of the body size range sampled are compared" (1998, p.580). The total volume of trabecular bone in joints has been found to scale in direct proportion to body mass (Rafferty and Ruff, 1994). Trabeculae, however, do not appear to have same relationships as whole bones. Swartz et al. argue that trabeculae may be comparable to other sub-organ-level structures (i.e., red blood cells and cross-sections of skeletal muscle fibers) and thus are largely scale-independent. Theoretical constraints to trabecular size include surface area requirements for calcium homeostasis and the range of influence for osteocytes signaling for modeling/remodeling. This study does not support these arguments as representing major theoretical themes for the human ontogenetic pattern of trabecular thickness relative to body mass. There appears to be some scalar relationship between trabecular thickness and body mass evident primarily after gait is established.

Femoral bicondylar angle

Table 6.8 lists the skeletal data relating to the development of the femoral bicondylar angle from birth to age seven years. This age range was chosen on the basis of clinical and skeletal studies (Salenius and Vankka, 1975; Tardieu and Trinkaus, 1994; Tardieu et al., 2006). The femoral bicondylar angle is stated to be an epigenetic functional feature developing during early childhood growth related to the

acquisition and maturation of normal human bipedal walking (Tardieu, 1999). Reported skeletal samples exhibit a pattern of a femoral bicondylar angle of 0° at birth, followed by a steady increase later in infancy and into juvenile years. Skeletal samples reach low adult values by approximately four years of age (6-8°) (Tardieu and Trinkaus, 1994).

In a seminal clinical study, Salenius and Vankka (1975) measured the tibiofemoral angle clinically and roentgenographically in children between birth and age 13 years. The tibiofemoral angle is the clinical equivalent of the skeletal femoral bicondylar angle, incorporating both articular and metaphyseal regions of the femur and tibia. The tibiofemoral angle in newborn infants to nearly one year old was in pronounced varus alignment of near 15°, straightening to near neutral (0°) by one and one-half years, and changing to valgus alignment during the second and third years (10°). This may be associated with an overshoot; the valgus alignment corrects spontaneously reaching the average adult value by age six to seven years (6°).

The femoral bicondylar angle (FBA) has been studied primarily from a top-down perspective: the femur. Clinical, experimental, and computational data confirm that changes in bone density in the proximal tibia are associated with changes in angulation at the knee joint (Wu et al., 1990). Varus or neutral angulation (FBA = 0°) loads the medial tibial condyle more than the lateral and is associated with a relative increase in bone density in the medial condyle. Valgus angulation (FBA >0°) shifts loading towards the lateral condyle and is associated with a relative increase in bone density in the lateral condyle. This current study offers an opportunity to

examine trabecular bone changes from the bottom-up: the proximal tibia. Questions to be asked are: (1) does the development of the femoral bicondylar angle have a signal in the trabecular bone microarchitecture of the proximal tibia, and (2) do the relative values between the medial and lateral volumes of interest (VOI) change with the development of the femoral bicondylar angle? The femoral bicondylar angle was assessed by direct skeletal measurement in femurs having adequate preservation as described in the Chapter 5. Using an admittedly oversimplified model, the proximal tibial bone volume fraction lateral to medial (PTL/M) ratio was calculated by dividing the BV/TV value of the lateral VOI by the BV/TV value of the medial VOI. A ratio of ≤ 1 is consistent with neutral/varus alignment (FBA = 0°) and a ratio of >1 is consistent with valgus alignment (FBA $\geq 1°$).

Burial No.	Age	FBA (°)	BV/TV M	BV/TV L	PTL/M Ratio
10/72	0.1	0	0.4117	0.3933	0.956
14B/72	0.1		0.4606	0.4452	0.967
9/72	0.25	0	0.4041	0.3893	0.963
5/71	0.25	0	0.4393	0.4871	
8/72	0.4		0.2958	0.2575	0.871
15AB/73	0.4	1	0.4362	0.4333	0.993
15A+B/73	0.4		0.4361	0.4269	0.979
12/73	0.4		0.2975	0.245	0.824
5/72	0.4	0.5	0.2609	0.241	0.924
7/73	0.7		0.2596	0.2299	0.886
8/73	0.9		0.2416		
4/72	1.3		0.2841	0.248	**1**
9/73	1.3	0.5	0.2613	0.2615	**1.001**
4/73	1.3	0.5	0.2359	0.252	**1.068**
8/76	1.3	4	0.334	0.2967	0.888
7/76	1.3	5	0.288	0.2911	**1.011**
15/72	1.3	1	0.3397	0.3221	0.948
3/72	2.1	6	0.2881	0.3081	**1.069**
6/80	2.1	3	0.3759	0.3843	**1.022**
14/74	2.75	5	0.2087	0.2353	**1.127**
6/71	4.7	4	0.2812	0.2328	0.828
13/72	6.8	3	0.3784	0.3779	0.999
2/73	6.8	2	0.3266	0.3004	0.92

Table 6.8 Femoral Bicondylar Angle Skeletal Data

The values for PTL/M equal to or greater than 1 are in bold type in Table 6.8. Examination of the raw data confirms a femoral bicondylar angle of 0° at birth and an increase of the angle from approximately one to four years consistent with previous studies. Figure 6.35 is a bivariate plot of femoral bicondylar angle (metaphyseal) versus age. The data is best described by a non-linear asymptotic curve giving results very similar to the plot with Lowess smoothed lines indicating the general pattern of increase in the femoral bicondylar angle with age (cf. Tardieu and Trinkaus, 1994). It

should be emphasized, however, that the femoral bicondylar angle for this study was evaluated by direct skeletal measurement. Measurement by radiographic methods would likely give more data precision and less "noise." This is planned as a component of follow-up studies to this research.

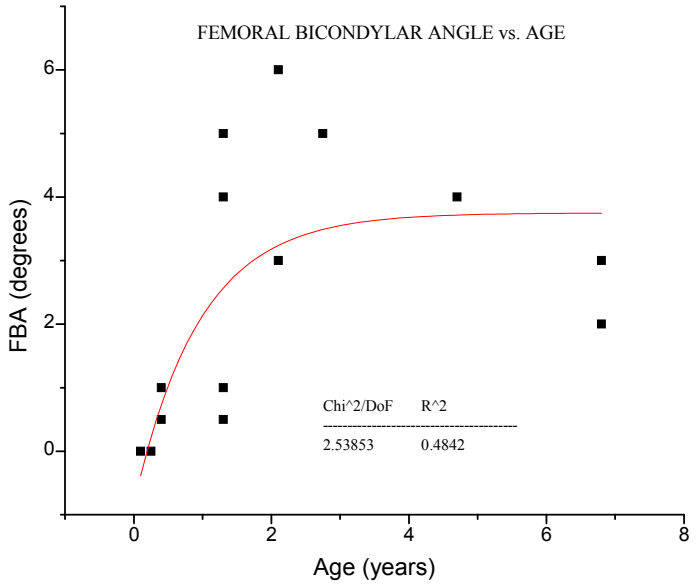

Figure 6.35 FBA and AGE. Black squares represent individual femora. Red [black] line represents the nonlinear asymptotic curve.

Interest in this side-bar to the major focus intensified when initial BV/TV data demonstrated a relatively sudden shift in the relative bone volume fractions between the medial and lateral VOIs during the same chronological period in which the femoral bicondylar angle was developing. The proximal tibia ratio described above (PTL/M) is plotted against the femoral bicondylar angle in Figure 6.36. Although the results are not statistically significant and are apt to be hampered by femoral bicondylar angle skeletal measurement imprecision as well as ratio "noise,"

a biologically significant general pattern may be perceived with low PTL/M ratios associated with low femoral bicondylar angles and vice versa. The data imply a trabecular bone signal in the proximal tibia associated with the femoral bicondylar angle consisting of a change in the relative bone volume fraction between the medial and tibial condyles, occurring between two to three years of age. The development of the femoral bicondylar angle appears to make an important contribution to the pattern of variation in trabecular bone during early growth. The average ratio in older subadults/adults (7-24 years old) is 0.934, suggesting some adjustment of alignment over time.

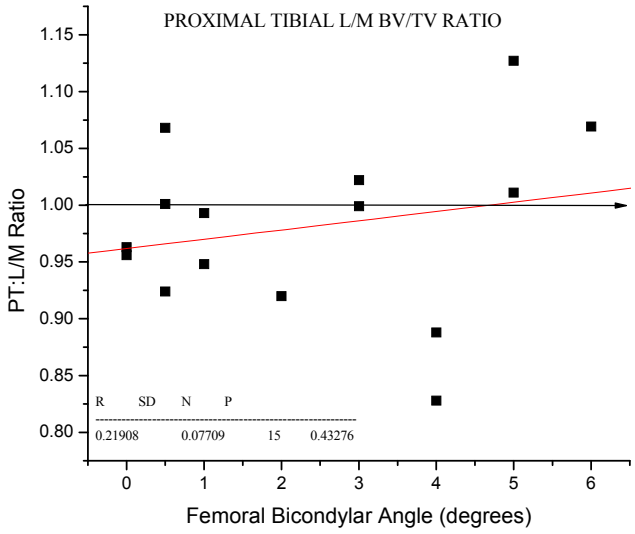

Figure 6.36 Femoral Bicondylar Angle. Black squares represent individual femora.

Intra-tibial heterogeneity

The development of within-tibial trabecular heterogeneity is a reflection, in part, of the continuous ontogenetic adaptation of trabecular bone to bipedalism. Ryan and Krovitz (2006) studied localized variation within the trabecular structure of the proximal femur using multiple VOIs located throughout the metaphysis. They suggested that age-related differential heterogeneity was a way to describe developmental changes. Their results demonstrated increasing heterogeneity for the structural parameters of BV/TV, SVD DA, and Tb.N. Tr.Th, on the other hand, did not exhibit any defined pattern. The comprehensive examination of intra-tibial heterogeneity is a large scale project outside the scope of this dissertation research: requiring a dataset on the order of 4-8 times larger than that of the current investigation.

The intention of this portion of the current research project is to *highlight* selected areas of ontogenetic change evident on examination of transverse slice images. Figure 6.37A displays a scan image from a neonatal individual demonstrating a relatively homogeneous trabecular structure. Figure 6.37B displays a scan image from a young adult (21years) demonstrating trabecular variation. Regions of selected interest are the posterior aspects of the condyles relative to the anterior aspects and the central intercondylar region. Variation in proximal tibial trabecular structure was studied in this project using four secondary VOIs located adjacent to the growth plate or subchondral plate as described in Chapter 5. They are positioned in the center of the anterior and posterior quadrants of the medial and lateral tibial condyles and are

smaller than the primary medial and lateral VOIs. These are positioned to examine the differential effects of bipedal gait-related loading. Analyses compare age-related changes in posterior structural properties to those of the anterior structural properties. A fifth secondary VOI is positioned in the center of the tibial plateau. It is the same size as the primary VOIs and is meant to examine an area of the tibia which experiences minimal direct weight-bearing loading. The structural pattern of this VOI is compared to that of primary VOIs. The structural parameters studied are BV/TV and SVD DA. A subset of the skeletal sample consisting of eight individuals was used in this analysis. Two individuals from each of the four maturity stage-related group were chosen based on preservation and spacing seriation as broadly as possible. VOIs of the two oldest individuals are in the subchondral position.

Results suggest that tibial trabecular bone develops non-random regional variation chronologically associated with the maturation of gait kinematics. The regional tibial trabecular microarchitecture adapts to the changing mechanical loads (or lack thereof). The development of mature gait kinematics as an interpretive framework will be discussed in detail in the chapter to follow. Tibial structure records this continuum: changing from a relatively homogeneous trabecular pattern to one with segments of increased bone volume (i.e. posteriorly) combined with regions of decreased bone volume (i.e. central). Table 6.9 lists the entire sample with the selected individuals in **bold** in order for the reader to place the subsample into the larger context. Tables 6.10, 6.11, and 6.12 list the structural data for medial (anterior/posterior), lateral (anterior/posterior), and central VOIs respectively.

medial

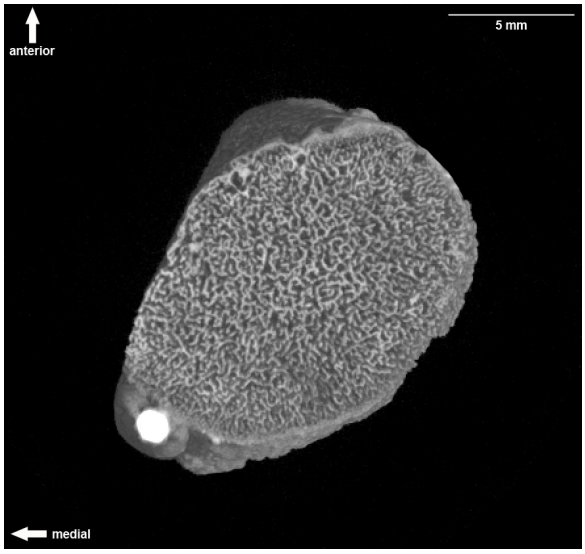

A.

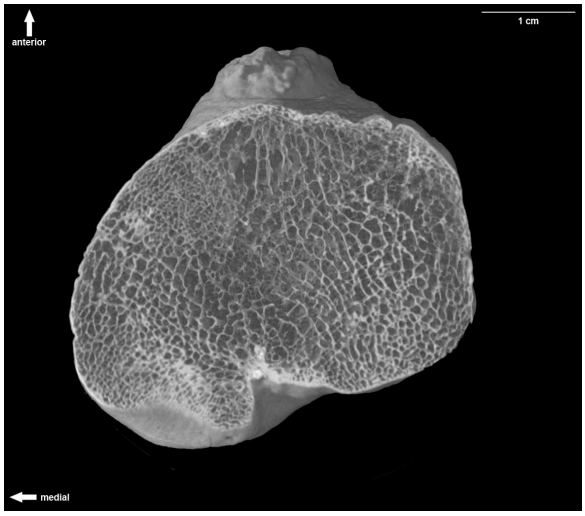

B.

posterior

Figure 6.37 Transverse CT slices: (A) neonatal individual with homogeneous trabecular structure, (B) 21 year old individual with region trabecular variation.

Burial No.	Age	Group
10/72	**0.1**	**I**
14B/72	0.1	1
9/72	0.25	1
5/71	0.25	1
8/72	0.4	1
15AB/73	0.4	1
15A+B/73	**0.4**	**1**
12/73	0.4	1
5/72	0.4	1
7/73	0.7	II
8/73	0.9	II
4/72	**1.3**	**II**
9/73	1.3	II
4/73	1.3	II
8/76	1.3	II
7/76	1.3	II
15/72	1.3	II
3/72	2.1	II
6/80	**2.1**	**II**
14/74	2.75	III
6/71	4.7	III
13/72	6.8	III
2/73	**6.8**	**III**
7/80	9.8	III
1/81	9.8	III
SM3	9.8	III
15/74	**9.8**	**III**
9/75	14.3	IV
7/81	14.3	IV
9/77	14.3	IV
SM18	16.9	IV
SM16	**16.9**	**IV**
SM9B	16.9	IV
474	19	IV
3A/76	**21**	**IV**
9/74	24	IV

Table 6.9 Tibial Heterogeneity Subsample

Burial No.	BV MA	SVD MA	BV MP	SVD MP	MBVP/A
10/72	0.4075	6.4151	0.3876	5.8703	0.951
15A+B/73	0.4399	6.6715	0.4364	7.3691	0.992
4/72	0.3221	9.0989	0.2638	2.996	0.819
6/80	0.366	3.8585	0.4191	5.0331	1.145
2/73	0.3033	3.7891	0.3639	3.4527	1.2
15/74	0.3476	5.5977	0.4108	9.0715	1.182
SM16	0.3981	5.6348	0.4018	3.2373	1.01
3A/76	0.3785	5.1904	0.4191	1.3312	1.107

Table 6.10 Skeletal Data: Medial (Anterior/Posterior) VOIs. MA is medioanterior, MP is medioposterior, and MBVPA is medial bone volume ratio.

Burial No.	BV LA	SVD LA	BV LP	SVD LP	LBVP/A
10/72	0.4137	6.1307	0.3893	4.2676	0.941
15A+B/73	0.441	7.6255	0.4355	8.0902	0.988
4/72	0.2566	3.6638	0.2683	5.3686	1.046
6/80	0.3973	2.261	0.4254	3.7821	1.07
2/73	0.2987	6.4662	0.3752	6.0901	1.256
15/74	0.3661	8.2907	0.4158	4.2187	1.136
SM16	0.2875	2.3316	0.4157	1.399	1.446
3A/76	0.3183	5.4262	0.4176	1.3346	1.312

Table 6.11 Skeletal Data: Lateral (Anterior/Posterior) VOIs. LA is lateroanterior, LP is lateroposterior, and LBVP/A is lateral bone volume ratio.

Burial No.	BV/TV C	SVD C
10/72	0.3869	8.8688
15A+B/73	0.4113	10.3973
4/72	0.2372	4.9916
6/80	0.3691	2.752
2/73	0.2418	2.7847
15/74	0.3068	4.2082
SM16	0.1905	2.416
3A/76	0.242	2.5775

Table 6.12 Skeletal Data: Central VOI

Anterior/posterior differentiation

The posterior regions of both tibial condyles (more notable in the lateral condyle than the medial) are the sites of developmental changes patterned by increasing bone volume fraction followed by decreasing anisotropy. The chronology of these particular changes parallels that of the maturation of bipedal gait and suggests local trabecular bone functional adaptation under varying ontogenetic-related mechanical loading conditions. This differential in tibial microarchitecture is quantified by the usual structural parameters as well as the bone volume fraction posterior/anterior ratio (BVP/A). The ratio is calculated by dividing the posterior VOI BV/TV by the anterior VOI BV/TV. A ratio >1 indicates that the bone volume fraction of the posterior VOI is greater than that of the anterior VOI. Ratio plots were generated using raw data and log transformed data, with identical results. Raw data scatterplots are demonstrated. Graphic representations of the results of scatterplots from this limited subset are clarified by a variable point adjacent average data smoothing procedure from the OriginLab Graphics program. No other statistical procedures were thought to be appropriate because of small and selected sample size. This approach is validated by the concordance of the general ontogenetic pattern of these plots with those of the complete sample discussed earlier in this chapter. The variances that are present offer a fascinating insight into trabecular bone ontogeny and functional adaptation.

Figures 6.38 A/B and 6.39 A/B display scatter plots for the BV/TV and SVD DA of the anteromedial and posteromedial VOIs, respectively. Both the medial and

lateral condyle secondary VOIs have the same pattern; results from the secondary medial VOIs are plotted below. Bone volume fraction in the anterior aspect of the medial tibial condyle exhibits the now familiar pattern of the primary VOIs with an early and rapid decrease followed by a more gradual increase. The BV/TV of the posterior aspect of the condyle does demonstrate an early decline in value followed by a relatively rapid increase to near maximum values which then remain stable. Anisotropy patterns similarly: the anterior VOI following the pattern of the primary VOIs. The SVD DA of the posterior VOIs becomes relatively more isotropic with age. The combination of these patterns suggests an age-related differentiation of microarchitecture within the proximal tibia.

Figure 6.40 AB are plots of the bone volume fraction posterior/anterior ratio from the medial and lateral condyle indicating a shift to the relative predominance of posterior BV/TV compared to the anterior BV/TV in early childhood. This descriptive presentation will be discussed further in the following chapter.

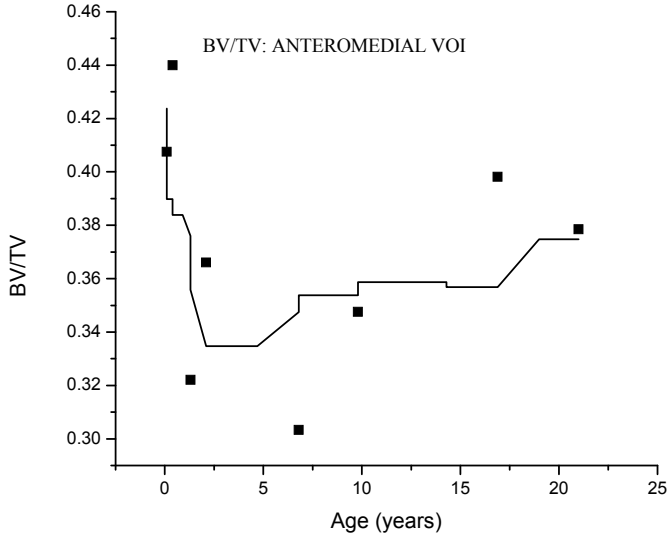

A.

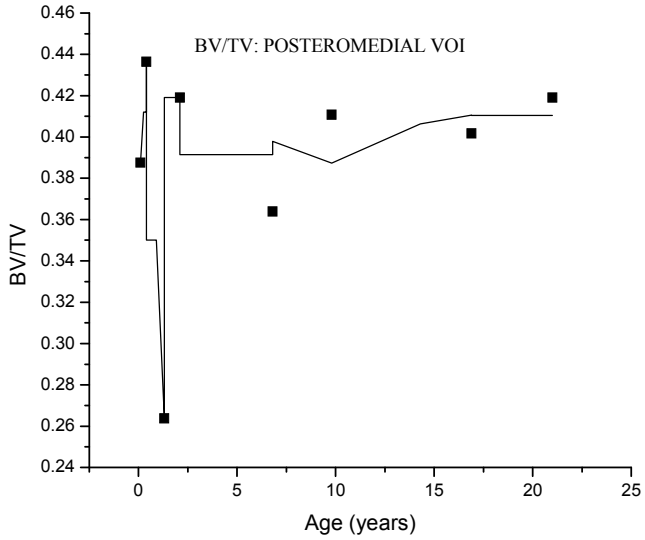

B.

Figure 6.38 BV/TV: (A) anteromedial VOI and (B) posteromedial VOI. Black squares represent individual tibiae and black line is smoothed data.

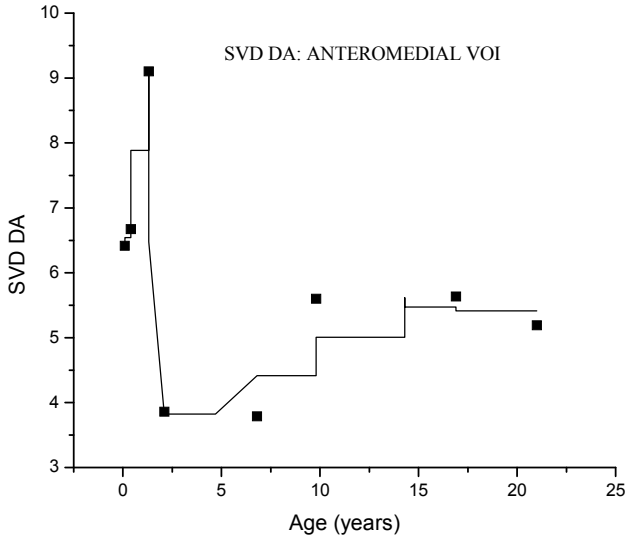

A.

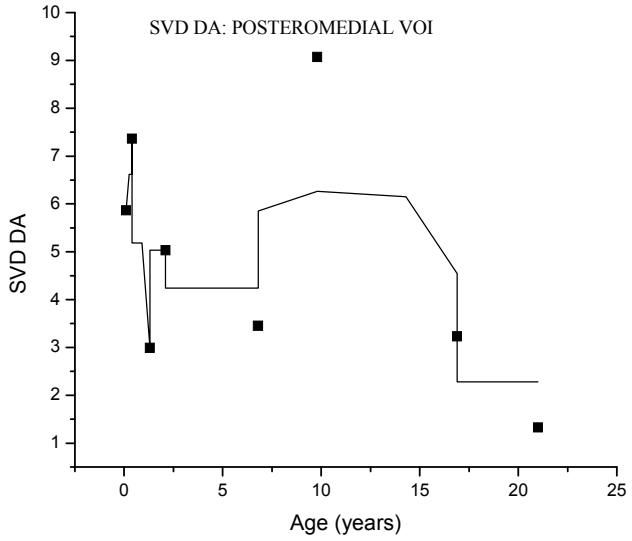

B.

Figure 6.39 SVD DA (A) anteromedial VOI and (B) posteromedial VOI. Black squares represent individual tibiae and black line is smoothed data.

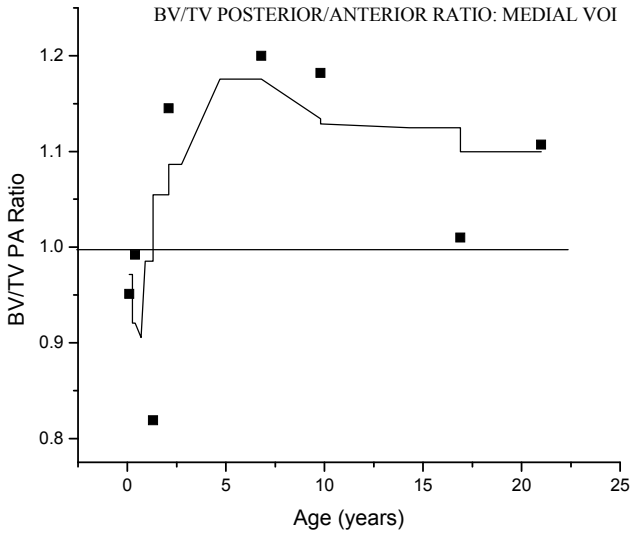

A.

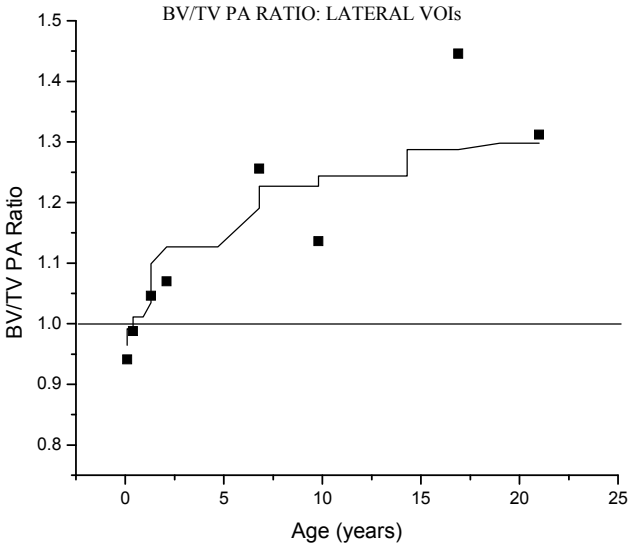

B.

Figure 6.40 BV/TV POSTERIOR/ANTERIOR RATIO. (A) medial ratio and (B) lateral ratio. Black squares represent individual tibiae and black line is smoothed data.

Central (intercondylar) VOI

An interesting question asked of this sample and data subset is: what is the ontogenetic pattern of trabecular bone in a region of the proximal tibia subjected to relatively low weight-bearing mechanical forces? This can be thought of as an internally-controlled natural experiment within the tibia, comparing the influence of weight-bearing forces (primary medial and lateral VOIs) on trabecular architecture to the influence of the relative lack thereof (central VOI). Direct examination of scan slices and reconstructions indicate an apparent decrease of bone volume in the central intercondylar region of the tibia of young adults compared to infants.

Figures 6.41 A/B and 6.42 A/B visually display the ontogenetic pattern of structural parameters BV/TV and SVD DA of the central VOI compared to that of the primary medial VOI. The Figure 6.41 A/B plots indicate that the bone volume fraction of the intercondylar region continues a decreasing trajectory from infancy to young adulthood. Components of this decline appear to be the age-related development, in general, of less thick and fewer trabeculae: the result of an "underloaded" (re)modeling process (Frost and Jee, 1994). Both sets of plots are best described by a non-linear exponential-decay curve. The small size of this sample and dataset precludes additional meaningful statistical analysis.

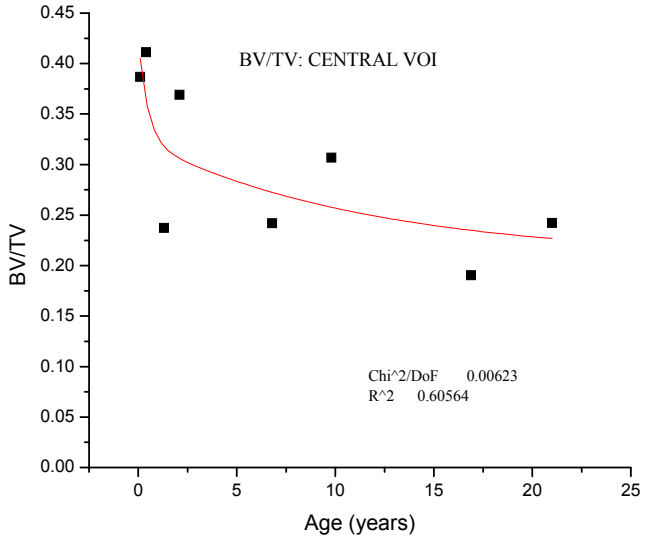

A.

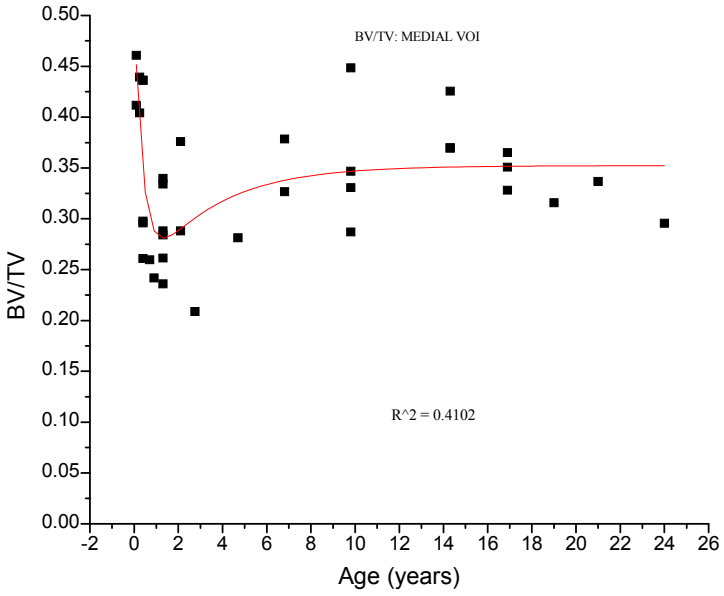

B.

Figure 6.41 BV/TV: (A) Central and (B) Primary Medial VOI. Black squares represent individual tibiae. Red [black] line represents the exponential-decay curve.

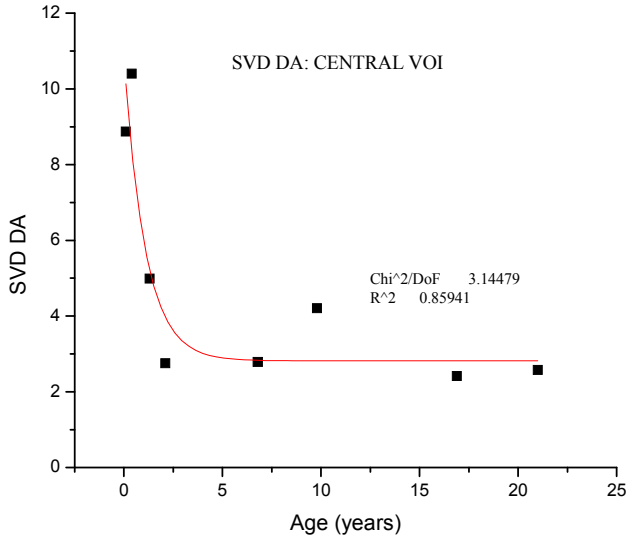

A.

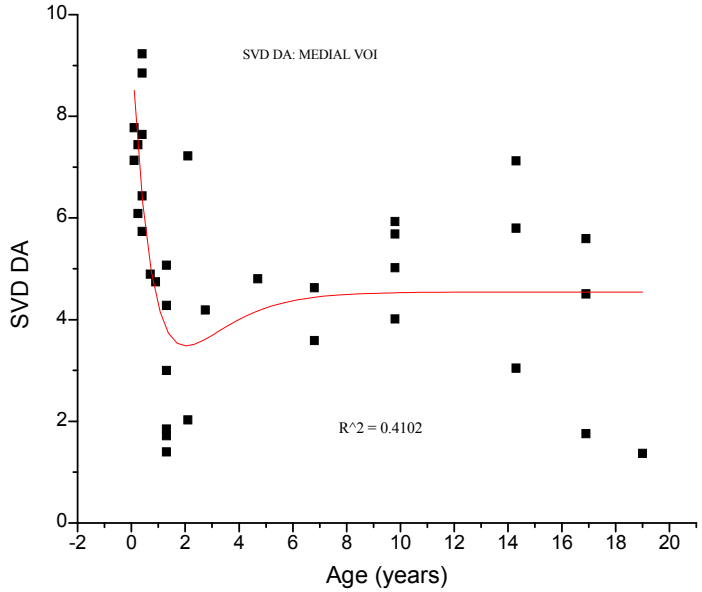

B.

Figure 6.42 SVD DA: (A) Central VOI and (B) Primary Medial VOI. Black squares represent individual tibiae. Red [black] line represents the exponential-decay curve

The Figure 6.42 A/B plots of SVD DA demonstrate that the trabecular microarchitecture of the unloaded central VOI decreases rapidly during the first year of life, then remains relatively isotropic from late infancy. The absence of distinct orthogonal weight-bearing loads and/or the combination of multidirectional forces in the intercondylar region of the proximal tibia is clearly reflected by the lack of directionality in the trabecular structure.

The exposition of the ontogenetic pattern and quantification of the differential functional adaptation of trabecular bone of the proximal tibia has been highlighted by this heterogeneity analysis. MicroCT-derived microarchitectural and 3D structural analyses are exciting new techniques for skeletal biology and bioarchaeology as revealed by the results of this research. It is important, however, to the application of these procedures to make explicit any potential data-altering limitations of the microCT methodology.

SOURCES OF ERROR

Resolution dependency of microstructural properties

This reported research suggests that for the range of in-line resolution used in this project (22-80 μm) the influence of that resolution, although presently unknown, is likely to be minimal. The dataset of the current research was challenged for indications [or lack thereof] of resolution dependency by several procedures: (1)

examining the transition zones of one field of reconstruction (FOR) to another looking for parameter values consistently larger or smaller than expected (Appendix A), (2) examining the sequential parameter values in groups containing more than one FOR (groups II and III), (3) examining the dataset for sequential maturity-related changes in parameter values within a single FOR, and (4) discussions with Richard Ketcham, principle research scientist and director of the UTCT scanning facility. This assessment suggests that mean trabecular thickness is the structural parameter most likely to have some resolution dependency in the transition range of maximum change in resolution (x2): 22- 40 μm. Figure 6.43 displays the relevant plot with the FORs indicated. The region of likely resolution dependency is marked by a black line in the lower left between resolutions of 22 and 40 μm. This researcher argues that the influence does not appear to change the overall ontogenetic patterns demonstrated by the results of this research. This topic is an area for future research in order to account for the CT blurring-effect both within and between slices and the resulting effect on the structural parameters of trabecular bone.

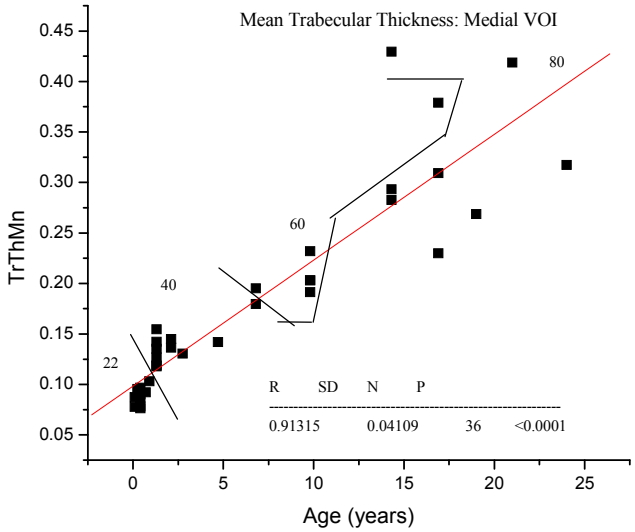

Figure 6.43 Tr.Th. Mn: Medial VOI. Black squares represent individual tibiae. Red [black] line represents the linear regression line. Small black lines separate the FORs, which are indicated as 22, 40, 60, and 80.

VOI Positioning

The non-homologous positioning of the VOIs in older individuals just distal to the articular subchondral plate, as opposed to beneath the growth plate, had a clear effect on the anisotropy parameters in these older individuals. The horizontal components of the growth plate are well-demonstrated by the rose diagrams and corresponding degree of anisotropy. The overall pattern, however, appears to be minimally affected. The VOI-positioning influence on bone volume fraction, trabecular thickness, and trabecular number, although not precisely known, also did

not appear to change the overall trends of this research. The patterns of change are the message.

SUMMARY

This research has generated a new body of quantitative morphologic data describing the changes in trabecular bone microarchitecture and structural parameters during the time span of human growth and development. MicroCT-derived morphometrics include bone volume fraction, star volume distribution degree of anisotropy, trabecular thickness, and trabecular number. The image-related and quantitative data demonstrate the reorganization and differentiation of trabecular structure beginning at about one year of age, stimulated by ongoing development, the acquisition and maturation of normal walking, and later in childhood associated with increasing body mass. The key results are as follows:

- Bone Volume Fraction is highest at birth, lowest at one year, and then increases to reach the range of average adult values by approximately age eight.
- Star Volume Distribution Degree of Anisotropy parallels the pattern of bone volume fraction.
- Trabecular Thickness is least at birth and continues to increase throughout skeletal ontogeny.
- Trabecular Number is highest at birth, rapidly decreases during the first year of life, and then progressively decreases throughout ontogeny.

- Intra-tibial trabecular variation is associated with the onset and maturation of normal human walking and the development of the femoral bicondylar angle.
- Increasing body mass is associated with increasing trabecular thickness after early childhood and after the bipedal gait has been established.

The advanced technologies used in this research have robust capabilities for uncovering the response of trabecular bone to changing circumstances, such as the microarchitectural reply to the development of the femoral bicondylar angle or the maturation of gait kinematics. The results of this study document the pattern of ontogenetic trabecular bone morphogenesis and adaptation at the microstructural level. Some of the implications of these results for anthropologically-directed research in human ontogeny and bioarchaeology are considered in the next chapter.

CHAPTER 7

DISCUSSION

The recent availability of high-resolution computed tomography and three-dimensional structural analyses have turned research interest towards exploring human quantitative data on the growth and development of trabecular bone with particular attention to the ontogenetic effects of body size and locomotor behavior on trabecular architecture (Ryan and Krovitz, 2006). The ontogenetic trabecular research presented in this dissertation complements those studying ontogenetic effects in the metaphyseal region of the distal femur forming the bicondylar angle (Tardieu, 1999), the development of epiphyseal morphology (Carter et al., 1996), and age changes in long bone strength and length proportions as related to bipedalism (Ruff, 2003a,b).

The results of this study document a pattern of ontogenetic reorganization of trabecular bone in the proximal tibia in which the initial primary relatively-dense spongy bone is diminished and then structurally differentiated into [re]modeled bone with few, thicker components within a more complex fabric anisotropy. It should be emphasized that the *primary eigenvector* of the trabecular architecture of the proximal tibia, as demonstrated by the 3D rose diagrams, *remains consistently*

aligned and relatively parallel to the longitudinal axis of the tibia throughout ontogeny, with a superior/inferior orientation. The slight anteroposterior and/or mediolateral components to the primary eigenvectors appear to be positional and related to the corresponding shape of the tibia. For example, the primary eigenvector of the center of the medial plateau has a small mediolateral/superoinferior component; the primary eigenvector of the center of the lateral plateau has a small lateromedial/superoinferior component. The changes in degree of anisotropy (SVD DA) values reflect the increasing or decreasing contributions of the primary and tertiary eigenvectors, describing more lattice-like or plate-like trabecular structures.

Instrumental developmental forces include, but are not limited to, the combination of genetic patterning modified by epigenetic processes; both intrinsic (hormonal, gene regulatory control) and extrinsic (body mass, locomotor behavior). This research is concerned with the latter influences on trabecular architecture. This chapter places the data derived from this research into several interpretive frameworks in order to explore essential questions: What does this all mean in regard to this setting? What are the implications for anthropology in general? The results are reviewed *vis a vis* the initial hypotheses for this study, exemplifying the research journey with a focus on the importance of the endochondral ossification process. The ontogenetic pattern for trabecular bone is discussed in terms of a broader development context, including how trabecular patterns are related to brain development. A detailed view into the current understanding of the maturation and kinematics of human walking and their association with trabecular patterning is

undertaken. Finally, a consideration of the anthropological implications of a trabecular bone research agenda, along with suggestions for future research is presented.

HYPOTHESES

This study aims to develop quantifiable, repeatable, predictable morphological and scan image data on ontogenetic microarchitectural changes to relative bone volume and anisotropy in human trabecular bone structure from a Late Prehistoric Ohio Valley archaeological subadult skeletal sample. This will highlight the dynamic relationships and sequences between growth/development, general functional activities, and trabecular distribution/architecture. Hypotheses, linked to previous study results demonstrating that bone mass increases early and that trabecular directionality increases later, are tested in this project to characterize the temporal sequence of cancellous bone parameter change (BV/TV and DA) during human growth and development (see Huiskes et al., 2000 and Tanck et al., 2001):

1. *Infancy (0-1 year: pre-walking) is characterized by homogeneous, thin, relatively low density (low BV/TV) primary trabeculae with random orientation (low DA).*
2. *Early childhood (1-5 years): increased body mass, beginning and independent walking is characterized by increasingly dense (higher BV/TV) secondary remodeled trabeculae with multiaxial anisotropic orientation (low DA).*

3. Middle childhood (6-10 years): increased body mass, adult gait pattern, independent activities) is characterized by statistically significant increased bone volume (higher BV/TV) and an increase in anisotropy (higher DA).

4. Late puberty/early adult (15-20 years): increased body mass related to pubertal growth spurt, fully active adult lifestyle is characterized by statistically significant increased bone volume (higher BV/TV) and statistically significant increase in anisotropy (higher DA).

It should be noted that these hypotheses were generated based upon the data foundations of computer stimulation studies (Huiskes et al., 2000) and juvenile animal models (Tanck et al., 2001). These studies did *not* account for the now evident importance of delayed locomotor maturation to the ontogenetic pattern of human trabecular bone. This was first explicitly discussed by Ryan and Krovitz (2006) confirming earlier work which had studied the trabecular architecture of the ulnar coronoid process from dogs ranging in age between 4 and 24 weeks old (Wolschrijn and Weijs, 2004). The results of the current study corroborate the importance of initial unloading (no walking) and delayed loading (beginning bipedal walking) sequence as an important force in adaptation of the trabecular bone structure. Each initial hypothesis is compared to the final dataset, the *actual age ranges*, and subsequent analyses.

Infancy (0-1 year: pre-walking) is characterized by homogeneous, thin, relatively low density (low BV/TV) primary trabeculae with random orientation (low DA).

The age-related group for this hypothesis became restricted to 0.0-0.5 years as the design of this study became more consistent and reasoned and the actual age range for the dataset became evident. This resulted in overall more biologically meaningful maturity-staged groups. The hypothesis as it stands is nearly 50% predictive. Trabecular bone at infancy *is* homogeneous and thin; it does *not*, however, have an initially low bone volume fraction or isotropic fabric orientation. The microstructural data of this research consistently demonstrate a high bone density (BV/TV) at birth, continuing into early infancy. There is a striking anisotropic character to the primary trabeculae reflecting the parallel columnar organization of the endochondral ossification process and microstructure as well as the underlying shape-patterning of the proximal tibia. This is thought to be result of modeling/remodeling mechanisms based on differential strain experienced by bone trabeculae during a period of life characterized by dependency, changes in the material properties of bone, and the relative lack of weight-bearing activity on the lower limbs (Frost and Jee, 1994a, 1994b; Miller et al., 2007; Mulder et al., 2007). It is upon this substrate that further ontogenetic-related trabecular structural changes occur.

Early childhood (1-5 years): increased body mass, beginning and independent walking is characterized by increasingly dense (higher BV/TV) secondary remodeled trabeculae with multiaxial anisotropic orientation (low DA).

Similar to the first hypothesis, this age-related group became defined as 0.8-2.1 years coincident with the developmental events leading up to the initiation and

early acquisition of bipedalism. This chronological period, the secotrant (first two years of life), is characterized by complex transitions and reversals of the bone volume fraction (BV/TV) and the degree of anisotropy (SVD DA). This hypothesis for early childhood is *not* supported by the data pattern and tends to oversimplify trabecular reorganization. The initial portion of late infancy/early childhood is the stage in which BV/TV and SVD DA are both near their lowest values. Beginning at around 1- 1 ½ years, these structural parameters begin to increase as a response to the mechanical forces introduced by bipedal walking. These parameters are quite variable during this phase and have no clear pattern discernable in relationship to body mass, reflecting the importance of changes in mechanical loading relative to those of body size in this age group. This general pattern of initial decline, rapid increase followed by a more gradual increase has also been demonstrated as an ontogenetic pattern of change in femoral/humeral cortical strength studies using different techniques and study samples (Ruff, 2003a, b; Sumner and Andriacchi, 1996). The chronologies follow those of the adoption of bipedal gait. These studies in the aggregate suggest the importance of mechanical loading in both the patterning of trabecular microarchitecture as well as cortical strength. The consistencies of the results of this investigation with those in the literature involving research of different bone envelopes enhance the credibility of the results of this dissertation research.

Additional attention needs to be directed towards understanding the BV/TV patterning in this age group. Although this study is focused on trabecular bone geometry and 3D microarchitecture, changes in bone material properties are

occurring rapidly and simultaneously. The degree of decrease in BV/TV in mid-late infancy prior to walking may be modulated by the age-related increase in bone material properties (Currey and Butler, 1975; Ruff, 2003b), making tibial trabeculae relatively stiffer and stronger (Ding et al., 1997). This "underloaded" state, according to current models of bone (re)modeling, may then result in resorption of now redundant smaller trabeculae. This status is reversed with the onset of walking, increasing BV/TV in order to stabilize bone strain.

Middle childhood (5-10 years): increased body mass, adult gait pattern, independent activities) is characterized by statistically significant increased bone volume (higher BV/TV) and an increase in anisotropy (higher DA).

The age range for this hypothesis was modified slightly: 2.75-9.8 years. BV/TV and SVD DA both increased from the low values of the early/middle secotrant to be within the range of normal young adults. Important operative factors may be maturation of walking capabilities, increasing body and muscle mass, and the onset of more structured physical activities: essential bone functional adaptation. This hypothesis is supported by the data. Tests for statistical significance between age-related groups show significance between Groups I and II and Groups I and III. On reflection of the dataset, it is evident that testing for statistical significance should be viewed critically. It is not necessarily a meaningful analysis. Each group, as defined, is bounded by specific and often differing hormonal systems, bone shape, nutritional factors, [in] dependency, and levels of functional behavioral activity. In the opinion of this researcher, this has some of the attributes of an "apples-to-

oranges" comparison. I argue, however, that the ontogenetic patterns have biological significance, in the absence of statistical significance.

Late puberty/early adult (15-20 years): increased body mass related to pubertal growth spurt, fully active adult lifestyle is characterized by statistically significant increased bone volume (higher BV/TV) and statistically significant increase in anisotropy (higher DA).

The age range for this hypothesis is changed only by the addition of three young adults (ages 19-24 years) into the sample functioning as a sort of "target" towards which trabecular reorganization is heading [has headed]. The fact that all three young adults are female introduces a level of bias (currently unknown) in the structural parameters which are otherwise from a pooled-sex sample. They are best used as a general indicator of a portion of the adult range of values as opposed to a "bull's-eye." This hypothesis is not supported by the data, although the data in this group may be skewed by non-homologous VOI sampling. BV/TV and SVD DA reach the range of adult values by approximately age eight with no consistent pattern of change in late adolescence/ maturity age ranges. Although changes in trabecular number and trabecular thickness were not part of the initial hypotheses, it should be noted that these structural parameters decrease or increase, respectively, throughout the entire age range studied. The interrelated quantitative patterns thus described display a complex developmental weave in regards to age, body mass, and functional behavioral skills which have been imposed upon the essential underlying process of endochondral ossification. The results are discussed within the framework of recently published research on growth plate structure and function.

Endochondral ossification redux

"Formation of cancellous bone at the growth plate is the defining event of its morphogenesis" (Schaffler et al., 1993, p. 150). The highly regulated multistep process of endochondral ossification sets the basic trabecular bone scaffold upon which all subsequent biologically and mechanically driven modeling/remodeling occurs. The journey of trabecular bone morphogenesis from growth plate cartilage to the secondary spongiosa is thought to be highly conserved, quantitatively predictable, and very similar among mammalian species (Byers et al., 2000; Salle et al., 2002; Schaffler et al., 1993). The age-related sizes and shapes of long bones are controlled by local paracrine regulators, system hormones, and mechanical forces. An overview of endochondral ossification was presented in Chapter 2.

Descriptive qualitative histomorphometric data on the growth plate and associated metaphyseal region during human growth and development are well established in the scientific literature (Atkinson, 1967; Felts, 1954; Hall, 2005; Kneissel et al., 1977; Sontag, 1994). Quantitative age-related histomorphometric data, in contrast, are relatively limited with an initial focus on the structural aspects of trabecular bone at the costochondral junction and iliac crest in infants and children (Byers et al, 2000; Fazzalari et al., 1997; Glorieux et al., 2000; Gruber and Rimoin, 1989; Kember and Sissons, 1976; Parfitt et al., 2000). It should be noted that metaphyseal bone at these locations differs from that in long bone metaphyses in the absence of a diaphysis and associated trabecular resorption (Salle, 2002). Noting this exception, these studies found that trabecular bone mass (BV/TV) increases with age

via an increase in trabecular thickness until skeletal maturity (Glorieux et al. 2000; Kneissel et al., 1977; Sontag, 1994).

Byers et al. (2000) use quantitative histomorphometric analysis to describe the age-related integrated cartilage-to-bone transformation process from birth to adolescence using costochondral junctions from 46 children from age 11 days to 13.5 years. Their results suggests that proliferative, hypertrophic, and primary spongiosa regions of the growth plate/metaphysis are the "active growth unit," in which changes are primarily achieved by an increase in cartilage septa and trabecular thickness producing an increase in volume fraction. The bone volume fraction and trabecular thickness were found to increase with age. Trabecular number decreased with age. The secondary spongiosa was characterized by a more stable consolidation of trabecular structure. These findings validate the positioning of the primary VOIs of this research in a position as close to the growth plate as possible and support the general ontogenetic pattern demonstrated. Byers et al. (2000) noted that trabecular bone structural parameters changed most rapidly during the first year of life: a prominent feature of this dissertation research project as well. It is during this period that rapid growth velocity and a marked change in biomechanical influences on trabecular bone coincide.

The microCT and Quant 3D methods of this dissertation research reveal a more complex ontogenetic pattern with the trabecular bone fraction decreasing and then increasing during the first year of life. The decrease is associated with a rapid attrition in trabecular number. The initial (and ultimate) trabecular number appears to

be determined early in development, possibly under relatively strict constraints. It is related to the numerical density of cartilage septae which become ossified (Byers et al, 2000). The increase in BV/TV is associated with continuously increasing trabecular thickness.

This ontogenetic trabecular bone choreography is described by the mechanical usage endochondral ossification model described by Frost and Jee (1994a, b) and Wong and Carter (1990). This model assumes that the endochondral ossification sequences have a "master control" to guide them- mechanical strain. Mechanical usage effects on trabecular bone result in a mechanically adapted state, which is defined by Frost and Jee (1994a, p. 441) as, "the fit among mechanical usage, bone architecture, and bone mass that tends to keep typical peak bone strains within the range between the minimum effective strain range for remodeling (MESr) and the minimum effective strain range for modeling drifts (MESm)." This model accounts for the demonstrated ontogenetic pattern characterized by the early loss of relatively underloaded small trabeculae (decreasing BV/TV) and the recovery (increasing BV/TV) by increased trabecular thickness. Frost and Jee (1994, p. 444) suggest, and this research supports, that the early age-related loss of primary spongiosa "may stem, at least in part, from fitting an originally redundant trabecular bone mass to a subject's typical mechanical usage."

Two additional points of interest in applying the endochondral ossification model to the results of this research lie in the center of the intercondylar region of the proximal tibia and in the metaphyseal cortex. Frost and Jee (1994) argue that the

completed primary spongiosa carries the complete loads of the growth plate (also see Hayes et al., 1978). As distance from the growth plate increases (into the secondary spongiosa), the loads are progressive transferred to the cortex, in essence deloading the center of the tibia. The results reported in this research suggest that this is an age-related phenomenon. The bone volume fraction of the proximal tibia is relatively homogeneous at birth with the central portion decreasing in bone fraction in the first year of life. The BV/TV in this region remains relatively low, possibly from load transfer to the cortices, thus emphasizing the structural effect of "under loading."

Longitudinal bone growth by endochondral ossification requires not only the formation of new trabecular bone, but also metaphyseal cortical bone. Baron and coworkers (2003) have demonstrated that the longitudinal growth of the metaphyseal cortex occurs by coalescence of trabecular bone formed at the periphery of the growth plate. This coalescence is associated with increased osteoblast surface on the peripheral endochondral trabecular bone, possibly due to inductive effects of nearby periosteum. The scan images generated by this research suggest that this process may also be age-related with merging of peripheral trabeculae occurring between 6 months and one year of age (Figure 7.1A/B).

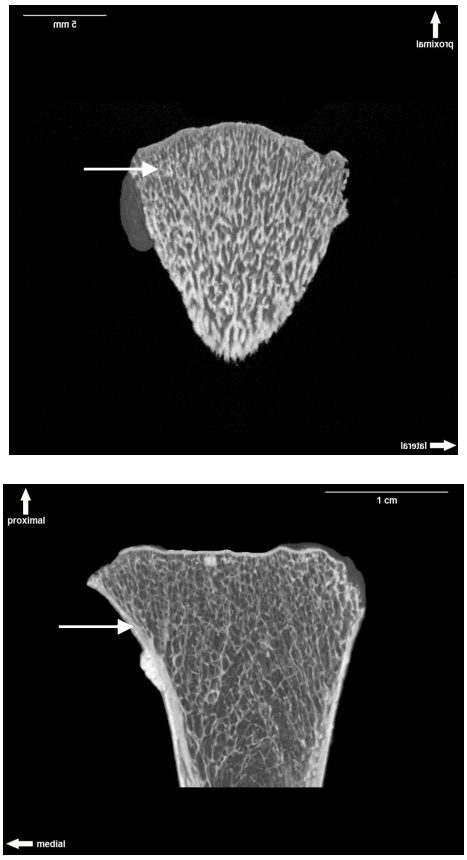

Figure 7.1 (A) Mid-coronal image of neonatal tibia demonstrates no significant coalescence of peripheral trabecular. (B) Mid coronal image of 1.3 year old tibia with complete metaphyseal cortex and trabecular coalescence evident. Arrows are directed towards medial metaphyseal cortex.

GENERAL DEVELOPMENTAL PROCESSES

The ontogenetic pattern demonstrated is not unique to the skeletal domain. The ontogenetic pattern for trabecular bone organization can be thought of in rather simplistic terms as a process in which an abundance of raw material is introduced during fetal development: reorganized and differentiated by further growth and functional requirements until a stable configuration (hopefully) is reached. This

process is demonstrated empirically in this research. Similar results have also been obtained from computer models of long bone growth in which ontogenetic patterns were generated from several loading regimes (Carter et al., 1989; Carter and Beaupre, 2001). This is not a unique process; it fits into the broader context of general developmental procedures exemplified (in part) by ontogenetic/embryonic changes in fibrous tissue (Grinnel, 2000), the vascular tree (Bejan, 2000), and brain development (Parker, 2000).

Connective tissue (e.g., ligaments and tendons) is shaped by function in a similar way as is trabecular bone, although the starting points may differ. Fibroblasts instead of osteoblasts are the operators. These versatile cells prior to structural organization, *in vitro,* are frequently displayed in a "bugsplat" format (Turner, 2007). They have the capability to restructure themselves as necessary in order to regulate tension along secreted fibrous proteins (collagen). They are tension homeostasis regulators (Grinnell, 2000). The fibroblasts tension the collagen fibers by gripping on fibronectin "footholds." Fibronectins are powerful attractors of other fibroblasts. The well-endowed threads have more fibronection and attract yet more fibroblasts. The fibers which do not attract many fibroblasts eventually are lost by attrition. What has started out as a random organization of collagen fibers differentiates into a reticular meshwork of directionally organized meshwork of a "few heavily invested skeins of collagen I, interspersed with comparatively open spaces" (Turner, 2007, p. 53) (Figure 7.2). This looks very much like trabecular bone reorganization.

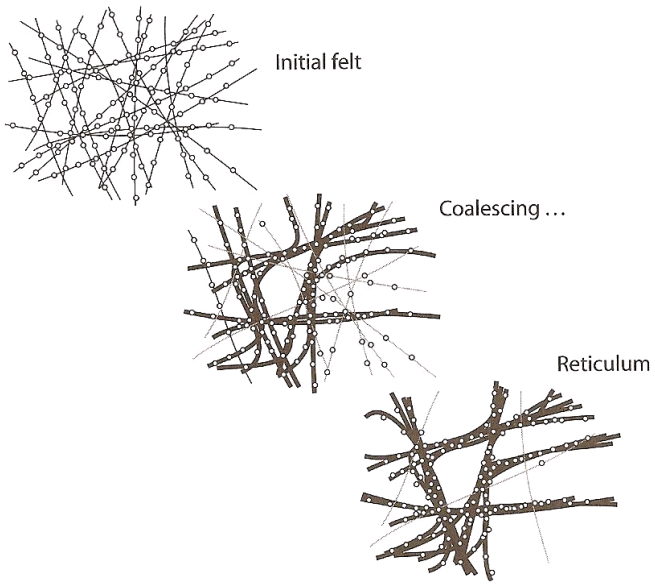

Figure 7.2 Collagen reorganization from random small collagen fibers to an organized mesh of thick, collagen "ropes" (from Turner, 2007).

The development of motor and cognitive skills from infancy into childhood, so important to trabecular bone differentiation, depends upon the growth, maturation, and differentiation of skeletal, musculature, and nervous system tissues. It is instructive to compare the ontogenetic pattern for trabecular bone to the growth curves for these various tissues offered by Bogin (1999, p. 73) (Figure 7.3). Even though the Bogin curves are plotting percent gain since birth compared to a complex pattern of decrease/increase for the various parameters describing the ontogenetic pattern for trabecular bone as a tissue, it should be noted that by interpolation the chronology of the developmental processes for trabecular bone re-organization could fit within the interval of body maturation. Each tissue has its own developmental chronology. What is striking, however, is the convergence of human developmental

events in the age range of six to eight years. This includes eruption of the first permanent molar and incisor, cessation of brain growth (not maturation), a mid-childhood growth spurt, and increasing cognitive and behavioral independency (Bogin and Smith, 2000; Smith and Tompkins, 1995). Fitting trabecular bone into the "mix" lends additional support to the suggestion that the ontogenetic patterning of trabecular bone should not be viewed in isolation, but within the broader context of the suite of general developmental processes- an area for further research.

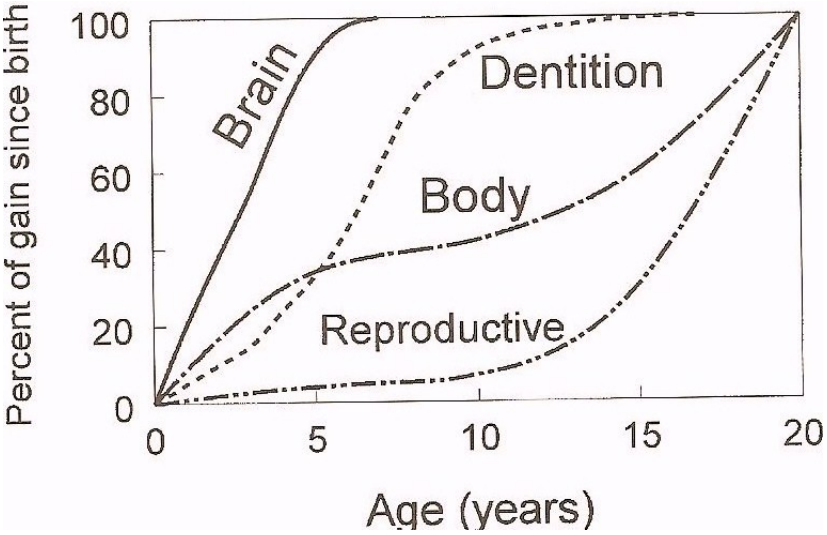

Figure 7.3 Growth curves for different body tissues (From Bogin, 1999, p. 73). The "Body" curve represents growth in stature or total body weight.

BONE-BRAIN CONNECTION

The organization and maturation of the human brain have important associations with the ontogenetic pattern of trabecular bone microstructure: two are discussed. The first is that the brain's developmental reorganization has similarities to that of trabecular bone: from a relatively dense, randomly organized neuronal structure to the differentiated mature brain. As in the example of connective tissue, the starting points may differ. The second association is the linkages of progressive brain maturity with the onset and maturation of locomotor behavior, which, as this research project reveals, is so very important to the ontogenetic pattern of trabecular bone architecture.

Developmental organization of the brain

Human brain development has been researched by autopsy series, electroencephalogram studies, neurocognitive performance, and most recently MRI scanning (Gogtay et al., 2004). A number of parallels exist with the ontogenetic pattern of trabecular bone structure as demonstrated in this study. Firstly, brain and trabecular development from infancy to young adulthood are structurally and functionally non-linear processes. This fits into the expectations of mathematical models describing the general human growth curve for height and weight (Preece and Baines, 1978). Secondly, MRI gray matter density (neurons with dendritic and synaptic processes and supporting architecture) studies demonstrate high initial density followed by loss of cortical gray matter density over time with increased "synaptic pruning" during adolescence and early adulthood and continuing. White

matter density and volume increases with age during adolescence (Sowell et al., 2003). While the timing of brain reorganization differs from that of trabecular bone, the functional relationships have a degree of similarity. Think of substituting trabecular number for gray matter (neuron/synapse) density and trabecular thickness for white matter volume.

Thirdly, brain development progresses in a localized, region-specific manner coinciding with functional maturation (Gogtay et al., 2004). The regions associated with more primary functions (e.g. motor cortex) develop earlier than those concerned with more integrative tasks. Within the motor area, nerve cells controlling the movements of the arms and upper trunk develop ahead of those controlling the legs (Tanner, 1990). This "top-down" gradient accounts for the infant's capacity to control its arms early on. The leg areas are still relatively delayed up to two years. Longitudinal MRI studies of normal brain development in children demonstrate a chronological pattern of maturation which agrees with regionally relevant milestones in cognitive and functional development. This is especially germane to the results of this dissertation research project in which a significant portion of early ontogenetic changes in trabecular bone microarchitecture are linked to onset of locomotor behavior (or lack of), which in turn, are linked to age-related brain developmental patterns.

The successful development of motor (and other) functions requires the smooth and rapid flow of neural impulses throughout the brain integrating the spatially segregated regions involved in these functions. The speed of neural

transmission depends on both the synapse and the structural properties of the connecting fibers (axon diameter and thickness of the insulating myelin sheath). Postmortem (Paus et al., 1999) and MRI (Evans, 2006) human studies demonstrate that axon diameter and myelin sheath undergo rapid growth during the first two years of life suggesting a shortening of the central conduction time in major fiber pathways, such as those of the corpus callosum, cerebellum or the corticospinal tract- the latter two so important in motor pathways. Figure 7.4 demonstrates sequential MRI scan images from a single individual at 3, 6, 9, and 12 months of age. The NIH MRI study of normal brain development has generated longitudinal age-related images showing by 18 months of age a myelination signal pattern similar (but not identical) to the adult pattern. The main difference lies in the subcortical white matter which is not as well myelinated as in the adult (Almli et al., 2007). These findings indicate a chronological concordance of the ontogenetic patterns of both brain and trabecular bone. Myelination and therefore the speed of neural transmission both precede trabecular bone reorganization, but both processes are on rather similar time scale and pattern.

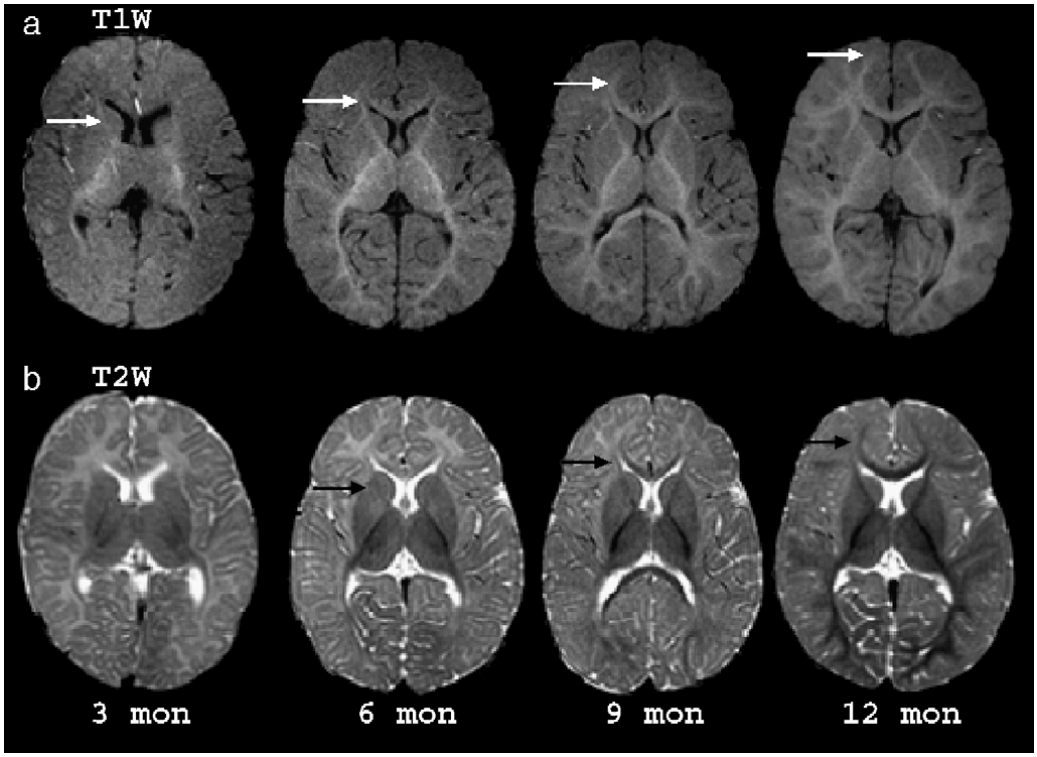

Figure 7.4 Brain maturation illustrated on MRI images from a single participant of the NIH MRI Brain Development Cooperative Group study at 3, 6, 9, and 12 months of age. Row "a" T1W images show the maturational trends of increasing myelination (whiter). This age-related process proceeds from occipital to frontal lobes (caudal-to-rostral) and from central to subcortical white matter (medial-to-lateral). The white arrows indicate the progression of myelination into the frontal lobe. Row "b" T2W images show a similar trend. The black arrows indicate myelin maturation which is manifested as a signal reduction (darker). (image and caption adapted from Almli et al., 2007).

To complete the analogy between brain and trabecular bone development, there is no reason to assume that the link between maturation (or change) of structure and appearance (or change) of function suddenly ceases at any age. Bone functional adaptation on a life-history scale has been well-accepted (Ruff, 2006). Evidence is accumulating that suggests that a major influence on brain development and

remodeling is *use* (i.e., brain functional adaptation) (Tanner, 1990). The nervous system developmental patterns of cell connectivity, like trabecular bone microarchitecture, are the results of (but not limited to) genetic patterning, biochemical influences, and functional activity.

LOCOMOTOR SKILLS

The development of the mature gait in humans has been identified in this research as a key component in the early ontogenetic pattern of proximal tibial trabecular bone. After approximately age 8, this pattern falls into the range of adult values, with the exceptions of trabecular thickness which continues to increase in association with increasing age and body mass and trabecular number which moves in the opposite direction. These results enhance existing research indicating concomitant changes in femoral shaft metaphyseal alignment (e.g. bicondylar angle). The patterned structural changes in trabecular bone, in addition, correspond to the development of diaphyseal strength characteristic researched by Ruff (2003b). This has been discussed in a previous section.

Developmental motor milestones have important implications for the types and magnitudes of loads generated. There is significant individual (Sutherland et al., 1988) and possibly cultural variation (Tracer et al., 2000) for these events. Important to the framework of this research is the suggestion by recent investigations that there are no significant gender differences of the age of onset of independent ambulation

(Stanitski et al., 2000). This supports the validity of results from a pooled-sex sample. The motor developmental pattern is as follows:

1. six months: onset of upright sitting
2. nine months: crawling
3. one year: unassisted bipedal walking
4. four years: mature adult-like gait (Sutherland, 1997)

Locomotion in the developmental phase between 6-12 months is characterized by crawling and "cruising" in which the upper limb (humerus) is an important component to weight-bearing. Humeral cortical strength growth trajectories reflect these early demands (Ruff, 2003b). Ryan et al. (2007) in a quantitative microCT study in the juvenile human femur and humerus also established a pattern of an early increase in the structural and mechanical properties of the humerus with a decrease after one year of age.

The early gait pattern is mechanically inefficient, increasing the mechanical demands on the femur, manifested by both increasing cortical strength in the shaft (Ruff, 2003b) and increasing microstructural/mechanical properties in the proximal trabecular bone (Ryan et al., 2007). The fully developed gait pattern is present by age four to eight years, depending on the researcher (Hallemans et al., 2005; Stansfield et al., 2006; Sutherland, 1997; Wollacott and Assaiante, 2002). It is characterized by a narrow mediolateral base of support, predictable limb stability, an adult-like cadence, and mechanical efficiency (Sutherland, 1997). It is after this pattern has stabilized that those changes in femoral strength become more closely correlated to increases in

body size (Ruff, 2003b). This dissertation research indicates that it is after this pattern has stabilized that changes in the trabecular bone parameters of BV/TV and SVD DA remain within the range of adult values (about 8 years). Trabecular thickness, however, appears to continue to increase in association with body mass. These findings are consistent with those for cortical bone and suggest that the mechanical loading as a result of locomotor behavior is a key component of the ontogenetic pattern of adaptation of trabecular bone structure.

Knee kinematics

Kinematics is the branch of mechanics concerned with motion; kinetics is the branch of mechanics concerned with force. Can linkages be made between trabecular three-dimensional microstructural parameters and specific events within a maturing gait? The pattern of heterogeneity in trabecular bone of the proximal tibia demonstrated in this research follows the chronology of maturing gait kinematics at the knee. Of specific interest is the empirical BV/TV ratio data from the anterior/posterior secondary VOIs of the medial and lateral condyles. These data imply that the initial relative homogeneity of the trabecular structure in neonates subsequently remodels, favoring the posterior portions of the condyles, beginning in the age range of 1.5-2.5 years. Changes in the lateral condyle tend to precede those in the medial. This regional differentiation continues into skeletal maturity. There are some disclaimers to be made at this point: this dataset is cross-sectional, the sample is small, and the individuals are a selected subset. Sampling bias masking individual variability may be significant. The general assumption (well supported in the

literature) made is that trabecular remodeling reflects the mechanical forces experienced. A case can be made for the idea that posterior condylar remodeling reflects a shift towards a more posterior loading pattern of the proximal tibia (Hurwitz et al., 1998; Lai et al, 2005). The discussion to follow should be considered speculative: associative, not correlative - requiring further research. Nevertheless, the implications of the sensitivity of the methods used in this study to early changes in trabecular microstructure are compelling.

The task ahead is to look for specific gait characteristics which may account for loading of the posterior portion of the proximal tibial plateau during development of the mature gait occurring within the 1.5-2.5 age range. The proximal tibial contact area (adults: no data exists for children) has been shown to transfer from an anterior pair of tibio-femoral surfaces at 10° of knee flexion to a posterior pair between 10-30° of knee flexion: laterally more so than medially (Freeman and Pinskerova, 2005). The estimated and measured forces at the human knee (adults: no data exists for children) ranges from 1.9 to 7.2 times body weight. during level walking (Komistek et al., 2005). This suggests that changes in the weight-bearing *knee flexion range* may be important in differential load transfer to the posterior portion of the condyles.

The human gait studies of Sutherland and co-workers (Sutherland et al., 1988; Sutherland, 1997) have added valuable insight. Examining age-related changes (beginning at age 1 year) in sagittal movements at the knee, these researchers note, "The primary change in the knee flexion/extension curve by age is gradual development of an initial knee *flexion wave*" (emphasis mine) (Sutherland, 1997, p.

166). The flexion wave is a term used to describe the flexion of the knee during loading response and subsequent extension during the mid-stance phase of gait. This is considered to have a shock absorbing effect. Sutherland states there is only a hint of an initial knee-flexion wave in one year olds. The knee essentially remains in a 10° flexed position at foot-strike. By 1 ½ years the flexion wave has developed, with further flexion evident by three years of age (20-30°). At four years of age, children show a totally mature knee flexion wave in stance phase (Figure 7.5 A/B). This chronology of gait development in regards to knee flexion appears to have close parallels to the chronology of trabecular structural changes being discussed. Of course, temporal concordance is not causality. The possible linkages are, however, intriguing and await further research.

One important area of such linkages is the pattern of tibio-femoral loading during normal human gait (in adults) and activities such as stair climbing (Taylor et al., 2004). Figure 7.6 depicts data demonstrating high contact forces generated in the knee joint in the initial loading phase of the gait cycle, associated with the knee flexion wave. The average resultant peak force during walking in this study was 3.1 times body weight (Taylor et al., 2004). The data show greatly increased loading with stair climbing (5.4 times body weight), compared to that seen during normal walking. This emphasizes the *potential* importance of specific types of activities and joint position to knee joint loading, and by inference, to the trabecular architecture of the proximal tibia. However, the data of this study do not allow any inferences on specific activity patterns other than those associated with gait.

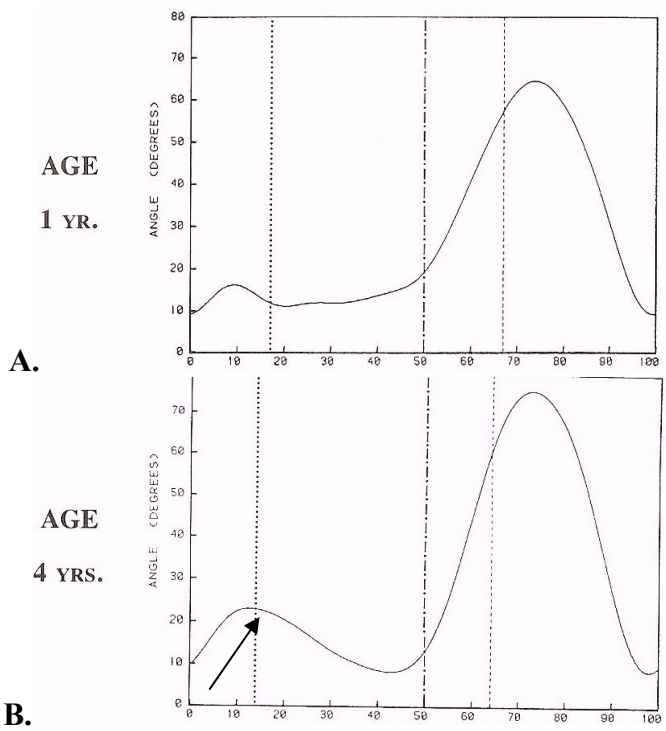

Figure 7.5 Knee joint angles in flexion and extension during gait cycle of one year old (A) and four year old (B). X axis is percent of a single gait cycle. Y axis is knee angle in degrees. The broken vertical lines indicate approximate timings of (from left to right): opposite (left) toe-off, opposite (left) foot-strike, and (right) toe-off. The black arrow is directed toward the mature initial flexion wave present at 4 years of age, but not at one year (Sutherland et al., 1988).

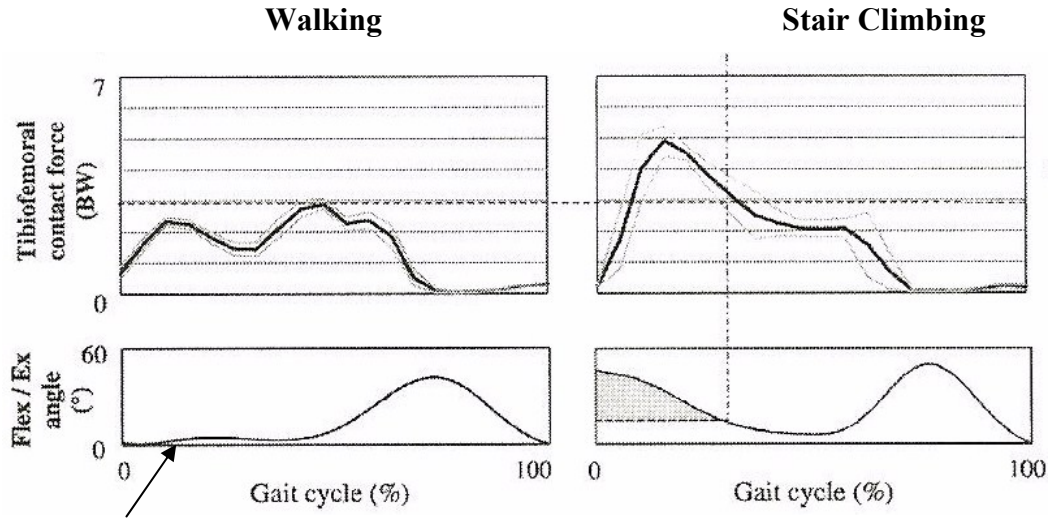

Figure 7.6 Tibio-femoral contact forces and knee joint position during both normal walking and stair climbing. The dotted horizontal lines correspond to the average peak axial force during walking. Forces are shown in body weight (BW). Flex/Ex angle is the knee joint position. The black arrow is directed towards the gait cycle knee flexion wave (Taylor et al., 2004).

NEW INSIGHTS FOR SKELETAL BIOLOGY

Discussion up to this point has been focused on the quantitative aspects of this research in terms of trabecular bone microarchitecture, skeletal biology, and locomotor behavior. I would now like to turn to the "big picture" and consider the anthropological implications of the early results and future possibilities of the trabecular bone research agenda.

Life history perspective

One of the strengths of this project is the harnessing of new analytical methods to address concerns related to human skeletal growth and development. The juvenile skeletal series from SunWatch presented a valuable sample for the study of ontogenetic patterning in trabecular bone microstructure in a Late Prehistoric agricultural village. The data presented might be regarded as 3D microstructural "reference values" for the proximal tibial metaphysis during growth and development for a prehistorical maize agricultural setting. This is a biocultural milieu which is characterized by the increased prevalence of dental disease, bioarchaeological stress indicators, early growth disturbance, and relatively short adult stature. It is unknown at this time if the results of this research can be generalized. It is unknown, but possible that there are cross-cultural differences in the timing of onset of locomotors skills (Tracer et al., 2000), which could be manifested by culturally-related variations in aspects of the ontogenetic pattern of trabecular bone microarchitecture. These questions await further research with expanded sample sizes, comparisons with other skeletal elements from the same individuals, and comparisons between groups of people living under different circumstances (Ryan and Krovitz, 2006).

A longer time scale, in terms of human lifespan, may present additional opportunities for documenting and interpreting patterns of lifestyle, physical activity, and health from skeletal remains: *the life history perspective*. Trabecular bone morphology reflects lifelong accumulated strain history superimposed upon the changes occurring during growth and development. Analysis of trabecular

microarchitecture and directionality (anisotropy) has the potential to provide a window into the assessment of human behavior and physical activity in the archaeological context over the life course of individuals, groups, and populations. The broad research framework is to explore trabecular bone adaptation from a life course perspective extending from the maternal-fetal environment to birth, childhood, adolescence, young adulthood, and later adult life (Ben-Shlomo and Kuh, 2002). This includes studies of growth and development, human variation, the effects of lifestyle change, aging and senescence, and chronic degenerative conditions; incorporating the influences of socially structured health and disease, diet and nutrition, mobility and sedentism, and workload.

This research perspective uses mechanobiology of cancellous bone as the theoretical scaffold, providing the continuity in a life course of change through the processes of growth, modeling, remodeling, and skeletal adaptation. Mechanobiological factors during ontogeny, responsible for the development of skeletal mass and distribution, are also in play at the opposite stages of life: aging, senescence, and the development of osteoarthritis (Beaupre et al. 2000). This sets the stage for research into the prevalence, causes, and consequences of variation in human cancellous bone adaptation over a life course perspective. A common characteristic of a broad-spectrum research agenda is that more questions are generated than are answered.

Maternal-fetal environment

Research over the past four decades has demonstrated that perturbations early in life "could have long-term, irreversible consequences" and "also that the insult must occur during a critical period of development to have maximal effect" (Gillman, 2005, p. 1848). Two essential critical periods are fetal development and adolescent growth and maturation (Cameron and Demerath, 2002; Worthman and Kuzara, 2005). First generation studies on early origins of later disease concentrated on associations between birth weight and disease occurrence decades later (Barker, 1998; Gluckman and Hanson, 2004; Hales and Barker, 2001). These researchers found relationships between low birth weight and later obesity, type 2 diabetes mellitus, and ischemic cardiovascular disease, proposing that this phenomenon was a consequence of the "thrifty phenotype hypothesis" (Hales and Barker, 2001). This hypothesis identifies fetal adaptation to a deficient intrauterine environment as a general biological process associated with later-life disease. These early studies were criticized for having too narrow of a focus and ignoring socioeconomic variables (Gillman, 2002).

Current research is focused on a broad range of prenatal determinants on postnatal outcomes, including maternal diet, placental function and blood flow, and fetal metabolism (Gillman, 2005) as well as late consequences of variations in postnatal growth and development (Barker et al., 2005). Gluckman, Hanson et al. (2005) have proposed a scheme outlining a broader set of developmental and evolutionary strategies based on the capacity for a single genotype to produce

different phenotypes in different environments. This form of developmental plasticity may be an adaptive response early in life with an effect later in life (Bateson, et al., 2004). These are termed "predictive adaptive responses" (PARs) in which the phenotype is "not necessarily advantageous in the environment concurrent with or immediately following the inducing cue, but is likely to be advantageous in an anticipated future environment (Gluckman et al., 2005). These human PARs may have become increasingly inappropriate in recent human circumstances, contributing to disease conditions in later life.

Is there data to suggest that trabecular bone microstructure is influenced by maternal-fetal perturbations? A close inspection of the dataset for the primary medial VOIs in the youngest individuals (Appendix A, Group I) reveals that the range for bone volume fraction value is quite narrow. These BV/TVs fall into a limited range of 0.4041- 0.4606, consistent with other microCT studies of fetal or juvenile trabecular bone (Nuzzo et al., 2003; Ryan and Krovitz, 2006). This suggests that the fetal endochondral ossification process is relatively constrained, conserved, and stereotypical. There are three individual in this group, however, who have much lower BV/TVs (Burials 8_72, 0.2958; 12_73, 0.2975; and 5_72, 0.2609). Possible explanations for this disparity include, but are not limited to, normal individual variation, preservation issues, erroneous maturity estimation (older than indicated), chronic illness (not evident), and/or low initial bone volume fraction as a reflection of maternal factors. Clearly, several individuals do not make a series. And it is not the expectation to settle this line of reflection from this

research. However, an exploration of what is known in regards to the fetal origins of low bone mass may be useful for the consideration of the question of whether (or not) BV/TV at birth can possibly be used as a general indicator of maternal well-being or a more specific indicator within a population of a differential in maternal health- questions of interest to Anthropology.

Recent research has taken on the quantitative study of human fetal bone development by histomorphometric (Salle et al., 2002) and microCT methods (Nuzzo et al., 2003). These techniques demonstrate an extremely rapid rate of trabecular bone metabolism, cell division, and modeling especially in the last trimester of fetal development, manifested by increasing bone volume fraction, trabecular thickness, brisk matrix mineralization, and increasing hydroxyapatite crystal size. Research into the fetal origins of reduced bone mass commonly use the measure of bone mineral density (BMD) derived from dual energy X-ray absorptiometry (DEXA) or ultrasound scanning. Although BMD is *not* the equivalent of 3D microstructural measurements, the general trends should be consistent (Nuzzo et al., 2003).

There is now evidence to suggest that environmental influences during early life (intrauterine) interact with the genome in establishing the functional level of a variety of metabolic processes involved in skeletal growth, including neonatal bone mass (Cooper et al., 2002; Javaid and Cooper, 2002). After adjusting for gestational age, neonatal bone density is positively associated with birth weight, birth length, and placental weight. Maternal factors negatively associated with

neonatal bone density are maternal smoking, maternal nutrition at 18 weeks gestation, and high maternal physical activity (Godfrey et al., 2001). Neonatal bone density has been demonstrated to be lower among winter births than among summer birth. This is associated with winter month maternal vitamin D deficiency (Javaid and Cooper, 2002).

Mechanisms for the induction of fetal programming in regards to skeletal development are thought to include: (1) a nutrient environment (in the most general sense) which may permanently alter gene expression important to the activity of metabolic enzymes or the responsiveness of various tissues within the growth plate to endocrine systems such as growth hormone/insulin-like growth factor I, hypothalamic-pituitary- adrenal, and gonadal. Vitamin D_3 responsiveness is also likely to be a factor. And (2), a nutrient environment which may permanently reduce cell numbers in the growth plate. The high growth rates of the fetus are mostly the result of cell replication. Fewer cells equal a reduced capacity for growth and, in addition, the slowing of whatever growth that is occurring is considered a major adaptation to undernutrition (Cooper et al., 2002).

The important element from a bioarchaeological perspective is that undernutrition and other adverse influences arising in fetal life can have a permanent effect on body structure. Evidence is accumulating from human studies of consequences on intrauterine skeletal mineralization and neonatal bone density. Undernutrition is a key variable in the study of human variation; so important to research agendas within physical anthropology and a possible lynch-pin in neonatal

trabecular bone volume. The question remains: is there data to suggest that trabecular bone microstructure is influenced by maternal-fetal perturbations? The answer is a very provisional yes, awaiting comparative studies of trabecular bone structure under differing environmental, cultural, and nutritional situations.

Bone functional adaptation

Fast-forward in life history to the interval which encompasses the prepubertal to young-adult years in which skeletal tissues are highly responsive to mechanical loads generated by physical activity. The assessment of levels of physical activity (mobility) and workload is an important issue in the bioarchaeological research agenda (Larsen, 1997). Current bioarchaeological methods for assessing physical activity levels from archaeological skeletal remains include cortical robusticity (Ruff et al., 1993), long bone diaphyseal geometry (Ruff and Hayes, 1983; Ruff, 2000), enthesiopathies (Stirland, 1998; Weiss, 2003), and degenerative joint disease (Larsen, 1997). Bioarchaeological analyses have documented the wide-ranging changes of human skeletal adaptations, stress, and health indicators during the time period embracing the foraging to farming transition (Larsen, 1997). Agricultural populations are generally characterized by sedentism; foragers by mobility. Agricultural populations have different demands on their musculoskeletal system than do hunter-gatherer populations. Studies have been directed towards demonstrating that behavioral changes (degree of mobility

and intensity of physical activity) associated with new subsistence technology have resulted in skeletal adaptations (Bridges et al., 2000).

Bioarchaeological researchers using long bone diaphyseal geometric biomechanical analyses have had conflicting results in demonstrating the relationship of form to function (Larsen, 1997; Ruff et al., 1984; Larsen and Ruff, 1994). Georgia coast studies suggested that the population-based patterns of long bone strength decrease in agriculturalists (Ruff and Larsen, 1990; Ruff et al., 1984); northwest Alabama studies suggested the opposite (Bridges, 1989; Bridges et al., 2000). Ruff (1999) in a meta-analysis of North American research on this topic reported that subsistence has no significant effect on lower limb robusticity. But that there is an influence related to sex, sexual dimorphism, and terrain topography. The current position of trabecular bone analyses in anthropology may be similar to that of the initial use of long bone geometry to assess mobility in archaeological skeletal samples (Ruff, pers. comm.). That is, an "introductory offering," building gradual acceptance, followed by critique and subsequent refinement.

Daily cyclic loading of cancellous bone is produced by customary and habitual activities (walking, running, climbing, and carrying) applied consistently over a long period of time with bone formation, resorption, and directionality determined by the specifics of the daily stress stimulus. For example, changes in load magnitudes result in changes of bone density and thickness (Theintz et al., 1992; Brahm et al., 1998; Duppe et al., 1997; Bass et al., 1999; Sundberg et al.,

2001) and changes in load direction results in changes of architectural pattern (Carter and Beaupre, 2001; Jacobs, 2000; Pontzer et al., 2006; Ruimerman et al., 2005; van der Meulen and Huiskes, 2002). The results of this study show that microCT and Quant 3D are particularly robust technologies for cancellous bone analysis, capable of demonstrating quantitative morphological patterns related to mechanical loading regimes. I argue that the advances in trabecular bone microstructural analyses may offer new insights from skeletal remains in interpreting the level of physical activity, extent of mobility, customary work load, and external demands on juvenile and adult populations.

An example of this type of study would assess skeletal adaptation (loading history and 3D trabecular bone microstructure parameters) during the foraging to farming transition in the Ohio Valley, comparing quantitative datasets between Late Archaic and Late Prehistoric groups. Research during the past two decades has indicated that eastern North America, including the Ohio Valley, was an independent center for plant domestication (Gremillion, 2004; Smith 2001). The fundamental post-Pleistocene shift from reliance on wild resources to intensive food production had profound consequences for human societies and lifestyles (Smith, 1989, 1992). Understanding the complex patterns of this larger social transformation associated with the "coevolutionary interactions between humans and plants" (O'Brien, 1987, p.177) is a major research question for anthropology. How does trabecular bone adaptation reflect cultural and economic change? How do divergent living strategies (mobility/sedentism) alter growth and development

of cancellous bone microarchitecture? What are the trabecular bone quantitative parameter characteristics related to physical activity from childhood to adulthood in hunter-gatherers versus intensive agriculturalists? Is this knowable? The "reference" dataset from the current research derived from SunWatch village, in which intensive maize agriculture was practiced, sets an initial foundation upon which some of these questions may be addressed- possibly enhancing the interpretations of lifestyle in past populations.

Adult-onset conditions

Another fast forward in life history to "mature" adult years brings to the fore two conditions intimately related to trabecular bone microarchitecture: osteoporosis and osteoarthritis. These conditions are of interest to the understanding of health and disease patterns in later life for extant and past populations. There has been a recent shift in the osteoporosis bone strength paradigm from a primary focus on bone density as measured by dual energy x-ray absorptiometry (DEXA) to the consideration of bone strength to be related to *both* bone structure (quality) and bone density. Important elements of bone quality are trabecular architecture, mineralization, bone turnover, and damage accumulation (Sebba, 2007). Microarchitectural studies reveal an age-related loss of trabecular number affecting primarily horizontal trabeculae. This results in a progressive deficit in bone strength. The current research results have two points of convergence on the investigation of osteoporosis and attendant fracture risk as a

manifestation of skeletal health in past populations. The first is the utility of examining trabecular three-dimensional volume and architecture via microCT scanning for understanding the complexities of age and sex-related changes in trabecular bone over the life course in archaeological contexts. The second, and most direct connection with the current ontogenetic project, are the data that link poor childhood skeletal growth to the later onset of osteoporosis and hip fracture risk (Cooper et al., 1997; Javaid and Cooper, 2002). This is an extension of the fetal-programming perspective. To paraphrase a marketing slogan: "That which happens to trabecular bone early in life, stays in trabecular bone." This investigative field is wide open.

The articular cartilage degradation evident in osteoarthritis is associated with changes in trabecular microstructure that are at variance to age-related or a simple "wear-and-tear" process. Age-related characteristics of human tibial trabecular bone consist of a decline in bone mass and an increase in the degree of anisotropy (Ding, 2000). This second phenomenon can be interpreted as functional adaptation to the first, suggesting that the microstructure of trabecular bone "re-organizes continually to adapt to the mechanical loading environment in aging bone" (Ding, 2000, p. 31). Osteoarthritis is associated with a thickening of the subchondral bone plate and an acceleration of bone turnover (decreased bone volume and mineralization) in the microstructure of subchondral trabecular bone (Li and Aspden, 1997). Bone mineral density increases in both the axial and peripheral skeletal with the osteoarthritis progression (Dequeker, 1997). The causal

relationship between cartilage destruction and subchondral plate and trabecular changes in osteoarthritis remains unclear at this time. This combination of trabecular changes is associated with progressive *symptomatic* osteoarthritis (Buckland-Wright et al., 2007), as opposed to age-related changes which may or may not have correlative symptoms. Thus it may be possible to design a bioarchaeological research project using microCT and Quant 3D analyses on skeletal elements (tibiae) with macroscopic evidence for "degenerative joint disease" sorting out age-related joint changes from those of likely symptomatic progressive osteoarthritis. As evident in earlier discussions, the dataset from this current research gives some indication of the starting point for trabecular bone microstructure at skeletal maturity, from which to gauge age-related or pathophysiological changes. These deliberations, having commenced at the beginning of life's journey, come to a close near the destination.

SUMMARY

The ontogenetic patterning of trabecular bone demonstrated by this research is an integral component of human growth and development, life history cycles, behavioral maturation, and biocultural circumstances. Growth is indicated by the quantitative increase in size or mass. Development is indicated by the reorganization of the trabecular structure from a homogeneous immature structure to a differentiated, heterogeneous, functionally adapted configuration.

The implications of the results of this research for human biology, aging and disease, and bioarchaeology were discussed. The outline for an anthropologically-related trabecular bone research program has been suggested. Concluding remarks remain.

CHAPTER 8

SUMMARY AND CONCLUSIONS

The objective of this dissertation project, to establish new quantitative data on the ontogenetic pattern of trabecular bone in the proximal tibia, has been successfully achieved. The morphometric structural parameters for bone volume fraction, bone fabric directionality (degree of anisotropy), trabecular number, and trabecular thickness were measured directly or calculated from microCT scan data. The findings of this research indicate that, at birth, human tibial trabecular bone is relatively dense, being constructed of numerous, small, directionally-oriented trabeculae. The first year of life is witness to a marked reduction in bone volume, trabecular number, and directional organization. These reach their lowest point at around six months of age.

The initiation and subsequent maturation of normal human walking provides the physical stimulus for the reorganization and differentiation of the trabecular structure. This begins around one year of age and is largely completed by the age of eight. The quantitative measures during this developmental phase demonstrate that the bone volume fraction and degree of anisotropy gradually increase to the adult range of values. Trabecular number decreases throughout ontogeny and trabecular

thickness increases throughout ontogeny. The results further suggest that intra-tibial trabecular variation increases in concert with the full elaboration of the human bipedal gait. Increasing body mass becomes important primarily after early childhood, after the earlier influence of walking. Reorganization of tibial trabecular bone by the process of bone functional adaptation, as well growth and development, results ultimately in fewer, thicker, trabeculae with a greater degree of complexity in structure.

LIMITATIONS AND STRENGTHS

Limitations to the current study are those which, by necessity, are related to archaeological juvenile skeletal samples – relatively small sample sizes (overall and within maturity-related groups), sample mortality and preservation bias, lack of precision in age estimation, and no sex assessments prior to age 17. The cross-sectional nature of this study increases the probabilities for nonrandom sampling and masks individual variability in growth patterns. The sample is more fine-grained for younger individuals because of demographic (high fertility and infant mortality) and methodological (maturity staging is skewed toward the younger groups) factors. These latter issues are not necessarily limitations as ontogenetic patterning of trabecular bone exhibits the highest variability during the secotrant. Overall, these limitations appear to have an unknown (and currently unknowable), but modest effect on the ontogenetic pattern displayed. The subchondral VOI positioning in the older age groups with the epiphysis present is likely to have had

an effect on the degree of anisotropy data. This is an area of future research. Similarly, the CT resolution influence on trabecular thickness in ontogenetic studies, presently unknown, needs further clarification and research.

The results of this study indicate a morphological pattern signal for the trabecular bone of the proximal tibia which is quite strong and consistent with previous observations for the proximal femur (Ryan and Krovitz, 2006), humeral and femoral shafts (Ruff, 2003 b), and recent animal models (Wolschrijn and Weijs, 2004). Strengths of the current study reside, in part, in the recent developments in 3D imaging technique which has made true three-dimensional quantification of trabecular bone microstructure possible. Structural parameters, such as architectural anisotropy, bone volume fraction, and trabecular thickness can be calculated directly from CT scan-related images. These methods, which are unbiased and free of assumptions, enable a detailed and flexible quantification of ontogenetic patterning.

In addition, there are characteristics of the SunWatch village skeletal remains which enhance the natural experiment perspective of this project. Some important factors include the relative genetic homogeneity (common ancestral group) of the SunWatch skeletal sample, the putative egalitarian nature of village life, the relatively short duration of village occupation (~ 40 years), and the excellent skeletal preservation of juvenile remains. Last, but not least, the seriation of the skeletal remains by population-specific maturity stages (Sciulli, 2007) has proven to be a major asset to this project. The orderliness and relative lack of noise

in the dataset provides an independent validation of the seriation procedure. It contributes notably to the demonstration and quantification of the ontogenetic pattern of trabecular bone.

CONCLUSIONS

Lifestyle, physical activity, and behavior are essential components of bioarchaeological interpretation of skeletal remains (Larsen, 1997). Much about how ancient populations lived their daily lives is available to researchers by deciphering the data embedded in the human skeleton. This project represents a natural experiment of ontogeny and mechanical loading: infants going from not walking to walking, small body mass to large body mass, and dependency in activity to adult activity. The study develops new quantitative and structural knowledge about the development and remodeling of normal trabecular structure as demonstrated in a subadult archaeological skeletal sample. The data of this research produces a temporal sequence in the variation in bone volume fraction, degree of anisotropy, trabecular thickness, and trabecular number as a reflection of ontogeny and as associated with the timing and acquisition of normal functional activities. The pattern is the message.

The intellectual merit of this study centers on its potential of using recent advances in mechanobiological modeling, non-invasive micro-imaging techniques, and computational methodologies to advance understanding of socially structured human behavior, environmental influences, and skeletal response during ontogeny in ancient populations. This study is focused on the problem of ontogenetic

changes in trabecular bone in a temporal, social, and environmentally-specific analysis of the Late Prehistoric SunWatch village. The project is not about SunWatch *per se*; it is about skeletal ontogeny using SunWatch juvenile skeletal remains. Trabecular bone analysis using microCT and computational 3-D structural analyses permits previously inaccessible skeletal phenomena (i.e. accurate loading history throughout ontogeny) to be examined and interpreted in a problem focused, population-based, biocultural framework. The application of mechanobiological principles in the context of human skeletal ontogeny provides portals for deciphering aspects of tissue differentiation, endochondral growth and ossification, and bone growth and adaptation (Carter and Beaupre, 2001). Finally, this project forms the basis for expanded studies in physical anthropology relative to physical activity, structural adaptation, and health. It presents the future promise to clarify issues in the relationship between ontogeny and loading history throughout the entire life course of various populations during important transitions in human lifeways, as well as in differing environmental and cultural circumstances.

Trabecular bone analysis is situated within a broad framework of research in the arena of musculoskeletal biology. The broader impacts of this project have society-wide and possibly global implications in three general areas. First, the quantification of trabecular architecture of past populations can provide baselines for extant and future populations. Trabecular bone is a dynamic tissue, undergoing continuous change; this characteristic has important implications to the understanding of skeletal adaptations during ontogeny in populations of varying

genetic and environmental background. Secondly, the study of trabecular bone differentiation, maintenance, and adaptation can, by extension to contemporary adult populations, have important public health-related relevance by contributing to research and understanding of such globally prevalent conditions as osteoporosis and osteoarthritis (Beaupre et al., 2000). Architectural changes in cancellous bone have been implicated in both of these disorders (Brandt, 2003; Ding et al., 2003). Thirdly, trabecular bone analysis is on the forefront of skeletal regenerative and implant longevity research (Papaloucas et al., 2004).

For final consideration, this study enhances the infrastructure of research in physical anthropology by incorporating recent technological and methodological advances in trabecular bone analysis, lending these towards understanding skeletal adaptation and ontogeny. A multidisciplinary approach is fostered by enlarging upon existing, and developing "next-generation," technologies, methodologies, and infrastructures to be shared by anthropology, engineering, mathematics, and skeletal biology.

LIST OF REFERENCES

Abel TJ, Koralewski JM, and DeMuth GB. 2000. Cemetery Ridge: An Early Village Site Located in Sandusky County, Ohio. In: RA Genheimer, editor. Cultures Before Contact. Columbus: Ohio Archaeological Council. pp. 384- 403.

Adams M, BJ F, and Morrison H. 2000. Mechanical Initiation of Intervertebral Disc Degeneration. Spine *25:*1625-1636.

Aiello L, and Dean C. 2002. An Introduction to Human Evolutionary Anatomy. London: Elsevier.

Agarwal S, and Stout S, editors. 2003. Bone Loss and Osteoporosis: An Anthropological Perspective. New York: Kluwer Academic.

Allman J. 1968. The Incinerator Village Site. Ohio Archaeologist *18:*50-56.

Allport S. 2003. The Primal Feast: Food, Sex, Foraging, and Love. Lincoln, NE: iUniverse.

Almli C, Rivkin M, and McKinstry R. 2007. The NIH MRI Study of Normal Brain Development (Objective-2): Newborns, Infants, Toddlers, and Preschoolers. Neuroimage *35*:308-325.

Ammann P, Bourrin S, Bonjour J, Meyer J, and Rizzoli R. 2000. Protein Undernutrition-Induced Bone Loss is Associated with Decreased IGF-I Levels and Estrogen Deficiency. Journal of Bone and Mineral Research *15*:683-690.

Anderson M, Green W, and Messner M. 1963. Growth and Predictions of Growth in the Lower Extremities. Journal of Bone and Joint Surgery *45-A:*1-14.

Armelagos G, Carlson D, and Van Gerven D. 1982. The Theoretical Foundations and Development of Skeletal Biology. In: Spencer F, editor. A History of American Physical Anthropology 1930-1980. New York: Academic Press. Pp. 305-328.

Atkinson P. 1967. Variation in Trabecular Structure of Vertebrae with Age. Calcified Tissue Research *1:*24-32.

Aveni A. 2003. Archaeoastronomy in the Ancient Americas. Journal of Archaeological Research *11*:149-192.

Barker A, and Pauketat T, editors. 1992. Lords of the Southeast: Social Inequality and the Native Elites of Southeastern North America: Archaeological Papers of the American Anthropological Association Number 3.

Barker D. 1998. Mothers, Babies, and Disease in Later Life. Second Edition. New York: Churchill Livingstone.

Barker D, et al. 2005. Trajectories of Growth among Children Who Have Coronary Events as Adults. The New England Journal of Medicine *353:*1802-1809.

Baron J. 2003. Regulation of Skeletal Growth (abstract). Grant Number: 1Z01HD000640-08. http://crisp.cit.nih.gov (7/2/2007).

Barry III H, and Paxson L. 1971. Infancy and Early Childhood: Cross-Cultural Codes 2. Ethnology *10:*466-508.

Barry III H, Child I, and Bacon M. 1959. Relation of Child Training to Subsistence Economy. American Anthropologist *61:*51-63.

Bass S. 2000. The Prepubertal Years: A Uniquely Opportune Stage of Growth When the Skeleton is Most Responsive to Exercise? Sports Medicine *30:*73-78.

Bass S, Delmas PD, Pearce G, Hendrich E, Tabensky A, and Seeman E. 1999. The Differing Tempo of Growth in Bone Size, Mass, and Density in Girls is Region-Specific. Journal of Clinical Investigation *104:*795- 804.

Bass S, Eser P, and Daly R. 2005. The Effect of Exercise and Nutrition on the Mechanostat. Journal of Musculoskeletal and Neuronal Interaction *5*:239-254.

Bass S, Pearce G, Bradney M, Hendrich E, Delmas P, Harding A, and Seeman E. 1998. Exercise Before Puberty May Confer Residual Benefits in Bone Density in Adulthood: Studies in Active Prepubertal and Retired Female Gymnasts. Journal of Bone and Mineral Research *13*: 500-507.

Bass S, Saxon L, and Daly RM, et al. 2002. The Effect of Mechanical Loading on the Size and Shape of Bone in Pre-, Peri-, and Postpubetal Girls: A Study in Tennis Players. Journal of Bone and Mineral Research *17:*2274- 2280.

Bass W. 1995. Human Osteology: A Laboratory and Field Manual, Fourth Edition. Columbia: Missouri Archaeological Society.

Bateson P, Barker D, et al. 2004. Developmental Plasticity and Human Health. Nature *430:*419-421.

Baunach D. 2001. Gender Inequality in Childhood: Toward a Life Course Perspective. Gender Issues *Summer:*62-86.

Beaupre' G, Orr T, and Carter D. 1990. An Approach for Time-Dependent Bone Modeling and Remodeling-Theoretical Development. Journal of Orthopaedic Research *8:*651-661.

Beaupre' G, Stevens S, and Carter D. 2000. Mechanobiology in the Development, Maintenance, and Degeneration of Articular Cartilage. Journal of Rehabilitation Research and Development *37:*145-152.

Bejan A. 2000. Shape and Structure: From Engineering to Nature. Cambridge: Cambridge University Press.

Bender M, Baerreis D, and Steventon R. 1981. Further Light on Carbon Isotopes and Hopewell Agriculture. American Antiquity *46(2):*346-353.

Benjamini Y. 1988. Opening the Box of a Box plot. The American Statistician *42:*257-262.

Benn D.1994. Fabric Shape and the Interpretation of Sedimentary Fabric Data. Journal of Sedimentary Research *A64*:910-915.

Ben-Shlomo Y, and Kuh D. 2002. A Life Course Approach to Chronic Disease Epidemiology: Conceptual Models, Empirical Challenges and Interdisciplinary Perspectives. International Journal of Epidemiology *31:*285-293.

Berti P, Leonard W, and Berti W (1998) Stunting in an Andean Community: Prevalence and Etiology. American Journal of Human Biology *10:*229-240.

Bertram J, and Biewener A. 1988. Bone Curvature: Sacrificing Strength for Load Predictability? Journal of Theoretical Biology *131:*75-92.

Bertram J, and Swartz S. 1991. The "Law of Bone Transformation": A Case of Crying Wolff? Biological Review *66*.

Biewener A, Fazzalari N, Konieczynski D, and Baudinette R. 1996. Adaptive Changes in Trabecular Architecture in Relation to Functional Strain Patterns and Disuse. Bone *19:*1-8.

Bocquet-Appel J, and Masset C. 1982. Farewell to Paleodemography. Journal of Human Evolution *11:*321-333.

Bogin B. 1999a. Evolutionary Perspective on Human Growth. Annual Review of Anthropology *28:*109-153.

Bogin B. 1999b. Patterns of Human Growth Second Edition. Cambridge: Cambridge University Press.

Bogin B, and Smith H. 2000. Evolution of the Human Life Cycle. In: Stinson F, Bogin B, Huss-Ashmore R, and O'Rourke, editors. Human Biology: An Evolutionary and Biocultural Perspective. New York: Wiley-Liss. P 377-424.

Bogin B, Smith P, Silva M, and Loucky J. 2002. Rapid Change in Height and Body Proportions of Maya American Children. American Journal of Human Biology *14:*753-761.

Boos N, Weissbach S, and Rohrbach H (2002) Classification of Age-Related Changes in Lumbar Intervertebral Discs. Spine *27:*2631-2644.

Bourrin S, Ammann P, Bonjour J, and Rizzoli R. 2000. Dietary Protein Restriction Lowers Plasma Insulin-Like Growth Factor I (IGF-I), Impairs Cortical Bone Formation, and Induces Osteoblastic Resistance to IGF-I in Adult Female Rats. Endocrinology *141*:3149-3155.

Boyd D. 1996. Skeletal Correlates of Human Behaviors in the Americas. Journal of Archaeological Methods and Theory *3:*189-251.

Boyle W, Simonet W, and Lacey D. 2003. Osteoclast Differentiation and Activation. Nature *432:*337-342.

Brahm, H., Mallmin H, Michaelsson K, Strom H, and Ljunghall S. 1998. Relationship Between Bone Mass Measurements and Lifetime Physical Activity in a Swedish Population. Calcified Tissue International *62:*400- 412.

Braidwood R. 1960. The Agricultural Revolution. Scientific American. *203:*130-148.

Brandt K, Doherty M, and Lohmander L, editors. 2003. Osteoarthritis Second Edition. Oxford: Oxford University Press.

Breitburg E. 1992. Vertebrate Faunal Remains. In: Henderson AG, editor. Fort Ancient Cultural Dynamics in the Middle Ohio Valley. Madison: Prehistory Press. pp. 209-241.

Bressani, R. 1967. The Prevention of Protein Malnutrition. In: Turk KL, and Crowder LV, editors. Rural Development in Tropical Latin America. Ithaca: Cornell University Press. pp. 185-193.

Bridges P. 1989. Changes in Activities with the Shift to Agriculture in the Southeastern United States. Current Anthropology *30:*385-394.

Bridges P. 1995. Skeletal Biology and Behavior in Ancient Humans. Evolutionary Anthropology *4:*112-120.

Bridges PS, Blitz JH, and Solano MC. 2000. Changes in Long Bone Diaphyseal Strength with Horticultural Intensification in West-Central Illinois. American Journal of Physical Anthropology *112:*217-238.

Brock S, and Ruff C. 1988. Diachronic Patterns of Change in Structural Properties of the Femur in the Prehistoric American Southwest. American Journal of Physical Anthropology *75:*113-127.

Broida, Mary O'Neal. 1983. Maize in Kentucky Fort Ancient Diets: An Analysis of Carbon Isotope Ratios in Human Bone. Lexington: University of Kentucky.

Broida, Mary O'Neal. 1984. An Estimate of the Percents of Maize in the Diets of Two Kentucky Fort Ancient Villages. In: Pollak D, Hockensmith CD, and Sanders TN, editors. Late Prehistoric Research in Kentucky. Frankfort: Kentucky Heritage Council. pp. 68-83.

Buckland_Wright J, Messent E, Bingham C, Ward R, and Tonkin C. 2007. A 2 yr Longitudinal Ragiographic Study Examining the Effect of a Biphosphonate (Risedronate) upon Subchondral Bone Loss in Osteoarthritic Knee Patients. Rheumatology *46:*257-264.

Buikstra J, and Ubelaker D. 1994. Standards for Data Collection from Human Skeletal Remains. Fayettville: Arkansas Archaeological Survey Research Series No.44.

Burr D. 1992. Orthopedic Principles of Skeletal Growth, Modeling, and Remodeling. In: Carlson D, and Goldstein S, editors. Bone Biodynamics in Orthodontic and Orthopedic Treatment. Ann Arbor: Center for Human Growth and Development, The University of Michigan. pp. 15-49.

Burr D. 2002. Targeted and Nontargeted Remodeling. Bone *30:*2-4.

Burr D, Forwood M, Fyhrie D, et al. 1997. Bone Microdamage and Skeletal Fragility in Osteoporotic and Stress Fractures. Journal of Bone and Mineral Research *12:*6-15.

Burr D, Milgrom C, Fyhrie M, et al. 1996. In Vivo Measurement of Human Tibial Strains During Vigorous Activity. Bone *18:*405-410.

Burr D, Robling A, and Turner C. 2002. Effects of Biomechanical Stress on Bones in Animals. Bone *30:*781-786.

Burton M, and White D. 1984. Sexual Division of Labor in Agriculture. American Anthropologist *86:*568-583.

Byers S, Moore A, Byard R, and Fazzalari N. 2000. Quantitative Histomorphometric Analysis of the Human Growth Plate From Birth to Adolescence. Bone *27*:495-501.

Cameron N, and Demerath E. 2002. Critical Periods in Human Growth and Their Relationship to Diseases of Aging. Yearbook of Physical Anthropology *45:*159-184.

Cameron N, editor. 2002. Human Growth and Development. New York: Academic Press.

Carskadden J, and Morton J (2000) Fort Ancient in the Central Muskingum Valley of Eastern Ohio: A View from the Philo II Site. In: Genheimer RA, editor. Cultures Before Contact. Columbus: Ohio Archaeological Council. pp. 158-193.

Carter D, and Beaupre' G. 2001. Skeletal Function and Form: Mechanobiology of Skeletal Development, Aging, and Regeneration. Cambridge: Cambridge University Press.

Carter D. and Hayes, W. 1977. The Compressive Behavior of Bone as a Two-Phase Porous Structure. Journal of Bone and Joint Surgery *59A:*954-962.

Carter D, Orr T, and Fyhrie D. 1989. Relationships Between Loading History and Femoral Cancellous Bone Architecture. Journal of Biomechanics *22*:231-244.

Carter D, van der Meulen M, and Beaupre' G. 1996. Mechanical Factors in Bone Growth and Development. Bone *18:*5S-10S.

Cassidy C. 1984. Skeletal Evidence for Prehistoric Subsistence Adaptation in the Central Ohio River Valley. In: Cohen M, and Armelagos G, editors. Paleopathology at the Origins of Agriculture. New York: Academic Press. pp. 307-343.

Church F, and Nass Jr J. 2002. Central Ohio Valley During the Late Prehistoric Period. In: Hart J, and Rieth C, editors. Northeast Subsistence-Settlement Change: AD 700-1300. Albany: SUNY. pp. 11-42.

Cleaver O, and Melton D. 2003. Endothelial Signaling During Development. Nature Medicine *9:*661-668.

Clegg M, and Aiello L. 1999. A Comparison of the Nariokotome *Homo erectus* With Juveniles From a Modern Human Population. American Journal of Physical Anthropology *110:*81-93.

Cobb C. 2003. Mississippian Chiefdoms: How Complex? Annual Review of Anthropology *32:*63-84.

Cohen M. 1989. Health and the Rise of Civilization. New Haven: Yale University Press.

Cohen M. 1994. The Osteological Paradox Reconsidered. Current Anthropology *35:*629-637.

Cohen M, and Armelagos G, editors. 1984. Paleopathology at the Origins of Agriculture. New York: Academic Press.

Cohen M. 1977. The Food Crisis in Prehistory, Overpopulation and the Origins of Agriculture. New Haven: Yale University Press.

Conard A. 1985. A Preliminary Report on the Incinerator Site (33My57): Stable Carbon Isotope Ratios used in Dietary Reconstruction. M.A. Thesis. Cincinnati: University of Cincinnati.

Conard A. 1988. Analysis in Dietary Reconstruction. In: Heilman JM, Lileas MC, and Turnbow CA, editors. A History of 17 Years of Excavation and Reconstruction – A Chronicle of 12th Century Human Values and the Built Environment, vol. I. Dayton: Dayton Museum of Natural History. pp. 112-156.

Conroy G, and Vannier M. 1984. Noninvasive Three-Dimensional Computer Imaging of Matrix-Filled Fossil Skulls by High-Resolution Computed Tomography. Science *226:*456-458.

Cook R. 2004. Upper Mississippian Village Structure and Formation Spatial Analysis of Sunwatch, a Fort Ancient Site in Southwest Ohio. Ph.D. Dissertation. East Lansing: Michigan State University.

Cook R. 2007a. Single Component Sites with Long Sequences of Radiocarbon Dates: The SunWatch Site and Middle Fort Ancient Village Growth. American Antiquity *72*:439-460.

Cook R. 2007b. SunWatch: Fort Ancient Development in the Mississippian World. University of Alabama Press, Tuscaloosa (in press).

Cooke R, and Sunderhaus T. 1999. Cultural Interaction Within a Fort Ancient Village: Spatial Analysis of the Incinerator Site Ceramic Assemblage. Chicago: Society for American Archaeology.

Cooke C, and Zanker C. 2004. Energy Balance, Bone Turnover, and Skeletal Health in Physically Active Individuals. Medicine and Science in Sports and Exercise *36*:1372-1381.

Cooper C, Fall C, Egger R, Hobbs R, Eastell R, and Barker D. 1997. Growth in Infancy and Bone Mass in Later Life. Annals of Rheumatic Disorders *56:*17-21.

Cooper C, Javaid M, Taylor P, et al. 2002. The Fetal Origins of Osteoporotic Fracture. Calcified Tissue International *70:*391-394.

Count E. 1943. Growth Patterns of the Human Physique: An Approach to Kinetic Anthropometry. Human Biology *15:*1-32.

Cowan C. 1987. First Farmers of the Middle Ohio Valley: Fort Ancient Societies, A.D. 1000-1670. Cincinnati: Cincinnati Museum of Natural History.

Cruz-Orive L, Karlsson L, Larsen S, Wainschtein F. 1992. Characterizing Anisotropy: A New Concept. Micron and Microscopica Acta *23*:75-76.

Currey J, and Butler G. 1975. The Mechanical Properties of Bone Tissue in Children. Journal of Bone and Joint Surgery *57A:*810-814.

Dancey WS, editor. 1994. The First Discovery of America: Archaeological Evidence of the Early Inhabitants of the Ohio Area. Columbus: Ohio Archaeological Council. Dayton, Ohio: Dayton Museum of Natural History. p 299-313.

Demes B, Qin Y, Stern Jr JT, Larson SG, and Rubin CT. 2001. Patterns of Strain in the Macaque Tibia During Functional Activity. American Journal of Physical Anthropology *116:*257-265.

Dequeker J. 1997. Inverse Relationship of Interface Between Osteoporosis and Osteoarthritis. Journal of Rheumatology *24:*795-798.

Derevenski J. 1994. Where are the Children? Accessing Children in the Past. Archaeological Review from Cambridge *13:*7-20.

Derevenski J. 1997. Engendering Children, Engendering Archaeology. In: Moore J, and Scott E, editors. Invisible People and Processes. London: Leicester University Press. p 192-202.

Ding M, Dalstra M, Danielson C, Kabel C, Hvid I, and Linde F. 1997. Age Variation in the Properties of Human Tibial Trabecular Bone. Journal of Bone and Joint Surgery *79B:*995-1002.

Ding M, Odgaard A, and Hvid I. 2003. Changes in the Three-Dimensional Microstructure of Human Tibial Cancellous Bone in Early Osteoarthritis. Journal of Bone and Joint Surgery *85-B:*906-912.

Ding M, Odgaard A, Danielson CD, and Hvid I. 2002. Mutual associations among microstructural, physical and mechanical properties of human cancellous bone. Journal of Bone and Joint Surgery *84-B:*900-907.

Ding M. 2000. Age Variations in the Properties of Human Tibial Trabecular Bone and Cartilage. Acta Orthopaedica Scandinavica Supplementum No 292 71:1-45.

Donahue H, Chen Q, Jacobs C, Saunders M, and Yellowley C. 2003. Bone Cells and Mechanotransduction. In: Rosier R, and Evans C, editors. Molecular Biology in Orthopaedics. Rosemont: AAOS. pp. 179-190.

Drooker P. 1997. The View from Madisonville. Ann Arbor: University of Michigan.

Ducher G, and Bass S. 2007. Exercise During Growth: Compelling Evidence for the Primary Prevention of Osteoporosis. BoneKEy *June 4*:171-180.

Ducy P, et al. 2000. Leptin Inhibits Bone Formation Through a Hypothalamic Relay: a Central Control of Bone Mass. Cell *100:*197-207.

Ducy P, Schinke T, and Karenty G. 2000. The Osteoblast: A Sophisticated Fibroblast under Central Surveillance. Science *289:*1501-1504.

Dunn M. 1988. Burials- The Human Factor. In: Heilman J, Lileas M, and Turnbow C, editors. A History of 17 Years of Excavation and Reconstruction- A Chronicle of 12th Century Human Values and the Built Environment. Dayton: Dayton Museum of Natural History. pp. 299-313.

Dunnell R. 1972. The Prehistory of Fishtrap, Kentucky. New Haven: Yale University.

Duong L, and Rodan G. 2001. Regulation of Osteoclasts Formation and Function. Reviews in Endocrine and Metabolic Disorders *2*:95-104.

Duppe H, Cooper C, Gardsell P, and Johnell O. 1997. The Relationship Between Childhood Growth, Bone Mass, and Muscle Strength in Male and Female Adolescents. Calcified Tissue International *60:*405- 409.

ESB. 1978. Inaugural Document for the Formation of the European Society of Biomechanics. ESB Archives.

Essenpreis P. 1978. Fort Ancient Settlement: Differential Response at Mississippian--Late Woodland Interface. In: Smith B, editor. Mississippian Settlement Patterns. New York: Academic Press. pp 141-167.

Essenpreis P. 1982. The Anderson Village Site: Redefining the Anderson Phase of the Fort Ancient Tradition of the Middle Ohio Valley. Cambridge: Harvard University.

Essenpreis P. 1988. An Introduction to the Fort Ancient Cultural Complexes of the Middle Ohio Valley. In: Heilman JM, Lileas MC, and Turnbow CA, editors. A History of 17 Years of Excavation and Reconstruction- A Chronicle of 12th Century Human Values and the Built Environment. Dayton: Dayton Museum of Natural History.

Evans A. 2006. The NIH MRI Study of Normal Brain Development. Neuoimage *30*:184-202.

Evans-Eargle S. 1998. Mortuary Data as Indicators of Social Organization at the Incinerator Site (33MY57). Unpublished M.A. thesis. Columbia: University of South Carolina.

Eveleth P, and Tanner J. 1990. Worldwide Variation in Human Growth. Cambridge: Cambridge University Press.

Fajardo R, Muller R, Ketcham R, and Colbert M. 2005. Allometry of Anthropoid Femoral Neck Architecture using 3D MicroCT. American Journal of Physical Anthropology Suppl. *40:*101.

Fajardo RJ, and Muller R. 2001. Three-Dimensional Analysis of Nonhuman Primate Trabecular Architecture Using Micro-computed Tomography. American Journal of Physical Anthropology *115:*327-336.

Fajardo RJ, Ryan TM, and Kappelman J. 2002. Assessing the Accuracy of High-resolution X-ray Computed Tomography of Primate Trabecular Bone by Comparisons with Histological Sections. American Journal of Physical Anthropology *118:*1-10.

Farrow D. 1986. A Study of Monongahela Subsistence Patterns Based on Mass Spectrometric Analysis. Midcontinental Journal of Archaeology *11(2):*153-179.

Fazzalari N, Moore A, Byers S, and Byard R. 1997. Quantitative Analysis of Trabecular Morphogenesis in the Human Costochondral Junction During the Postnatal Period in Normal Subjects. Anatomical Record *248A*:1-12.

Feldkamp L, Goldstein S, Parfitt A, et al. 1989. The Direct Examination of Three Dimensional Bone Architecture in vitro by Computed Tomography. Journal of Bone and Mineral Research *4:*3-11.

Felts W. 1954. The Prenatal Development of the Human Femur. American Journal of Anatomy *94:*1-44.

Finch C, and Rose M. 1995. Hormones and the Physiological Architecture of Life History Evolution. The Quarterly Review of Biology *70:*1-52.

Fitting J, and Cleland C. 1969. Late Prehistoric Settlement Patterns in the Upper Great Lakes. Ethnohistory *16:*289-302.

Fitzgerald C. 1998. Do Enamel Microstructures Have Regular Time Dependency? Conclusions from the Literature and a Large-Scale Study. Journal of Human Evolution *35:*371-386.

Fitzgerald C, and Rose J. 2000. Reading Between the Lines: Dental Development and Subadult Age Assessment Using the Microstructural Growth Markers of Teeth. In: Katzenberg M, and Saunders S, editors. Biological Anthropology of the Human Skeleton. New York: Wiley-Liss. pp. 163-186.

Flannery K. 1973. The Origins of Agriculture. Annual Review of Anthropology *2:*271-310.

Forwood M, and Burr D. 1993. Physical Activity and Bone Mass: Exercises in Futility? Bone and Mineral *21:*89-112.

Forwood M, and Turner C. 1995. Skeletal Adaptations to Mechanical Usage: Results From Tibial Loading in Rats. Bone *17:*197S-205S.

Forwood M, Baxter-Jones A, Beck T, et al. 2006. Physical Activity and Strength of the Femoral Neck During the Adolescent Growth Spurt: A Longitudinal Analysis. Bone *38:*576-583.

Fowler M. 1969. Middle Mississippian Agricultural Fields. American Antiquity *34:*365-375.

Francis C. 1939. Growth of the Human Tibia. American Journal of Physical Anthropology *25:*323-331.

Freeman M, and Pinskerova V. 2005. The Movement of the Normal Tibio-Femoral Joint. Journal of Biomechanics *38:*197-208.

Frigge M, Hoaglin D, and Iglewicz B. 1989. Some Implementations of the Boxplot. The American Statistician *43:*50-54.

Fritton J. Myers E, Wright T, and van der Meulen, M. 2005. Loading Induces Site-Specific Increases in Mineral Content Assessed by Microcomputed Tomography of the Mouse Tibia. Bone *36*: 1030-1038

Frost H. 1969. Tetracycline-Based Histological Analysis of Bone Remodeling. Calcified Tissue Research *3:*211-237.

Frost H. 1986. Intermediary Organization of the Skeleton. Boca Raton: CRC Press.

Frost H. 1987. Bone "mass" and the "mechanostat": A Proposal. Anatomical Record *219:*1-9.

Frost H. 1988. Vital Biomechanics: Proposed General Concepts for Skeletal Adaptations to Mechanical Usage. Calcified Tissue International *42:*145-156.

Frost H. 1989. Skeletal Structural Adaptations to Mechanical Usage (SATMU): 2. Redefining Wolff's Law: The Remodeling Problem. Anatomical Record *226:*414-422.

Frost H. 2003. On Changing Views About Age-Related Bone Loss. In: Agarwal S, and Stout S, editors. Bone Loss and Osteoporosis: An Anthropological Perspective. New York: Kluwer Academic. pp. 19-32.

Frost H, and Jee W. 1994a. Perspectives: A Vital Biomechanical Model of the Endochondral Ossification Mechanism. The Anatomical Record *240:*435-446.

Frost H, and Jee W. 1994b. Perspectives: Applications of a Biomechanical Model of the Endochondral Ossification Mechanism. The Anatomical Record *240:*447-455.

Frost HM. 1998. Perspectives: A Proposed General Model of the "Mechanostat" (Suggestions from a New Skeletal-Biological Paradigm). Anatomical Record *244:*139-147.

Fyhrie D, and Kimura J. 1999. Cancellous Bone Biomechanics. Journal of Biomechanics *32:*1139-1148.

Garn S. 1980. Human Growth. Annual Review of Anthropology *9:*275-292.

Gartley R. 1977. Ceramics from the Richards Site and the Philo Phase of the Fort the Fort Ancient Tradition. In: Carskadden J, and Morton J, editors. The Richards Site and the Philo Phase of the Fort Ancient Tradition. Zanesville: Muskingum Valley Archaeological Survey. pp. 17-38.

Gartley R, Carskadden J, and Morton J. 1976. Ceramics from the Philo II Site. Pennsylvania Archaeologist *46(1-2):*55-75.

Genheimer R, editor. 2000. Cultures Before Contact: The Late Prehistory of Ohio and Surrounding Regions. Columbus: Ohio Archaeological Council, Inc.

Genoves S. 1967. Proportionality of the Long Bones and Their Relation to Stature Among Mesoamericans. American Journal of Physical Anthropology *26:*67-78.

Gibson L. 1985. The Mechanical behavior of Cancellous Bone. Journal of Biomechanics *18*: 317-328.

Giesen M, and Sciulli P. 1988. Long Bone Growth in a Late Archaic Skeletal Sample. Paper presented at the 57th Annual Meeting of the American Association of Physical Anthropologists.

Giesen M. 1992. Late Prehistoric Populations in the Ohio Area: Biological Affinities and Stress Indicators. Ph.D. Dissertation.

Gillman M. 2002. Epidemiological Challenges in Studying the Fetal Origins of Adult Chronic Disease. International Journal of Epidemiology *31:*294-299.

Gillman M. 2005. Developmental Origins of Health and Disease. The New England Journal of Medicine *353:*1848-1850.

Gindhart P. 1973. Growth Standards for the Tibia and Radius in Children Aged One Month through Eighteen Years. American Journal of Physical Anthropology *39:*41-48.

Glasbey C, and Horgan G. 1995. Image Analysis for the Biological Sciences. New York: Wiley.

Glorieux F, Travers R, Taylor A, et al. 2000. Normative Data for Iliac Bone Histomorphometry in Growing Children. Bone *26*:103-109.

Gluckman P, and Hanson M. 2004. Developmental Origins of Disease Paradigm: A Mechanistic and Evolutionary Perspective. Pediatric Research *56:*311-317.

Gluckman P, Hanson M, and Spences H. 2005. Predictive Adaptive Responses and Human Evolution. Trends in Ecology and Evolution *20:*527-533.

Godfrey K, Walker-Bone K, Robinson S, et al. 2001. Neonatal Bone Mass: Influence of Parental Birthweight, Maternal Smoking, Body Composition, and Activity During Pregnancy. Journal of Bone and Mineral Research *16:*1694-1703.

Gogtay N, Giedd J, Lisk L, et al. 2004. Dynamic Mapping of Human Cortical Development During Childhood Through Early Adulthood. Proceedings of the National Academy of Sciences of the United States of America *101*:8174-8179.

Goldstein S, Mathews L, Kuhn J, and Hollister S. 1991. Trabecular Bone Remodeling: An Experimental Model. Journal of Biomechanics *24S:*135-150.

Goldstein S, Wilson D, Sonstegard D, and Mathews L. 1983. The Mechanical Properties of Human Tibial Trabecular Bone as a Function of Metaphyseal Location. Journal of Biomechanics *16:*965-969.

Goodman A. 1993. On the Interpretation of Health from Skeletal Remains. Current Anthropology *34:*281-288.

Goodman A, and Armelagos G. 1989. Infant and Childhood Morbidity and Mortality Risks in Archaeological Populations. World Archaeology *21:*225-243.

Goss A. 1988. Astronomical Alignments at the Incinerator Site. In: Heilman JM, Lileas MC, and Turnbow CA, editors. A History of 17 Years of Excavation and Reconstruction – A Chronicle of 12th Century Human Values and the Built Environment, vol. I. Dayton: Dayton Museum of Natural History. pp. 314-355.

Gowland R, and Knusel C, editors. 2006. Social Archaeology of Funerary Remains. Oxford: Oxbow.

Graybill J. 1980. Marietta Works, Ohio, and the Eastern Periphery of Fort Ancient. Pennsylvania Archaeologist *50(1-2):*51-60.

Graybill J. 1981. The Eastern Periphery of Fort Ancient (A.D. 1050-1650): A Diachronic Approach to Settlement Variability. Seattle: University of Washington.

Graybill J. 1986. Fort Ancient – East: Origins, Change, and External Correlations. Columbus: Midwestern Archaeological Conference.

Gremillion K. 2004. Seed Processing and the Origins of Food production in Eastern North America. American Antiquity *69:* 215-233.

Greulich W, and Pyle S. 1959. Radiographic Atlas of Skeletal Development of the hand and Wrist. Stanford: Stanford University Press.

Griffin J. 1943. The Fort Ancient Aspect: Its Cultural and Chronological Position in Mississippi Valley Archaeology. Ann Arbor: University of Michigan Press.

Griffin J. 1967. Eastern North American Archaeology: A Summary. Science *156:*175-191.

Griffin J. 1978. Late Prehistory of the Ohio Valley. In: Trigger BG, editor. Northeast. Handbook of North American Indians. Washington: Smithsonian Institution. pp. 547-559.

Griffin J. 1992. Fort Ancient Has No Class: The Absence of an Elite Group in Mississippian Societies in the Central Ohio Valley. In: Barker A, and Pauketat T, editors. Lords of the Southeast: Social Inequality and the Native Elites of Southeastern North America. Washington: American Anthropological Association. pp. 53-59.

Grinnell F. 2000. Fibroblast-Collagen-Matrix Contraction: Growth-Factor Signaling and Mechanical Loading. Trends in Cell Biology *10:*362-365.

Grooms T. 1999. What's In a Pit?: An Imitative Experimental Study of Fort Ancient Storage. Cincinnati: University of Cincinnati.

Gruber H, and Rimoin D. 1989. Quantitative Histology of Cartilage Cell Columns in the Human Costochondral Junction: Findings in Newborn and pediatric Subjects. Pediatric Research *25*:202-204.

Halekoh U, and Vach W. 2004. A Bayesian Approach to Seriation Problems in Archaeology. Computational Statistics and Data Analysis *45:*651-673.

Hales C, and Barker D. 2001. The Thrifty Phenotype Hypothesis. British Medical Bulletin *60:*5-20.

Hall B. 2005. Bones and Cartilage: Developmental and Evolutionary Skeletal Biology. San Diego: Elsevier.

Hallemans A, De Clereq D, and Aerts P. 2005. 3D Joint Dynamics of Walking in Toddlers: A Cross-Sectional Study Spanning the First Rapid Development Phase of Walking. Gait and Posture *22:*107-118.

Hallgrimson B, K W, and Hall B. 2002. Canalization, Developmental Stability, and Morphological Integration in Primate Limbs. American Journal of Physical Anthropology *35S:*131-158.

Hallgrimsson B, and Hall B, editors. 2005. Variation: A Central Concept in Biology. Burlington: Elsevier Academic Press.

Hara T, Tanck E, Homminga J, Huiskes R. 2002 The Influence of Microcomputed Tomography Threshold Variations on the Assessment of Structural and Mechanical Trabecular Bone Properties. Bone *31:*107-109.

Harada S, and Rodan G. 2003. Control of Osteoblast Function and Regulation of Bone Mass. Nature *423:*349-355.

Hawkes K, and Paine R, editors. 2006. The Evolution of Human Life History. Santa Fe: School of American Research Press.

Hayes W, Swenson L, and Schurman D. 1978. Axisymmetric Finite Element Analysis of the lateral Tibial Plateau. Journal of Biomechanics *11:*21-33.

Heilman J, and Hoefer R. 1981. Astronomical Alignments in a Fort Ancient Settlement at the Incinerator Site in Dayton, Ohio. Philadelphia: Society for American Archaeology.

Heilman J, Lileas M, and Turnbow C, editors. 1988. A History of 17 Years of Excavation and Reconstruction - A Chronicle of 12th Century Human Values and the Built Environment. Dayton: Dayton Museum of Natural History.

Heller M, Taylor W, Perka C, and Duda G. 2003. The Influence of Alignment on the Musculo-Skeletal Loading Conditions at the Knee. Archives of Surgery *388*:291-297.

Hemphill B, and Larsen C, editors. 1999. Prehistoric Lifeways in the Great Basin Wetlands. Salt Lake City: University of Utah Press.

Hendee W. 1983. The Physical Principles of Computed Tomography. Boston: Little, Brown, and Co.

Henderson A, editor. 1992. Fort Ancient Cultural Dynamics in the Middle Ohio Valley. Madison: Prehistory Press.

Henderson A, editor. 1992. Introduction. In Fort Ancient Cultural Dynamics in the Middle Ohio Valley. Madison: Prehistory Press. pp. 1-8.

Henderson A. 1998. Middle Fort Ancient Villages and Organizational Complexity in Central Kentucky. Lexington: University of Kentucky.

Henderson A, and Pollack D. 2001. Fort Ancient. In: Peregrine PN, and Ember M, editors. Encyclopedia of Prehistory, vol. 6. New York: Kluwer Academic/Plenum Publishers. pp. 174-194.

Henderson A, Pollack D, and Turnbow C. 1992. Chronology and Cultural Patterns. In: Henderson A, editor. Fort Ancient Cultural Dynamics in the Middle Ohio Valley. Madison: Prehistory Press. pp. 253-280.

Henderson A, and Turnbow C. 1992. Previous Fort Ancient Chronologies. In: Henderson A, editor. Fort Ancient Cultural Dynamics in the Middle Ohio Valley. Madison: Prehistory Press.

Hewlett B, and Lamb M, editors. 2005. Hunter-Gatherer Childhoods. New Brunswick: Transaction.

Hildebrand T, Laib A, Muller R, Dequeker J, and Ruegsegger P. 1999. Direct Three-Dimensional Morphometric Analysis of Human Cancellous Bone Microstructural Data from Spine, Femur, Iliac Crest, and Calcaneus. Journal of Bone and Mineral Research *14:*1167-1174.

Hillson S. 1992. Studies of Growth in Dental Tissues. Journal of Human Ecology *2 (special issue):*7-24.

Hillson S. 1996. Dental Anthropology. Cambridge: Cambridge University Press.

Hind K, and Burrows M. 2007. Weight-bearing Exercise and Bone Mineral Accrual in Children and Adolescents: A Review of Controlled Trials. Bone *40*:14-27.

Hoerr N, Pyle, S, and Francis C. 1962, Radiographic Atlas of Skeletal Development of the Foot and Ankle: A Standard of Reference. Springfield: C.C. Thomas.

Holliday T, and Falsetti A. 1995. Lower Limb Length of European Early Modern Humans in Relation to Mobility and Climate. Journal of Human Evolution *29:*141-153.

Holliday T, and Ruff C. 2001. Relative Variation in Human Proximal and Distal Limb Segment Lengths. American Journal of Physical Anthropology *116*:26-33.

Holt B. 2003. Mobility in Upper Paleolithic and Mesolithic Europe: Evidence From the Lower Limb. American Journal of Physical Anthropology *122:*200-215.

Hooton E, and Willoughby C. 1920. Indian Village Site and Cemetery near Madisonville, Ohio. Papers of the Peabody Museum of American Archaeology and Ethnology. VIII. Cambridge: Harvard University.

Hoppa R, and FitzGerald C, editors. 1999. Human Growth in the Past: Studies from Bones and Teeth. Cambridge: Cambridge University Press.

Hoppa R, and Vaupel J, editors. 2002. Paleodemography: Age Distributions from Skeletal Samples. Cambridge: Cambridge University Press.

Hounsfield G. 1973. Computerized Transverse Axial Scanning (tomography): Part I. Description of System. British Journal of Radiology *46*: 1016-1022.

Howell N. 1986. Demographic Anthropology. Annual Review of Anthropology *15:*219-246.

Hrdlička A. 1896. Study of the Normal Tibia. American Anthropologist *11:*307-312.

Hudson C. 1976. The Southeastern Indians. Knoxville: University of Tennessee Press.

Huiskes R. 2000. If Bone is the Answer, Then What is the Question? Journal of Anatomy *197:*145-156.

Huiskes R, Ruimerman R, Van Lenthe G, and Janssen J. 1998. Indirect Osteoclast-Osteoblast Coupling Through Mechanical Stress Relates Trabecular Morphogenesis and Adaptation to Bone Turn-Over. Bone *23*.

Huiskes R, Rulmerman R, van Lenthe G, and Jannsen J. 2000. Effects of mechanical forces on maintenance and adaptation of form in trabecular bone. Nature *405:*704-706.

Hummert J. 1983. Cortical Bone Growth and Dietary Stress Among Subadults From Nubia's Batn El Hajar. American Journal of Physical Anthropology *62:*167-176.

Hurwitz D, Sumner D, Andriacchii T, and Sugar D. 1998. Dynamic Knee Loads During Gait Predict Proximal Tibial Bone Distribution. Journal of Biomechanics *31:*423-430.

Hutchinson D, Larsen C, Schoeninger M, and Norr L. 1998. Regional Variation in the Pattern of Maize Adoption and Use in Florida and Georgia. American Antiquity *63:*397-416.

Jackes M. 2000. Building the Bases for Paleodemographic Analysis: Adult Age Determination. In M Katzenberg and S Saunders (eds.): Biological Anthropology of the Human Skeleton. New York: Wiley-Liss.

Jackes M, Lubell D, and Meiklejohn C. 1997. Healthy but Mortal: Human Biology and the First Farmers of Western Europe. Antiquity *71:*639-659.

Jacobs C. 2000. The Mechanobiology of Cancellous Bone Structural Adaptation. Journal of Rehabilitation Research and Development *37:*1-16.

Jacobs C, and Eckstein F. 1997. Computer Simulation of Subchondral Bone Adaptation to Mechanical Loading in an Incongruous Joint. Anatomical Record *249:*317-326.

Jacobs C, Simo JC, Beaupre G, and Carter D. 1997. Adaptive Bone Remodeling Incorporating Simultaneous Density and Anisotropy Considerations. Journal of Biomechanics *30:*603-613.

Jacobs K. 1993. Human Postcranial Variation in the Ukrainian Mesolithic-Neolithic. Current Anthropology *34:*311-324.

Janz K, Burns T, Levy S, et al. 2004. Everyday Activity Predicts Bone Geometry in Children: The Iowa Bone Development Study. Medicine and Science in Sports and Exercise *36:*1124-1131.

Javaid M, and Cooper C. 2002. Prenatal and Childhood Influences on Osteoporosis. Best Practice and Research Clinical Endocrinology and Metabolism *16:*349-367.

Jee W. 2001. Integrated Bone Tissue Physiology: Anatomy and Physiology. In: Cowin S, editor. Bone Biomechanics Handbook, Second Edition. Boca Raton: CRC Press. pp. 1-68.

Jee W, and Li X. 1990. Adaptation of Cancellous Bone Overloading in the Adult Rat: A Single Photon Absorptiometry and Histomorphometry Study. Anatomical Record *227:*418-426.

Jee W, Li X, and Schaffer M. 1991. Adaptation of Diaphyseal Structure With Aging and Increased Mechanical Usage in the Adult Rat: A Histomorphometrical and Biomechanical Study. Anatomical Record *230:*332-338.

Jelliffe D. 1969. The Secotrant- A Possible New Age Category in Early Childhood. Journal of Pediatrics *74:*808-810.

Johnson A, and Earle T. 2000. The Evolution of Human Societies: From Foraging Group to Agrarian State, Second Edition. Stanford: Stanford University Press.

Johnson F. 1961. Sequence of Epiphyseal Union in a Prehistoric Kentucky Population from Indian Knoll. Human Biology *33:*66-81.

Johnston F, and Zimmer L. 1989. Assessment of Growth and Age in the Immature Skeleton. In: Iscan M, and Kennedy K, editors. Reconstruction of Life From the Skeleton. New York: Alan R. Liss. pp. 11-21.

Jones D, and German R. 2005. Variation in Ontogeny. In: Hallgrimsson B, and Hall B, editors. Variation: A Central Concept in Biology. Amsterdam: Elsevier. pp. 71-84.

Jones H, Priest J, Tichenor C, and Nagel D. 1977. Humeral Hypertrophy in Response to Exercise. Journal of Bone and Joint Surgery *59A:*204-208.

Jurmain R. 1999. Stories from the Skeleton: Behavioral Reconstruction in Human Osteology. Amsterdam: Gordon and Breach.

Kamp K. 1998. Social Hierarchy and Burial Treatments: A Comparative Assessment. Cross-Cultural Research *32:*79-115.

Kamp K. 2001. Where Have All the Children Gone?: The Archaeology of Childhood. Journal of Archaeological Method and Theory *8:*1-34.

Kamp K, Timmerman N, Lind G, Graybill J, and Natowaky I. 1999. Discovering Childhood: Using Fingerprints to Find Children in the Archaeological Record. American Antiquity *64:*309-315.

Kato Y, Shimazu A, Iwamoto M, et al. 1990. Role of 1,25-Dihydroxycholecalciferol in Growth-plate Cartilage: Inhibition of Terminal Differentiation of Chondrocytes in Vitro and in Vivo. Proceedings of the National Academy of Science USA *87:*6522-6526.

Katzenberg M, Schwarcz H, Knyf M, and Melbye F. 1995. Stable Isotope Evidence for Maize Horticulture and Paleodiet in Southern Ontario, Canada. American Antiquity *60(2):*335-350.

Keaveny T, Morgan E, Niebur G, and Yeh O. 2001. Biomechanics of Trabecular Bone. Annual review of Biomedical Engineering *3:*307-333.

Kelly J. 1990a. Range Site Community Patterns and the Mississippian Emergence. In: Smith BD, editor. The Mississippian Emergence. Washington: Smithsonian Institution Press. pp. 67-112.

Kelly J. 1990b. The Emergence of Mississippian Culture in the American Bottom. In: Smith BD, editor. The Mississippian Emergence. Washington: Smithsonian Institution Press. pp. 113-152.

Kelly J. 1998. The Third Culture. Science *279:*992-993.

Kelly R. 1995. The Foraging Spectrum: Diversity in Hunter-Gatherer Lifeways. Washington: Smithsonian Institution Press.

Kember N, and Sissons H. 1976. Quantitative Histology of the Human Growth Plate. Journal of Bone and Joint Surgery *58B*:426-435.

Kennedy K. 1989. Skeletal Markers of Occupational Stress. In: Iscan M, and Kennedy K, editors. Reconstruction of Life From the Human Skeleton. New York: Alan R. Liss. pp. 128-160.

Kennedy K. 1998. Markers of Occupational Stress: Conspectus and Prognosis of Research. International Journal of Osteoarchaeology *8:*305-310.

Kennedy W. 2000. Interpreting Fort Ancient Settlement Variability. Kent: Kent State University.

Ketcham R, and Carlson W. 2001. Acquisition, Optimization and Interpretation of X-ray Computed Tomographic Imagery: Applications to the Geosciences. Computers and Geosciences *27:*381-400.

Ketcham R, and Ryan T. 2004. Quantification and Visualization of Anisotropy in Trabecular Bone. Journal of Microscopy *213:*158-171.

Ketcham R, Ryan T, Maga M, and Gordon A. 2002. Quantification of Anisotropy in Trabecular Bone Fabrics. American Journal of Physical Anthropology *34 (Suppl):*93-94.

Kneissel M, Roschager P, Steiner W, et al. 1997. Cancellous Bone Structure in the Growing and Aging Lumbar Spine in a Historic Nubian Population. Calcified Tissue International *61:*95-100.

Knick S. 1976. Paleopathology of North American Indians at Incinerator Site, Fort Ancient Culture, Montgomery County, Ohio. St Louis: American Association of Physical Anthropologists.

Knick S. 1977. Paleopathological Evidence of Familial Relationships in a Prehistoric Population. Seattle: American Association of Physical Anthropologists.

Knusel C. 2000. Bone Adaptation and Its Relationship to Physical Activity in the Past. In: Cox M, and Mays S, editors. Human Osteology in Archaeology and Forensic Science. London: Greenwich Media. pp. 381-401.

Koletzko B, Dodds P, Akerblom H, and Ashwell M, editors. 2005. Early Nutrition and Its Later Consequences: New Opportunities. Berlin: Springer.

Komistek R, Kane T, Mahfouz M, Ochoa J, and Dennis D. 2005. Knee Mechanics: A Review of Past and Present Techniques to Determine In Vivo Loads. Journal of Biomechanics *38:*215-228.

Kontulainen S, MacDonald H, Khan K, and McKay H. 2005. Examining Bone Surfaces Across Puberty. Journal of Bone and Mineral Research *20:*1202-1207.

Kontulainen S, Sievanen H, Kannus P, Pasanen M, and Vuori I. 2002. Effect of Long-Term Impact-Loading on Mass, Size, and Estimated Strength of Humerus and Radius of Female Racquet-Sports Players: A Pheripheral Quantitative Computed Tomography Study Between Young and Old Starters and Controls. Journal of Bone and Mineral Research *17*:2281-2289.

Kopperdahl D, and Keaveny T. 1998. Yield Strain Behavior of Trabecular Bone. Journal of Biomechanics *31:*601-608.

Korstjens C, Geraets W, Ginkel F, et al. 1995. Longitudinal Analysis of Radiographic Trabecular Pattern by Image Processing. Bone *17:*527-532.

Kosa F. 1989. Age Estimation From the Fetal Skeleton. In: Iscan M, editor. Age Markers in the Human Skeleton. Springfield: Charles C. Thomas. pp. 21-54.

Kothari M, Keaveny TM, Lin JC, Newitt DC, Genant HK, and Majumdar S. 1998. Impact of Spatial Resolution on the Prediction of Trabecular Architecture Parameters. Bone *22:*437-443.

Kozarek SE, Dancey WS, Minichillo T, and Pape W. 1994. Phase IV Data Recovery of an Early Holocene Lithic Cluster in North Central Ohio. In: Dancey WS, editor. The First Discovery of America. Columbus: Ohio Archaeological Council. pp. 157-166.

Kramer K. 2005. Maya Children: Helpers at the Farm. Cambridge: Harvard University Press.

Kriska AM, Sandler RB, Cauley JA, et al. 1988. The Assessment of Historical Physical Activity and Its Relation to Adult Bone Parameters. American Journal of Epidemiology *127:*1053-1063.

Lai L, and Mitchell J. 2005. Indian Hedgehog: Its Roles and Regulation in Endochondral Bone Development. Journal of Cellular Biochemistry *96:*1163-1173.

Lai Y, Qin L, Yeung H, Lee K, and Chan K. 2005. Regional Differences in Trabecular BMD and Micro-Architecture of Weight-bearing Bone Under Habitual Gait Loading- A pQCT and MicroCT Study in Human Cadavers. Bone *37:*274-282.

Laib A, and Ruegsegger P. 1999. Calibration of Trabecular Bone Structure Measurements of In Vivo Three-Dimensional Peripheral Quantitative Computed Tomography With 28-um-Resolution Microcomputed Tomography. Bone *24:*35-39.

Lallo J. 1979. Disease and Mortality at the Anderson Village Site. Ohio Journal of Science *79:*256-261.

Lambert P, editor. 2000. Bioarchaeological Studies of Life in the Age of Agriculture. Tuscaloosa: University of Alabama Press.

Lampl M, and Johnston F. 1996. Problems in the Aging of Skeletal Juveniles: Perspectives From Maturation Assessments of Living Children. American Journal of Physical Anthropology *101:*345-355.

Lanou A, Berkow S, and Barnard N. 2005. Calcium, Dairy Products, and Bone Health in Children and Young Adults: A Reevaluation of the Evidence. Pediatrics *115*:736-743.

Lanyon L. 1982. Mechanical Function and Bone Remodeling. In: Sumner-Smith G, editor. Bone in Clinical Orthopaedics. Philadelphia: Saunders. pp. 273-304.

Lanyon L. 1996. Using Functional Loading to Influence Bone Mass and Architecture Objectives, Mechanisms and Relationship with Estrogen of the Mechanically Adaptive Process in Bone. Bone *18:*37S-43S.

Larsen C. 1995. Biological Changes in Human Populations with Agriculture. Annual Review of Anthropology *24:*185-213.

Larsen C. 1997. Bioarchaeology: Interpreting Behavior from the Human Skeleton. Cambridge: Cambridge University Press.

Larsen C. 2002. Bioarchaeology: The Lives and Lifestyles of Past People. Journal of Archaeological Research *10:*119-166.

Larsen C, and Kelly R. 1995. Bioarchaeology of the Stillwater Marsh: Prehistoric Human Adaptation in the Western Great Basin. New York: Anthropological Papers of the American Museum of Natural History.

Larsen C, editor. 2001. Bioarchaeology of Spanish Florida: The Impact of Colonialism. Gainesville: University Press of Florida.

Larsen C, Kelley R, Ruff C, Schoeninger M, and Hutchinson D. 1996. Biobehavioral Adaptations in the Western Great Basin. In: Reitz E, Newsom L, and Scudder S, editors. Case Studies in Environmental Archaeology. New York: Plenum Press. pp. 149-174.

Layton M, Goldstein S, Goulet R, et al. 1988. Examination of Subchondral Bone Architecture in Experimental Osteoarthritis by Microscopic Computed Axial Tomography. Arthritis and Rheumatism *31:*1400-5.

Ledley R, DiChiro G, Luessenhop A, and Twigg H. 1974. Computerized Transaxial X-ray Tomography of the Human Body. Science *186:*207-212.

Legge S. 2005. Estimating Puberty in a Prehistoric Skeletal Collection. Annals of Human Biology *32:*383-389.

Lepper BT. 1988. Early Paleo-Indian Foragers of Midcontinental North America. North American Archaeologist *9*.

Lerner R. 1984. On the Nature of Human Plasticity. Cambridge: Cambridge University Press.

Leung C, and Lam F. 1996. Performance Analysis for a Class of Iterative Image Thresholding Algorithms. Pattern Recognition *29:*1523-1530.

Lewis A, and Garn S. 1960. The Relationship Between Tooth Formation and Other Maturational Factors. Angle Orthodontist *30:*70-77.

Li B, and Aspden R. 1997. Composition and Mechanical Properties of Cancellous Bone From The Femoral Head of Patients With Osteoporosis or Osteoarthritis. Journal of Bone and Mineral Research *12:*641-651.

Lieberman D. 1997. Making Behavioral and Phylogenetic Inferences From Hominid Fossils: Considering the Developmental Influence of Mechanical Forces. Annual Review of Anthropology *26:*185-210.

Lieberman D, Devlin M, and Pearson O. 2001. Articular Area Responses to Mechanical Loading: Effects of Exercise, Age, and Skeletal Location. American Journal of Physical Anthropology *116:*266-277.

Lieberman D, Polk J, and Demes B. 2004. Predicting Long Bone Loading From Cross-Sectional Geometry. American Journal of Physical Anthropology *123:*156-171.

Lileas, MC. 1988a. Early Development of the Incinerator Site. In: Heilman JM, Lileas MC, and Turnbow CA, editors. A History of 17 Years of Excavation and Reconstruction: A Chronicle of 12th Century Human Values and the Built Environment. Dayton, Ohio: Dayton Museum of Natural History. pp. 25-35.

Lileas, MC. 1988b. History of the Dayton Museum of Natural History's Involvement with the Incinerator Site. In: Heilman JM, Lileas MC, and Turnbow CA, editors. A History of 17 Years of Excavation and Reconstruction: A Chronicle of 12th Century Human Values and the Built Environment. Dayton, Ohio: Dayton Museum of Natural History. pp. 36-54.

Lillehammer G. 1989. A Child is Born. The Child's World in an Archaeological Perspective. Norwegian Archaeological Review *22:*89-105.

Link T, Majumdar S, Lin J, Newitt D, et al. 1998. A Comparative Study of Trabecular Bone Properties in the Spine and Femur Using High-Resolution MRI and CT. Journal of Bone and Mineral Research *13:*122-132.

Liversidge H. 1994. Accuracy of Age Estimation from Developing Teeth of a Population of Known Age (0-5.4 years). International Journal of Osteoarchaeology *4:*37-45.

Lloyd T, Beck T, Lin H, et al. 2002. Modifiable Determinants of Bone Status in Young Women. Bone *30:*416-421.

Lovejoy C, and Heiple K. 1970. The Blain Mound. In: Prufer O, and Shane O, editors. Blain Village and the Fort Ancient Tradition in Ohio. Kent, Ohio: Kent State University. pp. 151-184.

Lovejoy C, and Heiple K. 1981. The Analysis of Fractures in Skeletal Populations with an Example from the Libben Site, Ottawa, Ohio. American Journal of Physical Anthropology *55:*529-541.

Lovejoy C, Burstein A, and Heiple K. 1976. The Biomechanical Analysis of Bone Strength: A Method and Its Application to Platycnemia. American Journal of Physical Anthropology *44:*489-506.

Lovejoy C, Cohn M, and White T. 1999. Morphological Analysis of the Mammalian Postcranium: A Developmental Perspective. Proceedings of the National Academy of Sciences of the United States of America *96:*13247-13252.

Lovejoy C, McCollum M, Reno P, and Rosenman B. 2003. Developmental Biology and Human Evolution. Annual Review of Anthropology *32:*85-109.

Lovejoy C, Meindl R, Mensforth R, and Barton T. 1985. Multifactorial Determination of Skeletal Age at Death: A Method and Blind Tests of Its Accuracy. American Journal of Physical Anthropology *68:*1-14.

Lovejoy C, Meindl R, Pryzbeck T, et al. 1977. Paleodemography of the Libben Site, Ottawa County, Ohio. Science *198:*291-293.

Lovejoy C, Russell K, and Harrison M. 1990. Long Bone Growth Velocity in the Libben Population. American Journal of Human Biology *2:*533-542.

Lucy S. 1994. Children in Early Medieval Cemeteries. Archaeological Review from Cambridge *13:*21-34.

MaCaulay J. 1990. The Palaeoethnobotany of the Hine Village Site, A Fort Ancient Component in the Middle Ohio Valley. Toronto: University of Toronto.

MacKelvie K, Petit M, Khan K, Beck T, and McKay H. 2004. Bone Mass and Structure are Enhanced Following a 2-Year Randomized Controlled Trial of Exercise in Prepubertal Boys. Bone *34:*755-764.

MacLatchy L, and Muller R 2002. A Comparison of the Femoral Head and Neck Trabecular Architecture of Galago and Perodicticus Using Micro-Computed Tomography. Journal of Human Evolution *43:*89-105.

MacNeil J, and Boyd S. 2007. Load Distribution and the predictive Power of Morphological Indices in the Distal Radius and Tibia by High Resolution Peripheral Quantitative Computed Tomography. Bone *41*:129-137.

Maga M, Kappelman J, Ryan T, and Ketcham R. 2006. Preliminary Observations on the Calcaneal Trabecular Microarchitecture of Extant Large-Bodied Hominoids. American Journal of Physical Anthropology *129:*410-417.

Majumdar S, Kothari M, Augat P, Newitt D, et al. 1998. High-Resolution Magnetic Resonance Imaging: Three-Dimensional Trabecular Bone Architecture and Biomechanical Properties. Bone *22:*445-454.

Malina R, Bouchard C, and Bar-Or O. 2004. Growth, Maturation, and Physical Activity. Champaign: Human Kinetics.

Maresh M. 1955. Linear Growth of Long Bones of Extremities from Infancy Through Adolescence. American Journal of Diseases of Children *89:*725-742.

Marotti G. 1996. The Structure of Bone Tissues and the Cellular Control of their Deposition. Italian Journal of Anatomy and Embryology *101:*25-79.

Martin R 2000. Toward a Unifying Theory of Bone Remodeling. Bone *26:*1-6.

Martin R 2003. Functional Adaptation and Fragility of the Skeleton. In: Agarwal S, and Stout S, editors. Bone Loss and Osteoporosis: An Anthropological Perspective. New York: Kluwer Academic. pp. 121-138.

Martin R, Burr D, and Sharkey N. 1998. Skeletal Tissue Mechanics. New York: Springer.

Massaro E, and Rogers J, editors. 2004. The Skeleton. Totowa, NJ: Humana Press.

Massart D, Smeyers-Verbeke J, Capron X, and Schlesler K. 2007. Visual Presentation of Data by Means of Box Plots. Practical Data Handling: htttp://www.lcgceurope.com:6/6/2007.

Mauras N, Rogel A, Haymond M, and Veldhuis J. 1996. Sex Steroids, Growth Hormone, Insulin-Like Growth factor-1: Neuroendocrine and Metabolic Regulation in Puberty. Hormone Research *45*:74-80.

Mays S. 1999. A Biomechanical Study of Activity Patterns in a Medieval Human Skeletal Assemblage. International Journal of Osteoarchaeology *9:*68-73.

Mazurier A, Nakatsukasa M, Bondioli L, Rook L, and Macchiarelli R. 2007. Structural Signature of Bipedal Training in the Tibial Plateau of a Japanese Macaque. American Journal of Physical Anthropology *44 Suppl:*167.

McCaa R. 2002. Paleodemography of the Americas: From Ancient Times to Colonialism and Beyond. In: Steckel R, and Rose J, editors. The Backbone of History: Health and Nutrition in the Western Hemisphere. Cambridge: Cambridge University Press. pp. 94-124.

McCammon R. 1970. Human Growth and Development. Springfield, IL: Charles C. Thomas.

McKern, WC. 1939. The Midwestern Taxonomic Method as an Aid to Archaeological Culture Study. American Antiquity *4:*301-313.

Mehta G, Roach H, Langley-Evans S, et al. 2002. Intrauterine Exposure to a Maternal Low Protein Diet Reduces Adult Bone Mass and Alters Growth Plate Morphology in Rats. Calcified Tissue International *71:*493-498.

Meindl R, and Russell K. 1998. Recent Advances in Method and Theory in Paleodemography. Annual Review of Anthropology *27:*375-399.

Melsen F, Mosekilde L, and Eriksen E. 1995. Spatial Distribution of Sinusoids in Relation to Remodeling Sites: Evidence for Specialized Sinusoidal Structures Associated With Formative Sites. Journal of Bone and Mineral Research *10 (S):*S209.

Mensforth R. 1985. Relative Tibia Long Bone Growth in the Libben and Bt-5 Prehistoric Skeletal Populations. American Journal of Physical Anthropology *68:*247-262.

Mensforth R, Lovejoy C, Lallo J, and Armelagos G. 1978. The Role of Constitutional Factors, Diet, and Infectious Disease in the Etiology of Porotic Hyperostosis and Periosteal Reactions in Prehistoric Infants and Children. Medical Anthropology *2:*1-59.

Mielke J, Armelagos G, and Van Gerven D.1972. Trabecular Involution in Femoral Heads of a Prehistoric (X-Group) Population from Sudanese Nubia. American Journal of physical Anthropology *36*:39-44

Miller L, Little W, Schirmer A, et al., 2007. Accretion of Bone Quantity and Quality in the Developing Mouse Skeleton. Journal of Bone and Mineral Research *22 (7):*1037-1045.

Mills W. 1904. Explorations of the Gartner Mound and Village Site. Ohio State Archaeological and Historical Publications *13(2):*128-189.

Mills W. 1906. Baum Prehistoric Village. Ohio State Archaeological and Historical Publications *15:*45-136.

Milner G. 2004. The Moundbuilders: Ancient Peoples of Eastern North America. London: Thames and Hudson.

Milner G, Anderson E, and Smith V. 1991. Warfare in Late Prehistoric West Central Illinois. American Antiquity *56(4):*581-603.

Milner G, Humpf D, and Harpending H. 1989. Pattern Matching of Age-at-Death Distribution in Paleodemographic Analysis. American Journal of Physical Anthropology *80:*49-58.

Milner G, Wood J, and Bolden J. 2000. Paleodemography. In: Katzenberg M, and Saunders S, editors. Biological Anthropology of the Human Skeleton. New York: Wiley-Liss. pp. 467-497.

Moore J, and Scott E, editors. 1997. Invisible People and Processes: Writing Gender into European Archaeology. London: Leicester University Press.

Moorehead W. 1908. Fort Ancient, Part II. Andover: Phillips Academy.

Moorrees C, Fanning E, and Hunt Jr. E. 1963a. Age Variation of Formation Stages for Ten Permanent Teeth. Journal of Dental Research *42:*1490-1502.

Moorrees C, Fanning E, and Hunt Jr. E. 1963b. Formation and Resorption of Three Deciduous Teeth in Children. American Journal of Physical Anthropology *21:*205-213.

Morgan R. 1946. Fort Ancient. Columbus: The Ohio State Archaeological and Historical Society.

Morrow V. 1996. Rethinking Childhood Dependency: Children's Contributions to the Domestic Economy. The Sociological Review:58-77.

Mulder L, Koolstra J, Weijs W, and Van Eijden T. 2005. Architecture and Mineralization of Developing Trabecular Bone in the Pig Mandibular Condyle. Anatomical Record *285A*;659-667.

Mulder L, Koolstra J, den Toonder J, and van Eijden T. 2007. Intratrabecular Distribution of Tissue Stiffness and Mineralization in Developing Trabecular Bone. Bone *41:*256-265.

Mullender M, and Huiskes R. 1997. Osteocytes and Bone Lining Cells: Which are the Best Candidates for Mechano-Sensors in Cancellous Bone? Bone *6:*527-532.

Mullender M, Meer D, Huiskes R, and Lips P. 1996. Osteocyte Density Changes in Aging and Osteoporosis. Bone *18:*109-113.

Muller R. 2003. Bone Architecture Assessment: Current and Future Trends. Osteoporosis International *14 (Suppl 5):*S89-S99.

Muller R, and Ruegsegger P. 1995. Three-Dimensional Finite Element Modeling of Non-invasively Assessed Trabecular Bone Structures. Medical Engineering and Physics *17:*126-133.

Muller R, Hildebrand T, and Ruegsegger P. 1994. Non-invasive Bone Biopsy: A New Method to Analyze and Display the Three-Dimensional Structure of Trabecular Bone. Physics in Medicine and Biology *39:*145-164.

Muller R, Koller B, Hildebrand T, et al. 1996. Resolution Dependency of Microstructural Properties of Cancellous Bone Based on Three-Dimensional μ-Tomography. Technology and Health Care *14*:113-119.

Murdock G, and Morrow D. 1970. Subsistence Economy and Supportive Practices: Cross-Cultural Codes 1. Ethnology.9:302-330.

Murdock G, and Provost C. 1973. Factors in the Division of Labors by Sex: A Cross-Cultural Analysis. Ethnology *12:*203-225.

Murdock G, and White D. 1969. Standard Cross-Cultural Sample. Ethnology *8:*329-369.

Murdock G, and Wilson S. 1972. Settlement Patterns and Community Organization: Cross-Cultural Codes 3. Ethnology *11:*254-295.

Nafei A, Danielson C, Linde F, and Hvid I. 2000a. Properties of Growing Trabecular Ovine Bone. Journal of Bone and Joint Surgery *82-B:*910-920.

Nafei A, Kabel J, Odgaard A, Linde F, and Hvid I. 2000b. Properties of Growing Trabecular Ovine Bone. Part II: Architectural and Mechanical Properties. Journal of Bone and Joint Surgery [Br] *82-B:*921-927.

Nashida S, and Endo N. 1999. Number of Osteoprogenitor Cells in Human Bone Marrow Markedly Decreases After Skeletal Maturation. Journal of Bone and Mineral Metabolism *17:*171-177.

Nass Jr. J. 1988. Fort Ancient Agricultural Systems and Settlement: A View from Southwestern Ohio. North American Archaeologist *9:*319-347.

Nass Jr. J. 1989. Household Archaeology and Functional Analysis as Procedures for Studying Fort Ancient Communities in the Ohio Valley. Pennsylvania Archaeologist *59:*1-13.

Nass Jr. J, and Yerkes RW. 1995. Social Differentiation in Mississippian and Fort Ancient Communities. In: Rogers JD, and Smith BD, editors. Mississippian Communities and Households. Tuscaloosa: University of Alabama Press. pp. 58-80.

Neumann G. 1960. Origins of the Indians of the Middle Mississippi Area. Proceedings of the Indian Academy of Science *69:*66-68.

Niebur G, Feldstein M, et al. 2000. High-Resolution Finite Element Models with Tissue Strength Asymmetry Accurately Predict Failure of Trabecular Bone. Journal of Biomechanics *33:*1575-1583.

Nuzzo S, Meneghini C, Braillon P, Mobilo S, and Peyrin F. 2003. Microarchitectural and Physical Changes During Fetal Growth in Human Vertebral Bone. Journal of Bone and Mineral Research *18:*760-769.

O'Brien MJ. 1987. Sedentism, Population Growth, and Resource Selection in the Woodland Midwest: A Review of Coevolutionary Developments. Current Anthropology *28:*177-197.

Odgaard A. 1997. Three-Dimensional Methods for Quantification of Cancellous Bone Architecture. Bone *20 :*315-328.

O'Donnell J. 2004. Ohio's First Peoples. Athens: Ohio University Press.

Olsen B, Reginato A, and Wang W. 2000. Bone Development. Annual Review of Cell and Developmental Biology *16:*191-220.

O'Shea J. 1989. The Role of Wild Resources in Small-Scale Agricultural Systems: Tales From the Lakes and the Plains. In: Halstead P, and O'Shea J, editors. Bad Year Economics: Cultural Responses to Risk and Uncertainty. Cambridge: Cambridge University Press. pp. 57-67.

O'Shea J, and Halstead P. 1989. Conclusions: Bad Year Economics. In: Halstead P, and O'Shea J, editors. Bad Year Economics: Cultural Responses to Risk and Uncertainty. Cambridge: Cambridge University Press. pp. 123-126.

Owsley D. 1989. Temporal Variation in Femoral Cortical Thickness of North American Plains Indians. In: Iscan M, and Kennedy K, editors. Reconstruction of Life from the Skeleton. New York: Alan R. Liss. pp. 105-110.

Owsley D, and Jantz L. 1983. Formation of the Permanent Dentition in Ankara Indians: Timing Differences That Affect Dental Age Assessments. American Journal of Physical Anthropology *61:*467-471.

Panter-Brick C. 1998. Biological Anthropology and Child Health: Context, Process, and Outcome. In: Panter-Brick C, editor. Biosocial Perspectives on Children. Cambridge: Cambridge University Press. pp. 66-101.

Panter-Brick C, editor. 1998. Biosocial Perspectives on Children. Cambridge: Cambridge University Press.

Papaloucas C, Earnshaw P, Tonkin C, and Buckland-Wright, J. 2004. Quantitative Radiographic Assessment of Cancellous Bone Changes in the Proximal Tibia After Total Knee Arthroplasty: A 3-Year Follow-up Study. Calcified Tissue International *74:* 429-436.

Papathanasiou A. 2005. Health Status of the Neolithic Population of Alepotrypa Cave, Greece. American Journal of Physical Anthropology *126:*377-390.

Papathanasiou A, Larsen C, and Norr L. 2000. Bioarchaeological Inferences from a Neolithic Ossuary from Alepotrypa Cave, Diros, Greece. International Journal of Osteoarchaeology *10:*210-228.

Paquette S. 1981. An Analysis of Demographic and Pathological Correlation at Incinerator Site, Fort Ancient Culture, Montgomery County, Ohio. SunWatch. Dayton: Dayton Museum of Natural History.

Parfitt A. 1994. Osteonal and Hemi-Osteonal Remodeling: The Spatial and Temporal Framework for Signal Traffic in Adult Human Bone. Journal of Cellular Biochemistry *55:*273-286.

Parfitt A. 2000. The Mechanism of Coupling: A Role for the Vasculature. Bone *26:*319-323.

Parfitt A. 2002. Targeted and Nontargeted Bone Remodeling: Relationship to Basic Multicellular Unit Origination and Progression. Bone *30:*5-7.

Parfitt A. 2003. New Concepts of Bone Remodeling: A Unified Spatial and Temporal Model with Physiologic and Pathophysiologic Implications. In: Agarwal S, and Stout S, editors. Bone Loss and Osteoporosis: An Anthropological Perspective. New York: Kluwer Academic. pp. 3-17.

Parfitt A, et al. 1987. Bone Histomorphometry Nomenclature, Symbols, and Units. Report of the ASBMR Histomorphometry Nomenclature Committee. Journal of Bone and Mineral Research *2:*595-610.

Parfitt A, Travers R, Rauch F, and Glorieux F. 2000. Structural and Cellular Changes During Bone Growth in Healthy Children. Bone *27:*487-494.

Park R. 1998. Size Counts: The Miniature Archaeology of Childhood in Inuit Societies. Antiquity *72:*269-281.

Parker S, Langer J, and McKinney M, editors. 2000. Biology, Brains, and Behavior: The Evolution of Human Development. Sante Fe: School of American Research Press.

Pathi S, Rutenberg J, Johnson R, and A V. 1999. Interaction of Ihh and BMP Noggin Signaling During Cartilage Differentiation. Developmental Biology *209:*239-253.

Paul, J. 1976. Force Actions Transmitted by Joints in the Human Body. Proceedings of the Royal Society of London, Series B, Biological Sciences *192*:163-192.

Paus T, Zijdenbos A, Worsley K, et al. 1999. Structural Maturation of Neural Pathways in Children and Adolescents: In Vivo Study. Science *283*:1908-1911.

Pearson O. 2000. Activity, Climate, and Postcranial Robusticity. Current Anthropology *41:*569-607.

Pearson O, and Lieberman D. 2004. The Aging of Wolff's "Law": Ontogeny and Responses to Mechanical Loading in Cortical Bone. Yearbook of Physical Anthropology *47:*63-99.

Peebles C, and Kus S. 1977. Some Archaeological Correlates of Ranked Societies. American Antiquity 42:421-448.

Perzigian A, Tench P, and Braun D. 1984. Prehistoric Health in the Ohio River Valley. In: Cohen M, and Armelagos G, editors. Paleopathology at the Origins of Agriculture. New York: Academic Press. pp. 347-366.

Peterson J. 2002. Sexual Revolution: Gender and Labor at the Dawn of Agriculture. Walnut Creek: AltaMira Press.

Pfau R, and Sciulli P. 1994. A Method for Establishing the Age of Subadults. Journal of Forensic Sciences *39:*165-176.

Phenice T. 1969. A Newly Developed Visual Method of Sexing the *Os pubis.* American Journal of Physical Anthropology *30:*297-302.

Pollack D, and Henderson AG. 1992. Toward a Model of Fort Ancient Society. In: Henderson AG, editor. Fort Ancient Cultural Dynamics in the Middle Ohio Valley. Madison: Prehistory Press. pp. 281-294.

Pollack D, and Henderson AG (2000) Insights into Fort Ancient Culture Change: A View from South of the Ohio River. In: Genheimer RA, editor. Cultures Before Contact: The Late Prehistory of Ohio and Surrounding Regions. Columbus: Ohio Archaeological Council. pp. 194-227.

Pontzer H, Lieberman D, et al. 2005. The Effect of a "Bent-Knee" Gait on Trabecular Orientation: An Experimental Test of Wolff's Law. American Journal of Physical Anthropology *40 (S):*167.

Pontzer H, Lieberman DE, Momin E, Devlin MJ, et al. 2006. Trabecular Bone in the Bird Knee Responds with High Sensitivity to Changes in Load Orientation. Journal of Experimental Biology *209:*57-65.

Preece M, and Baines M. 1978. A New Family of Mathematical Models Describing the Human Growth Curve. Annals of Human Biology *5*:1-24.

Prufer O, and Shane III O, editors. 1970. Blain Village and the Fort Ancient Tradition in Ohio. Kent: The Kent State University Press.

Pruffle. 2007. Models for Anisotropic Materials. http://pruffle.mit.edu/3.00/Lecture_07-web/node3.html (4/11/2007).

Pyle S, and Hoerr N. 1955. Radiographic Atlas of Skeletal Development of the Knee. Springfield: C.C. Thomas.

Rafferty K, and Ruff C. 1994. Articular Structure and Function in *Hylobates, Colobus, and Papio*. American Journal of Physical Anthropology *94:*395-408.

Ramsey-Styer D. 1995. Seasonal Behavior at the Incinerator Site (33My57), an A.D. 1250 Fort Ancient Site in Southwestern Ohio. Columbia: University of South Carolina.

Raxter M, Auerbach B, and Ruff C. 2006. Revision of the Fully Technique for Estimating Statures. American Journal of Physical Anthropology *130:*374-384.

Redmond BG. 2000. Reviewing the Late Prehistory of Ohio. In: Genheimer RA, editor. Cultures Before Contact. Columbus: Ohio Archaeological Council. pp. 426-437.

Rhodes J, and Knusel C. 2005. Activity-Related Skeletal Change in Medieval Humeri: Cross-Sectional and Architectural Alterations. American Journal of Physical Anthropology *128:*536-546.

Richman B., Nakatsukasa M, Ketcham R, and Hirakawa T. 2004. Trabecular Bone Structure in Human and Chimpanzee Knee Joints. American Journal of Physical Anthropology *123:*167.

Richman B, Nakatsukasa M, Griffin N, Ogihara N, and Ketcham R. 2005. Trabecular Bone Structure in a Bipedally Trained Macaque. American Journal of Physical Anthropology *40S*: 175-176.

Ridler T, and Calvard S. 1978. Picture Thresholding Using an Iterative Selection Method. IEEE Transactions on Systems, Man, and Cybernetics *SMC-8*: 630-632.

Robbins L, and Neumann G. 1972. The Prehistoric People of the Fort Ancient Culture of the Central Ohio Valley. Ann Arbor: University of Michigan.

Robbins L. 1975. The Investigation of Infanticide in an Ohio Fort Ancient Site: A Demonstration of Archaeological/Physical Anthropologist Field Synergy. Dallas: Society for American Archaeology.

Roberts C, and Cox M. 2003. Health and Disease in Britain: From Prehistory to the Present Day. Phoenix Mill: Sutton.

Roberts C, and Manchester K. 1995. The Archaeology of Disease. Stroud: Sutton.

Robertson JA. 1980. Chipped Stone and Socio-cultural Interpretations. Chicago: University of Illinois.

Robertson JA. 1984. Chipped Stone and Functional Interpretations: A Fort Ancient Example. Midcontinental Journal of Archaeology *9:*251-267.

Roesler H. 1987. The History of Some Fundamental Concepts in Bone Biomechanics. Journal of Biomechanics *20:*1025-1034.

Rogers J, and Smith B, editors. 1995. Mississippian Communities and Households. Tuscaloosa: University of Alabama Press.

Rosier R, and Evans C, editors. 2003. Molecular Biology in Orthopaedics. Rosemont: AAOS.

Rossen J. 1992. Botanical Remains. In: Henderson AG, editor. Fort Ancient Cultural Dynamics in the Middle Ohio Valley. Madison: Prehistory Press. pp. 189-208.

Roughley P. 2004. Biology of Intervertebral Disc Aging and Degeneration. Spine *29:*2691-2699.

Rousseeuw P, Ruts I, and Tukey J. 1999. The Bagplot: A Bivariate Boxplot. The American Statistician *53:*382-387.

Roux W. 1881. Der Kampf der Teile im Organismus. Leipzig: Englemann.

Rowe T, Kappelman J, Carlson W, Ketcham R, and Denison C. 1997. High-Resolution Computed Tomography: A Breakthrough Technology for Earth Scientists. Geotimes (23-27).

Rubin CT, Turner A, Mallinckrodt C, et al. 2002. Mechanical Strain, Induced Noninvasively in the High Frequency Domain, Is Anabolic to Cancellous Bone, But Not Cortical Bone. Bone *30:*445-452.

Ruegsegger P, Koller B, and Muller R. 1996. A Microtomographic System for the Nondestructive Evaluation of Bone Architecture. Calcified Tissue International *58:*24-29.

Ruff C. 1987. Sexual Dimorphism in Human Lower Limb Bone Structure: Relationship to Subsistence Strategy and Sexual Division of Labor. Journal of Human Evolution *16*.

Ruff C. 1994. Biomechanical Analysis of Northern and Southern Plains Femora: Behavioral Implications. In: Owsley D, and Jantz R, editors. Skeletal Biology in the Great Plains: Migration, Warfare, Health, and Subsistence. Washington: Smithsonian Institution Press. pp. 235-244.

Ruff C. 1994. Morphological Adaptation to Climate in Modern and Fossil Hominids. Yearbook of Physical Anthropology *37:*65-107.

Ruff C. 1995. Limb Bone Structure: Influence of Sex, Subsistence, and Terrain. American Journal of Physical Anthropology *38 (s20):*186.

Ruff C. 1999. Skeletal Structure and Behavioral Patterns of Prehistoric Great Basin Populations. In: Hemphill B, and Larsen C, editors. Prehistoric Lifeways in the Great Basin Wetlands. Salt Lake City: University of Utah Press. pp. 290-320.

Ruff C. 2000. Body Size, Body Shape, and Long Bone Strength in Modern Humans. Journal of Human Evolution *38:*269-290.

Ruff C. 2002. Biomechanical Analyses of Archaeological Human Skeletons. In: Katzenberg M, and Saunders S, editors. Biological Anthropology of the Human Skeleton. New York: Wiley-Liss. pp. 71-102.

Ruff C. 2002. Long Bone Articular and Diaphyseal Structure in Old World Monkeys and Apes. I: Locomotor Effects. American Journal of Physical Anthropology *119:*305-342.

Ruff C. 2002. Variation in Human Body Size and Shape. Annual Review of Anthropology *31:*211-232.

Ruff C. 2003a. Growth in Bone Strength, Body size, and Muscle Size in a Juvenile Longitudinal Sample. Bone *33:*317-329.

Ruff C. 2003b. Ontogenetic Adaptation to Bipedalism: Age Changes in Femoral-to-Humeral Length and Strength Proportions in Humans, with a Comparison to Baboons. Journal of Human Evolution *45:*317-349.

Ruff C. 2005. Growth Tracking of Femoral and Humeral Strength From Infancy Through Late Adolescence. Acta Paediatrica *94:*1030-1037.

Ruff C. 2005. Mechanical Determinants of Bone Form: Insights from Skeletal Remains. Journal of Musculoskeletal Neuronal Interaction *5:*202-212.

Ruff C. 2007. Body Size Prediction From Juvenile Skeletal Remains. American Journal of Physical Anthropology *133:*698-716.

Ruff C, and Hayes W. 1983. Cross-Sectional Geometry of Pecos Pueblo Femora and Tibiae- A Biomechanical Investigation: I. Method and General Patterns of Variation. American Journal of Physical Anthropology *60:*359-381.

Ruff C, and Hayes W. 1983. Cross-Sectional Geometry of Pecos Pueblo Femora and Tibiae- A Biomechanical Investigation: II. Sex, Age, and Side Differences. American Journal of Physical Anthropology *60:*383-400.

Ruff C, and Larsen C. 2001. Reconstructing Behavior in Spanish Florida: The Biomechanical Evidence. In: Larsen C, editor. Bioarchaeology of Spanish Florida. Gainesville: University of Florida Press. pp. 113-145.

Ruff C, and Leo F. 1986. Use of Computed Tomography in Skeletal Structure Research. Yearbook of Physical Anthropology *29:*181-196.

Ruff C, Holt B, Sladek V et al. 2006. Body Size, Body Proportions, and Mobility in the Tyrolean “Iceman.” Journal of Human Evolution *51:* 91-101.

Ruff C, Holt B, and Trinkaus E. 2006. Who's Afraid of the Big Bad Wolff?: "Wolff's Law" and Bone Functional Adaptation. American Journal of Physical Anthropology 129: 484-498.

Ruff C, Larsen C, and Hayes W. 1984. Structural Changes in the Femur With the Transition to Agriculture on the Georgia Coast. American Journal of Physical Anthropology *64:*125-136.

Ruff C, Trinkaus E, Walker A, and Larsen C. 1993. Postcranial Robusticity in *Homo.* I: Temporal Trends and Mechanical Interpretation. American Journal of Physical Anthropology *91:*21-53.

Ruff C, Walker A, and Trinkaus E. 1994. Postcranial Robusticity in *Homo.* III. Ontogeny. American Journal of Physical Anthropology *93*.

Ruimerman R, Hilbers P, van Reitbergen B, and Huiskes R. 2005. A Theoretical Framework for Strain-Related Trabecular Bone Maintenance and Adaptation. Journal of Biomechanics *38:*931-941.

Ryan T, and van Rietbergen B. 2005. Mechanical Significance of Femoral Head Trabecular Bone Structure in *Loris* and *Galago* Evaluated Using Micromechanical Finite Element Models. American Journal of Physical Anthropology *1261:*82-96.

Ryan T, van Rietbergen B, and Krovitz G. 2007. Mechanical Adaptation of the Trabecular Bone in the Growing Human Femur and Humerus. American Journal of Physical Anthropology *44 Suppl:*203.

Ryan TM, and Ketcham R. 2002a. The Three-Dimensional Structure of Trabecular Bone in the Femoral Head of Strepsirrhine Primates. Journal of Human Evolution *43:*1-63.

Ryan TM, and Ketcham R. 2002b. Femoral Head Trabecular Bone Structure in Two Omomyid Primates. Journal of Human Evolution *43:*241-263.

Ryan TM, and Krovitz GE. 2005. Ontogeny of Three-Dimension Trabecular Bone Architecture in the Human Proximal Femur. American Journal of Physical Anthropology *Supplement 40:*180-181.

Ryan T and Krovitz G. 2006. Trabecular Bone Ontogeny in the Human Proximal Femur. Journal of Human Evolution *51:*591-602.

Ryan TM, and van Rietbergen B. 2005. Mechanical Significance of Femoral Head Trabecular Bone Structure in *Loris* and *Galago* Evaluated Using Micromechanical Finite Element Models. American Journal of Physical Anthropology *121:*82-96.

Salenius P, and Vankka E. 1975. The Development of the Tibiofemoral Angle in Children. Journal of Bone and Joint Surgery *57A:*259-261.

Salle B, Rauch F, Travers R, Bouvier R, and Glorieux F. 2002. Human Fetal Bone Development: Histomorphometric Evaluation of the Proximal Femoral Metaphysis. Bone *30:*823-828.

Saunders S. 2000. Subadult Skeletons and Growth-Related Studies. In: Katzenberg M, and Saunders S, editors. Biological Anthropology of the Human Skeleton. New York: Wiley-Liss.

Saunders S, and Hoppa R. 1993. Growth Deficit in Survivors and Non-survivors: Biological Mortality Bias in Subadult Skeletal Samples. Yearbook of Physical Anthropology *36:*127-151.

Saunders S, and Melbye F. 1990. Subadult Mortality and Skeletal Indicators of Health in Late Woodland Ontario Iroquois. Canadian Journal of Archaeology *14:*61-74.

Schaffler M, Wenzel T, Fazzalari N, and Fyhrie D. 1993. Quantitative Characteristics of Cancellous Bone Morphogenesis. Trans Orthop Res Soc *18*:150.

Scheuer L, and Black S. 2000. Developmental Juvenile Osteology. Amsterdam: Elsevier.

Scheuer L, and MacLaughlin S. 1994. Age Estimation from the Pars Basilaris of the Fetal and Juvenile Occipital Bone. International Journal of Osteoarchaeology *4:*377-380.

Schour I, and Massler M. 1941. The Development of the Human Dentition. Journal of the American Dental Association *28:*1153-1160.

Schroeder S. 1999. Maize Productivity in the Eastern Woodlands and Great Plains of North America. American Antiquity *64(2):*499-516.

Schurr M, and Powell M. 2005. The Role of Changing Childhood Diets in the Prehistoric Evolution of Food Production: An Isotopic Assessment. American Journal of Physical Anthropology *126:*278-294.

Schurr M, and Schoeninger M. 1995. Associations between Agricultural Intensification and Social Complexity: An Example from the Prehistoric Ohio Valley. Journal of Anthropological Archaeology *14:*315-339.

Schwartz J. 1995. Skeleton Keys: An Introduction to Human Skeletal Morphology, Development, and Analysis. Oxford: Oxford University Press. pp. 185-222.

Sciulli P. 1990. Standardization of Long Bone Growth in Children. International Journal of Osteoarchaeology *4:*257-259.

Sciulli P. 1992. Estimating Age of Occurrence of Enamel Defects in Deciduous Teeth. Journal of Paleopathology. Special Publication *2:*31-39.

Sciulli P. 2007. Relative Dental Maturity and Associated Skeletal Maturity in Prehistoric Native Americans of the Ohio Valley Area. American Journal of Physical Anthropology *132:*545-557.

Sciulli P, and Aument B. 1987. Paleodemography of the Duff Site (33L0111). Midcontinental Journal of Archaeology *12:*117-144.

Sciulli P, and Giesen M. 1993. An Update on Stature Estimation in Prehistoric Native Americans of Ohio. American Journal of Physical Anthropology *92:*395-399.

Sciulli P, and Oberly J. 2002. Native Americans in Eastern North America: The Southern Great Lakes and Upper Ohio Valley. In: Steckel R, and Rose J, editors. The Backbone of History: Health and Nutrition in the Western Hemisphere. Cambridge: Cambridge University Press. pp. 440-480.

Sciulli P, and Schneider KN. 1985. Cranial Variation in the Terminal Late Archaic of Ohio. American Journal of Physical Anthropology *66:*429-443.

Sciulli P, and Schuck R. 2001. Terminal Late Archaic Mortuary Practices: II. The Boose Cemetery. Pennsylvania Archaeologist *71:*29-42.

Sciulli P, Schneider K, and Mahaney M. 1990. Stature Estimation in Prehistoric Native Americans of Ohio. American Journal of Physical Anthropology *83:*275-280.

Sciulli P, Schuck R, and Geisen M. 1993. Terminal Late Archaic Mortuary Practices at Kirian-Treglia (33AL39). Pennsylvania Archaeologist *63:*53-63.

Scott E. 1999. The Archaeology of Infancy and Infant Death. Oxford: Archaeopress.

Seaman MF, Dancey WS. 2000. The Late Woodland Period in Southern Ohio: Basic Issues and Prospects. In: Emerson TE, McElrath DL, Fortier AC, editors. Late Woodland Societies: Tradition and Transformation across the Midcontinent. Lincoln: University of Nebraska Press. pp. 583-611.

Shane III O. 1988. An Interim Summary Report of the Vertebrate Faunal Remains from the Incinerator Site (33 My 57), Montgomery County, Ohio. In: Heilman J, Lileas M, and Turnbow C, editors. A History of 17 Years of Excavation and Reconstruction – A Chronicle of 12th Century Human Values and the Built Environment, vol. I. Dayton: Dayton Museum of Natural History. pp. 157-213.

Shefelbine S, Tardieu C, and Carter D. 2002. Development of the Femoral Bicondylar Angle in Hominid Bipedalism. Bone *30*: 765-770.

Shelburne K, Torry M, and Pandy M. 2005. Muscle, Ligament, and Joint-Contact Forces at the Knee During Walking. Medicine and Science in Sports and Exercise *37*:1948-1956.

Sherwood R, Meindl R, Robinson H, and May R. 2000. Fetal Age: Methods of Estimation and Effects of Pathology. American Journal of Physical Anthropology *113:*305-315.

Sholtis S, and Weiss K. 2005. Phenogenetics: Genotypes, Phenotypes, and Variation. In: Hallgrimsson B, and Hall B, editors. Variation: A Central Concept in Biology. Amsterdam: Elsevier. pp. 499-518.

Skedros J, Hunt K, and Bloebaum R. 2004. Relationships of Loading History and Structural and Material Characteristics of Bone: Development of the Mule Deer Calcaneus. Journal of Morphology *259:*281-307.

Smit T, Schneider E, and Odgaard A. 1998. Star Length Distribution: A Volume-Based Concept for the Characterization of Structural Anisotropy. Journal of Microscopy *191*:249-257;

Smith B. 1989. Origins of Agriculture in Eastern North America. Science *246:*1566-1571.

Smith B. 1992. Rivers of Change: Essays on Early Agriculture in Eastern North America. Washington: Smithsonian Institution Press.

Smith B. 1995. The Emergence of Agriculture. New York: Scientific American Library.

Smith B. 2001. Low-Level Food Production. Journal of Archaeological Research *9:*1-43.

Smith BH. 1991. Standards of Human Tooth Formation and Dental Age Assessment. In: Kelley M, and Larsen C, editors. Advances in Dental Anthropology. New York: Wiley-Liss. pp. 143-168.

Smith BH, and Tompkins R. 1995. Toward a Life History of the Hominidae. Annual Review of Anthropology. *24:*257-279.

Smith C. N/A. Field Notes on File. Dayton: Dayton Society of Natural History.

Smith P, and Avishai G. 2005. The Use of Dental Criteria for Estimating Postnatal Survival in Skeletal Remains of Infants. Journal of Archaeological Science *32:*83-89.

Smith P, Bloom R, and Berkowitz. 1984. Diachronic Trends in Humeral Cortical Thickness. Journal of Human Evolution *13:*603-611.

Smith S, and Buschang P. 2004. Variation in Longitudinal Diaphyseal Long Bone Growth in Children Three to Ten Years of Age. American Journal of Human Biology *16:*648-657.

Smith S, and Buschang P. 2005. Longitudinal Models of Long Bone Growth During Adolescence. American Journal of Human Biology *17:*731-745.

Sofaer J. 2006. Gender, Bioarchaeology, and Human Ontogeny. In: Gowland R, and Knusel C, editors. Social Archaeology of Funerary Remains. Oxford: Oxbow. pp. 155-167.

Sommerfeldt D, and Rubin C. 2001. Biology of Bone and How It Orchestrates the Form and Function of the Skeleton. European Spine Journal *10:*S86-S95.

Sone T, Imai Y, Joo Y, et al. 2006. Side-to-Side Differences in Cortical Bone Mineral Density of Tibiae in Young Male Athletes. Bone *38:*708-13.

Sontag W. 1994. Age-Dependent Morphometric Change in the Lumbar Vertebrae of Male and Female Rats: Comparison with the Femur. Bone *15*:593-601.

Sowell E, Peterson B, Thompson P, Welcome S, Henkenius A, and Toga A. 2003. Mapping Cortical Change Across the Human Life Span. Nature Neuroscience *6*:309-315.

Spoor F, Wood B, and Zonneveld F. 1994. Implications of Early Hominid Labyrinthine Morphology for the Evolution of Human Locomotion. Nature *369:*645-648.

Stanitski D, Nietert P, Stanitski C, Nadjarian R, and Barfield W. 2000. Relationship of Factors Affecting Age of Onset of Independent Ambulation. Journal of Pediatric Orthopedics *20:*686-688.

Stansfield B, Hillman S, Hazlewood M, and Robb J. 2006. Regression Analysis of Gait Parameters with Speed in Normal Children Walking at Self-selected Speeds. Gait and Posture *23:*288-294.

St-Arnaud R. 2003. Transcriptional Control of the Osteoblast Phenotype. In: Rosier R, and Evans C, editors. Molecular Biology in Orthopaedics. Rosemont: AAOS. pp. 191-209.

Stearns S, editor. 1999. Evolution in Health and Disease. Oxford: Oxford University Press.

Steckel R. 1987. Growth Depression and Recovery: The Remarkable Case of American Slaves. Annals of Human Biology *14:*111-132.

Steckel R, and Rose J, editors. 2002. The Backbone of History: Health and Nutrition in the Western Hemisphere. Cambridge: Cambridge University Press.

Steckel R, Rose J, Larsen C, and Walker P. 2002. Skeletal Health in the Western Hemisphere From 4000 B.C. to the Present. Evolutionary Anthropology *11:*142-155.

Stevens S, and Williams G. 1999. Hormone Regulation of Chondrocyte Differentiation and Endochondral Bone Formation. Molecular and Cellular Endocrinology *151:*195-204.

Stevenson P. 1924. Age Order of Epiphyseal Union in Man. American Journal of Physical Anthropology *7:*53-93.

Stewart T. 1934. Sequence of Epiphyseal Union, Third Molar Eruption, and Suture Closure in Eskimos and American Indians. American Journal of Physical Anthropology *19:*433-453.

Stinson S. 2000. Growth Variation: Biological and Cultural Factors. In: Stinson S, Bogin B, Huss-Ashmore R, and O'Rourke D, editors. Human Biology: An Evolutionary and Biocultural Perspective. New York: Wiley-Liss. pp. 425-464.

Stinson S, Bogin B, Huss-Ashmore R, and O'Rourke D, editors. 2000. Human Biology: An Evolutionary and Biocultural Perspective. New York: Wiley-Liss.

Stirland A. 1998. Musculoskeletal Evidence for Activity: Problems of Evaluation. International Journal of Osteoarchaeology *8:*354-362.

Stock J, and Pfeiffer S. 2001. Linking Structural Variability in Long Bone Diaphyses to Habitual Behaviors: Foragers From the Southern African Later Stone Age and the Andaman Islands. American Journal of Physical Anthropology *115:*337-348.

Stokes I, and Iatridis J. 2004. Mechanical Conditions That Accelerate Intervertebral Disc Degeneration: Overload *Versus* Immobilization. Spine *29:*2724-2732.

Stothers D, and Bechtel S. 1987. Stable Carbon Isotope Analysis: An Inter-Regional Perspective. Archaeology of Eastern North America. *15:*137-154.

Stout S, and Lueck R. 1995. Bone Remodeling Rates and Skeletal Maturation in Three Archaeological Skeletal Populations. American Journal of Physical Anthropology *98:*161-171.

Sumner D, and Andriacchii. 1996. Adaptation to Differential Loading: Comparison of Growth-Related Changes in Cross-Sectional Properties of the Human Femur and Humerus. Bone *19:*121-126.

Sundberg M, Gardsell P, Johnell O, Karlsson MK, et al. 2001. Peripubertal Moderate Exercise Increases Bone Mass in Boys but Not in Girls: A Population-Based Intervention Study. Osteoporosis International *12:*230-238.

Sutherland D, Olshen R, Biden E, and Wyatt M. 1988. The Development of Mature Walking. London: Mac Keith Press.

Sutherland D. 1997. The Development of Mature Gait. Gait and Posture *6:*163-170.

Swartz S, Parker A, and Huo C. 1998. Theoretical and Empirical Scaling Patterns and Topological Homology in Bone Trabeculae. Journal of Experimental Biology *209:*573-590.

Tanck E, Hannink G, Ruimerman R, Buma P, et al. 2006. Cortical Bone Development Under the Growth Plate is Regulated by Mechanical Load Transfer. Journal of Anatomy *208:*73-79.

Tanck E, Homminga J, Van Lenthe G, and Huiskes R. 2001. Increase in Bone Volume Fraction Precedes Architectural Adaptation in Growing Bone. Bone *28:*650-654.

Tanner J. 1990. Foetus into Man: Physical Growth from Conception to Maturity, Revised and Enlarged. Cambridge: Harvard University Press.

Tardieu C, and Trinkaus E. 1994. Early Ontogeny of the Human Bicondylar Angle. American Journal of Physical Anthropology *95:*183-195.

Tardieu C, Glard Y, Garron E, et al. 2006. Relationship between Formation of the Femoral Bicondylar Angle and Trochlear Shape: Independence of Diaphyseal and Epiphyseal Growth. American Journal of Physical Anthropology *130:*491-500.

Tardieu C. 1999. Ontogeny and Phylogeny of Femoro-Tibial Characters in Human and Hominid Fossils: Functional Influence and Genetic Determinism. American Journal of Physical Anthropology *110:*365-377.

Tatarek B, and Sciulli P. 2000. Comparison of Population Structure in Ohio's Late Archaic and Late Prehistoric Periods. American Journal of Physical Anthropology *112:*363-376.

Taylor W, Heller M, Bergmann G, and Duda G. 2004. Tibio-Femoral Loading During Human Gait and Stair Climbing. Journal of Orthopaedic Research *22*: 625-632.

Taylor S, and Walker P. 2001. Forces and Moments Telemetered From Two Distal Femoral Replacements During Various Activities. Journal of Biomechanics *34*:839-848.

Teitelbaum S. 2000. Bone Resorption by Osteoclasts. Science *289:*1504-1508.

Theintz G, Buchs B, Rizzoli R, et al. 1992. Longitudinal Monitoring of Bone Mass Accumulation in Healthy Adolescents: Evidence for a Marked Reduction after 16 Years of Age at the Levels of Lumbar Spine and Femoral Neck in Female Subjects. Journal of Clinical Endocrinology and Metabolism *75:*1060- 1065.

Tompkins R. 1999. Human Population Variability in Relative Dental Development. American Journal of Physical Anthropology *99:*79-102.

Tracer D, Wyckoff S, Wimmer M, and Gardner S. 2000. Prone to Crawl: Cultural Contingency and Early Life Locomotor Development. American Journal of Human Biology *12:*278.

Trinkaus E. 1999. Diaphyseal Cross-Sectional Geometry of Near Eastern Middle Paleolithic Humans: The Femur. Journal of Archaeological Science *26:*409-424.

Trinkaus E, and Ruff CB. 1999. Diaphyseal Cross-sectional Geometry of Near Eastern Middle Paleolithic Humans: The Femur. Journal of Archaeological Science *26:*409-424.

Trinkaus E, Churchill S, and Ruff C. 1994. Postcranial Robusticity in *Homo.* II: Humeral Bilateral Asymmetry and Bone Plasticity. American Journal of Physical Anthropology *93:*1-34.

Trussel H. 1979. Comments on 'Picture Thresholding Using an Iterative Selection Method.' IEEE Transactions on Systems, Man, and Cybernetics *SMC-9*:311.

Tsekhmistrenko T. 1999. Quantitative Changes in Human Cerebellar Pyriform Neurons from Birth to the Age of 20 Years. Neuroscience and Behavioral Physiology *29:*405-409.

Tufte. 1983. The Visual Display of Quantitative Information: Graphic Press.

Tufte. 1990. Envisioning Information: Graphic Press.

Turnbow C. 1988. The Muir Site Ceramics. In: Turnbow CA, and Sharp WE, editors. Muir: An Early Fort Ancient Site in the Inner Bluegrass. Lexington: University of Kentucky Program for Cultural Resource Assessment. Pp. 97-178.

Turner C, and Robling A. 2003. Designing Exercise Regimens to Increase Bone Strength. Exercise and Sport Scientific Review *31*.

Turner C, Robling A, Duncan R, and Burr D. 2002. Do Bone Cells Behave Like a Neuronal Network? Calcified Tissue International *70:*435-442.

Turner J. 2007. The Tinkerer's Accomplice: How Design Emerges From Life Itself. Cambridge: Harvard University Press.

Ubelaker D. 1986. Estimating Age at Death from Immature Human Skeletons: An Overview. Journal of Forensic Sciences *32:*1254-1263.

Ubelaker D. 1989. The Estimation of Age at Death from Immature Human Bone. In: Iscan M, editor. Age Markers in the Human Skeleton. Springfield: Charles C. Thomas. pp. 55-70.

Uchiyama T, Tanizawa T, Muramatsu H, Endo N, Takahashi HE, and Hara T. 1999. Three-Dimensional Microstructural Analysis of Human Trabecular Bone in Relation to its Mechanical Properties. Bone *25:*487-491.

Ulijaszek S, Johnston F, and Preece M, editors. 1998. The Cambridge Encyclopedia of Human Growth and Development. Cambridge: Cambridge University Press.

Ulrich D, van Rietbergen B, Laib A, and Ruegsegger P. 1999. The Ability of Three-Dimensional Structural Indices to Reflect Mechanical Aspects of Trabecular Bone. Bone *25:*55-60.

Uusi-Rasi, Sievanen H, and Heinonen A. 2006. Long-Term Recreational Gymnastics Provides a Clear Benefit in Age-Related Functional Decline and Bone Loss. A Prospective 6-Year Study. Osteoporosis International *17:*1154-1164.

Valdimarsson O, Alborg H, Duppe H, et al. 2005. Reduced Training is Associated with Increased Loss of BMD. Journal of Bone and Mineral Research *20:*906-12.

van der Linden JC, Day JS, Verhaar J, and Weinans H. 2004. Altered Tissue Properties Induce Changes in Cancellous Bone Architecture in Aging and Diseases. Journal of Biomechanics *37:*367-374.

van der Merwe J, and Vogel J. 1978. C Content of Human Collagen as a Measure of Prehistoric Diet in Woodland North America. Nature *276(2):*815-816.

van der Meulen M, and Huiskes R. 2002. Why Mechanobiology? A Survey Article. Journal of Biomechanics *35:*401-414.

van der Meulen M, Beaupre G, and Carter D. 1993. Mechanobiologic Influences in Long Bone Cross-Sectional Growth. Bone *14:*635-642.

van der Meulen M, Morgan T, Yang X, Baldini T, and et al. 2006. Cancellous Bone Adaptation to In Vivo Loading in a Rabbit Model. Bone *38*: 871-877.

van Rietbergen B, Odgaard A, Kabel J, and Huiskes R. 1998. Relationships Between Bone Morphology and Bone Elastic Properties can be Accurately Quantified using High-Resolution Computer Reconstructions. Journal of Orthopedic Research *16:*23-28.

van Rietbergen B, Weinans H, Huiskes R, and Odgaard A. 1995. A New Method to Determine Trabecular Bone Elastic Properties and Loading Using Micromechanical Finite-Element Models. Journal of Biomechanics *28:*69-81.

Wagner G. 1987. Uses of Plants by the Fort Ancient Indians. St. Louis: Washington University.

Wagner GE. 1988. Paleoethnobotanical Research at the Incinerator Site. In: Heilman JM, Lileas MC, and Turnbow CA, editors. A History of 17 Years of Excavation and Reconstruction: A Chronicle of 12th Century Human Values and the Built Environment. Dayton: Dayton Museum of Natural History. pp. 72-111.

Wagner G. 1996. Feast or Famine? Seasonal Diet at a Fort Ancient Community. In: Rietz E, Newson L, and Scudder S, editors. Case Studies in Environmental Archaeology. New York: Plenum Press. pp. 255-271.

Waldron T. 1994. Counting the Dead: The Epidemiology of Skeletal Populations. Chichester: John Wiley and Sons.

Walker R, Gurven M, Migliano, et al. 2006. Growth Rates and Life History in Twenty-Two Small-Scale Societies. American Journal of Human Biology *18:*295-311.

Ward K, Roberts S, Adams J, and Mughal M. 2005. Bone Geometry and Density in the Skeleton of Pre-pubertal Gymnasts and School Children. Bone *36*:1012-1018.

Weiss E. 2003. Understanding Muscle Markers: Aggregation and Construct Validity. American Journal of Physical Anthropology *121:*230-240.

Weiss E. 2005. Humeral Cross-Sectional Morphology From 18th Century Quebec Prisoners of War: Limits to Activity Reconstruction. American Journal of Physical Anthropology *126:*311-317.

Weiss K. 1998. In Search of Human Variation. Genome Research *8:*691-697.

Welch M, Page B, and Martin L. 1981. Sex Differences in the Ease of Socialization: An Analysis of the Efficiency of Child Training Processes in Preindustrial Societies. Journal of Social Psychology *113:*3-12.

Wescott D. 2005. Effect of Mobility on Femur Midshaft External Shape and Robusticity. American Journal of Physical Anthropology *000 (online):*NA.

West-Eberhard M. 2003. Developmental Plasticity and Evolution. Oxford: Oxford University Press.

Wheeler D, and Lyday R. 1989. Evaluating the Measurement Process, Second Edition. Knoxville: SPC Press.

Wheelersburg R. 1992. An Archaeobotanical Study of Fort Ancient Subsistence in Southwestern Ohio: the State Line Site. Pennsylvania Archaeologist *62(2):*45-65.

White T. 2000. Human Osteology, Second Edition. San Diego: Academic Press. pp.338-378.

White T, and Folkens P. 2005. Human Bone Manual. Burlington: Elsevier.

Wittry WL. 1969. The American Woodhenge. In: Fowler ML, editor. Cahokia Archaeology. Urbana: University of Illinois. pp. 43-48.

Wolfe L, and Gray J. 1982. Subsistence Practices and Human Sexual Dimorphism of Stature. Journal of Human Evolution *11:*575-580.

Wolff J. 1892. The Law of Bone Remodeling. Berlin: Springer-Verlag.

Wolschrijn C, and Weijs W. 2004. Development of the Trabecular Structure Within the Ulnar Medial Coronoid Process of Young Dogs. Anatomical Record *278A*:514-519.

Wolschrijn C, and Weijs W. 2005. Development of the Subchondral Bone Layer of the Medial Coronoid Process of the Canine Ulna. Anatomical Record *284A*:439-445.

Wong M, and Carter D. 1990. A Theoretical Model of Endochondral Ossification and Bone Architectural Construction in Long Bone Ontogeny. Anatomy and Embryology *181:*523-532.

Wood J, Milner G, Harpending H, and Weiss K. 1992. The Osteological Paradox: Problems in Inferring Prehistoric Health From Skeletal Samples. Current Anthropology *33:*343-358.

Wood J. 1998. A Theory of Preindustrial Population Dynamics. Current Anthropology *39:*99-135.

Woods A, Omernik J, Brockman C, Gerber T, Hosteter W, and Azevedo S. 2000. Map-Ecoregions of Indiana and Ohio. Washington: United States Environmental Protection Agency.

Woollacott M, and Assaiante C. 2002. Developmental Changes in Compensatory Responses to Unexpected Resistance to Leg Lift During Gait Initiation. Experimental Brain Research *144:*385-396.

Worthman C, and Kuzara J. 2005. Life History and the Early Origins of Health Differentials. American Journal of Human Biology *17:*95-112.

Wright L, and Yoder C. 2003. Recent Progress in Bioarchaeology: Approaches to the Osteological Paradox. Journal of Archaeological Research *11:*43-70.

Wu D, Burr D, Boyd R, and Radin E. 1990. Bone and Cartilage Changes Following Experimental Varus or Valgus Tibial Angulation. Journal of Orthopedic Research *8:*572-585.

Yellowley C, Li Z, Zhou Z, et al. 2000. Functional Gap Junctions Between Osteocytic and Osteoblastic Cells. Journal of Bone and Mineral Research *15:*209-2.

You L, Cowin S, Schaffer M, and Weinbaum S. 2001. A Model for Strain Amplification in the Actin Cytoskeleton of Osteocytes due to Fluid Drag on Pericellular Matrix. Journal of Biomechanics *34:*1375-1386.

Zanker C, and Cooke C. 2004. Energy Balance, Bone Turnover, and Skeletal Health in Physically Active Individuals. Medicine and Science in Sports and Exercise *36*:1372-1381.

Zeller A. 1987. A Role for Children in Hominid Evolution. Man *22:*528-557.

Zysset PK. 2003. A Review of Morphology- Elastic Relationships in Human Trabecular Bone: Theories and Experiments. Journal of Biomechanics *36:*1469-1485.

APPENDIX A

SKELETAL SAMPLE DATABASE

DEFINITION OF VARIABLES

Variable	Definition
Damage M/L	Medial/lateral tibial damage
Burial Grp.	Burial group in SunWatch
D. Age D.	Dental age, deciduous
D. Age P.	Dental age, permanent
LB Age	Long bone length age
Fusion	Epiphyseal fusion age
Age Est.	Summary age estimate
Age	Age estimate (median)
Mat. Stg	Dental-based maturity stage
Seriation	Relative position within SunWatch sample
RL MF	Right/left, male/female
Group	Maturity-stage group
FOR	Field of reconstruction (mm)
BV/TV	Bone Volume Fraction
VOI	Volume of interest
M/L/C	Medial/lateral/central
BV/TV M/L	Bone volume fraction, medial/lateral VOI
SVD DA M/L	Star volume degree of anisotropy, medial/lateral VOI
E. M.	Elongation index, medial VOI
TrThMn	Mean trabecular thickness

TrThMx	Maximum trabecular thickness
TrN M/L	Trabecular number, medial/lateral VOI
MILF M/L	Mean intercept degree of anisotropy, medial/lateral VOI
BIC Angle	Femoral bicondylar angle
L>M	Lateral BV/TV > medial BV/TV
L/M	Lateral BV/TV/ medial BV/TV ratio
Log L/M	Log of L/M ratio
BV MA/MP/LA/LP/C	BV/TV medial or lateral anterior/posterior/central VOI
SVD MA/MP/LA/LP/C	SVD medial or lateral anterior/posterior/central VOI
BV M or LP/A	BV/TV posterior/anterior ratio, medial or lateral secondary VOI
Log BV	Log of BV/TV posterior/anterior ratio
SVD M or LP/A	SVD posterior/anterior ratio, medial or lateral secondary VOI
Log SVD	Log of SVD posterior/anterior ratio
Dist FMB	Distal femoral metaphyseal breadth (mm)
Fem. Head	Femoral head breadth (mm)
Bd. Mass	Body mass (kg)

Burial No.	Damage M/L	Burial Grp	D. Age D	D. Age P	LB Age	Fusion	Age Est.
10/72		7			35+/-6wks	<0.5-1.0	F-0.2
14B/72			0.2		35+/-6wks	<0.5-1.0	F-0.2
9/72		7	0.2-0.4		0.2	<0.5-1.0	0.2-0.3
5/71	?L intrusions	8	0.2-0.3		0.2	<0.5-1.0	0.2-0.3
8/72	ML	7	<0.2		0.2	<0.5-1.0	0.3-0.5
15AB/73		3	0.2-0.4		</=0.2		0.3-0.5
15A+B/73		3			</= 0.2		0.3-0.5
12/73		2	0.4-0.6	0.1	0.2-0.5	<0.5-1.0	0.3-0.5
5/72		7	0.3-0.6		0.2-0.5	<0.5-1.0	0.3-0.5
7/73		2	0.6-0.8			<0.5-1.0	0.6-0.8
8/73	L	2	0.6-0.9	0.6-1.3	0.5-1.0	</=0.5-1.0	0.8-1.0
4/72	L	7	0.6-0.9		0.3-0.5	</=0.5-3.0	1.1-1.6
9/73		2	0.6-1.1	0.6-1.3	0.5-1.0	</=0.5-3.0	1.1-1.6
4/73	L	3	0.6-1.1	0.8-0.9	0.5-1.0	</=0.5-3.0	1.1-1.6
8/76		6	0.8-1.2	0.8-1.7	0.5-1.5	</=0.5-3.0	1.1-1.6
7/76	L	6	1.0-1.5	1.3	0.5-1.0	0.5-3.0	1.1-1.6
15/72	L		0.8-1.3	1.3	1.0-2.0	</=0.5-3.0	1.1-1.6
3/72		7	1.4-2.2		1.0-1.5	>/=0.5-3.0	1.8-2.4
6/80		9	2.0-2.2		1.5-3.0	</=0.5-3.0	1.8-2.4
14/74		5	2.7		1.5-3.5	>/=0.5-3.0	2.5-3.0
6/71			>2.8	3.1-4.9	3.0-5.5	>/=0.5-3.0	4.3-5.1
13/72	L	4	>2.8	5.0-7.6	4.0-7.0	>/=3.0-6.5	6.0-7.5
2/73		3	2.8	5.0-7.6	3.0-6.0	>/=3.0-6.5	6.0-7.5
7/80	L>M	9	>2.8	6.2-8.3	4.5-8.5	<11.0-17.0	9.1-10.5
1/81		9	>2.8	9.6-12.4	5.0-8.5	<11.0-17.0	5.0-12.4
SM3					6.0-8.0	<11.0-17.0	9.1-10.5
15/74		8	>2.8	9.4-12.4	7.5-12.0	<11.0-17.0	9.1-10.5
9/75		4	>2.8	>13.5-13.9	10-13	>/=12.0-16	13.2-15.5
7/81			>2.8	14.8-15.2	>10.5	>/=12-17.0	13.2-15.5
9/77		11	>2.8	13.2	10.5-12.0	>/=11.0-17	13.2-15.5
SM18	L		>2.8	17.5-17.7		>/=13.0-17	16.2-17.6
SM16			>2.8	17.5-17.7	>12.0	>/=14.0-18	16.2-17.6
SM9B					>12.0	>/=18.0-2-	16.2-17.6
474		2					19
3A/76		3					21
9/74		2					24
EXCLUDE							
7/71	ML damage	8	0.9-1.1	0.4-0.6	0.2-0.5	<0.5-1.0	1.1-1.6
3/74	ML damage	2	2.2-2.8	3.1-4.4	1.5-3.5	>/=0.5-3.0	1.8-2.4
2/81	treponemal?	10	>2.8	17.5-17.7	>12.0	>/=18.0-20	16.2-17.6

Burial No.	Age	Mat. Stg	Seriation	RL MF	Group	FOR	BV/TV M
10/72	0.1	1	7	R	I	22	0.4117
14B/72	0.1	1	8	L	1	22	0.4606
9/72	0.25	1	21	R	1	22	0.4041
5/71	0.25	1	23	L	1	22	0.4393
8/72	0.4	2	29	R	1	22	0.2958
15AB/73	0.4	2	30	R	1	22	0.4362
15A+B/73	0.4	2	31	L	1	22	0.4361
12/73	0.4	2	42	R	1	22	0.2975
5/72	0.4	2	45	R	1	22	0.2609
7/73	0.7	3	48	R	II	22	0.2596
8/73	0.9	4	56	R	II	22	0.2416
4/72	1.3	5	61	L	II	40	0.2841
9/73	1.3	5	62	L	II	40	0.2613
4/73	1.3	5	63	R	II	40	0.2359
8/76	1.3	5	67	L	II	40	0.334
7/76	1.3	5	69	R	II	40	0.288
15/72	1.3	5	70	L	II	40	0.3397
3/72	2.1	6	76	R	II	40	0.2881
6/80	2.1	6	79	R	II	40	0.3759
14/74	2.75	7	84	R	III	40	0.2087
6/71	4.7	9	86	L	III	40	0.2812
13/72	6.8	11	87	R	III	60	0.3784
2/73	6.8	11	88	R	III	40	0.3266
7/80	9.8	12	89	R	III	60	0.4485
1/81	9.8	12	93	L	III	60	0.3305
SM3	9.8	12	94	L	III	60	0.287
15/74	9.8	12	95	L	III	60	0.3468
9/75	14.3	15	96	Le	IV	80	0.3699
7/81	14.3	15	97	L	IV	80	0.4255
9/77	14.3	15	98	R	IV	80	0.3693
SM18	16.9	16	99	Le	IV	80	0.365
SM16	16.9	16	102	Le	IV	80	0.3507
SM9B	16.9	16	103	L	IV	60	0.3281
474	19	-	-	L F	IV	80	0.3156
3A/76	21	-	-	R F	IV	80	0.3366
9/74	24	-	-	L F	IV	80	0.2955
EXCLUDE							
7/71	1.3	5	60	L			
3/74	2.1	6	81	L		40	0.2236
2/81	16.9	16	100	L		80	0.3995

Burial No.	SVDDA	E M	TrTh Mn	TrTh Mx	TrN M	MILF M	BiC Angle
10/72	6.5148	0.8025	0.0778	0.2639	5.1179	1.4851	0
14B/72	7.7742	0.8525	0.0873	0.2216	5.0443	1.5115	
9/72	7.1332	0.8282	0.0952	0.2792	4.2415	1.5914	0
5/71	6.0874	0.7806	0.0956	0.2931	4.5043	1.4618	0
8/72	7.4439	0.8107	0.0865	0.2891	3.4476	1.4895	
15AB/73	7.6417	0.8464	0.0762	0.2387	5.5363	1.5438	1
15A+B/73	5.7339	0.8136	0.0782	0.2372	5.4617	1.4501	
12/73	9.231	0.8397	0.0967	0.3083	2.9699	1.7042	
5/72	6.4366	0.7156	0.0902	0.3052	2.968	1.4807	0.5
7/73	8.8512	0.8646	0.0921	0.2517	2.6766	1.6295	
8/73	4.8926	0.7622	0.1031	0.2784	2.177	1.4758	
4/72	4.7457	0.5765	0.1187	0.4043	2.3089	1.408	
9/73	3.0029	0.5512	0.1178	0.3593	2.1869	1.2658	0.5
4/73	5.0708	0.7662	0.1267	0.3539	1.7588	1.4987	0.5
8/76	1.4019	0.1645	0.1422	0.3908	2.285	1.1749	4
7/76	4.2776	0.696	0.1354	0.5117	2.013	1.4692	5
15/72	1.8471	0.2643	0.1545	0.448	2.0797	1.1977	1
3/72	1.717	0.2814	0.1362	0.4743	2.1601	1.2349	6
6/80	2.0306	0.4745	0.1449	0.5286	2.4577	1.1254	3
14/74	7.2195	0.831	0.1305	0.4495	1.5697	1.3204	5
6/71	4.1905	0.7571	0.1419	0.4425	1.9312	1.2596	4
13/72	4.8028	0.5847	0.1952	0.7	1.8532	1.4292	3
2/73	4.6258	0.563	0.1796	0.6401	1.7108	1.3086	2
7/80	3.5887	0.6487	0.2319	0.7161	1.8607	1.2552	5
1/81	5.9331	0.7609	0.203	0.5722	1.6022	1.3163	5
SM3	5.0216	0.7348	0.1913	0.6341	1.4664	1.2551	
15/74	5.6836	0.7982	0.203	0.6404	1.7068	1.2897	3
9/75	4.013	0.138	0.4293	1.8456	0.9258	1.3668	
7/81	7.1248	0.8188	0.2933	0.9561	1.3725	1.4996	0.5
9/77	5.799	0.7584	0.2827	1.2861	1.2092	1.4242	2.5
SM18	3.0487	0.3215	0.3091	1.155	1.1074	1.4678	4
SM16	4.5041	0.647	0.3789	1.6524	0.9454	1.4497	
SM9B	5.5952	0.7887	0.2298	0.7061	1.3263	1.4476	
474	1.755	0.301	0.2686	1.1998	0.9709	1.5805	
3A/76	1.3673	0.151	0.4186	1.9205	0.7846	1.44	
9/74	13.0283	0.8233	0.3174	1.0248	0.9278	1.5893	
EXCLUDE							
7/71							
3/74	5.7505		0.1565	0.5002	1.3431		
2/81	11.545		0.3234	0.973	1.0904		

Burial No.	L>M	L/M	Log L/M	BV/TV L	SVD L	E L	TrTh MN	TrTh Mx
10/72		0.956	-0.020	0.3933	4.3401	0.7598	0.0788	0.2206
14B/72		0.967	-0.014	0.4452	7.2108	0.8337	0.0904	0.2358
9/72		0.963	-0.016	0.3893	9.2954	0.8611	0.0929	0.2587
5/71		**1.109***	0.045	0.4871	6.5367	0.8151	0.1063	0.3048
8/72		0.871	-0.06	0.2575	6.4801	0.751	0.0939	0.2931
15AB/73		0.993	-0.003	0.4333	10.1475	0.8648	0.0853	0.2323
15A+B/73		0.979	-0.009	0.4269	8.1035	0.8261	0.0806	0.2168
12/73		0.824	-0.084	0.245	8.7033	0.8557	0.0957	0.2947
5/72		0.924	-0.034	0.241	5.9625	0.8006	0.0884	0.2961
7/73		0.886	-0.053	0.2299	4.2553	0.6855	0.1019	0.2822
8/73								
4/72	L=M	**1**	0	0.248	3.2046	0.4703	0.1201	0.3544
9/73	L>M	**1.001**	0	0.2615	3.4891	0.6713	0.1141	0.3187
4/73	L>M	**1.068**	0.029	0.252	6.086	0.7492	0.1282	0.3583
8/76		0.888	-0.052	0.2967	2.5436	0.336	0.1356	0.414
7/76	L>M	**1.011**	0.005	0.2911	3.8551	0.5897	0.1268	0.3811
15/72		0.948	-0.023	0.3221	2.9556	0.4983	0.1562	0.5134
3/72	L>M	**1.069**	0.029	0.3081	4.5957	0.6389	0.135	0.3345
6/80	L.>M	**1.022**	0.009	0.3843	3.2213	0.674	0.1463	0.3967
14/74	L>M	**1.127**	0.052	0.2353	7.8451	0.7435	0.1299	0.5019
6/71		0.828	-0.082	0.2328	3.6072	0.3989	0.1348	0.4048
13/72		0.999	0	0.3779	3.075	0.401	0.2307	0.9789
2/73		0.92	-0.036	0.3004	6.3244	0.3749	0.173	0.5977
7/80		0.809	-0.092	0.3626	6.5612	0.3426	0.2308	0.8566
1/81		0.982	-0.008	0.3247	6.7363	0.3978	0.2109	0.7185
SM3	L>M	**1.006**	0.003	0.2888	9.4249	0.4501	0.2077	0.9374
15/74		0.974	-0.011	0.3377	7.2213	0.284	0.1986	0.5956
9/75		0.884	-0.054	0.3271	10.1058e	0.4335	0.4128	1.7103
7/81		0.916	-0.038	0.3899	6.1774	0.6399	0.2507	0.6479
9/77		0.891	-0.05	0.3291	2.7257	0.4498	0.2505	0.8957
SM18								
SM16		0.854	-0.069	0.2997	2.152	0.1195	0.3761	2.0326
SM9B		0.869	-0.061	0.2851	3.2475	0.4834	0.2317	0.7783
474	L>M	**1.02**	0.009	0.3218	3.9402	0.681	0.2897	1.2353
3A/76	L>M	**1.057**	0.024	0.3557	11.4669	0.7568	0.3181	1.0675
9/74	L>M	**1.001**	0	0.2958	4.4036	0.7502	0.2946	1.2328

EXCLUDE
7/71
3/74
2/81

Burial No.	TrN L	MILF L	BV MA	SVD MA	BV MP	SVD MP	BVMP/A
10/72	4.9331	1.5226	0.4075	6.4151	0.3876	5.8703	0.951
14B/72	4.75123	1.5331					
9/72	4.1646	1.7191					
5/71	4.2839	1.5221					
8/72	2.8217	1.5219					
15AB/73	4.9319	1.7422					
15A+B/73	5.1197	1.5833	0.4399	6.6715	0.4364	7.3691	0.992
12/73	2.5562	1.637					
5/72	2.6903	1.5507					
7/73	2.1179	1.4329					
8/73							
4/72	1.9351	1.3227	0.3221	9.0989	0.2638	2.996	0.819
9/73	2.3225	1.2908					
4/73	1.796	1.4832					
8/76	2.1138	1.2903					
7/76	2.105	1.3537					
15/72	1.9555	1.2616					
3/72	2.2167	1.3869					
6/80	2.5902	1.3043	0.366	3.8585	0.4191	5.0331	1.145
14/74	1.8271	1.4308					
6/71	1.7146	1.2661					
13/72	1.25	1.3451					
2/73	1.7037	1.5781	0.3033	3.7891	0.3639	3.4527	1.2
7/80	1.4974	1.6243					
1/81	1.5402	1.5703					
SM3	1.4011	1.6524					
15/74	1.6419	1.4039	0.3476	5.5977	0.4108	9.0715	1.182
9/75	0.9449	1.2157					
7/81	1.4939	1.4299					
9/77	1.2642	1.23					
SM18							
SM16	0.8441	1.1474	0.3981	5.6348	0.4018	3.2373	1.01
SM9B	1.1752	1.243					
474	1.071	1.3544					
3A/76	1.0775	1.5022	0.3785	5.1904	0.4191	1.3312	1.107
9/74	0.9461	1.3492					
EXCLUDE							
7/71							
3/74							
2/81							

Burial No.	log BV	SVDMP/A	log SVD	BV LA	SVD LA	BV LP	SVD LP
10/72	-0.0218	0.9151	-0.0385	0.4137	6.1307	0.3893	4.2676
14B/72							
9/72							
5/71							
8/72							
15AB/73							
15A+B/73	-0.0035	1.1046	0.0432	0.441	7.6255	0.4355	8.0902
12/73							
5/72							
7/73							
8/73							
4/72	-0.0867	0.3293	-0.4824	0.2566	3.6638	0.2683	5.3686
9/73							
4/73							
8/76							
7/76							
15/72							
3/72							
6/80	0.0588	1.3044	0.1154	0.3973	2.261	0.4254	3.7821
14/74							
6/71							
13/72							
2/73	0.0792	0.9112	-0.0404	0.2987	6.4662	0.3752	6.0901
7/80							
1/81							
SM3							
15/74	0.0726	1.6206	0.2097	0.3661	8.2907	0.4158	4.2187
9/75							
7/81							
9/77							
SM18							
SM16	0.0043	0.5745	-0.2407	0.2875	2.3316	0.4157	1.399
SM9B							
474							
3A/76	0.0441	0.2133	-0.671	0.3183	5.4262	0.4176	1.3346
9/74							
EXCLUDE							
7/71							
3/74							
2/81							

Burial No.	BVLP/A	log BV	SVDLP/A	log SVD	BV/TV C	SVD C	TrThC Mn
10/72	0.941	-0.0264	0.6961	-0.1573	0.3869	8.8688	0.0794
14B/72							
9/72							
5/71							
8/72							
15AB/73							
15A+B/73	0.988	-0.0052	1.0609	0.0257	0.4113	10.3973	0.0733
12/73							
5/72							
7/73							
8/73							
4/72	1.046	0.0195	1.4653	0.1659	0.2372	4.9916	0.1167
9/73							
4/73							
8/76							
7/76							
15/72							
3/72							
6/80	1.07	0.0294	1.6728	0.2234	0.3691	2.752	0.1364
14/74							
6/71							
13/72							
2/73	1.256	0.099	0.9418	-0.026	0.2418	2.7847	0.1568
7/80							
1/81							
SM3							
15/74	1.136	0.0554	0.5088	-0.2935	0.3068	4.2082	0.1841
9/75							
7/81							
9/77							
SM18							
SM16	1.446	0.1602	0.6	-0.2218	0.1905	2.416	0.2874
SM9B							
474							
3A/76	1.312	0.1179	0.246	-0.6091	0.242	2.5775	0.2472
9/74							
EXCLUDE							
7/71							
3/74							
2/81							

Burial No.	TrThC Mx	TrN C	MILF C	Dist FMB	Fem Head	Bd Mass
10/72	0.2148	4.6926	1.6881			
14B/72						
9/72						
5/71						
8/72						
15AB/73				18		5.68
15A+B/73	0.1849	5.2699	1.6688			
12/73						
5/72				25		7.3
7/73						
8/73						
4/72	0.5292	1.9363	1.3631			
9/73						
4/73						
8/76				35		9.18
7/76				30		8.24
15/72				37		9.56
3/72				40		10.92
6/80	0.4724	2.5518	1.2258	38		10.38
14/74				40		11.78
6/71				48.5		16.2
13/72						
2/73	0.5357	1.5505	1.293			
7/80				59		29.03
1/81				48		18.12
SM3						
15/74	0.5246	1.6134	1.3018	61		31.01
9/75						
7/81						
9/77						
SM18					48	66.8
SM16	1.2345	0.6932	1.1561			
SM9B					39	51.1
474					44	64.5
3A/76	0.8354	0.871	1.1999		41	57.9
9/74					42	60.1
EXCLUDE						
7/71						
3/74						
2/81						

APPENDIX B

SELECTED CT CORONAL SLICE AND SVD ROSE DIAGRAM IMAGES

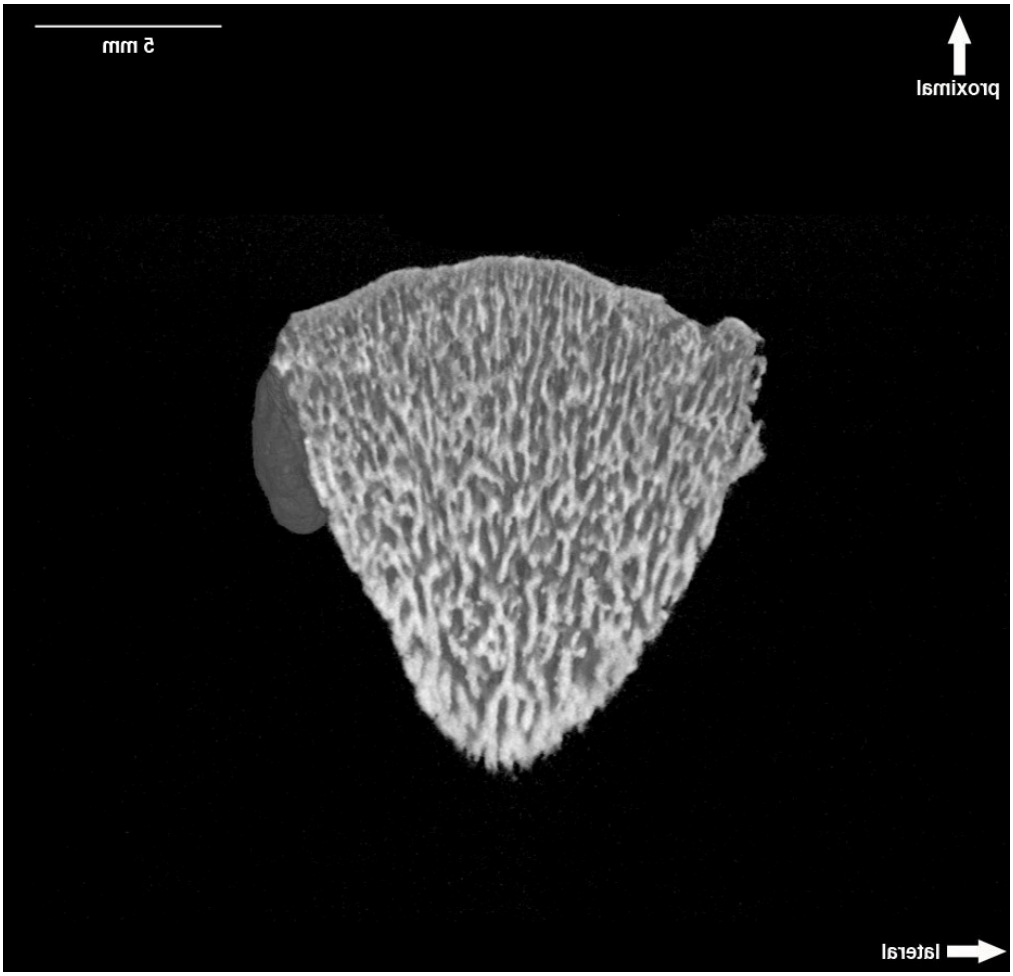

Figure B.1 Coronal scan slice. Burial 10_72. Age estimation is 0.00 years.

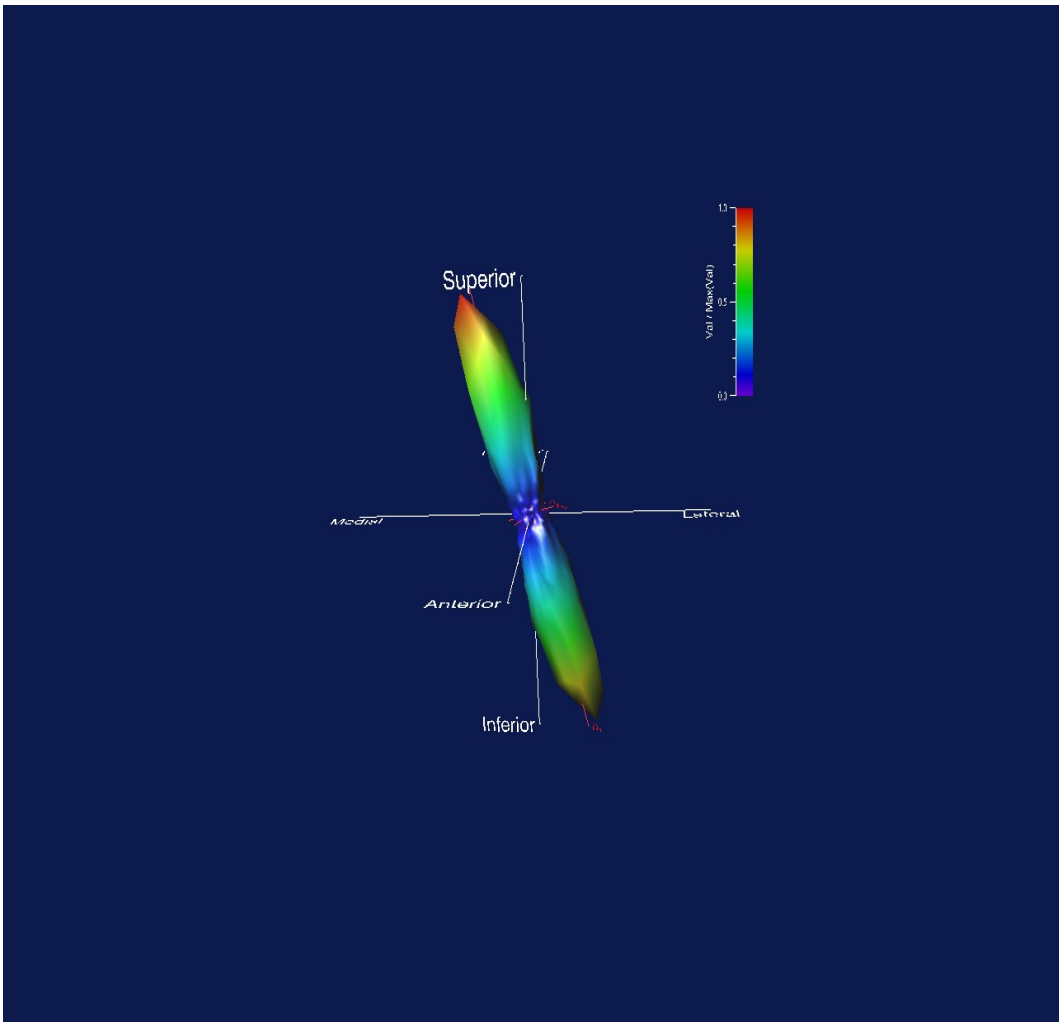

Figure B.2 SVD rose diagram. Burial 10_72. Age estimation is 0.00 years.

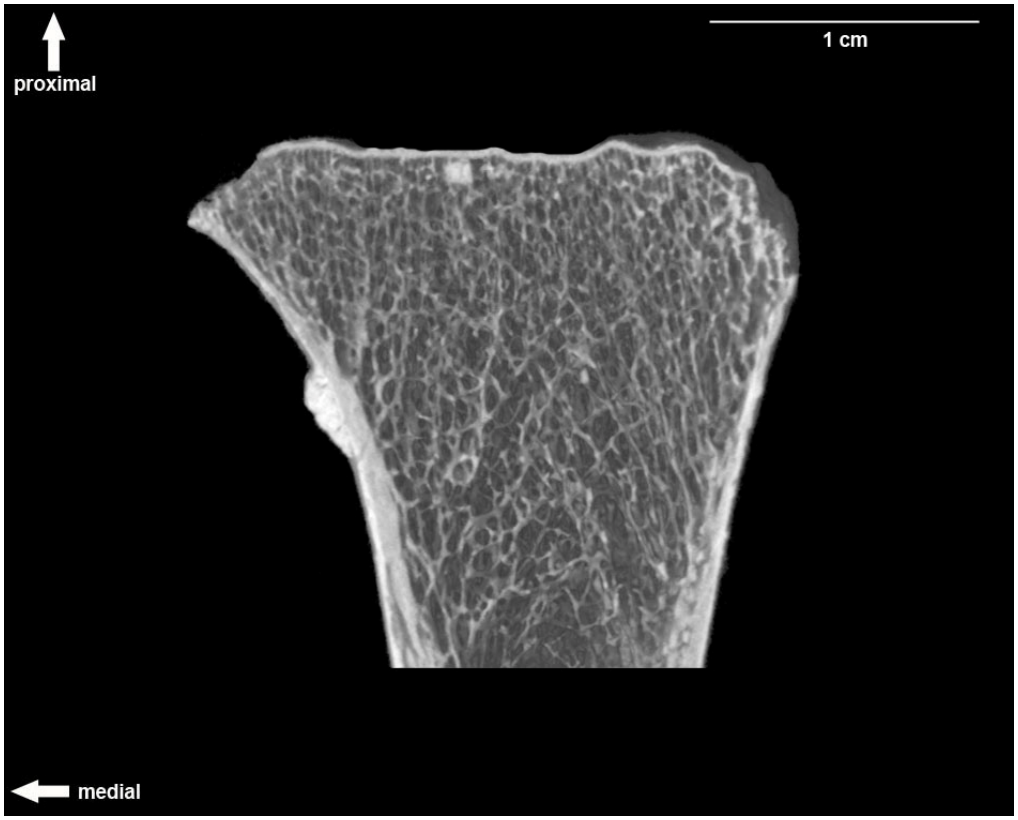

Figure B.3 Coronal scan slice. Burial 4_72. Age estimation is 1.3 years.

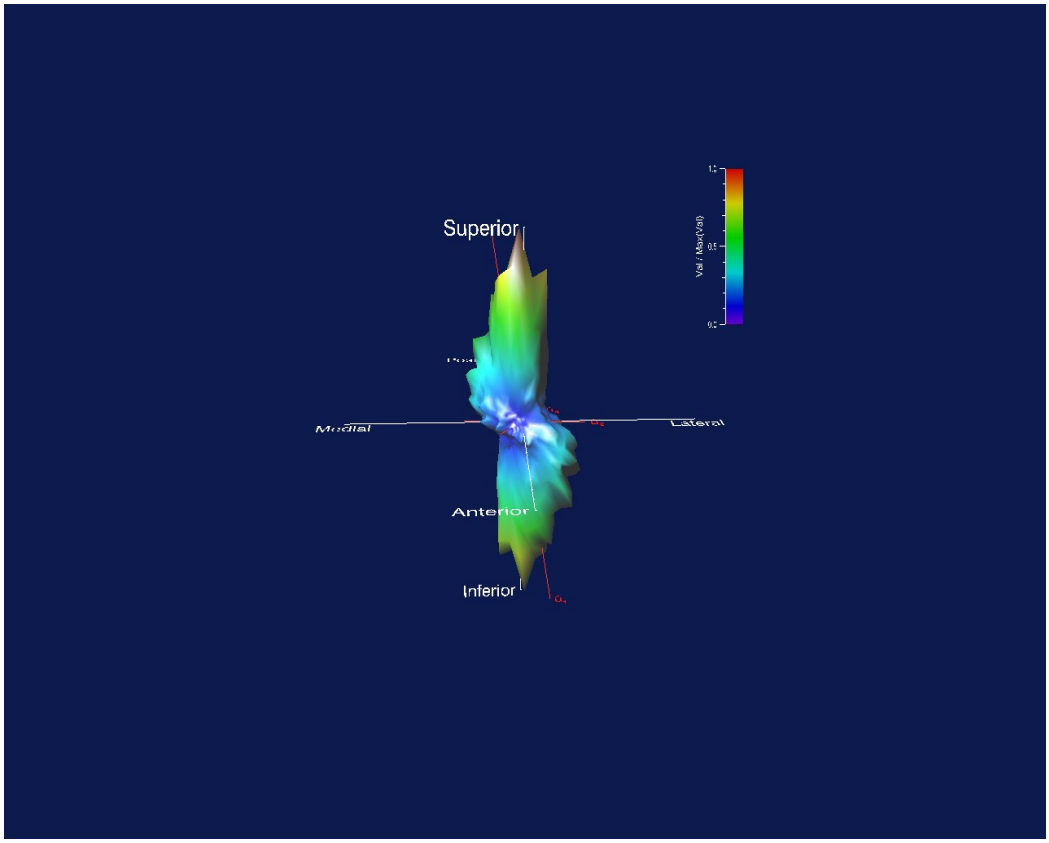

Figure B.4 SVD rose diagram. Burial 4_72. Age estimation is 1.3 years.

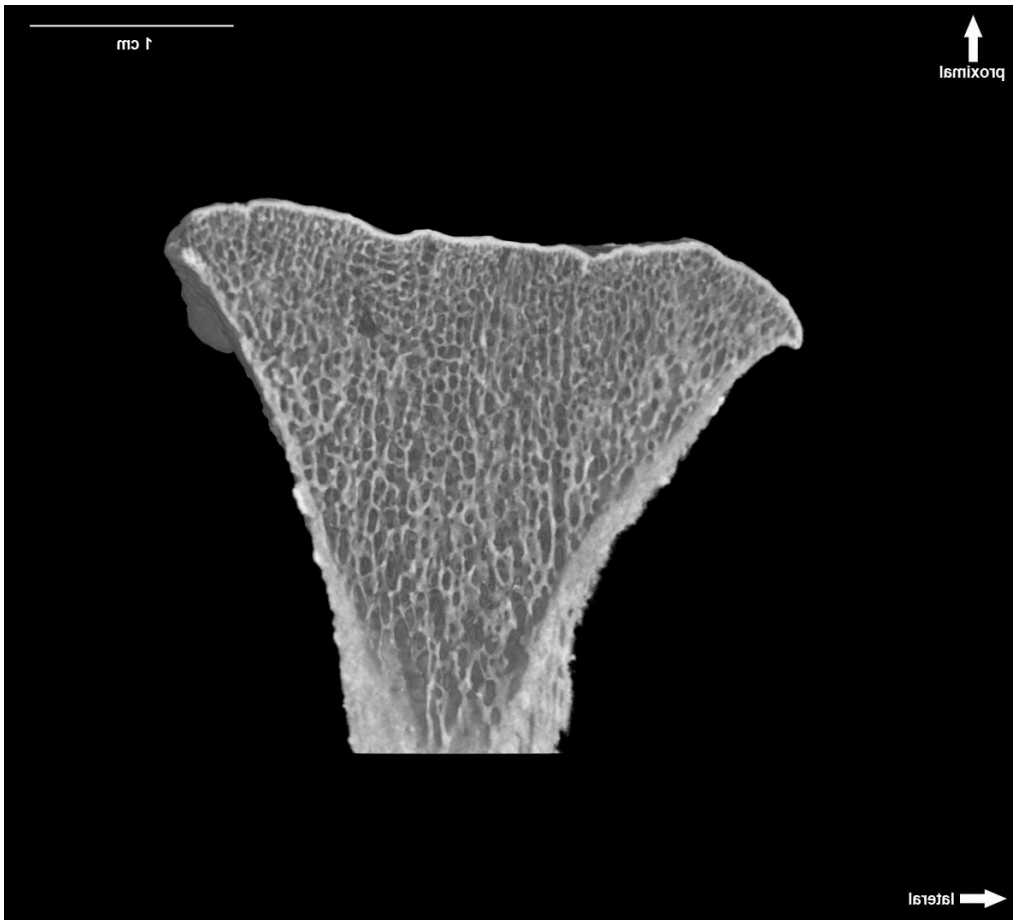

Figure B.5 Coronal scan slice. Burial 6_80. Age estimation is 2.1 years.

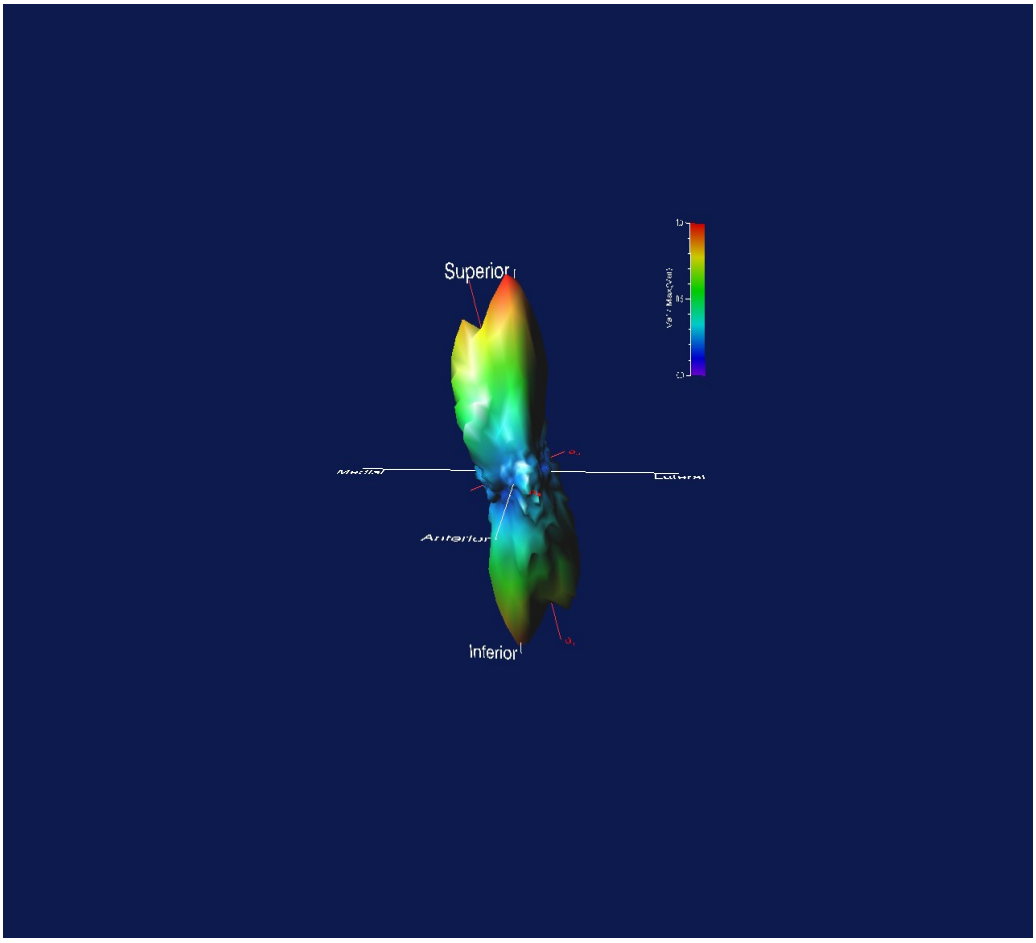

Figure B.6 SVD rose diagram. Burial 6_80. Age estimation is 2.1 years.

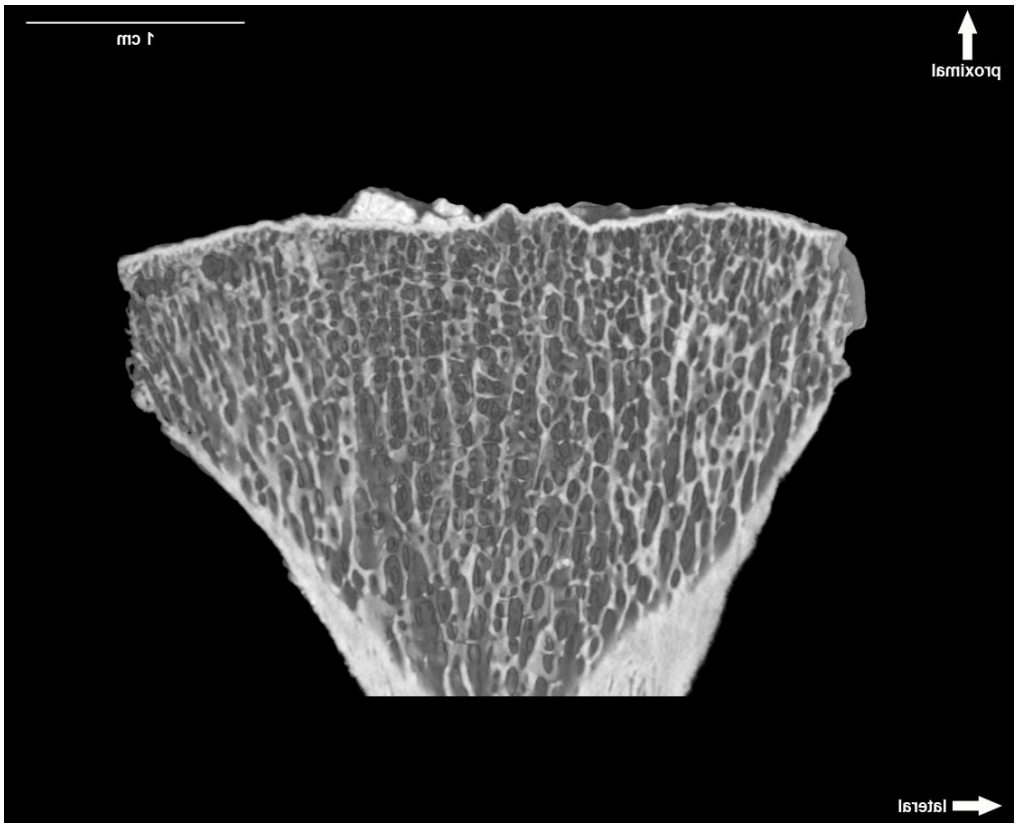

Figure B.7 Coronal scan slice. Burial 2_73. Age estimation is 7.0 years.

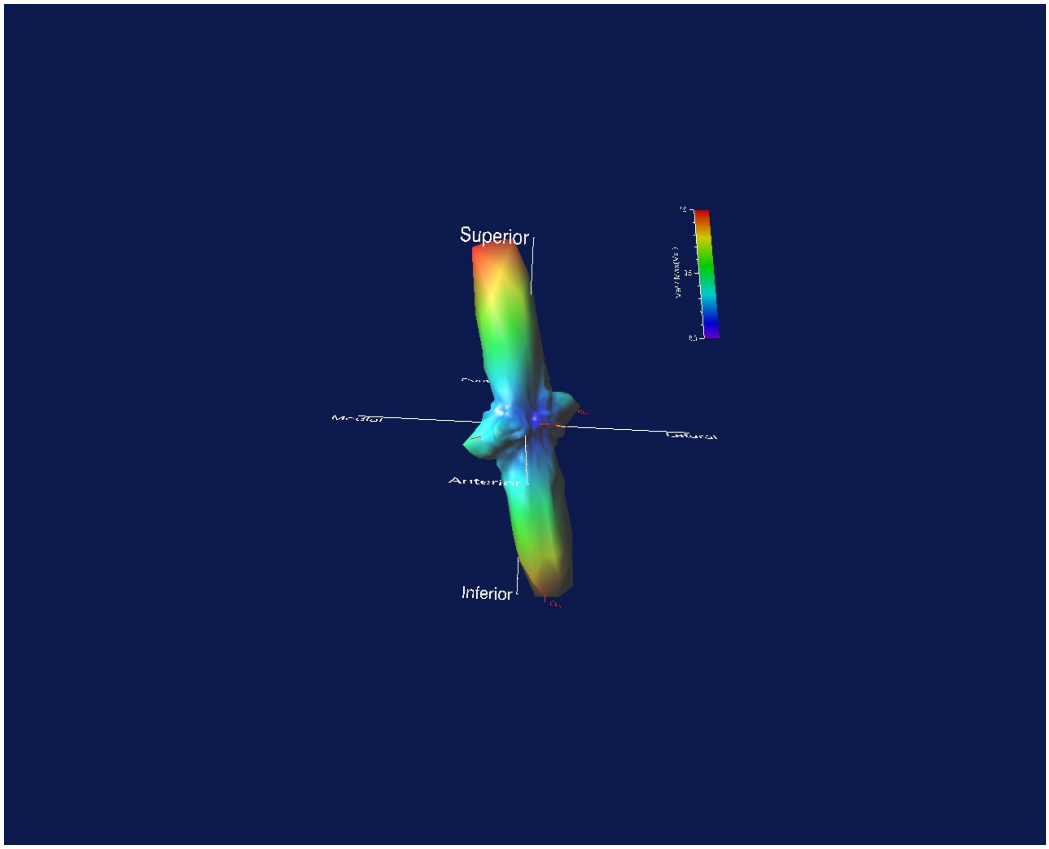

Figure B.8 SVD rose diagram. Burial 2_73. Age estimation is 7.0 years.

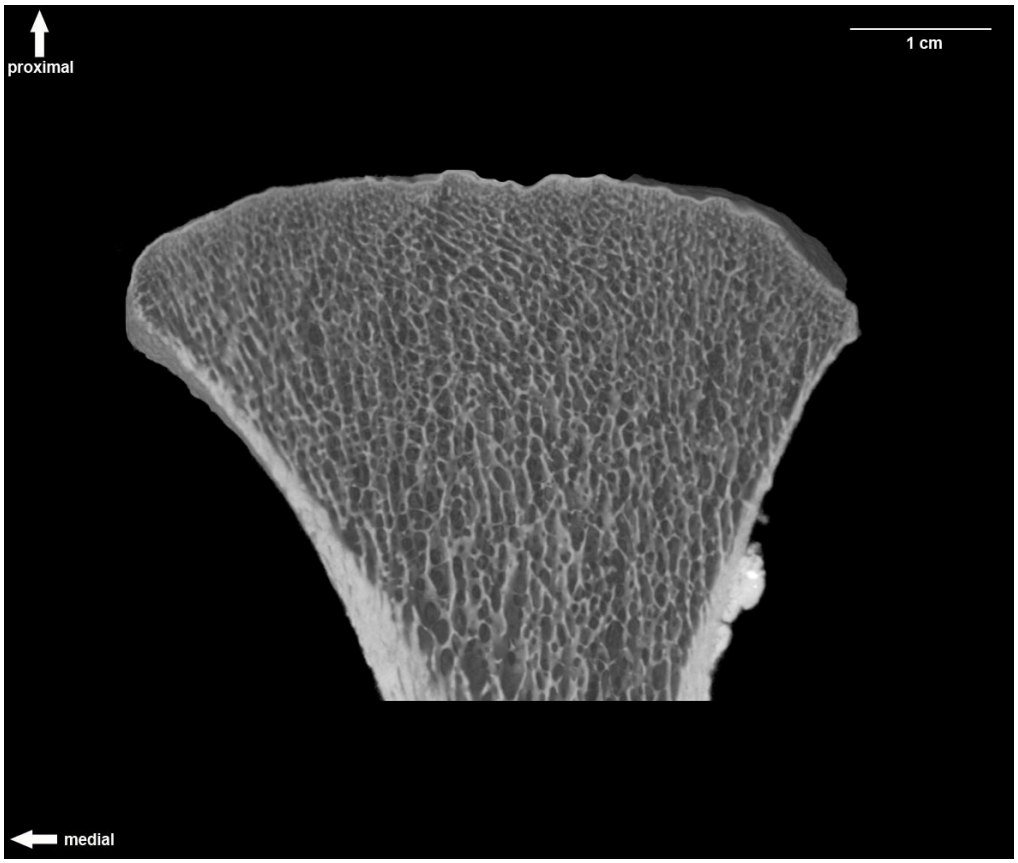

Figure B.9 Coronal scan slice. Burial 15_74. Age estimation is 10.0 years.

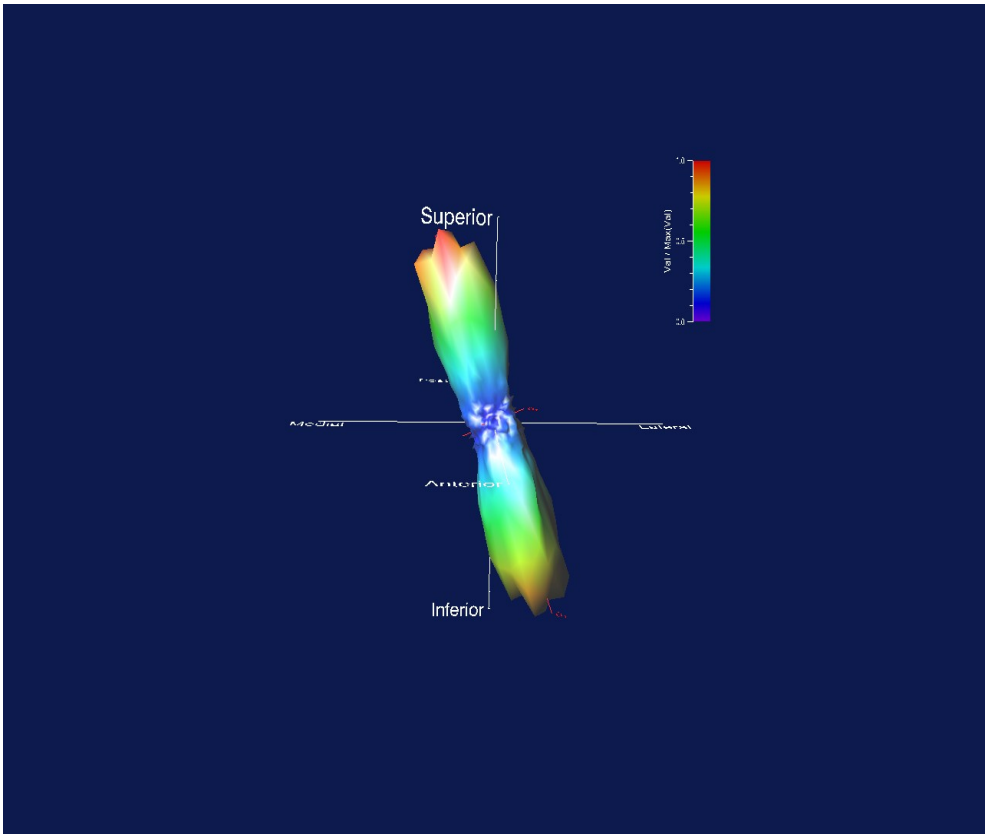

Figure B.10 SVD rose diagram. Burial 15_74. Age estimation is 10.0 years.

Figure B.11 Coronal scan slice. Burial SM_16. Age estimation is 17.0 years.

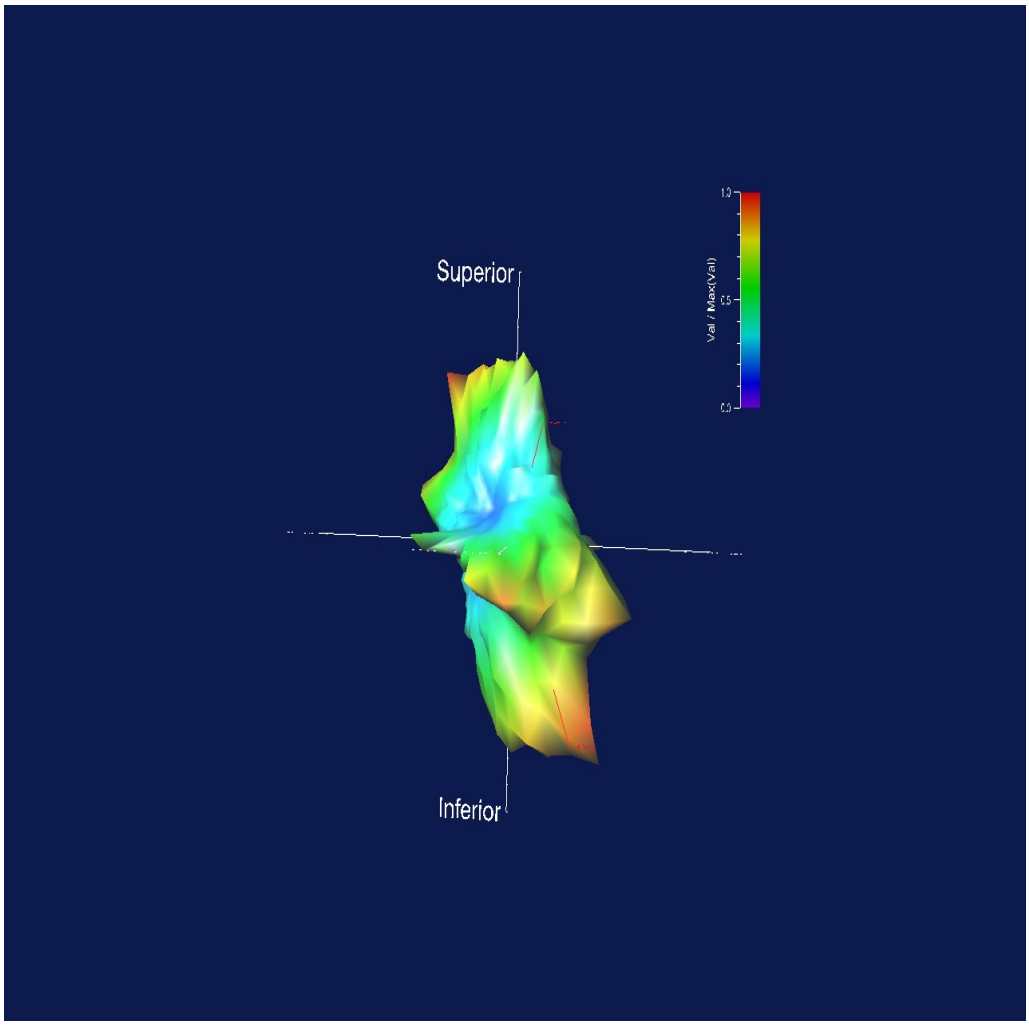

Figure B.12 SVD rose diagram. Burial SM_16. Age estimation is 17.0 years.

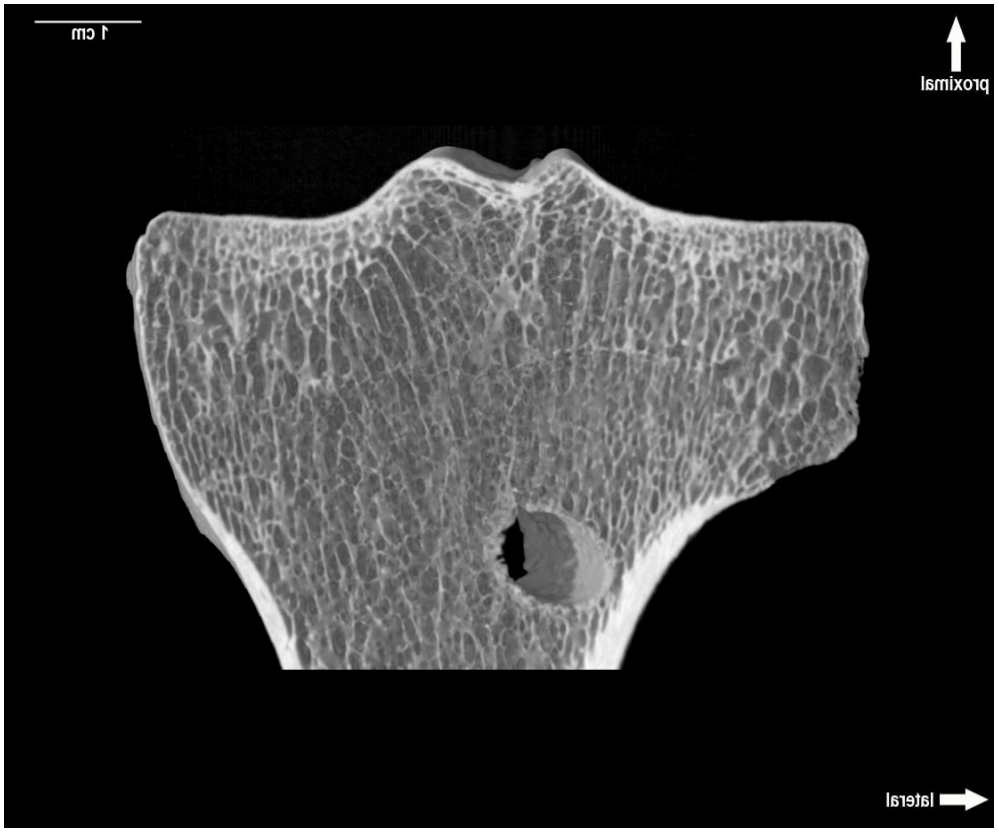

Figure B.13 Coronal scan slice. Burial 3A_76. Age estimation is 21.0 years.

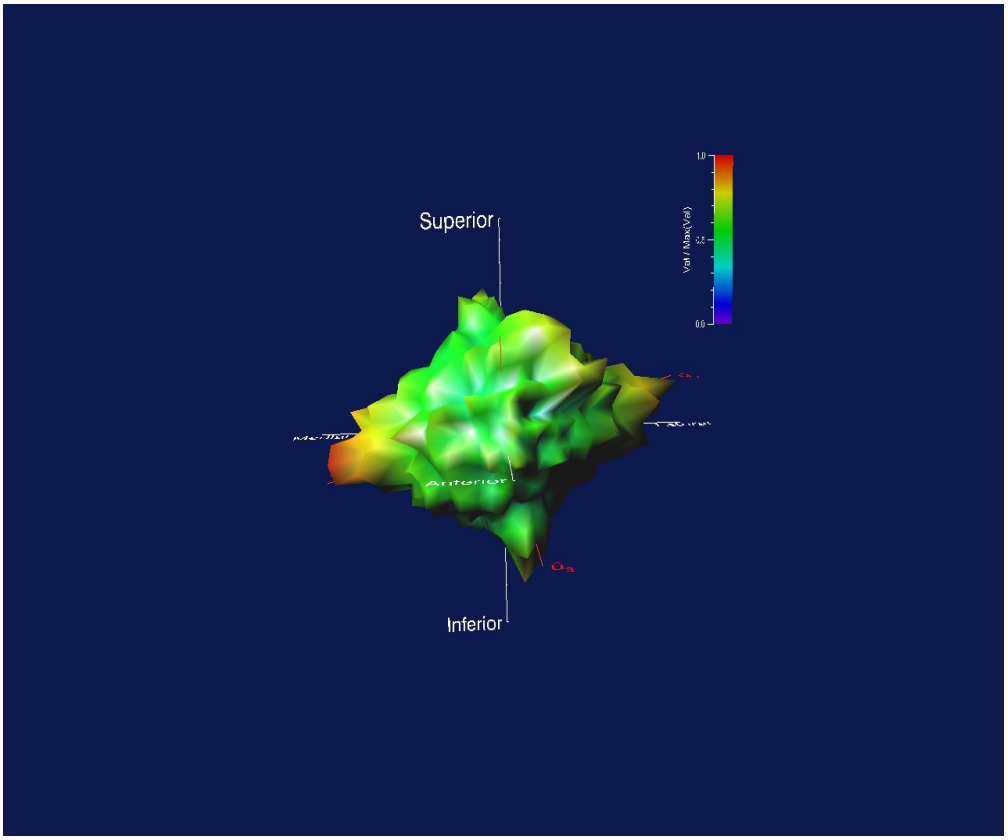

Figure B.14 SVD rose diagram. Burial 3A_76. Age estimation is 21.0 years.

APPENDIX C

LOG FILES: PRIMARY MEDIAL AND LATERAL VOLUMES OF INTEREST

10_72

medial

Star length and volume calcuations for sample: B10_72_0001
Threshhold range, BV/TV: 80.0000-169.000 0.411741
Uniform Orientations: 513
Vector sampling: Dense
Random Points: 2000
Data orientation (strike, dip, up): -42.0000 -180.000 0
SVD Eigenvalues: Eigenvectors Trend Plunge
0.740179 -0.332908 0.106668 0.936907 107.766 69.5384
0.146207 -0.565003 0.772911 -0.288758 323.833 16.7836
0.113615 -0.754947 -0.625485 -0.197040 230.358 11.3639
SVD Fabric Tensor:
0.193460 -0.0364826 -0.190110
-0.0364826 0.140214 0.0553437
-0.190110 0.0553437 0.666326
SVD DA I E Sum(tau)
6.51481 0.153496 0.802471 1.66079
SLD Eigenvalues: Eigenvectors Trend Plunge
0.447962 -0.339228 0.124348 0.932449 110.131 68.8199
0.287192 -0.599957 0.734866 -0.316265 320.771 18.4372
0.264846 -0.724552 -0.666715 -0.174684 227.380 10.0603
SLD Fabric Tensor:
0.293962 -0.0175761 -0.0536820
-0.0175761 0.279745 0.0160385
-0.0536820 0.0160385 0.426294
SLD DA I E Sum(tau)
1.69140 0.591225 0.358893 30.6556
Thickness (minimum line length at each point, non-zero points only)
Mean Variance Skewness Kurtosis Min Max
0.0777510 0.00137260 0.708512 0.589392 0.0214800 0.263869
Thickness histogram
bin num norm
0.0146594 46 0.0254707
0.0439782 607 0.336102
0.0732969 471 0.260797
0.102616 428 0.236988
0.131935 175 0.0968992
0.161253 59 0.0326689

0.190572 12 0.00664452
0.219891 5 0.00276855
0.249210 2 0.00110742
0.278528 1 0.000553710
MIL calculations for sample: B10_72_0001
Threshhold range, BV/TV: 80.0000-169.000 0.411741
Uniform Orientations: 513
Vector sampling: Dense
Random Points: 2000
Data orientation (strike, dip, up): -42.0000 -180.000 0
MIL Ellipse Eigenvectors: Trend Plunge

0.280120 -0.130983 -0.950987 115.061 71.9871
-0.825767 0.472300 -0.308288 299.768 17.9561
0.489532 0.871651 0.0241392 209.319 1.38321
MIL Ellipse Eigenvalues:
12.2060 33.5787 36.2518
MIL Ellipse (H) Eigenvalues:
0.458049 0.276164 0.265787
MIL Ellipse Tensor (M):
32.5422 1.92477 5.72509
1.92477 35.2429 -2.60602
5.72509 -2.60602 14.2513
MIL (H) DA I E Tb.N
1.72337 0.580259 0.397088 5.11791
MIL Fabric Eigenvectors: Trend Plunge
-0.287594 0.0893876 0.953572 107.266 72.4724
-0.743208 0.607161 -0.281064 309.247 16.3237
-0.604095 -0.789535 -0.108182 217.421 6.21055
MIL Fabric Eigenvalues:
0.421648 0.294433 0.283919
MIL Fabric Tensor:
0.301118 -0.00828492 -0.0355747
-0.00828492 0.288895 0.00994546
-0.0355747 0.00994546 0.409986
MIL (F) DA I E
1.48510 0.673356 0.301709

Lateral

Star length and volume calcuations for sample: B10_72_0001
Threshhold range, BV/TV: 78.0000-166.000 0.393254
Uniform Orientations: 513
Vector sampling: Dense
Random Points: 2000
Data orientation (strike, dip, up): -42.0000 -180.000 0
SVD Eigenvalues: Eigenvectors Trend Plunge

0.680003 0.168166 0.111062 0.979482 236.558 78.3735
0.163318 0.973376 0.138290 -0.182798 81.9140 10.5328
0.156679 -0.155754 0.984145 -0.0848493 351.007 4.86736
SVD Fabric Tensor:
0.177769 0.0106678 0.0850182
0.0106678 0.163261 0.0567609
0.0850182 0.0567609 0.658970
SVD DA I E Sum(tau)
4.34011 0.230409 0.759827 1.45419
SLD Eigenvalues: Eigenvectors Trend Plunge
0.437817 0.142563 0.114689 0.983119 231.184 79.4572
0.282865 0.114066 -0.988550 0.0987818 353.418 5.66902
0.279318 -0.983191 -0.0980571 0.154013 84.3045 8.85954
SLD Fabric Tensor:
0.282586 0.00219167 0.0222546
0.00219167 0.284869 0.0175249
0.0222546 0.0175249 0.432546
SLD DA I E Sum(tau)
1.56745 0.637979 0.353921 29.9076
Thickness (minimum line length at each point, non-zero points only)
Mean Variance Skewness Kurtosis Min Max
0.0788114 0.00149153 0.552241 -0.320442 0.0214800 0.220627
Thickness histogram
bin num norm
0.0122571 56 0.0315138
0.0367712 452 0.254361
0.0612853 338 0.190208
0.0857994 396 0.222847
0.110313 267 0.150253
0.134828 184 0.103545
0.159342 46 0.0258863
0.183856 35 0.0196961
0.208370 2 0.00112549
0.232884 1 0.000562746
MIL calculations for sample: B10_72_0001
Threshhold range, BV/TV: 78.0000-166.000 0.393254
Uniform Orientations: 513
Vector sampling: Dense
Random Points: 2000
Data orientation (strike, dip, up): -42.0000 -180.000 0
MIL Ellipse Eigenvectors: Trend Plunge
-0.128390 -0.114205 -0.985126 228.346 80.1056

0.830283 -0.555619 -0.0437969 123.790 2.51018
0.542353 0.823556 -0.166158 33.3669 9.56450
MIL Ellipse Eigenvalues:
11.1827 31.8206 33.7012
MIL Ellipse (H) Eigenvalues:
0.461074 0.273331 0.265595
MIL Ellipse Tensor (M):
32.0336 0.537367 -2.77976
0.537367 32.8270 -2.57923
-2.77976 -2.57923 11.8439
MIL (H) DA I E Tb.N
1.73600 0.576036 0.407187 4.93306
MIL Fabric Eigenvectors: Trend Plunge
0.0933302 0.0814615 0.992297 228.885 82.8839
-0.907263 0.417453 0.0510621 114.708 2.92691
0.410077 0.905040 -0.112868 24.3755 6.48067
MIL Fabric Eigenvalues:
0.429700 0.288094 0.282206
MIL Fabric Tensor:
0.288337 -0.00110831 0.0133869
-0.00110831 0.284211 0.0120480
0.0133869 0.0120480 0.427452
MIL (F) DA I E
1.52264 0.656752 0.329547

14B_72

medial

Star length and volume calcuations for sample: 14B_72_0001
Threshhold range, BV/TV: 103.000-194.000 0.460646
Uniform Orientations: 513
Vector sampling: Dense
Random Points: 2000
Data orientation (strike, dip, up): 176.0007.000001

SVD Eigenvalues:	Eigenvectors		Trend	Plunge
0.783592	-0.308677	0.483920	0.818865	147.467 54.9713
0.115614	-0.271440	0.780289	-0.563444	340.819 34.2943
0.100794	-0.911613	-0.396195	-0.109502	246.510 6.28663

SVD Fabric Tensor:

0.166944	-0.105132	-0.170321
-0.105132	0.269714	0.264054
-0.170321	0.264054	0.563342

SVD DA	I	E	Sum(tau)
7.77420	0.128631	0.852457	4.35148

SLD Eigenvalues:	Eigenvectors		Trend	Plunge
0.463022	-0.330749	0.494492	0.803792	146.223 53.4938
0.274054	-0.233726	0.782272	-0.577428	343.365 35.2698
0.262924	-0.914318	-0.378851	-0.143160	247.493 8.23073

SLD Fabric Tensor:

0.285422	-0.0347615	-0.0516945
-0.0347615	0.318664	0.0745051
-0.0516945	0.0745051	0.395915

SLD DA	I	E	Sum(tau)
1.76105	0.567845	0.408118	40.6023

Thickness (minimum line length at each point, non-zero points only)

Mean	Variance	Skewness	Kurtosis	Min	Max
0.0873130	0.00165621	0.441779	-0.346844	0.0218000	0.221573

Thickness histogram

bin num	norm
0.0123096	30 0.0165289
0.0369288	399 0.219835
0.0615479	283 0.155923
0.0861671	421 0.231956
0.110786	320 0.176309
0.135405	217 0.119559

0.160025 86 0.0473829

0.184644 47 0.0258953
0.209263 11 0.00606061
0.233882 1 0.000550964
MIL calculations for sample: 14B_72_0001
Threshhold range, BV/TV: 103.000-194.000 0.460646
Uniform Orientations: 513
Vector sampling: Dense
Random Points: 2000
Data orientation (strike, dip, up): 176.0007.000001
MIL Ellipse Eigenvectors: Trend Plunge
-0.277180 0.472518 0.836599 149.604 56.7827
-0.298519 -0.869976 0.392465 18.9389 23.1079
0.913267 -0.140957 0.382196 278.774 22.4698
MIL Ellipse Eigenvalues:
12.5444 31.4346 35.9430
MIL Ellipse (H) Eigenvalues:
0.449947 0.284238 0.265815
MIL Ellipse Tensor (M):

33.7436 1.89371 5.95407
1.89371 27.3065 -7.71031
5.95407 -7.71031 18.8720
MIL (H) DA I E Tb.N
1.69271 0.590770 0.368284 5.04427
MIL Fabric Eigenvectors: Trend Plunge
-0.313638 0.479877 0.819359 146.832 55.0207
0.291846 0.869847 -0.397732 18.5473 23.4365
0.903580 -0.114383 0.412868 277.215 24.3851
MIL Fabric Eigenvalues:
0.424736 0.294252 0.281012
MIL Fabric Tensor:
0.296278 -0.0182703 -0.0384712
-0.0182703 0.324127 0.0519302
-0.0384712 0.0519302 0.379595
MIL (F) DA I E
1.51145 0.661617 0.307211

Lateral

Star length and volume calcuations for sample: 14B_72_0001
Threshhold range, BV/TV: 96.0000-190.000 0.445191
Uniform Orientations: 513
Vector sampling: Dense
Random Points: 2000
Data orientation (strike, dip, up): 176.0007.000001

SVD Eigenvalues: Eigenvectors Trend Plunge
0.766282 0.0278676 0.339150 0.940320 184.697 70.1053
0.127450 0.0100177 0.940543 -0.339527 0.610229 19.8481
0.106268 -0.999561 0.0188816 0.0228132 91.0822 1.30721
SVD Fabric Tensor:
0.106783 0.00643755 0.0172232
0.00643755 0.200922 0.203720
0.0172232 0.203720 0.692295
SVD DA I E Sum(tau)
7.21082 0.138680 0.833678 4.18737
SLD Eigenvalues: Eigenvectors Trend Plunge
0.454655 0.0186849 0.337877 0.941005 183.165 70.2210
0.277077 -0.0734730 0.939089 -0.335730 355.526 19.6169
0.268268 -0.997122 -0.0628654 0.0423716 86.3925 2.42844
SLD Fabric Tensor:
0.268381 0.000568897 0.00349446
0.000568897 0.297314 0.0564834
0.00349446 0.0564834 0.434305
SLD DA I E Sum(tau)
1.69478 0.590047 0.390578 41.2858
Thickness (minimum line length at each point, non-zero points only)
Mean Variance Skewness Kurtosis Min Max
0.0904481 0.00167456 0.317686 -0.347894 0.0218000 0.235803
Thickness histogram
bin num norm
0.0131002 34 0.0186813
0.0393005 407 0.223626
0.0655008 248 0.136264
0.0917012 485 0.266484
0.117902 346 0.190110
0.144102 195 0.107143
0.170302 73 0.0401099
0.196503 26 0.0142857
0.222703 5 0.00274725
0.248903 1 0.000549451
MIL calculations for sample: 14B_72_0001
Threshhold range, BV/TV: 96.0000-190.000 0.445191
Uniform Orientations: 513
Vector sampling: Dense
Random Points: 2000
Data orientation (strike, dip, up): 176.0007.000001
MIL Ellipse Eigenvectors: Trend Plunge

-0.0395918	-0.304637	-0.951645	187.405	72.1095
-0.0990334	0.948899	-0.299637	354.042	17.4358
0.994296	0.0823815	-0.0677379	85.2636	3.88407

MIL Ellipse Eigenvalues:

9.88122	28.8640	32.6035

MIL Ellipse (H) Eigenvalues:

0.468249	0.273971	0.257780

MIL Ellipse Tensor (M):

32.5313	0.0773624	-0.967087
0.0773624	27.1277	-5.52408
-0.967087	-5.52408	11.6898

MIL (H) DA	I	E	Tb.N
1.81647	0.550520	0.414904	4.75123

MIL Fabric Eigenvectors:			Trend	Plunge
0.00992339	0.314177	0.949312	181.809	71.6794
0.0999475	0.944293	-0.313561	6.04190	18.2740
-0.994943	0.0979929	-0.0220306	275.625	1.26236

MIL Fabric Eigenvalues:

0.429759	0.289958	0.280283

MIL Fabric Tensor:

0.280394	0.00137924	0.00110489
0.00137924	0.303665	0.0417167
0.00110489	0.0417167	0.415941

MIL (F) DA	I	E
1.53331	0.652185	0.325300

medial

Star length and volume calcuations for sample: B9_72_0001
Threshhold range, BV/TV: 104.000-220.000 0.404106
Uniform Orientations: 513
Vector sampling: Dense
Random Points: 2000
Data orientation (strike, dip, up): -31.0000 180.0000

SVD Eigenvalues:	Eigenvectors		Trend	Plunge
0.762179	-0.262182	0.306252	0.915134	139.433
66.2248				
0.130971	-0.743449	0.540504	-0.393876	306.018
23.1959				
0.106850	-0.615259	-0.783623	0.0859727	38.1371
4.93196				

SVD Fabric Tensor:

0.165229	-0.0623118	-0.150171
-0.0623118	0.175360	0.178528
-0.150171	0.178528	0.659411

SVD DA	I	E	Sum(tau)
7.13318	0.140190	0.828162	6.12506

SLD Eigenvalues:	Eigenvectors		Trend	Plunge
0.461480	-0.268163	0.323999	0.907256	140.387
65.1288				
0.277181	-0.728063	0.548562	-0.411100	306.996
24.2740				
0.261339	-0.630882	-0.770782	0.0887872	39.3002
5.09384				

SLD Fabric Tensor:

0.284129	-0.0237160	-0.0439515
-0.0237160	0.287116	0.0552590
-0.0439515	0.0552590	0.428755

SLD DA	I	E	Sum(tau)
1.76583	0.566306	0.399366	45.3108

Thickness (minimum line length at each point, non-zero points only)

Mean	Variance	Skewness	Kurtosis	Min	Max
0.0952437	0.00225912	0.543703	0.0758488	0.0214800	0.279240

Thickness histogram

bin num	norm
0.0155133	58	0.0323661
0.0465400	460	0.256696
0.0775667	379	0.211496
0.108593	396	0.220982
0.139620	326	0.181920
0.170647	103	0.0574777

0.201673 47 0.0262277

0.232700 15 0.00837054
0.263727 7 0.00390625
0.294753 1 0.000558036
MIL calculations for sample: B9_72_0001
Threshhold range, BV/TV: 104.000-220.000 0.404106
Uniform Orientations: 513
Vector sampling: Dense
Random Points: 2000
Data orientation (strike, dip, up): -31.0000 180.0000
MIL Ellipse Eigenvectors: Trend Plunge
0.226437 -0.272250 -0.935204 140.249 69.2611
-0.740608 0.575493 -0.346854 307.849 20.2950
0.632634 0.771160 -0.0713178 39.3643 4.08968
MIL Ellipse Eigenvalues:
8.01667 23.6775 25.4084
MIL Ellipse (H) Eigenvalues:
0.466509 0.271450 0.262041
MIL Ellipse Tensor (M):

23.5672 1.80990 3.23831
1.80990 23.5460 -4.08259
3.23831 -4.08259 9.98925
MIL (H) DA I E Tb.N
1.78029 0.561705 0.418125 4.24151
MIL Fabric Eigenvectors: Trend Plunge
-0.226055 0.309063 0.923785 143.818 67.4859
-0.670277 0.638785 -0.377733 313.622 22.1933
-0.706843 -0.704581 0.0627574 45.0918 3.59810
MIL Fabric Eigenvalues:
0.438634 0.285741 0.275625
MIL Fabric Tensor:
0.288500 -0.0157196 -0.0314794
-0.0157196 0.295323 0.0440995
-0.0314794 0.0440995 0.416177
MIL (F) DA I E
1.59141 0.628372 0.348567

Lateral

Star length and volume calcuations for sample: B9_72_0001
Threshhold range, BV/TV: 104.000-215.000 0.389307
Uniform Orientations: 513
Vector sampling: Dense
Random Points: 2000
Data orientation (strike, dip, up): -31.0000 180.0000
SVD Eigenvalues: Eigenvectors Trend Plunge

0.802247 0.203644 0.161521 0.965630 231.580
74.9345
0.111447 0.0324612 -0.986869 0.158228 358.116
9.10405
0.0863062 -0.978507 0.000876516 0.206213 90.0513
11.9005
SVD Fabric Tensor:
0.116023 0.0227438 0.140915
0.0227438 0.129469 0.107739
0.140915 0.107739 0.754507
SVD DA I E Sum(tau)
9.29535 0.107581 0.861081 6.42479
SLD Eigenvalues: Eigenvectors Trend Plunge
0.480790 0.209902 0.172079 0.962461 230.655
74.2511
0.270178 -0.0387160 0.985081 -0.167679 357.749
9.65292
0.249032 -0.976956 -0.00206642 0.213432 89.8788
12.3236
SLD Fabric Tensor:
0.259274 0.00756452 0.0469576
0.00756452 0.276415 0.0348906
0.0469576 0.0348906 0.464311
SLD DA I E Sum(tau)
1.93064 0.517964 0.438053 44.1015
Thickness (minimum line length at each point, non-zero points only)
Mean Variance Skewness Kurtosis Min Max
0.0928604 0.00182260 0.327811 -0.342014 0.0214800 0.258677
Thickness histogram
bin num norm
0.0143709 25 0.0135796
0.0431128 450 0.244432
0.0718547 295 0.160239
0.100597 527 0.286257
0.129339 303 0.164584
0.158080 174 0.0945138
0.186822 49 0.0266160
0.215564 15 0.00814775
0.244306 2 0.00108637
0.273048 1 0.000543183
MIL calculations for sample: B9_72_0001
Threshhold range, BV/TV: 104.000-215.000 0.389307
Uniform Orientations: 513
Vector sampling: Dense
Random Points: 2000
Data orientation (strike, dip, up): -31.0000 180.0000
MIL Ellipse Eigenvectors: Trend Plunge
0.168037 0.152310 0.973943 227.811 76.8917

-0.170391 0.977609 -0.123485 350.113 7.09327
0.970943 0.145201 -0.190227 81.4946 10.9660
MIL Ellipse Eigenvalues:
6.72288 23.7898 25.8314
MIL Ellipse (H) Eigenvalues:
0.489775 0.260363 0.249862
MIL Ellipse Tensor (M):
25.2326 -0.148980 -3.17024
-0.148980 23.4369 -2.58812
-3.17024 -2.58812 7.67460
MIL (H) DA I E Tb.N
1.96018 0.510157 0.468403 4.16463
MIL Fabric Eigenvectors: Trend Plunge
0.197292 0.163680 0.966584 230.320 75.1464
0.140786 -0.980474 0.137296 351.829 7.89140
-0.970183 -0.108995 0.216483 83.5900 12.5026
MIL Fabric Eigenvalues:
0.458189 0.275279 0.266532
MIL Fabric Tensor:
0.274165 0.00498167 0.0367179
0.00498167 0.280075 0.0291447
0.0367179 0.0291447 0.445759
MIL (F) DA I E
1.71908 0.581707 0.399203

5_71

medial

Star length and volume calcuations for sample: B5_71_0001
Threshhold range, BV/TV: 112.000-255.000 0.460371
Uniform Orientations: 513
Vector sampling: Dense
Random Points: 2000
Data orientation (strike, dip, up): 172.000-6.00000 1

SVD Eigenvalues:	Eigenvectors		Trend	Plunge
0.679903	-0.567393	0.358696	0.741217	122.300
47.8351				
0.188579	-0.468816	-0.880725	0.0673343	28.0267
3.86089				
0.131517	-0.676961	0.309290	-0.667880	294.555
41.9037				

SVD Fabric Tensor:

0.320604	-0.0880476	-0.232431
-0.0880476	0.246336	0.142416
-0.232431	0.142416	0.433060

SVD DA	I	E	Sum(tau)
5.16969	0.193435	0.722638	125.127

SLD Eigenvalues:	Eigenvectors		Trend	Plunge
0.432582	-0.586164	0.377116	0.717074	122.756
45.8134				
0.302249	-0.527387	-0.849481	0.0156451	31.8334
0.896437				
0.265168	-0.615041	0.369005	-0.696821	300.962
44.1725				

SLD Fabric Tensor:

0.333003	-0.0203947	-0.0706740
-0.0203947	0.315736	0.0447795
-0.0706740	0.0447795	0.351261

SLD DA	I	E	Sum(tau)
1.63135	0.612988	0.301291	130.032

Thickness (minimum line length at each point, non-zero points only)

Mean	Variance	Skewness	Kurtosis	Min	Max
0.151146	0.00504136	0.475285	0.0309186	0.0237900	0.459339

Thickness histogram

bin num		norm
0.0255188	94	0.0519911
0.0765564	406	0.224558
0.127594	459	0.253872
0.178632	436	0.241150
0.229669	269	0.148783
0.280707	100	0.0553097

0.331745 32 0.0176991
0.382782 9 0.00497788
0.433820 2 0.00110619
0.484857 1 0.000553097
MIL calculations for sample: B5_71_0001
Threshhold range, BV/TV: 112.000-255.000 0.460371
Uniform Orientations: 513
Vector sampling: Dense
Random Points: 2000
Data orientation (strike, dip, up): 172.000-6.00000 1
MIL Ellipse Eigenvectors: Trend Plunge
-0.633160 0.386443 0.670649 121.397 42.1172
-0.598180 -0.794170 -0.107123 216.988 6.14949
-0.491212 0.468994 -0.733999 313.674 47.2227
MIL Ellipse Eigenvalues:
5.13646 9.20417 11.8789
MIL Ellipse (H) Eigenvalues:
0.415869 0.310667 0.273464
MIL Ellipse Tensor (M):
8.21884 0.379095 2.69163
0.379095 9.18503 -1.97497
2.69163 -1.97497 8.81565
MIL (H) DA I E Tb.N
1.52074 0.657573 0.252967 2.91476
MIL Fabric Eigenvectors: Trend Plunge
-0.598016 0.421224 0.681871 125.160 42.9900
-0.590888 -0.806505 -0.0200054 216.228 1.14630
-0.541506 0.414873 -0.731199 307.457 46.9870
MIL Fabric Eigenvalues:
0.397122 0.319441 0.283437
MIL Fabric Tensor:
0.336664 -0.0114792 -0.0459320
-0.0114792 0.327027 0.0332338
-0.0459320 0.0332338 0.336309
MIL (F) DA I E
1.40110 0.713726 0.195611

Lateral

Star length and volume calcuations for sample: B5_71_0001
Threshhold range, BV/TV: 111.000-219.000 0.486465
Uniform Orientations: 513
Vector sampling: Dense
Random Points: 2000
Data orientation (strike, dip, up): 172.000-6.00000 1
SVD Eigenvalues: Eigenvectors Trend Plunge
0.586776 0.131924 0.177229 0.975287 216.663 77.2358

0.243877 -0.905751 0.421312 0.0459577 114.946 2.63411
0.169346 0.402755 0.889430 -0.216107 24.3621 12.4805
SVD Fabric Tensor:
0.237755 -0.0186814 0.0506059
-0.0186814 0.195687 0.0735956
0.0506059 0.0735956 0.566557
SVD DA I E Sum(tau)
3.46495 0.288604 0.584378 178.591
SLD Eigenvalues: Eigenvectors Trend Plunge
0.397644 0.163369 0.216818 0.962445 216.998 74.2479
0.319449 -0.890084 0.453154 0.0490005 116.981 2.80865
0.282907 0.425512 0.864662 -0.267017 26.2024 15.4869
SLD Fabric Tensor:
0.314920 -0.0106747 0.0164467
-0.0106747 0.295805 0.0247540
0.0164467 0.0247540 0.389275
SLD DA I E Sum(tau)
1.40556 0.711460 0.196646 158.924
Thickness (minimum line length at each point, non-zero points only)
Mean Variance Skewness Kurtosis Min Max
0.167892 0.00583790 0.346116 -0.180511 0.0237900 0.454076
Thickness histogram
bin num norm
0.0252264 63 0.0344639
0.0756793 331 0.181072
0.126132 383 0.209519
0.176585 438 0.239606
0.227038 374 0.204595
0.277491 156 0.0853392
0.327944 56 0.0306346
0.378396 22 0.0120350
0.428849 4 0.00218818
0.479302 1 0.000547046
MIL calculations for sample: B5_71_0001
Threshhold range, BV/TV: 111.000-219.000 0.486465
Uniform Orientations: 513
Vector sampling: Dense
Random Points: 2000
Data orientation (strike, dip, up): 172.000-6.00000 1
MIL Ellipse Eigenvectors: Trend Plunge
-0.151969 -0.370972 -0.916125 202.276 66.3660
0.890466 -0.453625 0.0359767 296.995 2.06176
0.428924 0.810311 -0.399275 27.8937 23.5329

MIL Ellipse Eigenvalues:

6.17054	8.13532	9.64182

MIL Ellipse (H) Eigenvalues:

0.374406	0.326075	0.299519

MIL Ellipse Tensor (M):

8.36711	0.412834	-0.531542
0.412834	8.85410	-1.15515
-0.531542	-1.15515	6.72648

MIL (H) DA I E Tb.N

1.25002	0.799986	0.129088	2.82073

MIL Fabric Eigenvectors:

			Trend	Plunge
0.187362	0.379958	0.905830	206.248	64.9353
-0.908171	0.418417	0.0123374	114.737	0.706896
0.374327	0.824960	-0.423462	24.4063	25.0534

MIL Fabric Eigenvalues:

0.367712	0.326858	0.305429

MIL Fabric Tensor:

0.325290	-0.00370913	0.0103305
-0.00370913	0.318172	0.0215471
0.0103305	0.0215471	0.356538

MIL (F) DA I E

1.20392	0.830620	0.111103

8_72

medial

Star length and volume calcuations for sample: B8_72_0001
Threshhold range, BV/TV: 84.0000-255.000 0.295769
Uniform Orientations: 513
Vector sampling: Dense
Random Points: 2000
Data orientation (strike, dip, up): -11.0000 180.0001

SVD Eigenvalues:	Eigenvectors		Trend	Plunge
0.755494	0.237628	-0.289713	0.927146	320.641
67.9942				
0.143014	0.0160155	-0.953188	-0.301955	179.037
17.5751				
0.101492	0.971224	0.0866015	-0.221864	84.9046
12.8185				

SVD Fabric Tensor:

0.138432	-0.0456578	0.143886
-0.0456578	0.194110	-0.163718
0.143886	-0.163718	0.667457

SVD DA	I	E	Sum(tau)
7.44386	0.134339	0.810701	2.50347

SLD Eigenvalues:	Eigenvectors		Trend	Plunge
0.451620	0.238192	-0.301186	0.923337	321.661
67.4189				
0.286920	0.00765345	-0.950089	-0.311886	179.538
18.1730				
0.261460	0.971188	0.0813554	-0.223998	85.2116
12.9440				

SLD Fabric Tensor:

0.272250	-0.0138272	0.0417615
-0.0138272	0.301691	-0.0453388
0.0417615	-0.0453388	0.426058

SLD DA	I	E	Sum(tau)
1.72730	0.578937	0.364689	32.7129

Thickness (minimum line length at each point, non-zero points only)

Mean	Variance	Skewness	Kurtosis	Min	Max
0.0864760	0.00213390	0.741258	0.357904	0.0214800	0.289055

Thickness histogram

bin num	norm
0.0160586	160	0.0895355
0.0481759	489	0.273643
0.0802932	462	0.258534
0.112410	335	0.187465
0.144528	207	0.115837
0.176645	95	0.0531617

0.208762 30 0.0167879
0.240879 5 0.00279799
0.272997 3 0.00167879
0.305114 1 0.000559597
MIL calculations for sample: B8_72_0001
Threshhold range, BV/TV: 84.0000-255.000 0.295769
Uniform Orientations: 513
Vector sampling: Dense
Random Points: 2000
Data orientation (strike, dip, up): -11.0000 180.0001
MIL Ellipse Eigenvectors: Trend Plunge
0.185699 -0.276967 0.942765 326.159 70.5211
-0.0458744 0.955962 0.289881 177.253 16.8508
-0.981535 -0.0970794 0.164816 84.3515 9.48653
MIL Ellipse Eigenvalues:
5.89924 14.2292 17.0650
MIL Ellipse (H) Eigenvalues:
0.448061 0.288499 0.263440
MIL Ellipse Tensor (M):
16.6740 0.698645 -1.91709
0.698645 13.6169 2.12970
-1.91709 2.12970 6.90252
MIL (H) DA I E Tb.N
1.70081 0.587956 0.356115 3.44763
MIL Fabric Eigenvectors: Trend Plunge
0.223050 -0.272651 0.935901 320.714 69.3742
0.0627066 -0.954087 -0.292893 176.240 17.0313
0.972788 0.124017 -0.195712 82.7348 11.2863
MIL Fabric Eigenvalues:
0.419393 0.299046 0.281561
MIL Fabric Tensor:
0.288487 -0.00942830 0.0284516
-0.00942830 0.307724 -0.0302849
0.0284516 -0.0302849 0.403789
MIL (F) DA I E
1.48953 0.671354 0.286954

Lateral

Star length and volume calcuations for sample: B8_72_0001
Threshhold range, BV/TV: 84.0000-246.000 0.257534
Uniform Orientations: 513
Vector sampling: Dense
Random Points: 2000
Data orientation (strike, dip, up): -11.0000 180.0001
SVD Eigenvalues: Eigenvectors Trend Plunge
0.712579 -0.0795247 -0.139327 0.987048 29.7168
80.7684

0.177457 0.0311835 -0.990047 -0.137238 178.196
7.88803
0.109964 0.996345 0.0198660 0.0830779 268.858
4.76551
SVD Fabric Tensor:
0.113841 0.00459316 -0.0475909
0.00459316 0.187818 -0.0737025
-0.0475909 -0.0737025 0.698341
SVD DA I E Sum(tau)
6.48012 0.154318 0.750965 2.50492
SLD Eigenvalues: Eigenvectors Trend Plunge
0.438592 -0.0987780 -0.138826 0.985378 35.4327
80.1900
0.297876 0.0363303 -0.990064 -0.135844 177.898
7.80744
0.263532 0.994446 0.0223807 0.102840 268.711
5.90274
SLD Fabric Tensor:
0.265285 0.00116523 -0.0172088
0.00116523 0.300571 -0.0193284
-0.0172088 -0.0193284 0.434144
SLD DA I E Sum(tau)
1.66429 0.600858 0.320836 34.7227
Thickness (minimum line length at each point, non-zero points only)
Mean Variance Skewness Kurtosis Min Max
0.0939397 0.00210977 0.546085 0.0436809 0.0214800 0.293071
Thickness histogram
bin num norm
0.0162817 107 0.0583106
0.0488452 466 0.253951
0.0814087 448 0.244142
0.113972 428 0.233243
0.146536 251 0.136785
0.179099 91 0.0495913
0.211663 35 0.0190736
0.244226 6 0.00326975
0.276790 2 0.00108992
0.309353 1 0.000544959
MIL calculations for sample: B8_72_0001
Threshhold range, BV/TV: 84.0000-246.000 0.257534
Uniform Orientations: 513
Vector sampling: Dense
Random Points: 2000
Data orientation (strike, dip, up): -11.0000 180.0001
MIL Ellipse Eigenvectors: Trend Plunge
-0.110315 -0.176719 0.978060 31.9741 77.9758
-0.111351 0.980068 0.164523 173.518 9.46952
-0.987639 -0.0907582 -0.127794 264.750 7.34216

MIL Ellipse Eigenvalues:

4.05479	9.31763	11.5749

MIL Ellipse (H) Eigenvalues:

0.444140	0.292989	0.262872

MIL Ellipse Tensor (M):

11.4554	0.0997397	0.852741
0.0997397	9.17187	0.935822
0.852741	0.935822	4.32006

MIL (H) DA I E Tb.N

1.68957	0.591868	0.340323	2.82169

MIL Fabric Eigenvectors:

			Trend	Plunge
-0.0733848	-0.152006	0.985652	25.7701	80.2823
0.0894676	-0.985335	-0.145296	174.812	8.35444
0.993283	0.0775214	0.0859082	265.537	4.92825

MIL Fabric Eigenvalues:

0.420255	0.303600	0.276145

MIL Fabric Tensor:

0.277141	-0.000812787	-0.0107806
-0.000812787	0.306130	-0.0176607
-0.0107806	-0.0176607	0.416729

MIL (F) DA I E

1.52186	0.657089	0.277581

medial

Star length and volume calcuations for sample: B1_81_0001
Threshhold range, BV/TV: 58.0000-157.000 0.330521
Uniform Orientations: 513
Vector sampling: Dense
Random Points: 2000
Data orientation (strike, dip, up): 172.0000.000000 1

SVD Eigenvalues:	Eigenvectors		Trend	Plunge
0.710384	-0.191574	0.0262297	0.981128	97.7963
78.8510				
0.169884	-0.408459	0.906833	-0.103999	335.752
5.96950				
0.119732	0.892446	0.420674	0.163012	244.762
9.38177				

SVD Fabric Tensor:

0.149776	-0.0215445	-0.108888
-0.0215445	0.161380	0.0104705
-0.108888	0.0104705	0.688843

SVD DA	I	E	Sum(tau)
5.93313	0.168545	0.760857	576.227

SLD Eigenvalues:	Eigenvectors		Trend	Plunge
0.418069	-0.204430	0.0690459	0.976443	108.662
77.5390				
0.309177	-0.378712	0.914254	-0.143936	337.499
8.27568				
0.272754	0.902655	0.399215	0.160752	246.142
9.25056				

SLD Fabric Tensor:

0.284051	-0.0146624	-0.0270214
-0.0146624	0.303892	0.00500393
-0.0270214	0.00500393	0.412058

SLD DA	I	E	Sum(tau)
1.53277	0.652414	0.260463	203.138

Thickness (minimum line length at each point, non-zero points only)

Mean	Variance	Skewness	Kurtosis	Min	Max
0.202984	0.00796177	0.642595	0.252185	0.0585900	0.572195

Thickness histogram

bin num	norm
0.0317886	15	0.00823271
0.0953658	445	0.244237
0.158943	382	0.209660
0.222520	513	0.281559
0.286097	282	0.154775
0.349675	118	0.0647640
0.413252	45	0.0246981
0.476829	16	0.00878156

0.540406 5 0.00274424
0.603983 1 0.000548847
MIL calculations for sample: B1_81_0001
Threshhold range, BV/TV: 58.0000-157.000 0.330521
Uniform Orientations: 513
Vector sampling: Dense
Random Points: 2000
Data orientation (strike, dip, up): 172.0000.000000 1
MIL Ellipse Eigenvectors: Trend Plunge
0.143888 -0.117433 -0.982601 129.219 79.2965
-0.299055 0.941349 -0.156296 342.376 8.99194
0.943325 0.316340 0.100330 251.461 5.75817
MIL Ellipse Eigenvalues:
1.72794 2.73197 3.32815
MIL Ellipse (H) Eigenvalues:
0.397482 0.316114 0.286405
MIL Ellipse Tensor (M):
3.24170 0.194872 0.198379
0.194872 2.77778 -0.0969338
0.198379 -0.0969338 1.76857
MIL (H) DA I E Tb.N
1.38783 0.720548 0.204709 1.60216
MIL Fabric Eigenvectors: Trend Plunge
-0.133908 0.0983089 0.986105 126.284 80.4376
-0.332840 0.932802 -0.138193 340.363 7.94330
-0.933427 -0.346721 -0.0921890 249.623 5.28955
MIL Fabric Eigenvalues:
0.387587 0.317968 0.294445
MIL Fabric Tensor:
0.298721 -0.00852931 -0.0112172
-0.00852931 0.315813 0.00599723
-0.0112172 0.00599723 0.385466
MIL (F) DA I E
1.31633 0.759688 0.179622

Lateral

Star length and volume calcuations for sample: B1_81_0001
Threshhold range, BV/TV: 62.0000-152.000 0.324704
Uniform Orientations: 513
Vector sampling: Dense
Random Points: 2000
Data orientation (strike, dip, up): 172.0000.000000 1
SVD Eigenvalues: Eigenvectors Trend Plunge
0.571207 0.0579279 0.144096 0.987867 201.901 81.0656
0.343998 -0.201587 0.970833 -0.129790 348.270 7.45746

0.0847948 0.977756 0.191623 -0.0852862 78.9116
4.89248
SVD Fabric Tensor:
0.0969604 -0.0466679 0.0346168
-0.0466679 0.339198 0.0365787
0.0346168 0.0365787 0.563842
SVD DA I E Sum(tau)
6.73634 0.148448 0.397770 686.629
SLD Eigenvalues: Eigenvectors Trend Plunge
0.401750 -0.0435311 -0.213603 -0.975950 191.519
77.4088
0.370584 -0.218862 0.955186 -0.199297 347.095
11.4958
0.227666 0.974784 0.204922 -0.0883300 78.1280
5.06754
SLD Fabric Tensor:
0.234842 -0.0282588 0.0136297
-0.0282588 0.366004 0.00908398
0.0136297 0.00908398 0.399154
SLD DA I E Sum(tau)
1.76465 0.566686 0.0775752 223.317
Thickness (minimum line length at each point, non-zero points only)
Mean Variance Skewness Kurtosis Min Max
0.210886 0.0108435 1.058671.523440.0585900 0.718478
Thickness histogram
bin num norm
0.0399154 35 0.0188273
0.119746 634 0.341044
0.199577 556 0.299086
0.279408 376 0.202259
0.359239 152 0.0817644
0.439070 67 0.0360409
0.518901 27 0.0145239
0.598731 7 0.00376547
0.678562 4 0.00215169
0.758393 1 0.000537924
MIL calculations for sample: B1_81_0001
Threshhold range, BV/TV: 62.0000-152.000 0.324704
Uniform Orientations: 513
Vector sampling: Dense
Random Points: 2000
Data orientation (strike, dip, up): 172.0000.000000 1
MIL Ellipse Eigenvectors: Trend Plunge
0.00969307 0.301147 0.953529 181.844 72.4641
-0.174835 0.939395 -0.294906 349.457 17.1519
-0.984550 -0.163852 0.0617568 80.5512 3.54065
MIL Ellipse Eigenvalues:
1.35232 1.81325 4.46049

MIL Ellipse (H) Eigenvalues:

0.414214	0.357714	0.228072

MIL Ellipse Tensor (M):

4.37928	0.425710	-0.165220
0.425710	1.84252	-0.159143
-0.165220	-0.159143	1.40426

MIL (H) DA I E Tb.N

1.81615	0.550615	0.136403	1.54017

MIL Fabric Eigenvectors:

			Trend	Plunge
0.000125524	0.253184	0.967418	180.028	75.3340
-0.184551	0.950806	-0.248813	349.016	14.4073
-0.982823	-0.178507	0.0468447	79.7058	2.68499

MIL Fabric Eigenvalues:

0.390447	0.360902	0.248651

MIL Fabric Tensor:

0.252474	-0.0196924	0.00517164
-0.0196924	0.359219	0.00817539
0.00517164	0.00817539	0.388307

MIL (F) DA I E

1.57026	0.636836	0.0756710

15AB_73

medial

Star length and volume calcuations for sample: B15AB_73_0001
Threshhold range, BV/TV: 100.000-197.000 0.436248
Uniform Orientations: 513
Vector sampling: Dense
Random Points: 2000
Data orientation (strike, dip, up): -14.0000 -180.000 0

SVD Eigenvalues:	Eigenvectors		Trend	Plunge
0.778525	-0.262091	0.247294	0.932821	133.336
68.8788				
0.119597	0.313137	0.936102	-0.160183	18.4957
9.21752				
0.101878	0.912827	-0.250118	0.322780	285.323
18.8312				

SVD Fabric Tensor:

0.150096	-0.0386621	-0.166318
-0.0386621	0.158785	0.153433
-0.166318	0.153433	0.691120

SVD DA	I	E	Sum(tau)
7.64171	0.130861	0.846380	2.17724

SLD Eigenvalues:	Eigenvectors		Trend	Plunge
0.464910	-0.247478	0.247353	0.936788	134.986
69.5189				
0.275512	0.154027	0.964612	-0.214009	9.07227
12.3574				
0.259578	0.956572	-0.0913282	0.276819	275.454
16.0704				

SLD Fabric Tensor:

0.272532	-0.0102017	-0.0481281
-0.0102017	0.286967	0.0442894
-0.0481281	0.0442894	0.440501

SLD DA	I	E	Sum(tau)
1.79102	0.558341	0.407385	31.2991

Thickness (minimum line length at each point, non-zero points only)

Mean	Variance	Skewness	Kurtosis	Min	Max
0.0762281	0.00128904	0.721467	0.502981	0.0214800	0.238707

Thickness histogram

bin num	norm
0.0132615	43	0.0235875
0.0397846	547	0.300055
0.0663076	397	0.217773
0.0928307	466	0.255623
0.119354	251	0.137685
0.145877	77	0.0422381

0.172400 28 0.0153593
0.198923 11 0.00603401
0.225446 2 0.00109709
0.251969 1 0.000548546
MIL calculations for sample: B15AB_73_0001
Threshhold range, BV/TV: 100.000-197.000 0.436248
Uniform Orientations: 513
Vector sampling: Dense
Random Points: 2000
Data orientation (strike, dip, up): -14.0000 -180.000 0
MIL Ellipse Eigenvectors: Trend Plunge
-0.219204 0.271607 0.937112 141.094 69.5721
-0.288276 -0.935620 0.203743 17.1247 11.7559
-0.932119 0.225486 -0.283390 283.599 16.4626
MIL Ellipse Eigenvalues:
14.1488 39.7465 42.8217
MIL Ellipse (H) Eigenvalues:
0.460521 0.274764 0.264715
MIL Ellipse Tensor (M):
41.1884 0.877684 6.07057
0.877684 38.0145 -6.71180
6.07057 -6.71180 17.5141
MIL (H) DA I E Tb.N
1.73969 0.574815 0.403363 5.53629
MIL Fabric Eigenvectors: Trend Plunge
-0.210154 0.238947 0.948019 138.668 71.4450
0.0446020 0.971007 -0.234854 2.62997 13.5830
-0.976650 -0.00707187 -0.214718 269.585 12.3990
MIL Fabric Eigenvalues:
0.429171 0.292828 0.278001
MIL Fabric Tensor:
0.284707 -0.00694900 -0.0302729
-0.00694900 0.300612 0.0308628
-0.0302729 0.0308628 0.414681
MIL (F) DA I E
1.54378 0.647763 0.317690

Lateral

Star length and volume calcuations for sample: B15AB_73_0001
Threshhold range, BV/TV: 103.000-200.000 0.433304
Uniform Orientations: 513
Vector sampling: Dense
Random Points: 2000
Data orientation (strike, dip, up): -14.0000 -180.000 0
SVD Eigenvalues: Eigenvectors Trend Plunge
0.810531 0.0309505 0.148314 0.988456 191.787 81.2856

0.109594 -0.521574 0.846006 -0.110609 328.346 6.35041
0.0798750 -0.852645 -0.512129 0.103541 59.0094 5.94312
SVD Fabric Tensor:
0.0886596 -0.00975964 0.0240676
-0.00975964 0.117218 0.104335
0.0240676 0.104335 0.794122
SVD DA I E Sum(tau)
10.1475 0.0985465 0.864787 4.63601
SLD Eigenvalues: Eigenvectors Trend Plunge
0.485584 0.0464838 0.145318 0.988292 197.738 81.2240
0.266648 -0.610055 0.787556 -0.0871084 322.238 4.99728
0.247769 0.790994 0.598864 -0.125261 52.8706 7.19581
SLD Fabric Tensor:
0.255309 -0.00746412 0.0119284
-0.00746412 0.264500 0.0328591
0.0119284 0.0328591 0.480191
SLD DA I E Sum(tau)
1.95983 0.510249 0.450872 39.0033
Thickness (minimum line length at each point, non-zero points only)
Mean Variance Skewness Kurtosis Min Max
0.0853070 0.00152181 0.468628 -0.0888071 0.0214800 0.232342
Thickness histogram
bin num norm
0.0129079 35 0.0193263
0.0387236 433 0.239094
0.0645394 298 0.164550
0.0903551 484 0.267256
0.116171 316 0.174489
0.141987 162 0.0894533
0.167802 55 0.0303700
0.193618 19 0.0104914
0.219434 8 0.00441745
0.245250 1 0.000552181
MIL calculations for sample: B15AB_73_0001
Threshhold range, BV/TV: 103.000-200.000 0.433304
Uniform Orientations: 513
Vector sampling: Dense
Random Points: 2000
Data orientation (strike, dip, up): -14.0000 -180.000 0
MIL Ellipse Eigenvectors: Trend Plunge
-0.0245872 -0.139468 -0.989921 189.998 81.8585
-0.458997 0.881254 -0.112758 332.487 6.47430
0.888098 0.451598 -0.0856829 63.0466 4.91529

MIL Ellipse Eigenvalues:

9.42850	32.7865	36.7080

MIL Ellipse (H) Eigenvalues:

0.489461	0.262477	0.248061

MIL Ellipse Tensor (M):

35.8653	1.49266	-0.866924
1.49266	33.1319	-3.37660
-0.866924	-3.37660	9.92575

MIL (H) DA I E Tb.N

1.97315	0.506805	0.463742	4.93186

MIL Fabric Eigenvectors:

			Trend	Plunge
0.0213111	0.119985	0.992547	190.072	83.0004
-0.485298	0.869210	-0.0946555	330.824	5.43149
-0.874089	-0.479664	0.0767523	61.2438	4.40191

MIL Fabric Eigenvalues:

0.459220	0.277199	0.263582

MIL Fabric Tensor:

0.266877	-0.00524376	0.00476370
-0.00524376	0.276686	0.0221784
0.00476370	0.0221784	0.456437

MIL (F) DA I E

1.74223	0.573977	0.396371

15A+B_73

medial

Star length and volume calcuations for sample: 15A+B_73_0001
Threshhold range, BV/TV: 95.0000-188.000 0.436121
Uniform Orientations: 513
Vector sampling: Dense
Random Points: 2000
Data orientation (strike, dip, up): -162.000 0.000000 1

SVD Eigenvalues:	Eigenvectors		Trend	Plunge
0.734837	-0.333313	0.223157	0.916026	123.803
66.3518				
0.137005	-0.234579	0.921402	-0.309823	345.717
18.0486				
0.128158	-0.913168	-0.318149	-0.254768	250.792
14.7598				

SVD Fabric Tensor:

0.196045	-0.0470379	-0.184591
-0.0470379	0.165881	0.121491
-0.184591	0.121491	0.638074

SVD DA	I	E	Sum(tau)
5.73386	0.174403	0.813557	1.89616

SLD Eigenvalues:	Eigenvectors		Trend	Plunge
0.447506	-0.351639	0.219291	0.910089	121.949
65.5176				
0.277224	-0.444932	0.816201	-0.368581	331.404
21.6281				
0.275270	-0.823642	-0.534535	-0.189438	237.017
10.9200				

SLD Fabric Tensor:

0.296954	-0.0139909	-0.0547989
-0.0139909	0.284854	0.0337861
-0.0547989	0.0337861	0.418192

SLD DA	I	E	Sum(tau)
1.62570	0.615121	0.380513	31.4440

Thickness (minimum line length at each point, non-zero points only)

Mean	Variance	Skewness	Kurtosis	Min	Max
0.0782612	0.00139823	0.686900	0.297217	0.0214800	0.237163

Thickness histogram

bin num	norm
0.0131758	44	0.0245536
0.0395273	489	0.272879
0.0658787	434	0.242188
0.0922303	423	0.236049
0.118582	262	0.146205
0.144933	79	0.0440848

0.171285 44 0.0245536
0.197636 13 0.00725446
0.223988 3 0.00167411
0.250339 1 0.000558036
MIL calculations for sample: 15A+B_73_0001
Threshhold range, BV/TV: 95.0000-188.000 0.436121
Uniform Orientations: 513
Vector sampling: Dense
Random Points: 2000
Data orientation (strike, dip, up): -162.000 0.000000 1
MIL Ellipse Eigenvectors: Trend Plunge
-0.290680 0.219441 0.931317 127.050 68.6410
-0.0143241 -0.974234 0.225083 0.842354 13.0078
-0.956713 -0.0520869 -0.286333 266.884 16.6386
MIL Ellipse Eigenvalues:
13.7564 39.1898 40.5314
MIL Ellipse (H) Eigenvalues:
0.459759 0.272394 0.267847
MIL Ellipse Tensor (M):
38.2688 1.68917 7.25270
1.68917 37.9687 -5.17779
7.25270 -5.17779 17.2401
MIL (H) DA I E Tb.N
1.71650 0.582582 0.407530 5.46167
MIL Fabric Eigenvectors: Trend Plunge
-0.299858 0.211194 0.930313 125.158 68.4837
0.0537805 0.977379 -0.204544 3.14954 11.8028
0.952467 0.0113014 0.304433 269.320 17.7241
MIL Fabric Eigenvalues:
0.418218 0.293369 0.288413
MIL Fabric Tensor:
0.300098 -0.00795985 -0.0362654
-0.00795985 0.298937 0.0245129
-0.0362654 0.0245129 0.400965
MIL (F) DA I E
1.45007 0.689622 0.298527

Lateral

Star length and volume calcuations for sample: 15A+B_73_0001
Threshhold range, BV/TV: 97.0000-200.000 0.426927
Uniform Orientations: 513
Vector sampling: Dense
Random Points: 2000
Data orientation (strike, dip, up): -162.000 0.000000 1
SVD Eigenvalues: Eigenvectors Trend Plunge
0.770818 0.0215790 0.130276 0.991243 189.405
82.4119

0.134060 -0.205359 0.970910 -0.123133 348.057 7.07296
0.0951216 -0.978449 -0.200904 0.0477046 78.3968 2.73431
SVD Fabric Tensor:
0.0970784 -0.00586424 0.0154378
-0.00586424 0.143295 0.0826011
0.0154378 0.0826011 0.759626
SVD DA I E Sum(tau)
8.10350 0.123403 0.826081 2.69257
SLD Eigenvalues: Eigenvectors Trend Plunge
0.459406 0.00525129 0.153013 0.988210 181.966 81.1932
0.283878 -0.225214 0.963016 -0.147916 346.837 8.50614
0.256715 -0.974295 -0.221782 0.0395178 77.1761 2.26479
SLD Fabric Tensor:
0.258099 -0.00572841 0.00195672
-0.00572841 0.286652 0.0267795
0.00195672 0.0267795 0.455250
SLD DA I E Sum(tau)
1.78956 0.558798 0.382076 33.4446
Thickness (minimum line length at each point, non-zero points only)
Mean Variance Skewness Kurtosis Min Max
0.0805856 0.00138598 0.527930 -0.0471315 0.0214800 0.216838
Thickness histogram
bin num norm
0.0120466 48 0.0267261
0.0361397 391 0.217706
0.0602328 357 0.198775
0.0843259 447 0.248886
0.108419 299 0.166481
0.132512 158 0.0879733
0.156605 62 0.0345212
0.180698 24 0.0133630
0.204791 9 0.00501114
0.228885 1 0.000556793
MIL calculations for sample: 15A+B_73_0001
Threshhold range, BV/TV: 97.0000-200.000 0.426927
Uniform Orientations: 513
Vector sampling: Dense
Random Points: 2000
Data orientation (strike, dip, up): -162.000 0.000000 1
MIL Ellipse Eigenvectors: Trend Plunge
0.0412029 -0.149116 -0.987961 164.554 81.1004
-0.134681 0.978947 -0.153372 352.167 8.82239
0.990032 0.139379 0.0202525 261.986 1.16046

MIL Ellipse Eigenvalues:

10.2362	34.2710	39.0811

MIL Ellipse (H) Eigenvalues:

0.485838	0.265519	0.248643

MIL Ellipse Tensor (M):

38.9449	0.811415	1.07483
0.811415	33.8300	-3.52724
1.07483	-3.52724	10.8134

MIL (H) DA I E Tb.N

1.95396	0.511782	0.453481	5.11966

MIL Fabric Eigenvectors:

			Trend	Plunge
-0.0162897	0.130605	0.991301	172.891	82.4370
-0.187826	0.973383	-0.131331	349.078	7.54649
-0.982067	-0.188331	0.00867486	79.1442	0.497039

MIL Fabric Eigenvalues:

0.435716	0.289096	0.275188

MIL Fabric Tensor:

0.275721	-0.00288431	-0.00224912
-0.00288431	0.291104	0.0190053
-0.00224912	0.0190053	0.433175

MIL (F) DA I E

1.58334	0.631577	0.336502

12_73

medial

Star length and volume calcuations for sample: B12_73_0001
Threshhold range, BV/TV: 89.0000-223.000 0.297488
Uniform Orientations: 513
Vector sampling: Dense
Random Points: 2000
Data orientation (strike, dip, up): -31.9082 -180.000 0

SVD Eigenvalues:	Eigenvectors			Trend	Plunge
0.788231	-0.197561	0.136684	0.970715	124.678	76.0996
0.126379	-0.737835	0.631234	-0.239047	310.548	13.8303
0.0853900	-0.645422	-0.763453	-0.0238569	220.211	1.36703

SVD Fabric Tensor:

0.135136	-0.0380695	-0.127558
-0.0380695	0.114853	0.0870689
-0.127558	0.0870689	0.750011

SVD DA	I	E	Sum(tau)
9.23096	0.108331	0.839668	5.60415

SLD Eigenvalues:	Eigenvectors			Trend	Plunge
0.463028	-0.190175	0.155287	0.969391	129.233	75.7873
0.285050	-0.770052	0.588894	-0.245404	307.407	14.2057
0.251922	-0.608977	-0.793152	0.00758610	37.5168	0.434656

SLD Fabric Tensor:

0.279201	-0.0212571	-0.0326580
-0.0212571	0.268501	0.0269911
-0.0326580	0.0269911	0.452297

SLD DA	I	E	Sum(tau)
1.83798	0.544076	0.384379	41.9983

Thickness (minimum line length at each point, non-zero points only)

Mean	Variance	Skewness	Kurtosis	Min	Max
0.0967236	0.00227377	0.485948	-0.217803	0.0214800	0.308295

Thickness histogram

bin num	norm
0.0171275	52	0.0289855
0.0513825	512	0.285396
0.0856374	448	0.249721
0.119892	416	0.231884
0.154147	225	0.125418
0.188402	114	0.0635452

0.222657 22 0.0122631
0.256912 3 0.00167224
0.291167 1 0.000557414
0.325422 1 0.000557414
MIL calculations for sample: B12_73_0001
Threshhold range, BV/TV: 89.0000-223.000 0.297488
Uniform Orientations: 513
Vector sampling: Dense
Random Points: 2000
Data orientation (strike, dip, up): -31.9082 -180.000 0
MIL Ellipse Eigenvectors: Trend Plunge
0.153478 -0.134225 -0.978993 131.172 78.2354
-0.746628 0.633233 -0.203869 310.302 11.7633
0.647295 0.762234 -0.00302931 40.3382 0.173567
MIL Ellipse Eigenvalues:
3.64374 10.8766 13.8843
MIL Ellipse (H) Eigenvalues:
0.478221 0.276793 0.244986
MIL Ellipse Tensor (M):
11.9664 1.63297 1.08086
1.63297 12.4937 -0.957383
1.08086 -0.957383 3.94445
MIL (H) DA I E Tb.N
1.95204 0.512286 0.421202 2.96986
MIL Fabric Eigenvectors: Trend Plunge
-0.124894 0.159069 0.979336 141.863 78.3319
-0.739614 0.643012 -0.198764 311.003 11.4647
-0.661341 -0.749155 0.0373418 41.4375 2.14003
MIL Fabric Eigenvalues:
0.447336 0.290166 0.262497
MIL Fabric Tensor:
0.280516 -0.0168310 -0.0185406
-0.0168310 0.278615 0.0252583
-0.0185406 0.0252583 0.440869
MIL (F) DA I E
1.70415 0.586801 0.351346

Lateral

Star length and volume calcuations for sample: B12_73_0001
Threshhold range, BV/TV: 82.0000-208.000 0.245026
Uniform Orientations: 513
Vector sampling: Dense
Random Points: 2000
Data orientation (strike, dip, up): -31.9082 -180.000 0
SVD Eigenvalues: Eigenvectors Trend Plunge

0.794157 -0.0138416 0.149312 0.988693 174.704 81.3758
0.114594 0.370715 0.919086 -0.133610 21.9668 7.67826
0.0912484 -0.928643 0.364674 -0.0680739 291.440 3.90337
SVD Fabric Tensor:
0.0945915 0.00650169 -0.0107757
0.00650169 0.126640 0.100899
-0.0107757 0.100899 0.778769
SVD DA I E Sum(tau)
8.70325 0.114900 0.855703 3.07704
SLD Eigenvalues: Eigenvectors Trend Plunge
0.464417 -0.0129500 0.128637 0.991607 174.251 82.5716
0.277556 0.177139 0.976300 -0.124338 10.2838 7.14251
0.258027 -0.984101 0.174042 -0.0354297 280.029 2.03040
SLD Fabric Tensor:
0.258674 0.00303365 -0.00308046
0.00303365 0.280057 0.0239559
-0.00308046 0.0239559 0.461269
SLD DA I E Sum(tau)
1.79988 0.555592 0.402356 35.8058
Thickness (minimum line length at each point, non-zero points only)
Mean Variance Skewness Kurtosis Min Max
0.0956805 0.00201755 0.262436 -0.559526 0.0214800 0.294658
Thickness histogram
bin num norm
0.0163699 58 0.0312837
0.0491096 462 0.249191
0.0818494 437 0.235707
0.114589 463 0.249730
0.147329 317 0.170982
0.180069 92 0.0496224
0.212808 23 0.0124056
0.245548 1 0.000539374
0.278288 0 0.000000
0.311028 1 0.000539374
MIL calculations for sample: B12_73_0001
Threshhold range, BV/TV: 82.0000-208.000 0.245026
Uniform Orientations: 513
Vector sampling: Dense
Random Points: 2000
Data orientation (strike, dip, up): -31.9082 -180.000 0
MIL Ellipse Eigenvectors: Trend Plunge
0.00178870 -0.0531820 -0.998583 178.074 86.9497

0.0409399 0.997751 -0.0530644 2.34966 3.04179
0.999160 -0.0407869 0.00396195 272.338 0.227003
MIL Ellipse Eigenvalues:
2.40605 8.64978 10.0145
MIL Ellipse (H) Eigenvalues:
0.495645 0.261409 0.242946
MIL Ellipse Tensor (M):
10.0122 -0.0550209 0.0165547
-0.0550209 8.63439 -0.331804
0.0165547 -0.331804 2.42375
MIL (H) DA I E Tb.N
2.04015 0.490160 0.472588 2.55618
MIL Fabric Eigenvectors: Trend Plunge
-0.0168017 0.0763710 0.996938 167.593 85.5150
0.178659 0.981261 -0.0721592 10.3188 4.13801
-0.983768 0.176899 -0.0301312 280.194 1.72665
MIL Fabric Eigenvalues:
0.444511 0.283953 0.271536
MIL Fabric Tensor:
0.271981 0.00195496 -0.00305746
0.00195496 0.284501 0.0122906
-0.00305746 0.0122906 0.443518
MIL (F) DA I E
1.63702 0.610864 0.361200

medial

Star length and volume calcuations for sample: B572_0001
Threshhold range, BV/TV: 79.0000-255.000 0.260879
Uniform Orientations: 513
Vector sampling: Dense
Random Points: 2000
Data orientation (strike, dip, up): -65.0000 180.0000

SVD Eigenvalues:	Eigenvectors		Trend	Plunge
0.694561	-0.202512	0.194567	0.959757	133.854
73.6901				
0.197530	-0.866250	0.421502	-0.268230	295.947
15.5590				
0.107909	-0.456728	-0.885709	0.0831846	27.2785
4.77164				

SVD Fabric Tensor:

0.199219	-0.0558385	-0.0931988
-0.0558385	0.146040	0.0994171
-0.0931988	0.0994171	0.654742

SVD DA	I	E	Sum(tau)
6.43657	0.155362	0.715604	2.50321

SLD Eigenvalues:	Eigenvectors		Trend	Plunge
0.431700	-0.203629	0.191326	0.960172	133.216
73.7750				
0.299964	-0.854664	0.443660	-0.269658	297.434
15.6439				
0.268336	-0.477583	-0.875534	0.0731775	28.6114
4.19651				

SLD Fabric Tensor:

0.298212	-0.0183573	-0.0246515
-0.0183573	0.280542	0.0262271
-0.0246515	0.0262271	0.421246

SLD DA	I	E	Sum(tau)
1.60880	0.621580	0.305157	33.8795

Thickness (minimum line length at each point, non-zero points only)

Mean	Variance	Skewness	Kurtosis	Min	Max
0.0901820	0.00217955	0.659097	0.133175	0.0214800	0.305241

Thickness histogram

bin num	norm
0.0169578	94 0.0514505
0.0508734	535 0.292830
0.0847891	511 0.279693
0.118705	393 0.215107
0.152620	189 0.103448
0.186536	74 0.0405036

0.220452 24 0.0131363
0.254367 5 0.00273673
0.288283 1 0.000547345
0.322198 1 0.000547345
MIL calculations for sample: B572_0001
Threshhold range, BV/TV: 79.0000-255.000 0.260879
Uniform Orientations: 513
Vector sampling: Dense
Random Points: 2000
Data orientation (strike, dip, up): -65.0000 180.0000
MIL Ellipse Eigenvectors: Trend Plunge
0.158788 -0.123666 -0.979537 127.912 78.3891
-0.753792 0.625562 -0.201171 309.689 11.6054
0.637639 0.770311 0.00611310 219.617 0.350257
MIL Ellipse Eigenvalues:
4.19448 10.8398 12.5308
MIL Ellipse (H) Eigenvalues:
0.454418 0.282673 0.262909
MIL Ellipse Tensor (M):
11.3598 0.961065 1.04020
0.961065 11.7416 -0.797023
1.04020 -0.797023 4.46373
MIL (H) DA I E Tb.N
1.72842 0.578563 0.377945 2.96801
MIL Fabric Eigenvectors: Trend Plunge
-0.146145 0.128473 0.980885 131.318 78.7794
-0.622654 0.758545 -0.192123 320.619 11.0767
-0.768728 -0.638830 -0.0308633 230.273 1.76862
MIL Fabric Eigenvalues:
0.420222 0.295977 0.283801
MIL Fabric Tensor:
0.291436 -0.00831211 -0.0180995
-0.00831211 0.293059 0.0154169
-0.0180995 0.0154169 0.415506
MIL (F) DA I E
1.48069 0.675361 0.295664

Lateral

Star length and volume calcuations for sample: B572_0001
Threshhold range, BV/TV: 77.0000-255.000 0.241027
Uniform Orientations: 513
Vector sampling: Dense
Random Points: 2000
Data orientation (strike, dip, up): -65.0000 180.0000
SVD Eigenvalues: Eigenvectors Trend Plunge

0.731444 0.0536651 0.110363 0.992441 205.932
82.9510
0.145881 -0.747514 0.663408 -0.0333522 311.589
1.91130
0.122675 0.662075 0.740074 -0.118099 41.8160
6.78243
SVD Fabric Tensor:
0.137395 -0.00790274 0.0330013
-0.00790274 0.140303 0.0661642
0.0330013 0.0661642 0.722302
SVD DA I E Sum(tau)
5.96247 0.167716 0.800557 1.97814
SLD Eigenvalues: Eigenvectors Trend Plunge
0.442145 0.0545485 0.106741 0.992789 207.069
83.1153
0.287667 -0.678794 0.733153 -0.0415300 317.205
2.38018
0.270188 0.732300 0.671634 -0.112448 47.4743
6.45644
SLD Fabric Tensor:
0.278754 -0.00769730 0.00980506
-0.00769730 0.281543 0.0176903
0.00980506 0.0176903 0.439704
SLD DA I E Sum(tau)
1.63643 0.611086 0.349382 32.0187
Thickness (minimum line length at each point, non-zero points only)
Mean Variance Skewness Kurtosis Min Max
0.0883766 0.00204462 0.678187 0.315979 0.0214800 0.296061
Thickness histogram
bin num norm
0.0164478 97 0.0523475
0.0493435 535 0.288721
0.0822392 493 0.266055
0.115135 424 0.228818
0.148031 191 0.103076
0.180926 80 0.0431732
0.213822 23 0.0124123
0.246718 8 0.00431732
0.279613 1 0.000539665
0.312509 1 0.000539665
MIL calculations for sample: B572_0001
Threshhold range, BV/TV: 77.0000-255.000 0.241027
Uniform Orientations: 513
Vector sampling: Dense
Random Points: 2000
Data orientation (strike, dip, up): -65.0000 180.0000
MIL Ellipse Eigenvectors: Trend Plunge
0.0164532 -0.103580 -0.994485 170.974 83.9798

0.896887 -0.438106 0.0604689 296.034 3.46673
0.441953 0.892936 -0.0856910 26.3328 4.91576
MIL Ellipse Eigenvalues:
3.26279 9.47985 10.0883
MIL Ellipse (H) Eigenvalues:
0.463957 0.272190 0.263853
MIL Ellipse Tensor (M):
9.59702 0.250730 0.0786815
0.250730 9.89832 -0.686969
0.0786815 -0.686969 3.33565
MIL (H) DA I E Tb.N
1.75839 0.568702 0.413330 2.69030
MIL Fabric Eigenvectors: Trend Plunge
0.00653117 0.0944631 0.995507 183.955 84.5666
-0.902041 0.430236 -0.0349069 295.499 2.00043
0.431601 0.897760 -0.0880196 25.6761 5.04968
MIL Fabric Eigenvalues:
0.429244 0.293941 0.276815
MIL Fabric Tensor:
0.290756 -0.00655223 0.00153031
-0.00655223 0.281345 0.0140770
0.00153031 0.0140770 0.427898
MIL (F) DA I E
1.55065 0.644890 0.315213

7_73

medial

Star length and volume calcuations for sample: B7_73_0001
Threshhold range, BV/TV: 75.0000-255.000 0.259552
Uniform Orientations: 513
Vector sampling: Dense
Random Points: 2000
Data orientation (strike, dip, up): -28.0000 180.0000

SVD Eigenvalues:	Eigenvectors			Trend	Plunge
0.801020	-0.184822	0.0979337	0.977880	117.918	77.9265
0.108481	-0.718029	0.665935	-0.202402	312.844	11.6775
0.0904988	-0.671026	-0.739554	-0.0527604	222.219	3.02435

SVD Fabric Tensor:

0.124041	-0.0214590	-0.125802
-0.0214590	0.105288	0.0656210
-0.125802	0.0656210	0.770671

SVD DA	I	E	Sum(tau)
8.85116	0.112979	0.864571	3.74697

SLD Eigenvalues:	Eigenvectors			Trend	Plunge
0.466657	-0.216141	0.0892762	0.972272	112.443	76.4760
0.274858	-0.737413	0.637746	-0.222490	310.855	12.8553
0.258485	-0.639926	-0.765055	-0.0720096	219.911	4.12942

SLD Fabric Tensor:

0.277113	-0.0117166	-0.0410606
-0.0117166	0.266804	0.0157463
-0.0410606	0.0157463	0.456083

SLD DA	I	E	Sum(tau)
1.80535	0.553909	0.411007	37.2609

Thickness (minimum line length at each point, non-zero points only)

Mean	Variance	Skewness	Kurtosis	Min	Max
0.0920658	0.00191236	0.370448	-0.360050	0.0214800	0.251728

Thickness histogram

bin num	norm
0.0139849	30	0.0160858
0.0419547	487	0.261126
0.0699246	229	0.122788
0.0978944	511	0.273995
0.125864	354	0.189812
0.153834	160	0.0857909

0.181804 70 0.0375335

0.209774 16 0.00857909
0.237744 7 0.00375335
0.265713 1 0.000536193
MIL calculations for sample: B7_73_0001
Threshhold range, BV/TV: 75.0000-255.000 0.259552
Uniform Orientations: 513
Vector sampling: Dense
Random Points: 2000
Data orientation (strike, dip, up): -28.0000 180.0000
MIL Ellipse Eigenvectors: Trend Plunge
0.163311 -0.0971879 -0.981776 120.757 79.0447
-0.571720 0.801685 -0.174462 324.505 10.0474
0.804031 0.589793 0.0753601 233.738 4.32191
MIL Ellipse Eigenvalues:
2.77996 9.43065 10.8330
MIL Ellipse (H) Eigenvalues:
0.487921 0.264910 0.247170
MIL Ellipse Tensor (M):

10.1598 0.770547 1.15131
0.770547 9.85563 -0.572259
1.15131 -0.572259 3.02812
MIL (H) DA I E Tb.N
1.97403 0.506577 0.457064 2.67656
MIL Fabric Eigenvectors: Trend Plunge
-0.195689 0.0887757 0.976640 114.402 77.5913
-0.427104 0.888766 -0.166367 334.333 9.57664
-0.882773 -0.449682 -0.136005 243.006 7.81675
MIL Fabric Eigenvalues:
0.444029 0.283473 0.272498
MIL Fabric Tensor:
0.281068 -0.00714628 -0.0320028
-0.00714628 0.282519 0.0132493
-0.0320028 0.0132493 0.436413
MIL (F) DA I E
1.62948 0.613693 0.361589

Lateral

Star length and volume calcuations for sample: B7_73_0001
Threshhold range, BV/TV: 77.0000-255.000 0.229887
Uniform Orientations: 513
Vector sampling: Dense
Random Points: 2000
Data orientation (strike, dip, up): -28.0000 180.0000
SVD Eigenvalues: Eigenvectors Trend Plunge

0.645386 -0.157284 0.0637243 0.985495 112.055
80.2294
0.202945 -0.919780 0.353856 -0.169677 291.043
9.76907
0.151668 -0.359536 -0.933127 0.00295633 21.0718
0.169386
SVD Fabric Tensor:
0.207262 -0.0216377 -0.0685252
-0.0216377 0.160094 0.0279267
-0.0685252 0.0279267 0.632644
SVD DA I E Sum(tau)
4.25525 0.235004 0.685544 3.89250
SLD Eigenvalues: Eigenvectors Trend Plunge
0.416714 -0.137169 0.0362667 0.989884 104.810
81.8432
0.305009 -0.943683 0.298962 -0.141720 287.578
8.14738
0.278277 -0.301077 -0.953576 -0.00678392 197.523
0.388693
SLD Fabric Tensor:
0.304687 -0.00823049 -0.0152221
-0.00823049 0.280848 0.00383727
-0.0152221 0.00383727 0.414464
SLD DA I E Sum(tau)
1.49748 0.667787 0.268062 42.8955
Thickness (minimum line length at each point, non-zero points only)
Mean Variance Skewness Kurtosis Min Max
0.101933 0.00256454 0.431100 -0.180681 0.0214800 0.282163
Thickness histogram
bin num norm
0.0156757 52 0.0286501
0.0470272 430 0.236915
0.0783786 341 0.187879
0.109730 431 0.237466
0.141082 317 0.174656
0.172433 144 0.0793388
0.203784 60 0.0330578
0.235136 32 0.0176309
0.266487 7 0.00385675
0.297839 1 0.000550964
MIL calculations for sample: B7_73_0001
Threshhold range, BV/TV: 77.0000-255.000 0.229887
Uniform Orientations: 513
Vector sampling: Dense
Random Points: 2000
Data orientation (strike, dip, up): -28.0000 180.0000
MIL Ellipse Eigenvectors: Trend Plunge
0.124944 -0.0683777 -0.989805 118.690 81.8115

-0.856728 0.495723 -0.142391 300.055 8.18625
0.500405 0.865785 0.00335665 210.027 0.192322
MIL Ellipse Eigenvalues:
2.36034 5.22279 6.37607
MIL Ellipse (H) Eigenvalues:
0.438464 0.294761 0.266775
MIL Ellipse Tensor (M):
5.46689 0.524106 0.355938
0.524106 6.07389 -0.190381
0.355938 -0.190381 2.41842
MIL (H) DA I E Tb.N
1.64358 0.608430 0.327742 2.11794
MIL Fabric Eigenvectors: Trend Plunge
-0.156834 0.0600572 0.985797 110.954 80.3319
-0.869232 0.465472 -0.166647 298.169 9.59292
-0.468869 -0.883023 -0.0207982 207.967 1.19173
MIL Fabric Eigenvalues:
0.408559 0.306306 0.285136
MIL Fabric Tensor:
0.304167 -0.00972802 -0.0160154
-0.00972802 0.290168 0.00566501
-0.0160154 0.00566501 0.405666
MIL (F) DA I E
1.43286 0.697906 0.250277

8_73

medial

Star length and volume calcuations for sample: B8_73_0001

Threshhold range, BV/TV:	81.0000-255.000	0.241575
Uniform Orientations:	513	
Vector sampling:	Dense	
Random Points:	2000	
Data orientation (strike, dip, up):	-23.0000	180.0000

SVD Eigenvalues:	Eigenvectors		Trend	Plunge
0.693369	-0.161243	0.0878599	0.982996	118.586
79.4189				
0.164913	-0.968493	-0.205635	-0.140485	258.013
8.07590				
0.141718	0.189795	-0.974677	0.118249	348.981
6.79106				

SVD Fabric Tensor:

0.177817	-0.00319591	-0.0842818
-0.00319591	0.146958	0.0483139
-0.0842818	0.0483139	0.675226

SVD DA	I	E	Sum(tau)
4.89258	0.204391	0.762158	3.44885

SLD Eigenvalues:	Eigenvectors		Trend	Plunge
0.432600	-0.184651	0.0587310	0.981048	107.644
78.8273				
0.297719	-0.970408	-0.168936	-0.172535	260.124
9.93525				
0.269681	0.155602	-0.983876	0.0881874	351.013
5.05934				

SLD Fabric Tensor:

0.301639	0.00282963	-0.0248187
0.00282963	0.271043	0.0102043
-0.0248187	0.0102043	0.427318

SLD DA	I	E	Sum(tau)
1.60412	0.623396	0.311792	42.1097

Thickness (minimum line length at each point, non-zero points only)

Mean	Variance	Skewness	Kurtosis	Min	Max
0.103145	0.00237878	0.303953	-0.403736	0.0214800	0.278435

Thickness histogram

bin num	norm
0.0154686	45	0.0256996
0.0464058	373	0.213021
0.0773429	329	0.187893
0.108280	393	0.224443
0.139217	368	0.210166
0.170154	138	0.0788121

0.201092 82 0.0468304
0.232029 17 0.00970874
0.262966 5 0.00285551
0.293903 1 0.000571102
MIL calculations for sample: B8_73_0001
Threshhold range, BV/TV: 81.0000-255.000 0.241575
Uniform Orientations: 513
Vector sampling: Dense
Random Points: 2000
Data orientation (strike, dip, up): -23.0000 180.0000
MIL Ellipse Eigenvectors: Trend Plunge
0.218334 -0.0408709 -0.975018 100.603 77.1661
-0.942569 -0.267625 -0.199849 254.149 11.5281
-0.252771 0.962656 -0.0969552 345.288 5.56386
MIL Ellipse Eigenvalues:
2.60866 5.49234 6.63515
MIL Ellipse (H) Eigenvalues:
0.431742 0.297546 0.270712
MIL Ellipse Tensor (M):
5.42789 -0.252349 0.641882
-0.252349 6.54657 -0.221578
0.641882 -0.221578 2.76169
MIL (H) DA I E Tb.N
1.59484 0.627023 0.310824 2.17704
MIL Fabric Eigenvectors: Trend Plunge
-0.218334 0.00905783 0.975832 92.3756 77.3777
-0.934914 -0.288605 -0.206500 252.845 11.9173
0.279760 -0.957405 0.0714807 343.711 4.09904
MIL Fabric Eigenvalues:
0.414208 0.305134 0.280659
MIL Fabric Tensor:
0.308417 0.00633978 -0.0237285
0.00633978 0.282708 0.00263905
-0.0237285 0.00263905 0.408874
MIL (F) DA I E
1.47584 0.677580 0.263332

medial

Star length and volume calcuations for sample: B4_72_0001
Threshhold range, BV/TV: 54.0000-142.000 0.284145
Uniform Orientations: 513
Vector sampling: Dense
Random Points: 2000
Data orientation (strike, dip, up): 177.000-3.00000 1

SVD Eigenvalues:	Eigenvectors		Trend	Plunge
0.611927	-0.170432	0.146007	0.974492	130.586
77.0311				
0.259129	-0.779763	0.584642	-0.223971	306.861
12.9424				
0.128944	-0.602431	-0.798045	0.0142093	37.0485
0.814163				

SVD Fabric Tensor:

0.222130	-0.0713675	-0.0574799
-0.0713675	0.183738	0.0516734
-0.0574799	0.0516734	0.594132

SVD DA	I	E	Sum(tau)
4.74567	0.210718	0.576536	9.61208

SLD Eigenvalues:	Eigenvectors		Trend	Plunge
0.409587	-0.183609	0.168884	0.968383	132.608
75.5540				
0.320011	-0.814186	0.525873	-0.246084	302.858
14.2459				
0.270402	-0.550807	-0.833628	0.0409478	33.4541
2.34679				

SLD Fabric Tensor:

0.307980	-0.0255569	-0.0148080
-0.0255569	0.288091	0.0163430
-0.0148080	0.0163430	0.403929

SLD DA	I	E	Sum(tau)
1.51474	0.660181	0.218697	58.1240

Thickness (minimum line length at each point, non-zero points only)

Mean	Variance	Skewness	Kurtosis	Min	Max
0.118665	0.00297169	0.813025	0.745643	0.0390600	0.404270

Thickness histogram

bin num	norm
0.0224594	61	0.0346001
0.0673783	605	0.343165
0.112297	442	0.250709
0.157216	418	0.237096
0.202135	168	0.0952921
0.247054	53	0.0300624

0.291972 10 0.00567215
0.336891 3 0.00170164
0.381810 2 0.00113443
0.426729 1 0.000567215
MIL calculations for sample: B4_72_0001
Threshhold range, BV/TV: 54.0000-142.000 0.284145
Uniform Orientations: 513
Vector sampling: Dense
Random Points: 2000
Data orientation (strike, dip, up): 177.000-3.00000 1
MIL Ellipse Eigenvectors: Trend Plunge
-0.155802 0.0947848 0.983230 121.315 79.4922
0.834338 -0.520216 0.182359 301.944 10.5072
0.528777 0.848758 0.00196825 211.923 0.112772
MIL Ellipse Eigenvalues:
3.25770 5.74641 7.34037
MIL Ellipse (H) Eigenvalues:
0.413373 0.311243 0.275384
MIL Ellipse Tensor (M):
6.13168 0.752126 0.382903
0.752126 6.87232 -0.229273
0.382903 -0.229273 3.34048
MIL (H) DA I E Tb.N
1.50108 0.666188 0.247066 2.30888
MIL Fabric Eigenvectors: Trend Plunge
-0.122820 0.0777453 0.989379 122.334 81.6420
-0.851245 0.504253 -0.145297 300.641 8.35445
-0.510194 -0.860049 0.00424779 30.6770 0.243381
MIL Fabric Eigenvalues:
0.398156 0.319061 0.282783
MIL Fabric Tensor:
0.310811 -0.0166741 -0.00953260
-0.0166741 0.292705 0.00621645
-0.00953260 0.00621645 0.396484
MIL (F) DA I E
1.40799 0.710231 0.198652

Lateral 384 500 95 62

Star length and volume calcuations for sample: B4_72_0001
Threshhold range, BV/TV: 57.0000-151.000 0.247954
Uniform Orientations: 513
Vector sampling: Dense
Random Points: 2000
Data orientation (strike, dip, up): 177.000-3.00000 1
SVD Eigenvalues: Eigenvectors Trend Plunge
0.542968 -0.365956 0.141213 0.919856 111.100 66.9050

0.287600 -0.227061 -0.972098 0.0588986 13.1473
3.37659
0.169432 -0.902507 0.187309 -0.387809 281.725
22.8183
SVD Fabric Tensor:
0.225550 0.00677913 -0.127322
0.00677913 0.288546 0.0417548
-0.127322 0.0417548 0.485904
SVD DA I E Sum(tau)
3.20463 0.312049 0.470319 9.12685
SLD Eigenvalues: Eigenvectors Trend Plunge
0.399790 -0.352065 0.122848 0.927878 109.236
68.1065
0.318024 -0.216300 -0.975193 0.0470413 12.5059
2.69626
0.282186 -0.910639 0.184138 -0.369904 281.432
21.7097
SLD Fabric Tensor:
0.298440 0.00247315 -0.0387830
0.00247315 0.318043 0.0117614
-0.0387830 0.0117614 0.383517
SLD DA I E Sum(tau)
1.41676 0.705835 0.204522 57.4039
Thickness (minimum line length at each point, non-zero points only)
Mean Variance Skewness Kurtosis Min Max
0.120103 0.00349067 0.767038 0.0859218 0.0390600 0.354419
Thickness histogram
bin num norm
0.0196899 51 0.0288788
0.0590698 590 0.334088
0.0984496 242 0.137033
0.137829 393 0.222537
0.177209 306 0.173273
0.216589 113 0.0639864
0.255969 49 0.0277463
0.295349 15 0.00849377
0.334729 6 0.00339751
0.374109 1 0.000566251
MIL calculations for sample: B4_72_0001
Threshhold range, BV/TV: 57.0000-151.000 0.247954
Uniform Orientations: 513
Vector sampling: Dense
Random Points: 2000
Data orientation (strike, dip, up): 177.000-3.00000 1
MIL Ellipse Eigenvectors: Trend Plunge
0.231193 -0.127672 -0.964495 118.909 74.6863
0.159337 0.982936 -0.0919198 9.20773 5.27406
-0.959772 0.132428 -0.247591 277.856 14.3350

MIL Ellipse Eigenvalues:

2.29167	4.29528	4.83025

MIL Ellipse (H) Eigenvalues:

0.413354	0.301928	0.284718

MIL Ellipse Tensor (M):

4.68098	-0.00885588	0.573898
-0.00885588	4.27200	-0.264263
0.573898	-0.264263	2.46422

MIL (H) DA I E Tb.N

1.45181	0.688798	0.269566	1.93515

MIL Fabric Eigenvectors:

			Trend	Plunge
-0.269928	0.0990925	0.957768	110.159	73.2891
-0.197052	-0.979323	0.0457874	11.3767	2.62435
-0.942502	0.176371	-0.283873	280.599	16.4915

MIL Fabric Eigenvalues:

0.391854	0.311882	0.296264

MIL Fabric Tensor:

0.303835	0.000456917	-0.0248537
0.000456917	0.312181	0.00837194
-0.0248537	0.00837194	0.383984

MIL (F) DA I E

1.32265	0.756057	0.204088

Medial

Star length and volume calcuations for sample: B9_73_0001
Threshhold range, BV/TV: 54.0000-139.000 0.261250
Uniform Orientations: 513
Vector sampling: Dense
Random Points: 2000
Data orientation (strike, dip, up): -177.000 -6.00000 1

SVD Eigenvalues:	Eigenvectors		Trend	Plunge
0.561233	-0.0947646	-0.00853547	0.995463	84.8532
84.5401				
0.251867	0.729110	-0.681438	0.0635658	313.064
3.64451				
0.186900	-0.677804	-0.731826	-0.0707995	222.805
4.05991				

SVD Fabric Tensor:

0.224798	-0.0319754	-0.0323016
-0.0319754	0.217095	-0.00599471
-0.0323016	-0.00599471	0.558106

SVD DA	I	E	Sum(tau)
3.00285	0.333017	0.551226	7.26646

SLD Eigenvalues:	Eigenvectors		Trend	Plunge
0.394894	-0.113462	-0.0281993	0.993142	76.0427
83.2860				
0.312311	0.693022	-0.718517	0.0587727	316.035
3.36937				
0.292795	-0.711932	-0.694938	-0.101067	225.692
5.80060				

SLD Fabric Tensor:

0.303482	-0.00939086	-0.0107100
-0.00939086	0.302952	-0.00368348
-0.0107100	-0.00368348	0.393566

SLD DA	I	E	Sum(tau)
1.34870	0.741453	0.209129	54.9080

Thickness (minimum line length at each point, non-zero points only)

Mean	Variance	Skewness	Kurtosis	Min	Max
0.117770	0.00310013	0.762601	0.118784	0.0390600	0.353903

Thickness histogram

bin num	norm
0.0196613	30 0.0163399
0.0589839	616 0.335512
0.0983064	314 0.171024
0.137629	390 0.212418
0.176952	313 0.170479
0.216274	124 0.0675381
0.255597	35 0.0190632

0.294919 8 0.00435730
0.334242 5 0.00272331
0.373564 1 0.000544662
MIL calculations for sample: B9_73_0001
Threshhold range, BV/TV: 54.0000-139.000 0.261250
Uniform Orientations: 513
Vector sampling: Dense
Random Points: 2000
Data orientation (strike, dip, up): -177.000 -6.00000 1
MIL Ellipse Eigenvectors: Trend Plunge
0.0572338 0.0681571 -0.996032 40.0213 84.8939
-0.737871 0.674932 0.00378526 132.449 0.216880
-0.672511 -0.734726 -0.0889200 222.469 5.10148
MIL Ellipse Eigenvalues:
3.15543 5.37106 5.94019
MIL Ellipse (H) Eigenvalues:
0.400751 0.307167 0.292082
MIL Ellipse Tensor (M):

5.62120 0.272569 0.160339
0.272569 5.66800 0.187594
0.160339 0.187594 3.17748
MIL (H) DA I E Tb.N
1.37205 0.728835 0.233523 2.18693
MIL Fabric Eigenvectors: Trend Plunge
-0.0380957 -0.0534914 0.997841 35.4579 86.2346
0.852429 -0.522823 0.00451714 301.522 0.258814
-0.521453 -0.850761 -0.0655149 211.505 3.75642
MIL Fabric Eigenvalues:
0.383065 0.314314 0.302621
MIL Fabric Tensor:
0.311235 -0.00504756 -0.00301293
-0.00504756 0.306047 -0.00432138
-0.00301293 -0.00432138 0.382718
MIL (F) DA I E
1.26582 0.789999 0.179475
Star length and volume calcuations for sample: B9_73_0001
Threshhold range, BV/TV: 49.0000-130.000 0.261454
Uniform Orientations: 513
Vector sampling: Dense
Random Points: 2000
Data orientation (strike, dip, up): -177.000 -6.00000 1
SVD Eigenvalues: Eigenvectors Trend Plunge
0.619095 -0.121499 -0.107911 0.986708 48.3896 80.6478
0.203468 0.936134 -0.342936 0.0777666 290.119 4.46020

0.177437 -0.329986 -0.933140 -0.142686 199.475
8.20329
SVD Fabric Tensor:
0.206769 -0.00256623 -0.0510527
-0.00256623 0.185641 -0.0477206
-0.0510527 -0.0477206 0.607589
SVD DA I E Sum(tau)
3.48909 0.286607 0.671346 5.45128
SLD Eigenvalues: Eigenvectors Trend Plunge
0.406929 -0.110718 -0.0922420 0.989562 50.2014
81.7144
0.304674 0.961850 -0.260579 0.0833273 285.158
4.77984
0.288397 -0.250173 -0.961036 -0.117574 194.591
6.75209
SLD Fabric Tensor:
0.304909 -0.00286908 -0.0116820
-0.00286908 0.290511 -0.0111729
-0.0116820 -0.0111729 0.404580
SLD DA I E Sum(tau)
1.41100 0.708717 0.251284 49.9102
Thickness (minimum line length at each point, non-zero points only)
Mean Variance Skewness Kurtosis Min Max
0.114066 0.00284277 0.748530 0.101915 0.0390600 0.318700
Thickness histogram
bin num norm
0.0177056 0 0.000000
0.0531167 627 0.344505
0.0885278 275 0.151099
0.123939 378 0.207692
0.159350 303 0.166484
0.194761 155 0.0851648
0.230172 55 0.0302198
0.265584 16 0.00879121
0.300995 10 0.00549451
0.336406 1 0.000549451
MIL calculations for sample: B9_73_0001
Threshhold range, BV/TV: 49.0000-130.000 0.261454
Uniform Orientations: 513
Vector sampling: Dense
Random Points: 2000
Data orientation (strike, dip, up): -177.000 -6.00000 1
MIL Ellipse Eigenvectors: Trend Plunge
0.102432 0.0883017 -0.990813 49.2368 82.2276
-0.0216100 0.996015 0.0865312 178.757 4.96408
-0.994505 -0.0125480 -0.103932 269.277 5.96561
MIL Ellipse Eigenvalues:
3.49710 6.23865 6.62431

MIL Ellipse (H) Eigenvalues:

0.403994	0.302471	0.293534

MIL Ellipse Tensor (M):

6.59132	-0.0199851	0.318104
-0.0199851	6.21733	0.240362
0.318104	0.240362	3.55141

MIL (H) DA I E Tb.N

1.37631	0.726581	0.251298	2.32245

MIL Fabric Eigenvectors:

			Trend	Plunge
-0.144162	-0.0703638	0.987049	63.9834	80.7689
0.0731208	-0.995499	-0.0602866	175.799	3.45627
-0.986849	-0.0634828	-0.148658	266.319	8.54915

MIL Fabric Eigenvalues:

0.389826	0.308167	0.302007

MIL Fabric Tensor:

0.303865	0.000442393	-0.0125233
0.000442393	0.308547	-0.00572951
-0.0125233	-0.00572951	0.387588

MIL (F) DA I E

1.29078	0.774723	0.209474

medial

Star length and volume calcuations for sample: B4_73_0001
Threshhold range, BV/TV: 58.0000-139.000 0.235905
Uniform Orientations: 513
Vector sampling: Dense
Random Points: 2000
Data orientation (strike, dip, up): -16.0000 180.0000

SVD Eigenvalues:	Eigenvectors			Trend	Plunge
0.698830	0.0206145	0.0630461	0.997798	198.106	86.1967
0.163355	-0.627392	0.777862	-0.0361876	321.112	2.07385
0.137814	0.778431	0.625264	-0.0555899	51.2273	3.18671

SVD Fabric Tensor:

0.148106	-0.0117355	0.0121195
-0.0117355	0.155498	0.0345730
0.0121195	0.0345730	0.696395

SVD DA	I	E	Sum(tau)
5.07081	0.197207	0.766245	10.0834

SLD Eigenvalues:	Eigenvectors			Trend	Plunge
0.429790	0.0107882	0.0868760	0.996161	187.079	84.9777
0.293465	-0.613613	0.787169	-0.0620044	322.063	3.55487
0.276745	0.789533	0.610588	-0.0618003	52.2833	3.54316

SLD Fabric Tensor:

0.283058	-0.00793247	0.00228086
-0.00793247	0.288260	0.0124288
0.00228086	0.0124288	0.428681

SLD DA	I	E	Sum(tau)
1.55302	0.643909	0.317189	60.0106

Thickness (minimum line length at each point, non-zero points only)

Mean	Variance	Skewness	Kurtosis	Min	Max
0.126707	0.00368642	0.726475	0.124339	0.0390600	0.353903

Thickness histogram

bin num	norm
0.0196613	25	0.0140371
0.0589839	537	0.301516
0.0983064	280	0.157215
0.137629	344	0.193150
0.176952	392	0.220101
0.216274	118	0.0662549

0.255597 48 0.0269512
0.294919 26 0.0145985
0.334242 10 0.00561482
0.373564 1 0.000561482
MIL calculations for sample: B4_73_0001
Threshhold range, BV/TV: 58.0000-139.000 0.235905
Uniform Orientations: 513
Vector sampling: Dense
Random Points: 2000
Data orientation (strike, dip, up): -16.0000 180.0000
MIL Ellipse Eigenvectors: Trend Plunge
0.0155484 -0.0589154 -0.998142 165.216 86.5067
-0.211988 0.975375 -0.0608737 347.738 3.48997
0.977149 0.212541 0.00267613 257.729 0.153331
MIL Ellipse Eigenvalues:
1.67187 3.62239 4.34214
MIL Ellipse (H) Eigenvalues:
0.434806 0.295392 0.269802
MIL Ellipse Tensor (M):
4.30915 0.151268 0.0321532
0.151268 3.64813 -0.114293
0.0321532 -0.114293 1.67911
MIL (H) DA I E Tb.N
1.61158 0.620510 0.320635 1.75884
MIL Fabric Eigenvectors: Trend Plunge
-0.000197885 0.0802902 0.996772 179.859 85.3947
-0.220117 0.972321 -0.0783643 347.244 4.49455
-0.975474 -0.219422 0.0174808 77.3229 1.00163
MIL Fabric Eigenvalues:
0.418048 0.303020 0.278932
MIL Fabric Tensor:
0.280099 -0.00515774 0.000388071
-0.00515774 0.302602 0.00929815
0.000388071 0.00929815 0.417299
MIL (F) DA I E
1.49874 0.667225 0.275154

Lateral

Star length and volume calcuations for sample: B4_73_0001
Threshhold range, BV/TV: 61.0000-188.000 0.251992
Uniform Orientations: 513
Vector sampling: Dense
Random Points: 2000
Data orientation (strike, dip, up): -16.0000 180.0000
SVD Eigenvalues: Eigenvectors Trend Plunge

0.706678 -0.0142919 -0.0488039 0.998706 16.3224
87.0851
0.177206 -0.693716 -0.718838 -0.0450549 223.981
2.58233
0.116115 0.720107 -0.693462 -0.0235824 133.920
1.35130
SVD Fabric Tensor:
0.145636 0.0308763 -0.00651995
0.0308763 0.149089 -0.0268059
-0.00651995 -0.0268059 0.705275
SVD DA I E Sum(tau)
6.08601 0.164311 0.749240 11.7936
SLD Eigenvalues: Eigenvectors Trend Plunge
0.436761 0.0231077 -0.0419903 0.998851 331.176
87.2528
0.294727 0.753557 0.657304 0.0101991 228.903
0.584375
0.268511 0.656976 -0.752455 -0.0468308 138.875
2.68419
SLD Fabric Tensor:
0.283488 0.0128220 0.00408490
0.0128220 0.280134 -0.00688100
0.00408490 -0.00688100 0.436378
SLD DA I E Sum(tau)
1.62660 0.614778 0.325198 62.1505
Thickness (minimum line length at each point, non-zero points only)
Mean Variance Skewness Kurtosis Min Max
0.128191 0.00367587 0.690455 0.144119 0.0390600 0.358331
Thickness histogram
bin num norm
0.0199073 22 0.0132770
0.0597219 490 0.295715
0.0995365 255 0.153893
0.139351 390 0.235365
0.179166 303 0.182861
0.218980 115 0.0694025
0.258795 56 0.0337960
0.298609 14 0.00844900
0.338424 11 0.00663850
0.378239 1 0.000603500
MIL calculations for sample: B4_73_0001
Threshhold range, BV/TV: 61.0000-188.000 0.251992
Uniform Orientations: 513
Vector sampling: Dense
Random Points: 2000

Data orientation (strike, dip, up): -16.0000 180.0000
MIL Ellipse Eigenvectors: Trend Plunge

0.0617085 0.0495066 -0.996866 51.2611 85.4624
-0.687632 -0.721812 -0.0784130 223.611 4.49735
-0.723432 0.690316 -0.0104996 313.658 0.601594
MIL Ellipse Eigenvalues:
1.61739 4.02516 4.43161
MIL Ellipse (H) Eigenvalues:
0.446824 0.283239 0.269937
MIL Ellipse Tensor (M):
4.22871 -0.210338 0.151201
-0.210338 4.21295 0.115881
0.151201 0.115881 1.63250
MIL (H) DA I E Tb.N
1.65529 0.604125 0.366107 1.79595
MIL Fabric Eigenvectors: Trend Plunge
-0.0167000 -0.0253750 0.999539 33.3501 88.2592
-0.794128 -0.607073 -0.0286797 232.604 1.64345
0.607520 -0.794241 -0.0100129 142.587 0.573706
MIL Fabric Eigenvalues:
0.420618 0.295790 0.283592
MIL Fabric Tensor:
0.291323 0.00593860 -0.00200948
0.00593860 0.288176 -0.00326307
-0.00200948 -0.00326307 0.420502
MIL (F) DA I E
1.48318 0.674226 0.296774

8_76

medial

Star length and volume calcuations for sample: B8_76_0001
Threshhold range, BV/TV: 71.0000-159.000 0.334453
Uniform Orientations: 513
Vector sampling: Dense
Random Points: 2000
Data orientation (strike, dip, up): 175.0001.000001

SVD Eigenvalues:	Eigenvectors	Trend	Plunge
0.392335	-0.639159	0.0232529	0.768723	92.0835	50.2393
0.327813	-0.443085	0.805853	-0.392782	331.197	23.1277
0.279852	0.628610	0.591660	0.504765	226.734	30.3158

SVD Fabric Tensor:

0.335220	-0.0187969	-0.0469200
-0.0187969	0.311059	-0.0131703
-0.0469200	-0.0131703	0.353721

SVD DA	I	E	Sum(tau)
1.40194	0.713299	0.164456	35.7359

SLD Eigenvalues:	Eigenvectors	Trend	Plunge
0.357254	-0.445750	0.0252124	0.894802	93.2373	63.4830
0.330206	-0.506852	0.816821	-0.275506	328.180	15.9922
0.312540	0.737840	0.576339	0.351320	232.006	20.5680

SLD Fabric Tensor:

0.325963	-0.00781628	-0.0153677
-0.00781628	0.324355	-0.00296672
-0.0153677	-0.00296672	0.349682

SLD DA	I	E	Sum(tau)
1.14307	0.874840	0.0757115	93.5686

Thickness (minimum line length at each point, non-zero points only)

Mean	Variance	Skewness	Kurtosis	Min	Max
0.142155	0.00479069	0.654605	0.0134642	0.0390600	0.390781

Thickness histogram

bin num	norm
0.0217101	24	0.0134303
0.0651302	487	0.272524
0.108550	311	0.174035
0.151970	422	0.236150
0.195390	280	0.156687
0.238811	158	0.0884163
0.282231	61	0.0341354

0.325651 33 0.0184667
0.369071 10 0.00559597
0.412491 1 0.000559597
MIL calculations for sample: B8_76_0001
Threshhold range, BV/TV: 71.0000-159.000 0.334453
Uniform Orientations: 513
Vector sampling: Dense
Random Points: 2000
Data orientation (strike, dip, up): 175.0001.000001
MIL Ellipse Eigenvectors: Trend Plunge
0.221433 -0.0673108 -0.972850 106.908 76.6183
-0.286558 0.949080 -0.130890 343.199 7.52105
-0.932122 -0.307762 -0.190869 251.728 11.0035
MIL Ellipse Eigenvalues:
4.05177 5.42872 6.16635
MIL Ellipse (H) Eigenvalues:
0.373898 0.323018 0.303083
MIL Ellipse Tensor (M):
6.00209 0.232128 0.427857
0.232128 5.49235 -0.0468371
0.427857 -0.0468371 4.15240
MIL (H) DA I E Tb.N
1.23365 0.810604 0.136079 2.28500
MIL Fabric Eigenvectors: Trend Plunge
-0.185511 0.0744708 0.979816 111.872 78.4689
0.348599 -0.927282 0.136479 339.397 7.84415
-0.918730 -0.366881 -0.146060 248.231 8.39869
MIL Fabric Eigenvalues:
0.364126 0.325948 0.309925
MIL Fabric Tensor:
0.313738 -0.00592820 -0.00908955
-0.00592820 0.324003 0.00192713
-0.00908955 0.00192713 0.362259
MIL (F) DA I E
1.17488 0.851149 0.104848

lateral

Star length and volume calcuations for sample: B8_76_0001
Threshhold range, BV/TV: 62.0000-253.000 0.296763
Uniform Orientations: 513
Vector sampling: Dense
Random Points: 2000
Data orientation (strike, dip, up): 175.0001.000001
SVD Eigenvalues: Eigenvectors Trend Plunge

0.486115 -0.179875 0.172609 0.968427 133.819
75.5641
0.322769 -0.0418180 0.982253 -0.182840 357.562
10.5352
0.191116 0.982800 0.0733859 0.169465 265.730
9.75670
SVD Fabric Tensor:
0.200891 -0.0145668 -0.0503810
-0.0145668 0.326926 0.0256675
-0.0503810 0.0256675 0.472182
SVD DA I E Sum(tau)
2.54356 0.393150 0.336024 21.4575
SLD Eigenvalues: Eigenvectors Trend Plunge
0.379241 -0.185236 0.194377 0.963278 136.379
74.4247
0.335334 -0.0357049 0.978264 -0.204267 357.910
11.7866
0.285424 0.982045 0.0722312 0.174270 265.793
10.0362
SLD Fabric Tensor:
0.288707 -0.00512114 -0.0163761
-0.00512114 0.336733 0.00759286
-0.0163761 0.00759286 0.374560
SLD DA I E Sum(tau)
1.32869 0.752620 0.115776 81.0051
Thickness (minimum line length at each point, non-zero points only)
Mean Variance Skewness Kurtosis Min Max
0.135627 0.00438691 0.861720 0.754062 0.0390600 0.413984
Thickness histogram
bin num norm
0.0229991 43 0.0235359
0.0689974 564 0.308703
0.114996 369 0.201970
0.160994 499 0.273125
0.206992 194 0.106185
0.252990 96 0.0525452
0.298989 38 0.0207991
0.344987 17 0.00930487
0.390985 6 0.00328407
0.436984 1 0.000547345
MIL calculations for sample: B8_76_0001
Threshhold range, BV/TV: 62.0000-253.000 0.296763
Uniform Orientations: 513
Vector sampling: Dense
Random Points: 2000
Data orientation (strike, dip, up): 175.0001.000001
MIL Ellipse Eigenvectors: Trend Plunge
0.211924 -0.104762 -0.971655 116.305 76.3256

0.0200653 0.994495 -0.102848 1.15587 5.90320
0.977080 0.00229945 0.212859 269.865 12.2900
MIL Ellipse Eigenvalues:
3.23957 4.11701 6.20770
MIL Ellipse (H) Eigenvalues:
0.383221 0.339940 0.276839
MIL Ellipse Tensor (M):
6.07355 0.0241771 0.615502
0.0241771 4.10740 -0.0882933
0.615502 -0.0882933 3.38334
MIL (H) DA I E Tb.N
1.38427 0.722401 0.112940 2.11377
MIL Fabric Eigenvectors: Trend Plunge
-0.174526 0.137302 0.975033 128.193 77.1699
0.00227950 -0.990171 0.139842 359.868 8.03868
-0.984650 -0.0266287 -0.172498 268.451 9.93308
MIL Fabric Eigenvalues:
0.371344 0.340860 0.287796
MIL Fabric Tensor:

0.290341 -0.00212184 -0.0142004
-0.00212184 0.341397 0.00383739
-0.0142004 0.00383739 0.368262
MIL (F) DA I E
1.29030 0.775011 0.0820933

lateral

Star length and volume calcuations for sample: B7_76_0001
Threshhold range, BV/TV: 65.0000-148.000 0.291085
Uniform Orientations: 513
Vector sampling: Dense
Random Points: 2000
Data orientation (strike, dip, up): -36.0000 -180.000 0

SVD Eigenvalues:	Eigenvectors		Trend	Plunge
0.598897	0.00182406	0.128890	0.991657	180.811
82.5938				
0.245750	0.625292	0.773734	-0.101716	38.9434
5.83797				
0.155353	-0.780389	0.620261	-0.0791824	308.478
4.54157				

SVD Fabric Tensor:

0.190699	0.0438395	-0.00494716
0.0438395	0.216839	0.0495770
-0.00494716	0.0495770	0.592462

SVD DA	I	E	Sum(tau)
3.85508	0.259398	0.589662	13.2039

SLD Eigenvalues:	Eigenvectors		Trend	Plunge
0.405676	-0.0129683	0.109639	0.993887	173.254
83.6615				
0.314324	-0.582201	-0.808936	0.0816395	35.7430
4.68281				
0.280000	-0.812942	0.577583	-0.0743222	305.393
4.26228				

SLD Fabric Tensor:

0.291656	0.0159868	-0.00325128
0.0159868	0.303972	0.0114279
-0.00325128	0.0114279	0.404373

SLD DA	I	E	Sum(tau)
1.44884	0.690206	0.225184	68.1218

Thickness (minimum line length at each point, non-zero points only)

Mean	Variance	Skewness	Kurtosis	Min	Max
0.126843	0.00357891	0.720473	0.210084	0.0390600	0.381057

Thickness histogram

bin num	norm
0.0211698	24	0.0137143
0.0635094	540	0.308571
0.105849	359	0.205143
0.148189	455	0.260000
0.190528	214	0.122286
0.232868	105	0.0600000
0.275207	34	0.0194286

0.317547 15 0.00857143
0.359887 3 0.00171429
0.402226 1 0.000571429
MIL calculations for sample: B7_76_0001
Threshhold range, BV/TV: 65.0000-148.000 0.291085
Uniform Orientations: 513
Vector sampling: Dense
Random Points: 2000
Data orientation (strike, dip, up): -36.0000 -180.000 0
MIL Ellipse Eigenvectors: Trend Plunge
0.0586031 -0.0360820 -0.997629 121.621 86.0538
0.595849 0.803074 0.00595617 216.574 0.341265
-0.800956 0.594785 -0.0685620 306.597 3.93140
MIL Ellipse Eigenvalues:
2.51105 5.14510 5.93540
MIL Ellipse (H) Eigenvalues:
0.425706 0.297400 0.276894
MIL Ellipse Tensor (M):
5.64305 -0.370924 0.197397
-0.370924 5.42125 -0.127044
0.197397 -0.127044 2.52724
MIL (H) DA I E Tb.N
1.53744 0.650434 0.301396 2.10501
MIL Fabric Eigenvectors: Trend Plunge
-0.0630599 0.0521557 0.996646 129.594 85.3060
-0.579317 -0.815080 0.00599955 35.4032 0.343751
-0.812660 0.576995 -0.0816135 305.375 4.68132
MIL Fabric Eigenvalues:
0.396549 0.310524 0.292927
MIL Fabric Tensor:
0.299245 0.00796803 -0.00657361
0.00796803 0.304900 0.00530028
-0.00657361 0.00530028 0.395856
MIL (F) DA I E
1.35374 0.738692 0.216935

medial

Star length and volume calcuations for sample: B7_76_0001
Threshhold range, BV/TV: 69.0000-166.000 0.287985
Uniform Orientations: 513
Vector sampling: Dense
Random Points: 2000
Data orientation (strike, dip, up): -36.0000 -180.000 0
SVD Eigenvalues: Eigenvectors Trend Plunge

0.650269 -0.0286293 0.0877394 0.995732 161.929
84.7045
0.197713 -0.460868 0.882787 -0.0910380 332.433
5.22333
0.152018 -0.887007 -0.461507 0.0151627 62.5122
0.868790
SVD Fabric Tensor:
0.162132 -0.0198424 -0.0122865
-0.0198424 0.191464 0.0398572
-0.0122865 0.0398572 0.646403
SVD DA I E Sum(tau)
4.27757 0.233778 0.695952 16.4477
SLD Eigenvalues: Eigenvectors Trend Plunge
0.415066 -0.0358132 0.0844464 0.995784 157.018
84.7371
0.307502 -0.464735 0.880720 -0.0914025 332.180
5.24430
0.277432 -0.884725 -0.466049 0.00770382 62.2209
0.441401
SLD Fabric Tensor:
0.284103 -0.0127238 -0.00363105
-0.0127238 0.301737 0.00915313
-0.00363105 0.00915313 0.414160
SLD DA I E Sum(tau)
1.49610 0.668404 0.259151 72.6763
Thickness (minimum line length at each point, non-zero points only)
Mean Variance Skewness Kurtosis Min Max
0.135357 0.00442665 1.004061.523620.0390600 0.511702
Thickness histogram
bin num norm
0.0284279 98 0.0578171
0.0852837 586 0.345723
0.142139 594 0.350442
0.198995 246 0.145133
0.255851 121 0.0713864
0.312707 36 0.0212389
0.369563 11 0.00648968
0.426418 1 0.000589970
0.483274 1 0.000589970
0.540130 1 0.000589970
MIL calculations for sample: B7_76_0001
Threshhold range, BV/TV: 69.0000-166.000 0.287985
Uniform Orientations: 513
Vector sampling: Dense
Random Points: 2000
Data orientation (strike, dip, up): -36.0000 -180.000 0
MIL Ellipse Eigenvectors: Trend Plunge
0.00886874 -0.0757921 -0.997084 173.326 85.6236

-0.457431 0.886370 -0.0714450 332.703 4.09699
0.889201 0.456731 -0.0268087 62.8130 1.53621
MIL Ellipse Eigenvalues:
2.03433 4.58796 5.97886
MIL Ellipse (H) Eigenvalues:
0.444603 0.296055 0.259342
MIL Ellipse Tensor (M):
5.68751 0.566596 -0.0105752
0.566596 4.86344 -0.210011
-0.0105752 -0.210011 2.05020
MIL (H) DA I E Tb.N
1.71435 0.583313 0.334113 2.01299
MIL Fabric Eigenvectors: Trend Plunge
-0.0117993 0.107300 0.994157 173.725 83.8030
-0.437830 0.893297 -0.101611 333.889 5.83193
-0.898980 -0.436471 0.0364390 64.1026 2.08826
MIL Fabric Eigenvalues:
0.409574 0.311660 0.278766
MIL Fabric Tensor:
0.285090 -0.0130307 -7.10330e-005
-0.0130307 0.306521 0.0109679
-7.10330e-005 0.0109679 0.408389
MIL (F) DA I E
1.46924 0.680626 0.239062

15_72

medial

Star length and volume calcuations for sample: B15_72_0001
Threshhold range, BV/TV: 68.0000-172.000 0.339722
Uniform Orientations: 513
Vector sampling: Dense
Random Points: 2000
Data orientation (strike, dip, up): -178.000 0.000000 1
SVD Eigenvalues: Eigenvectors Trend Plunge
0.439159 -0.174354 0.224721 0.958697 142.193 73.4753
0.323088 -0.506967 0.814169 -0.283044 328.090 16.4419
0.237754 -0.844148 -0.535378 -0.0280277 237.616 1.60608
SVD Fabric Tensor:
0.265808 -0.0431135 -0.0214206
-0.0431135 0.304490 0.0237259
-0.0214206 0.0237259 0.429702
SVD DA I E Sum(tau)
1.84712 0.541384 0.264303 54.7248
SLD Eigenvalues: Eigenvectors Trend Plunge
0.360442 -0.237639 0.404574 0.883090 149.571 62.0174
0.337973 -0.387498 0.794176 -0.468114 333.991 27.9119
0.301585 -0.890715 -0.453438 -0.0319551 243.021 1.83121
SLD Fabric Tensor:
0.310373 -0.0168567 -0.00575088
-0.0168567 0.334169 0.00750020
-0.00575088 0.00750020 0.355458
SLD DA I E Sum(tau)
1.19516 0.836709 0.0623360 108.694
Thickness (minimum line length at each point, non-zero points only)
Mean Variance Skewness Kurtosis Min Max
0.154528 0.00537595 0.619847 0.0831842 0.0390600 0.448013
Thickness histogram
bin num norm
0.0248896 25 0.0140845
0.0746689 474 0.267042
0.124448 352 0.198310
0.174227 490 0.276056
0.224007 244 0.137465
0.273786 118 0.0664789
0.323565 56 0.0315493

0.373345 10 0.00563380
0.423124 5 0.00281690
0.472903 1 0.000563380
MIL calculations for sample: B15_72_0001
Threshhold range, BV/TV: 68.0000-172.000 0.339722
Uniform Orientations: 513
Vector sampling: Dense
Random Points: 2000
Data orientation (strike, dip, up): -178.000 0.000000 1
MIL Ellipse Eigenvectors: Trend Plunge
-0.174843 0.478039 0.860761 159.910 59.4021
0.294811 -0.808700 0.509010 339.971 30.5979
0.939424 0.342758 0.000464510 249.955 0.0266145
MIL Ellipse Eigenvalues:
3.54819 4.00586 5.41413
MIL Ellipse (H) Eigenvalues:
0.363546 0.342149 0.294305
MIL Ellipse Tensor (M):
5.23469 0.491709 0.0694934
0.491709 4.06672 -0.188098
0.0694934 -0.188098 3.66677
MIL (H) DA I E Tb.N
1.23527 0.809541 0.0588575 2.07966
MIL Fabric Eigenvectors: Trend Plunge
-0.183800 0.469409 0.863639 158.617 59.7277
-0.257290 0.825001 -0.503165 342.679 30.2096
-0.948693 -0.314688 -0.0308609 251.649 1.76848
MIL Fabric Eigenvalues:
0.359647 0.340079 0.300274
MIL Fabric Tensor:
0.304915 -0.0135720 -0.00427148
-0.0135720 0.340449 0.00754602
-0.00427148 0.00754602 0.354636
MIL (F) DA I E
1.19773 0.834913 0.0544071

lateral

Star length and volume calcuations for sample: B15_72_0001
Threshhold range, BV/TV: 68.0000-184.000 0.322099
Uniform Orientations: 513
Vector sampling: Dense
Random Points: 2000
Data orientation (strike, dip, up): -178.000 0.000000 1
SVD Eigenvalues: Eigenvectors Trend Plunge

0.543470 -0.215920 0.0484789 0.975207 102.654
77.2149
0.272650 -0.340174 0.932458 -0.121671 339.957
6.98857
0.183880 0.915238 0.358011 0.184845 248.636
10.6521
SVD Fabric Tensor:
0.210917 -0.0319214 -0.0720434
-0.0319214 0.261908 0.00692912
-0.0720434 0.00692912 0.527175
SVD DA I E Sum(tau)
2.95556 0.338345 0.498317 50.3227
SLD Eigenvalues: Eigenvectors Trend Plunge
0.384626 -0.227746 0.0733660 0.970953 107.856
76.1564
0.326169 0.255410 -0.957741 0.132277 345.068
7.60117
0.289205 -0.939626 -0.278117 -0.199383 253.512
11.5009
SLD Fabric Tensor:
0.296565 -0.0106367 -0.0198518
-0.0106367 0.323625 0.00211438
-0.0198518 0.00211438 0.379810
SLD DA I E Sum(tau)
1.32994 0.751911 0.151983 105.954
Thickness (minimum line length at each point, non-zero points only)
Mean Variance Skewness Kurtosis Min Max
0.156173 0.00649410 0.840366 0.828846 0.0390600 0.513378
Thickness histogram
bin num norm
0.0285210 81 0.0454036
0.0855631 519 0.290919
0.142605 510 0.285874
0.199647 364 0.204036
0.256689 195 0.109305
0.313731 71 0.0397982
0.370773 27 0.0151345
0.427815 11 0.00616592
0.484857 5 0.00280269
0.541899 1 0.000560538
MIL calculations for sample: B15_72_0001
Threshhold range, BV/TV: 68.0000-184.000 0.322099
Uniform Orientations: 513
Vector sampling: Dense
Random Points: 2000
Data orientation (strike, dip, up): -178.000 0.000000 1
MIL Ellipse Eigenvectors: Trend Plunge
0.236639 -0.122603 -0.963831 117.389 74.5430

-0.179712 0.969366 -0.167430 349.497 9.63845
0.954833 0.212832 0.207357 257.434 11.9675
MIL Ellipse Eigenvalues:
2.85040 3.57114 5.11069
MIL Ellipse (H) Eigenvalues:
0.378756 0.338383 0.282861
MIL Ellipse Tensor (M):
4.93440 0.333777 0.469204
0.333777 3.63004 -0.0172253
0.469204 -0.0172253 2.96779
MIL (H) DA I E Tb.N
1.33902 0.746815 0.106593 1.95551
MIL Fabric Eigenvectors: Trend Plunge
-0.214003 0.135258 0.967423 122.294 75.3352
0.223000 -0.957450 0.183193 346.889 10.5558
-0.951038 -0.254939 -0.174735 254.994 10.0632
MIL Fabric Eigenvalues:
0.369364 0.337865 0.292771
MIL Fabric Tensor:
0.298521 -0.0118453 -0.0140150
-0.0118453 0.335511 0.00211284
-0.0140150 0.00211284 0.365968
MIL (F) DA I E
1.26162 0.792635 0.0852779

medial

Star length and volume calcuations for sample: B3_72_0001
Threshhold range, BV/TV: 61.0000-153.000 0.288100
Uniform Orientations: 513
Vector sampling: Dense
Random Points: 2000
Data orientation (strike, dip, up): -34.0000 180.0000

SVD Eigenvalues:	Eigenvectors			Trend	Plunge
0.434588	0.805339	-0.584011	-0.101778	125.949	5.84157
0.312303	0.486916	0.749586	-0.448368	33.0070	26.6390
0.253109	-0.338143	-0.311531	-0.888036	227.346	62.6275

SVD Fabric Tensor:

0.384845	-0.0637494	-0.0277982
-0.0637494	0.348266	-0.00910756
-0.0277982	-0.00910756	0.266889

SVD DA	I	E	Sum(tau)
1.71700	0.582411	0.281381	19.1190

SLD Eigenvalues:	Eigenvectors			Trend	Plunge
0.360313	-0.441627	0.256324	0.859805	120.131	59.2946
0.331062	-0.516341	0.711103	-0.477205	324.016	28.5030
0.308625	-0.733729	-0.654699	-0.181692	228.258	10.4683

SLD Fabric Tensor:

0.324688	-0.0140896	-0.0140983
-0.0140896	0.323366	0.00377763
-0.0140983	0.00377763	0.351946

SLD DA	I	E	Sum(tau)
1.16748	0.856544	0.0811830	72.8703

Thickness (minimum line length at each point, non-zero points only)

Mean	Variance	Skewness	Kurtosis	Min	Max
0.136221	0.00497791	0.999356	1.02277	0.0390600	0.474258

Thickness histogram

bin num	norm
0.0263477	51	0.0288298
0.0790431	662	0.374223
0.131738	456	0.257773
0.184434	352	0.198982
0.237129	130	0.0734878
0.289825	86	0.0486150
0.342520	22	0.0124364

0.395215 7 0.00395704
0.447911 2 0.00113058
0.500606 1 0.000565291
MIL calculations for sample: B3_72_0001
Threshhold range, BV/TV: 61.0000-153.000 0.288100
Uniform Orientations: 513
Vector sampling: Dense
Random Points: 2000
Data orientation (strike, dip, up): -34.0000 180.0000
MIL Ellipse Eigenvectors: Trend Plunge
0.195153 -0.194179 -0.961358 134.857 74.0201
-0.511607 0.816124 -0.268699 327.917 15.5869
0.836764 0.544275 0.0599256 236.958 3.43554
MIL Ellipse Eigenvalues:
3.38209 4.63978 6.00515
MIL Ellipse (H) Eigenvalues:
0.383989 0.327841 0.288170
MIL Ellipse Tensor (M):
5.54788 0.669493 0.304422
0.669493 4.99683 -0.190247
0.304422 -0.190247 3.48231
MIL (H) DA I E Tb.N
1.33251 0.750465 0.146224 2.16011
MIL Fabric Eigenvectors: Trend Plunge
-0.225941 0.212741 0.950627 133.276 71.9205
-0.519893 0.798931 -0.302359 326.947 17.5993
-0.823810 -0.562540 -0.0699089 235.673 4.00875
MIL Fabric Eigenvalues:
0.369959 0.330466 0.299575
MIL Fabric Tensor:
0.311518 -0.0162136 -0.0102616
-0.0162136 0.322478 0.00677224
-0.0102616 0.00677224 0.366004
MIL (F) DA I E
1.23494 0.809753 0.106751

lateral

Star length and volume calcuations for sample: B3_72_0001
Threshhold range, BV/TV: 58.0000-213.000 0.308112
Uniform Orientations: 513
Vector sampling: Dense
Random Points: 2000
Data orientation (strike, dip, up): -34.0000 180.0000
SVD Eigenvalues: Eigenvectors Trend Plunge

0.633417 0.0113661 0.0156283 0.999813 216.028
88.8927
0.228755 -0.172609 0.984899 -0.0134329 350.060
0.769670
0.137828 0.984925 0.172424 -0.0138921 80.0703
0.795983
SVD Fabric Tensor:
0.140601 -0.0153698 0.00584271
-0.0153698 0.226150 0.00654079
0.00584271 0.00654079 0.633248
SVD DA I E Sum(tau)
4.59571 0.217594 0.638856 21.2115
SLD Eigenvalues: Eigenvectors Trend Plunge
0.405800 0.0278633 0.0652467 0.997480 203.125
85.9316
0.319785 -0.196622 0.978731 -0.0585279 348.641
3.35532
0.274415 0.980083 0.194496 -0.0400996 78.7756
2.29816
SLD Fabric Tensor:
0.276271 -0.00849208 0.00417370
-0.00849208 0.318435 0.00595192
0.00417370 0.00595192 0.405294
SLD DA I E Sum(tau)
1.47878 0.676233 0.211965 77.5934
Thickness (minimum line length at each point, non-zero points only)
Mean Variance Skewness Kurtosis Min Max
0.134981 0.00356670 0.413146 -0.432935 0.0390600 0.334487
Thickness histogram
bin num norm
0.0185826 0 0.000000
0.0557478 434 0.252766
0.0929130 226 0.131625
0.130078 311 0.181130
0.167243 411 0.239371
0.204409 195 0.113570
0.241574 99 0.0576587
0.278739 25 0.0145603
0.315904 15 0.00873617
0.353069 1 0.000582411
MIL calculations for sample: B3_72_0001
Threshhold range, BV/TV: 58.0000-213.000 0.308112
Uniform Orientations: 513
Vector sampling: Dense
Random Points: 2000

Data orientation (strike, dip, up): -34.0000 180.0000
MIL Ellipse Eigenvectors: Trend Plunge

0.0242522 -0.00143749 -0.999705 93.3921 88.6079
-0.266623 0.963769 -0.00785393 344.536 0.450002
-0.963496 -0.266735 -0.0229903 254.526 1.31736
MIL Ellipse Eigenvalues:
2.85169 5.20317 7.04865
MIL Ellipse (H) Eigenvalues:
0.420809 0.311532 0.267660
MIL Ellipse Tensor (M):
6.91499 0.474366 0.0978911
0.474366 5.33447 0.00793782
0.0978911 0.00793782 2.85405
MIL (H) DA I E Tb.N
1.57218 0.636060 0.259684 2.21672
MIL Fabric Eigenvectors: Trend Plunge
-0.0287191 0.0446403 0.998590 147.245 86.9573
-0.244252 0.968405 -0.0503156 345.844 2.88409
-0.969286 -0.245353 -0.0169083 255.795 0.968819
MIL Fabric Eigenvalues:
0.393979 0.321958 0.284064
MIL Fabric Tensor:
0.286415 -0.00910426 -0.00268651
-0.00910426 0.319820 0.00305332
-0.00268651 0.00305332 0.393765
MIL (F) DA I E
1.38694 0.721012 0.182805

6_80

lateral

Star length and volume □alculations for sample: B6_80_0001
Threshhold range, BV/TV: 59.0000-126.000 0.384304
Uniform Orientations: 513
Vector sampling: Dense
Random Points: 2000
Data orientation (strike, dip, up): -16.0000 180.0001

SVD Eigenvalues:	Eigenvectors			Trend	Plunge
0.611101	-0.257197	-0.0943495	0.961742	69.8551	74.1002
0.199194	0.243313	-0.969483	-0.0300401	165.911	1.72143
0.189705	-0.935227	-0.226278	-0.272304	256.399	15.8014

SVD Fabric Tensor:

0.218142	0.00798728	-0.104305
0.00798728	0.202375	-0.0379610
-0.104305	-0.0379610	0.579483

SVD DA	I	E	Sum(tau)
3.22132	0.310432	0.674040	59.2091

SLD Eigenvalues:	Eigenvectors			Trend	Plunge
0.407788	-0.269083	-0.0810055	0.959704	73.2460	73.6794
0.305360	0.343249	-0.939091	0.0169749	339.922	0.972639
0.286852	-0.899875	-0.333985	-0.280499	249.638	16.2900

SLD Fabric Tensor:

0.297789	-0.00332968	-0.0311226
-0.00332968	0.303968	-0.00969673
-0.0311226	-0.00969673	0.398243

SLD DA	I	E	Sum(tau)
1.42160	0.703435	0.251180	106.653

Thickness (minimum line length at each point, non-zero points only)

Mean	Variance	Skewness	Kurtosis	Min	Max
0.146256	0.00425708	0.399553	-0.318293	0.0390600	0.396650

Thickness histogram

bin num	norm
0.0220361	20	0.0109230
0.0661083	441	0.240852
0.110181	325	0.177499
0.154253	435	0.237575
0.198325	350	0.191152

0.242397 184 0.100492
0.286469 58 0.0316767
0.330542 14 0.00764610
0.374614 3 0.00163845
0.418686 1 0.000546150
MIL calculations for sample: B6_80_0001
Threshhold range, BV/TV: 59.0000-126.000 0.384304
Uniform Orientations: 513
Vector sampling: Dense
Random Points: 2000
Data orientation (strike, dip, up): -16.0000 180.0001
MIL Ellipse Eigenvectors: Trend Plunge
0.166189 0.0410929 -0.985237 76.1113 80.1428
-0.128644 0.991496 0.0196544 172.607 1.12618
-0.977667 -0.123478 -0.170062 262.802 9.79142
MIL Ellipse Eigenvalues:
4.48955 7.26056 8.60302
MIL Ellipse (H) Eigenvalues:
0.398605 0.313443 0.287951
MIL Ellipse Tensor (M):
8.46719 0.143139 0.676916
0.143139 7.27635 0.140378
0.676916 0.140378 4.60958
MIL (H) DA I E Tb.N
1.38428 0.722397 0.213649 2.59019
MIL Fabric Eigenvectors: Trend Plunge
-0.207869 -0.0383326 0.977405 79.5516 77.7971
0.147358 -0.989055 -0.00745023 171.526 0.426871
-0.966993 -0.142480 -0.211243 261.618 12.1952
MIL Fabric Eigenvalues:
0.386200 0.317690 0.296110
MIL Fabric Tensor:
0.300471 -0.00242740 -0.0183276
-0.00242740 0.317353 -0.00321634
-0.0183276 -0.00321634 0.382176
MIL (F) DA I E
1.30425 0.766726 0.177394

medial

Star length and volume □alculations for sample: B6_80_0001
Threshhold range, BV/TV: 59.0000-143.000 0.375893
Uniform Orientations: 513
Vector sampling: Dense
Random Points: 2000
Data orientation (strike, dip, up): -16.0000 180.0000

SVD Eigenvalues: Eigenvectors Trend Plunge
0.495557 -0.0633916 0.184095 0.980862 160.999 78.7726
0.260393 -0.473164 0.859808 -0.191954 331.175 11.0669
0.244050 -0.878691 -0.476277 0.0326024 61.5410 1.86831
SVD Fabric Tensor:
0.248720 -0.00958358 -0.0141540
-0.00958358 0.264655 0.0427178
-0.0141540 0.0427178 0.486625
SVD DA I E Sum(tau)
2.03055 0.492477 0.474545 44.0203
SLD Eigenvalues: Eigenvectors Trend Plunge
0.370538 -0.0663095 0.222364 0.972706 163.395 76.5828
0.316764 -0.636131 0.741626 -0.212904 319.379 12.2926
0.312697 -0.768727 -0.632886 0.0922759 50.5357 5.29455
SLD Fabric Tensor:
0.314597 -0.00277165 -0.00317990
-0.00277165 0.317794 0.0118686
-0.00317990 0.0118686 0.367608
SLD DA I E Sum(tau)
1.18497 0.843900 0.145124 104.509
Thickness (minimum line length at each point, non-zero points only)
Mean Variance Skewness Kurtosis Min Max
0.144905 0.00409303 0.613355 0.863702 0.0390600 0.528570
Thickness histogram
bin num norm
0.0293650 51 0.0283491
0.0880949 559 0.310728
0.146825 634 0.352418
0.205555 407 0.226237
0.264285 116 0.0644803
0.323015 27 0.0150083
0.381745 2 0.00111173
0.440475 1 0.000555864
0.499205 1 0.000555864
0.557935 1 0.000555864
MIL calculations for sample: B6_80_0001
Threshhold range, BV/TV: 59.0000-143.000 0.375893
Uniform Orientations: 513
Vector sampling: Dense
Random Points: 2000
Data orientation (strike, dip, up): -16.0000 180.0000
MIL Ellipse Eigenvectors: Trend Plunge

0.0742677	-0.232302	-0.969804	162.271	75.8841
-0.402941	0.882579	-0.242266	335.461	14.0203
0.912208	0.408766	-0.0280568	65.8625	1.60774

MIL Ellipse Eigenvalues:

4.89037	6.38498	6.74677

MIL Ellipse (H) Eigenvalues:

0.366764	0.320980	0.312255

MIL Ellipse Tensor (M):

6.67779	0.160690	0.0983898
0.160690	6.36478	-0.340865
0.0983898	-0.340865	4.97956

MIL (H) DA	I	E	Tb.N
1.17456	0.851379	0.124832	2.45774

MIL Fabric Eigenvectors:			Trend	Plunge
-0.0984561	0.211306	0.972448	155.017	76.5193
-0.361445	0.902868	-0.232781	338.182	13.4609
-0.927181	-0.374405	-0.0125175	248.011	0.717218

MIL Fabric Eigenvalues:

0.358337	0.323261	0.318401

MIL Fabric Tensor:

0.319423	-0.00241707	-0.00341470
-0.00241707	0.324147	0.00718476
-0.00341470	0.00718476	0.356431

MIL (F) DA	I	E
1.12543	0.888551	0.0978853

medial

Star length and volume □alculations for sample: B3_74_0001
Threshhold range, BV/TV: 59.0000-255.000 0.223609
Uniform Orientations: 513
Vector sampling: Dense
Random Points: 2000
Data orientation (strike, dip, up): 173.0005.000001

SVD Eigenvalues:	Eigenvectors		Trend	Plunge
0.678314	-0.0281388	0.119107	0.992483	166.708
82.9702				
0.203727	-0.680029	-0.729995	0.0683258	42.9705
3.91783				
0.117958	-0.732645	0.672994	-0.101537	312.570
5.82770				

SVD Fabric Tensor:

0.158065	0.0406992	-0.0196344
0.0406992	0.171613	0.0619626
-0.0196344	0.0619626	0.670322

SVD DA	I	E	Sum(tau)
5.75046	0.173899	0.699657	67.4367

SLD Eigenvalues:	Eigenvectors		Trend	Plunge
0.393691	-0.0428229	0.110963	0.992901	158.897
83.1691				
0.322091	-0.606728	-0.792457	0.0623945	37.4387
3.57727				
0.284218	-0.793755	0.599749	-0.101260	307.074
5.81171				

SLD Fabric Tensor:

0.298360	0.0176898	-0.00608846
0.0176898	0.309350	0.0101886
-0.00608846	0.0101886	0.392290

SLD DA	I	E	Sum(tau)
1.38517	0.721930	0.181868	102.458

Thickness (minimum line length at each point, non-zero points only)

Mean	Variance	Skewness	Kurtosis	Min	Max
0.156470	0.00578952	0.751360	0.745983	0.0390600	0.500242

Thickness histogram

bin num	norm
0.0277912	55 0.0302697
0.0833737	509 0.280132
0.138956	441 0.242708
0.194539	482 0.265272
0.250121	223 0.122730
0.305704	62 0.0341222
0.361286	28 0.0154100

0.416869 13 0.00715465
0.472451 3 0.00165107
0.528034 1 0.000550358
MIL calculations for sample: B3_74_0001
Threshhold range, BV/TV: 59.0000-255.000 0.223609
Uniform Orientations: 513
Vector sampling: Dense
Random Points: 2000
Data orientation (strike, dip, up): 173.0005.000001
MIL Ellipse Eigenvectors: Trend Plunge
-0.00320630 -0.132532 -0.991173 181.386 82.3818
0.224331 0.965821 -0.129867 13.0762 7.46193
0.974508 -0.222768 0.0266343 282.876 1.52621
MIL Ellipse Eigenvalues:
1.30175 1.79890 2.33950
MIL Ellipse (H) Eigenvalues:
0.385119 0.327608 0.287274
MIL Ellipse Tensor (M):
2.31229 -0.117569 0.0124515
-0.117569 1.81700 -0.0685150
0.0124515 -0.0685150 1.31087
MIL (H) DA I E Tb.N
1.34060 0.745936 0.149334 1.34308
MIL Fabric Eigenvectors: Trend Plunge
-0.00164825 0.125411 0.992104 179.247 82.7949
0.183205 0.975351 -0.122989 10.6382 7.06464
-0.983073 0.181556 -0.0245836 280.464 1.40868
MIL Fabric Eigenvalues:
0.377652 0.328898 0.293450
MIL Fabric Tensor:
0.294640 0.00631666 -0.000936397
0.00631666 0.328496 0.00622423
-0.000936397 0.00622423 0.376864
MIL (F) DA I E
1.28694 0.777040 0.129098

14_74

medial

Star length and volume calcuations for sample: B14_74_0001
Threshhold range, BV/TV: 52.0000-174.000 0.208869
Uniform Orientations: 513
Vector sampling: Dense
Random Points: 2000
Data orientation (strike, dip, up): -27.0000 180.0000

SVD Eigenvalues:	Eigenvectors		Trend	Plunge
0.764797	-8.22754e-006	0.0301055	0.999547	179.984
88.2748				
0.129269	-0.0826432	0.996127	-0.0300032	355.257
1.71931				
0.105935	-0.996579	-0.0826060	0.00247982	85.2616
0.142083				

SVD Fabric Tensor:

0.106094	-0.00192110	5.24398e-005
-0.00192110	0.129685	0.0191290
5.24398e-005	0.0191290	0.764221

SVD DA	I	E	Sum(tau)
7.21953	0.138513	0.830977	18.6398

SLD Eigenvalues:	Eigenvectors		Trend	Plunge
0.416659	0.000417967	0.0327442	0.999464	180.731
88.1234				
0.294951	0.127157	0.991349	-0.0325315	7.30923
1.86425				
0.288390	-0.991883	0.127102	-0.00374929	277.302
0.214819				

SLD Fabric Tensor:

0.288496	0.000828888	2.64408e-005
0.000828888	0.294976	0.00398620
2.64408e-005	0.00398620	0.416528

SLD DA	I	E	Sum(tau)
1.44478	0.692149	0.292103	64.8214

Thickness (minimum line length at each point, non-zero points only)

Mean	Variance	Skewness	Kurtosis	Min	Max
0.130535	0.00392266	0.641558	0.230288	0.0390600	0.449511

Thickness histogram

bin num	norm
0.0249728	55 0.0295381
0.0749185	679 0.364662
0.124864	366 0.196563
0.174810	511 0.274436
0.224755	200 0.107411
0.274701	36 0.0193340
0.324647	8 0.00429646

0.374592 4 0.00214823
0.424538 2 0.00107411
0.474484 1 0.000537057
MIL calculations for sample: B14_74_0001
Threshhold range, BV/TV: 52.0000-174.000 0.208869
Uniform Orientations: 513
Vector sampling: Dense
Random Points: 2000
Data orientation (strike, dip, up): -27.0000 180.0000
MIL Ellipse Eigenvectors: Trend Plunge
-0.0372481 -0.0133064 -0.999217 250.341 87.7332
-0.229563 -0.973056 0.0215155 13.2745 1.23284
0.972581 -0.230185 -0.0331898 103.315 1.90199
MIL Ellipse Eigenvalues:
1.50928 2.83540 3.14749
MIL Ellipse (H) Eigenvalues:
0.412871 0.301226 0.285902
MIL Ellipse Tensor (M):

3.12877 -0.0705262 -0.0594310
-0.0705262 2.85170 -0.0152478
-0.0594310 -0.0152478 1.51170
MIL (H) DA I E Tb.N
1.44410 0.692473 0.270412 1.56970
MIL Fabric Eigenvectors: Trend Plunge
0.0711957 0.0398564 0.996666 240.759 85.3199
0.377090 0.923971 -0.0638863 22.2013 3.66291
-0.923436 0.380381 0.0507533 112.388 2.90920
MIL Fabric Eigenvalues:
0.393081 0.309217 0.297702
MIL Fabric Tensor:
0.299823 0.00428256 0.00649055
0.00428256 0.307684 0.00310910
0.00649055 0.00310910 0.392493
MIL (F) DA I E
1.32038 0.757355 0.213352

lateral

Star length and volume calcuations for sample: B14_74_0001
Threshhold range, BV/TV: 53.0000-186.000 0.235326
Uniform Orientations: 513
Vector sampling: Dense
Random Points: 2000
Data orientation (strike, dip, up): -27.0000 180.0000
SVD Eigenvalues: Eigenvectors Trend Plunge

0.722562 0.101548 -0.0921637 0.990552 312.227
82.1179
0.185335 0.209419 -0.971408 -0.111851 167.834
6.42204
0.0921031 0.972539 0.218798 -0.0793436 77.3209
4.55084
SVD Fabric Tensor:
0.102693 -0.0248668 0.0612330
-0.0248668 0.185435 -0.0474264
0.0612330 -0.0474264 0.711872
SVD DA I E Sum(tau)
7.84514 0.127467 0.743502 17.8724
SLD Eigenvalues: Eigenvectors Trend Plunge
0.421584 0.0872265 -0.0540499 0.994721 301.784
84.1102
0.316368 -0.195849 0.978109 0.0703212 168.677
4.03243
0.262048 0.976747 0.200949 -0.0747314 78.3746
4.28579
SLD Fabric Tensor:
0.265346 -0.0111578 0.0130942
-0.0111578 0.314482 -0.00484115
0.0130942 -0.00484115 0.420173
SLD DA I E Sum(tau)
1.60880 0.621580 0.249573 64.2895
Thickness (minimum line length at each point, non-zero points only)
Mean Variance Skewness Kurtosis Min Max
0.129939 0.00430543 0.814881 0.737384 0.0390600 0.501861
Thickness histogram
bin num norm
0.0278812 146 0.0796943
0.0836435 640 0.349345
0.139406 543 0.296397
0.195168 341 0.186135
0.250930 118 0.0644105
0.306693 30 0.0163755
0.362455 11 0.00600437
0.418217 2 0.00109170
0.473980 0 0.000000
0.529742 1 0.000545852
MIL calculations for sample: B14_74_0001
Threshhold range, BV/TV: 53.0000-186.000 0.235326
Uniform Orientations: 513
Vector sampling: Dense
Random Points: 2000
Data orientation (strike, dip, up): -27.0000 180.0000
MIL Ellipse Eigenvectors: Trend Plunge
-0.127898 0.106186 -0.986086 309.701 80.4311

0.233505 -0.963079 -0.133995 166.371 7.70052
0.963907 0.247394 -0.0983807 75.6053 5.64593
MIL Ellipse Eigenvalues:
1.83745 3.66792 4.81310
MIL Ellipse (H) Eigenvalues:
0.429988 0.304337 0.265676
MIL Ellipse Tensor (M):
4.70198 0.297945 -0.339453
0.297945 3.71737 0.163794
-0.339453 0.163794 1.89912
MIL (H) DA I E Tb.N
1.61847 0.617868 0.292220 1.82709
MIL Fabric Eigenvectors: Trend Plunge
0.0905589 -0.104254 0.990419 319.021 82.0625
0.247944 -0.960830 -0.123810 165.530 7.11202
0.964532 0.256781 -0.0611626 75.0923 3.50655
MIL Fabric Eigenvalues:
0.404182 0.313328 0.282490
MIL Fabric Tensor:
0.285384 -0.00849535 0.00996800
-0.00849535 0.312282 -0.00889678
0.00996800 -0.00889678 0.402334
MIL (F) DA I E
1.43078 0.698919 0.224785

medial

Star length and volume calcuations for sample: B6_71_0001
Threshhold range, BV/TV: 62.0000-157.000 0.281217
Uniform Orientations: 513
Vector sampling: Dense
Random Points: 2000
Data orientation (strike, dip, up): -178.000 0.000000 1
SVD Eigenvalues: Eigenvectors Trend Plunge
0.674968 -0.172272 0.0691055 0.982622 111.858 79.3030
0.163959 -0.0925254 -0.994261 0.0537026 5.31660 3.07842
0.161073 -0.980694 0.0816661 -0.177677 274.760 10.2345
SVD Fabric Tensor:
0.176349 -0.00585241 -0.0870057
-0.00585241 0.166380 0.0347418
-0.0870057 0.0347418 0.657271
SVD DA I E Sum(tau)
4.19046 0.238637 0.757086 47.5228
SLD Eigenvalues: Eigenvectors Trend Plunge
0.409146 -0.177923 0.0795727 0.980822 114.096 78.7607
0.296155 -0.977707 -0.127233 -0.167036 262.586 9.61553
0.294699 0.111501 -0.988676 0.100436 353.565 5.76430
SLD Fabric Tensor:
0.299714 -0.00143924 -0.0197344
-0.00143924 0.295448 0.00896309
-0.0197344 0.00896309 0.404839
SLD DA I E Sum(tau)
1.38835 0.720280 0.276163 90.7479
Thickness (minimum line length at each point, non-zero points only)
Mean Variance Skewness Kurtosis Min Max
0.141899 0.00454452 0.638099 0.232470 0.0390600 0.442488
Thickness histogram
bin num norm
0.0245827 37 0.0200869
0.0737480 567 0.307818
0.122913 413 0.224213
0.172079 487 0.264387
0.221244 213 0.115635
0.270409 85 0.0461455
0.319575 29 0.0157438

0.368740 8 0.00434311
0.417905 2 0.00108578
0.467071 1 0.000542888
MIL calculations for sample: B6_71_0001
Threshhold range, BV/TV: 62.0000-157.000 0.281217
Uniform Orientations: 513
Vector sampling: Dense
Random Points: 2000
Data orientation (strike, dip, up): -178.000 0.000000 1
MIL Ellipse Eigenvectors: Trend Plunge
0.136053 -0.0443213 -0.989710 108.044 81.7733
-0.0707028 0.996017 -0.0543231 355.940 3.11402
-0.988176 -0.0773661 -0.132377 265.523 7.60699
MIL Ellipse Eigenvalues:
2.43175 4.29864 4.55809
MIL Ellipse (H) Eigenvalues:
0.402812 0.302968 0.294219
MIL Ellipse Tensor (M):

4.51743 0.0310930 0.285321
0.0310930 4.29652 -0.0792340
0.285321 -0.0792340 2.47453
MIL (H) DA I E Tb.N
1.36909 0.730413 0.247867 1.93117
MIL Fabric Eigenvectors: Trend Plunge
-0.104460 0.0495010 0.993296 115.355 83.3620
0.0449184 -0.997506 0.0544346 357.422 3.12042
-0.993514 -0.0503037 -0.101976 267.101 5.85298
MIL Fabric Eigenvalues:
0.385348 0.308712 0.305940
MIL Fabric Tensor:
0.306812 -0.000534865 -0.00823258
-0.000534865 0.308893 0.00375390
-0.00823258 0.00375390 0.384295
MIL (F) DA I E
1.25955 0.793932 0.198874

lateral

Star length and volume calcuations for sample: B6_71_0001
Threshhold range, BV/TV: 55.0000-249.000 0.232759
Uniform Orientations: 513
Vector sampling: Dense
Random Points: 2000
Data orientation (strike, dip, up): -178.000 0.000000 1
SVD Eigenvalues: Eigenvectors Trend Plunge

0.532395 0.113883 0.199957 0.973164 209.663
76.6963
0.320012 0.224014 -0.959479 0.170930 346.858
9.84189
0.147593 -0.967909 -0.198536 0.154062 78.4083
8.86239
SVD Fabric Tensor:
0.161236 -0.0282966 0.0492486
-0.0282966 0.321707 0.0466016
0.0492486 0.0466016 0.517057
SVD DA I E Sum(tau)
3.60719 0.277224 0.398921 20.8375
SLD Eigenvalues: Eigenvectors Trend Plunge
0.381436 0.0676973 0.283137 0.956687 193.447
73.0751
0.343258 0.201508 -0.943006 0.264828 347.938
15.3568
0.275306 -0.977145 -0.174852 0.120893 79.8548
6.94365
SLD Fabric Tensor:
0.278552 -0.0108782 0.0104998
-0.0108782 0.344241 0.0117780
0.0104998 0.0117780 0.377208
SLD DA I E Sum(tau)
1.38550 0.721761 0.100092 74.8171
Thickness (minimum line length at each point, non-zero points only)
Mean Variance Skewness Kurtosis Min Max
0.134781 0.00394630 0.595435 0.00371218 0.0390600 0.404838
Thickness histogram
bin num norm
0.0224910 41 0.0225399
0.0674730 513 0.282023
0.112455 362 0.199010
0.157437 493 0.271028
0.202419 242 0.133040
0.247401 117 0.0643211
0.292383 39 0.0214404
0.337365 9 0.00494777
0.382347 2 0.00109951
0.427329 1 0.000549753
MIL calculations for sample: B6_71_0001
Threshhold range, BV/TV: 55.0000-249.000 0.232759
Uniform Orientations: 513
Vector sampling: Dense
Random Points: 2000
Data orientation (strike, dip, up): -178.000 0.000000 1
MIL Ellipse Eigenvectors: Trend Plunge
0.0593073 0.304312 0.950724 191.028 71.9385

-0.152272 0.944013 -0.292664 350.837 17.0175
-0.986558 -0.127411 0.102325 82.6411 5.87306
MIL Ellipse Eigenvalues:
2.16898 2.62625 4.10500
MIL Ellipse (H) Eigenvalues:
0.379409 0.344801 0.275790
MIL Ellipse Tensor (M):
4.06391 0.177626 -0.175062
0.177626 2.60791 -0.151573
-0.175062 -0.151573 2.22842
MIL (H) DA I E Tb.N
1.37572 0.726894 0.0912165 1.71459
MIL Fabric Eigenvectors: Trend Plunge
-0.0664735 -0.330345 -0.941517 191.377 70.3078
0.150145 -0.936171 0.317869 350.888 18.5341
-0.986427 -0.120234 0.111830 83.0506 6.42082
MIL Fabric Eigenvalues:
0.365770 0.345328 0.288902
MIL Fabric Tensor:
0.290514 -0.00624331 0.00750381
-0.00624331 0.346743 0.00711660
0.00750381 0.00711660 0.362743
MIL (F) DA I E
1.26607 0.789847 0.0558872

medial

Star length and volume calcuations for sample: B13_72_0001
Threshhold range, BV/TV: 60.0000-138.000 0.378352
Uniform Orientations: 513
Vector sampling: Dense
Random Points: 2000
Data orientation (strike, dip, up): -43.0000 180.0000

SVD Eigenvalues:	Eigenvectors			Trend	Plunge
0.615948	-0.0458235	-0.0643034	0.996878	35.4742	85.4712
0.255805	0.703773	-0.710297	-0.0134673	135.264	0.771640
0.128247	-0.708945	-0.700959	-0.0778033	225.325	4.46231

SVD Fabric Tensor:

0.192450	-0.0623277	-0.0234874
-0.0623277	0.194619	-0.0300427
-0.0234874	-0.0300427	0.612930

SVD DA	I	E	Sum(tau)
4.80282	0.208211	0.584697	382.429

SLD Eigenvalues:	Eigenvectors			Trend	Plunge
0.404925	-0.0771292	-0.0323738	0.996495	67.2305	85.2017
0.328041	0.668745	-0.742979	0.0276235	318.010	1.58291
0.267033	-0.739481	-0.668532	-0.0789551	227.885	4.52851

SLD Fabric Tensor:

0.295138	-0.0299683	-0.00947123
-0.0299683	0.300855	-0.00570055
-0.00947123	-0.00570055	0.404007

SLD DA	I	E	Sum(tau)
1.51639	0.659463	0.189872	180.618

Thickness (minimum line length at each point, non-zero points only)

Mean	Variance	Skewness	Kurtosis	Min	Max
0.195154	0.00867649	0.867899	1.15275	0.0585900	0.700025

Thickness histogram

bin num	norm
0.0388903	53	0.0295924
0.116671	683	0.381351
0.194451	406	0.226689
0.272232	450	0.251256
0.350013	145	0.0809604
0.427793	38	0.0212172
0.505574	12	0.00670017

0.583354 0 0.000000
0.661135 3 0.00167504
0.738916 1 0.000558347
MIL calculations for sample: B13_72_0001
Threshhold range, BV/TV: 60.0000-138.000 0.378352
Uniform Orientations: 513
Vector sampling: Dense
Random Points: 2000
Data orientation (strike, dip, up): -43.0000 180.0000
MIL Ellipse Eigenvectors: Trend Plunge
0.0752438 -0.0484295 -0.995988 122.767 84.8662
-0.648765 0.756139 -0.0857791 319.371 4.92083
0.757260 0.652617 0.0254754 229.245 1.45979
MIL Ellipse Eigenvalues:
2.07154 3.36278 5.10609
MIL Ellipse (H) Eigenvalues:
0.412914 0.324083 0.263003
MIL Ellipse Tensor (M):
4.35516 0.866249 0.130399
0.866249 4.10224 -0.0332999
0.130399 -0.0332999 2.08301
MIL (H) DA I E Tb.N
1.56999 0.636945 0.215131 1.85324
MIL Fabric Eigenvectors: Trend Plunge
-0.100442 0.0104837 0.994888 95.9587 84.2040
0.646636 -0.759270 0.0732839 319.580 4.20263
-0.756157 -0.650691 -0.0694834 229.287 3.98432
MIL Fabric Eigenvalues:
0.394622 0.329258 0.276120
MIL Fabric Tensor:
0.299535 -0.0262140 -0.00932357
-0.0262140 0.306767 -0.00172073
-0.00932357 -0.00172073 0.393699
MIL (F) DA I E
1.42917 0.699708 0.165637

lateral

MIL calculations for sample: B13_72_0001
I range, BV/TV: 59.0000-255.000 0.377855
Uniform Orientations: 513
Vector sampling: Dense
Random Points: 2000
Data orientation (strike, dip, up): -43.0000 180.0000
MIL Ellipse Eigenvectors: Trend Plunge
-0.436710 0.405744 -0.802905 312.895 53.4084
-0.759610 0.311836 0.570746 112.319 34.8023

0.481952 0.859145 0.172025 209.291 9.90558
MIL Ellipse Eigenvalues:
0.972307 1.37012 2.29699
MIL Ellipse (H) Eigenvalues:
0.401120 0.337906 0.260974
MIL Ellipse Tensor (M):
1.50954 0.454273 -0.0626455
0.454273 1.98878 0.266584
-0.0626455 0.266584 1.14110
MIL (H) DA I E Tb.N
1.53701 0.650612 0.157594 1.24370
MIL Fabric Eigenvectors: Trend Plunge
0.391879 -0.424700 0.816126 317.302 54.6988
0.766438 -0.340001 -0.544952 113.923 33.0214
0.508925 0.839064 0.192267 211.238 11.0851
MIL Fabric Eigenvalues:
0.379665 0.339625 0.280710
MIL Fabric Tensor:
0.330515 -0.0318221 0.00704093
-0.0318221 0.305369 -0.0233828
0.00704093 -0.0233828 0.364116
MIL (F) DA I E
1.35252 0.739361 0.105462
MIL calculations for sample: B13_72_0001
I range, BV/TV: 59.0000-255.000 0.377855
Uniform Orientations: 513
Vector sampling: Dense
Random Points: 2000
Data orientation (strike, dip, up): -43.0000 180.0000
MIL Ellipse Eigenvectors: Trend Plunge
0.434454 -0.429968 0.791440 314.703 52.3203
-0.707311 0.381153 0.595343 118.319 36.5371
-0.557639 -0.818443 -0.138528 214.268 7.96265
MIL Ellipse Eigenvalues:
1.00402 1.38605 2.34863
MIL Ellipse (H) Eigenvalues:
0.399213 0.339770 0.261017
MIL Ellipse Tensor (M):
1.61327 0.510680 -0.0570040
0.510680 1.96020 0.239139
-0.0570040 0.239139 1.16523
MIL (H) DA I E Tb.N
1.52946 0.653827 0.148901 1.25991
MIL Fabric Eigenvectors: Trend Plunge
0.377649 -0.441029 0.814171 319.427 54.5055
0.719936 -0.413099 -0.557710 119.847 33.8976
0.582299 0.796770 0.161506 216.160 9.29433
MIL Fabric Eigenvalues:

0.378323 0.340407 0.281270
MIL Fabric Tensor:
0.325763 -0.0337522 0.00609685
-0.0337522 0.310239 -0.0212248
0.00609685 -0.0212248 0.363998
MIL (F) DA I E
1.34505 0.743464 0.100223
Star length and volume □alculations for sample: B13_72_0001
I range, BV/TV: 59.0000-255.000 0.377855
Uniform Orientations: 513
Vector sampling: Dense
Random Points: 2000
Data orientation (strike, dip, up): -43.0000 180.0000
SVD Eigenvalues: Eigenvectors Trend Plunge
0.519677 0.192225 -0.121951 0.973744 302.392
76.8415
0.311310 0.180310 -0.970967 -0.157197 169.480
9.04426
0.169013 -0.964644 -0.205793 0.164655 77.9573
9.47721
SVD Fabric Tensor:
0.186596 -0.0331329 0.0616034
-0.0331329 0.308382 -0.0199216
0.0616034 -0.0199216 0.505021
SVD DA I E Sum(tau)
3.07478 0.325226 0.400955 913.368
SLD Eigenvalues: Eigenvectors Trend Plunge
0.401237 0.187556 -0.120628 0.974819 302.747
77.1148
0.327022 0.00369814 0.992510 0.122105 180.214
7.01362
0.271740 0.982247 0.0192965 -0.186597 88.8746
10.7543
SLD Fabric Tensor:
0.276296 -0.00272687 0.0237013
-0.00272687 0.328082 -0.00852788
0.0237013 -0.00852788 0.395622
SLD DA I E Sum(tau)
1.47655 0.677256 0.184965 259.568
Thickness (minimum line length at each point, non-zero points only)
Mean Variance Skewness Kurtosis Min Max
0.230731 0.0145163 1.107712.114330.0585900 0.978864
Thickness histogram
bin num norm
0.0543814 375 0.230769
0.163144 421 0.259077
0.271907 528 0.324923
0.380670 207 0.127385

0.489432	60	0.0369231
0.598195	23	0.0141538
0.706958	9	0.00553846
0.815720	1	0.000615385
0.924483	0	0.000000
1.03325	1	0.000615385

medial

Star length and volume calcuations for sample: B2_73_0001
Threshhold range, BV/TV: 70.0000-173.000 0.326574
Uniform Orientations: 513
Vector sampling: Dense
Random Points: 2000
Data orientation (strike, dip, up): -3.00000 -180.000 0
SVD Eigenvalues: Eigenvectors Trend Plunge
0.604906 -0.175421 0.150066 0.972989 130.546 76.6528
0.264327 -0.717973 -0.695719 -0.0221416 225.902 1.26872
0.130768 -0.673604 0.702464 -0.229787 316.201 13.2845
SVD Fabric Tensor:
0.214206 0.0542322 -0.0788040
0.0542322 0.206091 0.0712877
-0.0788040 0.0712877 0.579703
SVD DA I E Sum(tau)
4.62581 0.216178 0.563028 264.782
SLD Eigenvalues: Eigenvectors Trend Plunge
0.400910 -0.157274 0.163289 0.973962 136.075 76.8964
0.327685 0.727267 0.686351 0.00236842 226.658 0.135700
0.271405 0.668093 -0.708703 0.226700 316.690 13.1029
SLD Fabric Tensor:
0.304376 0.0247668 -0.0197405
0.0247668 0.301370 0.0206876
-0.0197405 0.0206876 0.394254
SLD DA I E Sum(tau)
1.47716 0.676973 0.182647 160.903
Thickness (minimum line length at each point, non-zero points only)
Mean Variance Skewness Kurtosis Min Max
0.179606 0.00897718 0.915066 1.272600.0390600 0.640129
Thickness histogram
bin num norm
0.0355627 313 0.175350
0.106688 352 0.197199
0.177814 547 0.306443
0.248939 335 0.187675
0.320064 160 0.0896359
0.391190 48 0.0268908
0.462315 17 0.00952381

0.533441 8 0.00448179
0.604566 4 0.00224090
0.675692 1 0.000560224
MIL calculations for sample: B2_73_0001
Threshhold range, BV/TV: 70.0000-173.000 0.326574
Uniform Orientations: 513
Vector sampling: Dense
Random Points: 2000
Data orientation (strike, dip, up): -3.00000 -180.000 0
MIL Ellipse Eigenvectors: Trend Plunge
0.102313 -0.141362 -0.984657 144.104 79.9503
0.702503 0.711086 -0.0290921 44.6521 1.66709
-0.704288 0.688748 -0.172061 314.361 9.90766
MIL Ellipse Eigenvalues:
1.89706 3.06487 3.92727
MIL Ellipse (H) Eigenvalues:
0.402940 0.317011 0.280050
MIL Ellipse Tensor (M):
3.48041 -0.401437 0.222155
-0.401437 3.45063 -0.264752
0.222155 -0.264752 1.95815
MIL (H) DA I E Tb.N
1.43881 0.695017 0.213255 1.71077
MIL Fabric Eigenvectors: Trend Plunge
-0.0658057 0.150165 0.986469 156.336 80.5637
-0.736001 -0.674852 0.0536317 47.4817 3.07435
-0.673774 0.722513 -0.154931 316.999 8.91277
MIL Fabric Eigenvalues:
0.384344 0.321939 0.293717
MIL Fabric Tensor:
0.309397 0.0131219 -0.00699707
0.0131219 0.308613 0.0124034
-0.00699707 0.0124034 0.381989
MIL (F) DA I E
1.30855 0.764203 0.162369

lateral

Star length and volume calcuations for sample: B2_73_0001
Threshhold range, BV/TV: 73.0000-177.000 0.300393
Uniform Orientations: 513
Vector sampling: Dense
Random Points: 2000
Data orientation (strike, dip, up): -3.00000 -180.000 0
SVD Eigenvalues: Eigenvectors Trend Plunge

0.560775 0.00958293 0.0795220 0.996787 186.871
85.4058
0.350557 -0.0549609 0.995368 -0.0788804 356.840
4.52421
0.0886681 -0.998443 -0.0540284 0.0139091 86.9026
0.796960
SVD Fabric Tensor:
0.0895025 -0.0139672 0.00564501
-0.0139672 0.351122 0.0168601
0.00564501 0.0168601 0.559376
SVD DA I E Sum(tau)
6.32443 0.158117 0.374871 228.762
SLD Eigenvalues: Eigenvectors Trend Plunge
0.405281 0.00603028 0.192420 0.981294 181.795
78.9004
0.361084 -0.0519399 0.980048 -0.191857 356.966
11.0611
0.233635 -0.998632 -0.0498114 0.0159042 87.1445
0.911284
SLD Fabric Tensor:
0.233985 -0.00628842 0.00228574
-0.00628842 0.362404 0.00844640
0.00228574 0.00844640 0.403611
SLD DA I E Sum(tau)
1.73468 0.576476 0.109054 150.559
Thickness (minimum line length at each point, non-zero points only)
Mean Variance Skewness Kurtosis Min Max
0.173042 0.00888510 0.976993 0.911930 0.0390600 0.597724
Thickness histogram
bin num norm
0.0332069 260 0.141921
0.0996207 457 0.249454
0.166034 527 0.287664
0.232448 296 0.161572
0.298862 172 0.0938865
0.365276 67 0.0365721
0.431690 35 0.0191048
0.498103 15 0.00818777
0.564517 2 0.00109170
0.630931 1 0.000545852
MIL calculations for sample: B2_73_0001
Threshhold range, BV/TV: 73.0000-177.000 0.300393
Uniform Orientations: 513
Vector sampling: Dense
Random Points: 2000
Data orientation (strike, dip, up): -3.00000 -180.000 0
MIL Ellipse Eigenvectors: Trend Plunge
0.0578517 -0.417714 -0.906735 172.115 65.0580

-0.0763681	0.903743	-0.421208	355.170	24.9109
0.995400	0.0936132	0.0203830	264.627	1.16794

MIL Ellipse Eigenvalues:

1.83614	2.24216	5.14399

MIL Ellipse (H) Eigenvalues:

0.399618	0.361630	0.238752

MIL Ellipse Tensor (M):

5.11600	0.280212	0.0801742
0.280212	2.19674	-0.148245
0.0801742	-0.148245	1.90955

MIL (H) DA I E Tb.N

1.67378	0.597452	0.0950600	1.70372

MIL Fabric Eigenvectors:

			Trend	Plunge
-0.0571169	0.454246	0.889043	172.833	62.7533
-0.0696093	0.886518	-0.457428	355.510	27.2213
-0.995938	-0.0880124	-0.0190154	264.950	1.08957

MIL Fabric Eigenvalues:

0.389858	0.363107	0.247036

MIL Fabric Tensor:

0.248064	-0.0108682	-0.00355657
-0.0108682	0.367727	0.0106090
-0.00355657	0.0106090	0.384209

MIL (F) DA I E

1.57814	0.633657	0.0686175

medial

Star length and volume calcuations for sample: B7_80_0001
Threshhold range, BV/TV: 76.0000-161.000 0.448468
Uniform Orientations: 513
Vector sampling: Dense
Random Points: 2000
Data orientation (strike, dip, up): -18.0000 -180.000 0

SVD Eigenvalues:	Eigenvectors		Trend	Plunge
0.613497	-0.177575	0.116603	0.977175	123.291
77.7348				
0.215550	-0.435848	-0.899580	0.0281405	25.8503
1.61254				
0.170953	-0.882328	0.420903	-0.210565	295.503
12.1554				

SVD Fabric Tensor:

0.193379	0.00832221	-0.0773382
0.00832221	0.213059	0.0492954
-0.0773382	0.0492954	0.593561

SVD DA	I	E	Sum(tau)
3.58869	0.278653	0.648654	1031.23

SLD Eigenvalues:	Eigenvectors		Trend	Plunge
0.395645	-0.163609	0.125592	0.978498	127.511
78.0970				
0.312988	-0.363106	-0.929900	0.0586417	21.3296
3.36185				
0.291367	-0.917271	0.345705	-0.197744	290.651
11.4050				

SLD Fabric Tensor:

0.297009	0.00515789	-0.0171544
0.00515789	0.311708	0.0116359
-0.0171544	0.0116359	0.391283

SLD DA	I	E	Sum(tau)
1.35789	0.736435	0.208916	276.096

Thickness (minimum line length at each point, non-zero points only)

Mean	Variance	Skewness	Kurtosis	Min	Max
0.231891	0.0116527	0.621250	0.116471	0.0585900	0.716085

Thickness histogram

bin num	norm	
0.0397825	18	0.0100671
0.119347	546	0.305369
0.198912	414	0.231544
0.278477	442	0.247204
0.358042	229	0.128076
0.437607	96	0.0536913
0.517172	33	0.0184564

0.596737 8 0.00447427
0.676302 1 0.000559284
0.755867 1 0.000559284
MIL calculations for sample: B7_80_0001
Threshhold range, BV/TV: 76.0000-161.000 0.448468
Uniform Orientations: 513
Vector sampling: Dense
Random Points: 2000
Data orientation (strike, dip, up): -18.0000 -180.000 0
MIL Ellipse Eigenvectors: Trend Plunge
0.167251 -0.0833330 -0.982386 116.485 79.2303
0.583198 0.811760 0.0304298 215.695 1.74377
-0.794926 0.578015 -0.184367 306.022 10.6242
MIL Ellipse Eigenvalues:
2.38288 3.81252 4.24862
MIL Ellipse (H) Eigenvalues:
0.393781 0.311315 0.294904
MIL Ellipse Tensor (M):
4.04810 -0.180456 0.298811
-0.180456 3.94829 -0.163512
0.298811 -0.163512 2.44762
MIL (H) DA I E Tb.N
1.33528 0.748905 0.209422 1.86071
MIL Fabric Eigenvectors: Trend Plunge
-0.126066 0.0783782 0.988921 121.870 81.4632
-0.668305 -0.743424 -0.0262733 221.954 1.50552
-0.733128 0.664212 -0.146101 312.177 8.40104
MIL Fabric Eigenvalues:
0.379811 0.317593 0.302597
MIL Fabric Tensor:
0.310521 0.00668748 -0.00936294
0.00668748 0.311359 0.00627778
-0.00936294 0.00627778 0.378120
MIL (F) DA I E
1.25517 0.796703 0.163814

lateral

Star length and volume calcuations for sample: B7_80_0001
Threshhold range, BV/TV: 68.0000-178.000 0.362638
Uniform Orientations: 513
Vector sampling: Dense
Random Points: 2000
Data orientation (strike, dip, up): -18.0000 -180.000 0
SVD Eigenvalues: Eigenvectors Trend Plunge

0.552545 -0.118376 0.489414 0.863980 166.403
59.7664
0.363241 -0.244630 0.828906 -0.503063 343.557
30.2028
0.0842136 -0.962364 -0.270906 0.0216028 74.2781
1.23785
SVD Fabric Tensor:
0.107474 -0.0837124 -0.0135601
-0.0837124 0.388106 0.0816792
-0.0135601 0.0816792 0.504419
SVD DA I E Sum(tau)
6.56124 0.152410 0.342605 1308.61
SLD Eigenvalues: Eigenvectors Trend Plunge
0.404786 -0.139636 0.562022 0.815250 166.047
54.6121
0.357290 -0.225863 0.783534 -0.578844 343.920
35.3693
0.237924 -0.964099 -0.264962 0.0175300 74.6329
1.00445
SLD Fabric Tensor:
0.247267 -0.0342193 -0.00338948
-0.0342193 0.363912 0.0223164
-0.00338948 0.0223164 0.388820
SLD DA I E Sum(tau)
1.70132 0.587779 0.117335 268.340
Thickness (minimum line length at each point, non-zero points only)
Mean Variance Skewness Kurtosis Min Max
0.230797 0.0135868 0.920386 1.129290.0585900 0.856576
Thickness histogram
bin num norm
0.0475876 110 0.0615557
0.142763 604 0.337997
0.237938 588 0.329043
0.333113 296 0.165641
0.428288 122 0.0682708
0.523463 48 0.0268607
0.618638 13 0.00727476
0.713813 5 0.00279799
0.808989 0 0.000000
0.904164 1 0.000559597
MIL calculations for sample: B7_80_0001
Threshhold range, BV/TV: 68.0000-178.000 0.362638
Uniform Orientations: 513
Vector sampling: Dense
Random Points: 2000

Data orientation (strike, dip, up): -18.0000 -180.000 0
MIL Ellipse Eigenvectors: Trend Plunge

0.140688 -0.440453 -0.886684 162.286 62.4594
-0.239941 0.853724 -0.462152 344.302 27.5260
0.960539 0.277771 0.0144258 253.871 0.826563
MIL Ellipse Eigenvalues:
1.23760 1.72997 4.22810
MIL Ellipse (H) Eigenvalues:
0.418965 0.354364 0.226671
MIL Ellipse Tensor (M):
4.02509 0.697036 0.0960361
0.697036 1.82720 -0.182281
0.0960361 -0.182281 1.34339
MIL (H) DA I E Tb.N
1.84834 0.541026 0.154193 1.49738
MIL Fabric Eigenvectors: Trend Plunge
-0.143025 0.539640 0.829658 165.156 56.0636
-0.259240 0.788582 -0.557614 341.802 33.8909
-0.955164 -0.294834 0.0271095 72.8459 1.55345
MIL Fabric Eigenvalues:
0.397802 0.357294 0.244904
MIL Fabric Tensor:
0.255585 -0.0347771 -0.00189654
-0.0347771 0.359321 0.0190345
-0.00189654 0.0190345 0.385094
MIL (F) DA I E
1.62432 0.615644 0.101830

1_81

medial

Star length and volume calcuations for sample: B1_81_0001
Threshhold range, BV/TV: 58.0000-157.000 0.330521
Uniform Orientations: 513
Vector sampling: Dense
Random Points: 2000
Data orientation (strike, dip, up): 172.0000.000000 1

SVD Eigenvalues:	Eigenvectors		Trend	Plunge
0.710384	-0.191574	0.0262297	0.981128	97.7963
78.8510				
0.169884	-0.408459	0.906833	-0.103999	335.752
5.96950				
0.119732	0.892446	0.420674	0.163012	244.762
9.38177				

SVD Fabric Tensor:

0.149776	-0.0215445	-0.108888
-0.0215445	0.161380	0.0104705
-0.108888	0.0104705	0.688843

SVD DA	I	E	Sum(tau)
5.93313	0.168545	0.760857	576.227

SLD Eigenvalues:	Eigenvectors		Trend	Plunge
0.418069	-0.204430	0.0690459	0.976443	108.662
77.5390				
0.309177	-0.378712	0.914254	-0.143936	337.499
8.27568				
0.272754	0.902655	0.399215	0.160752	246.142
9.25056				

SLD Fabric Tensor:

0.284051	-0.0146624	-0.0270214
-0.0146624	0.303892	0.00500393
-0.0270214	0.00500393	0.412058

SLD DA	I	E	Sum(tau)
1.53277	0.652414	0.260463	203.138

Thickness (minimum line length at each point, non-zero points only)

Mean	Variance	Skewness	Kurtosis	Min	Max
0.202984	0.00796177	0.642595	0.252185	0.0585900	0.572195

Thickness histogram

bin num	norm
0.0317886	15	0.00823271
0.0953658	445	0.244237
0.158943	382	0.209660
0.222520	513	0.281559
0.286097	282	0.154775
0.349675	118	0.0647640

0.413252 45 0.0246981
0.476829 16 0.00878156
0.540406 5 0.00274424
0.603983 1 0.000548847
MIL calculations for sample: B1_81_0001
Threshhold range, BV/TV: 58.0000-157.000 0.330521
Uniform Orientations: 513
Vector sampling: Dense
Random Points: 2000
Data orientation (strike, dip, up): 172.0000.000000 1
MIL Ellipse Eigenvectors: Trend Plunge
0.143888 -0.117433 -0.982601 129.219 79.2965
-0.299055 0.941349 -0.156296 342.376 8.99194
0.943325 0.316340 0.100330 251.461 5.75817
MIL Ellipse Eigenvalues:
1.72794 2.73197 3.32815
MIL Ellipse (H) Eigenvalues:
0.397482 0.316114 0.286405
MIL Ellipse Tensor (M):
3.24170 0.194872 0.198379
0.194872 2.77778 -0.0969338
0.198379 -0.0969338 1.76857
MIL (H) DA I E Tb.N
1.38783 0.720548 0.204709 1.60216
MIL Fabric Eigenvectors: Trend Plunge
-0.133908 0.0983089 0.986105 126.284 80.4376
-0.332840 0.932802 -0.138193 340.363 7.94330
-0.933427 -0.346721 -0.0921890 249.623 5.28955
MIL Fabric Eigenvalues:
0.387587 0.317968 0.294445
MIL Fabric Tensor:
0.298721 -0.00852931 -0.0112172
-0.00852931 0.315813 0.00599723
-0.0112172 0.00599723 0.385466
MIL (F) DA I E
1.31633 0.759688 0.179622

lateral

Star length and volume calcuations for sample: B1_81_0001
Threshhold range, BV/TV: 62.0000-152.000 0.324704
Uniform Orientations: 513
Vector sampling: Dense
Random Points: 2000
Data orientation (strike, dip, up): 172.0000.000000 1
SVD Eigenvalues: Eigenvectors Trend Plunge

0.571207 0.0579279 0.144096 0.987867 201.901
81.0656
0.343998 -0.201587 0.970833 -0.129790 348.270
7.45746
0.0847948 0.977756 0.191623 -0.0852862 78.9116
4.89248
SVD Fabric Tensor:
0.0969604 -0.0466679 0.0346168
-0.0466679 0.339198 0.0365787
0.0346168 0.0365787 0.563842
SVD DA I E Sum(tau)
6.73634 0.148448 0.397770 686.629
SLD Eigenvalues: Eigenvectors Trend Plunge
0.401750 -0.0435311 -0.213603 -0.975950 191.519
77.4088
0.370584 -0.218862 0.955186 -0.199297 347.095
11.4958
0.227666 0.974784 0.204922 -0.0883300 78.1280
5.06754
SLD Fabric Tensor:
0.234842 -0.0282588 0.0136297
-0.0282588 0.366004 0.00908398
0.0136297 0.00908398 0.399154
SLD DA I E Sum(tau)
1.76465 0.566686 0.0775752 223.317
Thickness (minimum line length at each point, non-zero points only)
Mean Variance Skewness Kurtosis Min Max
0.210886 0.0108435 1.058671.523440.0585900 0.718478
Thickness histogram
bin num norm
0.0399154 35 0.0188273
0.119746 634 0.341044
0.199577 556 0.299086
0.279408 376 0.202259
0.359239 152 0.0817644
0.439070 67 0.0360409
0.518901 27 0.0145239
0.598731 7 0.00376547
0.678562 4 0.00215169
0.758393 1 0.000537924
MIL calculations for sample: B1_81_0001
Threshhold range, BV/TV: 62.0000-152.000 0.324704
Uniform Orientations: 513
Vector sampling: Dense
Random Points: 2000
Data orientation (strike, dip, up): 172.0000.000000 1
MIL Ellipse Eigenvectors: Trend Plunge
0.00969307 0.301147 0.953529 181.844 72.4641

-0.174835 0.939395 -0.294906 349.457 17.1519
-0.984550 -0.163852 0.0617568 80.5512 3.54065
MIL Ellipse Eigenvalues:
1.35232 1.81325 4.46049
MIL Ellipse (H) Eigenvalues:
0.414214 0.357714 0.228072
MIL Ellipse Tensor (M):
4.37928 0.425710 -0.165220
0.425710 1.84252 -0.159143
-0.165220 -0.159143 1.40426
MIL (H) DA I E Tb.N
1.81615 0.550615 0.136403 1.54017
MIL Fabric Eigenvectors: Trend Plunge
0.000125524 0.253184 0.967418 180.028 75.3340
-0.184551 0.950806 -0.248813 349.016 14.4073
-0.982823 -0.178507 0.0468447 79.7058 2.68499
MIL Fabric Eigenvalues:
0.390447 0.360902 0.248651
MIL Fabric Tensor:

0.252474 -0.0196924 0.00517164
-0.0196924 0.359219 0.00817539
0.00517164 0.00817539 0.388307
MIL (F) DA I E
1.57026 0.636836 0.0756710

medial

Star length and volume calcuations for sample: SmithB3_0001
Threshhold range, BV/TV: 54.0000-134.000 0.287049
Uniform Orientations: 513
Vector sampling: Dense
Random Points: 2000
Data orientation (strike, dip, up): -165.000 0.000000 1

SVD Eigenvalues:	Eigenvectors		Trend	Plunge
0.682883	-0.103912	0.000844139	0.994586	90.4655
84.0353				
0.181128	0.415604	-0.908472	0.0441923	335.417
2.53286				
0.135989	-0.903590	-0.417946	-0.0940501	245.178
5.39665				

SVD Fabric Tensor:

0.149691	-0.0170910	-0.0556920
-0.0170910	0.173244	-0.00135308
-0.0556920	-0.00135308	0.677065

SVD DA	I	E	Sum(tau)
5.02160	0.199140	0.734759	235.717

SLD Eigenvalues:	Eigenvectors		Trend	Plunge
0.402517	-0.107522	-0.0168336	0.994060	81.1020
83.7520				
0.309589	0.338805	-0.940628	0.0207180	340.191
1.18714				
0.287894	-0.934692	-0.339020	-0.106842	250.064
6.13329				

SLD Fabric Tensor:

0.291710	-0.00670638	-0.0120989
-0.00670638	0.307122	-0.00234082
-0.0120989	-0.00234082	0.401168

SLD DA	I	E	Sum(tau)
1.39814	0.715236	0.230867	159.490

Thickness (minimum line length at each point, non-zero points only)

Mean	Variance	Skewness	Kurtosis	Min	Max
0.191295	0.00820268	0.790698	0.589923	0.0585900	0.634090

Thickness histogram

bin num	norm
0.0352272	41	0.0226895
0.105682	608	0.336469
0.176136	492	0.272274
0.246591	393	0.217488
0.317045	177	0.0979524
0.387499	71	0.0392916

0.457954 18 0.00996126
0.528408 4 0.00221361
0.598863 2 0.00110681
0.669317 1 0.000553403
MIL calculations for sample: SmithB3_0001
Threshhold range, BV/TV: 54.0000-134.000 0.287049
Uniform Orientations: 513
Vector sampling: Dense
Random Points: 2000
Data orientation (strike, dip, up): -165.000 0.000000 1
MIL Ellipse Eigenvectors: Trend Plunge
0.0967443 0.0606789 -0.993458 57.9037 83.4426
-0.00859053 0.998154 0.0601292 179.507 3.44723
-0.995272 -0.00271716 -0.0970869 269.844 5.57145
MIL Ellipse Eigenvalues:
1.41273 2.45733 2.64111
MIL Ellipse (H) Eigenvalues:
0.401672 0.304558 0.293770
MIL Ellipse Tensor (M):
2.62960 -0.00563522 0.118156
-0.00563522 2.45348 0.0630189
0.118156 0.0630189 1.42808
MIL (H) DA I E Tb.N
1.36730 0.731368 0.241775 1.46635
MIL Fabric Eigenvectors: Trend Plunge
-0.0615015 -0.0425854 0.997198 55.3002 85.7099
-0.0294111 -0.998578 -0.0444582 181.687 2.54811
-0.997674 0.0320628 -0.0601616 271.841 3.44909
MIL Fabric Eigenvalues:
0.382800 0.312197 0.305003
MIL Fabric Tensor:
0.305304 0.000414986 -0.00476180
0.000414986 0.312317 -0.00298436
-0.00476180 -0.00298436 0.382379
MIL (F) DA I E
1.25507 0.796769 0.184439

lateral

Star length and volume calcuations for sample: SmithB3_0001
Threshhold range, BV/TV: 53.0000-137.000 0.288767
Uniform Orientations: 513
Vector sampling: Dense
Random Points: 2000
Data orientation (strike, dip, up): -165.000 0.000000 1
SVD Eigenvalues: Eigenvectors Trend Plunge

0.603863 -0.0103361 0.365399 0.930793 178.380
68.5588
0.332065 -0.374094 0.861835 -0.342483 336.536
20.0282
0.0640714 -0.927333 -0.351744 0.127786 69.2279
7.34165
SVD Fabric Tensor:
0.101634 -0.0884418 0.0291423
-0.0884418 0.335198 0.104487
0.0291423 0.104487 0.563169
SVD DA I E Sum(tau)
9.42485 0.106103 0.450099 722.402
SLD Eigenvalues: Eigenvectors Trend Plunge
0.414608 0.0641185 -0.504480 -0.861039 172.757
59.4335
0.365179 -0.349794 0.796714 -0.492840 336.296
29.5274
0.220213 0.934630 0.332786 -0.125380 70.4011
7.20270
SLD Fabric Tensor:
0.238749 -0.0466880 0.0142588
-0.0466880 0.361704 0.0275198
0.0142588 0.0275198 0.399547
SLD DA I E Sum(tau)
1.88276 0.531134 0.119220 205.667
Thickness (minimum line length at each point, non-zero points only)
Mean Variance Skewness Kurtosis Min Max
0.207669 0.0134117 1.491953.426750.0585900 0.937440
Thickness histogram
bin num norm
0.0520800 408 0.224176
0.156240 583 0.320330
0.260400 577 0.317033
0.364560 159 0.0873626
0.468720 48 0.0263736
0.572880 23 0.0126374
0.677040 19 0.0104396
0.781200 2 0.00109890
0.885360 0 0.000000
0.989520 1 0.000549451
MIL calculations for sample: SmithB3_0001
Threshhold range, BV/TV: 53.0000-137.000 0.288767
Uniform Orientations: 513
Vector sampling: Dense
Random Points: 2000
Data orientation (strike, dip, up): -165.000 0.000000 1
MIL Ellipse Eigenvectors: Trend Plunge
0.102665 -0.508635 -0.854839 168.589 58.7420

-0.280440 0.809719 -0.515469 340.897 31.0288
0.954365 0.292651 -0.0595120 72.9521 3.41180
MIL Ellipse Eigenvalues:
1.11561 1.47786 3.76370
MIL Ellipse (H) Eigenvalues:
0.414374 0.360025 0.225601
MIL Ellipse Tensor (M):
3.55602 0.657343 -0.0980353
0.657343 1.57992 -0.197318
-0.0980353 -0.197318 1.22124
MIL (H) DA I E Tb.N
1.83675 0.544439 0.131160 1.40111
MIL Fabric Eigenvectors: Trend Plunge
-0.0796707 0.556223 0.827205 171.849 55.8127
-0.297150 0.778862 -0.552336 339.117 33.5274
-0.951501 -0.289809 0.103229 73.0603 5.92515
MIL Fabric Eigenvalues:
0.396308 0.363859 0.239832
MIL Fabric Tensor:
0.251777 -0.0356388 0.0100437
-0.0356388 0.363482 0.0186406
0.0100437 0.0186406 0.384742
MIL (F) DA I E
1.65244 0.605166 0.0818783

15_74

medial

Star length and volume calcuations for sample: B15_74_0001
Threshhold range, BV/TV: 55.0000-121.000 0.346758
Uniform Orientations: 513
Vector sampling: Dense
Random Points: 2000
Data orientation (strike, dip, up): 171.0008.000001

SVD Eigenvalues:	Eigenvectors		Trend	Plunge
0.725829	-0.340406	0.310192	0.887640	132.341
62.5782				
0.146466	-0.847429	0.307826	-0.432557	289.963
25.6300				
0.127705	-0.407415	-0.899458	0.158080	24.3684
9.09544				

SVD Fabric Tensor:

0.210486	-0.0680505	-0.173851
-0.0680505	0.187034	0.162188
-0.173851	0.162188	0.602480

SVD DA	I	E	Sum(tau)
5.68362	0.175944	0.798208	441.121

SLD Eigenvalues:	Eigenvectors		Trend	Plunge
0.425566	-0.368829	0.357157	0.858140	134.079
59.1084				
0.290660	-0.740053	0.445765	-0.503602	301.062
30.2386				
0.283774	-0.562394	-0.820812	0.0999043	34.4177
5.73366				

SLD Fabric Tensor:

0.306834	-0.0209500	-0.0423116
-0.0209500	0.303229	0.0419121
-0.0423116	0.0419121	0.389937

SLD DA	I	E	Sum(tau)
1.49967	0.666815	0.317003	195.127

Thickness (minimum line length at each point, non-zero points only)

Mean	Variance	Skewness	Kurtosis	Min	Max
0.203034	0.00831335	0.572060	0.106175	0.0585900	0.640419

Thickness histogram

bin num	norm
0.0355788	29	0.0155329
0.106737	564	0.302089
0.177894	467	0.250134
0.249052	480	0.257097
0.320210	219	0.117300
0.391367	82	0.0439207
0.462525	19	0.0101768

0.533683 5 0.00267809
0.604840 1 0.000535619
0.675998 1 0.000535619
MIL calculations for sample: B15_74_0001
Threshhold range, BV/TV: 55.0000-121.000 0.346758
Uniform Orientations: 513
Vector sampling: Dense
Random Points: 2000
Data orientation (strike, dip, up): 171.0008.000001
MIL Ellipse Eigenvectors: Trend Plunge
0.279283 -0.358817 -0.890647 142.105 62.9546
-0.437117 0.778361 -0.450649 330.682 26.7853
0.854944 0.515175 0.0605379 238.928 3.47069
MIL Ellipse Eigenvalues:
1.86323 3.34104 3.64694
MIL Ellipse (H) Eigenvalues:
0.406248 0.303377 0.290375
MIL Ellipse Tensor (M):
3.44937 0.282830 0.383426
0.282830 3.23196 -0.462736
0.383426 -0.462736 2.16988
MIL (H) DA I E Tb.N
1.39904 0.714773 0.253220 1.70682
MIL Fabric Eigenvectors: Trend Plunge
-0.316010 0.351154 0.881379 138.015 61.8091
-0.604925 0.641086 -0.472308 316.662 28.1842
-0.730893 -0.682422 0.00983237 46.9642 0.563362
MIL Fabric Eigenvalues:
0.388526 0.310227 0.301247
MIL Fabric Tensor:
0.313249 -0.0131675 -0.0217439
-0.0131675 0.315700 0.0242941
-0.0217439 0.0242941 0.371051
MIL (F) DA I E
1.28973 0.775358 0.201530

lateral

Star length and volume calcuations for sample: B15_74_0001
Threshhold range, BV/TV: 56.0000-132.000 0.337716
Uniform Orientations: 513
Vector sampling: Dense
Random Points: 2000
Data orientation (strike, dip, up): 171.0008.000001
SVD Eigenvalues: Eigenvectors Trend Plunge

0.539245 0.0461142 -0.500465 -0.864528 174.735
59.8288
0.386081 -0.448908 0.762755 -0.465495 329.522
27.7423
0.0746744 0.892387 0.409560 -0.189489 65.3473
10.9230
SVD Fabric Tensor:
0.138417 -0.117350 0.0465520
-0.117350 0.372208 0.0904360
0.0465520 0.0904360 0.489375
SVD DA I E Sum(tau)
7.22128 0.138480 0.284033 635.441
SLD Eigenvalues: Eigenvectors Trend Plunge
0.399516 0.123505 -0.661354 -0.739836 169.422
47.7175
0.369569 -0.401327 0.648566 -0.646761 328.251
40.2978
0.230915 0.907570 0.376795 -0.185318 67.4533
10.6797
SLD Fabric Tensor:
0.255819 -0.0498610 0.0205836
-0.0498610 0.362982 0.0243344
0.0205836 0.0243344 0.381199
SLD DA I E Sum(tau)
1.73014 0.577989 0.0749573 204.090
Thickness (minimum line length at each point, non-zero points only)
Mean Variance Skewness Kurtosis Min Max
0.198588 0.00815806 0.612736 -0.0336132 0.0585900 0.595566
Thickness histogram
bin num norm
0.0330870 36 0.0194700
0.0992609 530 0.286641
0.165435 400 0.216333
0.231609 471 0.254732
0.297783 261 0.141157
0.363957 104 0.0562466
0.430131 37 0.0200108
0.496305 8 0.00432666
0.562479 1 0.000540833
0.628653 1 0.000540833
MIL calculations for sample: B15_74_0001
Threshhold range, BV/TV: 56.0000-132.000 0.337716
Uniform Orientations: 513
Vector sampling: Dense
Random Points: 2000
Data orientation (strike, dip, up): 171.0008.000001
MIL Ellipse Eigenvectors: Trend Plunge
0.167135 -0.743143 -0.647923 167.325 40.3852

-0.270435 0.597408 -0.754963 335.645 49.0221
-0.948120 -0.301402 0.101124 72.3648 5.80392
MIL Ellipse Eigenvalues:
1.78705 2.22029 4.37219
MIL Ellipse (H) Eigenvalues:
0.394249 0.353699 0.252052
MIL Ellipse Tensor (M):
4.14260 0.668749 -0.159405
0.668749 2.17652 -0.274191
-0.159405 -0.274191 2.06042
MIL (H) DA I E Tb.N
1.56416 0.639321 0.102852 1.64190
MIL Fabric Eigenvectors: Trend Plunge
-0.141707 0.756607 0.638329 169.392 39.6673
-0.269649 0.590948 -0.760309 335.473 49.4914
0.952475 0.279867 -0.120277 73.6256 6.90809
MIL Fabric Eigenvalues:
0.376543 0.355241 0.268215
MIL Fabric Tensor:
0.276719 -0.0254820 0.00804288
-0.0254820 0.360619 0.0132175
0.00804288 0.0132175 0.362662
MIL (F) DA I E
1.40388 0.712310 0.0565721

medial

Star length and volume calcuations for sample: B9_75_0001
Threshhold range, BV/TV: 66.0000-219.000 0.369941
Uniform Orientations: 513
Vector sampling: Dense
Random Points: 2000
Data orientation (strike, dip, up): -4.84670 -0.000104587 0

SVD Eigenvalues:	Eigenvectors		Trend	Plunge
0.473667	-0.488111	0.856679	-0.166876	330.327
9.60623				
0.408299	0.822399	0.515471	0.240725	237.921
13.9293				
0.118034	-0.292244	0.0197381	0.956140	93.8639
72.9678				

SVD Fabric Tensor:

0.399083	-0.0256598	0.0864322
-0.0256598	0.456160	-0.0148231
0.0864322	-0.0148231	0.144758

SVD DA	I	E	Sum(tau)
4.01298	0.249191	0.138005	166916.

SLD Eigenvalues:	Eigenvectors		Trend	Plunge
0.346739	0.182545	0.721957	-0.667424	14.1897
41.8686				
0.337393	0.502180	-0.652069	-0.567998	142.399
34.6107				
0.315868	-0.845277	-0.231482	-0.481584	254.685
28.7889				

SLD Fabric Tensor:

0.322325	-0.00298003	-0.00990071
-0.00298003	0.341111	-0.00690264
-0.00990071	-0.00690264	0.336564

SLD DA	I	E	Sum(tau)
1.09773	0.910970	0.0269525	992.628

Thickness (minimum line length at each point, non-zero points only)

Mean	Variance	Skewness	Kurtosis	Min	Max
0.429275	0.104440	1.36491	1.46875	0.0781250	1.84556

Thickness histogram

bin num	norm	
0.102531	498	0.288194
0.307593	575	0.332755
0.512656	270	0.156250
0.717718	149	0.0862269
0.922780	105	0.0607639
1.12784	81	0.0468750
1.33291	33	0.0190972

1.53797 11 0.00636574
1.74303 5 0.00289352
1.94809 1 0.000578704
MIL calculations for sample: B9_75_0001
Threshhold range, BV/TV: 66.0000-219.000 0.369941
Uniform Orientations: 513
Vector sampling: Dense
Random Points: 2000
Data orientation (strike, dip, up): -4.84670 -0.000104587 0
MIL Ellipse Eigenvectors: Trend Plunge
0.218755 -0.0635153 -0.973711 106.191 76.8331
-0.0544397 0.995531 -0.0771691 356.870 4.42586
-0.974260 -0.0698896 -0.214319 265.897 12.3756
MIL Ellipse Eigenvalues:
0.527598 0.852252 1.23327
MIL Ellipse (H) Eigenvalues:
0.409689 0.322346 0.267965
MIL Ellipse Tensor (M):
1.19837 0.0304544 0.148709
0.0304544 0.852803 -0.0143712
0.148709 -0.0143712 0.561945
MIL (H) DA I E Tb.N
1.52889 0.654069 0.213194 0.925756
MIL Fabric Eigenvectors: Trend Plunge
-0.208412 0.0787045 0.974869 110.689 77.1278
0.0419075 -0.995123 0.0892989 357.589 5.12327
-0.977143 -0.0594655 -0.204097 266.517 11.7766
MIL Fabric Eigenvalues:
0.388194 0.327791 0.284015
MIL Fabric Tensor:
0.288617 -0.00353455 -0.0210025
-0.00353455 0.328011 0.00410317
-0.0210025 0.00410317 0.383372
MIL (F) DA I E
1.36681 0.731633 0.155599

lateral

Star length and volume calcuations for sample: B9_75_0001
Threshhold range, BV/TV: 63.0000-148.000 0.327119
Uniform Orientations: 513
Vector sampling: Dense
Random Points: 2000
Data orientation (strike, dip, up): -4.84670 -0.000104587 0
SVD Eigenvalues: Eigenvectors Trend Plunge

0.600439 0.173750 -0.984716 0.0120354 349.993
0.689596
0.340145 0.926814 0.159378 -0.340022 80.2427
19.8782
0.0594152 -0.332907 -0.0702335 -0.940340 258.087
70.1088
SVD Fabric Tensor:
0.316891 -0.0510988 -0.0873372
-0.0510988 0.591159 -0.0216252
-0.0873372 -0.0216252 0.0919502
SVD DA I E Sum(tau)
10.1058 0.0989528 0.433506 179561.
SLD Eigenvalues: Eigenvectors Trend Plunge
0.377635 0.407104 -0.912203 0.0463973 335.949
2.65933
0.335826 0.757938 0.309038 -0.574478 67.8176
35.0631
0.286539 -0.509702 -0.269039 -0.817204 242.173
54.8058
SLD Fabric Tensor:
0.329950 -0.0222850 -0.0197397
-0.0222850 0.367048 -0.0126056
-0.0197397 -0.0126056 0.303001
SLD DA I E Sum(tau)
1.31792 0.758773 0.110713 882.784
Thickness (minimum line length at each point, non-zero points only)
Mean Variance Skewness Kurtosis Min Max
0.412843 0.0993221 1.351871.164070.0781250 1.71028
Thickness histogram
bin num norm
0.0950154 467 0.269320
0.285046 625 0.360438
0.475077 236 0.136101
0.665108 131 0.0755479
0.855139 119 0.0686275
1.04517 94 0.0542099
1.23520 41 0.0236448
1.42523 14 0.00807382
1.61526 6 0.00346021
1.80529 1 0.000576701
MIL calculations for sample: B9_75_0001
Threshhold range, BV/TV: 63.0000-148.000 0.327119
Uniform Orientations: 513
Vector sampling: Dense
Random Points: 2000
Data orientation (strike, dip, up): -4.84670 -0.000104587 0
MIL Ellipse Eigenvectors: Trend Plunge
0.190677 -0.148582 0.970343 307.927 76.0112

-0.483615 0.845981 0.224572 150.245 12.9777
-0.854259 -0.512093 0.0894521 59.0590 5.13209
MIL Ellipse Eigenvalues:
0.699483 0.819958 1.15896
MIL Ellipse (H) Eigenvalues:
0.370302 0.342018 0.287680
MIL Ellipse Tensor (M):
1.06297 0.151715 -0.0481957
0.151715 0.906199 0.00184048
-0.0481957 0.00184048 0.709235
MIL (H) DA I E Tb.N
1.28720 0.776880 0.0763811 0.944882
MIL Fabric Eigenvectors: Trend Plunge
0.141537 -0.106424 0.984196 306.940 79.8000
-0.500319 0.850190 0.163884 149.524 9.43242
0.854194 0.515608 -0.0670875 58.8840 3.84672
MIL Fabric Eigenvalues:
0.362006 0.340228 0.297766
MIL Fabric Tensor:
0.309682 -0.0190292 0.00546707
-0.0190292 0.329186 -0.000812382
0.00546707 -0.000812382 0.361132
MIL (F) DA I E
1.21574 0.822544 0.0601614

medial

Star length and volume calcuations for sample: B7_81_0001
Threshhold range, BV/TV: 56.0000-146.000 0.425470
Uniform Orientations: 513
Vector sampling: Dense
Random Points: 2000
Data orientation (strike, dip, up): -173.000 -3.00000 1

SVD Eigenvalues:	Eigenvectors		Trend	Plunge
0.756705	-0.237673	0.0131163	0.971257	93.1588
76.2294				
0.137088	0.389464	0.917302	0.0829166	203.005
4.75623				
0.106207	0.889848	-0.397976	0.223126	294.096
12.8927				

SVD Fabric Tensor:

0.147636	0.00900466	-0.149165
0.00900466	0.132304	0.0106357
-0.149165	0.0106357	0.720060

SVD DA	I	E	Sum(tau)
7.12483	0.140354	0.818836	15078.7

SLD Eigenvalues:	Eigenvectors		Trend	Plunge
0.449133	-0.225779	0.0127855	0.974095	93.2411
76.9300				
0.283101	-0.203957	-0.978374	-0.0344322	191.776
1.97321				
0.267765	-0.952589	0.206448	-0.223504	282.228
12.9149				

SLD Fabric Tensor:

0.277649	0.00253662	-0.0397805
0.00253662	0.282475	0.00277544
-0.0397805	0.00277544	0.439876

SLD DA	I	E	Sum(tau)
1.67734	0.596183	0.369671	512.606

Thickness (minimum line length at each point, non-zero points only)

Mean	Variance	Skewness	Kurtosis	Min	Max
0.293263	0.0232663	1.00101	0.880939	0.0781250	0.956123

Thickness histogram

bin num	norm	
0.0531179	20	0.0114877
0.159354	590	0.338886
0.265590	468	0.268811
0.371826	361	0.207352
0.478061	165	0.0947731
0.584297	75	0.0430787
0.690533	41	0.0235497

0.796769 18 0.0103389
0.903005 2 0.00114877
1.00924 1 0.000574383
MIL calculations for sample: B7_81_0001
Threshhold range, BV/TV: 56.0000-146.000 0.425470
Uniform Orientations: 513
Vector sampling: Dense
Random Points: 2000
Data orientation (strike, dip, up): -173.000 -3.00000 1
MIL Ellipse Eigenvectors: Trend Plunge
0.170974 -0.0108320 -0.985216 93.6251 80.1356
-0.0457298 0.998775 -0.0189170 357.378 1.08393
-0.984214 -0.0482878 -0.170270 267.191 9.80349
MIL Ellipse Eigenvalues:
0.984598 2.26747 2.61460
MIL Ellipse (H) Eigenvalues:
0.440021 0.289956 0.270023
MIL Ellipse Tensor (M):
2.56623 0.0188745 0.274269
0.0188745 2.26813 -0.0108365
0.274269 -0.0108365 1.03231
MIL (H) DA I E Tb.N
1.62957 0.613658 0.341041 1.37248
MIL Fabric Eigenvectors: Trend Plunge
-0.156617 0.000691285 0.987659 90.2529 80.9893
0.0175469 -0.999840 0.00348225 358.995 0.199519
-0.987504 -0.0178755 -0.156580 268.963 9.00842
MIL Fabric Eigenvalues:
0.421382 0.297624 0.280994
MIL Fabric Tensor:
0.284443 -0.000306849 -0.0217148
-0.000306849 0.297618 3.79484e-005
-0.0217148 3.79484e-005 0.417939
MIL (F) DA I E
1.49961 0.666838 0.293697

lateral

Star length and volume calcuations for sample: B7_81_0001
Threshhold range, BV/TV: 52.0000-123.000 0.389904
Uniform Orientations: 513
Vector sampling: Dense
Random Points: 2000
Data orientation (strike, dip, up): -173.000 -3.00000 1
SVD Eigenvalues: Eigenvectors Trend Plunge

0.657046 -0.183028 0.362337 0.913900 153.200
66.0499
0.236592 -0.445815 0.797936 -0.405644 330.807
23.9315
0.106362 -0.876213 -0.481674 0.0154907 61.2014
0.887589
SVD Fabric Tensor:
0.150693 -0.0828468 -0.0685614
-0.0828468 0.261578 0.140201
-0.0685614 0.140201 0.587729
SVD DA I E Sum(tau)
6.17743 0.161880 0.639916 2297.87
SLD Eigenvalues: Eigenvectors Trend Plunge
0.418520 -0.190588 0.366460 0.910705 152.522
65.6029
0.326714 -0.412844 0.811760 -0.413044 333.043
24.3962
0.254766 -0.890638 -0.454700 -0.00342096 242.954
0.196007
SLD Fabric Tensor:
0.272977 -0.0355492 -0.0161538
-0.0355492 0.324168 0.0305270
-0.0161538 0.0305270 0.402855
SLD DA I E Sum(tau)
1.64276 0.608731 0.219358 339.295
Thickness (minimum line length at each point, non-zero points only)
Mean Variance Skewness Kurtosis Min Max
0.250659 0.0109602 0.578215 -0.0525358 0.0781250 0.647909
Thickness histogram
bin num norm
0.0359950 0 0.000000
0.107985 464 0.252037
0.179975 283 0.153721
0.251965 466 0.253123
0.323955 378 0.205323
0.395944 159 0.0863661
0.467934 56 0.0304183
0.539924 27 0.0146659
0.611914 7 0.00380228
0.683904 1 0.000543183
MIL calculations for sample: B7_81_0001
Threshhold range, BV/TV: 52.0000-123.000 0.389904
Uniform Orientations: 513
Vector sampling: Dense
Random Points: 2000
Data orientation (strike, dip, up): -173.000 -3.00000 1
MIL Ellipse Eigenvectors: Trend Plunge
0.169098 -0.429194 -0.887242 158.496 62.5287

-0.343347 0.818164 -0.461216 337.234 27.4656
0.923861 0.382623 -0.00901251 67.5028 0.516386
MIL Ellipse Eigenvalues:
1.34679 2.09448 3.47194
MIL Ellipse (H) Eigenvalues:
0.412421 0.330714 0.256865
MIL Ellipse Tensor (M):
3.24879 0.541182 0.100707
0.541182 2.15841 -0.289469
0.100707 -0.289469 1.50601
MIL (H) DA I E Tb.N
1.60559 0.622822 0.198115 1.49387
MIL Fabric Eigenvectors: Trend Plunge
-0.179254 0.387240 0.904386 155.161 64.7407
-0.342667 0.837134 -0.426363 337.739 25.2369
-0.922197 -0.386330 -0.0173650 247.270 0.994993
MIL Fabric Eigenvalues:
0.391672 0.334403 0.273925
MIL Fabric Tensor:
0.284810 -0.0255220 -0.0102527
-0.0255220 0.333964 0.0196507
-0.0102527 0.0196507 0.381226
MIL (F) DA I E
1.42985 0.699373 0.146217

9_77

medial

Star length and volume calcuations for sample: B9_77_0001
Threshhold range, BV/TV: 45.0000-130.000 0.369338
Uniform Orientations: 513
Vector sampling: Dense
Random Points: 2000
Data orientation (strike, dip, up): -47.0000 -180.000 0

SVD Eigenvalues:	Eigenvectors			Trend	Plunge
0.707189	-0.213872	-0.0307800	0.976377	81.8103	77.5213
0.170861	0.307570	-0.950790	0.0373990	342.074	2.14330
0.121950	-0.927178	-0.308303	-0.212815	251.607	12.2874

SVD Fabric Tensor:

0.153346	-0.0104508	-0.121647
-0.0104508	0.166720	-0.0193273
-0.121647	-0.0193273	0.679933

SVD DA	I	E	Sum(tau)
5.79902	0.172443	0.758394	8669.58

SLD Eigenvalues:	Eigenvectors			Trend	Plunge
0.427056	-0.217151	-0.0469272	0.975009	77.8057	77.1638
0.311794	0.372472	-0.927252	0.0383273	338.115	2.19653
0.261149	-0.902280	-0.371487	-0.218833	247.622	12.6405

SLD Fabric Tensor:

0.275999	-0.0158009	-0.0344035
-0.0158009	0.305059	-0.00939084
-0.0344035	-0.00939084	0.418942

SLD DA	I	E	Sum(tau)
1.63529	0.611511	0.269899	454.191

Thickness (minimum line length at each point, non-zero points only)

Mean	Variance	Skewness	Kurtosis	Min	Max
0.282703	0.0204547	1.24791	2.96131	0.0781250	1.28610

Thickness histogram

bin num	norm
0.0714500	404	0.228895
0.214350	601	0.340510
0.357250	517	0.292918
0.500150	168	0.0951841
0.643050	53	0.0300283
0.785950	16	0.00906516

0.928850 4 0.00226629
1.07175 1 0.000566572
1.21465 0 0.000000
1.35755 1 0.000566572
MIL calculations for sample: B9_77_0001
Threshhold range, BV/TV: 45.0000-130.000 0.369338
Uniform Orientations: 513
Vector sampling: Dense
Random Points: 2000
Data orientation (strike, dip, up): -47.0000 -180.000 0
MIL Ellipse Eigenvectors: Trend Plunge
0.178841 -0.0542278 -0.982382 106.868 79.2292
-0.373110 0.920160 -0.118717 337.928 6.81807
-0.910387 -0.387768 -0.144329 246.929 8.29843
MIL Ellipse Eigenvalues:
0.896145 1.38934 2.22383
MIL Ellipse (H) Eigenvalues:
0.410184 0.329431 0.260386
MIL Ellipse Tensor (M):
2.06519 0.299375 0.196297
0.299375 1.51336 0.0204299
0.196297 0.0204299 0.930753
MIL (H) DA I E Tb.N
1.57529 0.634803 0.196870 1.20919
MIL Fabric Eigenvectors: Trend Plunge
-0.181288 0.00462842 0.983419 91.4625 79.5517
0.346676 -0.935494 0.0683108 339.666 3.91697
-0.920299 -0.353311 -0.167990 248.998 9.67095
MIL Fabric Eigenvalues:
0.392899 0.331223 0.275878
MIL Fabric Tensor:
0.286376 -0.0180472 -0.0195522
-0.0180472 0.324315 -0.00300410
-0.0195522 -0.00300410 0.389309
MIL (F) DA I E
1.42418 0.702160 0.156979

lateral

Star length and volume calcuations for sample: B9_77_0001
Threshhold range, BV/TV: 46.0000-167.000 0.329149
Uniform Orientations: 513
Vector sampling: Dense
Random Points: 2000
Data orientation (strike, dip, up): -47.0000 -180.000 0
SVD Eigenvalues: Eigenvectors Trend Plunge

0.521629 0.201118 0.0665036 0.977307 251.703
77.7705
0.286994 -0.713762 0.693255 0.0997094 134.165
5.72243
0.191377 0.670892 0.717618 -0.186894 43.0726
10.7716
SVD Fabric Tensor:
0.253448 -0.0428958 0.0581074
-0.0428958 0.238792 0.0280739
0.0581074 0.0280739 0.507760
SVD DA I E Sum(tau)
2.72565 0.366884 0.449812 2120.59
SLD Eigenvalues: Eigenvectors Trend Plunge
0.374170 0.0554770 0.255308 0.965267 192.259
74.8548
0.340684 -0.620833 0.765968 -0.166913 320.975
9.60840
0.285147 0.781978 0.590009 -0.200997 52.9651
11.5953
SLD Fabric Tensor:
0.306826 -0.0251492 0.0105223
-0.0251492 0.323533 0.0148384
0.0105223 0.0148384 0.369640
SLD DA I E Sum(tau)
1.31220 0.762078 0.0894936 315.877
Thickness (minimum line length at each point, non-zero points only)
Mean Variance Skewness Kurtosis Min Max
0.250456 0.0157485 1.152571.786480.0781250 0.895731
Thickness histogram
bin num norm
0.0497628 56 0.0310938
0.149289 663 0.368129
0.248814 507 0.281510
0.348340 381 0.211549
0.447866 113 0.0627429
0.547391 50 0.0277624
0.646917 21 0.0116602
0.746443 7 0.00388673
0.845968 2 0.00111049
0.945494 1 0.000555247
MIL calculations for sample: B9_77_0001
Threshhold range, BV/TV: 46.0000-167.000 0.329149
Uniform Orientations: 513
Vector sampling: Dense
Random Points: 2000
Data orientation (strike, dip, up): -47.0000 -180.000 0
MIL Ellipse Eigenvectors: Trend Plunge
-0.0689603 0.386380 0.919758 169.881 66.8907

-0.607412 0.715102 -0.345948 319.655 20.2397
-0.791388 -0.582529 0.185378 53.6438 10.6832
MIL Ellipse Eigenvalues:
1.25084 1.42063 2.14211
MIL Ellipse (H) Eigenvalues:
0.370029 0.347213 0.282758
MIL Ellipse Tensor (M):
1.87168 0.337132 -0.0950765
0.337132 1.64011 -0.138252
-0.0950765 -0.138252 1.30179
MIL (H) DA I E Tb.N
1.30864 0.764151 0.0616605 1.26419
MIL Fabric Eigenvectors: Trend Plunge
0.162846 -0.450042 -0.878034 160.108 61.4061
0.578634 -0.677247 0.454445 319.490 27.0292
-0.799165 -0.582064 0.150123 53.9326 8.63405
MIL Fabric Eigenvalues:
0.360289 0.346793 0.292918
MIL Fabric Tensor:

0.312743 -0.0260498 0.00453380
-0.0260498 0.331274 0.0100407
0.00453380 0.0100407 0.355983
MIL (F) DA I E
1.23000 0.813008 0.0374591

medial

Star length and volume □alculations for sample: sm18_0001
I range, BV/TV: 61.0000-166.000 0.364988
Uniform Orientations: 513
Vector sampling: Dense
Random Points: 2000
Data orientation (strike, dip, up): 160.956-9.45886e-005 1

SVD Eigenvalues:	Eigenvectors		Trend	Plunge
0.498397	-0.187181	0.947854	-0.257947	348.829
14.9483				
0.338123	0.963175	0.228689	0.141407	256.643
8.12929				
0.163480	0.193023	-0.221979	-0.955755	138.991
72.8926				

SVD Fabric Tensor:

0.337231	-0.0209528	0.0399569
-0.0209528	0.473512	-0.0762381
0.0399569	-0.0762381	0.189257

SVD DA	I	E	Sum(tau)
3.04866	0.328013	0.321580	27908.2

SLD Eigenvalues:	Eigenvectors		Trend	Plunge
0.357657	-0.291750	-0.758689	0.582471	21.0340
35.6245				
0.341579	0.210492	-0.644962	-0.734654	161.925
47.2780				
0.300764	-0.933046	0.0917293	-0.347866	275.615
20.3568				

SLD Fabric Tensor:

0.307415	0.00705203	-0.0159798
0.00705203	0.350490	-0.00580260
-0.0159798	-0.00580260	0.342095

SLD DA	I	E	Sum(tau)
1.18916	0.840929	0.0449529	590.046

Thickness (minimum line length at each point, non-zero points only)

Mean	Variance	Skewness	Kurtosis	Min	Max
0.309070	0.0336900	1.41135	2.25123	0.0781250	1.15498

Thickness histogram

bin num	norm	
0.0641657	111	0.0633562
0.192497	716	0.408676
0.320828	485	0.276826
0.449160	229	0.130708
0.577491	92	0.0525114
0.705823	61	0.0348174
0.834154	37	0.0211187

0.962485 13 0.00742009
1.09082 7 0.00399543
1.21915 1 0.000570776
MIL calculations for sample: sm18_0001
I range, BV/TV: 61.0000-166.000 0.364988
Uniform Orientations: 513
Vector sampling: Dense
Random Points: 2000
Data orientation (strike, dip, up): 160.956-9.45886e-005 1
MIL Ellipse Eigenvectors: Trend Plunge
0.286506 -0.124665 -0.949933 113.515 71.7929
0.287050 0.957120 -0.0390317 16.6945 2.23692
-0.914066 0.261496 -0.310005 285.965 18.0596
MIL Ellipse Eigenvalues:
0.736477 1.17549 1.88360
MIL Ellipse (H) Eigenvalues:
0.413765 0.327510 0.258725
MIL Ellipse Tensor (M):
1.73109 -0.153576 0.320136
-0.153576 1.21709 -0.109392
0.320136 -0.109392 0.847388
MIL (H) DA I E Tb.N
1.59924 0.625295 0.208465 1.10738
MIL Fabric Eigenvectors: Trend Plunge
-0.258155 0.123596 0.958165 115.583 73.3684
-0.255071 -0.965311 0.0557944 14.8014 3.19844
-0.931823 0.229997 -0.280726 283.865 16.3035
MIL Fabric Eigenvalues:
0.399837 0.327761 0.272403
MIL Fabric Tensor:
0.284497 0.00956442 -0.0323093
0.00956442 0.325934 0.0121098
-0.0323093 0.0121098 0.389570
MIL (F) DA I E
1.46782 0.681285 0.180263

medial

Star length and volume □alculations for sample: B2_81_0001
I range, BV/TV: 51.0000-125.000 0.399454
Uniform Orientations: 513
Vector sampling: Dense
Random Points: 2000
Data orientation (strike, dip, up): 173.0001.000001

SVD Eigenvalues:	Eigenvectors	Trend	Plunge	
0.758007	-0.178007	0.000342280	0.984029	90.1102
79.7463				
0.176336	0.513875	0.852846	0.0926614	211.071
5.31673				
0.0656569	0.839194	-0.522162	0.151989	301.891
8.74218				

SVD Fabric Tensor:

0.116822	0.0484637	-0.116005
0.0484637	0.146159	0.00897971
-0.116005	0.00897971	0.737019

SVD DA	I	E	Sum(tau)
11.5450	0.0866178	0.767369	27753.6

SLD Eigenvalues:	Eigenvectors	Trend	Plunge	
0.454251	-0.181267	0.00410485	0.983425	91.2972
79.5537				
0.323550	-0.448818	-0.890123	-0.0790117	206.758
4.53176				
0.222199	-0.875046	0.455701	-0.163193	297.509
9.39225				

SLD Fabric Tensor:

0.250240	0.0403174	-0.0377721
0.0403174	0.302505	0.00806480
-0.0377721	0.00806480	0.447255

SLD DA	I	E	Sum(tau)
2.04434	0.489155	0.287728	663.599

Thickness (minimum line length at each point, non-zero points only)

Mean	Variance	Skewness	Kurtosis	Min	Max
0.323379	0.0213370	0.754337	0.839488	0.0781250	0.972997

Thickness histogram

bin num	norm	
0.0540554	18	0.00983607
0.162166	423	0.231148
0.270277	502	0.274317
0.378388	526	0.287432
0.486499	221	0.120765
0.594609	89	0.0486339

0.702720 30 0.0163934
0.810831 17 0.00928962
0.918942 3 0.00163934
1.02705 1 0.000546448
MIL calculations for sample: B2_81_0001
I range, BV/TV: 51.0000-125.000 0.399454
Uniform Orientations: 513
Vector sampling: Dense
Random Points: 2000
Data orientation (strike, dip, up): 173.0001.000001

MIL Ellipse Eigenvectors:			Trend	Plunge
0.162862	0.0103463	-0.986595	86.3650	80.6079
0.360113	0.930339	0.0692019	201.160	3.96815
-0.918583	0.366556	-0.147791	291.754	8.49893

MIL Ellipse Eigenvalues:
0.497834 1.06296 2.37189
MIL Ellipse (H) Eigenvalues:
0.466745 0.319422 0.213833
MIL Ellipse Tensor (M):
2.15243 -0.441684 0.268501
-0.441684 1.23877 -0.0651409
0.268501 -0.0651409 0.541474
MIL (H) DA I E Tb.N
2.18275 0.458137 0.315640 1.09035

MIL Fabric Eigenvectors:			Trend	Plunge
-0.122158	0.00801791	0.992478	93.7552	82.9681
-0.361577	-0.931608	-0.0369782	201.212	2.11918
-0.924305	0.363375	-0.116703	291.461	6.70185

MIL Fabric Eigenvalues:
0.430621 0.332042 0.237337
MIL Fabric Tensor:
0.252603 0.0317117 -0.0221673
0.0317117 0.319543 0.00480057
-0.0221673 0.00480057 0.427854
MIL (F) DA I E
1.81438 0.551152 0.228923

medial

Star length and volume calcuations for sample: sm16_0001
Threshhold range, BV/TV: 65.0000-255.000 0.350704
Uniform Orientations: 513
Vector sampling: Dense
Random Points: 2000
Data orientation (strike, dip, up): 172.0000.000000 1

SVD Eigenvalues:	Eigenvectors		Trend	Plunge
0.634918	-0.401778	0.0111561	0.915669	91.5905
66.3009				
0.224117	-0.511601	0.826589	-0.234552	328.245
13.5652				
0.140965	0.759499	0.562695	0.326398	233.466
19.0503				

SVD Fabric Tensor:

0.242466	-0.0373776	-0.171745
-0.0373776	0.197840	-0.0110755
-0.171745	-0.0110755	0.559694

SVD DA	I	E	Sum(tau)
4.50408	0.222021	0.647014	39902.3

SLD Eigenvalues:	Eigenvectors		Trend	Plunge
0.421530	-0.397481	0.00714960	0.917583	91.0305
66.5752				
0.307749	-0.508258	0.830847	-0.226643	328.544
13.0995				
0.270721	0.763991	0.556455	0.326612	233.932
19.0633				

SLD Fabric Tensor:

0.304113	-0.0160652	-0.0507379
-0.0160652	0.296290	-0.00598335
-0.0507379	-0.00598335	0.399598

SLD DA	I	E	Sum(tau)
1.55707	0.642234	0.269922	787.532

Thickness (minimum line length at each point, non-zero points only)

Mean	Variance	Skewness	Kurtosis	Min	Max
0.378880	0.0546940	1.433133.150190.0781250		1.65237	

Thickness histogram

bin num	norm	
0.0917981	410	0.230726
0.275394	598	0.336522
0.458991	412	0.231851
0.642587	231	0.129994
0.826183	72	0.0405177
1.00978	28	0.0157569
1.19338	15	0.00844119

1.37697 6 0.00337648
1.56057 4 0.00225098
1.74416 1 0.000562746
MIL calculations for sample: sm16_0001
Threshhold range, BV/TV: 65.0000-255.000 0.350704
Uniform Orientations: 513
Vector sampling: Dense
Random Points: 2000
Data orientation (strike, dip, up): 172.0000.000000 1
MIL Ellipse Eigenvectors: Trend Plunge
0.228941 0.0262101 -0.973087 83.4690 76.6772
-0.0730601 0.997281 0.00967272 175.810 0.554215
-0.970695 -0.0688793 -0.230233 265.941 13.3108
MIL Ellipse Eigenvalues:
0.469177 1.01444 1.29267
MIL Ellipse (H) Eigenvalues:
0.438111 0.297947 0.263942
MIL Ellipse Tensor (M):
1.24803 0.0153310 0.183655
0.0153310 1.01539 0.0183191
0.183655 0.0183191 0.512879
MIL (H) DA I E Tb.N
1.65988 0.602454 0.319928 0.945434
MIL Fabric Eigenvectors: Trend Plunge
-0.256870 -0.0500785 0.965148 78.9682 74.8287
0.0494519 -0.998030 -0.0386231 177.163 2.21349
-0.965180 -0.0378076 -0.258840 267.757 15.0013
MIL Fabric Eigenvalues:
0.407783 0.310929 0.281288
MIL Fabric Tensor:
0.289707 0.000164184 -0.0314168
0.000164184 0.311129 -0.00497131
-0.0314168 -0.00497131 0.399163
MIL (F) DA I E
1.44970 0.689799 0.237513

lateral

Star length and volume calcuations for sample: sm16_0001
Threshhold range, BV/TV: 61.0000-209.000 0.299651
Uniform Orientations: 513
Vector sampling: Dense
Random Points: 2000
Data orientation (strike, dip, up): 172.0000.000000 1
SVD Eigenvalues: Eigenvectors Trend Plunge

0.426405 0.143989 -0.340758 -0.929060 157.093
68.2887
0.375450 0.952356 -0.207356 0.223653 282.283
12.9237
0.198145 -0.268858 -0.917000 0.294665 16.3408
17.1375
SVD Fabric Tensor:
0.363690 -0.0462133 0.00723009
-0.0462133 0.232273 0.0640409
0.00723009 0.0640409 0.404037
SVD DA I E Sum(tau)
2.15199 0.464687 0.119500 32778.5
SLD Eigenvalues: Eigenvectors Trend Plunge
0.378530 0.0620145 0.190198 0.979785 198.059
78.4600
0.318933 -0.980910 0.192893 0.0246410 101.125
1.41197
0.302537 0.184307 0.962610 -0.198529 10.8390
11.4510
SLD Fabric Tensor:
0.318605 -0.00220587 0.00422113
-0.00220587 0.305896 0.0142395
0.00422113 0.0142395 0.375499
SLD DA I E Sum(tau)
1.25119 0.799241 0.157445 706.287
Thickness (minimum line length at each point, non-zero points only)
Mean Variance Skewness Kurtosis Min Max
0.376102 0.0703805 1.956685.427560.0781250 2.03262
Thickness histogram
bin num norm
0.112923 556 0.314836
0.338769 718 0.406569
0.564616 307 0.173839
0.790462 102 0.0577576
1.01631 42 0.0237826
1.24215 19 0.0107588
1.46800 15 0.00849377
1.69385 4 0.00226501
1.91969 2 0.00113250
2.14554 1 0.000566251
MIL calculations for sample: sm16_0001
Threshhold range, BV/TV: 61.0000-209.000 0.299651
Uniform Orientations: 513
Vector sampling: Dense
Random Points: 2000
Data orientation (strike, dip, up): 172.0000.000000 1
MIL Ellipse Eigenvectors: Trend Plunge
-0.137203 0.225451 0.964545 148.676 74.6973

-0.00253093	-0.973831	0.227261	0.148903	13.1359
0.990540	0.0287397	0.134183	268.338	7.71139

MIL Ellipse Eigenvalues:

0.593489	0.663026	0.863499

MIL Ellipse (H) Eigenvalues:

0.360341	0.340922	0.298737

MIL Ellipse Tensor (M):

0.858414	0.00785801	0.0358479
0.00785801	0.659658	-0.0143484
0.0358479	-0.0143484	0.601942

MIL (H) DA	I	E	Tb.N
1.20621	0.829040	0.0538918	0.844149

MIL Fabric Eigenvectors:			Trend	Plunge
0.159494	-0.187381	-0.969252	139.596	75.7550
0.0112953	-0.981410	0.191590	359.341	11.0456
-0.987134	-0.0415055	-0.154413	267.592	8.88274

MIL Fabric Eigenvalues:

0.352752	0.339801	0.307446

MIL Fabric Tensor:

0.308603	-0.00171272	-0.00693385
-0.00171272	0.340200	0.00214482
-0.00693385	0.00214482	0.351197

MIL (F) DA	I	E
1.14736	0.871564	0.0367144

medial

Star length and volume calcuations for sample: sm9b_0001
Threshhold range, BV/TV: 59.0000-197.000 0.328100
Uniform Orientations: 513
Vector sampling: Dense
Random Points: 2000
Data orientation (strike, dip, up): 172.0007.000001

SVD Eigenvalues:	Eigenvectors	Trend	Plunge	
0.719430	-0.262161	0.146206	0.953884	119.148 72.5319
0.151990	-0.0842901	0.981210	-0.173560	355.090 9.99488
0.128580	0.961336	0.125904	0.244911	262.539 14.1766

SVD Fabric Tensor:

0.169355	-0.0245831	-0.147412
-0.0245831	0.163748	0.0784155
-0.147412	0.0784155	0.666897

SVD DA	I	E	Sum(tau)
5.59518	0.178725	0.788736	2434.31

SLD Eigenvalues:	Eigenvectors	Trend	Plunge	
0.428788	-0.253876	0.147735	0.955888	120.196 72.9185
0.298051	-0.0307849	0.986532	-0.160647	358.213 9.24448
0.273161	0.966747	0.0702114	0.245909	265.846 14.2355

SLD Fabric Tensor:

0.283215	-0.00659300	-0.0376441
-0.00659300	0.300782	0.0180327
-0.0376441	0.0180327	0.416003

SLD DA	I	E	Sum(tau)
1.56973	0.637053	0.304899	301.843

Thickness (minimum line length at each point, non-zero points only)

Mean	Variance	Skewness	Kurtosis	Min	Max
0.229782	0.0127039	0.891548	0.861488	0.0585900	0.706080

Thickness histogram

bin num	norm	
0.0392267	22	0.0122494
0.117680	513	0.285635
0.196133	441	0.245546
0.274587	475	0.264477
0.353040	176	0.0979955
0.431493	102	0.0567929
0.509947	43	0.0239421

0.588400 16 0.00890869
0.666853 7 0.00389755
0.745306 1 0.000556793
MIL calculations for sample: sm9b_0001
Threshhold range, BV/TV: 59.0000-197.000 0.328100
Uniform Orientations: 513
Vector sampling: Dense
Random Points: 2000
Data orientation (strike, dip, up): 172.0007.000001
MIL Ellipse Eigenvectors: Trend Plunge
-0.246642 0.144588 0.958260 120.380 73.3875
0.0417111 -0.986307 0.159556 357.578 9.18111
-0.968208 -0.0793233 -0.237234 265.316 13.7233
MIL Ellipse Eigenvalues:
0.915094 2.00283 2.54104
MIL Ellipse (H) Eigenvalues:
0.439358 0.296981 0.263661
MIL Ellipse Tensor (M):
2.44119 0.0801251 0.380705
0.0801251 1.98348 -0.140581
0.380705 -0.140581 1.03429
MIL (H) DA I E Tb.N
1.66637 0.600105 0.324056 1.32631
MIL Fabric Eigenvectors: Trend Plunge
-0.224973 0.121144 0.966805 118.302 75.1958
-0.0482333 0.989640 -0.135229 357.210 7.77189
0.973171 0.0770552 0.216799 265.473 12.5211
MIL Fabric Eigenvalues:
0.406438 0.312796 0.280765
MIL Fabric Tensor:
0.287201 -0.00495415 -0.0271255
-0.00495415 0.313980 0.0104326
-0.0271255 0.0104326 0.398819
MIL (F) DA I E
1.44761 0.690794 0.230397

lateral

Star length and volume calcuations for sample: sm9b_0001
Threshhold range, BV/TV: 55.0000-149.000 0.285086
Uniform Orientations: 513
Vector sampling: Dense
Random Points: 2000
Data orientation (strike, dip, up): 172.0007.000001
SVD Eigenvalues: Eigenvectors Trend Plunge

0.548076 0.144964 0.0301356 0.988978 258.256
81.4853
0.283156 0.234976 0.969892 -0.0639967 13.6186
3.66925
0.168768 0.961130 -0.241663 -0.133518 104.114
7.67295
SVD Fabric Tensor:
0.183055 0.0277262 0.0526598
0.0277262 0.276716 0.00420463
0.0526598 0.00420463 0.540229
SVD DA I E Sum(tau)
3.24751 0.307928 0.483363 1239.79
SLD Eigenvalues: Eigenvectors Trend Plunge
0.383335 0.127339 0.0577985 0.990174 245.587
81.9613
0.331588 0.166281 0.982928 -0.0787599 9.60179
4.51729
0.285077 0.977822 -0.174677 -0.115555 100.128
6.63561
SLD Fabric Tensor:
0.287956 0.00832508 0.0117801
0.00832508 0.330342 0.00202272
0.0117801 0.00202272 0.381702
SLD DA I E Sum(tau)
1.34467 0.743675 0.134992 276.454
Thickness (minimum line length at each point, non-zero points only)
Mean Variance Skewness Kurtosis Min Max
0.231719 0.0126104 0.838020 1.149500.0585900 0.778335
Thickness histogram
bin num norm
0.0432408 55 0.0301535
0.129723 534 0.292763
0.216204 572 0.313596
0.302686 412 0.225877
0.389168 166 0.0910088
0.475649 50 0.0274123
0.562131 24 0.0131579
0.648613 7 0.00383772
0.735094 3 0.00164474
0.821576 1 0.000548246
MIL calculations for sample: sm9b_0001
Threshhold range, BV/TV: 55.0000-149.000 0.285086
Uniform Orientations: 513
Vector sampling: Dense
Random Points: 2000
Data orientation (strike, dip, up): 172.0007.000001
MIL Ellipse Eigenvectors: Trend Plunge
-0.140003 -0.150900 -0.978585 222.855 78.1211

-0.0790161 -0.983464 0.162957 4.59354 9.37856
-0.986993 0.100138 0.125764 95.7933 7.22490
MIL Ellipse Eigenvalues:
1.07430 1.26098 1.81523
MIL Ellipse (H) Eigenvalues:
0.371427 0.342833 0.285740
MIL Ellipse Tensor (M):
1.79725 -0.0587238 -0.0943742
-0.0587238 1.26229 -0.0205858
-0.0943742 -0.0205858 1.09098
MIL (H) DA I E Tb.N
1.29988 0.769303 0.0769830 1.17520
MIL Fabric Eigenvectors: Trend Plunge
0.132484 0.137379 0.981619 223.961 78.9974
0.0731354 0.986294 -0.147904 4.24083 8.50549
0.988483 -0.0913860 -0.120620 95.2820 6.92791
MIL Fabric Eigenvalues:
0.366711 0.338284 0.295005
MIL Fabric Tensor:
0.296495 0.00442704 0.00885718
0.00442704 0.338459 0.00335652
0.00885718 0.00335652 0.365046
MIL (F) DA I E
1.24307 0.804460 0.0775205

medial

Star length and volume calcuations for sample: B4_74_0001
Threshhold range, BV/TV: 56.0000-144.000 0.315580
Uniform Orientations: 513
Vector sampling: Dense
Random Points: 2000
Data orientation (strike, dip, up): -161.000 7.000001

SVD Eigenvalues:	Eigenvectors			Trend	Plunge
0.440768	0.571841	-0.538849	0.618578	313.299	38.2124
0.308083	-0.466581	-0.833824	-0.295023	209.230	17.1589
0.251150	-0.674759	0.119910	0.728232	100.077	46.7384

SVD Fabric Tensor:

0.325550	-0.0362787	0.0749101
-0.0362787	0.345790	-0.0491981
0.0749101	-0.0491981	0.328660

SVD DA	I	E	Sum(tau)
1.75500	0.569801	0.301032	11499.6

SLD Eigenvalues:	Eigenvectors			Trend	Plunge
0.383587	-0.261966	0.146023	0.953966	119.136	72.5475
0.326157	-0.375354	0.895241	-0.240109	337.253	13.8930
0.290256	0.889091	0.420976	0.179712	244.663	10.3530

SLD Fabric Tensor:

0.301719	-0.0156343	-0.0200886
-0.0156343	0.321019	0.00528398
-0.0200886	0.00528398	0.377262

SLD DA	I	E	Sum(tau)
1.32155	0.756687	0.149719	428.134

Thickness (minimum line length at each point, non-zero points only)

Mean	Variance	Skewness	Kurtosis	Min	Max
0.268554	0.0244637	1.70290	4.49046	0.0781250	1.19977

Thickness histogram

bin num	norm	
0.0666540	367	0.235407
0.199962	523	0.335471
0.333270	415	0.266196
0.466578	172	0.110327
0.599886	38	0.0243746
0.733194	21	0.0134702
0.866502	11	0.00705581

0.999810 10 0.00641437
1.13312 1 0.000641437
1.26643 1 0.000641437
MIL calculations for sample: B4_74_0001
Threshhold range, BV/TV: 56.0000-144.000 0.315580
Uniform Orientations: 513
Vector sampling: Dense
Random Points: 2000
Data orientation (strike, dip, up): -161.000 7.000001
MIL Ellipse Eigenvectors: Trend Plunge
-0.282695 0.264086 0.922140 133.051 67.2410
0.0412381 -0.957119 0.286745 357.533 16.6632
-0.958323 -0.119088 -0.259682 262.916 15.0512
MIL Ellipse Eigenvalues:
0.496087 0.949662 1.52243
MIL Ellipse (H) Eigenvalues:
0.435997 0.315121 0.248882
MIL Ellipse Tensor (M):
1.43943 0.0992295 0.260778
0.0992295 0.926152 -0.0927435
0.260778 -0.0927435 0.602593
MIL (H) DA I E Tb.N
1.75182 0.570835 0.277239 0.970923
MIL Fabric Eigenvectors: Trend Plunge
-0.298642 0.206267 0.931808 124.632 68.7185
-0.0789025 0.967685 -0.239497 355.339 13.8569
0.951098 0.145046 0.272717 261.329 15.8260
MIL Fabric Eigenvalues:
0.416758 0.319555 0.263686
MIL Fabric Tensor:
0.277686 -0.0136950 -0.0415406
-0.0136950 0.322516 0.0164726
-0.0415406 0.0164726 0.399798
MIL (F) DA I E
1.58051 0.632708 0.233236

lateral

Star length and volume calcuations for sample: B4_74_0001
Threshhold range, BV/TV: 48.0000-168.000 0.321767
Uniform Orientations: 513
Vector sampling: Dense
Random Points: 2000
Data orientation (strike, dip, up): -161.000 7.000001
SVD Eigenvalues: Eigenvectors Trend Plunge

0.635806 0.0672680 0.187615 0.979936 199.725
78.5034
0.202830 -0.503380 0.854378 -0.129021 329.494
7.41305
0.161364 -0.861443 -0.484601 0.151914 60.6402
8.73786
SVD Fabric Tensor:
0.174018 -0.0118460 0.0339675
-0.0118460 0.208333 0.0826556
0.0339675 0.0826556 0.617649
SVD DA I E Sum(tau)
3.94020 0.253794 0.680987 7354.15
SLD Eigenvalues: Eigenvectors Trend Plunge
0.407809 0.0479796 0.193413 0.979944 193.932
78.5054
0.315693 -0.219904 0.959048 -0.178522 347.086
10.2837
0.276498 -0.974341 -0.206929 0.0885470 78.0098
5.08002
SLD Fabric Tensor:
0.278696 -0.00704762 0.00771259
-0.00704762 0.317460 0.0181773
0.00771259 0.0181773 0.403844
SLD DA I E Sum(tau)
1.47491 0.678008 0.225881 457.319
Thickness (minimum line length at each point, non-zero points only)
Mean Variance Skewness Kurtosis Min Max
0.289726 0.0239509 1.386233.531200.0781250 1.23526
Thickness histogram
bin num norm
0.0686258 365 0.198370
0.205877 560 0.304348
0.343129 591 0.321196
0.480381 215 0.116848
0.617632 69 0.0375000
0.754884 26 0.0141304
0.892136 8 0.00434783
1.02939 1 0.000543478
1.16664 4 0.00217391
1.30389 1 0.000543478
MIL calculations for sample: B4_74_0001
Threshhold range, BV/TV: 48.0000-168.000 0.321767
Uniform Orientations: 513
Vector sampling: Dense
Random Points: 2000
Data orientation (strike, dip, up): -161.000 7.000001
MIL Ellipse Eigenvectors: Trend Plunge
-0.0429151 -0.280531 -0.958885 188.698 73.5132

-0.211585 0.940551 -0.265697 347.322 15.4084
0.976417 0.191483 -0.0997199 78.9046 5.72304
MIL Ellipse Eigenvalues:
0.768162 1.11239 1.61267
MIL Ellipse (H) Eigenvalues:
0.396643 0.329607 0.273749
MIL Ellipse Tensor (M):
1.58872 0.0893917 -0.0628766
0.0893917 1.10365 -0.102150
-0.0628766 -0.102150 0.800861
MIL (H) DA I E Tb.N
1.44893 0.690166 0.169008 1.07099
MIL Fabric Eigenvectors: Trend Plunge
0.00713130 0.267540 0.963520 181.527 74.4764
-0.177434 0.948593 -0.262082 349.405 15.1936
-0.984107 -0.169093 0.0542355 80.2504 3.10899
MIL Fabric Eigenvalues:
0.383730 0.332949 0.283321
MIL Fabric Tensor:
0.284888 -0.00816155 0.00299777
-0.00816155 0.335165 0.0135453
0.00299777 0.0135453 0.379946
MIL (F) DA I E
1.35440 0.738334 0.132334

medial

Star length and volume calcuations for sample: B3A_76_0001
Threshhold range, BV/TV: 64.0000-150.000 0.336567
Uniform Orientations: 513
Vector sampling: Dense
Random Points: 2000
Data orientation (strike, dip, up): -15.0000 180.0000

SVD Eigenvalues:	Eigenvectors		Trend	Plunge
0.387545	0.969952	0.119852	0.211726	262.956 12.2235
0.329023	-0.0367635	-0.788049	0.614514	2.67098 37.9166
0.283433	-0.240501	0.603833	0.759964	158.283 49.4610

SVD Fabric Tensor:

0.381444	0.0134239	0.0203509
0.0134239	0.313241	-0.0194358
0.0203509	-0.0194358	0.305316

SVD DA	I	E	Sum(tau)
1.36733	0.731355	0.151007	149310.

SLD Eigenvalues:	Eigenvectors		Trend	Plunge
0.361939	-0.119294	0.282766	0.951742	157.126 72.1275
0.323091	0.410056	0.887044	-0.212147	24.8098 12.2482
0.314970	-0.904225	0.364959	-0.221769	291.980 12.8129

SLD Fabric Tensor:

0.317004	0.00136951	-0.00603909
0.00136951	0.325116	0.0111119
-0.00603909	0.0111119	0.357880

SLD DA	I	E	Sum(tau)
1.14912	0.870231	0.107331	1090.69

Thickness (minimum line length at each point, non-zero points only)

Mean	Variance	Skewness	Kurtosis	Min	Max
0.418560	0.0971769	1.51296	2.30823	0.0781250	1.92049

Thickness histogram

bin num	norm
0.106694	491 0.296319
0.320082	571 0.344599
0.533469	274 0.165359
0.746857	145 0.0875075
0.960245	90 0.0543150
1.17363	52 0.0313820

1.38702 23 0.0138805
1.60041 5 0.00301750
1.81380 5 0.00301750
2.02718 1 0.000603500
MIL calculations for sample: B3A_76_0001
Threshhold range, BV/TV: 64.0000-150.000 0.336567
Uniform Orientations: 513
Vector sampling: Dense
Random Points: 2000
Data orientation (strike, dip, up): -15.0000 180.0000
MIL Ellipse Eigenvectors: Trend Plunge
-0.173431 0.422799 0.889473 157.697 62.8071
-0.114099 -0.905704 0.408267 7.18021 24.0960
0.978214 -0.0306824 0.205318 271.797 11.8481
MIL Ellipse Eigenvalues:
0.377886 0.633385 0.881936
MIL Ellipse (H) Eigenvalues:
0.412034 0.318258 0.269708
MIL Ellipse Tensor (M):
0.863539 0.0112748 0.0893340
0.0112748 0.587946 -0.0976508
0.0893340 -0.0976508 0.441722
MIL (H) DA I E Tb.N
1.52770 0.654579 0.227592 0.784559
MIL Fabric Eigenvectors: Trend Plunge
-0.178605 0.408205 0.895248 156.369 63.5403
0.0623982 0.912746 -0.403735 3.91084 23.8119
-0.981940 -0.0162474 -0.188492 269.052 10.8648
MIL Fabric Eigenvalues:
0.400005 0.322208 0.277787
MIL Fabric Tensor:
0.281859 -0.00638067 -0.0206612
-0.00638067 0.335160 0.0282944
-0.0206612 0.0282944 0.382981
MIL (F) DA I E
1.43997 0.694460 0.194490

lateral

Star length and volume calcuations for sample: B3A_76_0001
Threshhold range, BV/TV: 56.0000-138.000 0.355667
Uniform Orientations: 513
Vector sampling: Dense
Random Points: 2000
Data orientation (strike, dip, up): -15.0000 180.0000
SVD Eigenvalues: Eigenvectors Trend Plunge

0.751626 0.00659483 0.117408 0.993062 183.215
83.2468
0.182827 0.280374 0.953033 -0.114538 16.3934
6.57696
0.0655474 -0.959868 0.279184 -0.0266331 286.217
1.52614
SVD Fabric Tensor:
0.0747965 0.0318689 0.000726942
0.0318689 0.181526 0.0671904
0.000726942 0.0671904 0.743677
SVD DA I E Sum(tau)
11.4669 0.0872075 0.756758 19614.1
SLD Eigenvalues: Eigenvectors Trend Plunge
0.433452 0.00752923 0.133818 0.990977 183.220
82.2975
0.325419 0.323104 0.937523 -0.129055 19.0158
7.41497
0.241128 -0.946334 0.321160 -0.0361783 288.746
2.07332
SLD Fabric Tensor:
0.249939 0.0257270 -0.00207979
0.0257270 0.318660 0.0153057
-0.00207979 0.0153057 0.431401
SLD DA I E Sum(tau)
1.79760 0.556298 0.249238 571.739
Thickness (minimum line length at each point, non-zero points only)
Mean Variance Skewness Kurtosis Min Max
0.318063 0.0250993 0.790445 0.572086 0.0781250 1.06747
Thickness histogram
bin num norm
0.0593039 97 0.0531507
0.177912 536 0.293699
0.296520 552 0.302466
0.415127 357 0.195616
0.533735 178 0.0975342
0.652343 69 0.0378082
0.770951 29 0.0158904
0.889559 6 0.00328767
1.00817 0 0.000000
1.12677 1 0.000547945
MIL calculations for sample: B3A_76_0001
Threshhold range, BV/TV: 56.0000-138.000 0.355667
Uniform Orientations: 513
Vector sampling: Dense
Random Points: 2000
Data orientation (strike, dip, up): -15.0000 180.0000
MIL Ellipse Eigenvectors: Trend Plunge
-0.0197637 -0.145075 -0.989223 187.758 81.5808

0.171289	0.974297	-0.146308	9.97116	8.41302
0.985023	-0.172335	0.00559400	279.924	0.320514

MIL Ellipse Eigenvalues:

0.639317	1.14075	1.83613

MIL Ellipse (H) Eigenvalues:

0.427589	0.320103	0.252309

MIL Ellipse Tensor (M):

1.81526	-0.119481	-0.00597163
-0.119481	1.15085	-0.0726314
-0.00597163	-0.0726314	0.650088

MIL (H) DA	I	E	Tb.N
1.69470	0.590074	0.251377	1.07745

MIL Fabric Eigenvectors:			Trend	Plunge
-0.00226200	0.136266	0.990670	179.049	82.1671
0.231087	0.963929	-0.132060	13.4814	7.58864
-0.972930	0.228632	-0.0336696	283.224	1.92949

MIL Fabric Eigenvalues:

0.404436	0.326327	0.269237

MIL Fabric Tensor:

0.272286	0.0126751	-0.00204519
0.0126751	0.324793	0.0109838
-0.00204519	0.0109838	0.402921

MIL (F) DA	I	E
1.50216	0.665710	0.193132

lateral

Star length and volume calcuations for sample: B9_74_0001
Threshhold range, BV/TV: 47.0000-156.000 0.295771
Uniform Orientations: 513
Vector sampling: Dense
Random Points: 2000
Data orientation (strike, dip, up): 176.000-5.00000 1

SVD Eigenvalues:	Eigenvectors		Trend	Plunge
0.677107	0.168994	0.0172547	0.985466	264.170
80.2196				
0.169130	0.0174573	0.999637	-0.0204966	1.00049
1.17445				
0.153763	0.985462	-0.0206675	-0.168632	91.2015
9.70827				

SVD Fabric Tensor:

0.168714	0.00179418	0.0871511
0.00179418	0.169274	0.00858406
0.0871511	0.00858406	0.662011

SVD DA	I	E	Sum(tau)
4.40356	0.227089	0.750217	7928.69

SLD Eigenvalues:	Eigenvectors		Trend	Plunge
0.414718	0.161992	0.0142951	0.986688	264.957
80.6409				
0.306632	0.0278906	0.999429	-0.0190587	1.59851
1.09205				
0.278650	0.986398	-0.0306067	-0.161501	91.7773
9.29405				

SLD Fabric Tensor:

0.282243	0.00109514	0.0217337
0.00109514	0.306628	0.00138622
0.0217337	0.00138622	0.411130

SLD DA	I	E	Sum(tau)
1.48831	0.671903	0.260626	460.467

Thickness (minimum line length at each point, non-zero points only)

Mean	Variance	Skewness	Kurtosis	Min	Max
0.294607	0.0209816	1.21340	3.06187	0.0781250	1.23284

Thickness histogram

bin num	norm
0.0684913	319 0.177716
0.205474	496 0.276323
0.342457	682 0.379944
0.479439	207 0.115320
0.616422	61 0.0339833
0.753405	17 0.00947075
0.890387	9 0.00501393

1.02737 2 0.00111421
1.16435 1 0.000557103
1.30134 1 0.000557103
MIL calculations for sample: B9_74_0001
Threshhold range, BV/TV: 47.0000-156.000 0.295771
Uniform Orientations: 513
Vector sampling: Dense
Random Points: 2000
Data orientation (strike, dip, up): 176.000-5.00000 1
MIL Ellipse Eigenvectors: Trend Plunge
-0.0561178 -0.0488790 -0.997227 228.944 85.7321
0.0782510 -0.995944 0.0444127 355.508 2.54550
0.995353 0.0755416 -0.0597150 85.6599 3.42345
MIL Ellipse Eigenvalues:
0.584632 0.911046 1.22939
MIL Ellipse (H) Eigenvalues:
0.401498 0.321629 0.276873
MIL Ellipse Tensor (M):
1.22541 0.0230408 -0.0371883
0.0230408 0.912083 -0.0173466
-0.0371883 -0.0173466 0.587575
MIL (H) DA I E Tb.N
1.45012 0.689599 0.198929 0.946099
MIL Fabric Eigenvectors: Trend Plunge
0.0966987 0.00791487 0.995282 265.321 84.4323
0.0682854 -0.997665 0.00129941 356.084 0.0744506
-0.992969 -0.0678376 0.0970133 86.0917 5.56721
MIL Fabric Eigenvalues:
0.386297 0.327392 0.286311
MIL Fabric Tensor:
0.287438 -0.00272219 0.00962652
-0.00272219 0.327206 0.000734385
0.00962652 0.000734385 0.385356
MIL (F) DA I E
1.34922 0.741169 0.152486

medial

Star length and volume calcuations for sample: B9_74_0001
Threshhold range, BV/TV: 53.0000-144.000 0.295538
Uniform Orientations: 513
Vector sampling: Dense
Random Points: 2000
Data orientation (strike, dip, up): 176.000-5.00000 1
SVD Eigenvalues: Eigenvectors Trend Plunge

0.797810 -0.337485 -0.0346958 0.940691 84.1302
70.1680
0.140953 -0.684474 0.695074 -0.219927 315.440
12.7047
0.0612368 -0.646219 -0.718101 -0.258325 221.984
14.9707
SVD Fabric Tensor:
0.182477 -0.0293009 -0.221839
-0.0293009 0.100636 -0.0362262
-0.221839 -0.0362262 0.716887
SVD DA I E Sum(tau)
13.0283 0.0767560 0.823326 25913.2
SLD Eigenvalues: Eigenvectors Trend Plunge
0.459352 -0.354927 -0.0316667 0.934357 84.9016
69.1246
0.298332 -0.637705 0.739025 -0.217194 319.209
12.5443
0.242316 0.683636 0.672933 0.282494 225.452
16.4091
SLD Fabric Tensor:
0.292437 -0.0239598 -0.0642167
-0.0239598 0.273127 -0.0154128
-0.0642167 -0.0154128 0.434436
SLD DA I E Sum(tau)
1.89567 0.527518 0.350537 568.570
Thickness (minimum line length at each point, non-zero points only)
Mean Variance Skewness Kurtosis Min Max
0.317402 0.0272510 0.855031 0.609804 0.0781250 1.02478
Thickness histogram
bin num norm
0.0569321 55 0.0296017
0.170796 561 0.301938
0.284661 548 0.294941
0.398525 320 0.172228
0.512389 228 0.122713
0.626253 89 0.0479010
0.740118 39 0.0209903
0.853982 11 0.00592034
0.967846 6 0.00322928
1.08171 1 0.000538213
MIL calculations for sample: B9_74_0001
Threshhold range, BV/TV: 53.0000-144.000 0.295538
Uniform Orientations: 513
Vector sampling: Dense
Random Points: 2000
Data orientation (strike, dip, up): 176.000-5.00000 1
MIL Ellipse Eigenvectors: Trend Plunge
0.277290 0.0816223 -0.957313 73.5979 73.1987

-0.457875 0.887188 -0.0569824 332.702 3.26662
-0.844666 -0.454130 -0.283382 241.736 16.4621
MIL Ellipse Eigenvalues:
0.350941 1.05100 1.33852
MIL Ellipse (H) Eigenvalues:
0.478494 0.276498 0.245008
MIL Ellipse Tensor (M):
1.20231 0.0944442 0.254655
0.0944442 1.10564 0.0917029
0.254655 0.0917029 0.432522
MIL (H) DA I E Tb.N
1.95297 0.512040 0.422150 0.927839
MIL Fabric Eigenvectors: Trend Plunge
-0.286355 -0.0739325 0.955267 75.5232 72.7978
0.476434 -0.876004 0.0750197 331.460 4.30236
-0.831271 -0.476604 -0.286072 240.172 16.6229
MIL Fabric Eigenvalues:
0.429768 0.298902 0.271330
MIL Fabric Tensor:
0.290580 -0.00815314 -0.0423543
-0.00815314 0.293354 -0.0130016
-0.0423543 -0.0130016 0.416065
MIL (F) DA I E
1.58393 0.631342 0.304503